LCH Laboratoire de Constructions Hydrauliques
Laboratory of Hydraulic Constructions

ÉCOLE POLYTECHNIQUE
FÉDÉRALE DE LAUSANNE

Communication 34

Interaction of side weir overflow with bed-load transport and bed morphology in a channel

Burkhard Rosier

Editeur : Prof. Dr A. Schleiss

Lausanne, 2007

Communications du Laboratoire de Constructions Hydrauliques ISSN 1661-1179
Ecole Polytechnique Fédérale de Lausanne
Editeur: Prof. Dr A. Schleiss

Preface

River training works on rivers can protect the flood plains up to a certain flood level called design flood. For higher discharges occurring during extreme events, the residual risk has to be managed by secondary protection measures. One possibility is to inundate, in a controlled way, zones which are less vulnerable and where damage remains moderate. This can be attained by overtopable river dykes or fuse plugs (erodible dykes), which can divert a part of the flow laterally in order to force controlled flooding of certain zones in the flood plain.

A side overflow from a river will reduce its sediment transport capacity and consequently sediment will deposit near the side weir. Such deposits or bed aggradation can increase the side overflow in a non-controlled way. In his research work, Dr. Burkhard Rosier studied for the first time systematically the interaction of a side weir overflow with bed-load transport and bed morphology in a channel. Based on the analysis of numerous experiments carried out in a laboratory flume, he was able to develop empirical models, which can predict the change of the bed morphology in the vicinity of the side weir and its effect on the side overflow. In order to analyse the experiments, new methods of data acquisition had to be developed based on a digital photogrammetry survey. Assuming a Maxwell distribution function of the shape of the local deposits in the longitudinal direction of the channel, an empirical relationship for the prediction of the mean bed aggradation in the vicinity of the side weir could be developed.

Knowing this $1D$-bed aggradation, the increase of the lateral side overflow can be determined. Since the deposits are not uniformly distributed over the channel width, an empirical relationship for the prediction of the $2D$ shape of the deposits in transverse direction has also been developed. In addition, an empirical relationship was found, which allows a direct estimation of the side overflow considering the interaction with local deposits. For engineering practice, these empirical relationships for the prediction of the deposits near a side weir are useful tools to rapidly estimate their effect on the side overflow without modelling the complex full interaction.

We would like to thank Prof. Yves Zech, Université Catholique de Louvain, Belgium, for his support and guidance as academic guest at the LCH-EPFL as well as Prof. Gerhard Jirka, Technical University

of Karlsruhe, Germany, Dr. Gian Reto Bezzola, Federal Office for the Environment, Switzerland, and Prof. Christophe Ancey, Environmental Hydraulics Laboratory, Switzerland, for their valuable comments as members of the thesis jury. We also gratefully thank the Swiss Innovation Promotion Agency (CTI) for the sustained funding in the framework of the research project DIFUSE and the Swiss Federal Office for Water and Geology (now Federal Office for the Environment) for its financial support.

Prof. Dr. Anton Schleiss

Das Schauspiel der Natur
ist immer schön

Aristoteles

Table of Contents

Abstract

Interaction of side weir overflow with bed-load transport and bed morphology in a channel

Side weirs, also known as a lateral weirs, and overflow dams are free overflow regulation and diversion devices commonly encountered in hydraulic engineering. They are set into the side of a channel or river allowing to spill a part of the discharge over their crest when the surface of the flow in the main-channel exceeds a certain level.

The lateral loss of water is reducing the sediment transport capacity in the main-channel yielding to aggradation and the formation of a local sediment deposit in the downstream weir alignment. The reduced cross section generates backwater effects and additional contraction and expansion losses. As a consequence, the head over the side weir rises and the side overflow discharge as well. The design discharge to be diverted over the weir is increased by this flow-sediment transport interaction.

Since the interaction of side overflow with bed-load and bed morphology in a channel has not been studied so far, systematic tests have been performed.

Three test series and one reference experiment without side weir have been carried out in a 20.00 m long, 1.50 m wide and 1.20 m high rectangular flume. The first test series consisted of a 3.00 m long side weir, the second one had a 6.00 m long weir and the third series was characterised by two weirs of 2.50 m length each. The approach discharge varied between $0.098\ m^3/s \leq Q_1 \leq 0.222\ m^3/s$. The overall flow regime has been subcritical. The average initial bottom slope was 0.21 %. The mobile bed was characterized by a median particle size of $d_{50} = 0.72\ mm$. During the experiments the water surface, the $2D$-velocity field, the side overflow discharge and sediment supply were measured. The final bed morphology has been recorded by means of digital photogrammetry.

Based on the systematic experimental flume study a one- and a two-dimensional empirical model for the prediction of the mobile bed evolution near the side weir have been developed. The models allow a simple and straightforward estimation of the interaction of a side overflow with bed-load transport and bed morphology in engineering practice.

The $1D$-model represents the overall mobile bed evolution in the weir reach. The model takes into account a deposit being uniform over the channel width. The height of the deposit only varies in longitudinal direction. In

addition to the $1D$-approach the $2D$-model incorporates the variation of the deposit over the channel width.

For the parameterisation of the two models a Maxwell-type distribution function is applied. Input parameters for both models such as the location and height of the maximum bed elevation and a shape factor are expressed in terms of non-dimensional geometric channel and side weir variables as well as hydraulic parameters and bed load transport relations. For the $2D$-approach an additional relationship considering the spanwise variation is developed.

To implement the models in numerical flow simulations expressions for the location of the empirical deposit relative to the side weir are established.

Regarding the impact of the deposit on the intensity of side overflow it has been found out that the spilled discharge might increase by a factor of up to ≈ 3 compared to fixed plane bed conditions. In this context about 25 % of the total increase are attributed to effects of form roughness and about 75 % to bed aggradation phenomena. In this regard the height of the deposit represents the most important parameter. The location of the deposit with respect to the position of the side weir has a smaller influence, whereas the downstream shape of the deposit is of minor importance.

To test the prediction accuracy of the models they have been implemented into $1D$-flow calculations. The predicted side overflow was about 85 % for the $1D$-model and about 91 % for the $2D$-model. The difference is mainly caused due to the implementation of the spanwise variation in the $2D$-model.

Besides the two models a simple relationship for direct estimation of side overflow discharge in presence of bed-load transport has been established.

The empirical models have been applied in a case study on the Rhone river upstream of Lake Geneva in Switzerland. In the case of a flat bed without deposit a protection for a flood event with a hundred year return period persists. Taking into account the mobile bed evolution a protection even for an extreme flood might be obtained. This presumes a sufficiently large storage volume of the retention bassin.

The skewed deposit induces the formation of an oscillatory erosion gutter downstream of the weir. For the description of the sine-generated evolution of the thalweg indicative expressions are proposed.

In order to test the capability of a numerical tool to reproduce the bed aggradation phenomena observed in the experiments, $1D$-numerical simulations with bed-load transport have been performed (DUPIRO). From these computations it can be concluded that the most experimental phenomena are captured with reasonable accuracy.

Keywords: Side overflow, side weir, lateral outflow, bed-load transport capacity, bed morphology, deposition, aggradation, local sedimentary deposit, flume experiments, empirical model, Maxwell distribution function.

Résumé

Interaction d'un déversoir latéral avec le transport solide par charriage et la morphologie du lit dans un canal

Les déversoirs latéraux et les digues submersibles sont des dispositifs couramment utilisés pour régler le niveau d'eau d'une rivière ou d'un canal pour en dévier une partie du débit. Ils sont habituellement placés dans la digue latérale. Ils déchargent une partie du débit du cours principal quand la surface d'eau dans ce dernier atteint le niveau de leur crête.

La réduction du débit dans le canal principal conduit à une diminution de la capacité de transport solide (charriage) de ce dernier. Il se forme une surélévation du lit par un dépôt sédimentaire local situé à l'extrémité aval du déversoir. La section transversale réduite produit des effets de remous et des pertes locales d'énergie liées à des effets de contraction et d'expansion. En conséquence, la charge augmente sur le déversoir latéral. Le débit de dimensionnement est majoré par cette interaction avec le transport solide.

L'effet entre le déversement latéral, le transport solide par charriage et la morphologie du lit dans un canal n'a jamais été étudiée jusqu'ici. Des essais systématiques sont donc réalisés pour quantifier cette interaction.

Quatre séries d'essais dont une de référence sans déversoir latéral sont effectuées dans un canal rectangulaire d'une longueur de 20.00 m, d'une largeur de 1.50 m et d'une hauteur de 1.20 m. La première série porte sur un déversoir latéral de 3.00 m de long et la seconde série sur un déversoir de 6.00 m. La troisième série étudie une géométrie caractérisée par deux déversoirs d'une longueur de 2.50 m chacun. Le débit d'approche varie entre $0.098\ m^3/s \leq Q_1 \leq 0.222\ m^3/s$. Le régime global d'écoulement est fluvial. La pente initiale moyenne vaut 0.21 %. Le lit mobile est caractérisé par une granulométrie $d_{50} = 0.72\ mm$. Les résultats enregistrent le niveau d'eau, le champ de vitesse $2D$, le débit latéral déversé et l'apport des sédiments. La morphologie finale du lit est mesurée par photogrammétrie digitale.

Sur la base des résultats expérimentaux, deux modèles empiriques ($1D$ et $2D$) de prévision de l'évolution du lit mobile près du déversoir latéral sont développés. Ces modèles permettent une évaluation simple et directe de la morphologie de lit et de l'interaction du débordement latéral avec le transport solide par charriage. Ces modèles sont facilement applicables par les ingénieurs praticiens.

Le modèle $1D$ représente l'évolution longitudinale du lit mobile dans la région du déversoir. Le modèle $2D$ permet une variation supplémentaire du

dépôt dans le sens transversal du canal.

Une distribution de Maxwell est appliquée pour paramétrer les deux modèles. Les paramètres d'entrée, (position et hauteur maximale du dépôt, facteur de forme) sont exprimés de manière adimensionnelle en fonction de la géométrie du canal et du déversoir ainsi que des paramètres hydrauliques et des relations de transport solide. Pour l'approche $2D$, un rapport additionnel est développé pour considérer la variation transversale du dépôt.

Pour l'implantation des modèles dans une modélisation numérique, des expressions algébriques sont établies pour le positionnement du dépôt.

La déposition au pied du déversoir latéral a généré une augmentation du débit déversé jusqu'à un facteur ≈ 3 par rapport à un lit plat et fixe. Dans le contexte de l'étude expérimentale, environ 25 % de l'augmentation du débit déversé est attribuée aux effets de rugosité de forme et environ 75 % est lié aux phénomènes d'alluvionnement. À cet égard, la hauteur du dépôt représente le paramètre le plus important. L'emplacement du dépôt par rapport à la position du déversoir latéral a une influence plus faible. La forme aval du dépôt n'a qu'une importance mineure.

La capacité des modèles empiriques est examinée à l'aide d'un modèle numérique de simulation $1D$. Les résultats numériques reproduisent les mesures à hauteur de ≈ 85 % pour le modèle empirique $1D$ et de ≈ 91 % pour le modèle empirique $2D$. La différence est principalement liée à la variation latérale possible dans le modèle $2D$.

De plus, une formule simple est établie pour estimer directement le débit déversé en présence d'un lit mobile.

Enfin, les modèles empiriques sont appliqués pour une étude de cas sur le Rhône suisse alpin supérieur à l'amont du Lac Léman. Dans le cas d'un lit plat sans dépôt, la protection est assurée pour une crue centennale. Avec l'impact d'un lit mobile, la protection augmente au niveau d'une crue extrême. Ceci implique un volume suffisant de la zone de retention.

Le dépôt transversal, biaisé par rapport à l'axe de l'écoulement principal, induit la formation d'une gouttière oscillante d'érosion à l'aval du déversoir. Pour la description de cette évolution sinusoïdale du thalweg, des expressions indicatives sont développées.

Afin d'examiner les possibilités d'un outil numérique pour reproduire les phénomènes d'alluvionnement du lit observés dans les expériences, des simulations numériques $1D$ avec transport solide par charriage sont effectuées (DUPIRO). Ces calculs reproduisent les principaux phénomènes expérimentaux de manière raisonnable.

Mots-clés: Déversoir latéral, charriage, morphologie du lit, alluvionnement, dépôt sédimentaire, modélisation physique, modèle empirique, distribution de Maxwell.

Zusammenfassung

Wechselwirkung eines seitlichen Überfalls mit dem Geschiebetransport und der Sohlenmorphologie in einem Gerinne

Die gezielte und kontrollierte Überflutung von Hochwasserrückhalteräumen mittels seitlicher Notentlastungen wie Streichwehren oder überströmbarer Dämme stellt ein effektives und weit verbreitetes Konzept zur Gefahrenabwehr im Hochwasserfall dar.

Der reduzierte Abfluss im Hauptgewässer bewirkt eine Verringerung der Geschiebetransportkapazität, was zu Sedimentablagerungen unterstrom des Entlastungsbauwerkes und der Entstehung eines lokalen Sedimentdepots führen kann. Die hierdurch hervorgerufene Querschnittsreduktion führt durch Verengungs- und Erweiterungseffekte zu lokalen Energieverlusten und somit zu einem Rückstau. In Verbindung mit der Bildung von Transportkörpern resultiert diese Wechselwirkung zwischen Strömung und alluvialer Flusssohle in einem unkontrollierten Anstieg der seitlichen Überfallintensität.

Die heute gängigen Bemessungskonzepte erfassen in der Regel nur hydrologische und hydraulische Aspekte, der Einfluss der Sohlenmorphologie bleibt weitgehend unberücksichtigt. Aus diesem Grund sind systematische hydraulische Modellversuche durchgeführt worden.

Insgesamt wurden drei Versuchsreihen sowie ein Referenzversuch ohne seitlichen Überfall durchgeführt. Der rechteckige Versuchskanal war 20.00 m lang, 1.50 m breit und 1.20 m hoch. Die erste Versuchsserie bestand aus einem 3.00 m langen, die zweite aus einem 6.00 m langen und die dritte aus zwei 2.50 m langen Wehren. Die Durchflüsse im strömenden Abflussregime variierten zwischen $0.098\ m^3/s \leq Q_1 \leq 0.222\ m^3/s$. Die mittlere Initialsohlenneigung betrug 0.21 %. Das Sohlenmaterial hatte einen mittleren Korndurchmesser von $d_{50} = 0.72\ mm$. Während der Experimente wurden die Wasserspiegellage, das $2D$-Strömungsfeld, die seitliche Überfallmenge sowie die Geschiebezugaberaten gemessen. Die Sohlenmorphologie am Ende jedes Versuches wurde mittels digitaler Photogrammetrie erfasst.

Basierend auf den physikalischen Modellversuchen ist ein ein- und ein zweidimensionales empirisches Modell zur Beschreibung der Sohlenentwicklung im Bereich des seitlichen Überfalls entwickelt worden. Dies erlaubt Ingenieuren aus der Praxis, den Effekt der Interaktion zwischen Strömung und beweglicher Sohle auf einfache Art und Weise abzuschätzen.

Der eindimensionale Ansatz ermöglicht die Vorhersage der Sohlenentwicklung in Längsrichtung. Im Gegensatz hierzu wird im zweidimensionalen Modell zusätzlich die Variation der lokalen Auflandung in Gerinnequerrichtung berücksichtigt.

Die Form des aufgelandeten Gerinneabschnitts kann mit einer Maxwell Verteilungsfunktion beschrieben werden. Eingangsparameter wie Lage und Höhe der maximalen Auflandung sowie ein Formfaktor werden mittels dimensionsloser hydraulischer und sedimentologischer Kenngrössen sowie Gerinne- und Wehrgeometrie erfassst. Für den $2D$-Ansatz wurde zusätzlich eine Beziehung zur Beschreibung der Breitenvariation entwickelt.

Für die Anwendung der Modelle in numerischen Strömungssimulationen sind geeignete Transferfunktionen aufgestellt worden.

Auf Grund der beweglichen Sohle kann die seitliche Überfallmenge bis zu etwa drei mal höher ausfallen als für eine unbewegliche glatte Sohle. In diesem Zusammenhang können ungefähr 25 % des Anstiegs auf Formrauheitseffekte und etwa 75 % auf Auflandungseffekte zurückgeführt werden. Hierbei spielen die Höhe und die Lage des Depots bzgl. des Wehres eine bedeutende Rolle. Die unterstromige Form des Depots ist von geringerer Bedeutung.

Um die Vorhersagequalität der Modelle zu untersuchen, sind die Modelle in $1D$-Strömungsprogramme implementiert worden. Für den $1D$-Ansatz sind ≈ 85 %, für den $2D$-Ansatz ≈ 91 % der seitlichen Überfallmenge berechnet worden. Die höhere Genauigkeit des $2D$-Modells basiert im wesentlichen auf der Berücksichtigung der Breitenvariation des Depots.

Neben den beiden Modellen ist ein einfacher Ansatz zur direkten Abschätzung der seitlichen Überfallmenge unter Berücksichtigung von Geschiebetransportprozessen entwickelt worden.

In einer Fallstudie an der Rhone oberhalb des Genfer Sees in der Schweiz konnte gezeigt werden, dass unter Berücksichtigung einer beweglichen Sohle ein Hochwasserschutz für ein Extremereignis möglich ist. In diesem Zusammenhang wird ein ausreichendes Retentionsvolumen vorausgesetzt. Im Fall einer ebenen Sohle ohne lokale Auflandung reicht der Schutzgrad hingegen lediglich bis zu einem hundertjährlichen Ereignis.

Das lokale Sedimentdepot induziert die Bildung einer oszillierenden Erosionsrinne unterhalb des Wehres. Zur Beschreibung dieser sinusförmigen Talwegentwicklung sind überschlägige Beziehungen aufgestellt worden.

$1D$-numerische Berechnungen mit Sedimenttransport (DUPIRO) haben gezeigt, dass die wesentlichen im Experiment beobachteten Phänomene mit zufriedenstellender Genauigkeit wiedergegeben werden.

Stichworte: Seitlicher Überfall, Streichwehr, Geschiebetransportkapazität, Sohlenmorphologie, Auflandung, lokales Sedimentdepot, Laborversuche, empirisches Modell, Maxwell Verteilungsfunktion.

Notations

Roman Symbols

A	flow area $[m^2]$
a_0	amplitude of longitudinal evolution of minimum / maximum bed elevation $[-]$
B	channel width $[m]$
b_0	parameter occurring in Equation 5.35 $[-]$
B_s	empirical roughness function depending on the particle or roughness Reynolds number Re^* (Yalin and da Silva (2001)) $[-]$
C	overall Chézy resistance coefficient $[m^{1/2}/s]$
c	$= v/u_*$, total dimensionless Chézy resistance factor (appearing e. g. in the Smart and Jäggi (1983) formula, Eq. A.138) $[-]$
c^*	maximum bed-load concentration $= 0.65$ $[ppm]$
C''	Chézy resistance coefficient associated with form drag (e. g. bed forms) only $[m^{1/2}/s]$
c''	$= c_\Delta$, dimensionless Chézy factor associated with form drag (e. g. bed forms) only, bed form component of c $[-]$
C'	Chézy resistance coefficient associated with grain or skin friction only $[m^{1/2}/s]$
c'	$= c_f$, dimensionless Chézy friction factor associated with grain or skin friction only, pure friction component of c $[-]$
c_0	longitudinal shift in x-direction $[-]$
c_b	bed-load concentration $[ppm]$
C_D	$= C_M$, side weir discharge coefficient, De Marchi coefficient of discharge $[-]$
C_Q	discharge coefficient for a sharp-crested weir $[-]$
cp	coupling point $[-]$

d	particle or grain diameter $[m]$
D_*	dimensionless particle parameter $[-]$
d_f	median fall diameter in Fig. A.3 ($d_f \approx d_{50}$) $[m]$
d_g	geometric mean size $[m]$
d_i	particle or grain diameter for which i % of the sediment is finer by weight $[m]$
d_s	sphere diameter $[m]$
E	specific energy ($y + v^2/2g$) $[m]$
f	overall Darcy-Weisbach resistance coefficient for a composite channel cross section $[-]$
f''	Darcy-Weisbach resistance coefficient associated with form drag (e. g. bed forms) only $[-]$
f'	Darcy-Weisbach resistance coefficient associated with grain or skin friction only $[-]$
f_b	Darcy-Weisbach resistance coefficient for the bed region $[-]$
f_w	Darcy-Weisbach resistance coefficient for the wall region $[-]$
Fr	flow Froude number $[-]$
Fr^*	$= \tau^* = \theta$, Shields factor, particle mobility parameter, dimensionless shear stress $[-]$
Fr_D	weir Froude number composed of side overflow discharge (Q_D) and weir crest length (L_D) $[-]$
Fr_d^*	densimetric Froude number of the particle $[-]$
Fr_p^*	particle Froude number occurring in the approach of Karim (1999), paragraph A.3.1 $[-]$
Fr_t	flow Froude number for beginning of transition regime according to Karim (1999), paragraph A.3.1 $[-]$
Fr_u	flow Froude number for beginning of upper regime according to Karim (1999), paragraph A.3.1 $[-]$
g	acceleration due to gravity $[m/s^2]$
H	total energy head ($z + y + v^2/2g$) $[m]$
h	pressure head (without velocity head) ($h = z + y$) $[m]$
h_D	pressure head (without velocity head) above side weir crest ($h_D = y - w_D$) $[m]$
h_Q	pressure head (without velocity head) above sharp-crested measuring weir ($h_Q = y - w_Q$) $[m]$

K	$= K_0\ g^{1/2}$, empirical roughness parameter related to gradation, shape and distribution of bed material, bed forms and flow conditions $[m^{1/2}/s]$
k	geometric roughness height $[m]$
K_0	dimensionless empirical roughness factor related to gradation, shape and distribution of bed material, bed forms and flow conditions $[-]$
K_c	pier contraction coefficient $[-]$
k_s	Nikuradse equivalent sand grain roughness $[m]$
k_s''	overall form roughness (ripples and dunes) $[m]$
$k_{s,d}''$	form roughness related to asymmetrical dunes $[m]$
$k_{s,r}''$	form roughness related to ripples $[m]$
$k_{st,b}$	Strickler resistance coefficient for the bed region $[m^{1/3}/s]$
$k_{st,b}'$	Strickler resistance coefficient for the bed region associated with grain or skin friction only $[m^{1/3}/s]$
$k_{st,b}''$	Strickler resistance coefficient for the bed region associated with form drag (e. g. bed forms) only $[m^{1/3}/s]$
$k_{st,eq}$	equivalent Strickler resistance coefficient for a composite channel cross section $[m^{1/3}/s]$
$k_{st,w}$	Strickler resistance coefficient for the wall region $[m^{1/3}/s]$
k_{st}	overall Strickler resistance coefficient for a composite channel cross section $[m^{1/3}/s]$
k_{st}'	Strickler resistance coefficient associated with grain or skin friction only $[m^{1/3}/s]$
k_{st}''	Strickler resistance coefficient associated with form drag (e. g. bed forms) only $[m^{1/3}/s]$
L	length (e. g. channel length) $[m]$
L_0	clear span of a gate bay or weir field between piers $[m]$
L_D	side weir crest length $[m]$
L_Q	crest length of a sharp-crested measuring weir $[m]$
$L_{D,tot}$	total side weir crest length, here $L_{D,tot} = L_{D1} + L_{D2}$ $[m]$
L_{D1}	side weir crest length for weir 1 $[m]$
L_{D2}	side weir crest length for weir 2 $[m]$
L_{eff}	effective length of e. g. a spillway or weir crest $[m]$

M $= w_D/E$, relative weir height according to Hager (1987b) [−]

m slope of the channel or river bank in the numerical model DUPIRO [−]

N $= y/E$, relative flow depth according to Hager (1987b) [−]

n overall Manning's resistance coefficient for a composite channel cross section $[s/m^{1/3}]$

n' Manning's resistance coefficient associated with grain or skin friction only $[s/m^{1/3}]$

n'' Manning's resistance coefficient associated with form drag (e. g. bed forms) only $[s/m^{1/3}]$

N^* dimensionless number to predict ripple-bed configuration according to Karim (1999), paragraph A.3.1 [−]

n^* shape factor of the Maxwell-type distribution function [−]

n_b Manning resistance coefficient for the bed region $[s/m^{1/3}]$

n_c number of side contractions [−]

n_D number of side weirs [−]

n_w Manning's resistance coefficient for the wall region $[s/m^{1/3}]$

p porosity [−]

Q volume fluid discharge $[m^3/s]$

q volume fluid discharge per unit width $[m^3/s/m]$

Q_D volume fluid discharge over a weir $[m^3/s]$

q_D volume fluid discharge per unit length over a side weir $[m^3/s/m]$

Q_r reduced volume fluid discharge accounting for wall roughness in the Meyer-Peter and Müller (1948) formula (Eq. A.127) $[m^3/s]$

q_r reduced volume fluid discharge per unit width accounting for wall roughness in the Smart and Jäggi (1983) formula (Eq. A.136) $[m^3/s]$

q_s volumetric solid discharge (total load) per unit width $[m^3/s/m]$

q_{cr} critical volume fluid discharge per unit width for incipient motion $[m^3/s/m]$

$Q_{D,tot}$ total volume fluid discharge over a weir, here $Q_{D,tot} = Q_{D1} + Q_{D2}$ $[m^3/s]$

Q_{D1} total volume fluid discharge over weir 1 $[m^3/s]$

Q_{D2} total volume fluid discharge over weir 2 $[m^3/s]$

$Q_{s,D}$ solid discharge (total load) per unit weight over a side weir $[kg/min]$

$q_{s,top}$	volumetric solid discharge (total load) per unit width at the top of a bed form (dune) according to Fredsøe (1982) $[m^3/s/m]$
Q_{sb}	solid discharge (bed-load) per unit weight $[kg/min]$
q_{sb}	volumetric solid discharge (bed-load) per unit width $[m^3/s/m]$
Q_{ss}	solid discharge (suspended load) per unit weight $[kg/min]$
q_{ss}	volumetric solid discharge (suspended load) per unit width $[m^3/s/m]$
q_{sw}	volumetric solid discharge (wash load) per unit width $[m^3/s/m]$
Q_s	solid discharge (total load) per unit weight $[kg/min]$
R_b	hydraulic radius related to the bed $[m]$
R_h	hydraulic radius $[m]$
Re	flow Reynolds number $[-]$
Re^*	particle or grain size Reynolds number ($Re^* = u^* \cdot d/\nu$) $[-]$
Re^*	roughness Reynolds number according to Yalin and da Silva (2001) ($Re^* = u^* \cdot k_s/\nu$) $[-]$
S	slope $[-]$
s	$= \rho_s/\rho$, specific or relative density $[-]$
S_0	bottom slope $[-]$
S_e	energy slope $[-]$
S_f	friction slope $[-]$
S_f''	friction slope associated with form drag (e. g. bed forms) only $[-]$
S_f'	friction slope associated with grain or skin friction only $[-]$
S_w	slope of water level $[-]$
$stdev$	standard deviation $[variable]$
T	dimensionless bed shear stress parameter, transport stage parameter $[-]$
t	time, duration of experiment $[min]$
T_b	duration of development of a bed form $[min]$
t_{stab}	stabilisation time of side overflow discharge (Q_D) $[min]$
U	wetted perimeter $[m]$
u	flow velocity $[m/s]$
u_*	bed shear velocity $[m/s]$
u_*'	bed shear velocity associated with grain or skin friction only $[m/s]$

U_b	wetted perimeter related to the bed $[m]$
u_b	mean bed form (dune) migration velocity $[m/s]$
u_D	velocity component of the spill flow $[m/s]$
u_p	particle velocity according to Van Rijn (1984a) $[m/s]$
U_w	wetted perimeter related to the wall $[m]$
$u_{*,cr}$	critical bed shear velocity according to Shields $[m/s]$
V	total volume ($V = V_p + V_s$) $[m^3]$
v	mean flow velocity $[m/s]$
V_p	volume of porosity $[m^3]$
V_s	volume of sediments $[m^3]$
v_x	flow velocity in longitudinal direction (direction of channel axis) $[m/s]$
v_y	flow velocity perpendicular to channel axis) $[m/s]$
$v_{y,b}$	transverse velocity near the bed $[m/s]$
$v_{y,s}$	transverse velocity near the surface $[m/s]$
w_D	side weir crest height $[m]$
w_Q	crest height of a sharp-crested measuring weir $[m]$
w_s	particle fall velocity $[m/s]$
X	$= Re^*$, particle or grain size Reynolds number used by Yalin and da Silva (2001) ($X = Re^* = u^* \cdot d/\nu$) $[-]$
x	direction of rectilinear flow, channel distance $[m]$
x^*	location of deposition height of the extracted deposit $[m]$
X^*	dimensionless parameter of the Maxwell-type distribution function $[-]$
x_a	upstream deposition length until maximum elevation $[m]$
x_b	downstream deposition length from maximum elevation $[m]$
x_{ϕ_D}	streamwise location of lateral outflow angle (ϕ_D) $[m]$
x_{cp}	horizontal coordinate of the coupling point $[m]$
x_{dep}	total deposition length $[m]$
Y	$= \theta$, mobility number, Shields factor, particle mobility parameter, dimensionless shear stress according to Yalin and da Silva (2001) $[-]$
y	flow depth $[m]$

y''	flow depth associated with with form drag (e. g. bed forms) only $[m]$
y'	flow depth associated with grain or skin friction only $[m]$
y_B	lateralwise position along channel width $[m]$
y_m	flow mixture depth of clear water and sediments in the Smart and Jäggi (1983) formula (Eq. A.139) $[m]$
Z	$= y/d$, relative depth, dimensionless flow depth according to Yalin and da Silva (2001) $[-]$
z	direction vertically perpendicular to x $[m]$
z^*	deposition height of the extracted deposit $[m]$
Z^*	dimensionless parameter of the Maxwell-type distribution function $[-]$

Greek Symbols

α	kinetic energy correction coefficient $[-]$
α_0	exponent in the Meyer-Peter and Müller (1948) formula = 1.5 $[-]$
α_d	dune stoss slope angle $[°]$
α_s	coefficient to determine the Nikuradse equivalent sand grain roughness (k_s) from different sediment sizes (d_i) $[-]$
α_{sc}	portion of transverse flow with respect to main flow, strength of secondary circulation $[-]$
β_d	dune lee slope angle $[°]$
β_{SF}	bed form shape factor according to Führböter (1967)$[-]$
Δ	bed form height $[m]$
δ	bed form steepness $[-]$
Δx^*	longitudinal displacement between deposit on left and right channel bank $[m]$
δ_b	saltation height $[m]$
Δ_d	dune height $[m]$
δ_d	dune steepness $[-]$
Δ_r	ripple height $[m]$
δ_r	ripple steepness $[-]$
η^*	relative flow intensity according to Yalin and da Silva (2001) ($\eta^* = Y/Y_{cr} = \theta/\theta_{cr}$) $[-]$

γ_d	dune shape factor according to Van Rijn (1984) ($\gamma_d = 0.7$ for field conditions) [−]
γ_r	ripple presence factor according to Van Rijn (1984) ($\gamma_r = 1.0$ for ripples alone, $\gamma_r = 0.7$ for ripples superimposed on dunes) [−]
γ_s	specific weight of grains in fluid ($\gamma_s = (\rho_s - \rho) \cdot g \approx 16186.5$) $[N/m^3]$
κ	$= 0.4$, constant of von Karman [−]
Λ	bed form length $[m]$
Λ_d	dune length $[m]$
λ_L	geometric length scale model factor [−]
Λ_r	ripple length $[m]$
Λ_{dep}	wavelength of longitudinal evolution of maximum bed elevation $[m]$
Λ_{ero}	wavelength of longitudinal evolution of minimum bed elevation (erosion gutter, thalweg) $[m]$
ν	kinematic viscosity coefficient of fluid $[m^2/s]$
ω	periodic variation of the cross sectional averaged longitudinal bed surface $[m]$
ω^*	window length of the moving average procedure $[m]$
ω_p	$= 2\pi/b_0$, periodicity [−]
Φ	Einstein factor, intensity of bed-load discharge, bed-load transport rate [−]
ϕ	varied flow function according to De Marchi (1934) [−]
ϕ^*	longitudinal displacement angle between deposit on left and right channel bank [°]
ϕ^*_{dep}	deflection angle of longitudinal evolution of maximum bed elevation [°]
ϕ^*_{ero}	deflection angle of longitudinal evolution of minimum bed elevation (erosion gutter, thalweg) [°]
ϕ_D	lateral outflow angle, deflection angle [°]
ϕ_n	natural angle of repose [°]
ϕ_r	angle of repose [°]
ϕ_t	torsion angle between channel axis velocity (v_x) and transverse velocity (v_y) [°]
$\phi_{z,LB}$	angle between maximum heights of deposits on right and left channel bank (transverse slope of deposit) [°]
ρ	density of fluid $[kg/m^3]$

ρ_s	density of sediment $[kg/m^3]$
σ_d	geometric standard deviation $[-]$
σ_g	geometric sorting coefficient $[-]$
τ	shear stress $[N/m^2]$
τ^*	$= Fr^* = \theta$, Shields factor, particle mobility parameter, dimensionless shear stress $[-]$
τ_0	overall bottom or bed shear stress $[N/m^2]$
τ_0''	bottom or bed shear stress associated with form drag (e. g. bed forms) only $[N/m^2]$
τ_0'	bottom or bed shear stress associated with grain or skin friction only $[N/m^2]$
τ_b	bottom or bed shear stress corrected with a side wall correction procedure $[N/m^2]$
τ_g	transport term in the Meyer-Peter and Müller (1948) formula (Eq. A.127) $[N/m^2]$
θ	$= Fr^* = \tau^*$, Shields factor, particle mobility parameter, dimensionless shear stress $[-]$
θ_0	bottom angle $[°]$
ϑ	sidewall correction coefficient $[-]$
Ξ^3	material number according to Yalin and da Silva (2001) ($\Xi^3 = X^2/Y = \gamma_s \cdot d^3/(\rho \cdot \nu^2)$) $[-]$

Subscripts

$1, 2$	suffixes, designating the beginning and end of a side weir (Fig. A.15, a)
cr	critical
ero, dep	erosion and deposition
ini, fin	initial and final condition
LB, RB	left and right channel bank
min, max	minimum and maximum value

1. Introduction

1.1. Context

Side overflows are free overflow regulation and diversion devices commonly encountered in hydraulic engineering. They are set into the side of a channel, river or dam allowing to spill a part of the discharge over their crest when the surface of the flow in the main-channel or reservoir exceeds a certain level.

Lateral overflow devices find their use in the following domains:

- Urban drainage systems (combined sewer overflow - CSO),
- Irrigation engineering (distribution channels),
- Lateral intakes (power stations),
- River bifurcations (flow diversion),
- River restoration (ecological floodings),
- Side overflow spillways at dams and
- Flood control management (peak flow reduction using retention bassins or flood plains, prevention of dyke overtopping at unforeseen locations, residual risk).

In the context of flood control management different overflow types and concepts exist:

- Fixed side weir,
- Overflow dams,
- Erodible dams (fuse plugs),
- Fixed side weir and fuse plug,
- Sluice gates,
- Tilting or overturning fuse gates and
- Syphons.

In river engineering usually mobile bed conditions are present and significant morphological bed changes might be induced by the side overflow device. Commonly, the lateral loss of water takes place on a rather short stretch. Consequently, the main-channel discharge and thus the bottom shear stress and the sediment transport capacity in the main-channel are suddenly reduced. As a result aggradation and the formation of a local sediment deposit near the weir or dam alignment can occur (Fig. 1.1). The increase of the mean bed elevation generates backwater effects. In addition, the local sedimentary deposit induces both, horizontal and vertical energy losses through contraction and expansion phenomena. Furthermore, the mobile bed surface might be covered with alluvial bed forms increasing overall flow resistance compared to plane bed conditions. As a consequence the upstream water level and the pressure head above the side overflow device rise and the spill discharge as well. Hence, the design discharge to be diverted over the overflow structure is increased in an unforeseen way by this flow-sediment transport interaction. Opposite to the side weir the main-channel flow might be accelerated and increased shear stresses are present yielding river bed and bank erosion (Fig. 1.1).

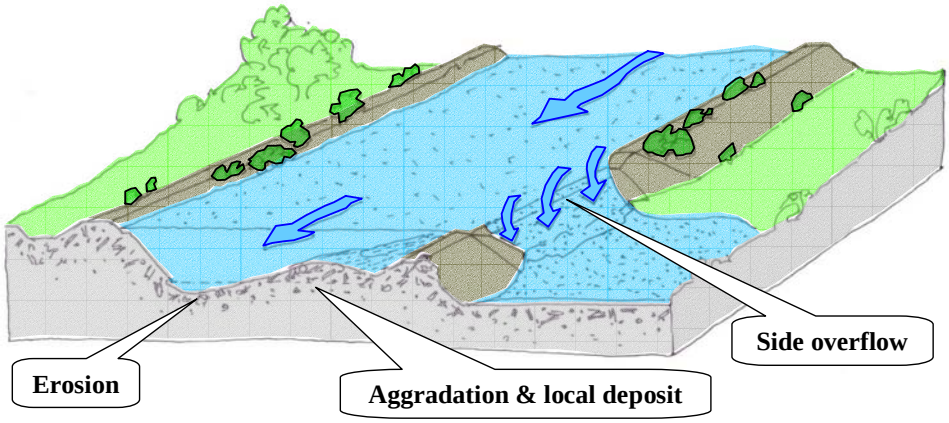

Figure 1.1: Basic processes as bed aggradation, local deposition and erosion in the main-channel near a side weir as a result of the interaction of flow with bed-load transport.

Since the background of the present investigation is the use of side weirs or overflow dams to control flow processes along a channel or river course, the morphological bed changes described above might result in an to early filling of retention bassins or flood plains designed to store a certain flood volume to reduce the peak flow. In a worst case scenario the available storage volume would already be filled up before the passage of the flood peak.

Due to these reasons the extent and the impact of the morphological bed changes on side overflow intensity have to be known and to be taken into account quantitatively when designing side weirs. In the framework of recent flood control concepts as for example the 3^{rd} correction of the river Rhone upstream of Lake Geneva in Switzerland, side weirs combined with fuse plugs are intended to be installed for the controlled flood peak reduction and filling of flood plains.

1.2. Aim of Present Research Work

Within the framework of the multidisciplinary flood protection research project DIFUSE (DIgues FUsibles et SubmersiblEs, Fuse plugs and overflow dams at rivers) four topics have been investigated by different research groups, namely:

- Establishment of design criteria for fuse plugs,
- Investigation of stability of submerged river dykes including scouring at the toe,
- Geometrical and aesthetical integration of overflow devices into landscape and
- Interaction of a side overflow with sediment transport.

The latter aspect has been investigated by the Laboratoire de Constructions Hydrauliques (LCH) at the Ecole Polytechnique Fédérale de Lausanne (EPFL).

Since very few investigations have been dealing with the interaction of a lateral overflow with bed-load transport in the main-channel, a systematic laboratory flume study has been conducted. The aim of these experiments was, on the one hand, to study and better understand the interaction of a side weir overflow with bed-load transport and bed morphology. On the other hand the flume tests served to collect and create a scientific data base upon which a dimensionless parameter analysis in order to find empirical relationships could be performed. Furthermore, the systematic tests allow the calibration of numerical models.

Within this analysis the scientific objectives of the research work can be summarized as follows:

- to develop an empirical $1D$-model for the prediction of the overall shape of the aggradation near the side weir,
- to develop an empirical model which accounts for the $2D$-effect of the local sedimentary deposit,

- to establish a calculation method for direct quantitative estimation of side spill discharge influenced by morphological bed changes in the main-channel,
- to account in an appropriate way for bed form induced roughness within the vicinity of the overflow reach and
- to give recommendations for the design of side overflow devices in river training works and flood protection measures.

The project supplies the scientific basis to take into account and quantify the interaction of a side weir overflow with bed-load transport and bed morphology in practical considerations. Therefore, the analysis is aimed to propose simple relationships based on reliable flume data that have good predicting ability for engineering purposes.

1.3. Structure of Research Report

After the introduction, the second chapter of the report consists of a literature review. In this chapter relevant domains interfering with side overflow on mobile bed conditions is briefly referred to. The relevant domains are sediment transport (bed-load), bed morphology (bed forms) and side weirs and spatially varied flow. In addition, some examples of prototype side overflows are introduced.

The third chapter refers to the theoretical background. Herein, basic approaches, methods and formulae necessary to investigate the different aspects occurring with the interaction of lateral overflow and bed-load transport and bed morphology are summarized. The points of interest in this regard are sediment transport (bed-load), flow resistance due to grain and form roughness as well as side weirs, spatially varied flow and the determination of a side weir discharge coefficient.

In the fourth chapter the experimental setup, the tested parameters, the test procedure and the measurement techniques are described.

The fifth chapter deals with data processing and the analysis of data obtained from the experiments. The analysis and results refer to side overflow intensity, the choice of an appropriate side weir discharge coefficient, the repartition of overflow discharge for the experiments with two weirs, three-dimensional flow pattern, bed-load transport, bed morphology and bed form induced flow resistance. Herein, different approaches and methods from literature are analyzed and compared with experimental results from the present study.

The sixth chapter is dedicated to the development of a $1D$- and $2D$-empirical model to describe the deposition phenomena in the side weir reach.

In addition a relationship for direct estimation of side overflow on mobile bed conditions is proposed. The chapter closes with a discussion regarding the influence of time, channel width and approach flow conditions.

The seventh chapter summarizes the different steps of calculation applying the empirical models in numerical flow simulations. To demonstrate the application procedure a computation example related to the experimental conditions is performed. Moreover, the empirical models are applied under prototype conditions in a case study on the Rhone river upstream of Lake Geneva in Switzerland.

In the eighth chapter some results from numerical steady and unsteady simulations with bed-load transport and a comparison with experimental results are presented.

Finally, in the last chapter the main developments concerning the interaction of a side overflow with bed-load and bed morphology are summarized and their constrictions and limits are highlighted. Before giving an outlook for further research recommendations for the application in engineering practice are given.

2. Literature Review

In the following paragraphs a brief review of research done in relevant domains with respect to the investigations of the present study is given. First, sediment transport (bed-load) in a channel and evolution of bed morphology is presented. Then existing studies on side weirs and spatially varied flow and the reciprocal interaction among them is referred to. At the end of the chapter some prototype examples of side overflows and fuse plugs are presented.

2.1. Sediment Transport in Channels and Rivers

Many textbooks give a good overview about sediment transport processes and formulae, e. g. Graf (1971), Yalin (1972), Zanke (1982), Graf (1984), Raudkivi (1990), Dittrich (1998), Graf and Altinakar (1998), Jäggi (1999/2000), Scheuerlein and Schöberl (2001) and Yalin and da Silva (2001).

The bed material used in the experimental investigations has been rather uniform. For this reason, a top layer or armoring effects are not treated explicitly. Suspended load has no distinct impact on the morphological processes taking place in the present study (aggradation of mean bed elevation, formation of a local sedimentary deposit). Therefore, only sediment transport formulae dealing with bed-load are considered herein.

Since bed-load transport is related to drag or traction (Graf (1971)), the first important contribution of the drag principle was advanced by Du Boys (1879). Investigating the Rhone river in France, stream flow depth and slope have been used to develop a quantitative bed-load formula.

Important investigations concerning incipient motion have been conducted by Hjulström (1935). The beginning of movement of sediments has been related to the grain diameter and mean flow velocity which was presumed to be about 40 % greater than the bottom velocity for a flow depth exceeding 1.0 m.

Shields (1936) performed laboratory tests with uniform grain size bed material. Based on these experiments and theoretical considerations, an incipient motion criterion has been developed using the grain size Reynolds number and a dimensionless shear stress parameter (Shields factor). Explicit formulations for the entire Shields diagram are given by Van Rijn (1984a), Yalin and da Silva (2001) and Cao et al. (2006).

Using both uniform sands and sand mixtures, Schoklitsch (1930) and Schoklitsch (1950) proposed the rate of sediment movement being proportional to the excess power. For this, an expression for the critical flow rate has been developed depending on the relative sediment density, the grain diameter and the energy slope (paragraph A.6.3).

Meyer-Peter and Müller (1948) (paragraph A.6.2) performed a large test series at bottom slopes between 0.04 % and 2.3 % and established the well-known Meyer-Peter and Müller (MPM) formula. The sediments used were characterized by a both uniform and wide grain size distribution.

Smart and Jäggi (1983) (paragraph A.6.4) extended the MPM-formula to channels with steeper slopes up to 20 %. In contrast to Meyer-Peter and Müller (1948), the value of the critical Shields parameter varies with the grain Reynolds number instead of being kept constant. Moreover, the influence of a wider grain size distribution has been incorporated in the formula. Currently, the Smart and Jäggi (1983) formula is one of the most widely used bed-load transport formulae in Switzerland.

Hunziker (1995) introduced a modified bed-load formula for wide sediment mixtures based on the one of Meyer-Peter and Müller (1948) introducing fractionwise sediment transport.

Based on dimensional analysis with empirically determined exponents, Ackers and White (1973) developed a bed-load transport formula having the discharge, flow velocity and flow depth and sediment characteristics as main input parameters.

Following the approach of Bagnold (1966), Van Rijn (1984a) assumed the motion of bed-load particles being dominated by gravity forces while the effect of turbulence on the overall trajectory is supposed to be of minor importance. Using the dimensionless particle diameter (D_*) and a transport stage parameter (T), the bed-load transport is proposed to be the product of the saltation height (δ_b), the particle velocity (u_b) and the bed-load concentration (c_b) (paragraph A.6.5).

2.2. Bed Morphology as a Result of Sediment Transport

Many attempts were made to explain and classify the type of bed forms generated under given flow conditions on a mobile bed. In the following paragraphs a review of bed form classification criteria and approaches dealing with bed form geometry is given. Moreover, the effect of bed forms on flow resistance is discussed.

2.2.1. Classification of Bed Forms

Bed forms occurring in channels and rivers can loosely be classified as plane bed, ripples, dunes and antidunes.

In a way similar to Shields (1936), Liu (1957) derived a relation to classify bed forms used at present. In this approach, the type of bed forms have been described in terms of a suspension parameter composed of the bed shear velocity (u_*) and the particle fall velocity (w_s) and a particle related Reynolds number (Re^*).

In this context it is worthwhile to mention a study by Garde and Ranga Raju (1963), wherein in addition to the parameters introduced by Liu (1957) the Froude number (Fr) is added. Later on, Garde and Ranga Raju (1966) proposed a diagram for the different flow regimes and hence, alluvial bed forms, depending on the ratio of hydraulic radius to grain diameter (R_h/d) and slope to relative density ($S/(s-1)$).

The Froude number is is often used as a flow criterion in open-channel flow. Following this idea, Engelund and Hansen (1967) applied the Froude number as a bed form classification parameter.

Simons and Richardson (1961) argued that the classification into a lower and upper regime connected by a transition zone would be more convenient than to work with tranquil and rapid flow regimes that are defined by the Froude number. This reasoning is based on the fact that extreme variability of flow conditions may occur in the same cross section. The most extensive experimental studies on bed forms were made by the U.S. Geological Survey at the Colorado State University (C.S.U.). As a result of this investigation, Simons and Richardson (1961) and Simons and Richardson (1966) (paragraph A.3.1) presented a bed form classification diagram which has been widely accepted (e. g. Henderson (1966)). The input parameters are the stream power ($\tau_0 \cdot v$) and the median fall diameter (d_f) which is often replaced by a characteristic grain diameter (e. g. d_m or d_{50}).

Kondratiev (1962) undertook the task of presenting and discussing some Soviet experimental research. In these investigations it has been shown that the Froude number and the grain diameter may be used as a bed form criterion.

A generalized empirical relation for bed forms incorporating about 20 Soviet and other investigations was presented by Znamenskaya (1962) and considerably extended by Znamenskaya (1969). The latter contribution includes a graph. For a given hydraulic condition (Fr and v) and a given sediment material the graph permits the determination of the kind of the resulting bed form, bed form velocity (u_b) and bed form steepness ($\delta = \Delta/\Lambda$).

Engelund (1966) considered bed forms in alluvial streams as a stability problem, accounting first for the hydraulics of a two-dimensional, sinusoidal

sand bed and then for the interaction of fluid flow and sand erosion. Stability conditions were investigated for different Froude number versus $c^{'}$-combinations ($c^{'}$ is referred to as the dimensionless Chézy friction factor, $c^{'} = C^{'}/g^{1/2} = v/u_{*}^{'}$) and have been plotted in a stability diagram. Thus, for a given set of hydraulic conditions, the prediction of the resulting bed form and its stability is possible.

Based on flume and field data, Van den Berg and Van Gelder (1989) used a dimensionless bed shear stress parameter ($\theta^{'}$) and a dimensionless particle parameter (D_{*}) to establish a diagram classifying bed form types.

The dimensionless particle parameter (D_{*}) has also been used by Van Rijn (1984b) (paragraph A.3.1). Furthermore, a transport stage parameter (T) has been introduced. Depending on these two parameters, a bed form classification method is proposed in an explicit (tabular) as well as in a graphical way.

Chiew (1991) stated that none of the classification diagrams (e. g. the one of Simons and Richardson (1966)) refer to non-uniform bed material. For this reason, a classification method for bed features in non-uniform sediments has been proposed.

Yalin (1992) plotted data from 27 sources on the log-log (B/y, y/d)-plane to identify existing regions of alternate bars, multiple bars and dunes (paragraph A.3.1). With reference to the present study, the application of this regime predictor only allows for the estimation of dunes; ripples and bed features of the transitional and upper regime are not included.

The bed regime predictor by Karim (1999) is based on graphical analysis of laboratory data (paragraph A.3.1). Two limiting Froude numbers for the beginning of the transition regime (Fr_t) and the beginning of the upper regime (Fr_u) were defined. Thus, dunes, transitional bed forms and antidunes can be identified. For the prediction of the ripple-bed configuration, a dimensionless number (N^{*}), being the product of the grain size Reynolds number (Re^{*}) and the particle Froude number ($Fr_p^{*} = (v/((s-1)gd_{50}))^{1/2}$), is proposed.

According to Yalin and da Silva (2001), ripples and dunes are caused by vertical turbulence. Introducing a group of several dimensionless variables, a method to determine the existence region of ripples and dunes has been developed (paragraph A.3.1). The results are presented in terms of equations and in graphical form.

2.2.2. Bed Form Geometry

The main parameters to describe bed form dimensions and geometry are bed form length, height, steepness as well as lee and stoss slope angle.

Since in the present study most bed features were located in the lower regime and quite a few in the transition regime, only dunes are considered in the literature review. For studies referring to ripples, the approaches of Yalin

(1985), Van Rijn (1993) and Yalin and da Silva (2001) might be referred to. These approaches are briefly presented in paragraph A.3.2.

Tsubaki and Shinohara (1959) proposed relationships for the relative dune height (Δ/y) and dune steepness (δ) depending on the dimensionless bed shear shear stress (θ').

Gill (1971) developed an equation for the relative dune height (Δ/y) being a function of the Froude number and the excess shear stress ($\tau_0 - \tau_{0,cr}$). Moreover, a power coefficient as well as a dune shape coefficient constitute the main input parameters.

Geometrical properties of bed forms have been studied by Yalin (1964). Performing experiments, dimensionless variables for length (Λ) and height (Δ) have been derived. The height was shown to be related to the shear stress (τ_0, $\tau_{0,cr}$), the latter depending on the flow depth. Again applying dimensional reasoning, the length of bed forms depends on the flow depth, the grain diameter and the particle Reynolds number. A constant relation being 6.3 for relative dune length (Λ/y) is given by Yalin (1972).

According to Ranga Raju and Soni (1976), the relative dune height, composed with the grain diameter (d_{50}) instead of the flow depth, is a function of the Froude number and the Shields factor (θ').

Allen (1968) investigated dune height and dune length. The relative dune height (Δ/y) and dune length (Λ/y) was found to only depend on flow depth.

Fredsøe (1982) explained dune geometry from a more theoretical point of view. Based on turbulence measurements downstream a rearward-facing step, a mathematical model being able to calculate dune shape of arbitrary height has been developed. Expressions given for relative dune height (Δ/y) and dune steepness (δ) depend on the dimensionless bed shear shear stress at the dune crest (θ'_{crest}) and the grain diameter (d_{50}).

Investigations by Van Rijn (1982) and Van Rijn (1984b) indicated that relative dune height (Δ/y) primarily is related to the grain diameter (d_{50}) and a transport stage parameter (T). With respect to relative dune length a constant value of 7.3 has been reported (paragraph A.3.2).

The approach by Julien and Klaassen (1995) lead to a constant value of 6.25 for relative dune length (Λ/y). The relative dune height (Δ/y) was found to depend on flow depth and the grain diameter (d_{50}).

Karim (1999) developed an expression for relative bed form height (Δ/y) for various flow regimes. Therein, bed form height is a function of energy slope (S), ratio of d_{50} and flow depth (d_{50}/y), Froude number and relative dune length (Λ/y).

The expression for relative dune length developed by Yalin and da Silva (2001) is composed in terms of the grain diameter (Λ/d_{50}). Furthermore, a dependency on the relative flow depth (y/d) and the grain Reynolds number has been found out. With respect to dune steepness a rather complex relation

has been established. The main input parameters were found to be a set of dimensionless variables.

In appendix A.3.2 and Table A.8 several approaches mentioned above and used for comparison with data from the present study are presented.

Another way to describe bed form geometry results from a stochastic point of view. Within this concept the variation of bed form shape is considered as the random variable of the probability distribution function (PDF). Bed from geometry is expressed by statistical distribution functions, e. g. Normal, Weibull, Gamma and Rayleigh, and then related to form resistance. Some references in this context are from Ashida and Tanaka (1967), Annambhotla et al. (1972), Wang and Shen (1980) and more recently from Van der Mark et al. (2005).

2.2.3. Influence of Bed Forms on Flow Resistance

Considering a bed with bed forms superimposed, a well-known theory to compute the overall or total resistance is given by Einstein (1950). Following the linear separation concept, the total resistance is assumed to be the sum of grain related and form related resistance (paragraph A.4).

Van Rijn (1993) stated that, basically, two approches to account for total bed roughness can be found in literature. The first group refers to methods based on bed form parameters such as bed form length, height and steepness. The second one is based on integral parameters such as mean depth, mean velocity and bed material size.

As far the first group is concerned, Engelund (1977) related the form friction coefficient (f'') to bed form parameters and developed an expression for dunes. Vanoni and Hwang (1967) also used the form friction coefficient and established a relation for ripples and dunes.

Using the equivalent sand grain roughness of Nikuradse, Van Rijn (1984b) developed an expression for the total roughness composed of the grain diameter (d_{90}) and a combination of bed form height and steepness (paragraph A.4.1).

Yalin and da Silva (2001) chose the dimensionless Chézy friction factor (c) to establish a relation for the grain roughness. The main input parameters are the grain size Reynolds number (Re^*) and the relative flow depth (y/d). The resistance due to form roughness is expressed in terms of bed form length and steepness (paragraph A.4.1).

Yu and Lim (2003) developed a new velocity formula in the form of a modified Manning equation. The influence of bed form geometry on flow resistance is directly incorporated. The main input parameters are the ratios R_b/d_{50} and $\theta/\theta cr$.

Referring to the second group, a functional relationship between v/u_*'' and the relative sediment density (s), the grain diameter (d_{35}), the hydraulic

radius ($R_h^{'}$) and the energy slope has been developed by Einstein (1950) and Einstein and Barbarossa (1952). This relationship was extended by Shen (1962) introducing a Reynolds number in terms of the settling velocity and modified by Yalin (1964) using the theory of dimensions.

With the aid of flume and field data, Garde and Ranga Raju (1966) suggested a relation in the form of the Manning equation. In this equation, a coefficient differing for ripples and dunes and for transition and antidunes has been proposed.

Engelund (1966) expressed the flow resistance due to bed forms with an expansion-loss equation in terms of the Carnot formula.

According to the approach developed by Engelund and Hansen (1967), the total resistance mainly depends on the ratio $\theta^{'}/\theta$ (paragraph A.4.2). Distinguishing between the lower and upper regime, expressions for the $\theta^{'}$ and θ-parameters were computed and plotted in a diagram.

Alam and Kennedy (1969) used the Froude number in the form $Fr = (v/(gd_{50}))^{1/2}$ and the ratio of the hydraulic radius related to the bed (R_b) and the grain diameter (d_{50}) to determine the contribution of $f^{''}$ to the total resistance (f).

Based on the analysis of river data, Smith and McLean (1977), proposed an expression for the equivalent sand grain roughness of Nikuradse (k_s) (paragraph A.4.2). The input parameters are the grain size (d_{50}) and the dimensionless excess bed shear stress ($\theta - \theta_{cr}$).

White et al. (1980) established a computational procedure which is based on the analysis of flume and field data of the lower regime.

Brownlie (1981) presented a method to predict the flow depth as a function of the main flow variables (paragraph A.4.2). Applying dimensional analysis and analyzing flume and field data, expressions for the lower and upper flow regime have been developed.

Wu and Wang (1999) proposed a method for the prediction of movable bed roughness in the lower flow regime. In this method, a roughness parameter is related to the non-dimensional shear stress ($\tau_0^{'}/\tau_{cr}$) and the flow Froude number.

As mentioned for bed form geometry in paragraph 2.2.2, form induced resistance might also be taken into account from the stochastic point of view.

2.3. Spatially Varied Flow and Side Weirs on fixed Bed

In this paragraph a literature review of spatially (gradually) varied flow with decreasing discharge is conducted. Special interest is laid on investigations

concerned with the determination of a side weir discharge coefficient.

Spatially (gradually) varied flow is characterised by a non-uniform discharge resulting from the addition or or diminution of water along the course of flow. The added or diminished water will cause disturbance in the energy or momentum content of the flow. Generally, two types of spatially varied flow occur: flow with increasing discharge and flow with decreasing discharge. In the present study only flow with decreasing discharge in the subcritical flow regime is discussed.

The theory of spatially varied flow with decreasing discharge was probably employed first in the design of lateral spillways or side spillway weirs. Laboratory tests on such structures were first made by Engels (1917) and Coleman and Smith (1923). Forchheimer (1930) has approached the problem analytically by assuming the energy line to be parallel to the spillway crest and to the channel bottom and also by assuming the flow profile along the spillway crest to be linear. Theoretically, De Marchi (1934) proved that the energy head along the spillway crest is essentially constant and that the flow profile is curved, rising in subcritical flow and dropping in supercritical flow. This theoretical investigation was further verified experimentally by Favre and Braendle (1937), Gentilini (1938) and Ferroglio (1941) for low Froude numbers. For $Fr > 0.5$, Hager and Volkart (1986) discovered serious disagreement. Theoretical and practical studies of the flow were also performed and advanced by Favre (1933), Favre (1937), Schmidt (1954), Schmidt (1955), Ackers (1957), Allen (1957), Collinge (1957), Frazer (1957) and many others.

Within the investigation of side overflow special interest is laid on the determination of the water surface profile along the side weir and an appropriate side overflow discharge coefficient (C_D). Basically, two concepts can be identified:

- Constant specific energy concept and
- momentum approach.

In principle, both concepts can be used to derive general dynamic equations for the steady spatially varied flow problem. This has been theoretically shown by Yen and Wenzel (1970). Cheong (1991) studied the side weir discharge coefficient in a trapezoidal channel on the basis of both concepts concluding C_D obtained from momentum considerations was very close to the one obtained by the energy method.

The first concept is a scalar relationship and has first been developed and theoretically proved by De Marchi (1934). According to the energy solution the average longitudinal (downstream) component u_D of the velocity of the spill flow at any section is assumed to be equal to the average velocity of flow

v in the main-channel (Fig. A.15). Therefore, the total energy of a unit mass of water remaining in the channel is unaffected by the spill that is occurring and, apart from friction losses, the total energy of the flow in the main-channel should remain constant.

For the second one, the first systematic investigations have been conducted by Favre (1933). The momentum approach is a vector relationship which equates the net momentum flux and all external forces acting on a control volume in the direction of flow.

In the following several contributions with respect to the two different concepts are presented. Many of them consist of an experimental part, especially when focusing on a relation for the discharge coefficient (C_D). For these, the basic experimental boundary conditions are summarized in Tables 2.1 and 2.2 (constant specific energy concept) and Tables 2.3 and 2.4 (momentum approach).

- Constant specific energy concept (Tab. 2.1 and 2.2):

  In a total of 200 experiments, Subramanya and Awasthy (1972) studied the spatially varied flow over side weirs of zero and finite height in two rectangular prismatic horizontal channels. The weirs were sharp edged and fully aerated on the downstream side. Assuming effects of the geometrical configuration of the flow (L_D/B, y_1/L_D, w_D/y_1 with L_D side weir crest length, B channel width, y_1 approach flow depth and w_D sill height) are negligible, a relation for C_D in sub- and supercritical flow with the approach Froude number as main input parameter is proposed. Herein, the discharge coefficient of a side weir of finite height is essentially the same as for a side weir with zero height. Furthermore, a relation for the lateral outflow angle (ϕ_D) is proposed.

  In contrast to Subramanya and Awasthy (1972), Nadesamoorthy and Thomson (1972) indicated that C_D is dependent on the channel width and propose a slightly different C_D-relation. This relation is valid for both sub- and supercritical flow conditions.

  Smith (1973) expanded the research from a prismatic horizontal channel (Subramanya and Awasthy (1972)) to arbitrary cross sectional shapes and a wide range of variables such as invert slope and side weir height. For this issue, a computational calculation procedure for sub- and supercritical flow conditions has been developed.

  Ranga Raju et al. (1979) studied the effect of a lateral constraint on the flow provided by the walls of a 90° branch channel. Thus, a new boundary condition has been introduced which has always been a free overfall in the previous investigations. The effective crest length has been taken into account introducing a correction factor for the true crest length. The main-channel geometry in experiments restricted to

subcritical flow has been rectangular and the weir crests have been sharp (7 experiments) and broad crested (15 experiments). The discharge coefficient was assumed to be a function the approach Froude number (Fr_1). For the broad crested weir, an empirical coefficient being a function of $y_1 - w_D$ and crest width was added to the C_D-relation. The value $y_1 - w_D$ was invariably maintained greater than 10.00 cm to eliminate effects of viscosity and surface tension that might be important at small heads. With respect to the constant specific energy approach, a difference between the up- and downstream weir corner of less than 2 % has been observed. Thus, this assumption has been concluded to be reasonable. The investigations resulted in a design procedure to determine the discharge to be passed into a branch channel.

Ramamurthy and Carballada (1980) developed a weir flow model based on the theory of flow through a lateral conduit outlet considering the variations in the angle of the outflowing jet. For this purpose, a two-dimensional lateral conduit outlet model is adopted. The side weir discharge coefficient was found to be highly dependant on the jet velocity ratio (main-channel velocity/overflow jet velocity) and on the ratio L_D/B. For the verification of the theoretical predictions an experimental study has been conducted. The model is applicable to lateral weirs that can be as long as the width of the parent channel.

Most of the research activities mentioned above referred to rectangular main-channel geometry. Cheong (1991) determined the side weir discharge coefficient in a prismatic trapezoidal main-channel for subcritical flow conditions. The tested parameters have been different Froude numbers, the crest lengths and side slopes of the main-channel. The investigations revealed that considerations from both the energy and the momentum concept yield almost no difference with respect to C_D. Finally, using the constant energy concept, an equation for C_D being related to the upstream Froude is proposed.

Uyumaz and Muslu (1985) extended the research to circular channels and investigated the flow over sharp crested side weirs both theoretically and experimentally (1600 combinaisons). A theoretical model developed is solved by a finite difference method. For practical use the results are presented in diagrammatic form. In the experimental study sub- and supercritical flow regimes have been present. In the subcritical regime the discharge coefficient was not significantly dependent on w_D/D-ratios (with D channel diameter) but highly a function of L_D/D. In the supercritical regime, C_D was strongly related to w_D/D and L_D/D. A discussion is found in Hager (1987a).

Uyumaz (1997) studied flow over side weirs in U-shaped channels in

the sub- and supercritical flow regime. Numerical models have been developed and compared to experimental results. Moreover, charts for practical engineering use are presented.

Not only the main-channel geometry and rectangular side weirs have been subject to numerous investigations. Kumar and Pathak (1987) studied the characteristics of sharp and broad crested triangular side weirs at the end of a 90° branch channel experimentally. The prismatic main-channel has been rectangular and the flow regime has been restricted to subcritical flow conditions. As done by Ranga Raju et al. (1979), the value $y_1 - w_D$ was maintained greater than 10.00 cm to eliminate effects of viscosity and surface tension. Relations between discharge coefficient and main-channel Froude number for different apex angles of the weir (60°, 90° and 120°) have been established. The effect of w_D/y on C_D was found to be insignificant for the sharp crested weir, thus corresponding to findings of Subramanya and Awasthy (1972). The parameter h_D/L, with h_D side weir pressure head and L crest width, was found to have an important influence on C_D for broad crested weirs. This influence is taken into account by a multiplication factor depending on h_D/L (with $h_D = y - w_D$ pressure head above side weir crest).

Uyumaz and Smith (1991) investigated the flow over side weirs in rectangular and circular channels numerically. The numerical models are solved by a finite difference method. Theoretical and experimental procedures for the determination of the length of side weirs in rectangular and circular delivery channels are proposed. Furthermore, it is shown that the rectangular channel side weir procedures should not be used for obtaining discharge and water surface profiles for side weirs in circular channels as has been proposed by Smith (1973) and El-Khashab and Smith (1976).

In addition to design procedures for flow over side weirs in rectangular and circular channels (Uyumaz and Smith (1991)), Uyumaz (1992) derived general expressions for the surface profile along side weirs in triangular-shaped channels.

Singh et al. (1994) studied the discharge coefficient for a rectangular sharp crested side weir located in a prismatic rectangular main-channel under subcritical flow conditions experimentally. Contrary to earlier findings (Subramanya and Awasthy (1972)), besides the upstream Froude number, C_D also depends on the ratio of sill height to upstream flow depth (w_D/y_1). A discussion is given in Jalili and Borghei (1996).

In the investigations mentioned above, the subject matter has always been a single side weir. Singh and Satyanarayana (1994) studied an automated field irrigation system using multiple side weirs. Analyzing

the characteristics of spatially varied flow along a main-channel with multiple side weir outlets, the roughness coefficient of the channel pertinent to spatially varied flow has been determined. Based on this analysis, a computer program has been developed to obtain the geometric parameters of the uniformly discharging weir outlets in a side weir irrigation system. The experiments (8 runs) conducted to evaluate the performance of the developed program showed deviations in the order of 5 to 10 %.

Swamee et al. (1994a) stated that various investigators have related the weir discharge coefficient with the main-channel's upstream Froude number. Thus, the dominant ratio of side weir head to weir height ($(y - w_D)/w_D$) has not been considered in previous investigations. Due to that reason, a concept of an elementary discharge coefficient for the discharge of an elementary rectangular strip along the weir crest is developed. Like that of a normal weir the elementary discharge coefficient has been related to the ratio of head to weir height only. The concept is based on a numerical solution of two ordinary differential equations for discharge and water depth. The constants in the elementary discharge coefficient have been obtained from 257 experiments for a sharp crested rectangular side weir placed in a horizontal rectangular main-channel.
Later on, Swamee et al. (1994b) extended the concept of an elementary C_D-value from rectangular sharp crested weirs to rectangular broad crested side weirs. Moreover, both configurations have been studied with unrestricted outflow (no branch channel, no side walls) and with restricted outflow. Furthermore, a triangular sharp crested weir has been investigated. To determine all relevant constants experiments have been conducted.

Side weirs located on straight channels have been largely investigated. Agaccioglu and Yüksel (1998) studied the hydraulic behavior of a rectangular sharp crested weir at various locations along a 180° bend. During the experiments in subcritical flow conditions, a stagnation zone has been observed at the side weir section along the inner side of the bend and standing waves were present downstream of the side weir. Both phenomena were reported to be highly dependent on the Froude number. With respect to the discharge coefficient, C_D was found to depend on the upstream Froude number, w_D/y_1 and L_D/B.

Based on more than 250 experiments in the subcritical flow regime, Borghei et al. (1999) investigated the influence of flow hydraulics and geometric channel and weir shape on the side weir discharge coefficient. The main-channel has been rectangular, the weir rectangular and sharp crested. It has been found out that the assumption of constant specific energy is acceptable, since the energy difference between the up- and

downstream weir corner was 3.7 %. The discharge coefficient was found to be a function of the upstream Froude number, w_D/y_1 and L_D/B, whereas the channel slope could be ignored.

Muslu (2001) presented a theoretical analysis for discharge over side weirs considering the lateral water surface elevation. For the derivation of generalized equations for the discharge and the water surface the weir has been divided into elementary strips. The validity of the proposed model has been checked using data presented by Subramanya and Awasthy (1972). Moreover, the equations developed were experimentally verified using the data from own laboratory studies and data presented by Hager (1982a) and Hager (1982b). The model quality has been increased taking into account the inclination of the deflected flow over the weir (Muslu (2003)). Muslu et al. (2004) reported that even better results have been obtained when the transition condition at the ends of the side weir consisted of no lateral surface slope. In addition, it is stated that the effect of water surface slope in lateral direction is of secondary importance as compared to the angle of the deflected jet along the weir. A discussion is given by Clemmens (2005).

Khorchani and Blanpain (2005) developed an expression for the discharge coefficient using artificial neural networks. The developed model has been calibrated and validated with experimental data.

More recently, Ramamurthy et al. (2006) established a new approach for the calculation of C_D for rectangular and circular side weirs using the multivariable nonlinear partial least square method (PLS). This method is used to determine the empirical equations relating C_D with the dimensionless weir parameters Fr_1, w_D/y_1 and L_D/B.

Table 2.1: Part I: Experimental boundary conditions for approaches based on the constant specific energy concept. *rect.* denotes rectangular, *circ.* circular, *trap.* trapezoidal, *sh.* sharp and *br.* broad.

Investigator	Main-channel characteristics					Side weir characteristics		
	Cross section	Bed type	L $[m]$	B $[m]$	S_0 $[\%]$	L_D $[m]$	w_D $[m]$	crest shape
Subramanya and Awasthy (1972)	rect.	cement	3.0/9.0	0.248/0.61	0.0	$0.10 - 0.15$	$***$	sharp
Ranga Raju et al. (1979)*	rect.	fixed	9.00	0.40/0.60/1.00	0.0	0.20/0.50	$0.05 - 0.25$	sh./br.
Ramamurthy and Carballada (1980)	rect.	fixed	4.32	0.25/0.46	0.0	$0.13 - 0.46$	$0.05 - 0.15$	sharp
Uyumaz and Muslu (1985)	circ.	concrete	10.90	$\varnothing$ 0.25	$0.0 - 2.0$	$0.15 - 0.85$	$0.06 - 0.14$	sharp
Kumar and Pathak (1987)*	rect.	fixed	9.00	0.50	0.3	$***$	$0.06 - 0.24$	sh./br.
Cheong (1991)	trap.	fixed	10.00	0.35/0.67[1)]	$***$	$0.28 - 0.97$	$***$	sharp
Singh et al. (1994)*	rect.	fixed	23.00	0.25	$***$	$0.10 - 0.20$	$0.06 - 0.12$	sharp
Singh and Satyanarayana (1994)*	rect.	fixed	23.00	0.25	0.0	$***$	$***$	$***$
Swamee et al. (1994a)	rect.	cement	9.00	0.50	0.0	$0.20 - 0.50$	$0.00 - 0.10$	sh./br.
Swamee et al. (1994b)**	rect.	cement	9.00	0.50	0.0	$0.20 - 0.50$	$0.00 - 0.60$	sharp
Borghei et al. (1999)	rect.	fixed	12.00	0.30	$-0.5 - 1.0$	$0.20 - 0.70$	$0.01 - 0.19$	sharp
Present study	rect.	mobile	18.00	1.50	$0.1 - 0.4$	3.0/5.0[2)]/6.0	0.09/0.10	sharp

*)restricted outflow (branch channel, sidewalls) **)with/without restricted outflow
1)main-channel base width 2)two side weirs of 2.50 m each

Table 2.2: Part II: Experimental boundary conditions for approaches based on the constant specific energy concept. *sub.* denotes subcritical, *super.* supercritical, *exp.* experimental, *theor.* theoretical and *num.* numerical.

Investigator	Dim.-less parameter combinations			Hydraulic characteristics			Type of study
	L_D/B [−]	w_D/y_1 [−]	y_1/L_D [−]	Q_1 $[m^3/s]$	Fr_1 [−]	Regime studied	
Subramanya and Awasthy (1972)	$0.2-1.0$	$0.2-0.96$	$0.1-2.4$	$***$	$0.02-4.30$	sub./super.	experimental
Ranga Raju et al. (1979)*	$***$	$***$	$***$	$***$	$***$	subcritical	experimental
Ramamurthy and Carballada (1980)	0.5/1.0	$***$	$***$	$***$	$***$	subcritical	exp./theor.
Uyumaz and Muslu (1985)	$0.6-3.4^{1)}$	$0.24-0.56^{2)}$	$***$	$***$	$0.10-2.00$	sub./super.	exp./theor.
Kumar and Pathak (1987)*	$***$	$***$	$***$	$0.02-0.12$	$0.09-0.69$	subcritical	experimental
Cheong (1991)	$***$	$***$	$***$	$0.003-0.075$	$0.29-0.99$	subcritical	experimental
Singh et al. (1994)*	$***$	$***$	$***$	$0.01-0.014$	$***$	subcritical	experimental
Singh and Satyanarayana (1994)*	$***$	$***$	$***$	$0.012-0.021$	$***$	subcritical	exp./num.
Swamee et al. (1994a)	$***$	$***$	$***$	$0.02-0.10$	$0.01-0.93$	subcritical	exp./theor.
Swamee et al. (1994b)**	$***$	$***$	$***$	$0.02-0.10$	$0.10-0.93$	subcritical	exp./theor.
Borghei et al. (1999)	$***$	$***$	$***$	$0.035-0.10$	$0.10-0.90$	subcritical	experimental
Present study	2.0/3.33/4.0	$0.57- \approx 1.00$	$0.02-0.05$	$0.098-0.222$	$0.55- \approx 1.00$	subcritical	exp./(num.)

*)restricted outflow (branch channel, sidewalls) **)with/without restricted outflow
1)L_D/D with D pipe diameter 2)w_D/D with D pipe diameter

- Momentum approach (Tab. 2.3 and 2.3):

  In experimental investigations in the sub- and supercritical flow regime El-Khashab and Smith (1976) found out that the longitudinal component of the velocity of the spill flow was invariably higher than the average channel velocity. Due to this difficulty with the energy concept a momentum approach was adopted to introduce relationships for the longitudinal velocity component of the spill flow and to develop a computational procedure. This computational procedure was based on a flow classification in three categories following the regime type and the ratio of spill discharge to upstream discharge (Q_D/Q_1). According to this, the subcritical regime can be divided by $Q_D/Q_1 < 0.5$ and $Q_D/Q_1 > 0.5$. The third category is represented by the supercritical flow regime. A discussion is given by Balmforth and Sarginson (1977).

  Balmforth and Sarginson (1983b) presented a theoretical model based on the traditional transverse weir equation. Two differential equations have been derived which have been solved using a fourth order Runge-Kutta method. An experimental study in a rectangular channel covering both sub- and supercritical flow conditions has been used for validation of the model. In another study, Balmforth and Sarginson (1983a) investigated the effect of streamline curvature on the water surface profile in supercritical conditions. Hager (1984) and Hager and Hager (1985) stated that the model equations and the numerical procedure is questionable.

  Hager (1987b) investigated the lateral outflow mechanism of side weirs using a one-dimensional approach. The effects of flow depth, approach velocity, lateral outflow direction as well as main-channel shape have been included to obtain expressions for the lateral outflow angle and the lateral discharge intensity. The theoretical solutions have been in fair agreement with experimental observations (Hager (1982a) and Hager (1982b)). Moreover, a distinction between sub- and supercritical flow conditions has been made.

  Etheridge (1996) proposed a computer-based methodology to account for submergence of the side overflow. Using published data defining the relationship between the degree of submergence of a weir and the reduction of the weir coefficient, a method to describe the water profile in the receiving channel is developed. The results have been compared with those obtained from physical scale models.

  Based on the momentum of El-Khashab and Smith (1976) and incorporating the Balmforth and Sarginson (1977) discussion, a mathematical model for spatially varied flow over a broad crested weir (overtopping of embankments) has been formulated by Das (1997).

Using laboratory experiments, the model has been tested for accuracy. Deviations in the order of magnitude of 3 to 10 % have been observed. The ratio of spill to approach discharge (Q_D/Q_1) varied between 0.06 and 0.99.

Table 2.3: Part I: Experimental boundary conditions for approaches based on the momentum concept.

Investigator	Main-channel characteristics					Side weir characteristics		
	Cross section	Bed type	L $[m]$	B $[m]$	S_0 $[\%]$	L_D $[m]$	w_D $[m]$	crest shape
El-Khashab and Smith (1976)	rectangular	fixed	21.30	0.46	mild/steep	1.20/2.30	$0.10 - 0.25$	sharp
Balmforth and Sarginson (1983b)	rectangular	fixed	$***$	1.00	$***$	$0.46 - 0.76$	$0.04 - 0.12$	sharp
Hager (1987b)	rectangular	fixed	$***$	0.30	$-0.5 - 2.0$	1.00	$0.00 - 0.20$	sharp
Das (1997)*	unsymmetric[1)]	fixed	$***$	0.60[2)]	$***$	3.13[3)]	0.36[4)]	broad
Present study	rectangular	mobile	18.00	1.50	$0.1 - 0.4$	3.0/5.0[5)]/6.0	0.09/0.10	sharp

*)restricted outflow (branch channel, sidewalls)
1)one side vertical wall, other side trapezoidal embankment with side weir 2)main channel base width 3)variable
4)initial height, later reduced 5)two side weirs of 2.50 m each

Table 2.4: Part II: Experimental boundary conditions for approaches based on the momentum concept. *sub.* denotes subcritical, *super.* supercritical, *exp.* experimental, *theor.* theoretical and *num.* numerical.

Investigator	Dim.-less parameter combinations			Hydraulic characteristics			Type of study
	L_D/B [−]	w_D/y_1 [−]	y_1/L_D [−]	Q_1 $[m^3/s]$	Fr_1 [−]	Regime studied	
El-Khashab and Smith (1976)	$***$	$***$	$***$	$***$	$***$	sub./super.	exp./num.
Balmforth and Sarginson (1983b)	$***$	$***$	$***$	$***$	$***$	sub./super.	exp./theor.
Hager (1987b)	3.33	$***$	$***$	≤ 0.045	$0.30 - 2.00$	sub./super.	exp./theor.
Das (1997)*	$0.58 - 5.22$	$***$	$***$	$***$	$0.14 - 0.84$	subcritical	exp./theor.
Present study	$2.0/3.33/4.0$	$0.57- \approx 1.00$	$0.02 - 0.05$	$0.098 - 0.222$	$0.55- \approx 1.00$	subcritical	exp./(num.)

*)restricted outflow (branch channel, sidewalls)

Although some single experimental boundary conditions are close to the ones of the present study the literature review indicates that all approaches assume a fixed channel bottom to describe side overflow intensity. This appears to be evident, since most of the studies refer to irrigation or drainage engineering. In fluvial hydraulics commonly a mobile bed is present, especially when natural rivers are investigated. For the purpose of e. g. flood control management the morphological behavior and aspects of bed-load transport have essentially to be taken into account.

2.4. Interaction of Side Overflow with Sediment Transport and Bed Morphology

First of all it has to be mentioned that very few systematic studies dealing with the interaction of side overflow, sediment transport and bed morphology exist. The only references being to some extent related to the underlying work are studies dealing with overbank flow, lateral intakes and river bifurcations.

With respect to overbank flow the shear layer between main-channel and flood plain is responsable for a momentum transfer from the main-channel onto the flood plain. This interaction causes a reduction in overall discharge capacity. Consequently, as for the present investigation, the formation of sedimentary deposits might occur. Concerning lateral intake studies and natural river bifurcations, the transverse pressure gradient in the vicinity of the intake induces regions of mean flow velocity gradients, depth varying surfaces of flow division and separation, vortices, zones of flow reversal and local sediment deposition. Another reference which has been a precursor of the present study is the work of Teiller (2000) who studied the interaction of side weir overflow on mobile bed conditions (see also Rosier et al. (2004a)).

The first studies dealing with overbank flow on fixed bed main-channel conditions have been mainly concerned with the separation of main-channel and flood plain flow. For this reason fictive separation walls have been introduced (Sellin (1964)). Nicollet and Uan (1979) proposed a correction coefficient for the estimation of the total discharge. Wormleaton and Merrett (1990) introduced a coefficient characterizing the difference of flow velocities between the flood plain and the main-channel.

Ackers (1993a) and Ackers (1993b)) developed a suite of design functions to estimate the conveyance of two-stage channels when in flood. The flow may lie in one of several regions of performance depending on the relative flow depths of flow on the flood plains and in the main-channel. The design procedure proposed allows to take into account this interaction between main-channel flow and the slower moving flood plain flow. The approach applies to

a wide range of geometries and different roughness between flood plain and main-channel.

With respect to studies having mobile bed conditions, extensive investigations have been carried out at the Flood Channel Facility (FCF) at HR Wallingford, UK.

Ervine et al. (1997) found out that for an increasing flow depth from inbank flow to shallow overbank flow the sediment transport rate increases even though the boundary shear stress reduces. This phenomenon is assumed to be related to an increase in turbulence and secondary cell behavior. Comparing shallow overbank flow with a deeper overbank flow, a more conventional relationship between excess boundary shear and sediment transport is revealed.

Benson et al. (1997) stated a rapid change of bed roughness due to the formation of dunes. Comparing average bed and and bank positions, overall changes in the channel dimensions are not major. A particularity has been the "freezing" of the mobile bed region permitting the measurement of hydraulic parameters in the absence of sediment.

The experimental results of Atabay and Knight (1998) consisted of comparative tests with mobile and rigid main-channel beds. The resistance coefficients in compound channels have been shown to vary significantly with flow depth. Furthermore, a distinction between global, zonal and local resistance coefficients is assumed to be important.

Knight et al. (1998) and Knight and Brown (2001) conducted large scale experiments concerning equilibrium sand channels with overbank flow. Within these experiments considerable temporal variations in water surface profiles, bed profiles, bed-load rate and cross sectional shape on duned beds have been observed.

Valentine et al. (2001) conducted experiments under similar conditions than Knight et al. (1998). According to their findings, reasonable agreement of friction data with theory has been observed, whereas sediment transport rates are underestimated. Observed bed forms were consistent with the Simons and Richardson (1961) diagram of bed form domains. In addition to two-dimensional sand waves flow-parallel ridges have been stated.

In contrast to the studies mentioned above, Wormleaton et al. (2004) investigated flow structures in a two-stage sinuous channel. The results give an insight into flow structures and sediment transport of meandering channels under overbank flow.

As far as investigations dealing with (lateral) water withdrawal are concerned, Kerssens and Van Urk (1986) developed a one-dimensional mathematical model to predict the spatial and temporal aggradation and degradation effects resulting from discharge reduction in rivers or open-channels.

Regarding lateral intake flows, Neary and Odgaard (1993) studied the three-dimensional flow structure at a 90° open-channel diversion. Later on, Neary et al. (1999) developed a $3D$-numerical model for lateral intake inflows. The model reproduced three-dimensional flow pattern and provides novel insights about the complex hydraulics and sedimentary transport processes, e. g. the formation of a local scour within the stagnation region at the downstream corner of the intake. Observations of similar type have been observed at the downstream weir corner in the present study.

Michell et al. (2006) conducted a case study about the sediment control at a water intake for a thermal power station. The power station had a chronic problem with alluvial bed sediment buildup at the station's river water intake structure. The intake's flow substantially affected the flow field at the site causing bed sediment on the one hand to be deposited at the intake and on the other hand to be drawn to the intake. The operation of the intake has shaped the bed in front of the intake such that it formed a stationary deposit that acted in a manner similar to a cambered ramp. This ramp exacerbated sediment ingestion by the intake as it guides sediment up to the intake sill elevation. Similar phenomena have been observed in the present study. The problem of sediment buildup at the intake structure has been solved by using submerged vanes (Odgaard and Wang (1991a), Odgaard and Wang (1991b)) and a skimming wall together with realignment of the riverbank upstream of the intake.

In addition to the above references an experimental and numerical study investigating the interaction of a side overflow with a mobile bed has been performed at the Laboratory of Hydraulic Constructions (LCH) by Teiller (2000) (also Rosier et al. (2004a))).

The testing facility (geometrical model scale $\approx 1:20$) has been installed in a 2.00 m wide, 30.00 m long and 1.20 m deep flume. The flume has been subdivided longitudinally into two separate channels. The first one being 1.00 m wide represents the actual testing facility including the mobile bed ($d_m = 0.70\ mm$) and the side weir with a length of $L_D = 1.00\ m$. The effective flume length was 20.00 m. The second one constitutes a lateral channel permitting to evacuate the diverted discharge. In Table 2.5 the main experimental parameters are summarized.

The lateral overflow is responsable for an elevation of the mobile bed in the weir alignment and significant morphological bed changes. Upstream of the side weir a rather stable bed elevation with more or less regular dunes has been observed. In the weir alignment the dunes were distorted which have been regular upstream of the weir. In the downstream region alternating erosion and deposition zones occurred. This meander-like erosion gutter develops from one channel side to the other before dumping out towards the channel exit. Similar phenomena can be stated for the present investigation (paragraph 5.9.2).

Although the processes observed are strongly transient the system

Table 2.5: Overview of experimental parameters used in the study of Teiller (2000).

N^o of experiment	n_D [−]	L_D [m]	w_D [m]	S_0 [%]	Q_1 [l/s]	t [min]	$Q_{D,max}/Q_1$ [%]	Q_{sb} [kg/min]
01	preliminary test, $Q_1 = 170\ l/s$							
02	1	1.00	0.15	0.20	175	50	8.57	2.96
03	1	1.00	0.15	0.20	150	50	15.33	2.80
04	1	1.00	0.15	0.20	200	30	14.00	4.33

develops towards a rather stable equilibrium condition, e. g. the temporal evolution of the pressure head above the weir crest revealed an increase with time before reaching a rather stable but higher level. The discharge diverted over the weir increased by about 28 % compared to the beginning of the experiments.

1D-numerical simulations using the program DEPERO (DEPôt - EROsion) developed at the LCH by Dubois (1999) captured most experimental trends with reasonable accuracy, e. g. the overall shape of the mobile bed as well as the intensity of diverted discharge have been reproduced satisfactorily (Teiller (2000), Rosier et al. (2004a)).

2.5. Prototype Examples of Side Overflows

In this paragraph some prototype examples of side weirs, overflow dams and tilting fuse gates are briefly presented.

The first two examples are located in France. In the valley of Orléans on the middle Loire a side weir has been implemented in the river dike (Fig. 2.1). The crest length of the side weir is 715 m. On a length of 575 m the crest level is 3.7 m lower than the surrounding dike. The masonry made weir is equipped with a 1.75 m high fuse plug located on the actual weir. The design discharge when the side weir enters into operation is given by $Q = 6000\ m^3/s$.

On the lower Rhone river in the south of France between Valence and Montélimar a concrete side weir in combination with a syphon has been installed to divert flow into a retention bassin (Fig. 2.2). For low discharges the syphon first enters into operation. For higher discharges exceeding the capacity of the syphon the side weir enters into operation.

In Switzerland several side weirs and overflow dams exist. Based on a heavy flood event in 1987 on the Reuss river in the canton of Uri, among other

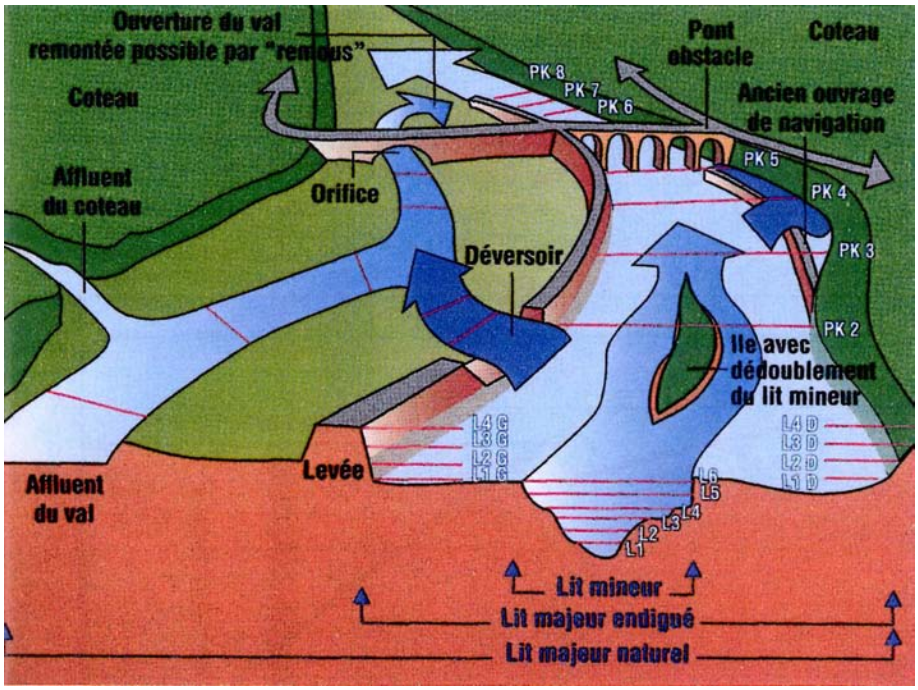

Figure 2.1: Definition sketch of the side weir on the middle Loire river, Orléans, France (Boisseau et al. (n.d.)).

Figure 2.2: Side weir on the lower Rhone river between Valence and Montélimar, France (photo: B. Rosier).

engineering protection works, the installation of a side overflow dam has been intended (VAW (1989), VAW (1995)). In Altdorf an overflow dam consisting of two 180 m long sections has been constructed. The spilled discharge is diverted on the highway (Bosshard (2000)).

In the framework of the 3^{rd} correction of the river Rhone upstream of Lake Geneva in the canton of Valais overflow dams and side weirs are planned to be installed (SRCE (2000)). Within this context an experimental scale study has been performed in 2005/2006 at the Laboratory of Hydraulic Constructions (LCH). The subject of this study has been the implementation of fuse plugs on the Rhone river close to the village of Viège.

In Figure 2.3 an overflow dam on the river Broye near Payerne in the west of Switzerland is presented. Besides flood control management, the main purpose of this structure is the ecological flooding to reestablish a riparian forest.

Figure 2.3: Overtopping dam on the river Broye, Payerne, Switzerland (photo: G. De Cesare).

In the centre of Switzerland, two lateral overflows equipped with tilting fuse gates are installed on the river Engelbergeraa. These devices have been in operation during the flood in August 2005 (Fig. 2.4).

In Figures 2.5 and 2.6 two examples of overflow dams in the south of Germany close to Karlsruhe are presented.

Figure 2.4: Side weirs equipped with tilting fuse gates on the river Engelbergeraa, centre of Switzerland (photo: Swiss air force).

Figure 2.5: Side overflow device on the river Alb, Karlsruhe, south of Germany (photo: B. Rosier).

Figure 2.6: Side overflow dam on the river Erlengraben, Karlsruhe, south of Germany (photo: B. Rosier).

2.6. Conclusion

Resuming, the literature review indicates that at the current stage of research lateral overflow on fixed bed conditions is well studied. The same accounts for expressions referring to the side weir discharge coefficient, sediment transport and bed morphology. Almost no investigations deal with the interaction of lateral overflow, sediment transport and bed morphology as a combined problem and no integral approach relating them to each other has been developed yet.

3. Theoretical Background

The theoretical background necessary for the investigation of a side overflow and its interaction with bed-load transport and bed morphology is presented in detail in appendix A.

The following important aspects relevant for the conduction of the present work have been studied:

- Appendix A.1: Bed material properties:
  - Particle size,
  - Particle fall velocity of sediments in still and flowing water,
  - Density and porosity of alluvial bed material and
  - Angle of repose of sediment particles.
- Appendix A.2: Flow equations and flow resistance:
  - Velocity distribution, bed shear stress and friction laws and
  - Granular skin roughness.
- Appendix A.3: Bed forms:
  - Classification of bed forms,
  - Geometry of bed forms and
  - Migration velocity of bed forms.
- Appendix A.4: Effective or total bed roughness:
  - Methods for bed roughness estimation based on grain and bed form parameters and
  - Methods for bed roughness estimation based on integral parameters.
- Appendix A.5: Side wall correction procedures:
- Appendix A.6: Sediment transport capacity:
  - Process of sediment transport,

  - Approach of Meyer-Peter and Müller (1948),
  - Approach of Schoklitsch (1950),
  - Approach of Smart and Jäggi (1983),
  - Approach of Van Rijn (1984a) and
  - Synopsis of bed-load transport equations.

- Appendix A.7: Side weirs and spatially varied flow:
  - Types of flow over a side weir,
  - Side weir equation and
  - Discharge coefficient of side weir.

4. Experimental Setup and Test Procedure

In this paragraph the reflections preceding the design and conception of the testing facility are described. In addition an overview of the laboratory flume, the tested parameters as well as the adopted measurement techniques and data acquisition systems is given. Finally, the testing procedure is described.

In this context it is worthy to mention that the concept of the experimental setup has been designed by Sheila Demierre, Ph.D. student at the LCH from 2000 to 2002. Sheila Demierre also conducted tests under fixed bed conditions as well as preliminary tests with a mobile bed. The experiments under mobile bed conditions have been performed by Frédéric Jordan. The measurement concept and the data acquisition devices (water level and flow velocity) have been designed by Daniel Hersberger. Both, Frédéric Jordan and Daniel Hersberger, have been engaged as research associates and Ph.D. students at the LCH at that time (2002/2003).

4.1. Model Scale and Reference Case

4.1.1. Model Scale Relations and Similitude

Usually, free surface hydraulic models are run according to the criterion of Froude similitude. This means that the same relationships for inertia and gravity forces apply in the prototype and in the model.

Introducing the geometrical length scale:

$$\lambda_L = \frac{L_{prototype}}{L_{model}} \tag{4.1}$$

Froude-scale models have to follow the relation:

$$Fr_L = \frac{v_L}{\sqrt{\lambda_g \cdot \lambda_L}} = 1 \tag{4.2}$$

Assuming that the acceleration due to gravity is equal in the prototype and in the model ($\lambda_g = 1$), the relations presented in Table 4.1 are obtained for a Froude-scale model (Kobus (1978)).

Table 4.1: Scale relations for a Froude model.

Type of parameter	Parameter	Froude-scale condition
geometric	length	$\lambda_L = L_{prototype}/L_{model}$
	area	$\lambda_A = \lambda_L^2$
cinematic	velocity	$\lambda_v = \lambda_L^{1/2}$
	discharge	$\lambda_Q = \lambda_L^{5/2}$
	time	$\lambda_t = \lambda_L^{1/2}$

In addition to the scale relations presented in Table 4.1, the roughness, e. g. the Strickler coefficient, has to be adequately transferred to the model scale:

$$\lambda_{k_{st}} = \lambda_L^{-1/6} \tag{4.3}$$

4.1.2. Reference Case

In order to design the experimental facility and the model conditions a relation to a real case appears to be necessary. This will also facilitate the transfer from theory to practical engineering studies.

The river referring to is the river Rhone upstream of Lake Geneva located in the canton of Valais between the villages of Viège and Le Bouveret in Switzerland.

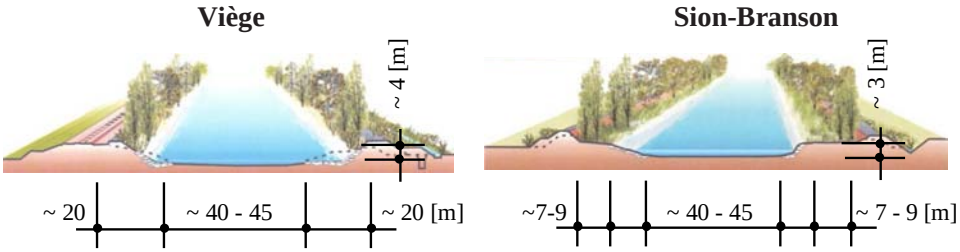

Figure 4.1: Characteristic cross sections of the Rhone river upstream of Lake Geneva (SRCE (2000)).

Characteristic geometric and hydraulic parameters for this river reach are presented in Figure 4.1 and Table 4.2. The average bottom slope is $S_0 = 0.2$ %.

The grain size distribution determined in Monthey yields a mean diameter of $d_{50} = 35\ mm$. With respect to hydraulic conditions typical design discharges have been determined according to studies conducted in the framework of the 3^{rd} correction of the river Rhone. The requested data is provided by SRCE (2000).

Table 4.2: Characteristic geometric and hydraulic parameters for the Rhone river in the reference reach.

Q $[m^3/s]$	B $[m]$	y $[m]$	A $[m^2]$	v $[m/s]$	Fr $[-]$
800	80.00	3.00	240	3.33	0.61
1000	80.00	3.50	280	3.57	0.61

4.1.3. Model Scale Factor

According to the reflections in the two preceding paragraphs and having the dimensions of the designated flume available at the Laboratory of Hydraulic Constructions (LCH) in mind, the model scale factor for the experimental investigation has been chosen as follows:

$$\lambda_L = \frac{L_{prototype}}{L_{model}} \approx \frac{50}{1} \tag{4.4}$$

4.2. Laboratory Flume

The experiments have been conducted in a recirculating rectangular prismatic glass-sided open-channel main flume being 40.00 m long, 2.00 m wide and 1.20 m deep (Canal Vevey). The flume slope was horizontal, the requested bottom slope of the mobile bed has been achieved by adjusting the sediment layer. The main flume was subdivided longitudinally into two separate channels. The first channel, 20.00 m long and 1.50 m wide, represents the actual testing facility with the mobile bed. The second one, 0.47 m wide, constitutes a lateral channel enabling to evacuate the laterally diverted discharge. The layout of the experimental setup is shown in Figures 4.2, 4.3 and 4.6.

The side weir was located on the right channel bank 5.00 m or 40 flow depths from the main-channel inlet (test series B). For test series C and D the position of the side overflow was 3.50 m or 32 flow depths and 26

flow depths, respectively, downstream from the main-channel inlet. The crest was horizontal and rectangular with a crest width of 0.025 m. The up-and downstream weir corner consisted of semi-circle profiles.

At the end of the mobile bed reach a plate has been installed to fix the sediments. The collection of bed material transported out of the main channel was attained by the arrangement of three restitution basins at the channel outlet.

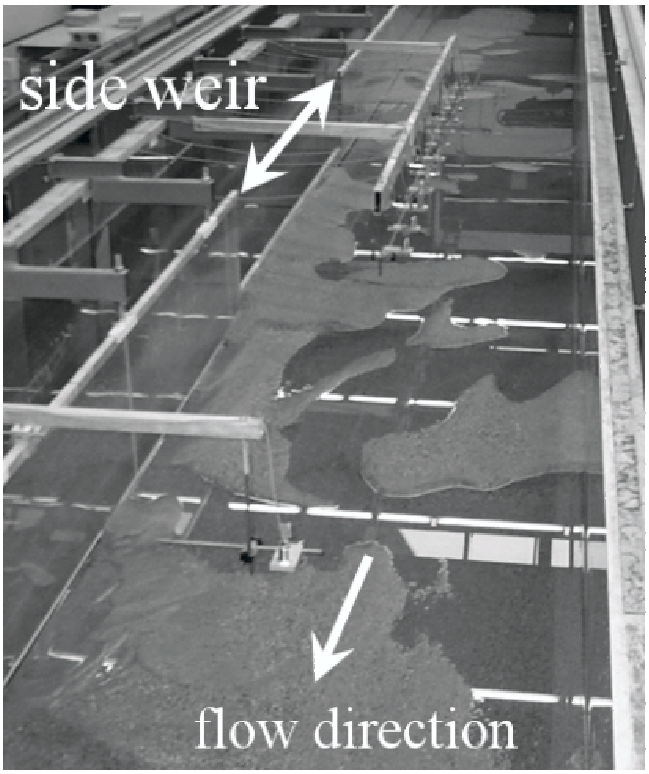

Figure 4.2: Laboratory setup with main channel and mobile bed, side weir and evacuation channel (see also Figs 4.3 and 4.6).

4.3. Tested Parameters

The following initial (!) parameters have been considered as test parameters (Tab. 4.3, for definition see Fig. 4.4):

- upstream discharge (Q_1),
- bottom slope (S_0),
- sill height of side weir (w_D),

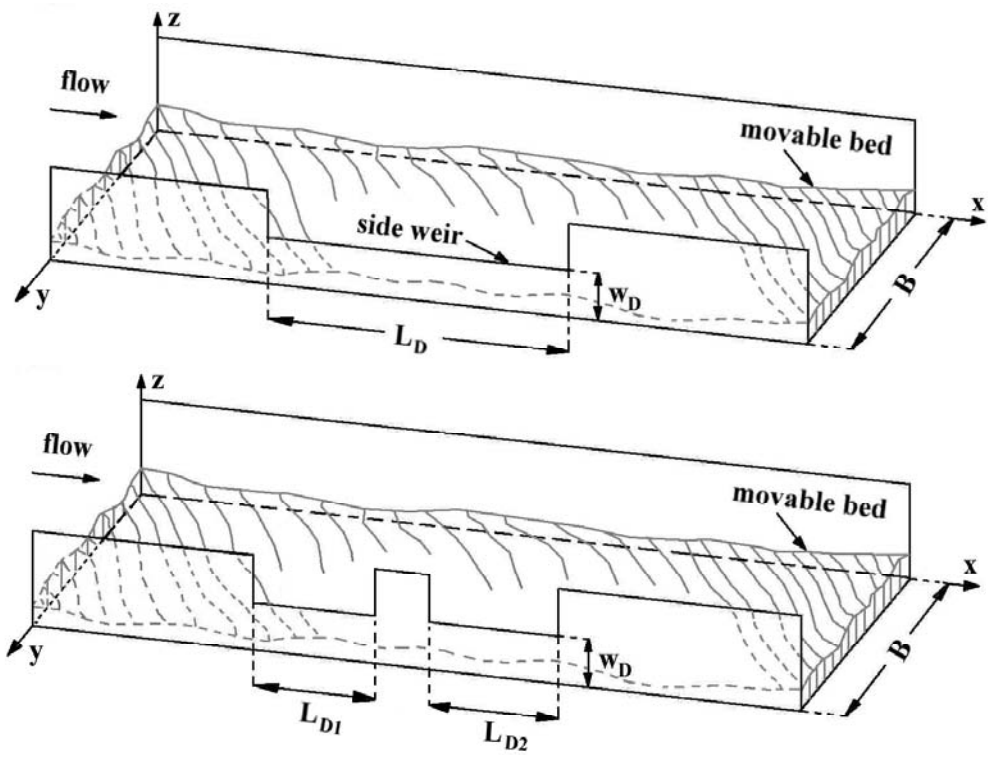

Figure 4.3: Definition sketch of experimental setup for one side weir (top) and two side weirs (bottom).

- weir crest length (L_D) and
- number of weirs (n_D).

The stepwise increase and decrease of the upstream discharge for test series C and D has been chosen to simulate the passage of a flood (flood hydrograph). The experiments have been stopped when the side overflow discharge has reached a rather stable value for a certain time increment (experiment duration t). The channel width (B) has been constant throughout all test series. Experiment $A01$ served as a reference test without side overflow.

4.4. Properties of Bed Material

The mobile bed consisted of sand material having the characteristics shown in Table 4.4. In Figure 4.5 the grain size distributions for the Rhone river and the experimental study are presented. The median particle size of $d_{50} = 0.72\ mm$ corresponds to coarse sand on the AGU-grain size scale (Tab. A.1). Measurements and indications of the company selling the bed

Table 4.3: Overview of test series and initial (!) parameters studied.

N^o of experiment	N^o of weirs n_D [$-$]	Length of weir crest L_D [m]	Sill height w_D [m]	Bottom slope S_0 [%]	Upstream discharge Q_1 [l/s]	Experiment duration t [min]
$A01$[1)]	$***$	$***$	$***$	0.2	153	120
$B01$	1	3.00	0.10	0.2	131	188
$B02$	1	3.00	0.10	0.2	181	183
$B03$	1	3.00	0.10	0.4	177	117
$B04$	1	3.00	0.10	0.1	98	245
$B05$	1	3.00	0.10	0.2	144	128
$B06$	1	3.00	0.10	0.3	148	138
$C01$	1	6.00	0.09	0.2	160	125
$C02$	1	6.00	0.09	0.2	197	120
$C03$	1	6.00	0.09	0.2	221	120
$C04$	1	6.00	0.09	0.2	179	120
$C05$	1	6.00	0.09	0.2	181	120
$D01$	2	2.50	0.09	0.2	166	125
$D02$	2	2.50	0.09	0.2	182	120
$D03$	2	2.50	0.09	0.2	222	120
$D04$	2	2.50	0.09	0.2	182	120
$D05$	2	2.50	0.09	0.2	150	120

[1)]reference case without side weir

material resulted in a sediment density of $\rho_s = 2650\ kg/m^3$. Using the measured bulk sediment density (sediment-air mixture) of $\rho_s = 1447\ kg/m^3$, the porosity has been determined to be $p = 45.4$ % (paragraph A.1.3)

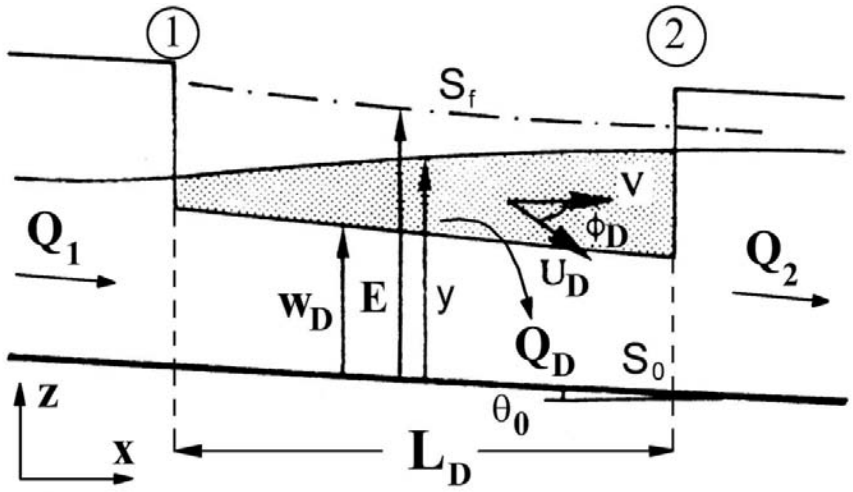

Figure 4.4: Definition sketch for tested parameters (from Sinniger and Hager (1989), modified).

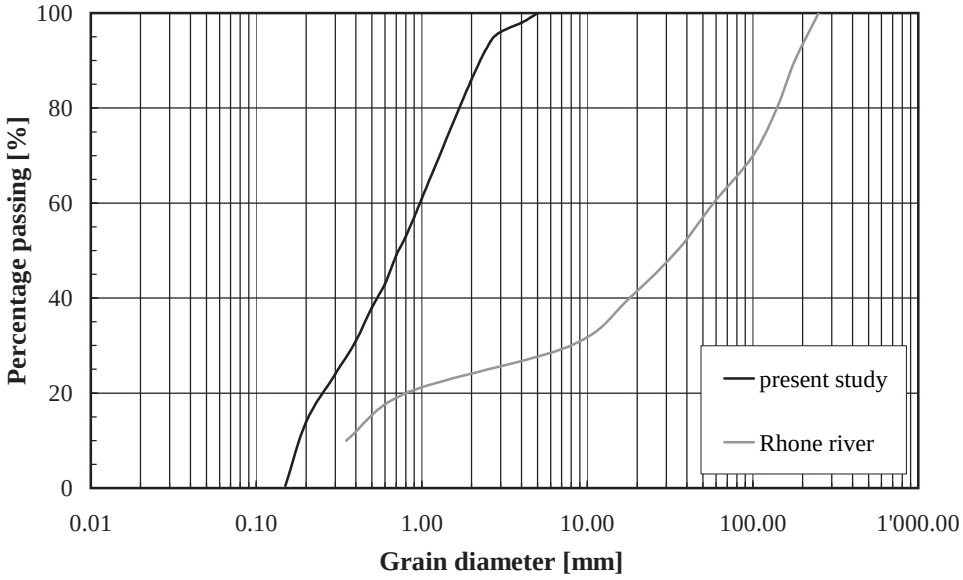

Figure 4.5: Grain size distribution for the Rhone river and the present study.

Table 4.4: Grain size distribution properties for the bed material used in the present study.

d_{10} [mm]	d_{16} [mm]	d_{30} [mm]	d_{35} [mm]	d_{50} [mm]	d_{65} [mm]	d_{84} [mm]
0.18	0.22	0.38	0.45	0.72	1.12	1.89
d_{85} [mm]	d_{90} [mm]	d_m [mm]	d_g [mm]		σ_d [$-$]	σ_g [$-$]
1.95	2.28	1.05	0.64		2.98	2.95

4.5. Sediment Supply

The sediment quantities to be supplied were estimated according to the formula of Smart and Jäggi (1983) (paragraph A.6.4) and adjusted during the tests in order to maintain both uniform flow and equilibrium transport conditions in the approach channel upstream of the side overflow. This has been controlled by water level measurements. In Table 4.5 average sediment quantities supplied during the entire experiment duration are listed.

4.6. Measurement Technique and Data Acquisition

In the following paragraphs the measurement techniques to gather upstream discharge, side overflow intensity, water level and flow depth, flow velocity and the final bed topography are presented. The disposition of water level and $2D$-flow flow field recordings are depicted in Figure 4.6.

4.6.1. Discharge and Overflow Intensity

The upstream discharge (Q_1) was delivered by the use of three pumps feeding one pipe controlled by an electromagnetic flow meter. A steady flow rate could therefore be easily set and maintained accurately throughout the duration of each test.

The side overflow discharge (Q_D) was determined using a standard sharp-crested measuring weir installed in the evacuation channel and equipped with an ultrasonic gauge (Fig. 4.6). The measurement procedure is explained in paragraph 5.1.3, the results are presented in paragraph 5.3.2.

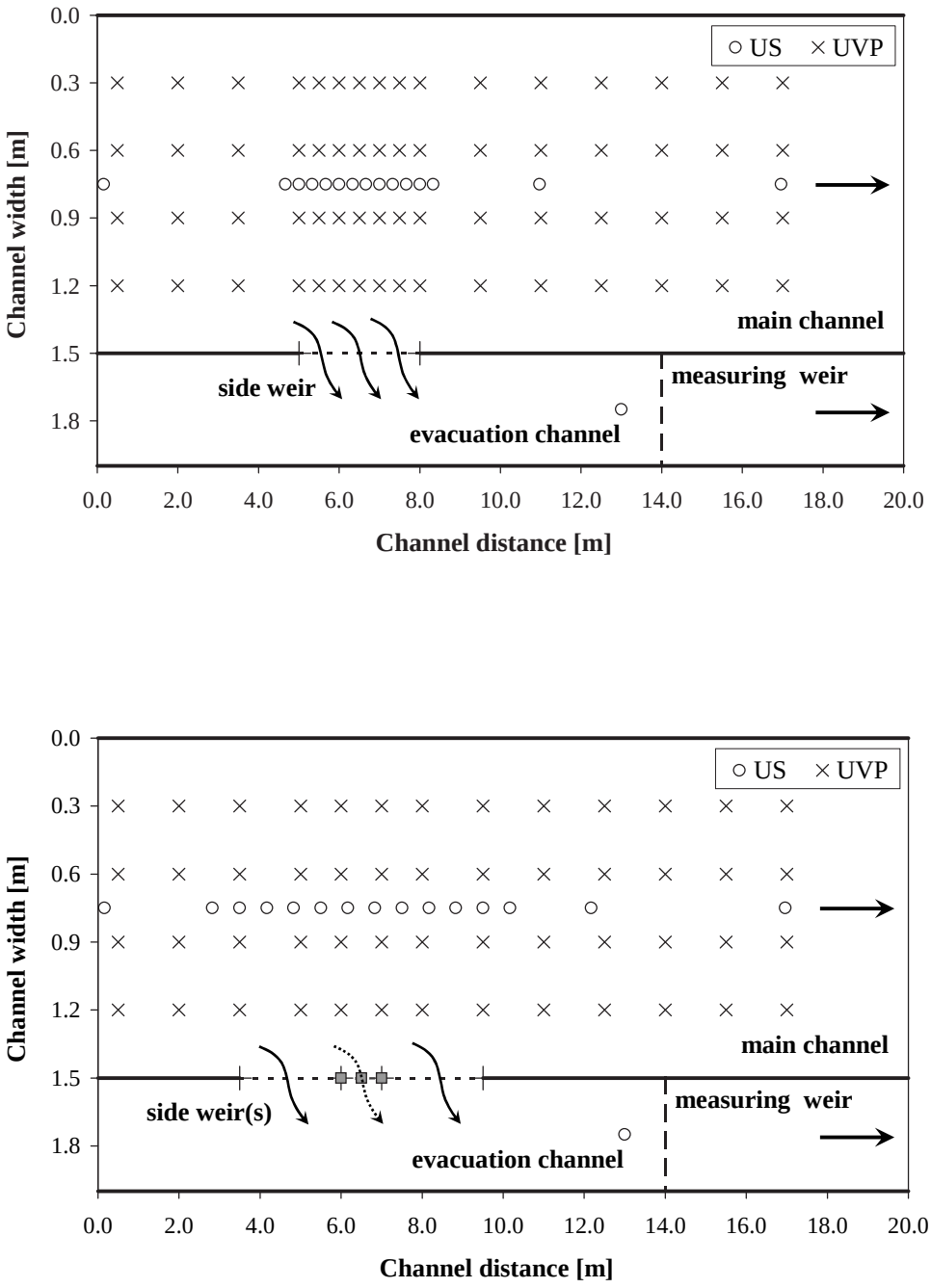

Figure 4.6: Plan view of the experimental setup and disposition of water level (US) and velocity (UVP) recordings for test series B (top) and test series C and D (bottom).

Table 4.5: Average sediment supply at the channel entrance ($Q_{sb,in}$) for the present study. $q_{sb,in}$ is calculated from $Q_{sb,in}$ using $\rho_s = 2650\ kg/m^3$ and $B = 1.50\ m$. Φ_{in} is obtained applying Equation A.124.

N^o of experiment	$Q_{sb,in}$ $[kg/min]$	$q_{sb,in}$ $\left[m^3/(s\ m)\right]$	Φ_{in} $[-]$
$A01$	15.25	$0.64 \cdot 10^{-4}$	0.468
$B01$	8.70	$0.37 \cdot 10^{-4}$	0.267
$B02$	17.73	$0.74 \cdot 10^{-4}$	0.544
$B03$	9.10	$0.38 \cdot 10^{-4}$	0.279
$B04$	9.67	$0.41 \cdot 10^{-4}$	0.297
$B05$	16.72	$0.70 \cdot 10^{-4}$	0.513
$B06$	17.61	$0.74 \cdot 10^{-4}$	0.541
$C01$	9.56	$0.40 \cdot 10^{-4}$	0.293
$C02$	42.69	$1.79 \cdot 10^{-4}$	1.310
$C03$	51.76	$2.17 \cdot 10^{-4}$	1.589
$C04$	39.82	$1.67 \cdot 10^{-4}$	1.222
$C05$	39.82	$1.67 \cdot 10^{-4}$	1.222
$D01$	27.04	$1.13 \cdot 10^{-4}$	0.830
$D02$	26.54	$1.11 \cdot 10^{-4}$	0.815
$D03$	39.82	$1.67 \cdot 10^{-4}$	1.222
$D04$	22.34	$0.94 \cdot 10^{-4}$	0.686
$D05$	19.91	$0.84 \cdot 10^{-4}$	0.611
average[1)]	24.93	$1.05 \cdot 10^{-4}$	0.765

[1)] without test series $A01$

4.6.2. Water Level and Flow Depth

Water levels along the main-channel as well as on the sharp-crested measuring weir in the evacuation channel were recorded continuously with a frequency of one measurement per second by the use of an ultrasonic gauge (US). The

voltage, ranging between 0 and 10 V, was transformed into a distance to a reference level being the crest of the side weir (elevation above flume bottom $z = 0.35\ m$) and the crest of the measuring weir ($-0.172\ m$ lower than the side weir crest), respectively. The error of the level measurement is less than $1\ mm$ (average $\pm\ 0.5\ mm$).

Altogether, 15 ultrasonic gauges were installed longitudinally in the centreline of the main-channel, two located upstream of the side weir, 10 in the weir reach and three downstream of the weir. One US-probe was located upstream of the measuring weir in the evacuation channel (Figs 4.6 and Tab. 4.6). The distance between each probe in the weir alignment was $1/3\ m$ for test series B and $2/3\ m$ for test series C and D.

The disposition of the US-probes in the channel centreline is due to the fact that for side overflow experiments reported in literature the flow depth has always been measured in the centreline (e. g. Subramanya and Awasthy (1972)). According to Ranga Raju et al. (1979) the effect of water surface draw-down is restricted to the immediate vicinity of the weir. As such, the flow depth at the centreline of the main-channel can be used as a reference depth.

Based on the water level measurements the flow depth is obtained by the use of the DEM. Indicative depth values during the experiments are given by the UVP-measurements.

4.6.3. Flow Velocity

Velocities were measured with an Ultrasonic Doppler Velocity Profiler (UVP) (Metflow SA, Model UVP-XW) allowing to obtain instantaneously a $1D$-velocity profile over the entire flow depth (Metflow (2000)). The probes had an emitting frequency of 2 MHz. For each $1D$-profile, 128 data points in time were recorded with a spatial resolution of 128 points over flow depth, representing 16384 data points (Fig. 4.7). The sampling time for one profile was 14 ms, hence for 128 profiles the sampling time was 1.8 sec. After 128 measured profiles the multiplexer switched to the next probe. Consequently, the measured $2D$-flow field was not instantaneous. However, with respect to the short recording time, an almost constant flow field might be assumed for average values. The acquisition frequency was 71 Hz. This would allow the analysis of turbulence characteristics.

Eight probes, each inclined by 30° to the vertical, were mounted on a measuring frame fixed on a traversing beam (Fig. 4.8). Due to the inclination, the vertical control volume yielded an approximate diameter of 7 cm. Four probes were orientated in the longitudinal channel direction and four perpendicular to the main-channel axis, thus allowing to constitute a $2D$-velocity field. The probes orientated in the channel axis were inclined opposite to the main flow direction to reduce disturbance induced by submergence of

Table 4.6: Measuring sections for water level (US) and velocity recordings (UVP). US-probe N^o 16 is located in the evacuation channel (measuring weir). The dashed lines indicate the up-and downstream weir corner, respectively.

Test series B				Test series C and D			
N^o US probe	x_i $[m]$	N^o UVP probe	x_i $[m]$	N^o US probe	x_i $[m]$	N^o UVP probe	x_i $[m]$
		1	0.50				
1	0.16	2	2.00	1	0.16	1	0.50
2	4.67	3	3.50	2	2.82	2	2.00
3	5.00	4	5.00	3	3.50	3	3.50
4	5.33	4*b*	5.50	4	4.17	4	5.00
5	5.67			5	4.83		
6	6.00	5	6.00	6	5.50		
7	6.33	5*b*	6.50	7	6.17	5	6.00
8	6.67			8	6.83	6	7.00
9	7.00	6	7.00	9	7.50		
10	7.33	6*b*	7.50	10	8.17	7	8.00
11	7.67			11	8.83		
12	8.00	7	8.00	12	9.50	8	9.50
13	8.33	8	9.50	13	10.17		
14	11.00	9	11.00	14	12.17	9	11.00
15	17.00	10	12.50	15	17.00	10	12.50
		11	14.00			11	14.00
		12	15.50			12	15.50
		13	17.00			13	17.00

the probes and to prevent air entrainment in the measuring volume. Velocity profiles were recorded every 30 minutes for 16 (test series B) and 13 (test series C and D) streamwise cross sections. For test series B three probes were located upstream of the weir, seven in the array of the weir (every 0.5 m) and

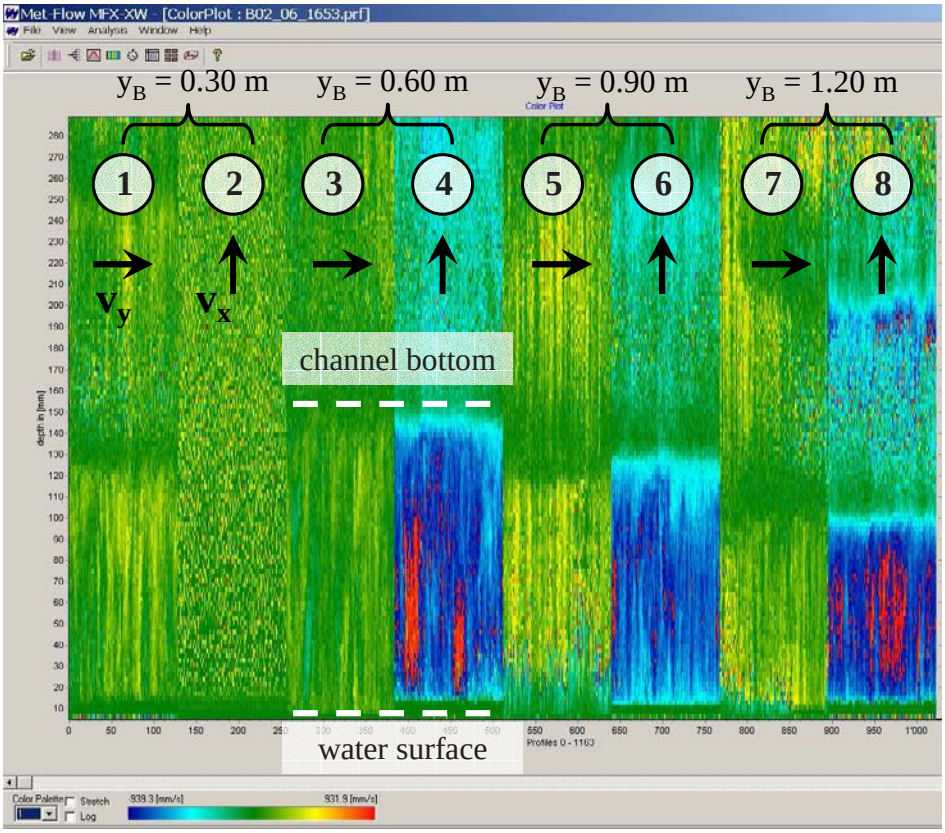

Figure 4.7: UVP software showing a sample file. For each laterwalwise position (e. g. $y_B = 0.60\ m$) two probes (e. g. probe N^o 3 and 4) constitute the $2D$-velocity field in the $x - y$-plane. One probe measured the transverse velocity (v_y), one the streamwise velocity (v_x). Probe N^o 2 has been out of order.

six in the downstream section of the channel. With respect to test series C and D two probes were installed upstream of the weir, six in the weir alignment and five downstream of the weir (Figs 4.6 and Tab. 4.6). Concerning the lateralwise disposition, every 0.30 m a probe was mounted.

The velocity measurements were also used to detect the bed. The bottom surface was obtained from the signal for which the velocity as well as the variance were close to zero (Hersberger (2002), Rosier et al. (2004d)). Thus, besides the high precision DEM obtained for the final bed topography, indicative values for the bottom elevation during the experiments could be obtained. Moreover, an indication for flow depth during the experiments was achieved. Using the DEM as a reference, absolute flow depths, e. g. with respect to the weir crest level, can be derived.

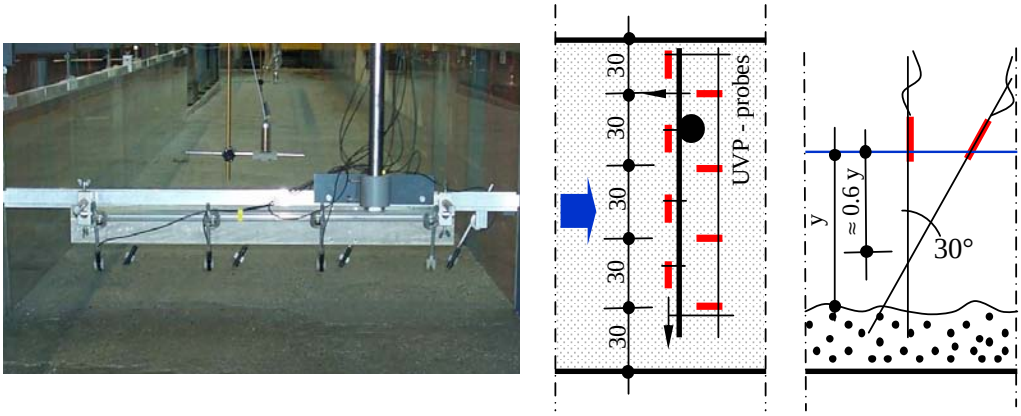

Figure 4.8: Disposition and configuration of UVP-probes on the measuring frame.

4.6.4. Bed Topography

As far as the monitoring of the river bed topography is concerned, a photogrammetrical approach has been applied serving as a three-dimensional surface measurement tool. Digital photogrammetry is based upon automated analysis of digital imagery using the basic principle of perspective projection. Two images of an object are acquired from two separate locations with known coordinates (Fig. 4.9). If at least five points (photocontrol points) at known object locations are clearly visible on both images a spatial resection can be carried out to derive the positions and orientations of the images (Fig. 4.10). By the help of automated stereo matching conjugate points can be identified and elevation coordinates can be extracted (Lane et al. (2001), Geisler et al. (2003)).

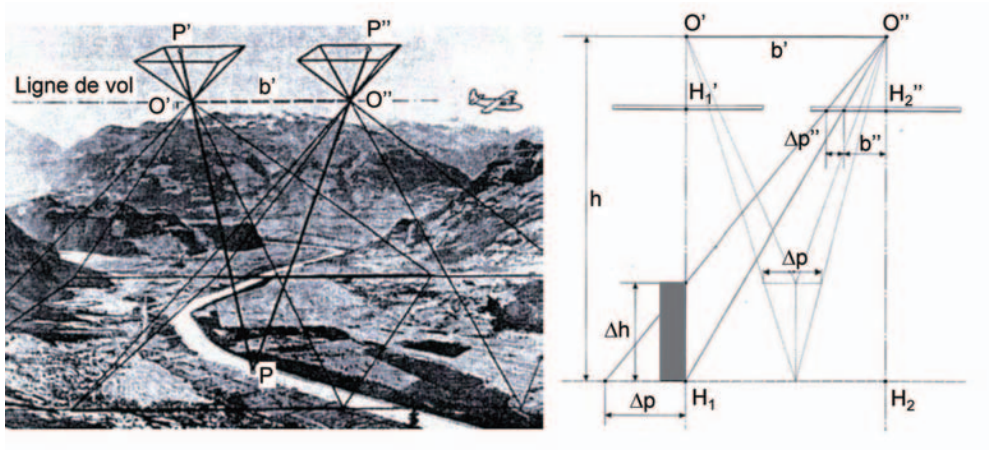

Figure 4.9: Digital photogrammetry and geometry of stereoscopic coverage (Kölbl (1988)).

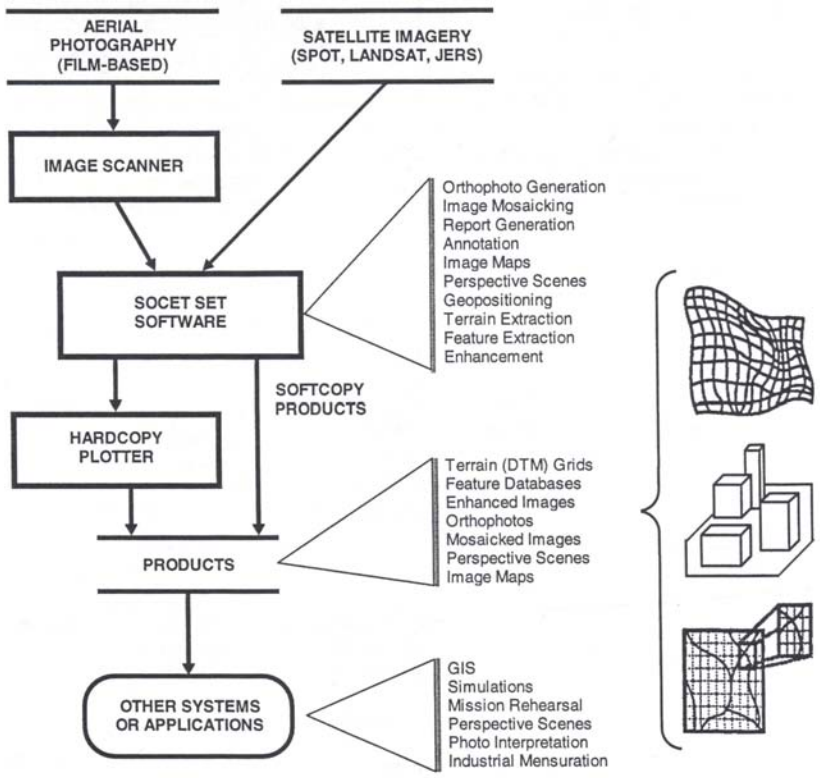

Figure 4.10: Basic steps for spatial resection used in the present study (Kölbl (1988)).

For the present study imagery was acquired with a Zeiss Jena UMK 10/1318 calibrated camera having a focal length of 64.32 mm. Five photographs with an overlap of 60 % have been taken to cover the whole channel. This has been done for the initial flat bed situation and after each experiment for the final bed situation after controlled drainage of the channel. 18 photocontrol points were distributed along the sidewalls of the channel and in the laboratory not to create unacceptable disturbances while inserted in the mobile bed. The resulting flying height of the camera (mounted at the gantry crane) to cover all photocontrol points was 6.50 m above the flume.

After image scanning (image size 130 x 180 mm) on a DSN 200 Helava-Leica scanner (resolution: pixel dimension 10 μm) the triangulation and orientation (position and aiming angles) process as well as the creation of the DEM have been performed on the photogrammetric workstation DPW 770 by Helava-Leica running on Unix. The program system used for the analysing process is called SocetSet. For the creation of the DEM a grid resolution of 2.5 x 2.5 cm has been chosen. This resolution corresponds to investigations conducted by Wormleaton et al. (2004). A summary of the stages of a photogrammetrical analysis is shown in Figure 4.11.

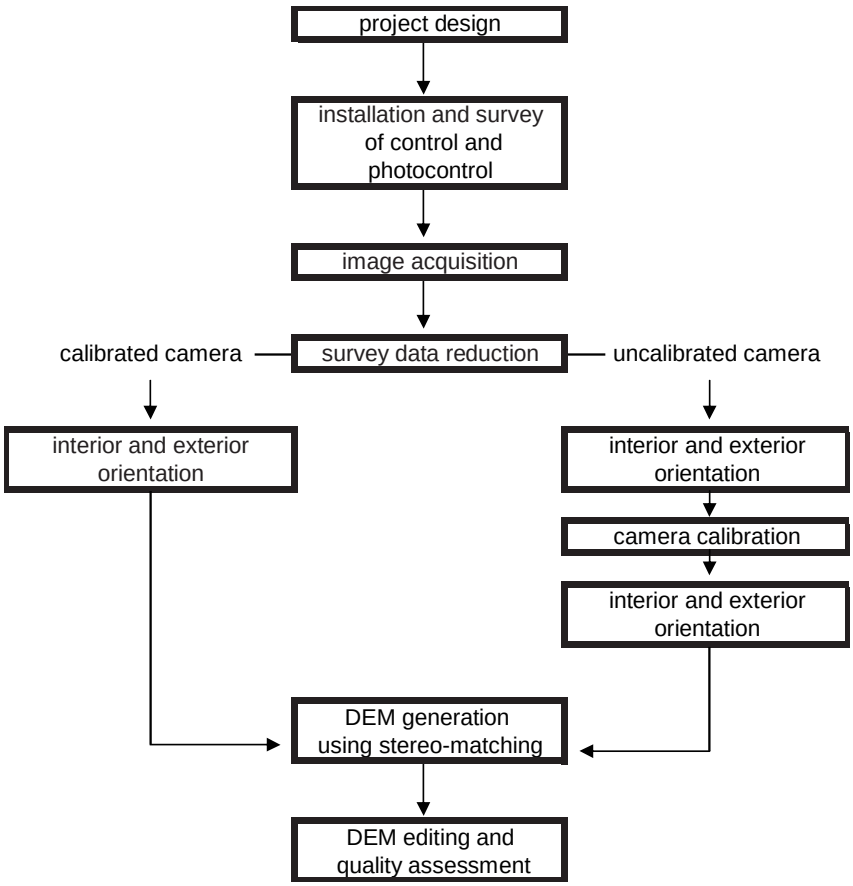

Figure 4.11: Basic stages in data collection using digital photogrammetry (Lane et al. (2001)).

4.6.5. Other Instrumentation

During all experiments photographs from different fixed points were taken. Thus, e. g. photographs taken through the glass-sided channel walls, served to estimate the bed form migration velocity. Moreover, special phenomena and observations were documented by video recordings.

4.6.6. Error Estimation

The accuracy of the water level measurements is $\pm$ 0.5 mm (paragraph 4.6.2), the precision of the digital elevation model has been determined to be $\pm$ 2.5 mm (paragraph 5.1.4). Hence, the error for the flow depth on the weir (h_D, pressure head) is about $\pm$ 3.0 mm.

Applying an average side overflow discharge coefficient of $C_D = 0.389$ (paragraph 5.3.2) and a mean flow depth on the weir of $h_{D,1} = 0.124$ m

the specific side overflow (q_D) according to the general equation of weirs (Eq. A.158) yields $q_D = 0.050\ m^2/s$. Taking into account the error of $\pm\ 3.0\ mm$ for the flow depth on the weir the overflow discharge is $q_D = 0.052\ m^2/s$ for $h_{D,1} = 0.124\ m + 3\ mm$ and $q_D = 0.048\ m^2/s$ for $h_{D,1} = 0.124\ m - 3\ mm$. As a consequence, the precision of the measured side overflow can be stated to be $q_D = 0.052\ m^2/s \pm\ 0.002\ m^2/s$ or $\pm\ 0.002/0.052 = \pm\ 3.85\ \%$.

4.7. Test Procedure

The channel facility originally possesses a horizontal slope. The initial slope of the mobile bed for each experiment has been created by adjusting the sediment layer to the requested slope. Within this procedure the sediment thickness in the middle of the side weir was fixed to 0.25 m, becoming thicker in the upstream direction and thinner in the downstream direction. The mean thickness of the sand layer was approximately 0.24 m. Once the requested slope of the mobile bed was created, the bed surface was flattened. At the channel inlet slightly upstream of the actual testing reach a coarser sediment layer to prevent the bed from erosion was introduced. At the channel exit a plate was installed to fix and keep the sediment layer in place.

Before slowly filling the main-channel with water a tilting gate at the exit of the channel facility was risen. Thus, the main-channel and the evacuation channel were carefully filled up with water until the horizontal side weir crest was reached. Then, the water level and velocity recordings were started. At this stage the reference level for the water level measurements, corresponding to the side weir crest height, was determined. In a next step the tilting gate was completely lowered and the discharge was increased to the requested one, being constant throughout the entire duration of the experiment. The overall flow regime was maintained subcritical, however, exceptionally locally supercritical flow conditions were observed.

The measuring frame carrying the UVP-probes was moved manually from one cross section to the next one, thus creating a continuous cycle passing every 30 minutes at each cross section.

The sediments were fed manually some distance upstream of the actual testing reach via a conveyer belt. As mentioned before the quantities to be supplied were estimated according to the formula of Smart and Jäggi (1983) and adjusted during each test in order to maintain both, uniform flow and equilibrium transport conditions in the approach channel upstream of the side overflow. In Table 4.5 mean sediment quantities supplied during the entire experiment duration are listed.

Regarding experiment duration, the time range chosen corresponds to the peak period when a lateral diversion structure such as a side weir is in operation. For this, characteristic peak flow durations observed in the

river Rhone upstream of Lake Geneva in Switzerland have been investigated. Moreover, the tests were run until a dynamic equilibrium was obtained. This was indicated by a rather stable spill discharge for a certain period of time. Attaining this condition, the assumption was made that the aggradation and the local sedimentary deposit were in an almost equilibrated state. For a longer duration, e. g. $t \rightarrow \infty$, the maximum bed elevation, being the most important parameter influencing the side over flow discharge, will not change in a considerable way. Probably, the downstream slope of the aggraded channel reach will become smoother due to sediment deposition with elapsing experiment time but this effect will be rather negligible compared to the maximum bed elevation. A discussion concerning the duration of the experiments is given in paragraph 6.10.1.

With respect to the side overflow intensity it is important to notice that the lateral overflow has never been submerged from downstream meaning free overfall conditions were always maintained. Otherwise, a reduction of the discharge coefficient (C_D) would have be taken into account, hence resulting in a reduced computed side overflow discharge (Q_D). This has been controlled by observation during the experiments and verified numerically according to USCE (n.d.).

The experiments were documented by photographs taken at different fixed locations as well as by video recordings.

5. Analysis and Results of the Experiments

5.1. Data Treatment

In this paragraph the treatment of raw data is described. Data processing for water levels and flow depth, flow velocity, side overflow discharge and bed topography was necessary to create the data base serving as the basis of this study. In paragraph 5.2 and appendix B an overview of characteristic data obtained from the data treatment process is given.

5.1.1. Flow Depth

Except eliminating erroneous water level values due to the passage of the UVP-measuring frame no particular data processing was required.

Since the water surface recordings (US-recordings) only yield a water level, the flow depth had to be determined by the use of the US-reference level (side weir crest level) and the digital elevation model (DEM) of the final bed morphology.

5.1.2. Flow Velocity

Due to the complexity of the flow field, especially near the side weir, several specific problems described below had to be solved.

The velocities in stream direction were rather high (up to $v_x = 1.20\ m/s$), those perpendicular to the main-channel axis an order of magnitude smaller (up to $v_y \approx \pm\ 0.20\ m/s$). Due to the lateral overflow and flow deviation induced by local sediment deposits and bed forms, both positive and negative velocities were encountered[1]. For this reason an adequate measurement

[1]Regarding streamwise velocities as obtained from the UVP-measuring device (raw data), negative velocities correspond to velocities in the direction of the main flow. For the analysis the negative streamwise velocities have been converted to positive velocities. There have been no positive streamwise velocities (raw data). As far as spanwise velocities are concerned, negative velocities (raw data) refer to velocities towards the left channel bank (opposite to the side weir), positive velocities refer to velocities towards the right channel bank (location of the side weir). The sign of the spanwise velocities has not been converted

domain had to be fixed to allow for good quality records of high as well as low velocities with positive and negative sign. The maximum detectable Doppler shift frequency is limited. This implies that there is a limitation on the maximum velocity that can be measured. The maximum velocity (v_{max}) can be either distributed two times the positive value (2 v_{max}), two times the negative value (2 ($-v_{max}$)) or equally ($\pm$ v_{max}). Due to the reason mentioned above the third option ($\pm$ v_{max}) has been chosen.

Since the value of the actual velocity cannot be reduced, a smaller component has been measured. This has been achieved by the inclination of the probes 30° to the vertical. Nevertheless, some velocity peaks were still higher than v_{max}. An interesting effect of the Doppler measurement device has therefore been revealed. If the measured velocity was higher than the maximum velocity the UVP-multiplexer shifted the measured value by $-$ 2 times the velocity range to the negative measurement domain and vice versa. If the sign of the velocity is known the recorded velocity can be corrected by shifting the negative (positive) values back to the positive (negative) domain (Fig. 5.1). This phenomenon has been described earlier by Rolland (1995) and Hersberger (2003). Consequently, this procedure was applied for the high streamwise velocities whose sign was clearly given (Rosier et al. (2004f)). For the transverse velocities no such treatment was necessary. In Figure 5.2 an example of the shifting process is given.

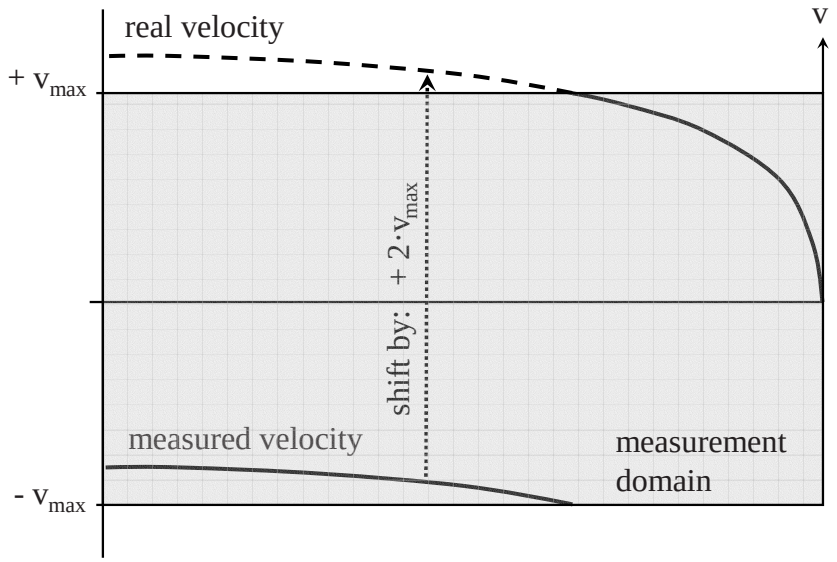

Figure 5.1: Correction of measured velocity exceeding the measurement domain by shifting back to its correct position.

The origin of the velocity profiles was not located immediately at the free water surface. This is due to the fact that the probes were submerged about

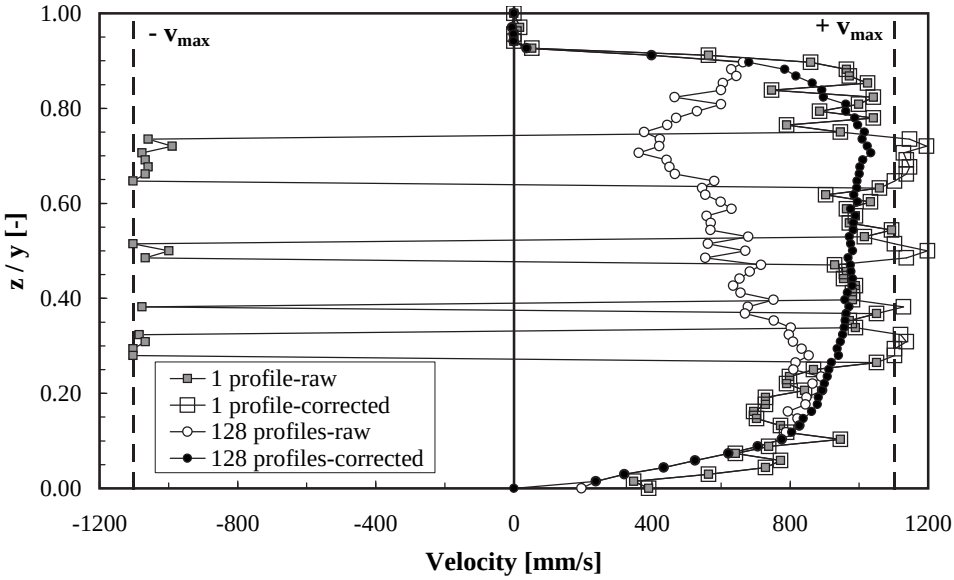

Figure 5.2: Example of the velocity shifting process applied in the present study.

10 *mm* followed by 5 *mm* minimum depth. The minimum depth is the distance between the emitting beam and the first measuring point (corresponding to the starting depth (window start) of the measuring window). Due to noise the first eight data points, having a channel distance of 2.22 *mm* each, were not included in the measurements. Consequently, the first velocity measurement was located 34 *mm* (in beam axis) below the water surface. This corresponds to 29 *mm* in vertical direction.

The UVP-measurements were also applied to detect the bed surface. The bottom surface was obtained from the signal for which the velocity as well as the variance were close to zero (Hersberger (2002)). Nevertheless, this criteria did not always match the case due to local fluctuations mainly close to the bed. Therefore, the velocity profiles had been analyzed visually on signal records. The combination of these three criteria gave fairly well results (Rosier et al. (2004d)).

5.1.3. Side Overflow Discharge

By the help of the sharp-crested measuring weir installed in the evacuation channel and applying the general equation of weirs, the discharge over a sharp-crested weir can be expressed by (Naudascher (1992)):

$$Q = \frac{2}{3} \cdot C_Q \cdot \sqrt{2g} \cdot h_Q^{3/2} \cdot L_Q \tag{5.1}$$

where C_Q discharge coefficient for sharp-crested weirs, g acceleration due to gravity, h_Q pressure head above weir crest, measured $3\ h_Q \div 4\ h_Q$ upstream of the weir, and L_Q crest length.

The discharge coefficient can be approximated according to the Rehbock-formula (Rehbock (1929)):

$$C_Q = 0.61 + 0.08 \cdot \frac{h_Q}{w_Q} \tag{5.2}$$

with w_Q sill height.

Besides this procedure, two other methods have been applied for comparison and verification (paragraph 5.3.2). The first one refers to the discharge difference $Q_1 - Q_2 = Q_D$ (with Q_1 approach discharge upstream of the weir, Q_2 discharge downstream of the weir and Q_D side overflow discharge). Q_1 is known and Q_2 has been calculated using water depths (y) from the US-measurements and velocities (v) from the UVP-measurements. Regarding the second method, the general equation of weirs (Eq. A.158) has been applied to a side overflow. Within this context, an appropriate side weir discharge coefficient (C_D) is required.

5.1.4. Digital Photogrammetry and Digital Elevation Model

As has been described in paragraph 4.6.4 the final bed morphology has been determined using digital photogrammetry. An advantage of digital photogrammetry is the spatial density of surface information. Automated stereo matching (Automatic Terrain Extraction - ATE, strategy: steep-dense) may significantly decrease data acquisition time but may also result in incorrect matches which need careful checking and perhaps manual editing of any derived digital elevation model (DEM). This process might be rather time-consuming.

The problem mentioned above has come across in the present study. A particular difficulty of the photogrammetric analysis was the considerably high relief of the bed surface due to the formation of bed forms. Especially the crest region and the lee side slope of dunes owing a steep gradient resulted in erroneous matches and poor elevation estimates. To cope with this problem the following technique has been adopted to obtain a correct DEM of high precision (Rosier et al. (2004e)).

A quality control feature for the automatic terrain extraction may indicate a successful automatic correlation or good measurement as well as the opposite. This tool is called Figure Of Merit (FOM). A FOM is a numerical value assigned by the terrain extraction process. FOMs are proportional to the average correlation coefficient, so in general the larger the number, the

better the measurement. As mentioned above, especially the lee side slope of dunes showed a low average correlation coefficient (Fig. 5.3). For this reason, DEM data points possessing an average correlation coefficient of 54 or less have been eliminated by the help of a macro written in Excel. The value of 54 has been chosen according to experiences made by Kölbl (personal communication by Prof. O. Kölbl, Laboratory of Photogrammetry, EPFL, Lausanne, Switzerland).

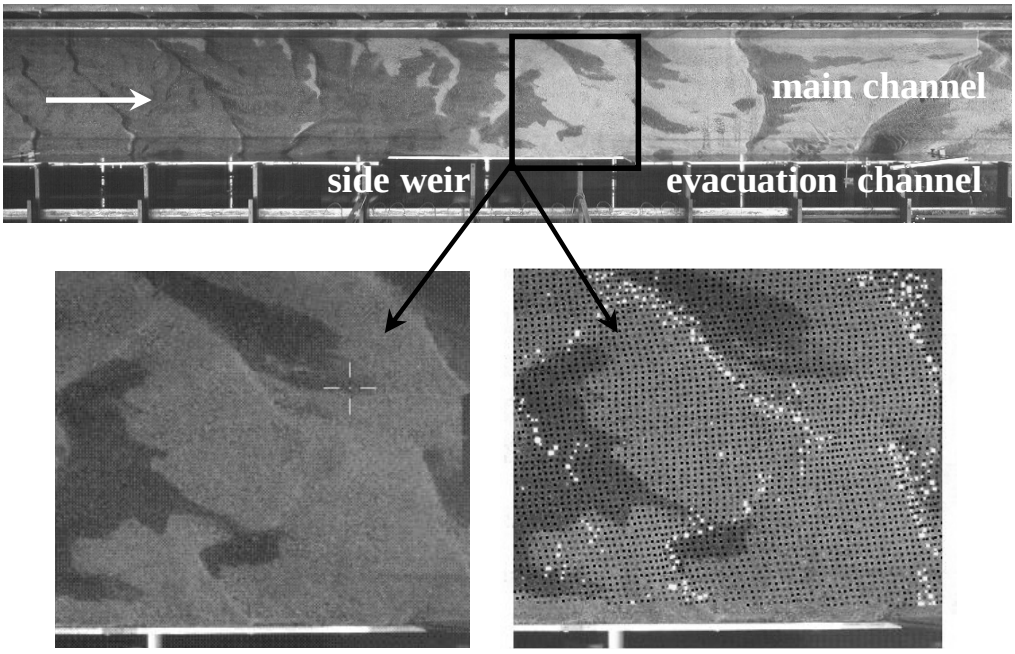

Figure 5.3: Top: Final bed surface. Bottom: Detailed view of the bed surface (left) and DEM with FOMs ≤ 54 (white) and FOMs > 54 (black) (right).

When the matches of poor quality were eliminated the DEM misses the most important information characterizing the dune covered bed surface (Fig. 5.4 and Fig. 5.5). To add the missing data points new values were interpolated from surrounding data points. For this, the software provides an interactive editing feature using stereo vision. The tool is called Geomorphic Editor. Linear features such as ridges and drains can be drawn manually by so called brake lines (Fig. 5.4). Applying this correction technique finally leads to a proper and precise DEM used for further analysis (Fig. 5.5).

Concerning the precision of the DEM obtained by the digital photogrammetric process, a vertical error of $\pm$ 2.5 mm can be assumed (oral communication by Prof. O. Kölbl, Laboratory of Photogrammetry, EPFL, Lausanne, Switzerland). This corresponds to about $\pm$ 3.5 d_{50}.

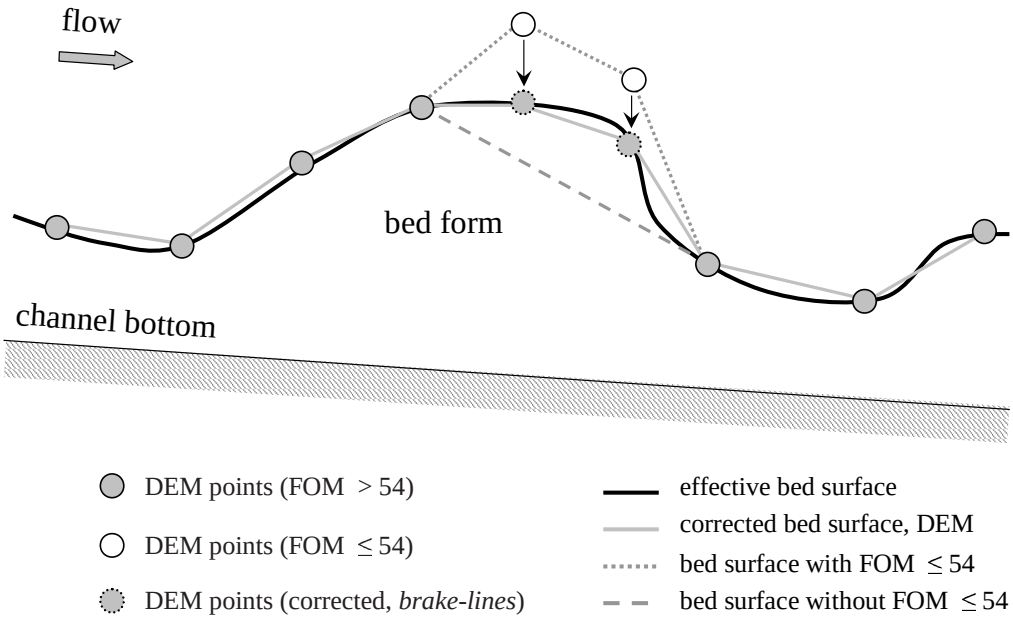

Figure 5.4: Influence of incorrect matches on the precision and quality of the DEM.

5.1.5. Determination of effective Weir Length

The aspect ratio of side weir crest length (L_D) to channel width (B, $B = 1.50\ m = constant$) for test series B is $L_D/B = 3.00\ m/1.50\ m = 2.00$. For test series C a ratio of $6.00\ m/1.50\ m = 4.00$ is obtained. In designing the flume experiments a certain influence of the number of side weirs ($n_D = 1$ or $n_D = 2$) has been assumed to be present. In analyzing the experiments it turns out that no significant impact of the number of weirs on bed morphology and flow characteristics could be observed for the configuration tested in series D. For this reason the weir length in test series D has been obtained by presuming no considerable influence of the $1.00\ m$ long separation wall between the two side overflows. Hence, L_D is the sum of the two side weir crest lengths, $L_D = L_{D1} + L_{D2} = 2.50\ m + 2.50\ m = 5.00\ m$. Consequently, L_B/B yields 3.33 (Tab. 5.1).

As can be seen in Table 5.1 the ratio L_D/B for test series D is located closer to C than to B. For a more equal L_D/B-repartition it would be preferable to have test series D being roughly situated in the middle between test series B and C. Due to this, an effective weir length has been studied (accounting for the presence of the vertical separation wall between the two weirs). Beside this aspect another reason to check the effective weir length was to verify whether the linear superposition of the two weir lengths is justified.

This verification has been done presuming a certain analogy to piers in

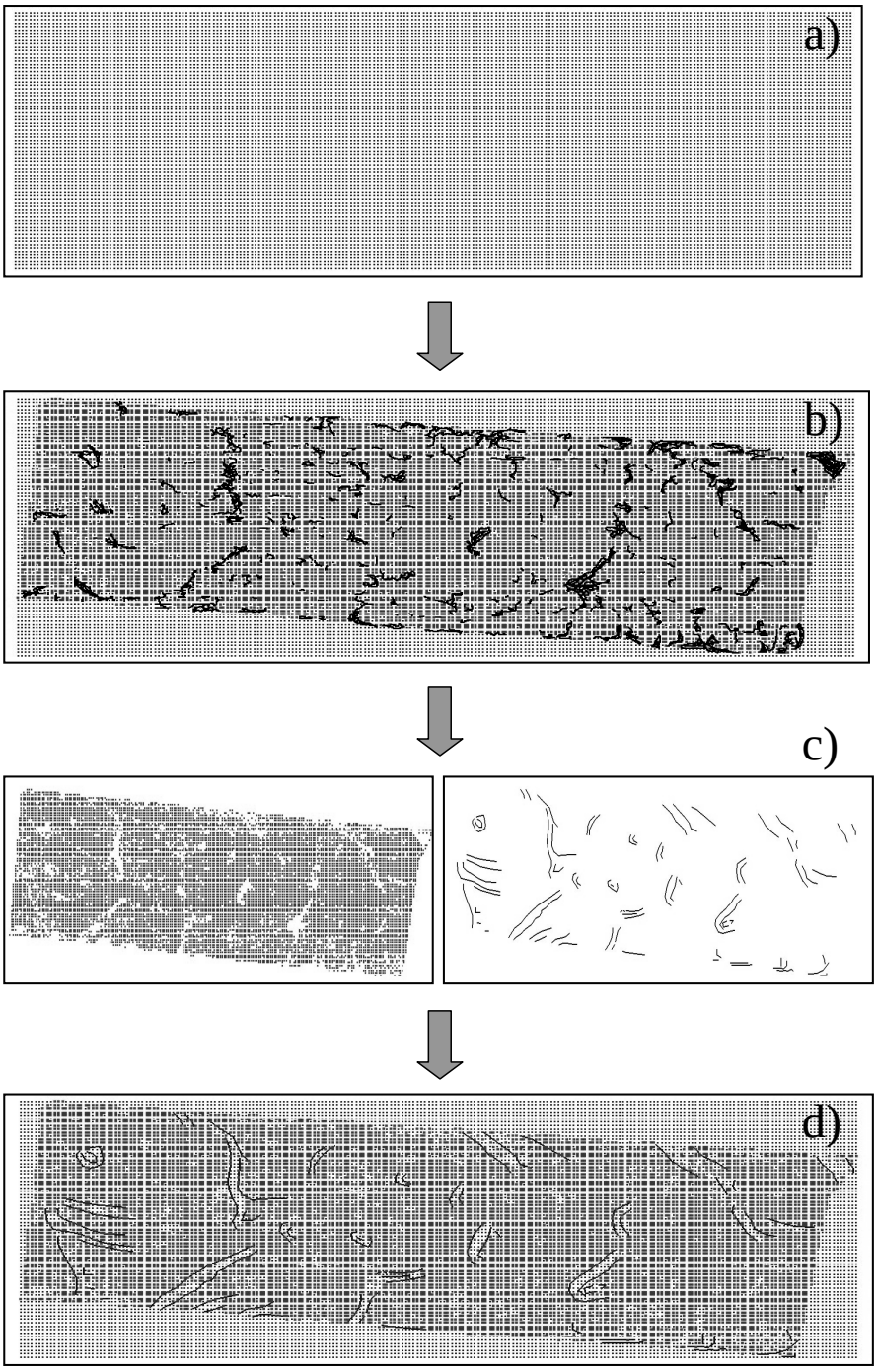

Figure 5.5: Correction technique to improve the DEM using an interactive stereo vision editing feature (brake lines): a) basic rectangular grid, b) basic grid (light) with flume and DEM with FOMs > 54 (dark) and FOMs ≤ 54 (black), c) DEM after elimination of incorrect matches (left) and edited linear features (brake lines) (right), d) final DEM.

Table 5.1: Aspect ratio of side weir crest length (L_D) to channel width (B) for the present study (L_D/B).

Test series	Side weir crest length L_D $[m]$	Channel width B $[m]$	Ratio L_D/B $[-]$
B	3.00	1.50	2.00
C	6.00	1.50	4.00
D	$2 \cdot 2.50 = 5.00$	1.50	3.33

gated spillways. The effect of the piers is to contract the flow and, hence, to alter the effective crest length of the spillway. The effective length of one bay of a gated spillway (corresponding to one side weir in the present study) may be expressed as (Chow (1973), Naudascher (1992)):

$$L_{eff} = L_0 - K_c \cdot n_c \cdot H_e \tag{5.3}$$

where L_0 is the clear span of the gate bay between piers, K_c is the pier contraction coefficient, n_c is the number of side contractions (equal to 2 for each gate bay) and H_e is the total head on the crest including the velocity head. The approximate K_c value given by Creager and Justin (1950) ranges from 0.1 for thick, blunt noses to 0.04 for thin or pointed noses and is 0.035 for round noses. These values apply to piers having a thickness equal to about 1/3 the head on the crest when all gates are open. When one gate is open and the adjacent gates are closed these values become roughly 2.5 times larger.

To obtain as large values as possible for the second term ($K_c \cdot n_c \cdot H_e$) in Equation 5.3 and thus a much smaller effective length L_{eff} than the clear span L_0, the following most unfavourable (= large) values from test series D are applied: pressure head (without velocity head) $h_D = 0.071\ m$ and perpendicular approach velocity (normal to side weir crest) $v_y = 0.251\ m/s$. The perpendicular approach velocity (v_y) corresponds to a velocity of $v_x = 0.848\ m/s$ in channel axis and a lateral outflow (deflection) angle of $\phi_D = 16.5°$ (paragraph 5.5), both measured in lateralwise position at $y_B = 1.20\ m$ (thus, not directly on the crest but 0.30 m from the side weir crest towards the channel centreline). Subsequently, the total energy head yields $H_e = h_D + v_y^2/2g = 0.074\ m$. Using furthermore $L_0 \equiv L_D = 2 \cdot 2.50\ m = 5.00\ m$, $K_c = 0.1$ (or $K_c = 0.1 \cdot 2.5 = 0.25$) and $n_c = 2 + 2 = 4$ (2 for each gate bay or

side weir field, respectively), the following effective lengths are obtained:

$$L_{eff} = \quad 5.0 - 0.1 \cdot 4 \cdot 0.074 \quad = 4.97 \ m \ \text{(for } \ K_c = 0.1) \tag{5.4}$$

or

$$L_{eff} = \quad 5.0 - 0.25 \cdot 4 \cdot 0.074 \quad = 4.93 \ m \ \text{(for } \ K_c = 0.25)$$

Using the values of 4.97 m and 4.93 m, respectively, L_D/B-values of 3.31 and 3.29, respectively, are obtained. These results are very close to $L_D/B = 3.33$ demonstrating that the assumption of $L_D = 2 \cdot 2.50 \ m = 5.00 \ m$ for test series D seems to be reasonable and no shifting towards the middle of series B and C, e. g. $L_D/B \approx 3.00$, might be possible. Nevertheless, it has to be kept in mind that the approach (Eq. 5.3) has originally been developed for overflow spillways and not for side weirs with a free overflow (lower nappe with atmospheric conditions!). Moreover, the condition that the approach (Eq. 5.3) applies to piers having a thickness equal to about 1/3 the head is not fulfilled ($1/3 \cdot H_e = 1/3 \cdot 0.074 \ m = 0.0247 \neq 1.00 \ m =$ length of the intermediate separation wall).

However, despite a certain lack of analogy this approach might serve as an indicator to get a rough idea about the order of magnitude of the error committed ($1 - (4.93 \ m/5.00 \ m) = 0.014 = 1.4 \ \%$) and whether a linear superposition of the two weirs lengths appears to be justified.

In addition to the approach mentioned above (analogy to piers in gated spillways) the effect of local energy losses due to sudden expansion/contraction effects (e. g. non-prismatic channel) or local obstructions (e. g. bridge pier) and constrictions (e. g. bridge abutment) in a rectangular channel has been considered.

This analogy does not seem to be physically based, since the flow does not rejoin behind the separation wall (free overflow!). Therefore, no flow separation occurs inducing free and unstable shear zones (boundary layer) resulting in an increased turbulent energy production and, hence, high internal shear stress combined with energy dissipation and energy losses. Moreover, these local losses might not be captured numerically, since a control volume is difficult to define. This could be possible on the main-channel side of the weir (water side) although an appropriate approach width in the main channel towards the side weir seems to be difficult to determine, since there is no well defined (sharp or solid) boundary (e. g. channel walls). After the overflow (on the air side of the weir) a definition of a control section seems to be rather delicate.

Eventually, a reduced effective overflow length might be present for a side overflow into a branch channel as shown in Figure 5.6, a. In this case the side walls of the branch channel are responsable for a flow separation zone resulting in a decreased overflow crest length. In the experimental study by Ranga Raju et al. (1979) an effective weir length which is 5.00 cm less than the true width

is proposed. In the present study a conventional free overflow without side walls has been present, hence, no flow separation occurs (Fig. 5.6, b).

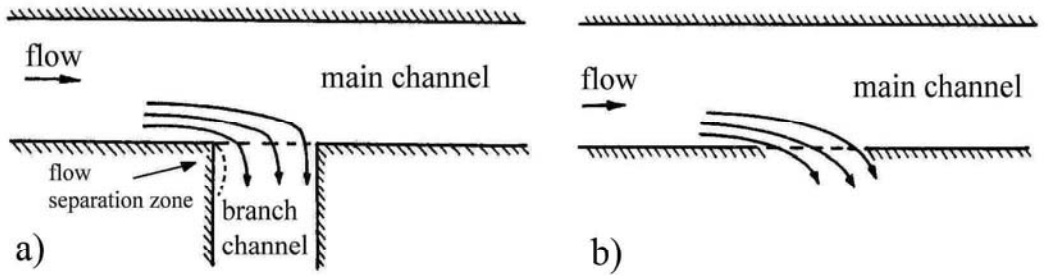

Figure 5.6: Streamline pattern over a side weir for a) branch channel and b) conventional side weir (from Ranga Raju et al. (1979), modified).

It may be concluded that the assumption of linear superposition of the two side weirs is justified and the error committed is less than 1.4 %.

5.2. Data Set used for Analysis of the Experiments

In this paragraph the data set obtained after data processing described in paragraph 5.1 is presented (see also appendix B). The characteristic data presented herein constitutes the data basis used for the analysis of the experiments. Besides the data set summarized in this paragraph a documentation of the final bed morphology (photographs, $3D$-view of the digital elevation model (DEM) and longitudinal bed surface profiles at different spanwise positions), the streamwise evolution of the water level elevation and the total energy head is given in appendix B.

It might be repeated that the following three test series, mainly characterized by different weir lengths (L_D), and a reference experiment without side weir have been conducted:

- Test series A: Reference case without side weir (1 experiment),
- Test series B: One side weir, crest length $L_D = 3.00\ m$ (6 experiments),
- Test series C: One side weir, crest length $L_D = 6.00\ m$ (5 experiments) and
- Test series D: Two side weirs, crest length $L_D = 2.50\ m$ each (5 experiments).

Table 5.2: Channel geometry, sediment supply and experiment duration for test series A, B, C and D.

N^o of exp.	Channel width B $[m]$	Bottom slope $S_{0,ini}$ [%]	Weir crest length L_D $[m]$	Weir height $w_{D,ini}$ $[m]$	N^o of weirs n_D $[-]$	Sediment supply $Q_{sb,in}$ $[kg/min]$	Exp. duration t $[min]$
A01	1.50	0.20	$***$	$***$	$***$	15.25	120
B01	1.50	0.20	3.00	0.10	1	8.70	188
B02	1.50	0.20	3.00	0.10	1	17.73	183
B03	1.50	0.40	3.00	0.10	1	9.10	117
B04	1.50	0.10	3.00	0.10	1	9.67	245
B05	1.50	0.20	3.00	0.10	1	16.72	128
B06	1.50	0.30	3.00	0.10	1	17.61	138
C01	1.50	0.20	6.00	0.09	1	9.56	125
C02	1.50	0.20	6.00	0.09	1	42.69	120
C03	1.50	0.20	6.00	0.09	1	51.76	120
C04	1.50	0.20	6.00	0.09	1	39.82	120
C05	1.50	0.20	6.00	0.09	1	39.82	120
D01	1.50	0.20	$2 \cdot 2.50$	0.09	2	27.04	125
D02	1.50	0.20	$2 \cdot 2.50$	0.09	2	26.54	120
D03	1.50	0.20	$2 \cdot 2.50$	0.09	2	39.82	120
D04	1.50	0.20	$2 \cdot 2.50$	0.09	2	22.34	120
D05	1.50	0.20	$2 \cdot 2.50$	0.09	2	19.91	120

Table 5.3: Flow parameters at the end of the experiments for test series A, B, C and D.

N^o of exp.	Upstream discharge Q_1 $[l/s]$	Overflow discharge $Q_{D,fin}$ $[l/s]$	Flow depth $y_{1,fin}$ $[m]$	Flow velocity $v_{1,fin}$ $[m/s]$	Froude number $Fr_{1,fin}$ $[-]$	Pressure head $h_{D,1,fin}$ $[m]$
A01	153	$***$	0.150	0.679	0.560	$***$
B01	131	22	0.130	0.673	0.597	0.026
B02	181	52	0.137	0.883	0.763	0.049
B03	177	41	0.146	0.806	0.672	0.039
B04	98	4	0.092	0.714	0.753	0.013
B05	144	37	0.118	0.812	0.754	0.035
B06	148	44	0.136	0.723	0.625	0.038
C01	160	30	0.100	1.063	1.072	0.037
C02	197	32	0.120	1.097	1.012	0.042
C03	221	71	0.084	1.744	1.916	0.048
C04	179	28	0.118	1.014	0.943	0.044
C05	181	38	0.116	1.042	0.978	0.039
D01	166	24	0.122	0.905	0.826	0.034
D02	182	33	0.138	0.879	0.755	0.048
D03	222	68	0.156	0.951	0.769	0.051
D04	182	67	0.131	0.929	0.821	0.040
D05	150	9	0.114	0.874	0.825	0.025

5.3. Intensity of measured Overflow Discharge

In this chapter the side overflow intensity and the determination and choice of an appropriate discharge coefficient are presented. Moreover, the influence of mobile bed conditions on spilled discharge is highlighted. In this context aggradation and deposition phenomena as well as bed form induced resistance is discussed.

5.3.1. Determination of Overflow Discharge from Experiments

For the present investigation the side overflow discharge (Q_D) can be determined according to the following three methods:

- a): Sharp-crested measuring weir in evacuation channel,
- b): $Q_D = Q_1 - Q_2$ (Q_1 and Q_2 discharge up- and downstream of weir) and
- c): Side weir equation (Eq. A.158).

Herein, Q_D has been determined following method (a) (paragraph 5.1.3). The other two methods have been applied for comparison and verification of method (a).

Concerning the second method (b), the downstream discharge Q_2 has been calculated applying the continuity equation ($Q = v\ A = v\ y\ B$). The water depth (y) has been obtained by subtracting the bottom elevation (final DEM) from the water surface elevation (US-measurements). The flow velocity (v) required has been obtained from UVP-measurements. The velocity could have been calculated by the use of the Strickler equation as well. To do so, an adequate k_{st}-value has to be chosen. The approach discharge (Q_1) is known, since it has been imposed.

With regard to the third method (c), the measured overflow depth ($h_{D,1}$) at the upstream weir corner (US-measurements) and an appropriate side weir discharge coefficient (C_D) are necessary. Q_D is then calculated according to Equation A.158. From several expressions available in literature (appendix A.7.3) an adequate relation for the determination of C_D is represented in the next paragraph (paragraph 5.3.2).

A comparison of the three methods is dealt with later on in paragraph 5.3.2.

Looking now at the transient evolution of the side overflow (Q_D). For plane fixed bed conditions the transient evolution of Q_D is constant. This

situation would correspond to the initial conditions at the very beginning of the experiments (although the bed is mobile and not fixed). In the case of mobile bed conditions bed forms rapidly form and aggradation of the bed in the weir reach occurs. Hence, the side overflow is no longer constant over time. In Figure 5.7 these phenomena are presented for emblematic experiments for each test series. Instead of Q_D the dimensionless ratio side overflow to approach discharge (Q_D/Q_1) is applied.

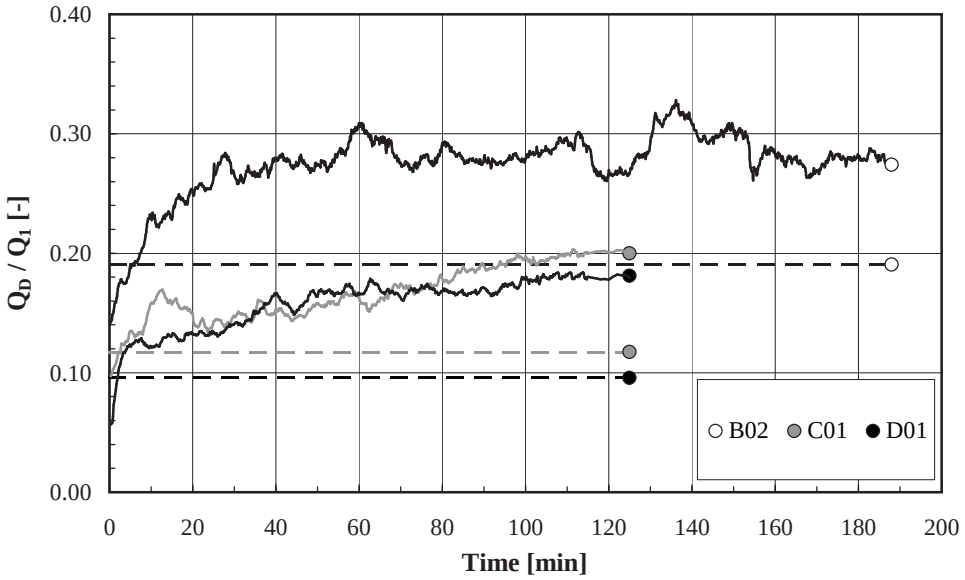

Figure 5.7: Transient evolution of the ratio diverted to approach discharge (Q_D/Q_1) for three emblematic experiments of each test series. The dashed lines indicate the Q_D/Q_1-ratio for plane fixed bed conditions. This situation corresponds to the initial experimental conditions (although the bed is mobile and not fixed).

It can be seen from Figure 5.7 that the ratio Q_D/Q_1 rapidly increases and stabilises after a certain time increment (t_{stab}). This time might be indicative for rather stable dynamic equilibrium flow and sediment transport conditions. For experiment $B02$ a difference between mobile and plane fixed bed conditions of $(Q_D/Q_1)_{mobile}/(Q_D/Q_1)_{fixed} = 0.29/0.19 = 1.51$ becomes evident. For $C01$ a value of $0.19/0.12 = 1.56$ and for $D01$ a ratio of $0.14/0.10 = 1.51$ is observed. Table 5.4 gives an overview of Q_D/Q_1-ratios and the stabilisation time (t_{stab}).

As far as the ratio Q_D/Q_1 is concerned the following relation is proposed by Singh and Satyanarayana (1994):

Table 5.4: Ratio of diverted to approach discharge (Q_D/Q_1) and time of stabilisation for the overflow discharge (t_{stab}). Q_D refers to the final (stabilized) experimental conditions.

N^o of exp.	Approach discharge Q_1 [l/s]	Overflow discharge Q_D $[l/s]$	Discharge ratio Q_D/Q_1 $[-]$	Duration of exp. t $[min]$	Stabilisation time for Q_D t_{stab} $[min]$	Time ratio t_{stab}/t $[-]$
$B01$	131	22	0.17	188	31	0.16
$B02$	181	52	0.29	183	41	0.22
$B03$	177	41	0.23	117	22	0.19
$B04$	98	4	0.04	245	72	0.29
$B05$	144	37	0.26	128	34	0.27
$B06$	148	44	0.30	138	25	0.18
$C01$	160	30	0.19	125	24	0.19
$C02$	197	32	0.16	120	18	0.15
$C03$	221	71	0.32	120	34	0.28
$C04$	179	28	0.16	120	20	0.17
$C05$	181	38	0.21	120	32	0.27
$D01$	166	24	0.14	125	49	0.39
$D02$	182	33	0.18	120	45	0.38
$D03$	222	68	0.31	120	31	0.26
$D04$	182	67	0.37	120	44	0.37
$D05$	150	9	0.06	120	46	0.38
average	170	38	0.21	138	36	0.26

$$\frac{Q_D}{Q_1} = 0.88 - 0.97 \cdot \frac{w_D}{y_1} \tag{5.5}$$

with w_D weir crest height and y_1 flow depth at the upstream weir corner. The maximum outflow ratio of $Q_D/Q_1 = 0.88$ is obtained for $w_D = 0.00$. For $w_D/y_1 = 0.91$, $Q_D/Q_1 = 0.00$. Hence, w_D has always to be smaller than 0.91 y_1 ($w_D \leq 0.91\ y_1$).

In Figure 5.8 the approach of Singh and Satyanarayana (1994) is compared with data from the present study. Some data points are not represented since negative values were obtained (condition $w_D \leq 0.91\ y_1$ not fulfilled). It can be derived from the Figure that until a Q_D/Q_1-ratio of ≈ 0.20 fairly well correlation is found, whereas for higher measured Q_D/Q_1-ratios Equation 5.5 considerably underestimates measured ratios. The deviation might be attributed to the experimental boundary conditions under which the relation has been developed. The most substantial differences to the present study are, among others, fixed plane bed conditions. Thus, the aggradation occurring in the present investigation and being responsable for higher outflow discharges than observed under fixed bed conditions is not reproduced.

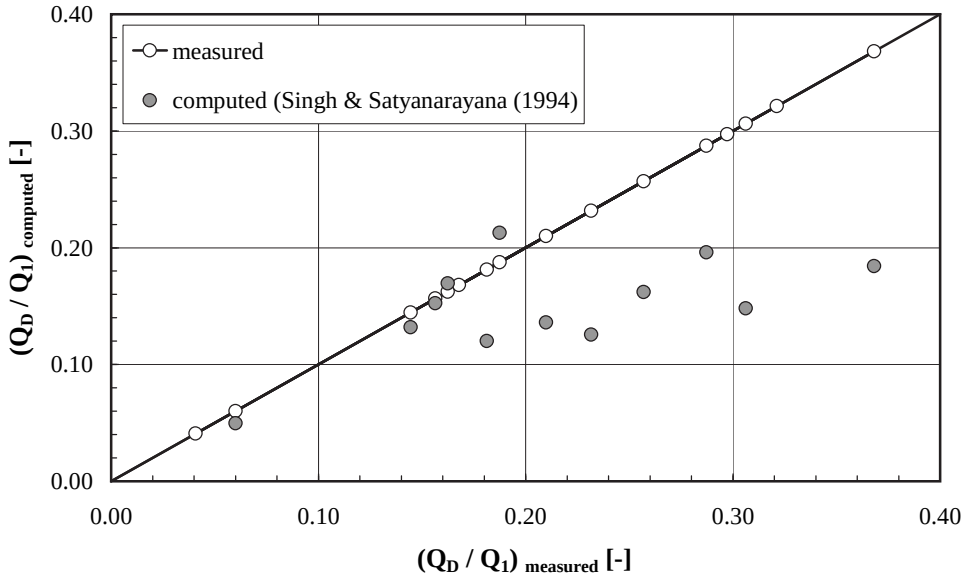

Figure 5.8: Comparison of diverted to approach discharge ratio (Q_D/Q_1) with the method of Singh and Satyanarayana (1994) (Eq. 5.5).

5.3.2. Determination of Side Weir Discharge Coefficient

Before determining the discharge coefficient (C_D) and conducting a comparison with available approaches from literature, it has to be stated that in some experiments the downstream water level in the evacuation channel has been rather high (e. g. experiment $C03$). A submerged weir overflow will reduce the discharge coefficient of the corresponding unsubmerged flow, hence, the overflow discharge is reduced. This has been verified by using a

chart developed by the U.S. Army Engineers Waterways Experimental Station (Chow (1973)). The verification indicated that the degree of submergence did not yet lead to a reduction of the discharge coefficient.

Referring now to the determination of the side weir discharge coefficient (C_D). Following De Marchi (1934), the specific energy (E) along the side weir crest is almost constant (constant energy concept) and the side weir discharge coefficient can be calculated according to Equation A.162. With respect to the constant energy approach, Ranga Raju et al. (1979) reported a maximum difference of the specific energy between the two ends of the weir being less than 2 %. El-Khashab and Smith (1976) stated a decrease by as much as 5 %. Borghei et al. (1999) found an average energy difference of 3.7 %. Furthermore, this also implies that the specific energy head at the downstream weir corner (E_2) is greater than the upstream one (E_1) (Fig. A.15). As mentioned in paragraph 5.8 an obstacle or local sedimentary deposit near the weir significantly influences the water level elevation and hence the specific energy head in the weir region. Thus E_2 might be, albeit less, smaller than E_1. For the present study the downstream specific energy head has always been smaller than the upstream one. Consequently, ϕ_2 is smaller than ϕ_1 and negative C_D-values using Equation A.162 are obtained (Rosier et al. (2005e)). For that reason C_D has been determined by the help of the general equation of weirs (Eq. A.158) using both measured pressure heads (h_D) and diverted discharges (Q_D).

In Figure 5.9 (top) and Table 5.5 the results of this analysis are presented and compared with different approaches from literature (appendix A.7.3). Referring to measured discharge coefficients, for test series B a C_D-value of 0.556 is obtained. For test series C and D the discharge coefficient equals to 0.257 and 0.320, respectively. The mean C_D-value corresponds to 0.389. It has to be noted that the approach Froude number (Fr_1) for experiments $C01$, $C02$ and $C03$ has been close to 1.00 (Tab. 5.3).

As far the comparison with approaches from literature is concerned rather great scattering becomes evident (Fig. 5.9, top). As often being the case this might be mainly attributed to the different boundary conditions under which the approaches have been established (paragraph 2.3, Tabs 2.1, 2.2, 2.3 and 2.4). The approaches apply adequately to one experiment but not all to another, hence no consistent trend can be identified. However, it follows that the discharge coefficient is best represented by the approaches of Subramanya and Awasthy (1972) (without $C01$, $C02$ and $C03$, since the approach is only valid for $Fr_1 \leq 1.00$) and Hager (1987b). The lowest correlation is obtained for the method of Singh et al. (1994). The analysis suggests that approaches incorporating the approach Froude number in terms of Fr_1^2 only, yield the best prediction quality (approach of Subramanya and Awasthy (1972) and Hager (1987b)). Using the Froude number in terms of Fr_1 leads to lower correlation (method of Ranga Raju et al. (1979)). Adding further parameters such as

weir height (w_D) and approach flow depth (y_1) (Singh et al. (1994), Swamee et al. (1994a)), specific energy (E_1) and weir crest length (L_D) (Frazer (1957)) or channel width (B) (Borghei et al. (1999)) does not seem to increase the correlation. This has also been demonstrated by Rosier et al. (2005e).

Table 5.5: Comparison of measured and computed side weir discharge coefficients (C_D). LSM denotes least squares method $\left(\sum(C_{D,measured} - C_{D,computed})^2\right)$.

Investigation	Eq. in study	Test series B C_D [−]	Test series C C_D [−]	Test series D C_D [−]	average C_D [−]	meas./ comp. [−]	LSM [−]
present study		0.556	0.257	0.320	0.389	1.00	0.00
Frazer (1957)	A.165	0.493	0.373	0.476	0.447	0.87	0.58
Subramanyana and Awasthy (1972)	A.166	0.392	0.137	0.319	0.283	1.38	0.37
Ranga Raju et al. (1979)	A.167	0.394	0.099	0.330	0.274	1.42	0.87
Hager (1987b)	A.168	0.412	0.365	0.398	0.392	0.99	0.44
Singh et al. (1994)	A.169	0.627	0.422	0.567	0.539	0.72	1.08
Borghei et al. (1999)	A.170	0.228	0.185	0.283	0.232	1.67	0.96
Swamee et al. (1994a)	A.171	0.422	0.425	0.423	0.423	0.92	0.52

Regarding the computed lateral outflow discharge (Q_D) based on the different weir coefficients (C_D) from literature, the expression of Subramanya and Awasthy (1972) (without $C01$, $C02$ and $C03$, since the approach is only valid for $Fr_1 \leq 1.00$) gives the best results (Fig. 5.9, bottom, Tab. 5.6). Ranga Raju et al. (1979) considerably overestimate the side overflow intensity. The other methods are located between these two limits (Fig. 5.9, bottom, Tab. 5.6). Within this context Q_D has been determined according to the general equation of weirs (Eq. A.158, for Hager (1987b) the coefficient 2/3 has to be omitted).

Knowing which C_D-approach gives the best results for the side overflow intensity, being the one of Subramanya and Awasthy (1972), the two methods (b) and c)) to determine the overflow discharge mentioned at the beginning of

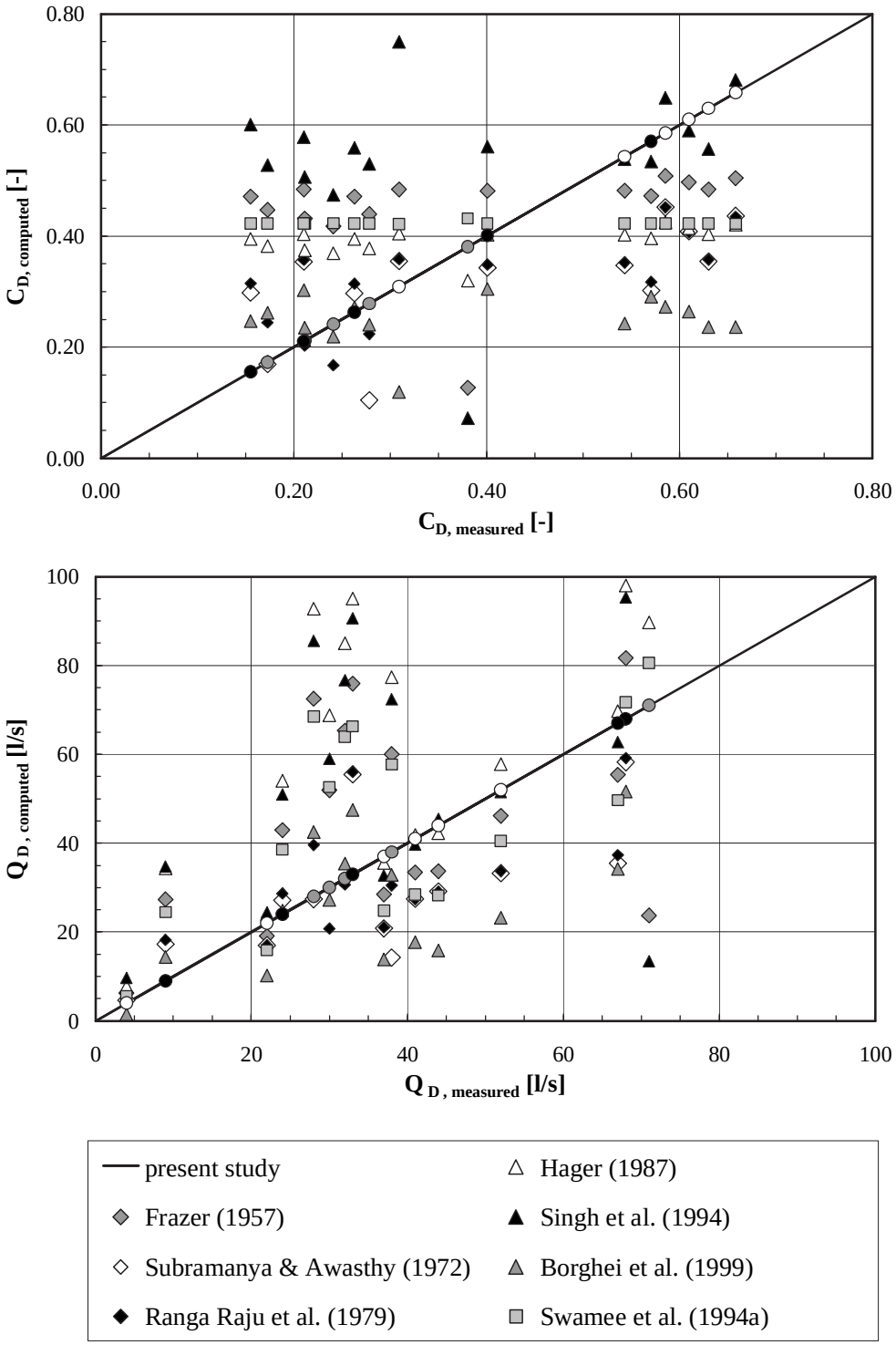

Figure 5.9: Comparison of measured and computed side weir discharge coefficients (C_D) (top) and corresponding side overflow intensities (Q_D) (bottom). The white circle corresponds to test series B, the grey one to C and the black circle to test series D.

Table 5.6: Comparison of measured and computed side overflow discharge (Q_D). Computed Q_D-values have been obtained by applying the general equation of weirs (Eq. A.158, for Hager (1987b) without the factor 2/3). LSM denotes least squares method $\left(\sum(Q_{D,measured} - Q_{D,computed})^2\right)$.

Investigation	Test series			average	meas./	LSM
	B	C	D		comp.	
	Q_D	Q_D	Q_D	Q_D		
	$[l/s]$	$[l/s]$	$[l/s]$	$[l/s]$	$[-]$	$\left[(l/s)^2\right]$
present study	33	40	40	38	1.00	0.00
Frazer (1957)	28	55	57	46	0.81	9433
Subra. & Awasthy (1972)	22	21	39	27	1.38	3278
Ranga Raju et al. (1979)	22	12	40	25	1.53	20968
Hager (1987b)	35	83	70	63	0.60	16765
Singh et al. (1994)	34	61	67	54	0.69	16197
Borghei et al. (1999)	14	26	34	25	1.51	10632
Swamee et al. (1994a)	24	65	50	46	0.81	6256

the paragraph can be compared with method (a). Method (a) is the one used in the present study. Method (b) and (c) are used for comparison only. From Figure 5.10 and Table 5.7 it can be derived that method (b) is significantly superior to method (c). In this context experiments $C01$, $C02$ and $C03$ could not be used since the approach of Subramanya and Awasthy (1972) is only valid for approach Froude numbers smaller or equal to 1.00 ($Fr_1 \leq 1.00$).

Finally it might be interesting to note that the measured ratio of initial discharge coefficient to final discharge coefficient ($C_{D,ini}/C_{D,fin} = 0.345/0.389 = 0.89$) is approximately in the same order of magnitude than the one for a sharp and broad round crested weir with perpendicular (!) approach flow conditions ($C_{D,ini}/C_{D,fin} = 0.64/0.79 = 0.81$). This might be explained by the fact that at the beginning of the experiments the side weir corresponds to a sharp-crested side weir, whereas at the end of the experiments the ramp-like deposit forming in front of the weir and the weir itself can be seen as one single overflow unit (Figs 5.38, 5.39). Note that the ratio 0.89 is rather indicative. However, a ratio of $C_{D,ini}/C_{D,fin} = 1.00$ would lead to the conclusion that other reasons than the deposit are the cause for an increased side overflow discharge.

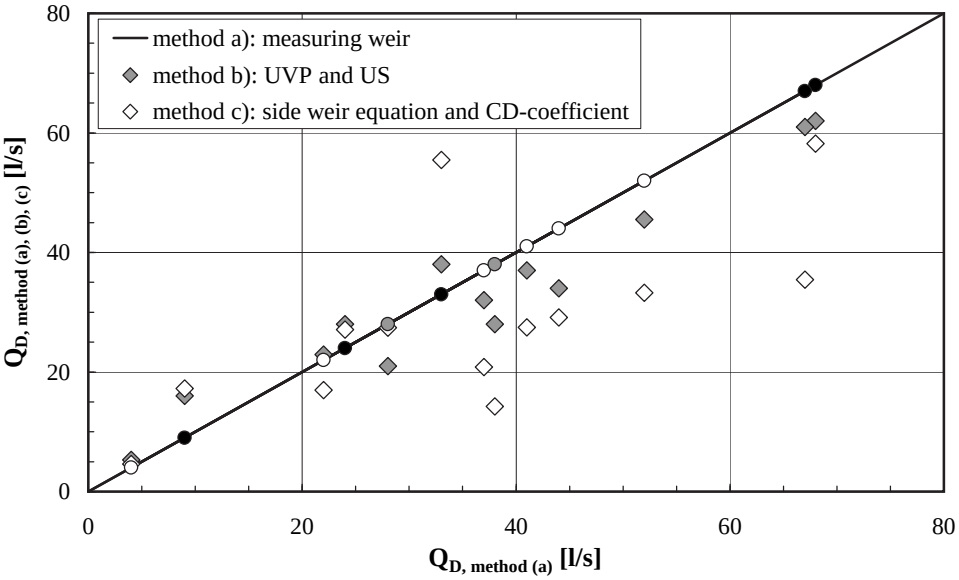

Figure 5.10: Comparison of method (a) with methods (b) and (c) for the determination of the side overflow discharge (Q_D). Method a): Sharp-crested measuring weir in evacuation channel (method used in this study). The white circle corresponds to test series B, the grey one to C and the black circle to test series D. Method b): $Q_D = Q_2 - Q_1$ using velocity (UVP) and water level measurements (US). Method c): Side weir equation and appropriate discharge coefficient (C_D) (here: Subramanya and Awasthy (1972)).

From this analysis it may be concluded that the side weir discharge coefficient (C_D) as proposed by several approaches from literature does not change significantly from one approach to the other. In contrast to this the calculation of spilled discharge (Q_D) based on different C_D-values might vary considerably depending on the C_D-approach chosen.

Table 5.7: Comparison of method (a) with methods (b) and (c) for the determination of the side overflow discharge (Q_D). Method a): Sharp-crested measuring weir in evacuation channel (method used in this study) ($Q_{D,a}$). Method b): $Q_D = Q_2 - Q_1$ using velocity (UVP) and water level measurements (US) ($Q_{D,b}$). Method c): Side weir equation and appropriate discharge coefficient (C_D) (here: Subramanya and Awasthy (1972)) ($Q_{D,c}$). LSM denotes least squares method $\left(\sum(Q_{D,a} - Q_{D,b,c})^2\right)$.

Test series	$Q_{D,a}$ $[l/s]$	$Q_{D,b}$ $[l/s]$	$Q_{D,c}$ $[l/s]$	$Q_{D,a}/Q_{D,b}$ $[-]$	$Q_{D,a}/Q_{D,c}$ $[-]$	LSM $\left[(l/s)^2\right]$ (b)	(c)
B	33	29	22	1.07	1.42	186	1042
C	33	25	21	1.35	1.84	149	564
D	40	41	39	0.90	1.01	162	1673
average	36	33	28	1.05	1.33	497*)	3278*)

*) sum

5.3.3. Influence of Aggradation and Flow Resistance on Overflow Discharge

In this paragraph it is investigated to which extent deposition effects and bed form induced resistance contribute to an elevated outflow intensity compared to fixed bed conditions.

In Figure 5.11 the contribution of grain and form roughness as well as aggradation effects and their impact on the measured side overflow discharge (Q_D) are represented. The portion of grain roughness and deposition has been directly derived from the experiments (initial and final situation). Since in the experiments form roughness and deposition occurred simultaneously, no explicit information for form roughness only can be obtained from the measurements. Hence, the portion of form roughness has been determined using the $1D$-numerical code DUPIRO (paragraph 8.1). In this context an adequate resistance coefficient (Strickler-value) accounting for form roughness had to be chosen. To do so, the reference experiment $A01$ without side overflow has been used. Moreover, Strickler-values from test series B, C and D determined far up- or downstream of the weir (and the deposition) have served to estimate form roughness.

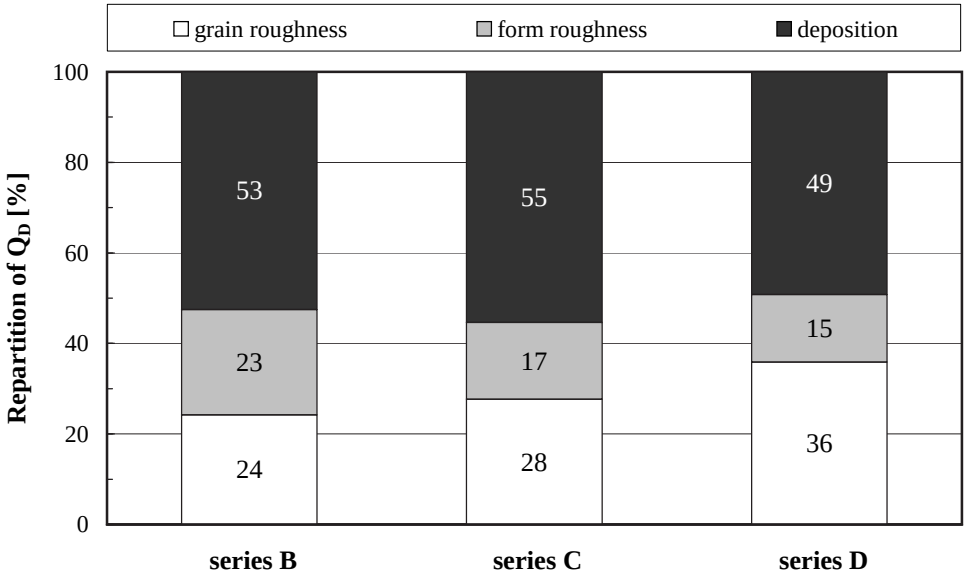

Figure 5.11: Influence of grain and form roughness as well as deposition on total measured side overflow discharge (Q_D).

The Figure indicates that granular skin friction and form roughness are of inferior importance with respect to side overflow intensity. Aggradation effects, e. g. local deposition near the weir, represent the main parameter to

explain increased Q_D-values. On average, the contribution of aggradation to the total side overflow is about 50 % (Rosier et al. (2005d)).

Figure 5.12 represents two different reference scenarios. The first (Fig. 5.12, left) refers to plane (fixed) bed conditions, the second to a bed form covered channel bottom (Fig. 5.12, right). This means that for the first scenario the portion of Q_D referring to grain roughness is fixed to zero, for the second scenario the portion of Q_D referring to form roughness is fixed to zero.

With respect to the first scenario having a plane bed as reference, about 25 % of the total overflow discharge are due to form roughness and about 75 % might be contributed to deposition effects. The scenario described does not appear to correspond to natural river conditions, especially in high flow situations. In sand bed rivers it is more likely to have a bed form covered bottom surface. The same accounts for gravel bed rivers of smaller grain size when the armor layer has been destroyed.

Assuming form roughness as the basic reference (second scenario), a side overflow increase of $\approx$ 50 % is observed. The remaining 50 % are already present in terms of form roughness.

The second scenario is the more realistic one and the portion of form roughness can be accounted for by the choice of an appropriate resistance factor. In contrast to this, the considerable portion of deposition is not known a-priori and the estimation of side overflow intensity will be rather inaccurate.

It may be concluded that these investigations underline the important effect of aggradation and the local sedimentary deposit on side overflow intensity. Hence, it appears to be necessary to be able to describe the flow-sediment interaction and to predict the extent of the deposition.

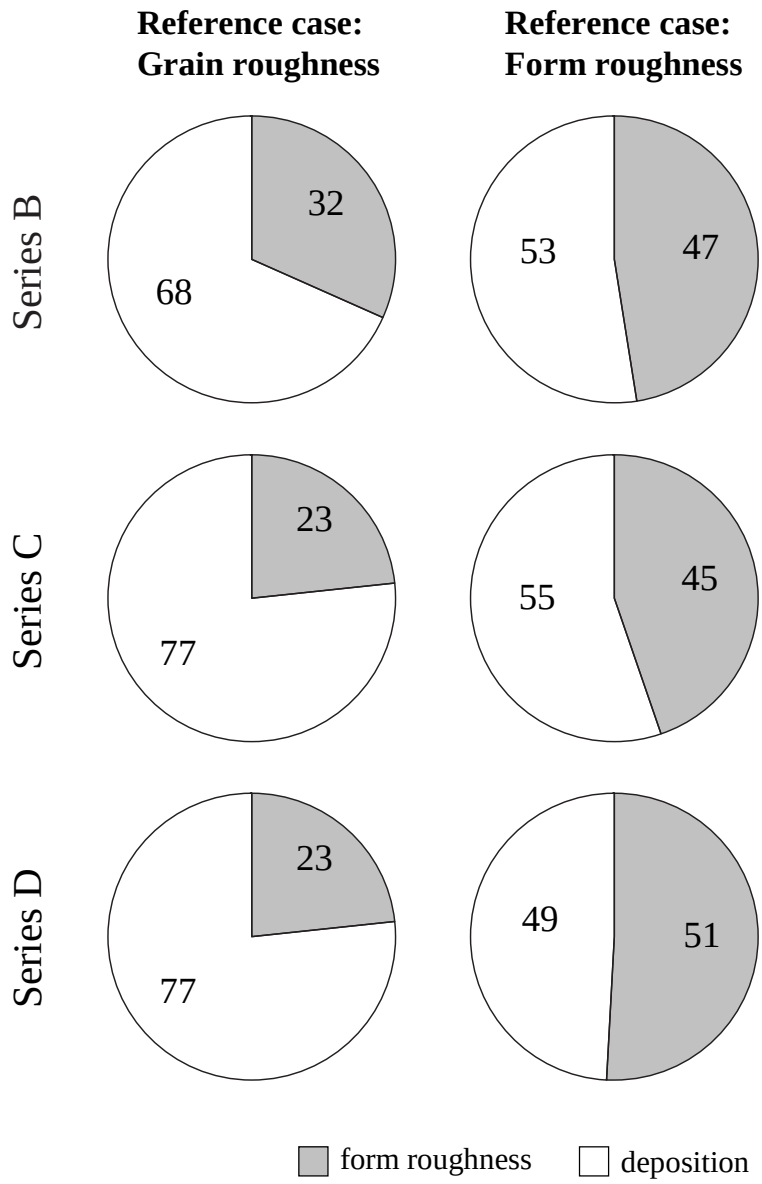

Figure 5.12: Influence of form induced roughness and deposition on side overflow discharge (Q_D) for two different reference bed conditions (scenarios). Left column: Plane bed with granular skin roughness. Right column: Bed form covered bottom surface.

5.3.4. Conclusion

The analysis showed that the ratio of overflow discharge to approach discharge (Q_D/Q_1) rapidly increases at the beginning of the experiments and stabilises after about 26 % of the total duration of the expriment. The average measured overflow ratio amounts to $\approx Q_D/Q_1 = 21\%$. Compared to fixed plane bed conditions the side overflow might increase by a factor of up to ≈ 3. Herein, about 25 % of the total increase can be attributed to form roughness effects induced by the formation of dunes and about 75 % to effects of local sediment deposition near the weir.

The investigation of the measured side weir discharge coefficient (C_D) revealed a value of 0.389. A comparison with several approaches from literature indicted that the C_D-value does not change significantly from one approach to the other.

5.4. Repartition of Overflow Discharge for two Side Weirs (Series D)

Since in test series D two side weirs have been present, the repartition of total overflow discharge on the two weirs is examined. In a first step the repartition of side overflow is investigated for the experiments with mobile bed conditions. In a second step a comparison with fixed bed conditions is performed.

5.4.1. Repartition of measured Overflow Discharge on mobile Bed Conditions

To determine the overflow discharge for weir 1 (Q_{D1}) and weir 2 (Q_{D2}) the general equation of weirs is applied (Eq. A.158). Assuming a rather constant side weir discharge coefficient (C_D) for both weirs the ratio Q_{D2}/Q_{D1} might be expressed as:

$$\frac{Q_{D2}}{Q_{D1}} \approx \left(\frac{h_{D,12}}{h_{D,1}}\right)^{3/2} \tag{5.6}$$

with $h_{D,1}$ and $h_{D,12}$ side weir pressure heads in section 1 and 12, respectively (Fig. 5.13, c).

Furthermore, the total side overflow discharge ($Q_{D,tot}$) is given by:

$$Q_{D,tot} = Q_{D1} + Q_{D2} \tag{5.7}$$

Replacing Q_{D2} in Equation 5.7 by the help of Equation 5.6 and rearranging for Q_{D1} and Q_{D2}, respectively, yields:

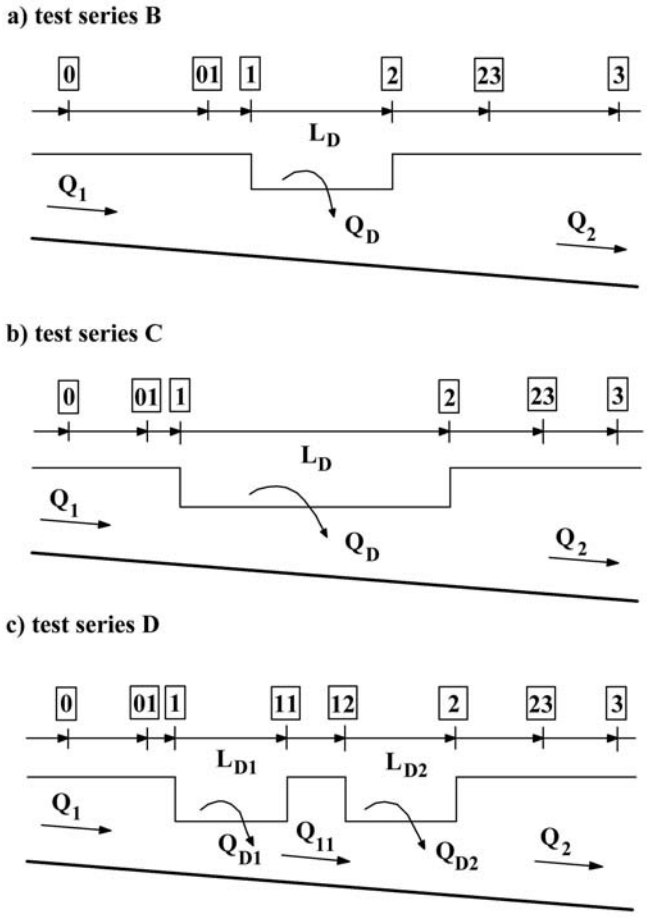

Figure 5.13: Definition sketch for the streamwise location of different cross sections. Part c) is used for the determination of the side overflow distribution for test series D.

$$Q_{D1} = \frac{Q_{D,tot}}{1 + \left(h_{D,12}/h_{D,1}\right)^{3/2}} \quad \text{and} \quad Q_{D2} = Q_{D,tot} - Q_{D1} \tag{5.8}$$

To determine whether weir 1 and weir 2 behave in the same way and whether the two weirs behave as one composed weir, the ratios of side overflow to approach discharge ($Q_{D,i}/Q_i$) versus crest length to pressure head ($L_{D,i}/h_{D,i}$) are investigated. Therefore, the following relations are introduced:

- Weir 1:

$$\frac{Q_{D1}}{Q_1} \quad \text{and} \quad \frac{L_{D1}}{h_{D,1}} \tag{5.9}$$

- Weir 2:

$$\frac{Q_{D2}}{Q_{11}} \quad \text{and} \quad \frac{L_{D2}}{h_{D,12}} \tag{5.10}$$

- Weir 1 + Weir 2:

$$\frac{Q_{D,tot}}{Q_1} \quad \text{and} \quad \frac{L_{D,tot}}{\left(\frac{(h_{D,1})^{3/2} + (h_{D,12})^{3/2}}{2}\right)^{2/3}} \tag{5.11}$$

In Equations 5.9, 5.10 and 5.11, Q_{11} is the approach main-channel discharge for weir 2, L_{D1} and L_{D2} are the weir crest lengths of weir 1 and weir 2 and $L_{D,tot}$ is the length of the composed weir ($L_{D,tot} = L_{D1} + L_{D2}$) (for definition see also Fig. 5.13, c).

The results from this analysis are presented in Figure 5.14. From the Figure it can be concluded that weir 1 and weir 2 behave similarly and that the composed weir acts in the same way than the two individual weirs. For an increasing side weir pressure head ($h_{D,i}$) and $L_D = const$ the ratio $L_{D,i}/h_{D,i}$ decreases and $Q_{D,i}/Q_{approach,i}$ increases. The sum of the $L_{D,i}/h_{D,i}$-ratios for the individual weirs results in the total overflow discharge.
Example: $L_{D1}/h_{D1} + L_{D2}/h_{D,12} \approx 100 + 100 = 200$. The corresponding discharge ratios are $Q_{D1}/Q_1 + Q_{D2}/Q_{11} = 3.17 + 2.92 = 6.09$. For $L_{D,i}/h_{D,i} \approx 200$ (composed weir), $Q_{D,tot}/Q_1 = 6.00$.

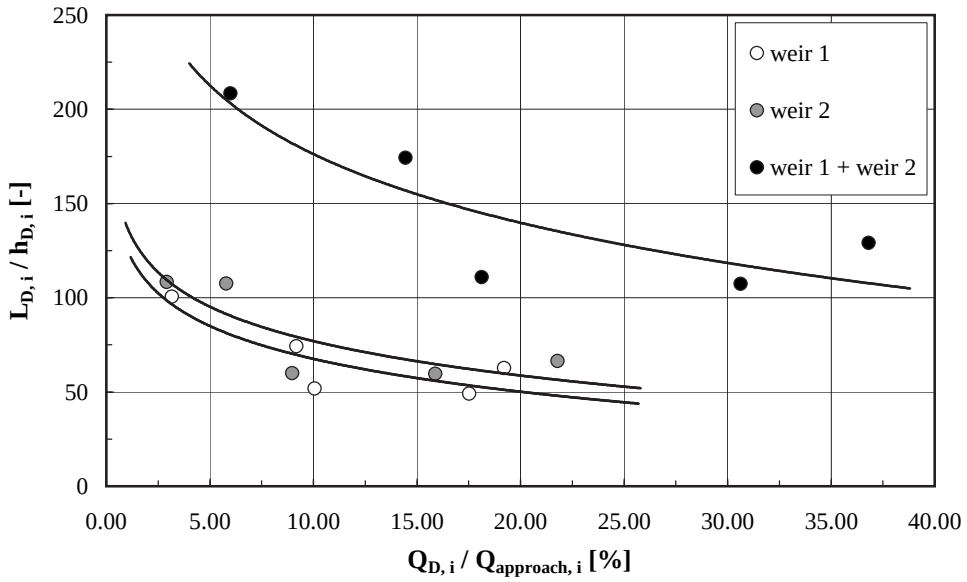

Figure 5.14: Interaction between weir 1 and weir 2 and weir 1 and weir 2 treated as one composed weir (Eqs 5.9, 5.10 and 5.11).

This fact is further demonstrated in Figure 5.15 using the following dimensionless expression for the side overflow discharge and the weir length:

$$\frac{Q_{D,i}}{L_{D,i}^{5/2} \cdot \sqrt{g}} \tag{5.12}$$

Note that Equation 5.12 is a kind of a Froude number.

It becomes evident that on average 55 % of the total side overflow are spilled over the first weir and that the remaining 45 % are diverted over the second one. This fact might serve to determine the repartition of Q_{D1} and Q_{D2}, being:

$$\frac{Q_{D2}}{Q_{D1}} = \frac{45}{55} = 0.82 \approx 4/5 \quad \text{or} \quad Q_{D2} \approx 4/5 \cdot Q_{D1} \tag{5.13}$$

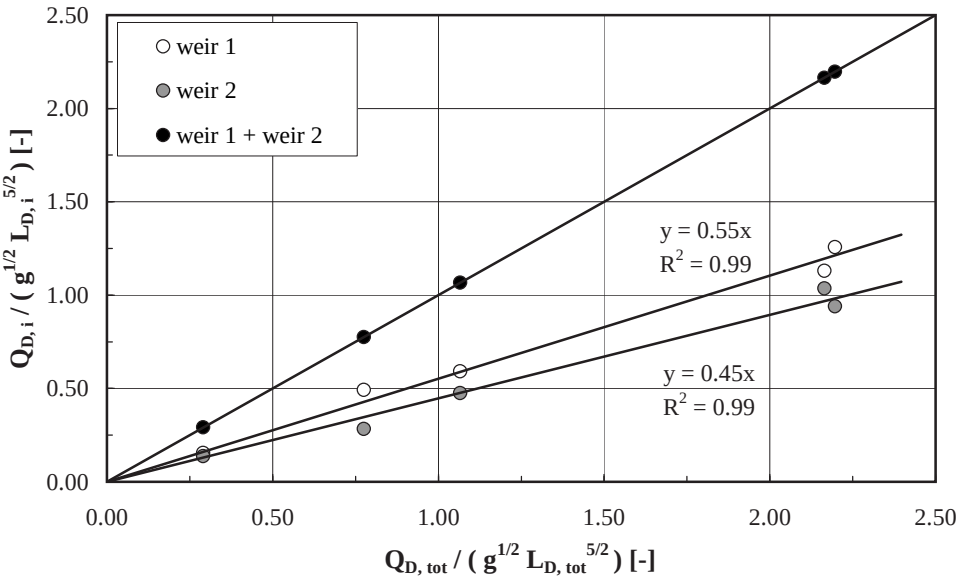

Figure 5.15: Behavior of weir 1 and weir 2 with respect to weir 1 and weir 2 treated as one composed weir (Eq. 5.12).

As has already been mentioned before, this distribution indicates that the two weirs behave approximately in the same manner. The first weir diverts 1/5 or 20 % more than the second one. For $Q_{D2}/Q_{D1} = 5/5 = 1.00$ the two weirs would participate uniformly in diverting $Q_{D,tot}$. In Figure 5.16 the repartition of the total overflow discharge diverted over weir 1 and weir 2 for each experiment of test series D is presented.

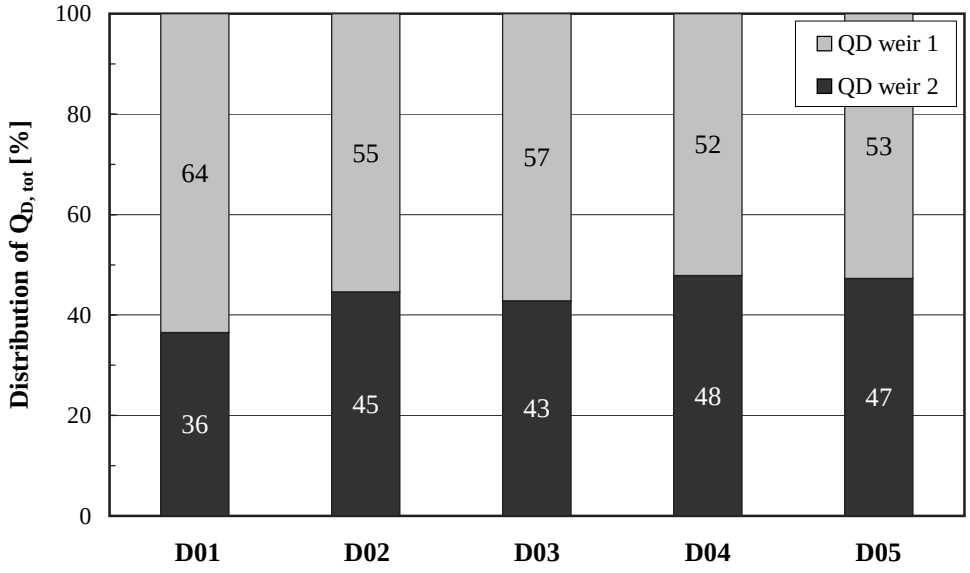

Figure 5.16: Repartition of side overflow discharge (Q_D) for test series D.

5.4.2. Repartition of Overflow Discharge on fixed Bed and Comparison with mobile Bed Conditions

The repartition of $Q_{D2}/Q_{D1} = 0.82$ as indicated in Equation 5.13 refers to mobile bed conditions and the formation of a sedimentary deposit. It is now interesting to investigate and to compare the discharge repartition for fixed bed conditions without aggradation.

To do so, Q_{D2}/Q_{D1}-ratios are generated for fixed plane bed conditions by simulations using the $1D$-numerical model DUPIRO. A detailed description of the numerical scheme is given in paragraph 8.1. For the computation the parameters approach discharge (Q_1), bottom slope (S_0), channel roughness (k_{st}) and total weir length ($L_{D,tot}$) were varied in the following ranges:

$$0.150\ m^3/s \leq Q_1 \leq 0.200\ m^3/s \tag{5.14}$$

$$0.001 \leq S_0 \leq 0.004$$

$$40\ m^{1/3}/s \leq k_{st} \leq 70\ m^{1/3}/s \tag{5.15}$$

$$4.0\ m \leq L_{D,tot} \leq 6.0 \tag{5.16}$$

The variation of Q_1 (0.150, 0.180 and 0.200 m^3/s), S_0 (0.001, 0.002, 0.004) and k_{st} (40, 60 and 70 $m^{1/3}/s$) corresponds to the experimental range. The channel width for all simulation runs was $B = 1.50\ m$ (like in

the present study). Regarding $L_{D,tot}$, the experimental value corresponds to $L_{D,tot} = 2.50\ m + 2.50\ m = 5.00\ m$ ($L_D/B = 3.33$). The values of $L_{D,tot} = 2.00\ m + 2.00\ m = 4.00\ m$ ($L_D/B = 2.67$) and $L_{D,tot} = 3.00\ m + 3.00\ m = 6.00\ m$ ($L_D/B = 4.00$) have been added to widen the parameter range. The $1.00\ m$ long separation wall between the two weirs was kept constant for the entire $L_{D,tot}$-range, thus corresponding to conditions from the experimental study. The bottom elevation in the middle of the separation wall was fixed to $z = 0.25\ m = constant$ while changing the invert slope. The crest level was kept constant at $z = 0.35\ m$. Hence, the resulting mean weir height was $w_D = 0.10\ m$ for all simulations.

For the sake of comparison, the following dimensionless parameter is introduced:

$$\frac{Q_1}{k_{st} \cdot L_{D,tot}^{8/3}} \cdot S_0^{-7/6} \tag{5.17}$$

with Q_1 approach discharge, k_{st} Strickler roughness coefficient, $L_{D,tot}$ total weir length and S_0 bottom slope.

Strickler-values for the present study have been determined using the GMS-Equation (Eq. A.24) with the energy slope (S_e) between sections 0 and 01 and flow depth ($y \approx R_h$) at section 01. In Table 5.8 these data are represented.

Table 5.8: Determination of Strickler-values for test series D upstream of the weir.

N° of experiment	Q_1 $[m^3/s]$	y $[m]$	S_e $[-]$	k_{st} $[m^{1/3}/s]$
$D01$	0.166	0.122	0.0031	66
$D02$	0.182	0.137	0.0041	52
$D03$	0.222	0.162	0.0032	54
$D04$	0.182	0.135	0.0026	67
$D05$	0.150	0.116	0.0036	60
average	0.180	0.135	0.0033	60

In Figure 5.17 results from the simulations and the present study are presented. Referring to the simulations, the Figure indicates that for mild slopes ($S_0 = 0.001$) the most uniform repartition of Q_{D1} and Q_{D2} is obtained (Q_{D2}/Q_{D1} close to 1.00). This means approximately the same fluid volumes are diverted over each of the two weirs ($Q_{D1} \approx Q_{D2}$). This repartition

appears to be almost insensitive of the approach discharge (Q_1), weir length ($L_{D,tot}$) and channel roughness (k_{st}). For steep slopes ($S_0 = 0.004$) and small discharges ($Q_1 = 0.150\ m^{1/3}/s$) the most non-uniform distribution is observed as indicated by the smallest Q_{D2}/Q_{D1}-ratios. Under these conditions the second weir might be partially or even completely dry (Q_{D2}/Q_{D1} close to 0.00).

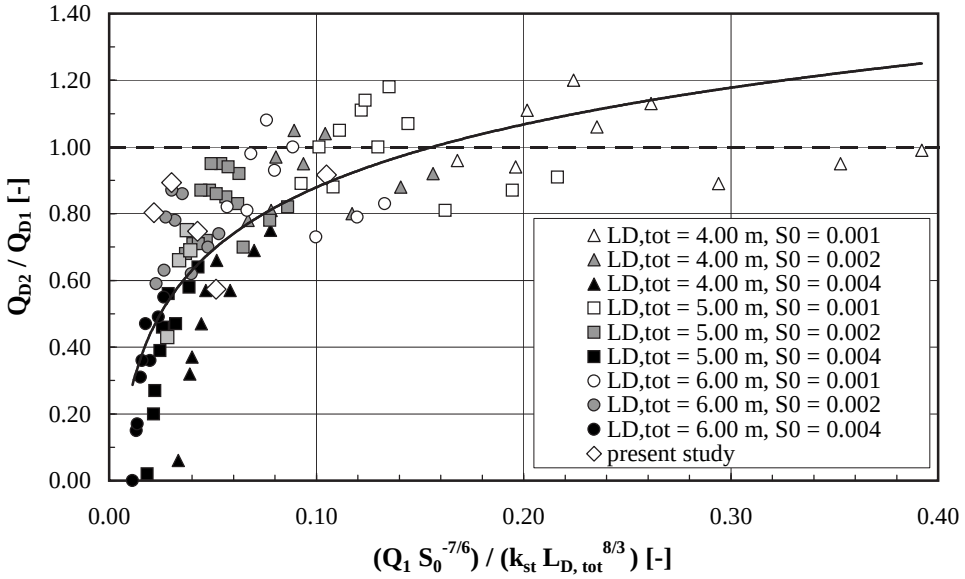

Figure 5.17: Comparison of side overflow repartition for two weirs under fixed and mobile bed conditions and different $L_{D,tot}$-values. The dashed line indicates $Q_{D2}/Q_{D1} = 1.00$. Fixed bed data was obtained from $1D$-numerical simulations, mobile bed data results from the present study (Eq. 5.18).

The data in Figure 5.17 suggest the following relation for the overflow repartition ($R^2 = 0.64$):

$$\frac{Q_{D2}}{Q_{D1}} = 0.27 \cdot ln\left(\frac{Q_1}{k_{st} \cdot L_{D,tot}^{8/3}} \cdot S_0^{-7/6}\right) + 1.51 \qquad (5.18)$$

Since the correlation of $R^2 = 0.64$ is rather moderate Figure 5.17 and Equation 5.18 are indicative and might mainly serve for an approximate estimation of the side overflow distribution for two weirs having a rather short separation wall ($L_{D,tot}/separation\ wall = 4.00 \div 6.00$).

Comparing mean Q_{D2}/Q_{D1}-ratios for fixed plane bed conditions (simulations) with those for mobile bed conditions (present study), the ratios summarized in Table 5.9 are obtained. It becomes evident that for mobile bed conditions a ratio of $Q_{D2}/Q_{D1} = 0.82$ is obtained, whereas for

fixed bed conditions a ratio of $Q_{D2}/Q_{D1} = 0.74$ is obtained. Consequently, the mobile bed and thus the deposit are responsable for a more uniform discharge distribution. In this context the so-called pseudo-uniform flow conditions as reported by Hager and Volkart (1986) are to mention. Pseudo-uniform flow condition might be achieved by proper modelling of the longitudinal channel geometry, e. g. linear channel width contraction (non-prismatic horizontal converging channel) or linear channel bottom increase (negative bottom inclination, non-prismatic vertical converging channel). Here, a negative bottom inclination induced by aggradation in the weir alignment is present.

Table 5.9: Side overflow repartition (Q_{D2}/Q_{D1}) for two weirs under fixed and mobile bed conditions (average values).

Study	Bed type	$L_{D,tot}/B$ [−]	S_0 [−]	Q_{D2}/Q_{D1} [−]
present	mobile	3.33	0.0033*)	0.82
Simulation (all)	fixed	2.67, 3.33, 4.00	0.0023**)	0.74
Simulation	fixed	3.33	0.001	0.99
Simulation	fixed	3.33	0.002	0.82
Simulation	fixed	3.33	0.004	0.40

*)mean energy slope S_e, **)mean bottom slope S_0

Looking only at experimental boundary conditions (Figure 5.18), hence $L_{D,tot}/B = 3.33$ ($L_{D,tot} = 5.00\ m$) and $S_0 = 0.0033$ (or $S_e = 0.0033$), the simulation runs with $S_0 = 0.002$ and $S_0 = 0.004$ are used for comparison. For these conditions an average Q_{D2}/Q_{D1}-ratio of $(0.82 + 0.40)/2 = 0.61$ is obtained for the fixed plane bed. Thus, the non-uniformity becomes even greater. Since $S_0 = 0.0033$ (experiments) is closer to $S_0 = 0.004$ than $S_0 = 0.002$ (simulations), an even smaller value of $Q_{D2}/Q_{D1} = 0.55$ is obtained by linear interpolation.

Concluding, the side overflow induced aggradation occurring under mobile bed conditions yields a significantly more uniform discharge repartition for the two weirs than for fixed plane bed conditions. Similar observations could also be made for the test series owing one side weir only (test series B and C).

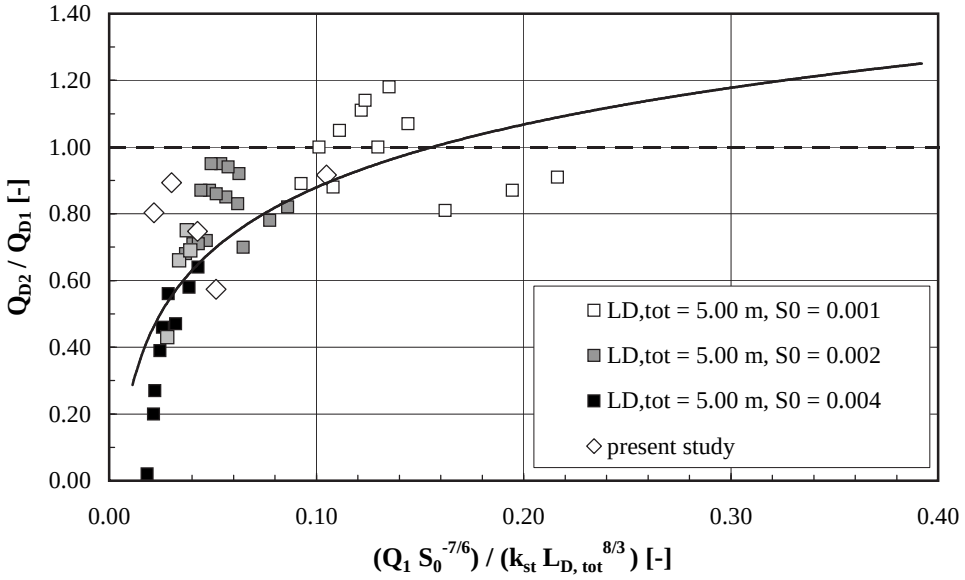

Figure 5.18: Comparison of side overflow repartition for two weirs under fixed and mobile bed conditions and $L_{D,tot} = 5.00\ m$. The dashed line indicates $Q_{D2}/Q_{D1} = 1.00$. Fixed bed data was obtained from $1D$-numerical simulations using DUPIRO, mobile bed data results from the present study.

5.4.3. Conclusion

For the mobile bed on average 55 % of the total side overflow are spilled over the first weir and about 45 % are diverted over the second one. Moreover, the two weirs behave similarly and the composed weir acts in the same way than the two individual weirs.

The investigation of the repartition of the overflow discharge for two weirs showed that the repartition on mobile bed conditions is considerably more uniform than for fixed plane bed conditions. The ratio of overflow discharge over the second weir to the one diverted over the first weir corresponds to $Q_{D2}/Q_{D1} = 0.82$ for the mobile bed and $Q_{D2}/Q_{D1} = 0.55$ for the fixed bed.

The reason for this more uniform repartition is the local sediment deposit near the weir inducing so-called pseudo-uniform flow conditions.

5.5. Lateral Outflow Angle

In this chapter measured lateral overflow angles are investigated and compared with two approaches from literature.

5.5.1. Measured Lateral Outflow Angles

Lateral outflow angles, defined as $tan\ \phi_D = v_y/v_x$ (see insert in Fig. 5.19 for definition) have been determined using the flow velocities (v_x, v_y) for the entire overflow water depth (pressure head above weir crest, h_D). In general this has been the part between $z/y = 0.75$ and 1.00 or approximately the upper 1/4 of the total flow depth (y) (Figs 5.26 and 5.27). The UVP-probes used for the determination of ϕ_D are located at $y_B = 1.20\ m$, thus not on the crest of the side weir but 0.30 m towards the channel centre line. In Table 5.10 measured outflow angles for the three test series are presented.

Table 5.10: Lateral outflow angles (ϕ_D) along the weir crest for the present study.

Test series	Minimum ϕ_D [°]	Maximum ϕ_D [°]	Mean ϕ_D [°]
B	−4	24	7
C	−1	4	2
D	−5	17	4
average	−3	15	4

A typical streamwise evolution of the outflow angle is shown in Figure 5.19. It can be seen that up- and downstream of the weir the deflection angle is close to zero. In the weir alignment the outflow angel increases towards its maximum located at $x_{\phi_{D,max}} = 7.00\ m$ or 2/3 L_D before decreasing towards the downstream weir corner. Regarding the entire data set (series B, C and D) the location of the maximum outflow angle ($x_{\phi_{D,max}}$) is represented by the ratios $x_{\phi_{D,max}}/L_D = 0.72$ (test series B), 0.80 (test series C) and 0.78 (test series D). This means that the location of the maximum outflow angle is shifted towards the downstream weir corner with increasing weir length:

$$x_{\phi_{D,max}}(series\ C) > x_{\phi_{D,max}}(series\ D) > x_{\phi_{D,max}}(series\ B) \tag{5.19}$$

To determine the average location of the maximum lateral outflow angle the following relation is suggested:

$$\frac{x_{\phi_{D,max}}}{L_D} = 0.76 \approx 3/4 \quad \text{or} \quad x_{\phi_{D,max}} \approx 3/4 \cdot L_D \tag{5.20}$$

The location of the maximum outflow angle is close to the location of the maximum elevation of the sedimentary deposit.

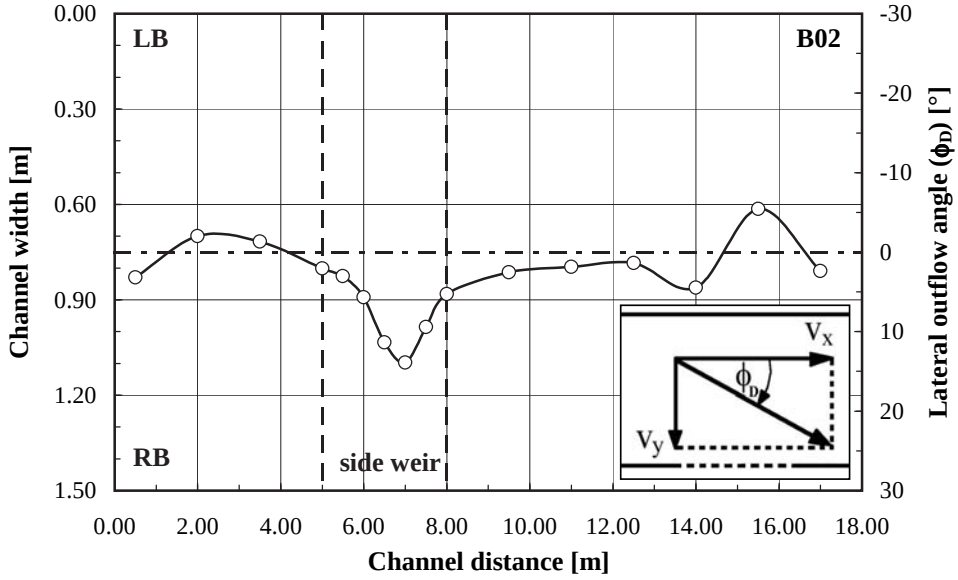

Figure 5.19: Streamwise evolution of the lateral outflow angle (ϕ_D) for test series $B02$. LB and RB denote left and right river bank, respectively.

5.5.2. Comparison of measured and predicted Lateral Outflow Angles

To compare outflow angles from the present investigation with relations from literature the approaches by Subramanya and Awasthy (1972) and Hager (1987b) are considered.

Using the approach Froude number in section 1 (Fr_1), Subramanya and Awasthy (1972) propose the following expression for the deflection angle (ϕ_D):

$$sin\ \phi_D = \sqrt{1 - \frac{3 \cdot Fr_1^2}{2 + Fr_1^2}} \tag{5.21}$$

Introducing the dimensionless variables:

$$N = \frac{y}{E} \quad \text{and} \quad M = \frac{w_D}{E} \tag{5.22}$$

the lateral outflow angle (ϕ_D) for a prismatic, nearly horizontal side weir, is given by Hager (1987b):

$$sin\ \phi_D = \left(\frac{N - M}{3 - 2 \cdot N - M} \right)^{1/2} \tag{5.23}$$

with y flow depth, E specific energy, w_D crest height and $N = y/E$ relative flow depth and $M = w_D/E$ relative weir height.

In Table 5.11 mean outflow angles resulting from the two approaches described above are summarized. Since the radicand in Equation 5.21 becomes negative for Froude numbers exceeding a value greater than 1.00 ($Fr_1 > 1.00$), experiments $C01$, $C02$ and $C03$ are not considered in the approach by Subramanya and Awasthy (1972). For the same reason experiment $B04$ could not be included applying the approach by Hager (1987b).

Table 5.11: Comparison of measured lateral outflow angles (ϕ_D) with two approaches from literature.

Author	Minimum ϕ_D [°]	Maximum ϕ_D [°]	Mean ϕ_D [°]
Subramanya and Awasthy (1972)	10	48	33
Hager (1987b)	17	30	25
present study	−3	15	4

Table 5.11 indicates that measured deflection angles from the present study are significantly smaller than those computed by approaches from literature. Regarding the approach of Subramanya and Awasthy (1972) measured angles only amount to $4/33 = 12$ % of computed values. For Hager (1987b) this ratio is $4/25 = 16$ %. Moreover, Hager (1982b) stated measured values in the range of $\phi_D = 26° \div 50°$.

The difference between computed and measured angles is mainly due to different geometric and hydraulic boundary conditions (Tables 2.1 to 2.4), e. g. different L_D/B- and y_1/L_D-ratios, horizontal bottom slope, non-movable bed and restricted outflow conditions (Fig. 5.6), weirs of zero height ($w_D = 0.00\ m$), weirs with dead end ($Q_D = Q_1$, $Q_2 = 0.00\ m^3/s$) and different Froude numbers (Fr_1). With respect to measured Froude numbers comparatively high values are observed ($0.55 \leq Fr_1 \leq 1.10$, mean Froude number $Fr_1 = 0.79$). This means the longitudinal velocity component is much greater than the lateral one ($v_x \gg v_y$), resulting in small lateral outflow angles.

For $Q_D/Q_1 < 0.5$, being the case for the present study, El-Khashab and Smith (1976) reported that a considerable part of the approach flow remains in the main channel and that there is a strong forward velocity which has a dominant effect on flow conditions. Moreover, as stated above, the UVP-probes used for the determination of ϕ_D are located at $y_B = 1.20\ m$, thus not on the crest of the side weir but $0.30\ m$ towards the channel centre line.

Since the two approaches from literature do not properly reflect the results of the present study, a new and more appropriate relation for mean outflow angles at high discharges and (implicitly!) mobile bed conditions is developed.

Within this context the outflow angle is supposed to be a function of channel and side weir geometry as well as flow conditions. To account for flow conditions the Froude number (Fr_1) is expected to represent an adequate parameter. Finally, the outflow angle is assumed to depend on a product of power relationships of the type:

$$sin\ \phi_D = y = f(x_i) = f\left(x_1^{\alpha} \cdot x_2^{\beta} \cdot x_3^{\gamma} \cdot x_4^{\delta} \cdot x_5^{\epsilon}\right) \tag{5.24}$$

Using dimensional analysis the coefficients x_1 through x_5 were found to be $x_1 = Q_1$, $x_2 = g$, $x_3 = B$, $x_4 = L_D$ and $x_5 = Fr_1$. The exponents α to ϵ were determined to be $\alpha = 1$, $\beta = -1/2$, $\gamma = -1/2$, $\delta = -2$ and $\epsilon = -1$. Hence, Equation 5.24 reads:

$$sin\ \phi_D = y = f(x) = f\left(Q_1 \cdot \frac{1}{\sqrt{g}} \cdot \frac{1}{\sqrt{B}} \cdot \frac{1}{L_D^2} \cdot \frac{1}{Fr_1}\right) \tag{5.25}$$

Finally, by curve fitting, a linear relationship has been identified:

$$sin\ \phi_D = y = f(x) = 16.91 \cdot x + 0.02 \tag{5.26}$$

Resuming, the following expression for the determination of lateral outflow angles at high discharges and (implicitly) mobile bed conditions is proposed (Fig. 5.20):

$$sin\ \phi_D = y = f(x) = 16.91 \cdot \left(\frac{Q_1}{\sqrt{g \cdot B} \cdot L_D^2} \cdot \frac{1}{Fr_1}\right) + 0.02 \tag{5.27}$$

Note that the term $Q_1/((gB)^{1/2}L_D^2)$ is defined like a Froude number. The R^2-value of Equation 5.27 is 0.75.

With $Q_1 = v_1 B y_1$ and $Fr_1 = v_1/(g y_1)^{1/2}$ Equation 5.27 might be expressed as:

$$sin\ \phi_D = y = f(x) = 16.91 \cdot \left[\left(\frac{B}{L_D}\right)^{1/2} \cdot \left(\frac{y_1}{L_D}\right)^{3/2}\right] + 0.02 \tag{5.28}$$

Since the second ratio of x in Equation 5.28 (y_1/L_D) is raised to the power of 3/2, the influence of flow conditions (y_1) is of greater importance than channel geometry (B), raised to the power of 1/2.

With respect to extreme values for $x = 0.00$, e. g. long weir crest (L_D) and B and $y_1 = const.$, Equation 5.28 yields $sin\ \phi_D = 0.02$ representing an outflow

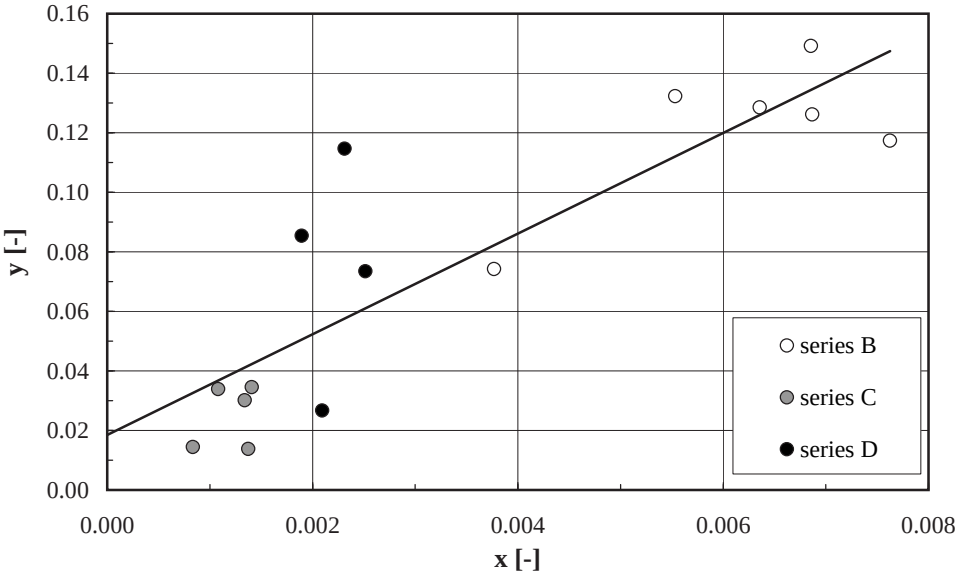

Figure 5.20: Approach for the estimation of the lateral outflow angle (ϕ_D) at high discharges and mobile bed conditions (Eqs 5.27 and 5.28).

angle of $\phi_D = 1.15°$. For great x-values the maximum of $sin\ \phi_D$ is given by 1.00 ($\phi_D = 90°$). This condition is achieved for $x = 0.06$. Consequently, the (theoretical) application range of Equation 5.28 is $0.00 \leq x \leq 0.06$ and $0.02 \leq y \leq 1.00$ (valid for $0.25 \leq B/L_D \leq 0.50$ and $0.014 \leq y_1/L_D \leq 0.049$).

Equation 5.27 (or 5.28) has been developed on the basis of measured outflow angles at $y_B = 1.20\ m$, thus not immediately at the weir but 0.30 m towards the channel center line. To estimate the outflow angle near the weir a logarithmic or linear extrapolation procedure is suggested. The choice of a logarithmic or linear extrapolation depends on the shape of the spanwise velocity distribution in the $x - y$-plane (plan view). Hence, computed angles according to Equation 5.27 (or 5.28) might be increased by a factor of 1.33 (logarithmic) or 1.52 (linear) to obtain the outflow angle near the weir ($y_B \approx 1.50\ m$):

$$\begin{aligned} \text{logarithmic extrapolation:} \quad & 1.33 \\ \text{linear extrapolation:} \quad & 1.52 \end{aligned} \tag{5.29}$$

In contrast to the approaches of Subramanya and Awasthy (1972) and Hager (1987b) an advantage of Equation 5.27 (or 5.28) is the explicit appearance of channel geometry (B), side weir geometry (L_D) and flow conditions (Q_1, Fr_1, y_1). In Equation 5.21 only flow variables (Fr) occur,

whereas in Equation 5.23 only flow conditions (y, E) and weir geometry (w_D) interfere.

5.5.3. Conclusion

The analysis of measured outflow angles indicated that the location of the maximum outflow angle is shifted towards the downstream weir corner with increasing weir length. The location of the maximum outflow angle is close to the location of the maximum elevation of the sedimentary deposit.

A comparison of measured and computed outflow angles showed that the measured angles are significantly smaller than predicted ones. The discrepancy is mainly due to different geometric and hydraulic boundary conditions, e. g. a non-movable bed, restricted outflow conditions and substantially smaller Froude numbers in the approaches from literature.

For that reason a new relationship based on channel and side weir geometry as well as flow variables has been developed. Since measured outflow angles have not been determined immediately at the weir crest a correction procedure for extrapolation is proposed.

5.6. Three-Dimensional Flow Field at Lateral Outflow

In this chapter the three-dimensional flow pattern for different zones in the main-channel are analyzed. Furthermore, the dividing stream plane separating the flow that enters the side weir from the flow that continues downstream is investigated. Finally, the strength of a secondary circulation is examined.

5.6.1. Flow Zones and Streamline Pattern in Channel with a Side Weir

According to the one-dimensional flow theory the surface profile in side weir channels is influenced by the local Froude number, the channel and lateral outflow geometries and the up- and downstream flow conditions (Hager and Volkart (1986)). Helpful information concerning the flow pattern in side weir channels can be derived from studies concerning lateral intake structures and open-channel diversions (Neary et al. (1999)). An analogy of flow structure at diversion channels and bend flows is assumed by Neary and Odgaard (1993).

Figure 5.21 shows the simplified, spatial flow mechanism in side weir channels for subcritical flow conditions (points (1) to (3) and (5)). In addition,

streamline pattern in presence of a submerged obstacle or deposit close to the weir are presented (point (4)).

To demonstrate typical flow pattern of the present study representative results using exemplarily test series $B04$ are presented in the following paragraphs.

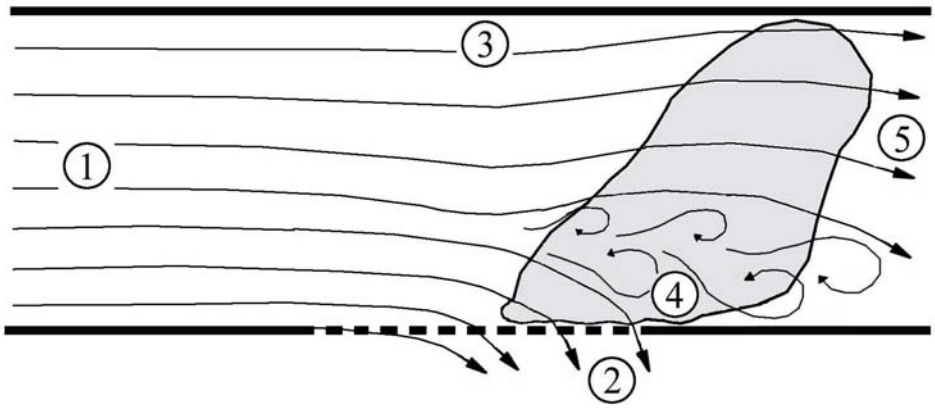

Figure 5.21: Different flow zones in a channel with a side weir and streamline pattern for a submerged obstacle (sediment deposit) located at the downstream weir corner. Zone 1 is the inflow zone, zone 2 is the lateral outflow zone, zone 3 a separation zone, zone 4 a stagnation or second separation zone and zone 5 the zone where the flow field re-establishes.

5.6.2. Flow Field upstream of Side Weir

- Zone 1 (Fig. 5.21):

  The extent of the inflow zone (1) depends on the magnitude of the downstream submergence. It is characterised by nearly uniform velocity distributions and almost horizontal transverse surface profiles (Hager and Volkart (1986)).

  In Figure 5.22 representative cross sectional streamwise and lateralwise velocity profiles for region (1) are presented. Since the longitudinal UVP-probe at $y_B = 0.30\ m$ was not operating, no signal has been obtained for v_x. The lateralwise velocity (v_y) on the left river bank at $y_B = 0.30\ m$ is always positive meaning orientated towards the right bank. The vertical distribution is homogeneous being rather close to zero ($v_y \approx 31\ mm/s$). As for $y_B = 0.30\ m$, the transverse velocity at $y_B = 0.60\ m$ is always positive and distributed almost homogenously throughout the entire water depth. For $y_B = 0.90\ m$, v_y is rather small as well with a slightly increasing bottom component towards the bank opposite of the weir.

Close to the right bank at $y_B = 1.20\ m$ the lateral velocity distribution is similar to the preceding spanwise positions. Resuming, the transverse component at all lateralwise locations is rather small varying between $v_y \approx\ 31\ mm/s$ and $\approx\ 111\ mm/s$. With respect to the longitudinal velocities (v_x) the profiles at all lateralwise locations are characterised by a nearly uniform distribution.

The flow field described above is presented in terms of isovels in Figures 5.23 and 5.30 (top). Both, the vertical and lateralwise velocity distribution is rather uniform. The center of maximum streamwise velocity is located almost in the middle of the channel and no significant transverse flow can be identified.

Referring to the difference between mean lateralwise and streamwise velocities, the streamwise velocity for $y_B = 0.60\ m$ is $v_x/v_y = 6.0$ times greater than the transverse one (Fig. 5.22, Tab. 5.12). Approaching the right channel bank this ratio decreases to $v_x/v_y = 4.8$ at $y_B = 0.90\ m$ and further decreases to $v_x/v_y = 4.4$ at $y_B = 1.20\ m$. In this context the depth averaged flow velocity is assumed to be located at $z/y = 0.368$ (see Fig. A.1).

To describe the distortion of the $2D$-velocity profile a torsion angle (ϕ_t) between the flow velocity in channel axis (v_x) and the transverse one (v_y), defined as $tan\ \phi_t = v_y/v_x$, is introduced (see insert in Fig. 5.27 for definition). Regarding this angle it is evident that at $y_B = 0.60\ m$ the angle is distributed nearly homogeneously over the flow depth with a mean value corresponding to $\phi_t = 12.3°$ (Fig. 5.22, Tab. 5.12). In the near-surface part of the profile a value of $\phi_t = 13.8°$ is measured. At the bottom between $z/y = 0.00$ and 0.20 this angle reaches 20.7° indicating a pronounced lateral flow component. Regarding the location at $y_B = 0.90\ m$, the vertical evolution of ϕ_t appears to be almost constant with a slightly increased component towards the left bank at the bottom. The average near-bed angle yields 5.3°. In the near-surface region a value of 12.2° is measured and the mean angle corresponds to 9.8°. On the right channel bank at $y_B = 1.20\ m$, increased values for all three angles are observed, namely 19.5° close to the surface, 26.0° close to the bed and 17.2° for the entire profile.

These results indicate that, although still rather far upstream of the side overflow, a certain, but slight, effect of the overflow device on the flow pattern might be identified. This fact is indicated by a decreased v_x/v_y-ratio and an increased near-surface torsion angle. Moreover, a considerable bed variability is manifested by both positive and negative transverse velocities as well as near-bed torsion angles.

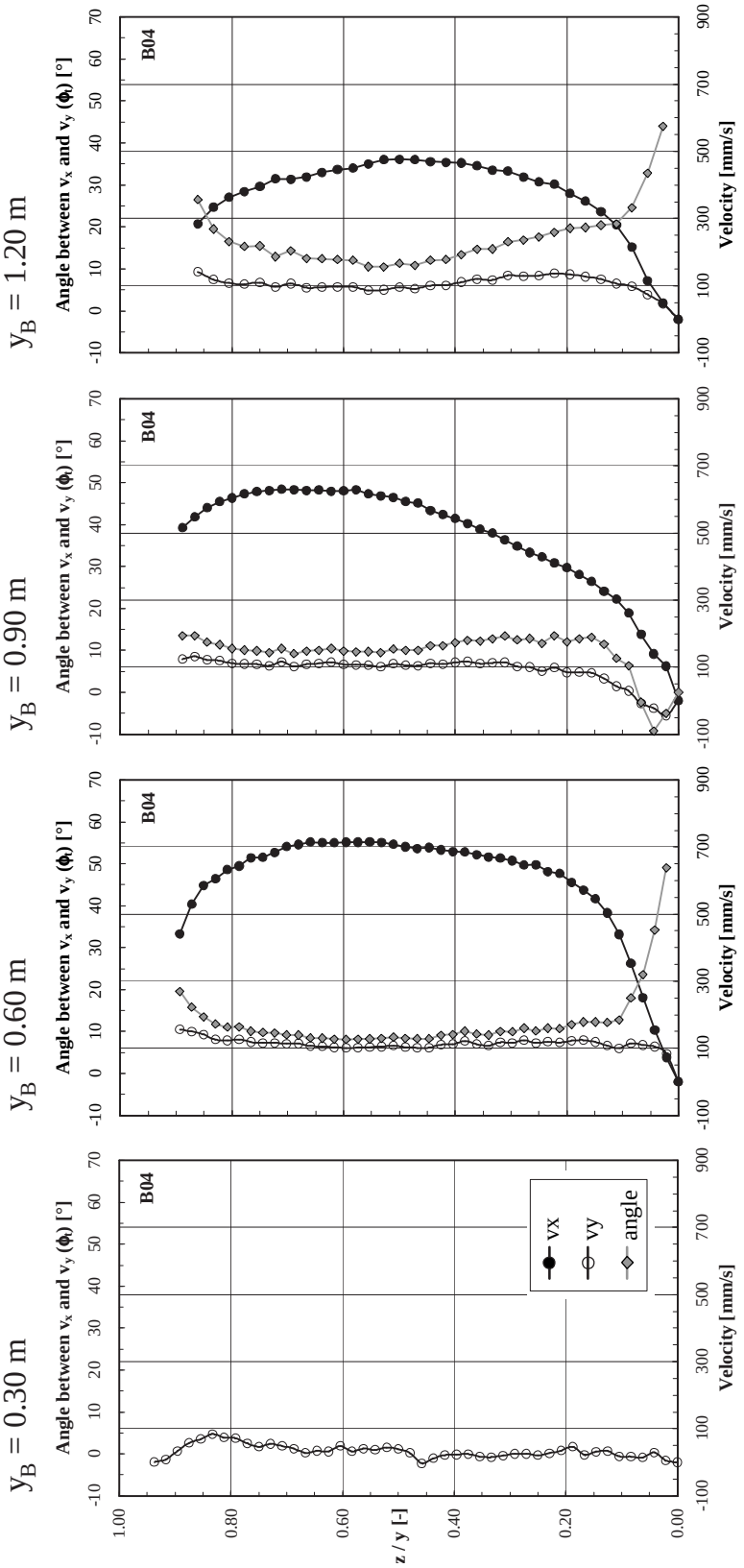

Figure 5.22: Normalised spanwise $2D$-velocity distribution and torsion angle (ϕ_t, definition see Fig. 5.27) upstream of the side weir at $x = 2.00\ m$ for experiment $B04$ (UVP-probe N^o 2).

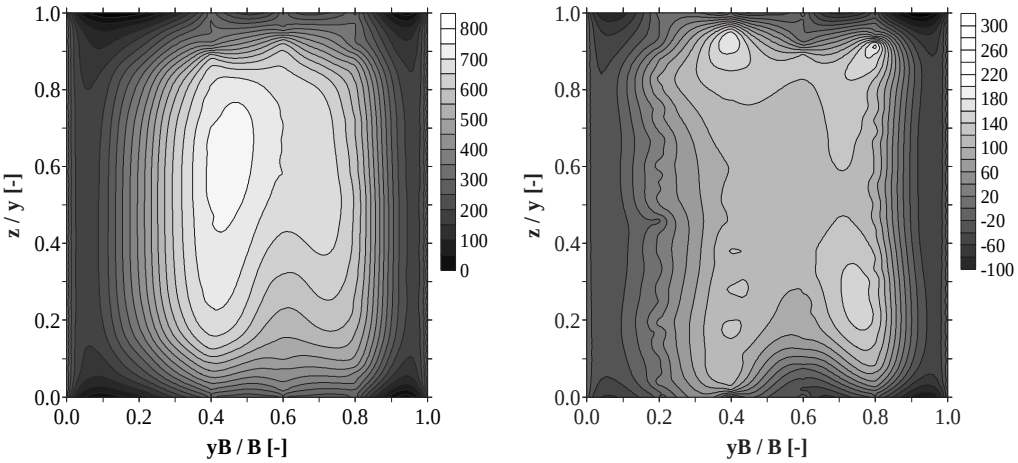

Figure 5.23: Streamwise (left) and lateralwise (right) isovels in $[mm/s]$ for experiment $B04$ upstream of the weir at $x = 2.00\ m$.

5.6.3. Flow Field at Side Weir

- Zone 2 (Fig. 5.21):

  The flow accelerates at the entrance of the side weir channel and potential energy is transformed into kinetic energy along the weir plane, thus forming the lateral outflow zone (2). Beside the increase in the magnitude of the velocities, the direction of the accelerating flow might deviate considerably from the channel axis. Streamlines are sloped and curved but lateral outflow may be approximated as potential flow (Hager and Volkart (1986)).

  In Figure 5.24 representative cross sectional streamwise and lateralwise velocity profiles for region (2) are shown. For the UVP-probe at $y_B = 0.30\ m$ no signal for v_x has been obtained. The transverse velocity (v_y) close to the left river bank ($y_B = 0.30\ m$) is almost zero with a slight positive component at the surface towards the right bank and a higher negative component at the bottom towards the left bank. Due to this skewed distribution a rather weak circulation cell might suggested to exist in the left channel region. The negative v_y-component at the bottom is the active force for erosion towards the left bank. At $y_B = 0.60\ m$, v_y is always positive and distributed almost homogenously throughout the entire water depth. A slightly higher component above the weir crest level in direction of the weir can be observed. For $y_B = 0.90\ m$ the transverse velocity towards the weir increases throughout the entire flow depth. The longitudinal velocities (v_x) at $y_B = 0.60\ m$ and $y_B = 0.90\ m$ are characterised by a nearly uniform distribution. Close to the weir at $y_B = 1.20\ m$ the lateral velocity distribution is similar to

the preceding position but a slightly higher positive component at the bottom than at the top is encountered. At the bottom the transverse component is even greater than the longitudinal one (v_x). This fact might be indicative for increased bed-load transport towards the weir, thus favoring the formation of a local sedimentary deposit.

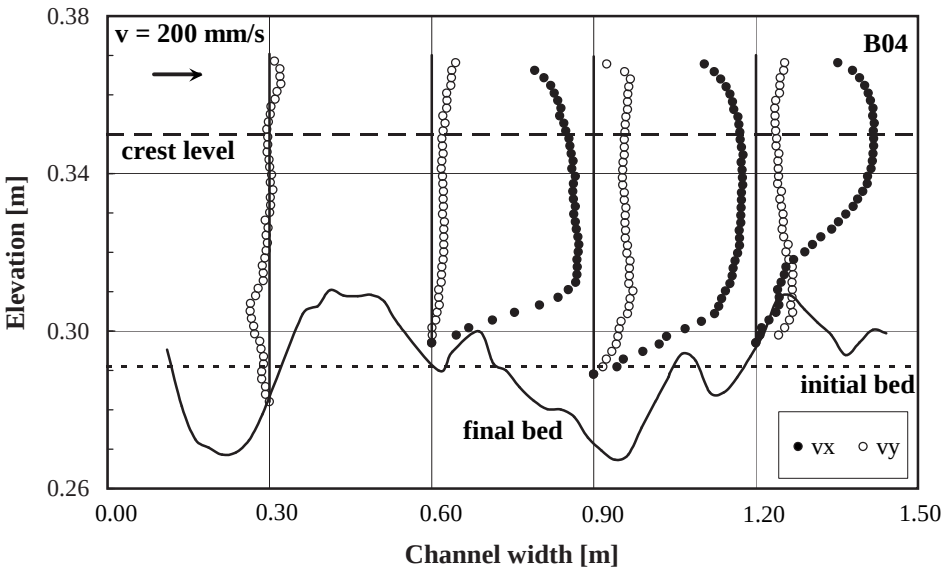

Figure 5.24: Cross sectional streamwise and lateralwise velocity distribution ($B04$, UVP-probe N^o $6b$, $x = 7.50\ m$). For some locations, e. g. $y_B = 0.90\ m$, the final bottom geometry does not correspond exactly to the origin of the velocity profile. This is due to the fact that the last UVP-sampling has been done slightly before the experiment has been stopped to take the photographs for the photagrammetric treatment to obtain the DEM.

Looking at the distribution of the isovels (Figs 5.25 and 5.30, middle) it turns out that the center of maximum streamwise velocity is slightly shifted from its central position at $x = 2.00\ m$ towards the weir. Moreover, an upwards displacement of the region of maximum flow velocity can be identified. The highest transverse velocities are encountered at the overflow. Close to the weir near the bed a strong transverse velocity component towards the right bank is present. Immediately at the wall the flow is reflected resulting in negative lateralwise velocities. Compared to the preceding cross section the flow field is characterised by considerable non-uniformity.

As far as the difference between mean lateralwise and streamwise velocities is concerned the streamwise velocity for $y_B = 0.60\ m$ is

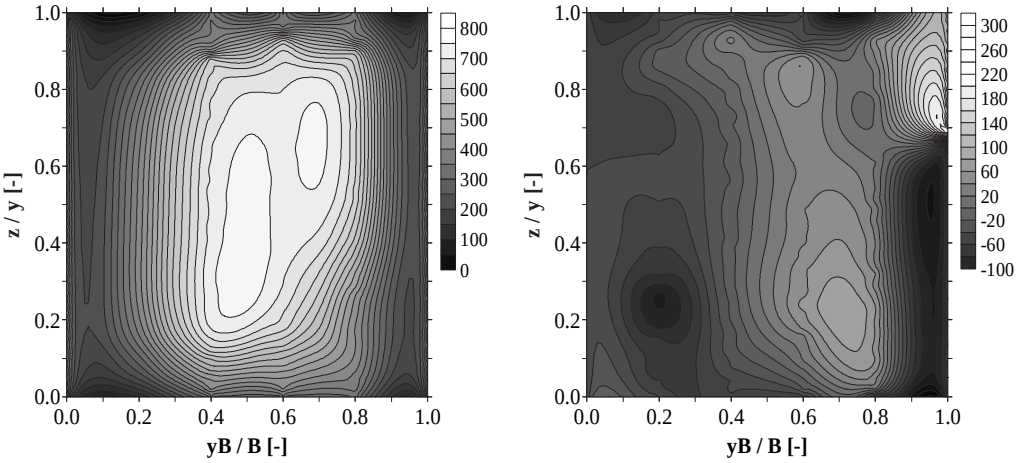

Figure 5.25: Streamwise (left) and lateralwise (right) isovels in $[mm/s]$ for experiment $B04$ in the weir reach at $x = 7.50\ m$.

$v_x/v_y = 12.1$ times greater than the transverse one (Fig. 5.26, Tab. 5.12). For $y_B = 0.90\ m$ this ratio decreases to $v_x/v_y = 4.5$ and further decreases to $v_x/v_y = 3.1$ at $y_B = 1.20\ m$. As said before the depth averaged flow velocity is assumed to be located at $z/y = 0.368$.

Looking at the torsion angle (ϕ_t) (Fig. 5.26, Tab. 5.13) it becomes evident that at $y_B = 0.60\ m$ the angle is distributed nearly homogeneously over the flow depth with a mean value corresponding to $\phi_t = 4.9°$. For the overflow part of the profile between the water surface and the weir crest a value of $\phi_t = 7.4°$ is measured. At the bottom between $z/y = 0.0$ and 0.20 this angle yields a value of 3.0°. With respect to $y_B = 0.90\ m$ the mean angle is $\phi_t = 14.0°$, the angle in the overflow part is $\phi_t = 13.1°$ and the near-bed value amounts to 18.9°. In the weir neighborhood at $y_B = 1.20\ m$, ϕ_t-values of 28.0° (mean) and $\phi_t = 12.1°$ (overflow part) are observed (for the overflow part at $y_B = 1.20\ m$ the torsion angle ϕ_t corresponds to the lateral outflow angle ϕ_D). In the bottom part ϕ_t mounts even up to 64.5° (mean). A detailed view of the flow pattern at $y_B = 1.20\ m$ is given in Figure 5.27 for test series $B01$ (the phenomena are similar to the ones described for series $B04$ but more pronounced). The mean ϕ_t-value is 30.3°, the one in the overflow part of the profile corresponds to $\phi_t = 16.1°$ and the near-bed angle ($z/y = 0.00 \div 0.20$) yields 51.8°. The ratio v_x/v_y (depth averaged flow velocity at $z/y = 0.368$) is 1.7.

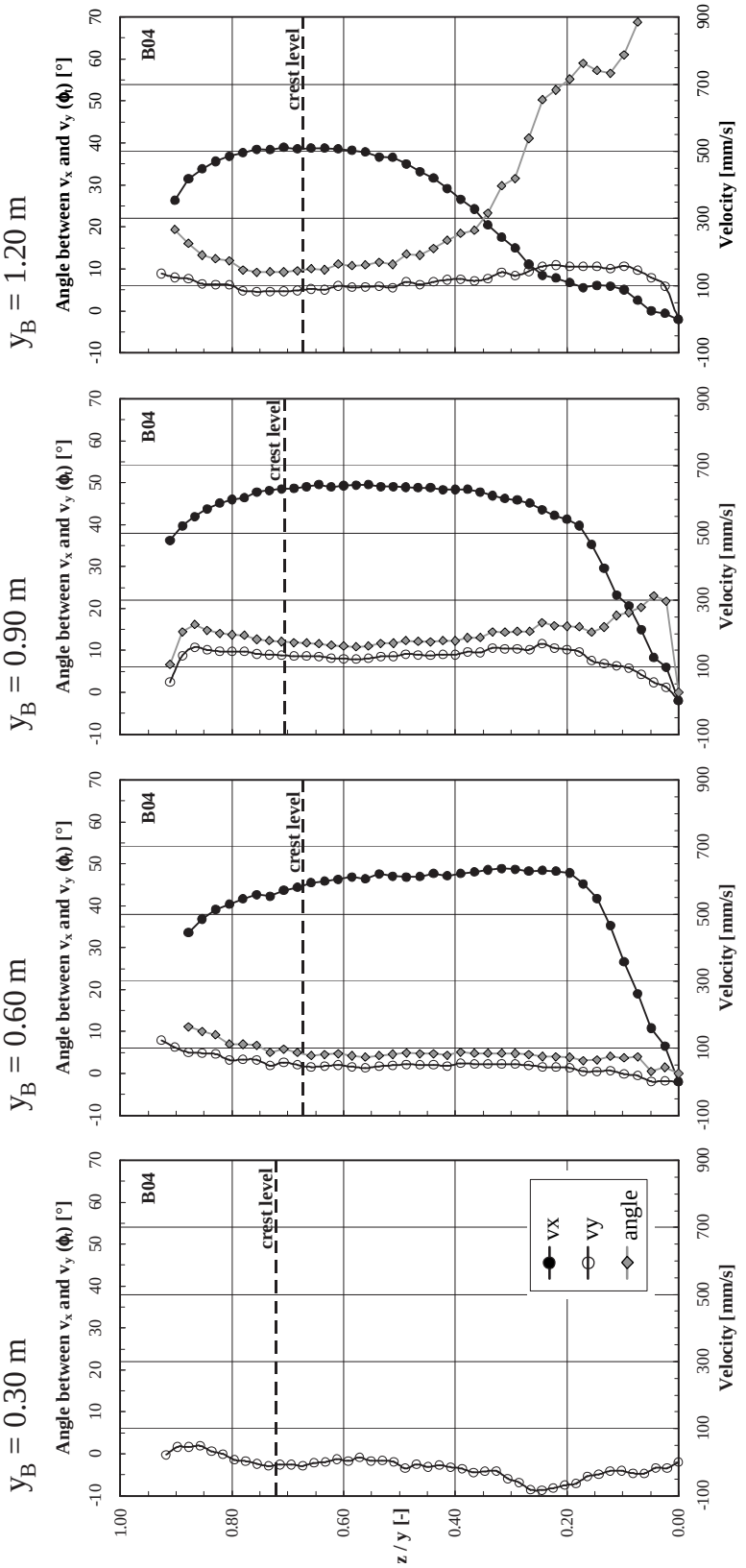

Figure 5.26: Normalised spanwise $2D$-velocity distribution and torsion angle (ϕ_t, definition see Fig. 5.27) in the weir reach at $x = 7.50\ m$ for experiment $B04$ (UVP-probe N^o $6b$).

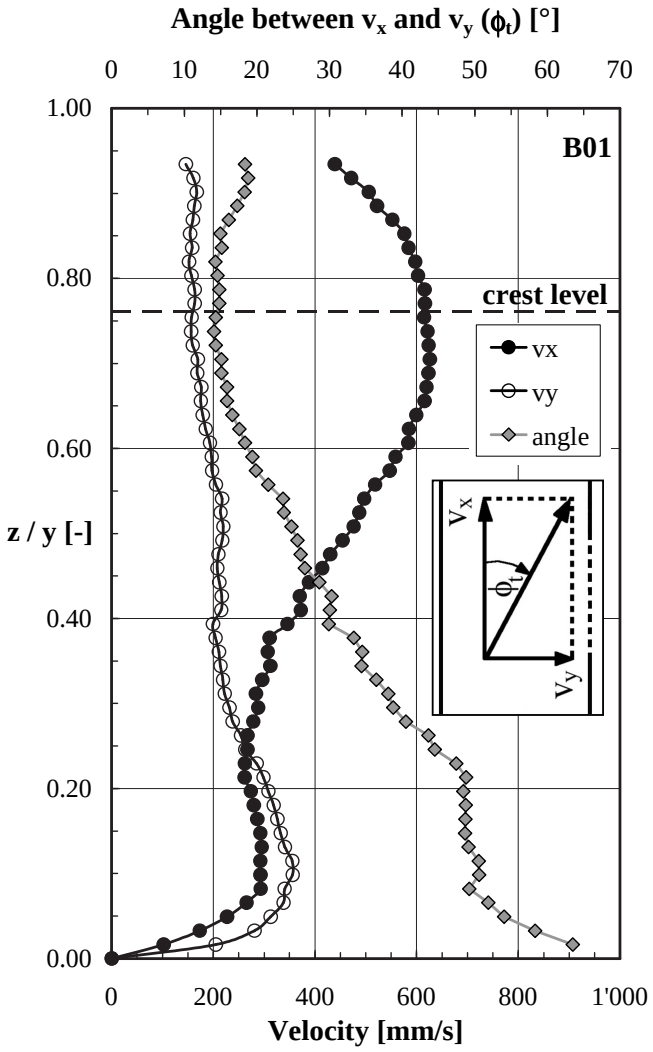

Figure 5.27: $2D$-velocity distribution and torsion angle (ϕ_t) between v_x and v_y close to the side overflow for experiment $B01$. The streamwise location of the profiles is at $x = 8.00\ m$ (downstream weir corner, section 2), the lateralwise position at $y_B = 1.20\ m$ (UVP-probe N^o 7). The flow depth at $y_B = 1.20\ m$ has been $y = 12.5\ cm$, the mean flow depth for the entire cross section $y = 14.8\ cm$.

5.6.4. Flow Field at opposite Bank of Side Weir and at downstream Weir Corner

- Zone 3 (Fig. 5.21):

  Particles situated opposite to the outflow zone, however, might not be able to follow the lateral outflow. Their movement is slowed and a separation zone (3) might develop. The flow going over the weir effectively pulls the flow that remains in the main-channel away from the opposite side of the channel. Subramanya and Awasthy (1972) stated a considerable effect of the side weir on the velocity distribution in the immediate neighborhood of the weir and observed a separation zone located at point (3). El-Khashab and Smith (1976) reported for Q_D/Q_1-values of about 0.70 that the velocity in the main-channel towards the end the weir has been that much retarded that separation and a dead water zone occurred. The location and size of that zone was found to depend on Fr_1 and L_D (Hager and Volkart (1986)).

  In this study, however, no such separation zone has been observed. This might be mainly attributed to the fact that lower Q_D/Q_1-ratios than 0.70 as reported by El-Khashab and Smith (1976) are present. Here, ratios varying between 0.04 and 0.37 with a mean ratio of 0.21 are measured. These rather small ratios compared to 0.70 are in accordance with elevated upstream Froude numbers ($0.55 \leq Fr_1 \leq 1.10$, mean Froude number $Fr_1 = 0.79$).

- Zone 4 (Fig. 5.21):

  Some streamlines do not leave the main-channel and might create a stagnation or second separation zone (4) with eventually reverse flow at the downstream weir corner at the obstacle location (Neary et al. (1999)).

  As mentioned before the streamwise velocity component is dominating the transverse one. For this reason no distinct stagnation zone with reverse flow has been observed. Nevertheless, scour has occurred immediately at the downstream weir corner due to significant downflow and impingement on the bed. Similar observations are reported by Neary et al. (1999).

5.6.5. Flow Field downstream of Side Weir

- Zone 5 (Fig. 5.21):

  Downstream of the side weir the flow field re-establishes, thus creating zone (5).

As shown in Fig. 5.28, the vertical distribution of the transverse velocity component at $y_B = 0.30\ m$ is always positive and homogeneous being rather close to zero ($v_y \approx\ 27\ mm/s$). Similar observations can be stated for the next section at $y_B = 0.60\ m$ but the average velocity is always negative ($v_y \approx\ -29\ mm/s$). At $y_B = 0.90\ m$, v_y is always positive being slightly higher in the upper part of the profile than in the lower part. Close to the right bank at $y_B = 1.20\ m$ the lateral velocity distribution is similar to the preceding positions. Regarding the streamwise velocities the profiles at all lateralwise location are characterised by a nearly uniform distribution.

The presentation of the isovels (Figs 5.29 and 5.30, bottom) indicates an almost uniform distribution of the streamwise velocity component with its center located towards the right bank and closer to the bottom than for the preceding cross section. The maximum transverse velocity component is situated right from the channel center as well. The flow field is rather uniform compared to the weir region but less than upstream of the weir. Hence, a week impact of the flow-sediment interaction induced by the weir is still present.

As far as the difference between depth averaged mean lateralwise and streamwise velocities is concerned, the streamwise component for $y_B = 0.60\ m$ is $v_x/v_y = -30.5$ times greater than the transverse one (Fig. 5.28, Tab. 5.12). Coming closer to the right channel bank this ratio first yields $v_x/v_y = 8.5$ at $y_B = 0.90\ m$ before slightly increasing to $v_x/v_y = 12.5$ at $y_B = 1.20\ m$.

With respect to the torsion angle (ϕ_t) small negative values for $y_B = 0.60\ m$ are observed. The almost constant distribution reveals a mean value of $\phi_t = -3.9°$, a near-surface angle of $-3.0°$ and a near-bed angle of $-6.9°$ (Fig. 5.28, Tab. 5.12). For the other two lateralwise locations at $y_B = 0.90\ m$ and $y_B = 1.20\ m$ no significant deviations from a vertically uniform distribution can be recognized. The average near-bed angles yield 3.8° and 8.5° for the respective locations. Considering the near-surface angle values of 12.5° and 6.5° are determined. The mean angles for the entire profile are 7.5° and 5.6°, respectively.

Concluding, the flow field downstream of the weir has fully re-established. This matter of fact is indicated by a uniform longitudinal velocity distribution and a transverse velocity component comprising both negative and positive values, thus showing no distinct tendency towards the left or right channel bank but representing typical bottom variations. Moreover, the $2D$-flow pattern is characterised by small torsion angles and an increased v_x/v_y-ratio compared to the upstream region and the weir alignment.

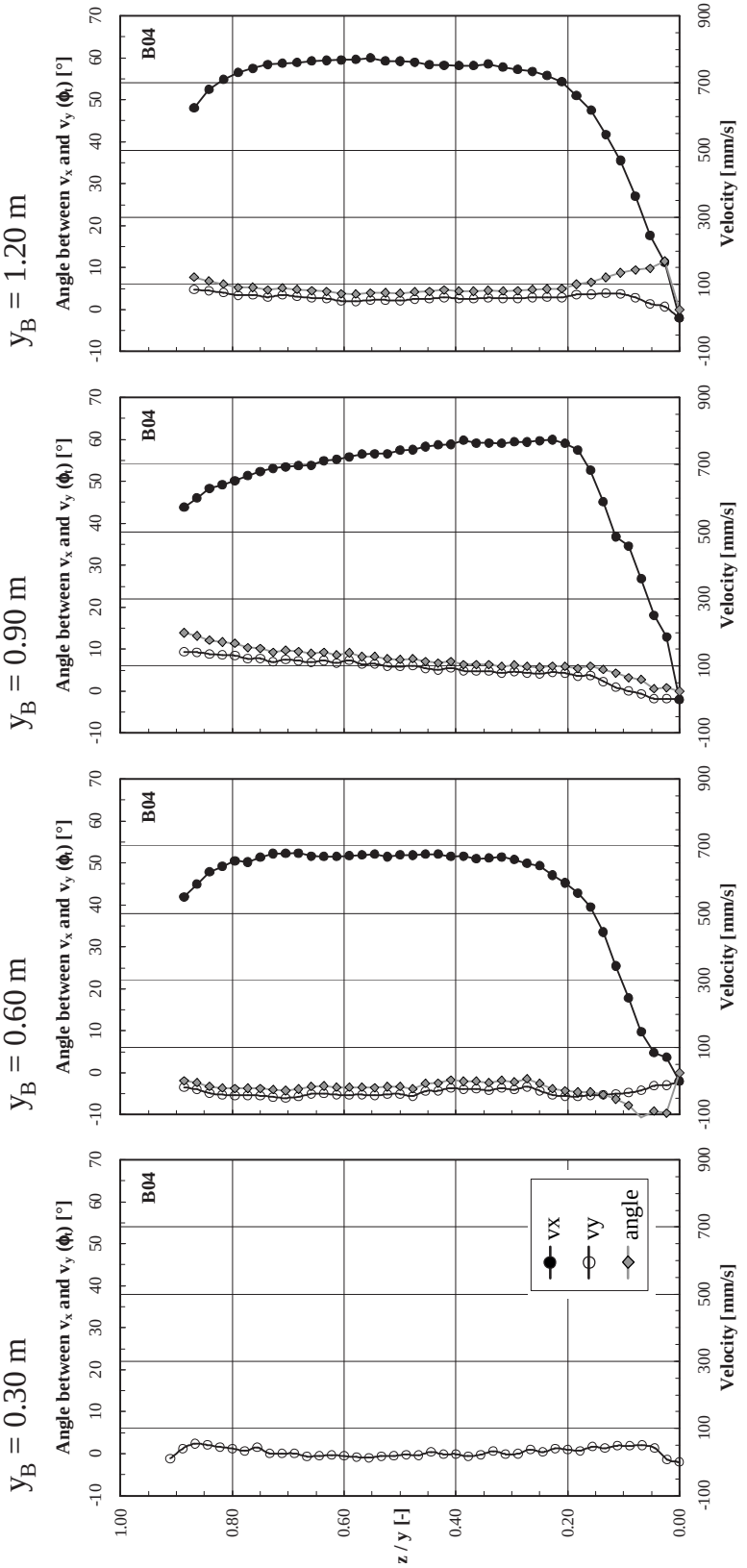

Figure 5.28: Normalised spanwise $2D$-velocity distribution and torsion angle (ϕ_t, definition see Fig. 5.27) downstream of the side weir at $x = 14.00\ m$ for exp. $B04$ (UVP-probe N^o 11).

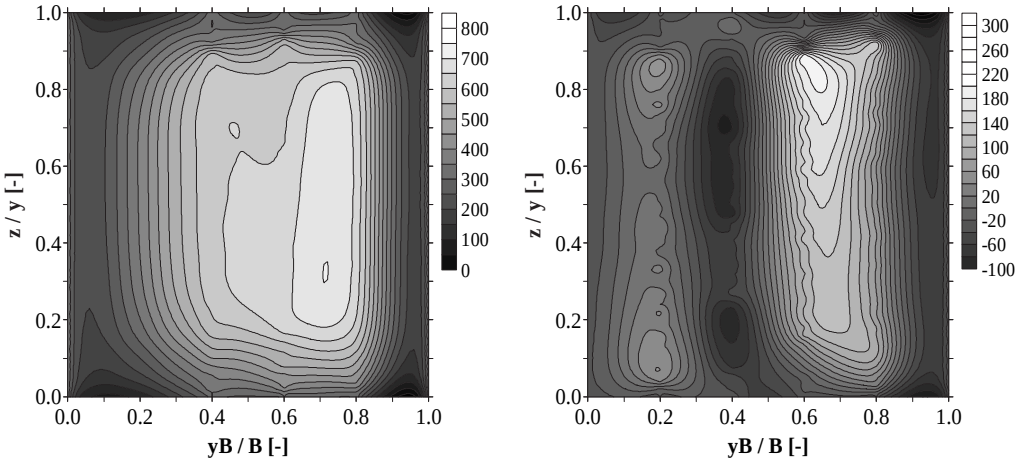

Figure 5.29: Streamwise (left) and lateralwise (right) isovels in $[mm/s]$ for experiment $B04$ downstream of the weir at $x = 14.00\,m$.

5.6.6. Summary of Flow Zones and Streamline Pattern

In this paragraph the three-dimensional flow field and streamline pattern described above are summarized in terms of Tables and Figures.

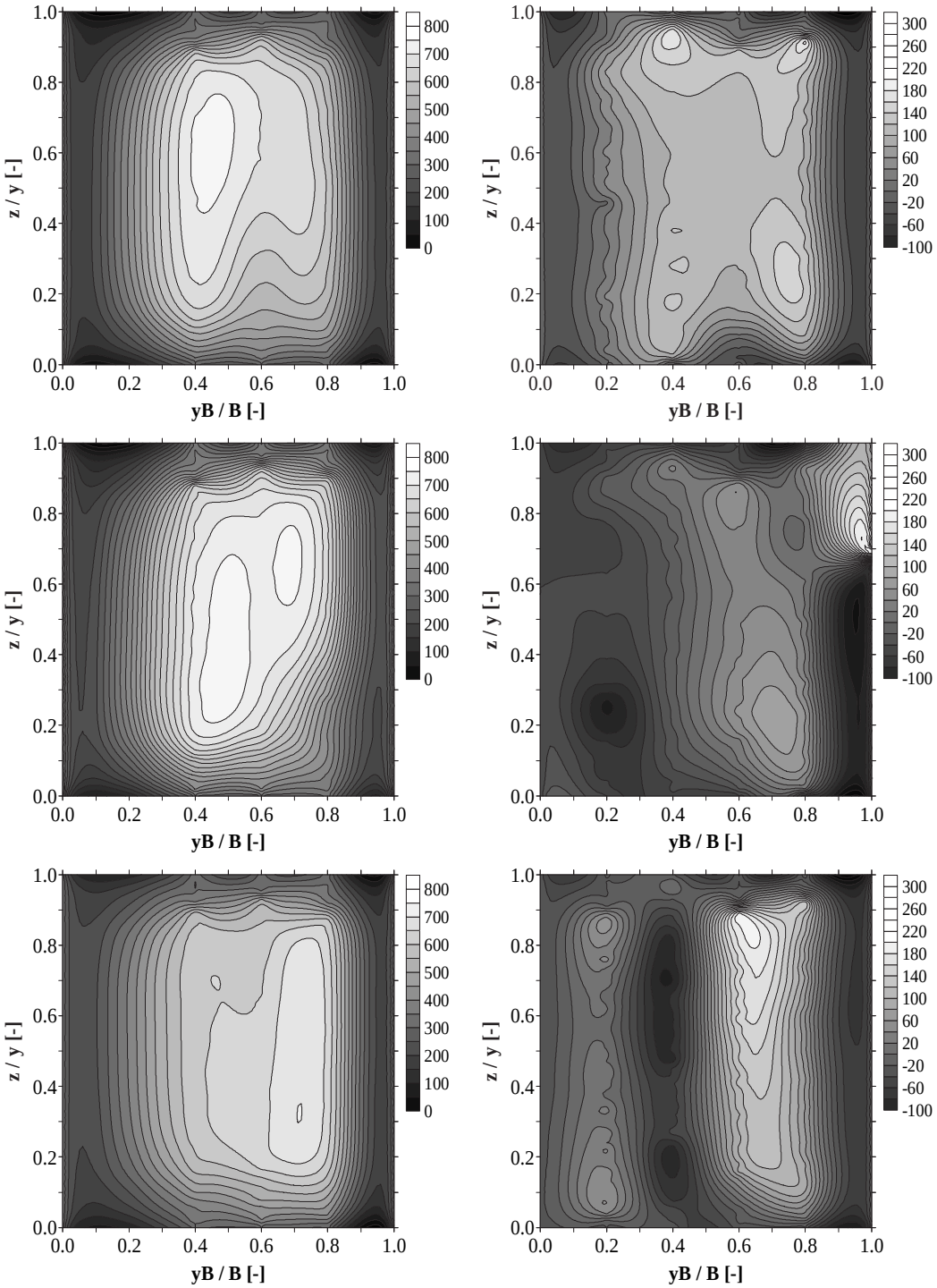

Figure 5.30: Synopsis of streamwise (left) and lateralwise (right) isovels for different cross sections in $[mm/s]$ for experiment $B04$. Top: Upstream of the weir at $x = 2.00\ m$. Middle: Downstream weir reach at $x = 7.50\ m$. Bottom: Downstream of the weir at $x = 14.00\ m$.

Table 5.12: Streamwise (v_x) and lateralwise (v_y) mean velocities and ratio v_x/v_y for test series $B04$. The mean velocities are measured at $z/y = 0.368 \approx 0.40$.

Spanwise position	v_x, v_y and v_x/v_y	Streamwise position of v_x, v_y and v_x/v_y		
		upstream	weir reach	downstream
		$x = 2.00\ m$	$x = 7.50\ m$	$x = 14.00\ m$
		$[mm/s]$, [-]	$[mm/s]$, [-]	$[mm/s]$, [-]
$y_B = 0.60\ m$	v_x	688	618	670
	v_y	115	51	−22
	v_x/v_y	6.0	12.1	−30.5
$y_B = 0.90\ m$	v_x	542	630	766
	v_y	113	140	90
	v_x/v_y	4.8	4.5	8.5
$y_B = 1.20\ m$	v_x	466	373	752
	v_y	106	119	60
	v_x/v_y	4.4	3.1	12.5

Table 5.13: Near-surface, near-bed and mean torsion angles (ϕ_t) at different lateralwise and streamwise channel positions for test series $B04$. The near-surface angle is measured at $z/y = 0.80 \div 1.00$, the near-bed angle at $z/y = 0.00 \div 0.20$ (without $z/y = 0.00$).

Spanwise position	Profile position	Streamwise position		
		ϕ_t upstream [°]	ϕ_t weir reach [°]	ϕ_t downstream [°]
$y_B = 0.60\ m$	near-surface	13.8	9.4	−3.0
	near-bed	20.7	3.0	−6.9
	average*	12.3	4.9	−3.9
$y_B = 0.90\ m$	near-surface	12.2	13.3	12.5
	near-bed	5.3	18.2	3.8
	average*	9.8	14.0	7.5
$y_B = 1.20\ m$	near-surface	19.5	14.7	6.5
	near-bed	26.0	64.5	8.5
	average*	17.2	28.0	5.6

*)without $z/y = 0.00$

5.6.7. Velocity Vectors and Dividing Stream Plane

To further study the flow structure in the overflow region velocity measurements at the following three depths are analyzed:

$$\begin{aligned} \text{near-surface:} \quad & z/y = 80\ \% \pm 5\ \% \\ \text{intermediate:} \quad & z/y = 40\ \% \pm 5\ \% \\ \text{near-bed:} \quad & z/y = 10\ \% \pm 5\ \% \end{aligned} \tag{5.30}$$

The intermediate depth corresponds approximately to the location of the mean flow velocity ($z/y = 0.368$), the near-surface one is located slightly above the weir crest.

The streamwise and transverse velocities (v_x, v_y) at $y_B/B = 0.40$, $0,60$ and 0.80 were used. Since for $y_B/B = 0.20$ the longitudinal UVP-probe (v_x) was out of order, velocities have been extrapolated from the three other probes. Depending on the physical meaning of the spanwise velocity distribution the extrapolation has been conducted by linear regression or a second order polynom. Near the wall at $y_B/B = 0.00$ and $y_B/B = 1.00$ both the streamwise and transverse velocities were supposed to be zero. Of course, this assumption is not true for the near-surface depth in the overflow region at $y_B/B = 1.00$. Hence, the extrapolated main-channel velocity provides the streamwise velocity component (v_x) while the measured pressure head (h_D) provides the spanwise velocity component ($v_y = (2gh_D)^{1/2}$). To add the streamwise and spanwise velocity components vectorially is a common procedure (Ramamurthy and Carballada (1980)).

In Figure 5.31 velocity vectors for the three different depths (Eq. 5.30) are shown. It can be seen that the directions of the velocity vectors near the bed deviate considerably from those near the surface. This deviation of the velocity profile is indicative of a secondary circulation. Neary and Odgaard (1993) stated that this secondary circulation is similar to that found in bend flows. As in bend flows the secondary circulation occurs because the higher-velocity surface water has a significant momentum in the direction of the main-channel flow and requires a greater force to turn it towards the outflow than the slower-velocity water near the bed.

The velocity vector trace plots indicate the location of the streamline dividing the flow that enters the side weir from the flow that continues downstream. As can be seen in Figure 5.31 its location in the main-channel changes over depth extending out farther near the bed than near the surface. The dividing streamlines form a surface, denoted hereafter as the dividing stream plane, that determines the portion of the main-channel flow withdrawn by the weir.

The extension of the dividing stream plane into the main-channel was defined by measurements at $1/3\ L_D = 1.00\ m$ upstream of the weir ($x =$

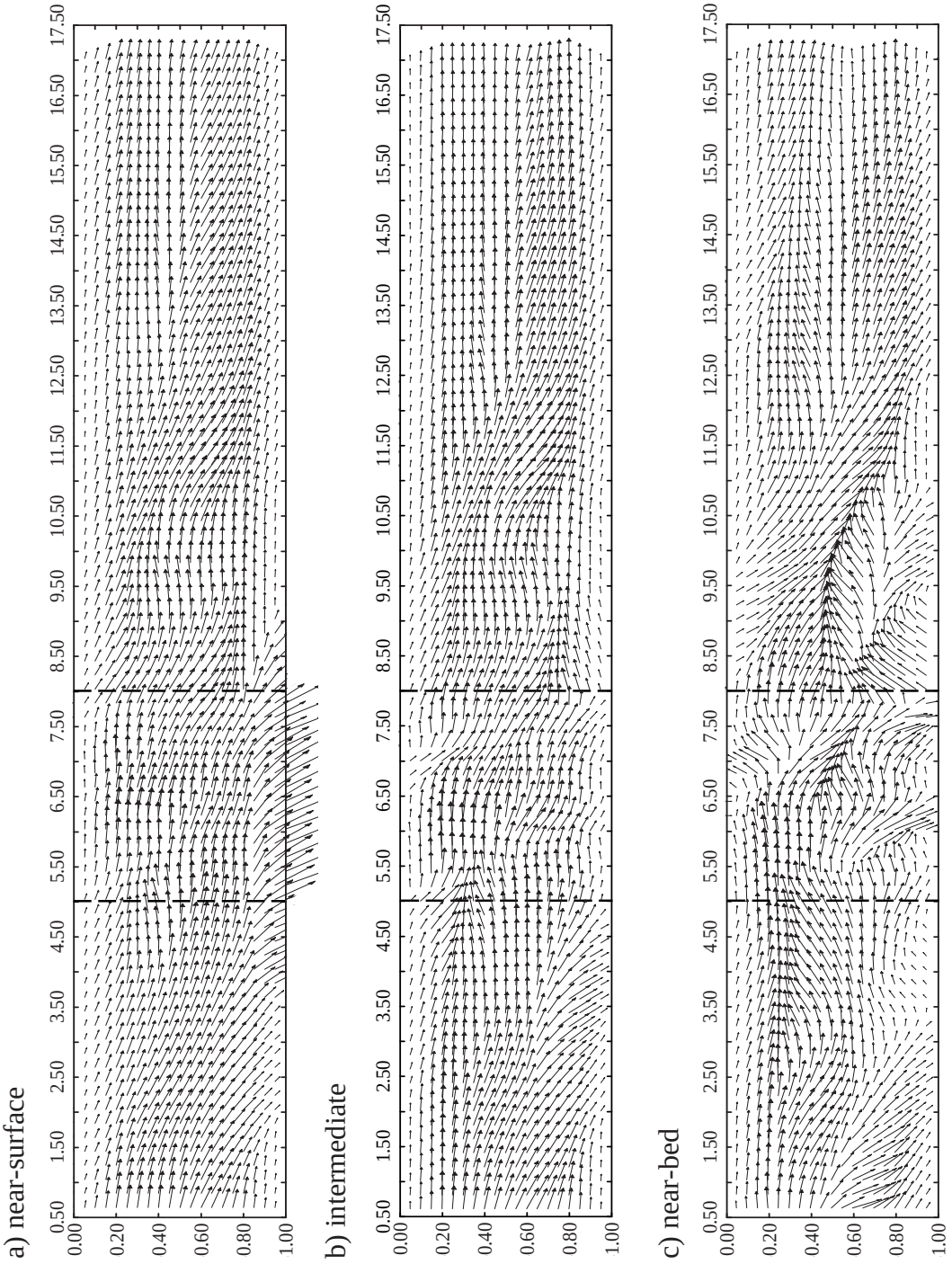

Figure 5.31: Plan view of measured velocity vectors at different water depths for experiment $B04$. The values $0.00 \div 1.00$ refer to the dimensionless channel width (y_B/B), the values $0.50 \div 17.50$ represent the channel length in $[m]$. The dashed line indicates the side weir position.

4.00 m). Thus, no flow has yet been withdrawn by the weir and the total fluid volume separated by the dividing stream plane and being diverted further downstream is still in the main-channel. Using Figure 5.31 the distance from the right wall of the main-channel to the dividing near-surface, intermediate and near-bed streamline was determined. Near the surface the dividing stream line is located at $y_B/B \approx 0.60$. For the intermediate depth its location is found at $y_B/B \approx 0.62$ and for the near-bed streamline a value of $y_B/B \approx 0.55$ has been measured. Hence, the dividing stream plane is closer to the wall at the surface than at the bottom. The shape as well as the vertical and transverse evolution of the dividing stream surface is presented in Figure 5.32.

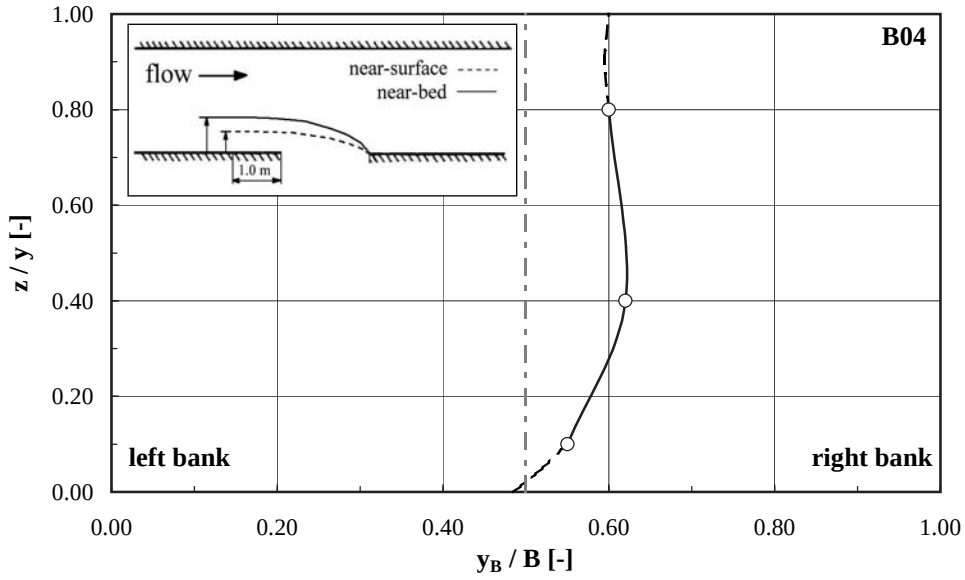

Figure 5.32: Shape and vertical as well as lateralwise evolution of the dividing stream surface at $x = 4.00$ m (1.00 m upstream of the weir) for experiment $B04$.

It follows that a greater part of the near-bed flow might be abstracted than near-surface flow. Surface flow continues with the main flow due to its higher momentum while the slower moving water near the bed flows towards as well as over the weir. Therefore, a disproportionate amount of sediments is transported in direction of the weir. Since the sediments are mainly transported as bed-load almost no bed material has passed the weir (Tab. 5.15). As a consequence the sediments are deposited in front of the weir, thus amplifying the magnitude of the deposit.

5.6.8. Intensity of Secondary Circulation at Side Weir

The analysis further shows that a dependency exists between the intensity of the secondary circulation and the discharge ratio Q_D/Q_1 (Fig. 5.33). The strength of the secondary circulation was taken as the difference between the transverse velocity measured near the surface ($v_{y,s}$) and that near the bed ($v_{y,b}$) at $y_B/B = 0.80$ ($y_B = 1,20\ m$) in the downstream reach of the weir (test series B: 80 % ÷ 100 % of L_D, test series C and D: 75 % ÷ 100 of L_D). $v_{y,s}$ and $v_{y,b}$ were determined at $z/y \approx$ 80 % and $z/y \approx$ 10 %, respectively. The strength of the secondary circulation ($v_{y,s} - v_{y,b}$) was normalized by the average main-channel velocity at section 01 ($v_{x,01}$) which is a measure of the inertia available to generate the secondary circulation. In addition, the reference case without side overflow (experiment $A01$) is represented in Figure 5.33. For this case ($Q_D/Q_1 = 0.00$) the secondary circulation is zero. The plot in Figure 5.33 suggests that the relationship between the secondary circulation and the discharge ratio follows the correlation ($R^2 = 0.60$):

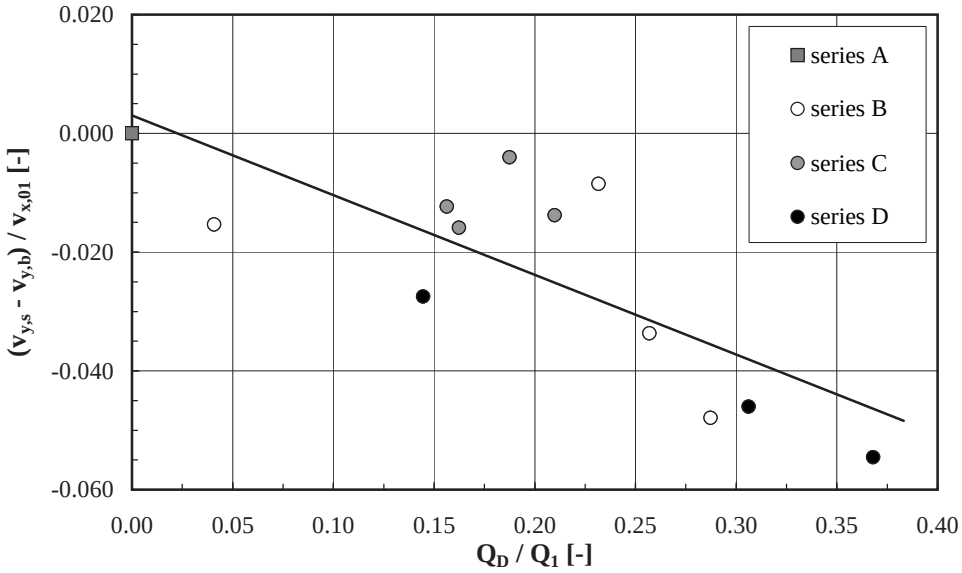

Figure 5.33: Effect of the discharge ratio Q_D/Q_1 on the intensity of the secondary circulation (Eq. 5.31).

$$\frac{v_{y,s} - v_{y,b}}{v_{x,01}} = -0.13 \cdot \frac{Q_D}{Q_1} + 0.003 \tag{5.31}$$

The data indicate that the strength of the secondary circulation, characterised by a greater difference $v_{y,s} - v_{y,b}$, increases with increasing discharge ratio and that incipient secondary circulation occurs at a threshold discharge ratio of $Q_D/Q_1 = 0.022$. Beyond this threshold, instabilities due to

centrifugal forces initiate three-dimensional behavior, specifically secondary circulation. It is worthy to mention that the R^2-value of 0.60 for Equation 5.31 is rather moderate. This is of less importance, since Equation 5.31 is not intended for design purposes but to roughly quantify and estimate the secondary circulation effect. Moreover it has to be kept in mind that usually rather great scattering is inherent to results obtained from mobile bed experiments. It is also for this reason that experiments $B01$, $B06$, $C03$, $D02$ and $D05$ could not be considered for the establishment of Equation 5.31.

Finally it has to be noted that the above analysis is similar to investigations carried out by Neary and Odgaard (1993) who studied the three-dimensional flow pattern at open-channel diversions. In contrast to the present study, the secondary circulation was analyzed in the diversion and not in the main-channel, hence $v_{y,s} - v_{y,b}$ was measured in the branch channel. Moreover, instead of Q_D/Q_1 the ratio of diversion channel velocity to main-channel velocity was used. However, it is interesting to note that Neary and Odgaard (1993) found a threshold value of 0.03 for the ratio of branch channel velocity and main-channel velocity being close to 0.022 from the present study.

Following the analogy of lateral water withdrawal with bend flows as stated by Neary and Odgaard (1993), another method used e. g. by Blanckaert and Graf (2001) to quantify the secondary circulation in bend flows is applied to the present data set.

Within this approach the strength of the secondary circulation is given by:

$$\alpha_{sc} = \frac{v_y(z_i) - v_y}{v_x} \tag{5.32}$$

with α_{sc} portion of the transverse flow component with respect to the streamwise velocity component, $v_y(z_i)$ transverse velocity at different depths z_i, v_y mean transverse velocity and v_x mean longitudinal velocity representing the inertia to generate secondary circulation.

In Figure 5.34 the results applying this criteria are presented. It follows that upstream of the weir ($x = 2.00\ m$) the range of α_{sc} varies from approximately -0.20 to 0.20. The maximum towards the right channel bank is found close to the surface, whereas the maximum orientated versus the left channel bank is located near the bed. In the weir region at $x = 7.50\ m$ the α_{sc}-range is considerably greater mounting up to $\approx$ 0.60 in the weir crest region. High values are also found close to the bed on the right bank indicating a strong near-bed transverse flow in direction of the weir. With respect to the downstream region ($x = 14.00\ m$) the smallest α_{sc}-range is present ($-0.15 \leq \alpha_{sc} \leq 0.15$). As for the upstream stretch, the maximum transverse flow compared to the streamwise one is situated near the surface and near the bed.

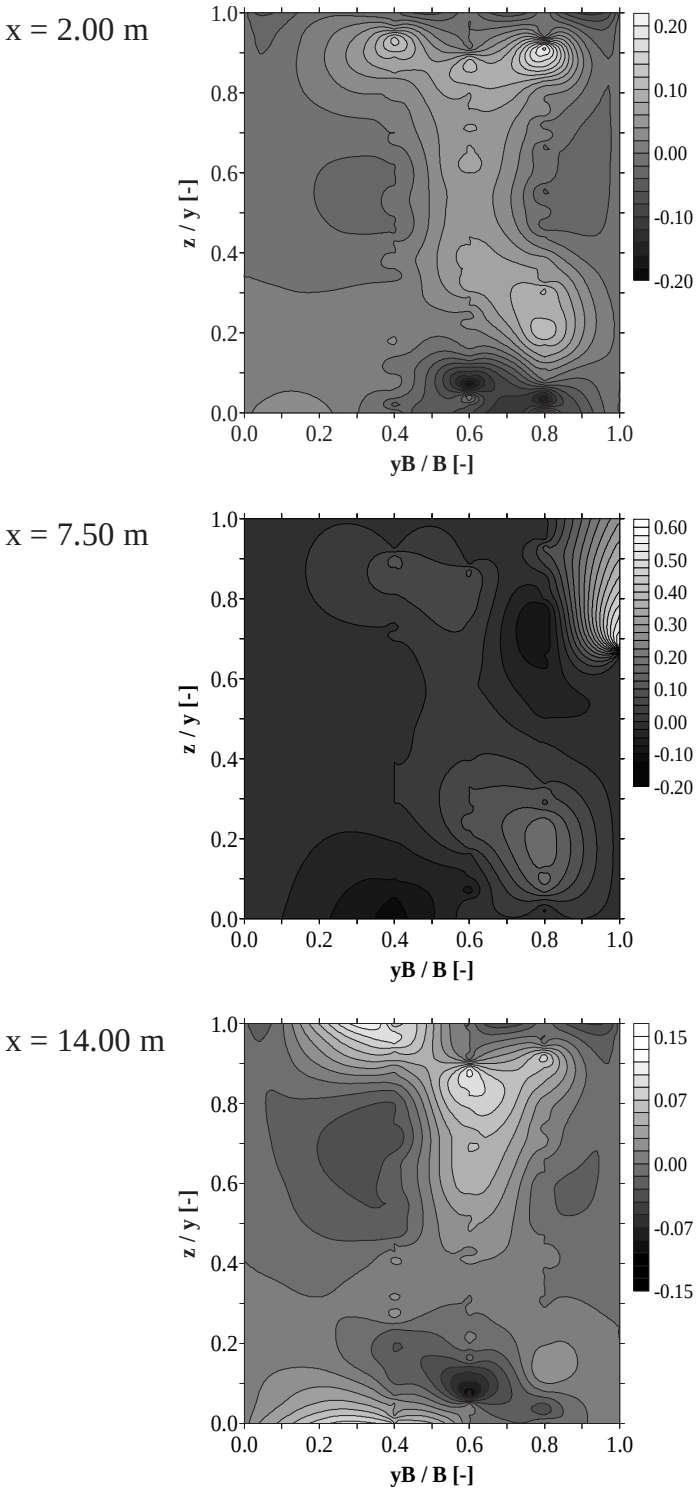

Figure 5.34: Portion of the transverse velocity component with respect to the streamwise velocity component (α_{sc}) (Eq. 5.32) at different streamwise cross sections for experiment $B04$. Note the different scales for α_{sc}!

Since the overflow region is the most interesting cross section, a detailed view of α_{cs} is given in Figure 5.35. The data shows that the strongest α_{cs}-values are found close to the surface and close to the bed. In between the transverse velocity component is rather moderate or even close to zero. The maximum value of $\alpha_{sc} = 0.18$ is found in the vicinity of the weir ($y_B/B = 0.80$) in the near-bed region. This considerable transverse flow component near the bed is responsable for the transport of sediments towards the weir, thus forming the deposit.

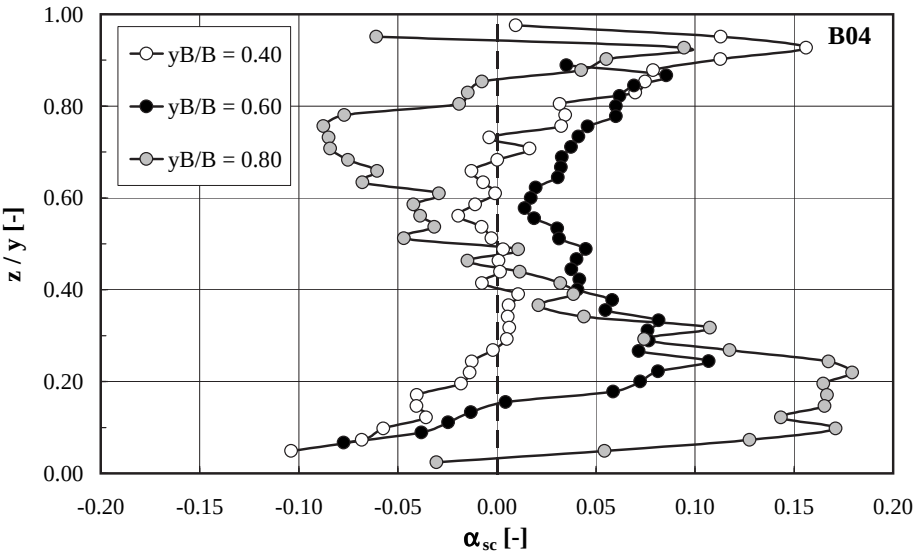

Figure 5.35: Portion of the transverse velocity component with respect to the streamwise velocity component (α_{sc}) for different lateralwise positions in the weir region at $x = 7.50\ m$ (experiment $B04$) (Eq. 5.32). The dashed line indicates $\alpha_{sc} = 0.00$ (no transverse flow component).

The similarity between diversion flows (e. g. branch channels and side weir channels) and bend flows may justify the application of relatively simple bend flow models to describe and predict the three-dimensional flow features at open-channel diversions.

5.6.9. Conclusion

The analysis demonstrates the existence of a weak transverse flow circulation superimposed by a strong streamwise current close to the weir. The transverse circulation increases from the left bank towards the side overflow on the right bank. The most considerable distortion of the $2D$-velocity profile is encountered in the near-bed region close to the side weir with a rather strong

velocity component towards the weir as indicated by a large torsion angle and a comparatively high secondary circulation effect. It is also in this zone where the otherwise strong streamwise velocity component reaches its minimum compared to the transverse velocity. The near-bed component of the secondary circulation appears to be the dominant mechanism by which sediment is transported to the weir where it accumulates to form the deposit.

However, it has to be noted that flow velocities in channel axis are highly dominant over the transverse ones. Consequently, the overall transverse flow phenomenon turns out to be rather weak, although being substantial close to the weir.

5.7. Sediment Transport and Sediment Transport Capacity

5.7.1. Observed Sediment Transport and Comparison with Approaches from Literature

As mentioned in paragraph 4.5 bed-load supply has been estimated according to the approach by Smart and Jäggi (1983). The sediment supply has then been adopted during the duration of the experiments in order to maintain both uniform flow and equilibrium sediment transport conditions in the approach channel reach upstream of the weir.

Since the sediment supply has been slightly modified during the experiments, it appears worthy to investigate which quantities have effectively been transported and which sediment transport formula corresponds in the best way to measured sediment quantities.

The upstream sediment supply was given in $[kg/min]$ (Tab. 4.5), the sediment volume (bulk volume) derived from the DEM is obtained in $[m^3]$ being the balance between the initial and final bed surface. For dimensional reasons one of the two quantities has to be converted. Since it is intended to perform the analysis in a non-dimensional way applying the Einstein factor (Φ, Equation A.124), the sediment supply is transformed from $[kg/min]$ into $[m^3/(s\ m)]$ using the channel width (B) and a measured sediment bulk density of $\rho_s = 1447\ kg/m^3$ (paragraph 4.4). The bulk density is applied because the volumes resulting from the DEM do not refer to pure sediments with $\rho_s = 2650\ kg/m^3$. The volumes derived from the DEM are related to time by the total experiment duration (duration of sediment supply). Thereafter, a stepwise sediment balance from the channel entrance to its exit is performed.

In Figure 5.36 an example of this procedure is presented. It becomes evident that the sediment transport upstream of the weir is almost constant.

As soon as the main-channel flow decreases at the side weir the sediment transport decreases as well and aggradation occurs. This phenomenon is continuous and most significant in the weir reach and a certain distance downstream of the weir. Towards the channel exit the intensity of sediment transport slightly increases as indicated by the flatter Φ-curve.

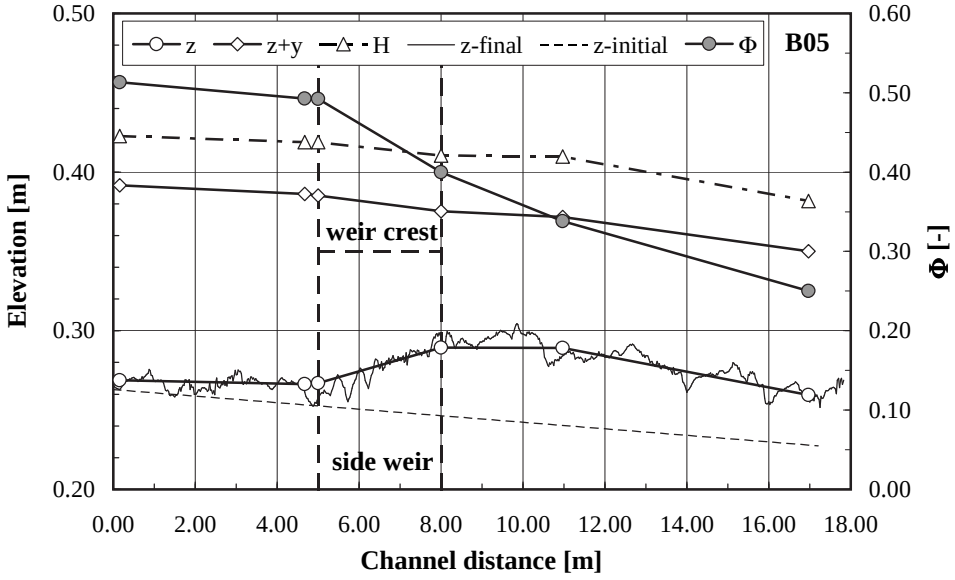

Figure 5.36: Streamwise evolution of dimensionless sediment transport rate (Φ) for experiment *B*05.

For the determination of transported sediment quantities and the comparison with approaches from literature presented in appendix A.6 section 01 is used as a reference (see Fig. 5.13 for definition). Hence, relevant input parameters such as flow depth, hydraulic radius, critical discharge for incipient motion, energy slope and flow resistance were derived from this cross section.

Although trivial, a shear stress exceeding the critical shear stress required to initiate bed-load motion is necessary as a prerequisite for the comparison of sediment transport formulae with results from the present study. For the experiments a mean dimensionless shear stress (θ, Shields factor) of $\theta = 0.213$ has been determined. This value exceeds conventional values assigned to the critical Shields factor ($\theta_{cr} = 0.047$ (Meyer-Peter and Müller (1948)), $\theta_{cr} = 0.05$ (Smart and Jäggi (1983)), $\theta_{cr} = 0.06$ (Shields (1936))) by a factor of more than 3.6.

For comparison measured sediment transport rates (q_{sb}, Φ) have to be transferred from bulk volumes into pure sediment volumes using a factor of $1-p = 1-0.454 = 0.546$ with p porosity (appendix A.1.3). Concerning values for the Einstein factor (Φ) from literature these values already refer to pure

sediment volumes. For their computation either the given equation (Meyer-Peter and Müller (1948), Smart and Jäggi (1983)) or equation A.124 with $d_m = 1.05\ mm$ has been used (Schoklitsch (1950), Van Rijn (1984a)).

With respect to side wall and bed form induced effects measured sediment transport rates need not to be corrected since these effects are already eliminated implicitly by the system. Hence, the net bottom shear stress available for sediment transport is exerting on the grains and the system represents the "reality". In the approach of Meyer-Peter and Müller (1948) both side wall and form roughness correction is taken into account by the factors Q_r/Q and $k_{st}/k_{st}^{'}$ (Eqs A.127 and A.129). Smart and Jäggi (1983) included side wall effects by introducing a reduced discharge (q_r) (Eqs A.136 and A.137). It is stated that no improvement was achieved by implementing a factor representing form roughness, hence the total resistance to flow is applied (parameter c). The bed-load equation of Van Rijn (1984a) considers both side wall as well as form roughness effects by the parameters R_b and $C^{'}$ (Eq. A.150). No specific correction procedure for side wall or form induced phenomena is stated by Schoklitsch (1950).

It has to be noted that the different side wall correction procedures as presented in appendix A.5 hardly vary from each other. The mean non-dimensional shear stress according to Shields (θ) for all test series, determined according to the side wall correction procedure of Einstein (1942) and Vanoni and Brooks (1957), yields $\theta = 0.198$. For the approach of Williams (1970) a value of $\theta = 0.213$ is obtained. Without any side wall correction the Shields factor is $\theta = 0.213$. Thus, the maximum difference is $1 - (0.198/0.213) \approx 7\ \%$.

Likewise, applying the different approaches from literature to the present data set no significant influence of side wall effects could be observed. Taking for example the MPM-approach without any side wall correction ($Q_r/Q = 1.00$) yields a Φ-value of 0.369. Taking into account the side wall correction procedure according to Einstein (1942) yields $\Phi = 0.314$. For Vanoni and Brooks (1957) Φ is 0.316 and for Williams (1970) a value of $\Phi = 0.366$ is obtained. The maximum difference is $1 - (0.314/0.369) \approx 15\ \%$. As will be shown later, this difference is negligible compared to measured absolute sediment transport rates.

Having the difference of $\approx 15\ \%$, the smooth glass-sided channel side walls and a rather great mean B/y-ratio of 12 in mind, a disregard of side wall effects seems to be justified. The B/y-ratio of $12 > 10$ also suggests that the flow depth (y) might be used instead of the hydraulic radius (R_h) (Naudascher (1992)). Hence, y instead of R_h is applied for the comparison.

Concerning form induced roughness the average total roughness (k_{st} or $k_{st,b}$ if side wall effects are removed) equals 63 $m^{1/3}/s$. The grain roughness ($k_{st}^{'}$ or $k_{st,b}^{'}$), determined according to Equation A.128 is 72 $m^{1/3}/s$, hence, $63/72 = 88\ \%$ of the total roughness. These calculations indicate that form

roughness represents a relatively small fraction of total roughness. Therefore, as for side wall effects, the disregard of form induced roughness might be acceptable. A more detailed investigation of form roughness due to bed forms is given in paragraph 5.10.6.

However, the comparison of measured and computed bed-load transport rates/capacity is performed using the original formulae from literature, including wall and form effects, if implemented (see above). Taking these effects into account refers to most unfavourable sediment transport conditions, viz highest transport capacity ("highest security factor"). In Figure 5.37 the comparison of measured and predicted sediment transport rates/capacity is presented. A synopsis is given in Table 5.14.

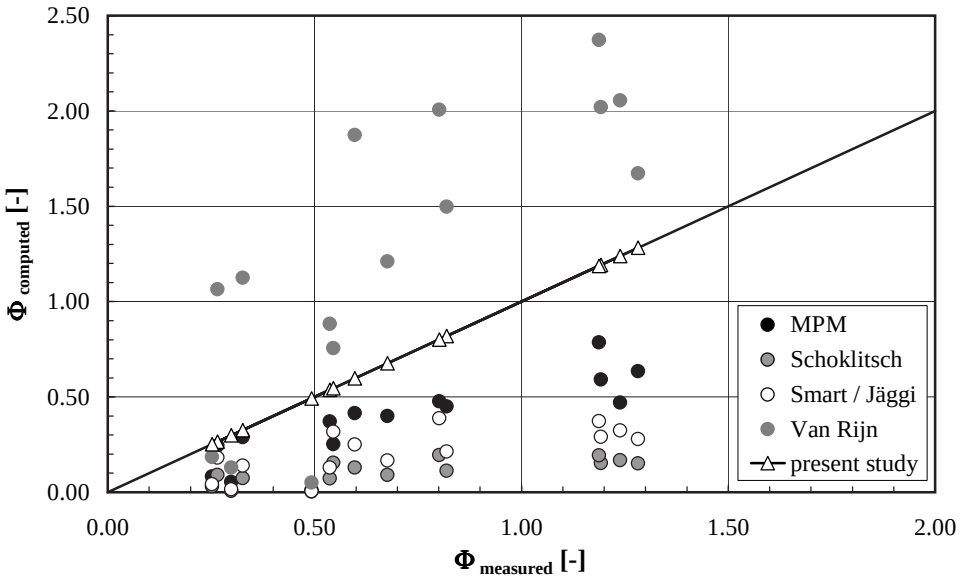

Figure 5.37: Comparison of measured and computed sediment transport rates/capacity (Φ).

From Figure 5.37 and Table 5.14 it becomes evident that all approaches yield satisfying results for small Φ-values. With increasing measured sediment transport rates the discrepancy increases. The approaches of Meyer-Peter and Müller (1948), Smart and Jäggi (1983) and (Schoklitsch (1950) underestimate the sediment transport rate, whereas according to the approach by Van Rijn (1984a) an overprediction is observed. The best correlation is found for the MPM-approach (LSM-value of 2.32), the lowest correlation for the one by Van Rijn (1984a) (LSM-value of 8.40).

Differences in this order of magnitude are common for bed-load equations and correspond to normally accepted values in the field of transport modelling, since the experimental boundary conditions may depart from the conditions under which the equations were formulated and several uncertainties could

Table 5.14: Comparison of measured and computed (original formulae) sediment transport rates/capacity (Φ) without experiments $A01$ (reference case) and $C03$. LSM denotes least squares method $\left(\sum(\Phi_{measured} - \Phi_{computed})^2\right)$.

Investigation	Eq. in study	Test series B Φ [−]	Test series C Φ [−]	Test series D Φ [−]	average Φ [−]	meas./ comp. [−]	LSM [−]
present study		0.411	0.979	0.827	0.701	1.00	0.00
MPM (1948)	A.130	0.204	0.523	0.443	0.369	1.90	2.32
Schoklitsch (1950)	A.133*	0.067	0.132	0.139	0.108	6.49	6.77
Smart & Jäggi (1983)	A.138	0.131	0.246	0.268	0.207	3.39	4.86
Van Rijn (1984a)	A.153*	0.668	1.562	1.729	1.260	0.56	8.40

*and Equation A.124

affect outcomes of model predictions. Lisle et al. (1997), e. g., found approximately 3 times higher transport rates than predicted by the MPM bed-load equation. Van Rijn (1984a) stressed that even under controlled flume conditions it is hardly possible to predict the transport rate with an inaccuracy less than a factor 2. In addition, actual transported sediment usually differs from potential capacity determined by transport functions.

Looking at the boundary conditions of the approaches from literature to explain the different correlations with the present study, in the approach by Meyer-Peter and Müller (1948) only flume data has been used. The slope range corresponds to conditions of the present investigation (mean initial bottom slope $S_0 = 0.21$ %). The sediment density also fits to the one of the present study. However, smaller as well as greater densities were applied by MPM. The grain diameter exceeds dimensions from this study (appendix A.6.2).

The approach of Schoklitsch (1950) is based on field and flume data and valid for $d \geq 6\ mm$ and moderate to strong slopes (0.3 to 10 %).

The bed-load equation of Smart and Jäggi (1983) is derived from flume experiments only. The grain diameters are greater than the ones from the underlying study, whereas the channel width as well as the discharge are smaller. The slope range corresponds to the one of Meyer-Peter and Müller (1948) but is extended up to 20 %. Moreover, the bed-load equation is valid for relative roughnesses $y/d_m < 100$. Herein, a mean value of $y/d_m = 119$ is

observed.

In the investigation of Van Rijn (1984a) both field and flume data is used. The range of the flume data (particle diameter, flow depth, Froude number) corresponds to experimental conditions of the present study.

Besides the different boundary conditions of the approaches from literature it has to be noted that the DEM of the final bed situation is used for the determination of measured Φ-values. These data do not represent an instantaneous situation but refer to an integration over the entire period of the experiment. Thus, slightly changing transient upstream flow and sediment supply conditions are incorporated in the DEM-data. The transient change of flow depth in the approach channel compared to mean flow depth is in the order of magnitude of ± 9%. With respect to sediment supply a maximum transient change of ± 15% with respect to average sediment supply can be stated.

It may be concluded that the boundary conditions of the MPM-approach appear to be rather close to those of the present study. The analysis further shows that the approach sediment transport characteristics can be best expressed by the bed-load formula of Meyer-Peter and Müller (1948) (appendix A.6.2, Eq. A.130) with a correction factor of 1.90 for the absolute transport quantity (Tab. 5.14).

5.7.2. Bed Material Transport over Side Weir

For the determination of sediment balances is it important to know whether bed material has been transported over the weir. From Table 5.15 it becomes evident that no significant transport over the weir occurred during the experiments. The quantities ($Q_{s,D}$), mainly composed of suspended load with small portions of bed-load are rather low compared to the total bed-load supplied at the channel entrance ($Q_{sb,in}$). However, the ramp-like deposit developing in front of the weir and occasionally mounting up to the weir crest might favor the transport of sediments over the weir (Figs 2.4, 5.38 and 5.39).

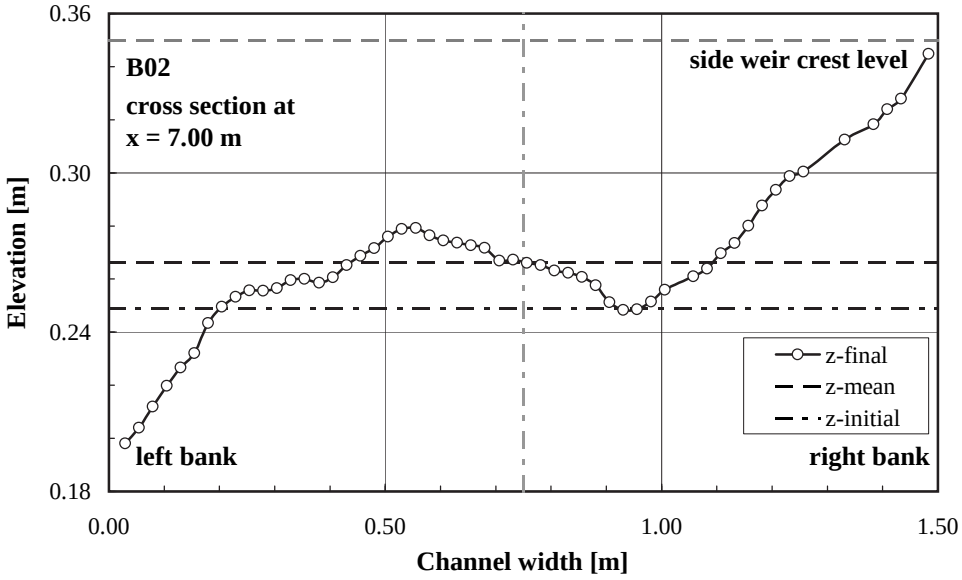

Figure 5.38: Formation of a ramp-like deposit in front of the side weir located on the right channel bank (experiment $B02$, $x = 7.00\ m$, $z_{mean} = 0.267\ m$, $z_{initial} = 0.249\ m$).

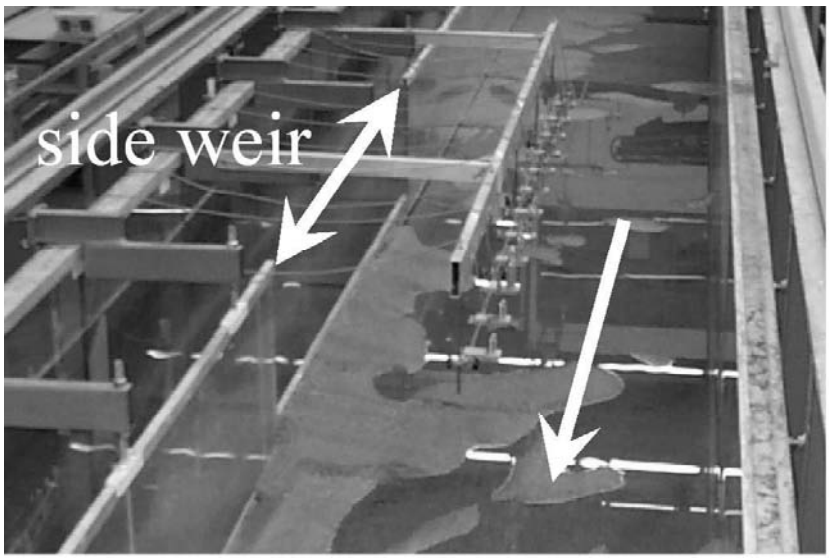

Figure 5.39: Formation of a ramp-like deposit in front of the side weir (experiment $B02$).

Table 5.15: Bed material (suspended and bed-load) transported over the side weir ($Q_{s,D}$) and comparison with bed-load material introduced at the channel entrance ($Q_{sb,in}$).

N^o of experiment	$Q_{sb,in}$ $[kg/min]$	$Q_{s,D}$ $[kg/min]$	$Q_{s,D}/Q_{sb,in}$ [%]
$A01$	15.25	$***$	$***$
$B01$	8.70	1.17	13.45
$B02$	17.73	0.63	3.54
$B03$	9.10	1.62	17.85
$B04$	9.67	1.25	12.95
$B05$	16.72	1.17	7.01
$B06$	17.61	1.67	9.47
$C01$	9.56	0.31	3.22
$C02$	42.69	1.24	2.91
$C03$	51.76	0.49	0.95
$C04$	39.82	1.36	3.42
$C05$	39.82	0.53	1.32
$D01$	27.04	0.10	0.37
$D02$	26.54	0.39	1.45
$D03$	39.82	1.23	3.08
$D04$	22.34	0.30	1.34
$D05$	19.91	0.33	1.63
average	24.93[1)]	0.86	5.25

[1)] without test series $A01$

5.7.3. Conclusion

The reflections in this paragraph make evident that as soon as the main-channel flow decreases at the side weir the sediment transport decreases as well and aggradation occurs. This phenomenon appears to be continuous and most significant in the weir reach and a certain distance downstream of the weir.

Furthermore, the calculations in this paragraph indicate that form roughness represents a relatively small fraction of total roughness and no significant influence of side wall effects could be observed. Therefore, the comparison of measured sediment transport rates with predicted sediment transport capacity could be performed without considering side wall and form roughness effects. Moreover, it turned out that the assumption of replacing the hydraulic radius with the flow depth is acceptable.

The analysis further shows that the approach sediment transport characteristics can be best expressed by the bed-load formula of Meyer-Peter and Müller (1948) with a correction factor of 1.90 for the absolute transport quantity.

The investigation whether sediment transport over the weir occurred showed that only rather small portions have been transited the weir (≈ 5 % of the upstream sediment supply). In this regard the ramp-like deposit developing in front of the weir might favor the transport of sediments over the weir.

5.8. Influence of a local Sediment Deposit on Performance of a Side Weir

As a precursor to the analysis of bed morphology, aggradation and their impact on side overflow intensity, the general situation of an obstacle formed by sediment deposits on the bed is investigated theoretically. This analysis is extended to the influence of an obstacle (sediment deposit) on side overflow. A sensibility study to get an idea about the effect of deposition shape, height and position with respect to spilled discharge has been performed using $1D$-numerical simulations (DUPIRO).

5.8.1. General Behavior of a Side Overflow in Presence of a local Sediment Deposit

The effect of a local deposit on flow conditions can be seen in Figure 5.40. In this Figure h denotes the pressure head ($h = z + y$) without velocity head (Eq. A.154). Compared to the normal flow situation ($h_{i,n}$) without a local deposit a $M1$-type backwater profile is first developed upstream of the

deposit. The upstream end point of the backwater curve is assumed to be at section 0. Between section 0 and 1 the flow is gradually varied. Near the local deposit somewhat downstream of section 1 the water begins to accelerate, deceleration might occur along the lower boundary and separation zones might be created downstream of the maximum elevation of the deposit resulting in local energy losses. At this point a certain analogy to flow separation in the trough region of bed forms (e. g. dunes) has to be mentioned (Fig. A.9). At the location of the local deposit the flow is rapidly varied, characterised by marked acceleration in direction normal to the streamlines. The longitudinal water surface drops rapidly in this region. The section of the maximum elevation of the deposit might be treated as a kind of control section and critical flow conditions might occur. Behind the deposit the flow begins to expand until it reaches downstream section 4 where uniform flow conditions are re-established. Between sections 2 and 4, the flow is gradually varied. Over the whole reach from sections 0 to 4 encompassed by the backwater effect of the deposit the total energy loss Δh is the same as that for uniform flow.

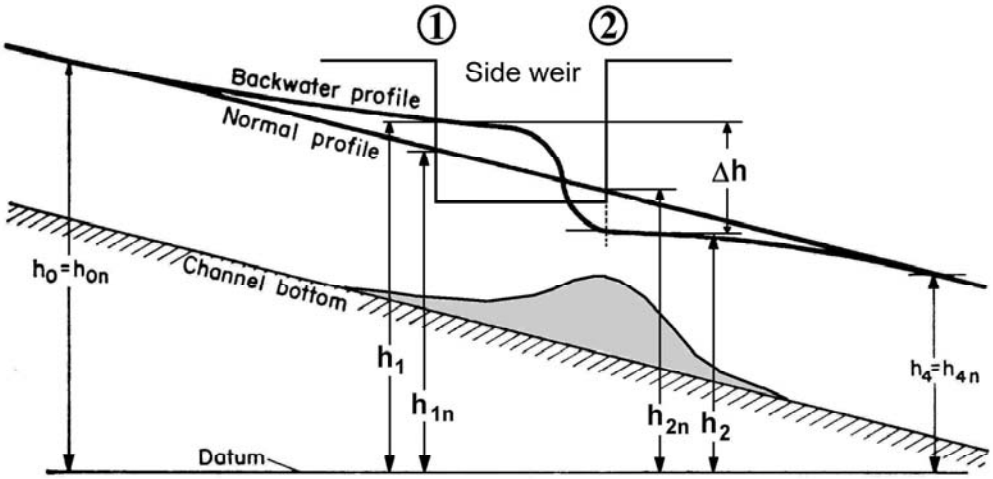

Figure 5.40: Definition sketch of flow over a local deposit without side weir. If a side weir is placed at the position shown in the Figure, the normal profile would be somewhat different as can be seen in Fig. A.14, a; whereas the backwater profile would be similar to the one shown in this Figure. h denotes the pressure head ($h = z + y$) without velocity head.

Assuming now a side weir is placed as shown in Figure 5.40. This situation corresponds to the one observed in the experimental investigations where a sedimentary deposit develops in the downstream weir alignment. In the case without side overflow the flow builds up a certain energy to be able to pass the local deposit. Thus, the pressure head between section 1 and 2 increases. If a

side weir is placed between section 1 and 2 the pressure head also increases, since the flow has to overcome the local deposit. The difference to the situation without overflow is that the required energy potential to overcome the deposit cannot be established, since no channel walls are present to allow for this increase in pressure head. Due to this geometrical boundary condition (= side weir) the increased pressure head for the case without side overflow is quasi transformed into an increased side overflow if a weir is present. This issue is presented graphically in Figure 5.41.

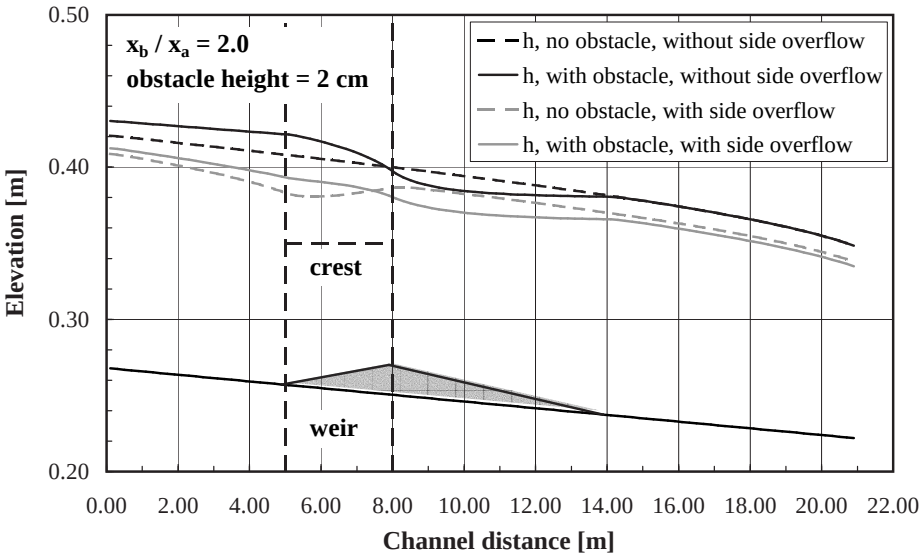

Figure 5.41: Influence of a triangular deposit on the water level for a channel with and without side overflow. For comparison the water levels without deposit are presented (dashed lines). Results from a $1D$-numerical simulation using DUPIRO.

Coming back to Figure 5.40 it can be seen that the pressure head in section 1 increases and keeps increased along the weir crest before dropping rapidly close to section 2. The part of the crest length characterised by an increased head compared to normal flow conditions is considerable longer than the crest length owing a decreased pressure head. This means the loss in pressure head close to section 2 ($\approx h_2 - h_{2n} < 0$) is largely compensated by the gain in head on the remaining crest length ($\approx h_1 - h_{1n} > 0$). It has to be noted that the normal profile would be somewhat different along the side weir (Fig. A.14, a), whereas the backwater profile would be similar to the one presented. Applying Equation A.158 to the case with and without deposit, corresponding to the initial and final situation in the experiments, and furthermore assuming an almost similar C_D-value for both situations (same weir crest shape, same channel width, neglecting slightly different approach

flow conditions and streamline curvature), the side overflow discharge (Q_D) (or q_D) is directly proportional to $(y - w_D)^{3/2} = h_D^{3/2}$:

$$\frac{Q_{D,fin}}{Q_{D,ini}} = \left(\frac{h_{D,fin}}{h_{D,ini}}\right)^{3/2} \tag{5.33}$$

with suffix ini for initial situation and fin for final situation. The assumption of an almost constant C_D-value is acceptable, since in general C_D has a rather small variation for different flow conditions (Naudascher (1992)).

In addition to different length ratios gaining or losing head the head does not increase/decrease linearly but is raised to the power of 3/2, thus amplifying this tendency.

To underline the impact of the exponent 3/2 a simple numerical example using Equation 5.33 may be presented with $h_{D,ini}$ and $h_{D,fin}$ being mean head values between sections 1 and 2:

$$h_{D,ini} = 2.0 \ m$$

$$h_{D,fin} = 3.0 \ m$$

$$\text{linear increase: } \left(\frac{3.0 \ m}{2.0 \ m}\right)^{1/1} = 1.50$$

$$\text{exponential increase: } \left(\frac{3.0 \ m}{2.0 \ m}\right)^{3/2} = 1.84$$

The examples shows that a head increase by a factor of 1.5 (corresponding to the increase from 2.0 m to 3.0 m) results, of course, in an increase of Q_D by a factor of 1.50 for the linear relation. The exponential relation yields a factor of 1.84, thus representing a difference of $50/84 = 60$ %.

5.8.2. Influence of Height, Shape and Location of a local Deposit on Side Overflow using 1D-Simulations

To get an idea about the different crest length ratios gaining or losing pressure head the following example resulting from a numerical simulation using DUPIRO is presented (Rosier et al. (2007b)). DUPIRO is a $1D$-numerical code jointly developed at the Laboratory of Hydraulic Constructions (LCH) and the Institute of Applied Hydrodynamics and Hydraulic Constructions (HACH), University of Liège, Belgium. A description of the numerical model

is given in paragraph 8.1. Using the experimental boundary conditions from Table 5.16 for the numerical simulations, the results presented in Figure 5.42 are obtained. The modelled channel reach has a length of $L = 22.00\ m$ with a spatial discretisation of $\Delta x_i = 0.10\ m$. Stable flow conditions have been obtained after 150 *sec*. The total simulation time has been 300 *sec*.

The $2D$ sedimentary deposit developing in the flume is modelled by a $1D$ fixed triangular symmetric deposit located at section 2. Considering the local deposit as a kind of bed form the approximation using a triangular shape seems to be reasonable, since the bed form shape factor (β_{SF}) (Eq. 5.34) of 0.50 for a triangular bed form corresponds fairly well to measured β_{SF}-factors, being in the order of magnitude of 0.57. Tang and Knight (2006) stated that the simple assumption of $\beta_{SF} = 0.50$ is approximately true for small-scale dunes in experimental flumes. According to Führböter (1967) the bed form shape factor (β_{SF}) is defined as follows:

$$\beta_{SF} = \frac{A}{\Lambda \cdot \Delta} \tag{5.34}$$

with A cross sectional area of bed form, Λ bed form length and Δ bed form height. For natural rivers where the bed forms have three-dimensional parabolic characteristics the β_{SF}-factor is closer to 0.66 (Tang and Knight (2006)). Zanke (1982) conducted dune experiments with a β_{SF}-value of 0.60, Wiesemann et al. (2006) reported a value of 0.55 (also for dune experiments).

The height of the triangular deposit represents measured heights, whereas the length is somewhat smaller compared to the laboratory tests. The height of the deposit is $z_{max} = 2.0\ cm$, thus 8.0 *cm* below the crest height of $w_D = 10\ cm$ or $2.0\ cm/10.0\ cm = 20\%$ of w_D. The length of the symmetric deposit (x_{dep}) is twice the weir length, thus $x_{dep} = 2\ L_D = 2 \cdot 3.0\ m = 6.0\ m$. The length repartition is $x_a = 1\ L_D$ upstream of z_{max} and $x_b = 1\ L_D$ downstream of z_{max}. The definition of the length, length ratio and height of the local deposit is given in Figure 5.43.

As can be seen in Figure 5.42 similar hydraulic conditions as presented schematically in Figure 5.40 occur. In section 2 at $x = 8.00\ m$ almost critical conditions are observed. The diverted discharge without deposit is $Q_D = 23.00\ l/s$. For the case of the deposit a value of $Q_D = 28.00\ l/s$ is determined. Consequently, the ratio $Q_{D,fin}/Q_{D,ini}$ is 1.22. Using $(h_{D,fin}/h_{D,ini})^{3/2} = (0.037\ m/0.032\ m)^{3/2}$ yields 1.24 (Fig. 5.44, $x_b/x_a = 1.00$). Regarding the crest length ratios, on 2.30 m of $L_D = 3.00\ m$ a higher head than at the initial situation is observed. This means $2.30\ m/3.00\ m = 77\ \%$ of the total length of $L_D = 3.0\ m$ contribute to a gain and only 23 % refer to pressure head losses.

For the case of a 3 *cm* high symmetric deposit ($3.0\ cm/10.0\ cm = 30\%$ of w_D) (not presented in Fig. 5.40) critical flow conditions occur at section 2.

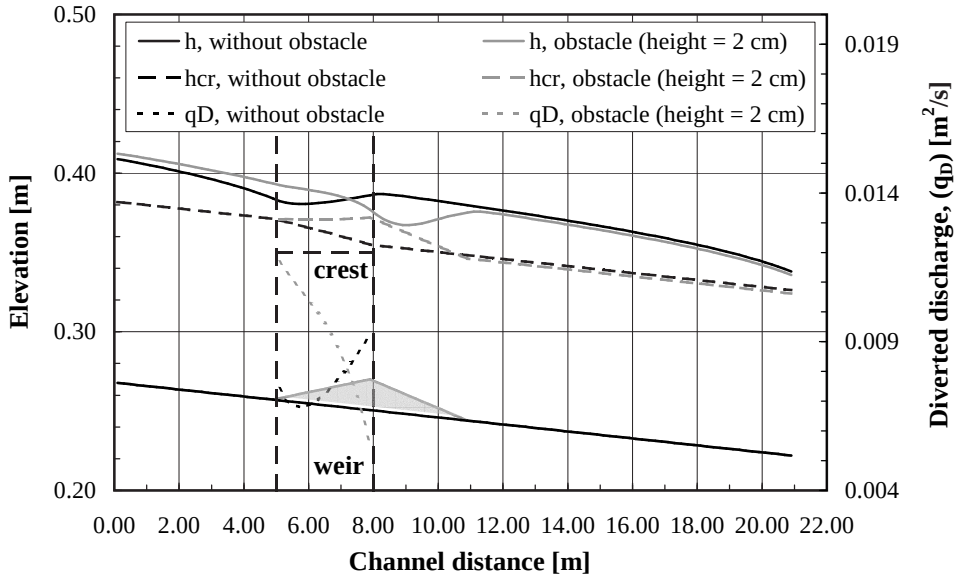

Figure 5.42: Influence of a $1D$ symmetric deposit on water level elevation and side overflow discharge (q_D). Results from a $1D$-numerical simulation using DUPIRO.

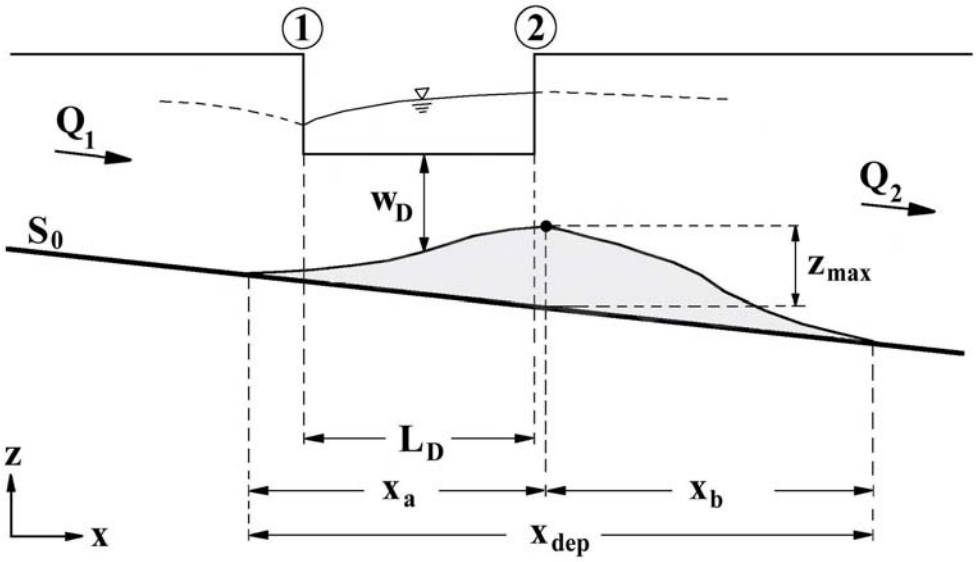

Figure 5.43: Definition sketch of local deposit and deposition length (x_{dep}), length ratio (x_b/x_a) and height (z_{max}) of deposit.

Table 5.16: Boundary conditions for a $1D$-numerical simulation of side overflow in presence of a $1D$ triangular deposit using DUPIRO.

Flow conditions		Channel geometry			Weir geometry		Geometry of deposit	
Q_1	$h_{1,ini}$	B	S_0	k_{st}	L_D	w_D	x_{dep}	z_{max}
$[l/s]$	$[m]$	$[m]$	$[-]$	$[m^{1/3}/s]$	$[m]$	$[m]$	$[m]$	$[m]$
181	0.141	1.50	0.0022	64.00	3.00	0.10	6.00	0.02

The ratio $Q_{D,fin}/Q_{D,ini} = (35\ l/s)/(23\ l/s)$ is 1.52 and $(h_{D,fin}/h_{D,ini})^{3/2} = (0.042\ m/0.032\ m)^{3/2}$ yields 1.50. The corresponding crest length ratios are 90 % (gain) and 10 % (loss).

In the above examples the triangular deposit has been symmetric. Considering now a nonsymmetric left skewed deposit (as observed in the experiments) with an upstream deposition length of $x_a = 1\ L_D$ and a downstream deposition length of $x_b = i\ L_D$ ($i = 2 \div 4$). The results obtained for these simulations are presented in Table 5.17 and Figure 5.44 (boundary conditions according to Tab. 5.16). It clearly appears that the influence of the height of the deposit on the ratio $Q_{D,fin}/Q_{D,ini}$ is of greater importance than a longer and smoother downstream deposition length. For the 2 *cm* high deposit the ratio $Q_{D,fin}/Q_{D,ini}$ increases from $x_b/x_a = 0.00$ (no deposit) to 1.00 with a slope of 21 % to continue with a milder slope of 6.8 %. With respect to the 3 *cm* high deposit, the ratio $Q_{D,fin}/Q_{D,ini}$ rapidly increases for $0.00 \leq x_b/x_a \leq 1.00$ with a slope of 52 % before further increasing with a milder slope of 6.6 %. Thus, from $x_b/x_a = 1.00$ on, both curves increase almost parallel but on different levels.

Until now, the maximum height of the local deposit has always been located at the downstream weir corner (section 2). Considering now different positions of the local deposit. This is important, since the part of the total crest length gaining or losing pressure head might be shifted along the weir crest, thus influencing the side overflow discharge. In the following the deposit is shifted once in the upstream direction of section 2 and once downstream of section2, each time by the factor $1/2\ L_D$. In Figures 5.45 and 5.46 the results for a shifted symmetric and a shifted nonsymmetric deposit are presented.

In both cases it becomes evident that for an upstream (downstream) transition of the deposit the water level drop-off or rise, respectively, is also shifted upstream (downstream). The impact of this up- and downstream transition on the side overflow intensity is presented in Table 5.18 and

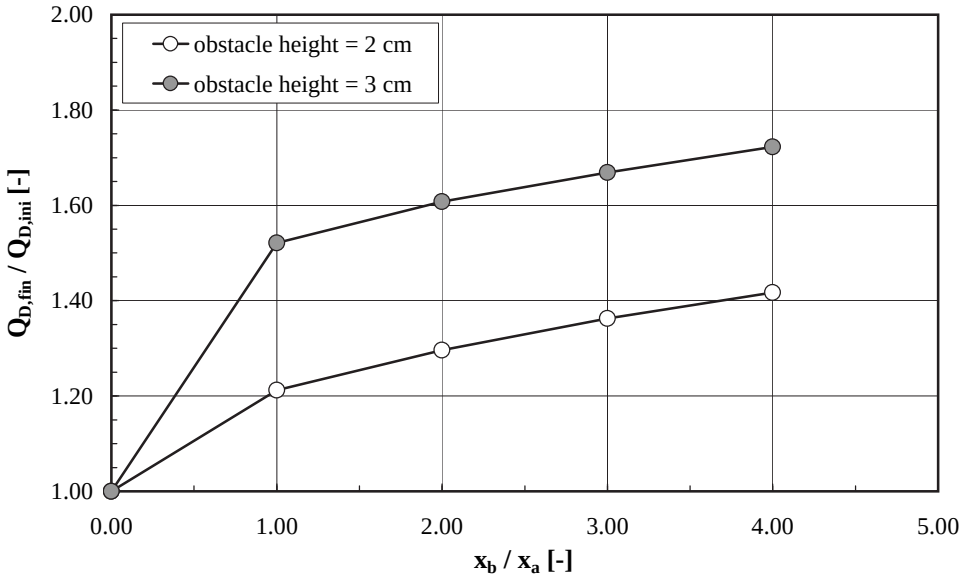

Figure 5.44: Relation between deposition length ratio (x_b/x_a) and diverted discharge ratio ($Q_{D,fin}/Q_{D,ini}$) for two different deposition heights ($1D$-numerical simulation using DUPIRO).

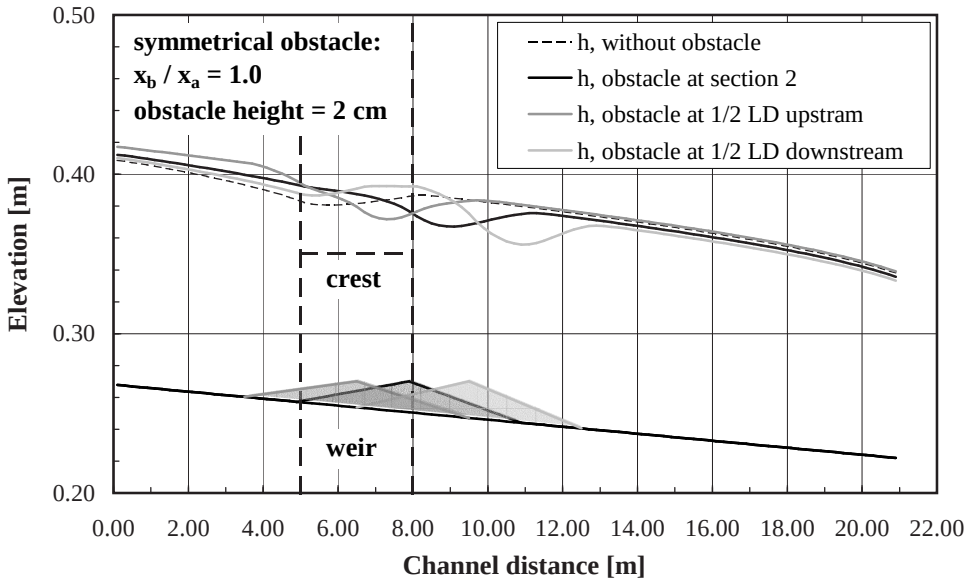

Figure 5.45: Influence of the location of the deposit on water level elevation for a symmetric deposit ($1D$-numerical simulation using DUPIRO).

Table 5.17: Influence of deposition length ratio (x_b/x_a) on diverted discharge ratio ($Q_{D,fin}/Q_{D,ini}$) for two deposits of different height ($1D$-numerical simulation using DUPIRO). The initial condition (denoted with *) always refers to flow conditions without deposit.

Length ratio	Height of deposit = 2 *cm*		Height of deposit = 3 *cm*	
x_b/x_a [−]	Q_D [l/s]	$Q_{D,fin}/Q^*_{D,ini}$ [−]	Q_D [l/s]	$Q_{D,fin}/Q^*_{D,ini}$ [−]
0.00*	22.88*	1.00*	22.88*	1.00*
1.00	27.73	1.21	34.81	1.52
2.00	29.65	1.30	36.79	1.61
3.00	31.17	1.36	38.19	1.67
4.00	32.42	1.42	39.41	1.72

Figure 5.47.

Table 5.18: Influence of deposition length ratio (x_b/x_a) and channel location on diverted discharge ratio ($Q_{D,fin}/Q_{D,ini}$) for a deposit of 2 *cm* height ($1D$-numerical simulation using DUPIRO). The initial condition (denoted with *) always refers to flow conditions without deposit. For $x_b/x_a = 4.00$ and $1/2\ L_D$ downstream no value occurs because the deposit was longer than the channel. To obtain discrete $Q_{D,fin}$-values, $Q^*_{D,ini} = 22.88\ l/s$ (Tab. 5.17) has to be used.

Length ratio	Section 2	1/2 L_D upstream	1/2 L_D downstream
x_b/x_a [−]	$Q_{D,fin}/Q^*_{D,ini}$ [−]	$Q_{D,fin}/Q^*_{D,ini}$ [−]	$Q_{D,fin}/Q^*_{D,ini}$ [−]
0.00*	1.00*	1.00*	1.00*
1.00	1.21	0.91	1.44
2.00	1.30	1.00	1.52
3.00	1.36	1.08	1.58
4.00	1.42	1.14	* * *

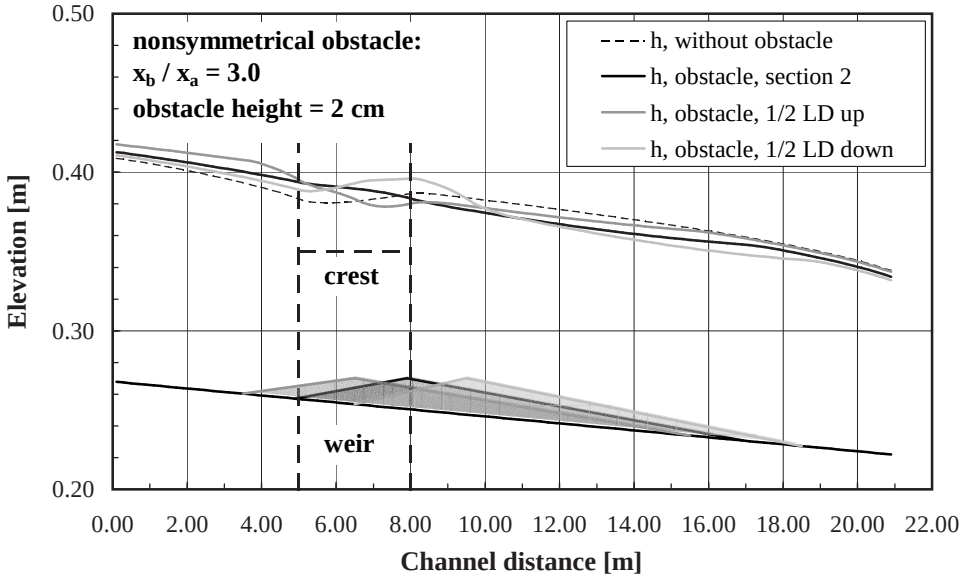

Figure 5.46: Influence of the location of the deposit on water level elevation for a nonsymmetric deposit ($1D$-numerical simulation using DUPIRO).

For the examples represented above (Tab. 5.17) a higher lateral outflow for the more pronounced deposit than for the smoother ones might have been expected. The reason for this would be attributed to local energy losses being higher for the symmetric pointed deposit than for the longer and smoother ones. Here, the transition from the top of the deposit to the downstream side is more gentle compared to the shorter deposits owing a rather sudden transition. As can be seen in Figure 5.48 the pressure head difference (Δh) between section 1 and 2 ($\Delta h = h_1 - h_2$) for the deposits located at section 2 and 1/2 L_D upstream of section 2 is positive and effectively decreases with increasing x_b/x_a-ratios. In contrast to this for increasing x_b/x_a-ratios the diverted discharge develops in the opposite direction (= increase).

For a local deposit at section 2 decreasing Δh-values mean that the water surface profile along the side weir crest is smoothed and becomes almost uniform (Fig. 5.46). Compared to the case without deposit this level is higher, thus resulting in an increased discharge ratio. In the extreme case Δh might drop to zero and the flow depth along the weir would be constant. This situation would correspond to so-called pseudo-uniform flow conditions as reported by Hager and Volkart (1986). For this configuration the maximum outflow discharge is obtained. The difference $H - h = v^2/2g$ then remains constant and so does the average velocity although the discharge varies with x along the weir crest. This pseudo-uniform condition might be achieved by proper modelling of the longitudinal channel geometry, e. g. linear channel

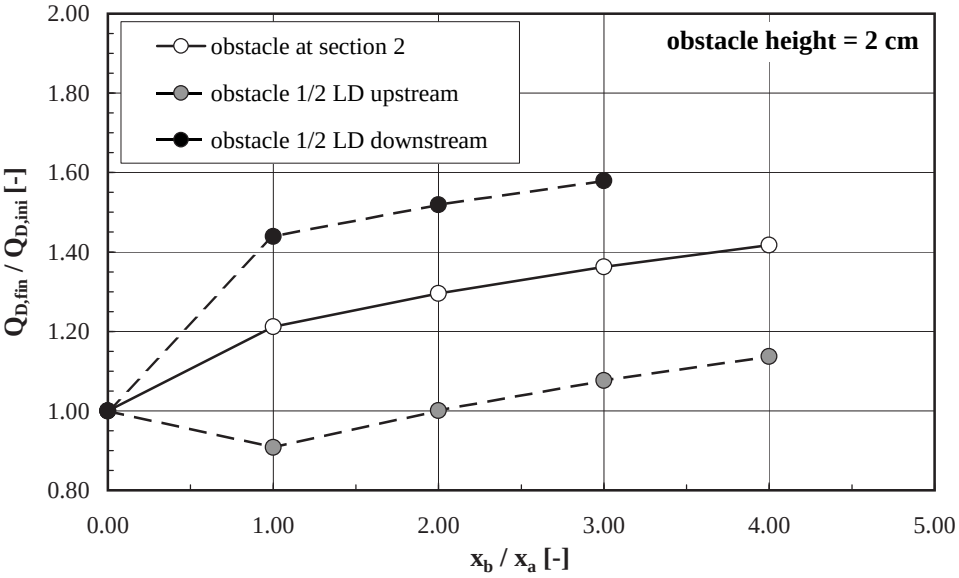

Figure 5.47: Influence of different deposition length ratios (x_b/x_a) and different channel locations on side overflow intensity ($Q_{D,fin}/Q_{D,ini}$) ($1D$-numerical simulation using DUPIRO).

width contraction from section 1 to 2 opposite to the weir (non-prismatic horizontal converging channel) or linear channel bottom increase (negative bottom inclination, non-prismatic vertical converging channel). The location of the obstacle at section 2 is similar to the latter case of locally negative bottom slope.

For the deposit shifted upstream, Δh is greater than for the deposit at section 2. For an almost similar h_1-value for both positions of the deposit the greater difference signifies a lower pressure head in section 2 than in section 1 (e. g. Fig. 5.46). Consequently, the water level along the crest declines and a lower discharge ratio is observed.

Contrary to these two situations, the deposits shifted downstream by 1/2 L_D reveal a negative pressure head difference. This means the head in section 2 is higher than in section 1 and the backwater effect induced by the deposit fully acts in the side weir crest region (e. g. Fig. 5.46). As a consequence, an elevated side weir discharge is produced.

Besides different locations of the deposit, increasing discharge ratios for longer, viz smoother, x_b/x_a-ratios and decreasing Δh-ratios might be explained by deploying the characteristics of a flow over a sharp crested aerated weir (perpendicular approach flow). In such a case the overfalling upper and lower nappe surfaces are subject to full atmospheric pressure. Designing overflow round crested weirs, the overflow surface is formed

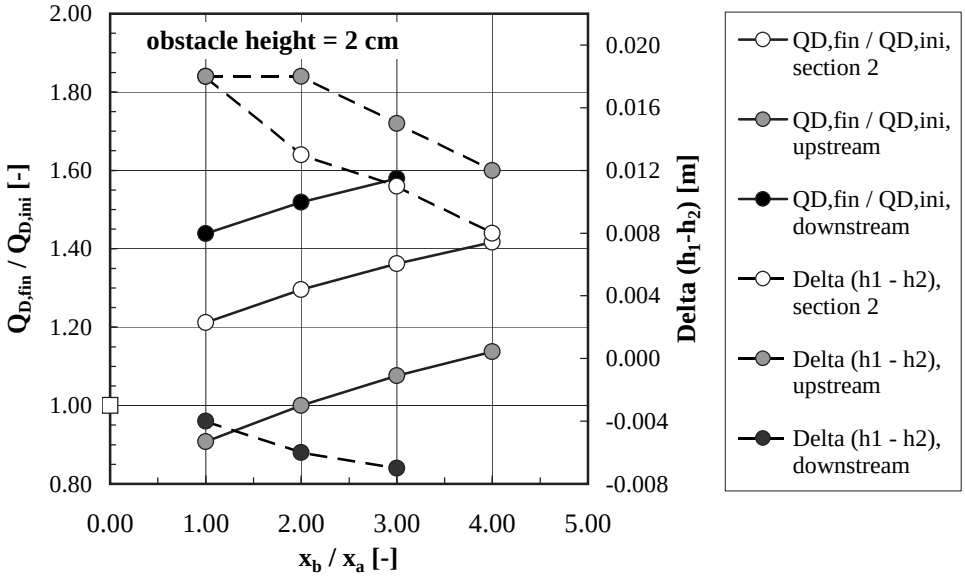

Figure 5.48: Influence of deposition length ratio (x_b/x_a) on diverted discharge ratio ($Q_{D,fin}/Q_{D,ini}$) and pressure head difference ($\Delta(h_1 - h_2)$ between section 1 and 2. For $x_b/x_a = 0.00$ (no deposit), $Q_{D,fin}/Q_{D,ini} = 1.00$ and $\Delta(h_1 - h_2) = -0.003\ m$ are obtained (white square) ($1D$-numerical simulation using DUPIRO).

according to the lower nappe profile of an aerated sharp crested weir. Consequently, the pressure on the overflow weir surface is supposed to be almost zero, thus representing optimal conditions from the constructional and hydraulic point of view. If the pressure head is lower or higher than the design head, an increased pressure or a pressure reduction is caused. Having these phenomena in mind, it can be argued that the flow which tends to drop after the deposit is kept on a higher level and in a way "carried" by the downstream part of the deposit (x_b).

Resuming, increasing head losses induced by decreasing deposition downstream length do not seem to have a gaining impact on the intensity of the side overflow. It is rather the "carrying"-effect of the extended downstream branch of the deposit which favors an increased side overflow.

With respect to the aforementioned, the traditional calculation of C_D as proposed by several authors in appendix A.7.3, using exclusively approach flow conditions in section 1 to determine basic input parameters, has to be used with carefulness. Since the backwater curve is very long and increases very smoothly in the upstream direction (towards section 0), thus inducing a rather mild slope along the weir crest, it covers a great part of the overflow crest length (in the example 77 % and 90 %). On the contrary, the rapidly

dropping water surface close to section 2 only covers a rather short ratio of the total crest length (in the example 23 % and 10 %).

Concluding and bearing in mind what has been discussed with respect to the influence of the exponent 3/2 in Equation 5.33, the explicit use of approach flow conditions at section 1 might, however, be acceptable.

A phenomenon which cannot be demonstrated using the $1D$-numerical model is the fact that great positive (negative) Δh-ratios indicate a high (small) streamwise velocity component (v_x) and a small (high) lateralwise one (v_y). Therefore, smaller (greater) side overflow ratios are obtained.

In this context it is worthy to mention that the entire discussion leaded above refers to a $1D$ local deposit, meaning the deposit does not change in lateralwise direction, viz, being constant over the channel width. In contrast to this, the flume experiments reveal a $2D$ sedimentary deposit, hence, the deposit varies along the channel width. Due to this, additional horizontal local energy losses induced by contraction and expansion effects occur, thus amplifying the impact of the deposit on the diverted discharge.

From the above investigations it can be concluded that the height and position of the deposit are of significant importance with respect to the side overflow intensity, whereas the shape of the deposit has less influence.

5.8.3. Conclusion

In this paragraph a triangular fixed local deposit of different shape (symmetric and non-symmetric) and height at different locations with respect to the side weir and its impact on the intensity of side overflow discharge has been investigated numerically applying the $1D$-numerical code DUPIRO.

From the computations it can be concluded that the height and the position of the local deposit are of considerable importance regarding side overflow intensity. The downstream shape of the deposit is of minor importance.

5.9. Bed Morphology

In this paragraph the sediment deposit observed in the experimental flume study is described. Since the impact of the deposit is not limited to the intensity of the side overflow discharge, the bed evolution downstream of the aggraded channel reach is investigated.

5.9.1. Description of local Deposit near Side Weir

Aggradation (and erosion) is caused by the disturbance of the equilibrium between sediment transport capacity of the main-channel (river) and sediment

supply. Assuming that the upstream supply of sediment will not be affected by the water withdrawal, in the (final) equilibrium conditions downstream of the side overflow the original amount of sediment has to be transported by a reduced flow. Of course, this is only valid if no sediments are transported over the weir (see paragraph 5.7.2 for sediment quantities transported over the weir). Thus, sediment is deposited in the weir reach and downstream of the weir the channel slope will increase to achieve equilibrium sediment transport conditions. Moreover, the normal depth will decrease as a result of the lateral loss of water. These phenomena are presented in Figures 5.36 and 5.49.

In Figure 5.49 typical final bed surface profiles for each test series are depicted. A $3D$-view of the final bed morphology is shown in Figure 5.50. Referring to Figure 5.49, upstream of the weir almost equilibrium sediment transport conditions can be observed. Immediately upstream of the weir the flow is attracted by the weir and slight erosion due to accelerated flow conditions is present. As soon as the weir is reached the main-channel discharge and hence sediment transport capacity is reduced and aggradation occurs. Maximum deposition is observed at the downstream weir corner. For test series D ($D02$) a rather small deposit at the first weir can be observed. This deposit is almost negligible with respect to the more pronounced deposit forming at the second weir. In the channel reach downstream of the weir decreased flow depth and reduced transport capacity is compensated by a steeper bottom slope to re-establish equilibrium transport conditions.

Assuming an analogy between bed forms and the deposit the shape of the aggradation might be roughly described by the bed form shape factor β_{SF} (Eq. 5.34) yielding a value of $\beta_{SF} = 0.57$ (paragraph 5.8.2).

5.9.2. Bed Evolution and sine-generated Flow Behavior downstream of Side Weir

Besides having an impact on the intensity of the diverted discharge the aggradation influences the downstream mobile evolution as well. The inclined and skewed sedimentary deposit being higher on the weir side than on the opposite channel bank (Figs 5.51 and 6.1, top) deviates the flow from the right bank to the left bank. Here, the flow is reflected by the flume wall. Through local flow acceleration bed sediment is mobilized and an oscillatory erosion gutter is initiated. The erosion gutter, corresponding to the thalweg (maximum erosion, z_{min}), continues in a periodic way in the downstream direction before being damped out. As a counterpart to the erosion gutter a line of maximum deposition is present (z_{max}). An example is given in Figures 5.51 and 5.52.

As mentioned before, the driving force for the initiation of the sine-generated erosion gutter is the skewness of the deposit. The skewness is

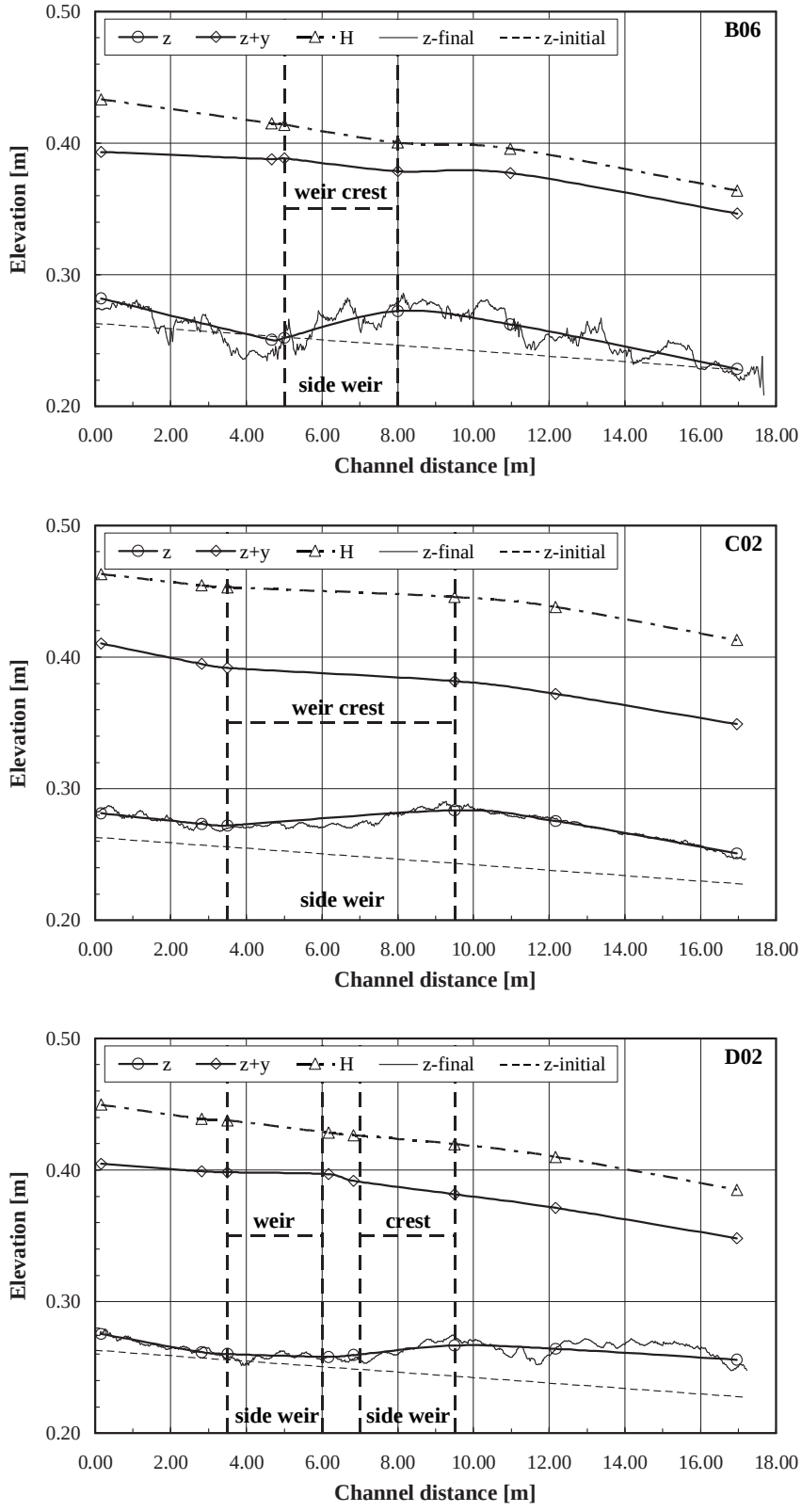

Figure 5.49: Final typical longitudinal bed surface profiles for test series B, C and D. The bold dashed lines indicate the side weir position and the crest height, respectively.

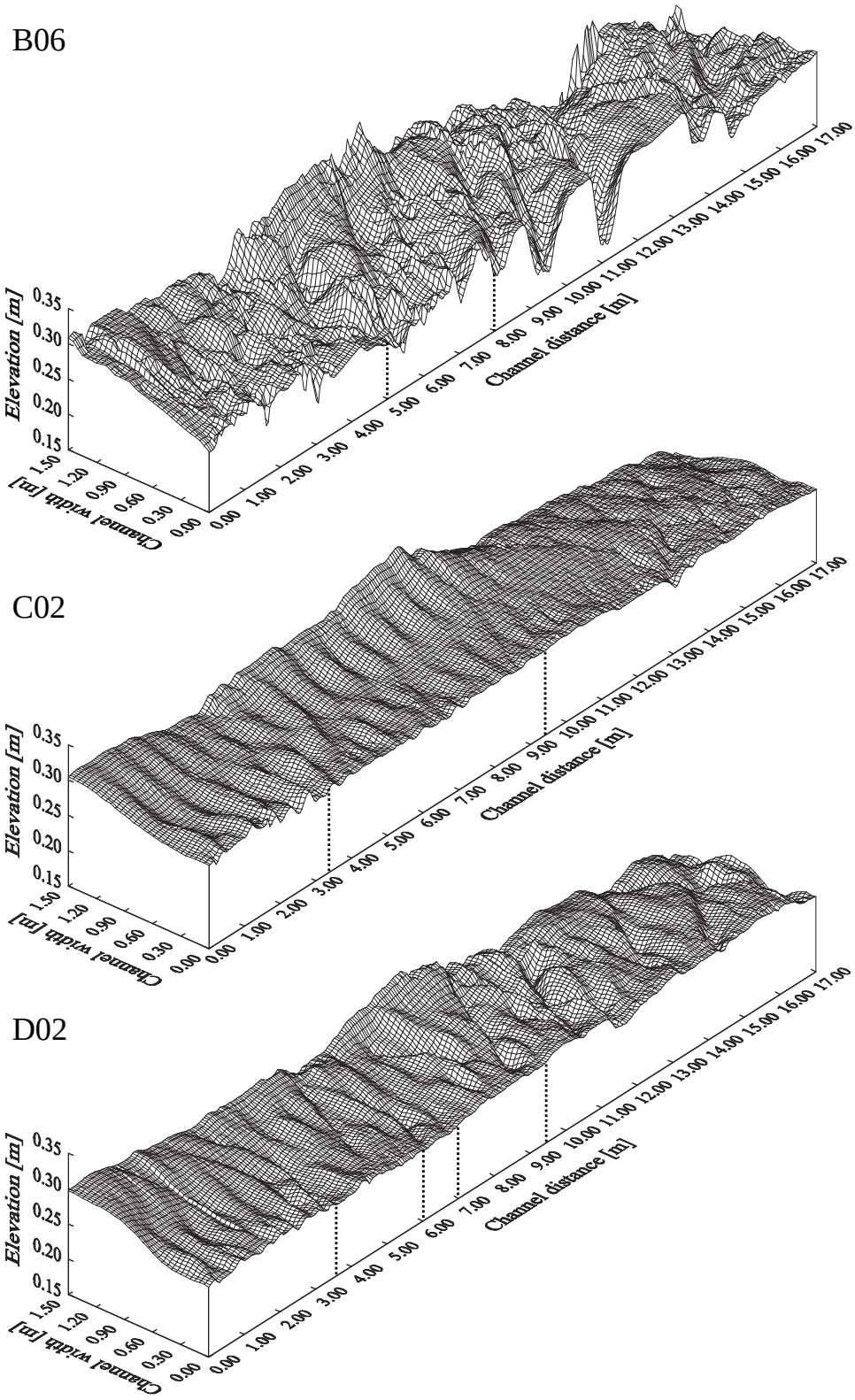

Figure 5.50: 3*D*-view of the final bed morphology for test series *B*, *C* and *D*. Flow is from left to right. The dashed line indicates the side weir location. Note: For better visibility of the deposit the left and right channel bank are inverted!

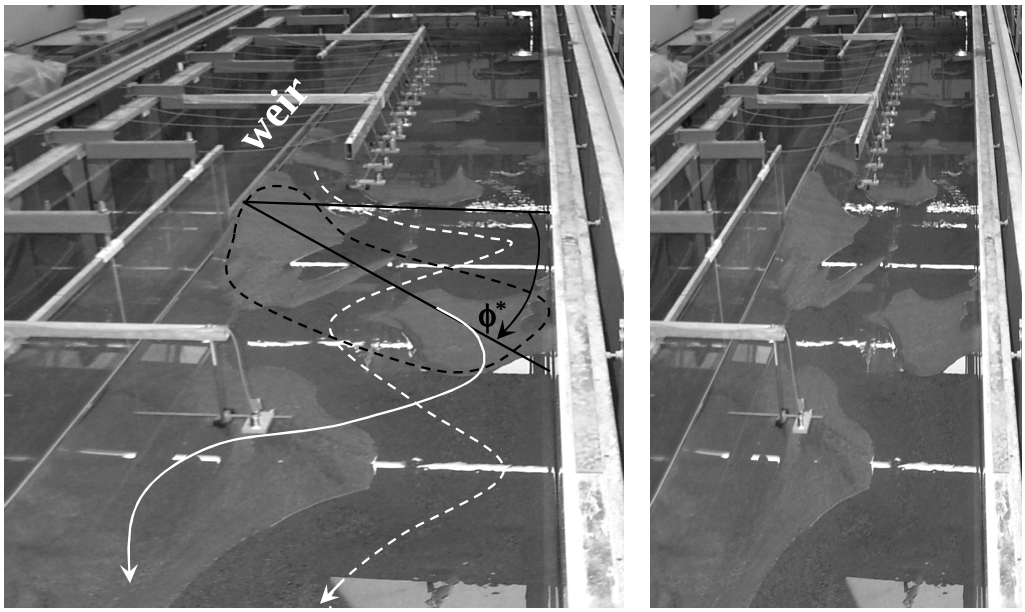

Figure 5.51: Left: Formation of an oscillatory erosion gutter (thalweg) downstream of the side weir for experiment $B01$ (white dashed line). The erosion gutter is initiated by the skewed deposit (black dashed line). As a counterpart to the erosion gutter a line of maximum deposition is presented (white solid line). Right: Undistorted original photograph taken at the end of the experiment after drainage of the flume.

expressed in terms of an angle (ϕ^*) describing the longitudinal shift of the deposit on the right and left channel bank (Figs 5.51, 5.52 and paragraph 6.7.1 and Tab. 6.6). Starting with the initial displacement angle (ϕ^*) of the deposit (Tab. 6.6) the erosion gutter develops in the downstream direction with the deflection angle ϕ^*_{ero}. The evolution of the line of maximum deposition is characterised by the deflection angle ϕ^*_{dep} (Fig. 5.52). In Figure 5.53 and Table 5.19 the initial displacement angle of the deposit (ϕ^*) and the longitudinal evolution of the erosion and deposition deflection angles (ϕ^*_{ero}, ϕ^*_{dep}) are presented for an emblematic experiment of each test series.

It can be derived from Figure 5.53 and Table 5.19 that for test series B close to the downstream weir corner the angles (ϕ^*_{ero}, ϕ^*_{dep}) closely follow the initial displacement angle of the deposit (ϕ^*). With increasing distance from the downstream weir corner ϕ^*_{ero} and ϕ^*_{dep} slightly decrease indicating a more tight shape of the erosion gutter and the line of maximum deposition. With respect to test series C the angles significantly increase compared to ϕ^*. Concerning test series D, ϕ^*_{ero} and ϕ^*_{dep} are rather narrow to the initial displacement angle of the deposit (ϕ^*) all along the downstream part of the channel. As far as the difference between ϕ^*_{ero} and ϕ^*_{dep} is concerned, both

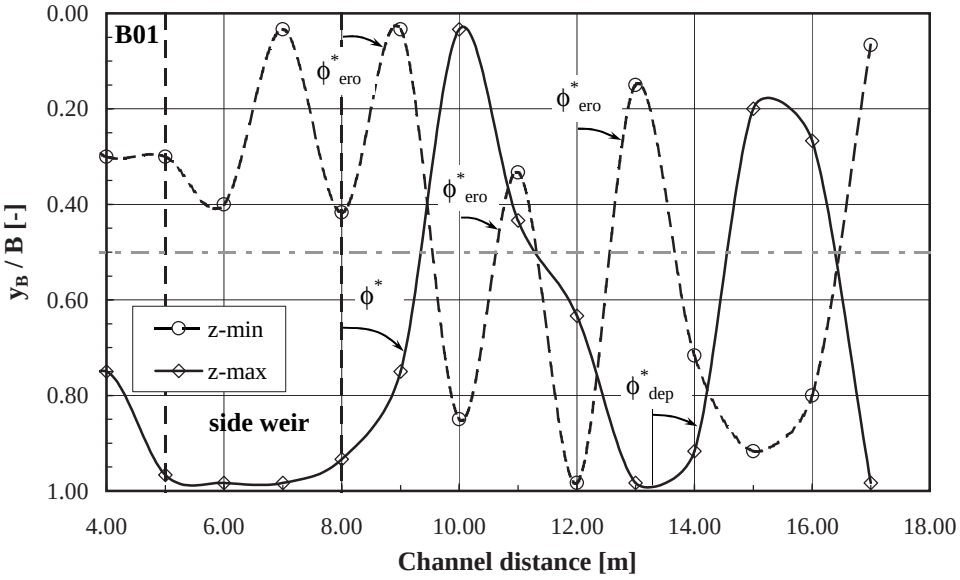

Figure 5.52: Plan view: Formation of an oscillatory erosion gutter (thalweg) (z_{min}) downstream of the side weir for experiment $B01$. As a counterpart to the erosion gutter the evolution of maximum deposition is presented (z_{max}). ϕ^* denotes the initial displacement angle of the deposit according to Table 6.6, ϕ^*_{ero} and ϕ^*_{dep} denote the erosion and deposition deflection angle.

Table 5.19: Deflection angles of the erosion gutter (ϕ^*_{ero}) and the line of maximum deposition (ϕ^*_{dep}) and comparison with the initial displacement angle (ϕ^*) of the deposit according to Table 6.6.

Test series	ϕ^* [°]	ϕ^*_{ero} [°]	ϕ^*_{dep} [°]	ϕ^*_{ero}/ϕ^* [−]	ϕ^*_{dep}/ϕ^* [−]
B	68	58	57	0.85	0.84
C	25	70	72	2.80	2.88
D	61	63	59	1.03	0.97

angles are in the same order of magnitude.

Since the plane shape of the erosion gutter and the line of maximum deposition downstream of the weir are periodic (Figs 5.51 and 5.52), a description by a sine-generated curve of the following type might be suggested (Fig. 5.54):

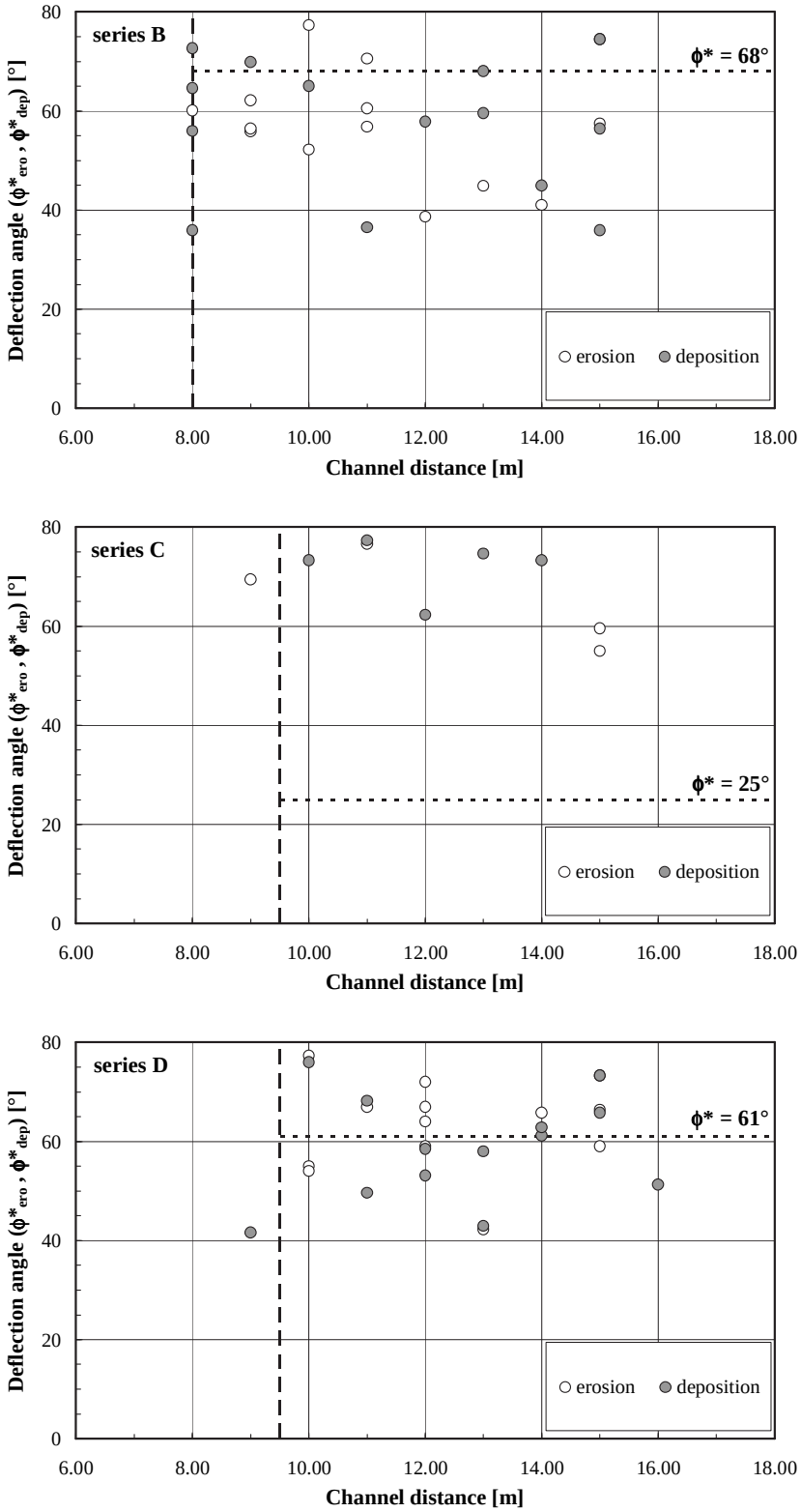

Figure 5.53: Streamwise evolution of the deflection angle of the erosion gutter (ϕ^*_{ero}) and the line of maximum deposition (ϕ^*_{dep}). The solid dashed line indicates the downstream weir corner, the tiny dashed line the initial displacement angle (ϕ^*) of the deposit according to Table 6.6.

$$y = a_0 \cdot sin\,(b_0 \cdot x + c_0) \tag{5.35}$$

with a_0 amplitude, $b_0 = 2\pi/\omega_p$, ω_p periodicity and c_0 longitudinal shift in x-direction.

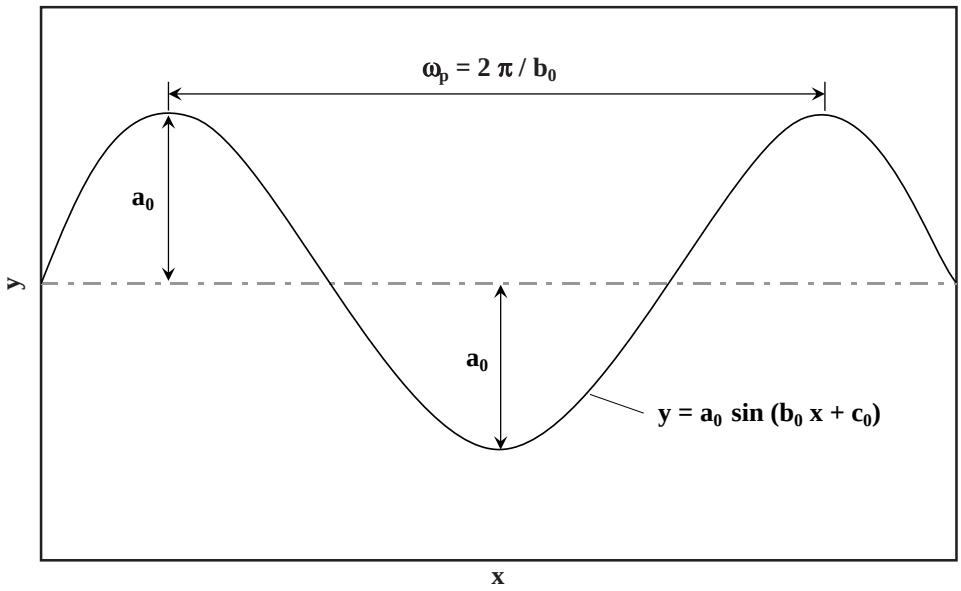

Figure 5.54: Definition sketch of a sine-generated curve to describe the plane shape of the erosion gutter and the line of maximum deposition downstream of the weir. a_0 is the amplitude, $\omega_p = 2\pi/b_0$ periodicity and c_0 the longitudinal shift in x-direction.

The origin of the sine-generated curve in the lateralwise direction (y-axis in Fig. 5.54) corresponds to the middle of the channel at $y_B/B = 0.50$ ($y_B/B = 0.00 \div 1.00$, e. g. Fig. 5.52). With reasonable approximation the origin in x-direction might be located at the downstream weir corner (section 2).

As far as the parameters occurring in Equation 5.35 are concerned, the amplitude (a_0) for both, the erosion gutter as well as the line of maximum deposition, can be expressed according to Table 5.20. Hence, a_0 starts from $y_B/B = 0.50$ (middle of the channel) with:

$$a_0 = \pm\, 0.83 \cdot B/L_D \tag{5.36}$$

For the parameter b_0 in Equation 5.35 the following relations have been found:

$$\begin{aligned} b_0 = &\quad 378 \cdot B/L_D \quad \text{erosion gutter} \\ b_0 = &\quad 43 \cdot L_D/B \quad \text{line of maximum deposition} \end{aligned} \tag{5.37}$$

Table 5.20: Amplitude (a_0) for the sine-generated erosion gutter and line of maximum deposition. B is channel width ($B = 1.50\ m = const.$) and L_D weir crest length ($L_D = 3.00\ m$ for test series B, $L_D = 6.00\ m$ for test series C and $L_D = 5.00\ m$ for test series D).

Test series	a_0 [–]	B/L_D [–]
B	$0.83 \cdot B/L_D$	0.50
C	$0.82 \cdot B/L_D$	0.25
D	$0.84 \cdot B/L_D$	0.30
average	$0.83 \cdot B/L_D$	

Hence, the periodicity ($\omega_p = 2\pi/b_0$) corresponds to:

$$\begin{aligned} \omega_p = &\ 2\pi \cdot 1/378 \cdot L_D/B \quad \text{erosion gutter} \\ \omega_p = &\ 2\pi \cdot 1/43 \cdot B/L_D \quad \text{line of maximum deposition} \end{aligned} \tag{5.38}$$

Note that in Equations 5.37 and 5.38 B/L_D and the inverse L_D/B are used.

The parameter c_0 has to be chosen in the way that the two sine-generated curves first develop to the river bank opposite to the weir. Herein, a constant value of $c_0 = 200$ has been used.

In Figures 5.55, 5.56 and 5.57 the measured erosion gutter and the line of maximum deposition as well as the corresponding computed sine-generated curves according to Equation 5.35 are presented. It can be seen that until a certain distance downstream of the end of the weir the computed curves for the erosion gutter correspond fairly well to the measured ones. As soon as the wavelength of the erosion gutter (Λ_{ero}) considerably increases the prediction quality decreases. Typical threshold distances counting from the downstream weir corner are given as follows:

$$\begin{aligned} \text{test series B:} &\ \approx 7/6 \cdot L_D \\ \text{test series C:} &\ \approx 1/4 \cdot L_D \\ \text{test series D:} &\ \approx 1/2 \cdot L_D \end{aligned} \tag{5.39}$$

(5.40)

For the line of maximum deposition no clear tendency could be observed.

Characteristic average wavelengths for the erosion gutter (Λ_{ero}) are summarized in Table 5.21. For the wavelength of the line of maximum deposition (Λ_{dep}) no well-defined relations could be identified. However, average Λ_{dep}-values in the range of $\Lambda_{dep} = 3,80\ m$ (test series B) and $\Lambda_{dep} = 2.50\ m$ (test series C and D) can be reported.

Table 5.21: Characteristic measured average wavelengths (Λ_{ero}) for the erosion gutter for test series B, C and D. L_D denotes the weir crest length.

Test series	Λ_{ero} [−]	L_D [m]
B	$0.21 \cdot \pi \cdot L_D$	3.00
C	$0.18 \cdot \pi \cdot L_D$	6.00
D	$0.17 \cdot \pi \cdot L_D$	5.00
average	$0.19 \cdot \pi \cdot L_D$	

Although from the hydraulic and sedimentary as well as the morphological point of view totally different, the plan view of the thalweg (and the corresponding deposition line) might suggest a comparison with meander theory. In that case an equation as proposed by e. g Yalin (1992) could be used instead of Equation 5.35. However, comparative calculations indicated better results applying Equation 5.35.

Finally it might be worthy to mention that accelerated flow conditions induced by the asymmetric convergent channel cross section (skewed deposit in the downstream weir alignment) could initiate additional sediment yield originating from bank erosion if no appropriate bank protection measures are provided. Since due to the lateral water withdrawal the overall sediment transport capacity is already reduced, these sediments are likely to accumulate shortly downstream of the weir when the flow field re-establishes. Consequently, the problem of sediment accumulation and thus increased diverted discharge would be intensified.

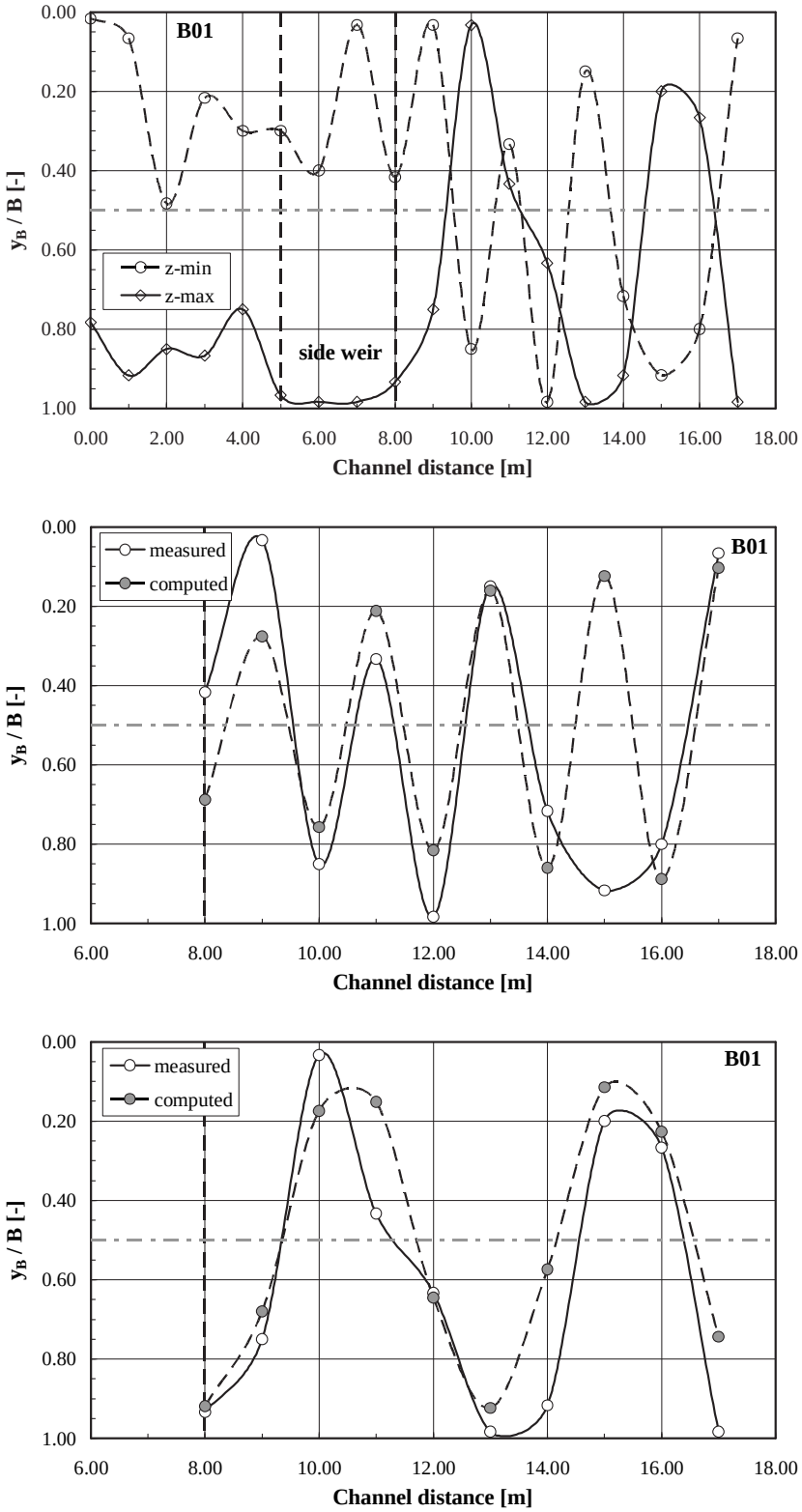

Figure 5.55: Measured and computed erosion gutter (thalweg) and line of maximum deposition for experiment $B01$. Top: Entire channel. z_{min} and z_{max} denote maximum erosion and deposition. Middle: Erosion gutter. Bottom: Deposition. The solid dashed line indicates the downstream weir corner.

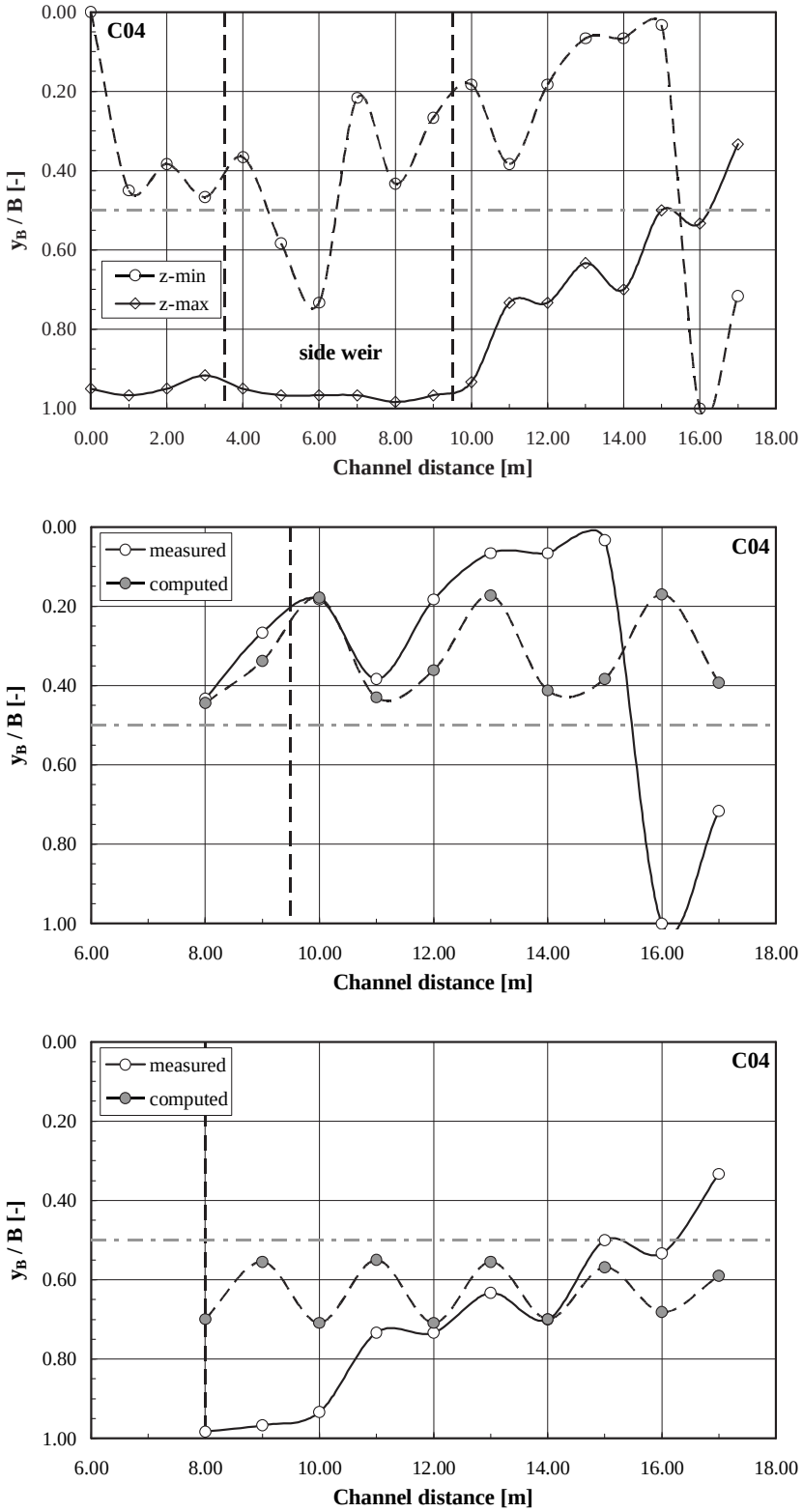

Figure 5.56: Measured and computed erosion gutter (thalweg) and line of maximum deposition for experiment $C04$. Top: Entire channel. z_{min} and z_{max} denote maximum erosion and deposition. Middle: Erosion gutter. Bottom: Deposition. The solid dashed line indicates the downstream weir corner.

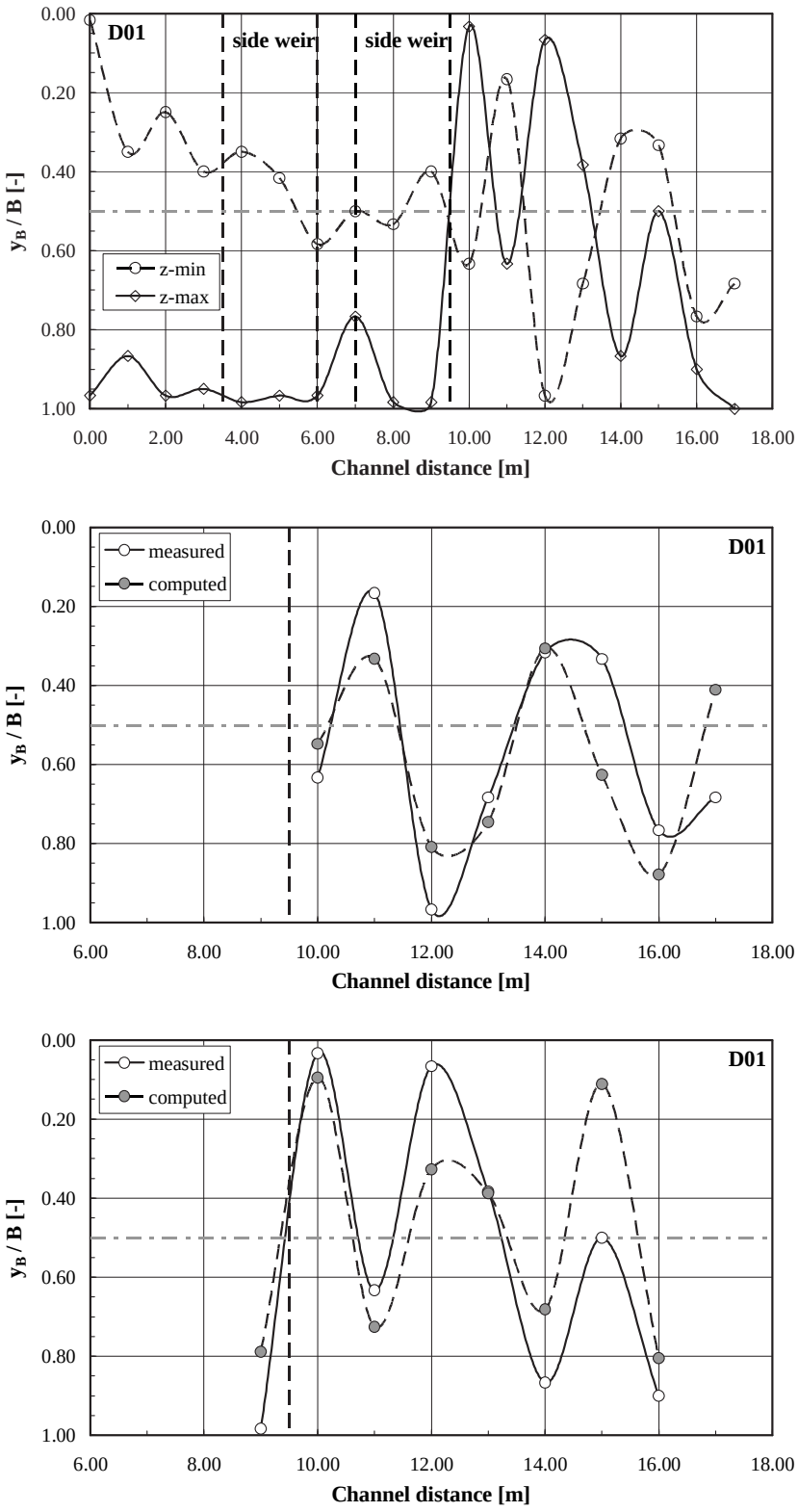

Figure 5.57: Measured and computed erosion gutter (thalweg) and line of maximum deposition for experiment *D*01. Top: Entire channel. z_{min} and z_{max} denote maximum erosion and deposition. Middle: Erosion gutter. Bottom: Deposition. The solid dashed line indicates the downstream weir corner.

5.9.3. Conclusion

The disturbance of the equilibrium between sediment transport capacity of the main-channel and sediment supply by the lateral loss of water induces the formation of a local sediment deposit. The maximum deposition is observed at the downstream weir corner.

The skewed local deposit is responsable for a meander-like erosion channel downstream of the weir. The oscillatory streamwise evolution is being damped out with increasing distance from the weir. For the description of the sine-generated plan shape of the erosion channel (thalweg) indicative expressions are proposed.

5.10. Bed Forms and Bed Form induced Flow Resistance

In this paragraph bed forms observed in the experiments are identified and compared with different classification methods. In a next step geometrical bed form characteristics such as bed form length, height, steepness and stoss as well as lee slope angle are investigated and tested against approaches from literature. In addition, the duration development and migration velocity of bed features is analyzed. In the last paragraph flow resistance due to bed forms is dealt with.

5.10.1. Identification of Bed Form Type

Herein, bed features observed in the experiments are identified and compared with different regime predictors or classification methods from literature as presented in appendix A.3.1.

For the comparison a distinction between the reach upstream of the weir, the weir alignment itself and the downstream weir reach is undertaken. In Tables 5.22, 5.23 and 5.24 the results are presented. In these Tables the following notation according to the original approaches is applied:

LR = lower regime	D = dune
TR = transition regime	RD = ripples superimposed on dunes
UR = upper regime	WD = washed-out dunes
NM = no motion	PB = plane bed
MD = mini dune	AD = anti dune

The analysis shows that for test series B the dominant bed features are dunes. Downstream of the weir ripples superimposed on dunes occur. For test

series C a slightly wavy or rather flat bed with washed-out dunes is identified. Series D represents an intermediate case with both dunes and washed-out dunes (or plane bed). Characteristic bed surfaces for all three test series are presented in Figure 5.58.

It has to be noted that the Froude number influences bed form pattern and it is a well-known phenomenon that bed forms generated at low velocities are washed out at high velocities. Especially for test series C high Froude numbers close to unity have been observed. The corresponding bed surface has been comparatively smooth with a roughness almost equal to grain roughness. It has further to be mentioned that for test series C the bed surface has not been loosed and flattened before starting a new experiment. Thus, the experiments were performed on the final bed topography of the preceding one. This is due to the fact that it was intended to simulate the passage of a flood hydrograph (each experiment corresponding to one step of the hydrograph).

Finally, no significant distinction in bed form type can be stated for the different channel reaches.

With respect to the classification approaches from literature the best regime predictors are given by Van Rijn (1984b) and Karim (1999). For the approach by Karim (1999) the factor N^* accounting for ripples equals $N^* = 345$ upstream of the weir, $N^* = 319$ in the weir reach and $N^* = 296$ downstream of the weir. Since $N^* < 80$ no ripples and only dunes occur. The Froude number as classification parameter yields satisfying results as well. Since the transition regime (washed-out dunes, plane bed) is not incorporated in the method by Yalin and da Silva (2001), the prediction accuracy is moderate. The same accounts for the regime predictor of Yalin (1992). Herein, from bed form pattern relevant for this study only dunes are taken into account. With respect to Simons and Richardson (1966) all relevant regimes are represented but the transition regime occurring in series C and D is not predicted correctly.

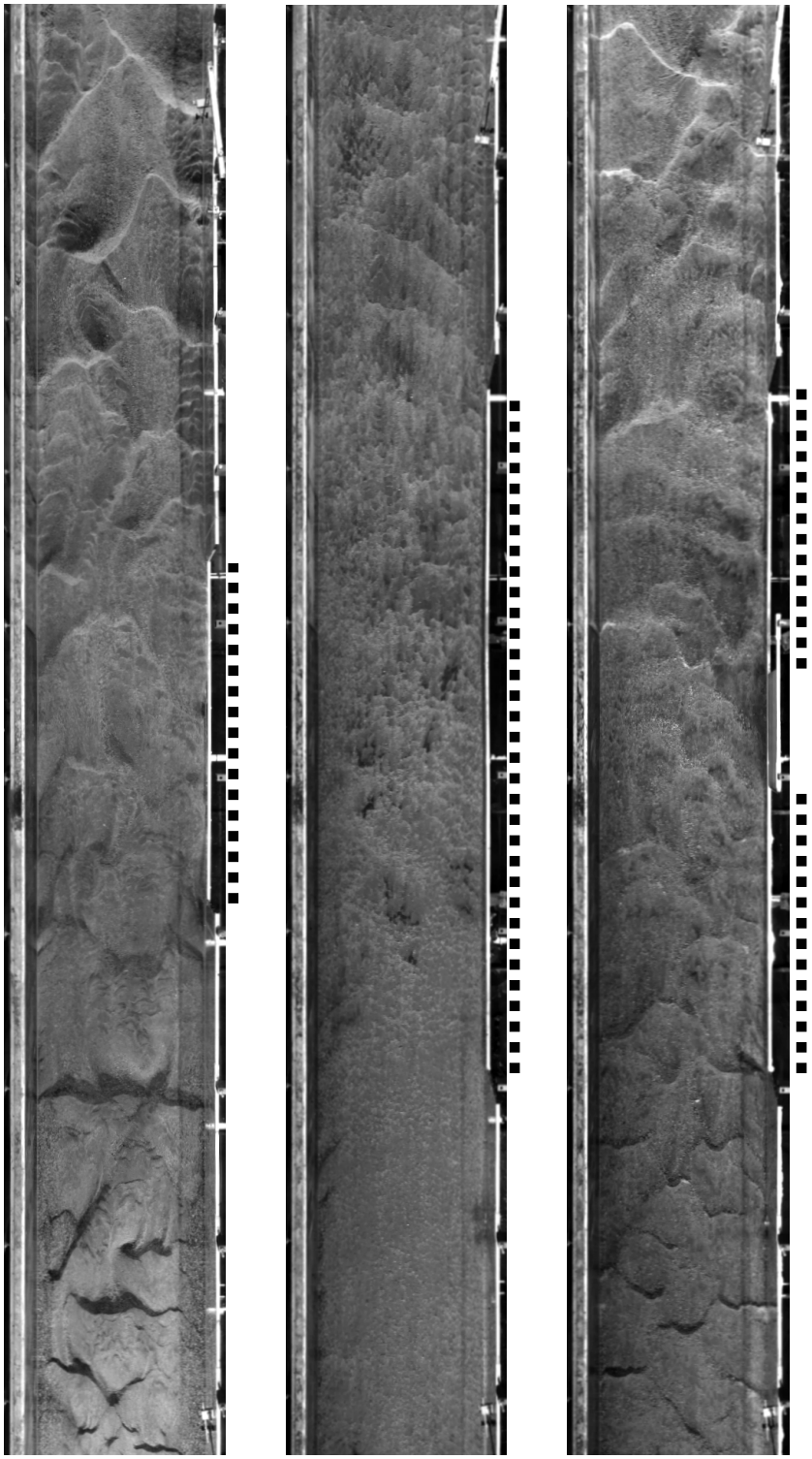

Figure 5.58: Characteristic examples of final bed morphology for test series B, C and D. Left: Test series B ($B03$). Middle: Test series C ($C05$). Right: Test series D ($D04$). Flow is from bottom to top. The dashed line indicates the position of the side weir(s).

Table 5.22: Upstream of side weir: Identification of bed form type for the present study and comparison with classification methods from literature. The notation follows the original approaches.

N^o of experiment	Present study	Froude number	Simons & Richardson (1966)	Van Rijn (1984b)	Yalin (1992)	Karim (1999)	Yalin & da Silva (2001)
*B*01	D	MD, D	D	D	D	LR, D	RD
*B*02	D	MD, D	D	D	D	TR, WD	RD
*B*03	D	MD, D	D	D	D	LR, D	D
*B*04	D	MD, D	D	D	D	LR, D	D
*B*05	D	MD, D	D	D	D	LR, D	RD
*B*06	D	MD, D	D	D	D	LR, D	D
*C*01	WD	PB	D	TR, WD	D	TR, WD	RD
*C*02	WD	PB	D	TR, WD	D	TR, WD	D
*C*03	WD, (D)	PB, (AD)	D	UR, PB	D	UR, PB	D
*C*04	WD, (D)	D, (PB)	D	D	D	TR, WD	D
*C*05	WD	PB	D	TR, WD	D	TR, WD	D
*D*01	WD, (D)	MD, D	D	D	D	TR, WD	D
*D*02	WD, (D)	MD, D	D	D	D	TR, WD	D
*D*03	WD, (D)	MD, D	D	D	D	TR, WD	D
*D*04	D	MD, D	D	D	D	TR, WD	D
*D*05	D	MD, D	D	D	D	TR, WD	D

LR = lower regime, TR = transition regime, UR = upper regime, NM = no motion, MD = mini dune, D = dune, RD = ripples superimposed on dunes, WD = washed-out dunes, PB = plane bed, AD = antidune

Table 5.23: Weir reach: Identification of bed form type for the present study and comparison with classification methods from literature. The notation follows the original approaches.

N^o of experiment	Present study	Froude number	Simons & Richardson (1966)	Van Rijn (1984b)	Yalin (1992)	Karim (1999)	Yalin & da Silva (2001)
*B*01	D	MD, D	D	D	D	LR, D	RD
*B*02	D	MD, D	D	D	D	LR, D	D
*B*03	D	MD, D	D	D	D	LR, D	D
*B*04	D	MD, D	D	D	D	LR, D	RD
*B*05	D	MD, D	NM	D	D	TR, WD	D
*B*06	D	MD, D	D	D	D	LR, D	D
*C*01	WD	PB	D	TR, WD	D	TR, WD	D
*C*02	WD	PB	D	TR, WD	D	TR, WD	RD
*C*03	WD	PB, (AD)	D	UR, PB	D	UR, PB	D
*C*04	WD, (D)	PB	D	TR, WD	D	TR, WD	D
*C*05	WD	PB	D	TR, WD	D	TR, WD	D
*D*01	WD, (D)	MD, D, (PB)	D	D	D	TR, WD	D
*D*02	WD, (D)	MD, D, (PB)	D	D	D	TR, WD	D
*D*03	WD, (D)	MD, D, (PB)	D	D	D	TR, WD	D
*D*04	D	MD, D, (PB)	D	D	D	LR, D	D
*D*05	D	MD, D, (PB)	D	D	D	TR, WD	RD

LR = lower regime, TR = transition regime, UR = upper regime, NM = no motion, MD = mini dune, D = dune, RD = ripples superimposed on dunes, WD = washed-out dunes, PB = plane bed, AD = antidune

Table 5.24: Downstream of side weir: Identification of bed form type for the present study and comparison with classification methods from literature. The notation follows the original approaches.

N^o of experiment	Present study	Froude number	Simons & Richardson (1966)	Van Rijn (1984b)	Yalin (1992)	Karim (1999)	Yalin & da Silva (2001)
*B*01	D, (RD)	MD, D	D	D	D	LR, D	RD
*B*02	D, (RD)	MD, D	D	D	D	LR, D	D
*B*03	D, (RD)	MD, D	D	D	D	TR, WD	D
*B*04	D	MD, D	D	D	D	TR, WD	RD
*B*05	D	MD, D, (PB)	D	D	D	TR, WD	RD
*B*06	D	MD, D	D	D	D	LR, D	D
*C*01	WD	PB	D	TR, WD	D	TR, WD	D
*C*02	WD, (D)	PB	D	TR, WD	D	TR, WD	D
*C*03	WD, (D)	PB, (AD)	D	UR, PB	D	TR, WD	D
*C*04	WD, (D)	PB	D	D	D	TR, WD	D
*C*05	WD, (D)	PB	D	TR, WD	D	TR, WD	RD
*D*01	D	PB	D	TR, WD	D	TR, WD	RD
*D*02	WD, (D)	PB	D	TR, WD	D	TR, WD	RD
*D*03	WD, (D)	MD, D	D	D	D	TR, WD	RD
*D*04	D	MD, D	D	D	D	LR, D	RD
*D*05	WD, (D)	PB	D	TR, WD	D	TR, WD	RD

LR = lower regime, TR = transition regime, UR = upper regime, NM = no motion, MD = mini dune, D = dune, RD = ripples superimposed on dunes, WD = washed-out dunes, PB = plane bed, AD = antidune

5.10.2. Measured Geometry of Bed Forms

Due to the importance of bed form resistance in determining the overall resistance in sand-bed flows (appendix A.4 and 5.10.6), the knowledge of bed form geometry is essential for estimating flow and water levels, especially during floods events in rivers.

In this paragraph only bed forms of the lower regime are considered. The dominant bed features of this regime are dunes. Since small scale bed forms such as ripples rarely occur in the present study (only in a few experiments of series B downstream of the weir, Tab. 5.24) these bed form pattern are not investigated. As for test series C and D no pronounced and well distinct dunes developed (Figs 5.58, 5.65) the analysis of bed form geometry refers to three emblematic experiments of test series B ($B01$, $B02$ and $B03$).

For the determination of dune geometry longitudinal bed elevation profiles were extracted for five different positions along the channel width, located at $y_B = 0.30\ m$, $y_B = 0.60\ m$, $y_B = 0.90\ m$ and $y_B = 1.20\ m$. Moreover, one profile in the channel centreline at $y_B = 0.75\ m$ was extracted (Fig. 5.65). Bed form identification possibilities such as alternate zero crossing or alternate changes of slope did not match properly for the present study. This is mainly due to the fact that sediment deposition takes place in the weir alignment and zero crossings with respect to the initially plane bed are excluded from being an appropriate criterion. Consequently, individual bed forms within a given bed profile were identified manually by searching the profile record for the presence of bed form lee slopes (Rosier et al. (2007a)). This approach proved to be effective due to the fundamental nature of the lee slope of a bed form.

For a detected lee slope the location of the corresponding bed form was taken as being given by the upstream trough of the same bed feature. The trough elevation for the bed form was taken as being given by the downstream limit of the lee slope. Similarly, the crest elevation was defined as the upstream limit of the lee slope. The bed form height (Δ_d) was calculated as the vertical difference between the crest and its subsequent trough. The bed form length (Λ_d) was determined as the longitudinal difference between two troughs. The resulting steepness is defined as $\delta_d = \Delta_d/\Lambda_d$. Knowing the bed form length, height and position of the crest, stoss and lee lope angles (α_d, β_d) were calculated according to $tan\ \alpha_d = \Delta_d/\Lambda_{d,1}$ and $tan\ \beta_d = \Delta_d/\Lambda_{d,2}$ (Fig. A.7). Typical dune pattern are shown in Figure 5.59.

Referring to measured dune dimensions, dune length (Λ_d), height (Δ_d) and steepness (δ_d) for experiments $B01$, $B02$ and $B03$ are depicted in Figure 5.60 and summarized in Table 5.25. It becomes evident that the distribution of dune length is rather uniform upstream of the weir and in the weir reach itself, whereas downstream of the overflow a dispersed repartition and greater Λ_d-values are encountered. For dune height similar observations

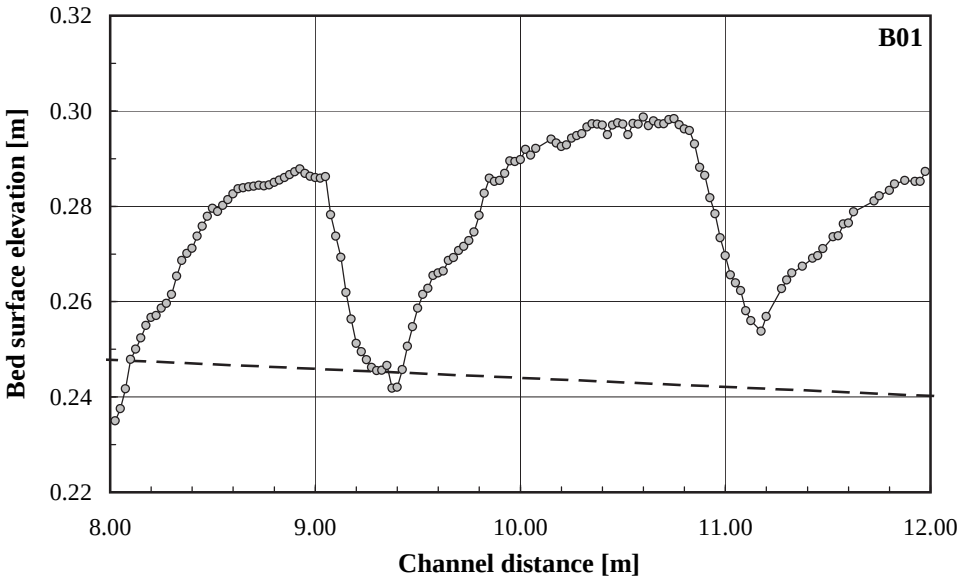

Figure 5.59: Dune pattern for experiment $B01$ downstream of the side weir. The dashed line represents the initial bed level.

can be stated with a slightly higher degree of scatter downstream of the weir. As far as dune steepness is concerned, the majority of data points is located in a band of $\delta_d \approx 0.02 \div 0.06$ with several values exceeding this range mounting up to $\delta_d = 0.011$ (or even 0.014).

In Figure 5.61 dune stoss slope (α_d) and lee slope angles (β_d) are illustrated. A summary is given in Table 5.25. As has been mentioned for dune length, height and steepness, a higher variability of stoss and lee slope angles is observed downstream of the weir.

To get an idea whether measured dune characteristics correspond to other investigations dealing with bed forms some data and values reported in literature are cited below.

In flume experiments performed by Wang and Shen (1980) Λ_d-values of 1.385 m and Δ_d-values of 0.074 m were observed. Stoss slope angles correspond to $\alpha_d = 5° \div 12°$ with a mean value of 8.5°

Van Rijn (1993) conducted flume experiments with artificial dunes (flume conditions: $B = 1.50\ m$, flume length 50 m, $y = 0.33\ m$, $v = 0.51\ m/s$, $S_w = 0.00095$, $Fr = 0.29$). The dune length was $\Lambda_d = 1.60\ m$, the height corresponds to $\Delta_d = 0.08\ m$. The lee side slope was $\beta_d = 26°$. A value of $\beta_d = 10°$ represents the minimum angle for lee side flow separation (Wilbers (2004)).

According to Fredsøe (1982), dune steepness (δ_d) will remain constant at a value of about 0.06 as long as all of the sediment is assumed to move as bed-load. Yalin (1992) pointed out that the dune steepness is always less

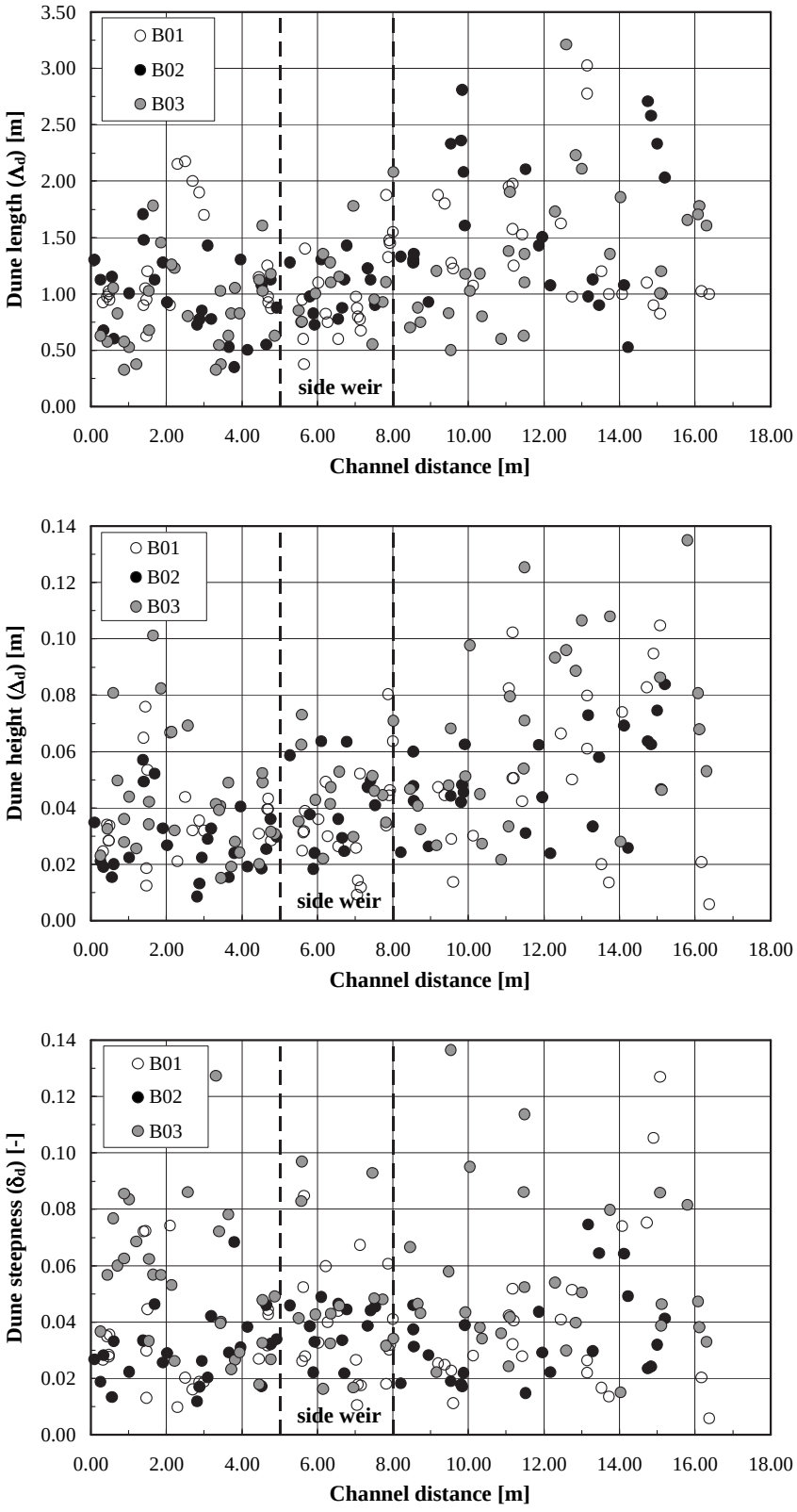

Figure 5.60: Streamwise evolution of dune length (Λ_d) (top), height (Δ_d) (middle) and steepness (δ_d) (bottom) for experiments $B01$, $B02$ and $B03$ (all lateralwise positions at y_B = 0.30 m, 0.60 m, 0.75 m, 0.90 m and 1.20 m).

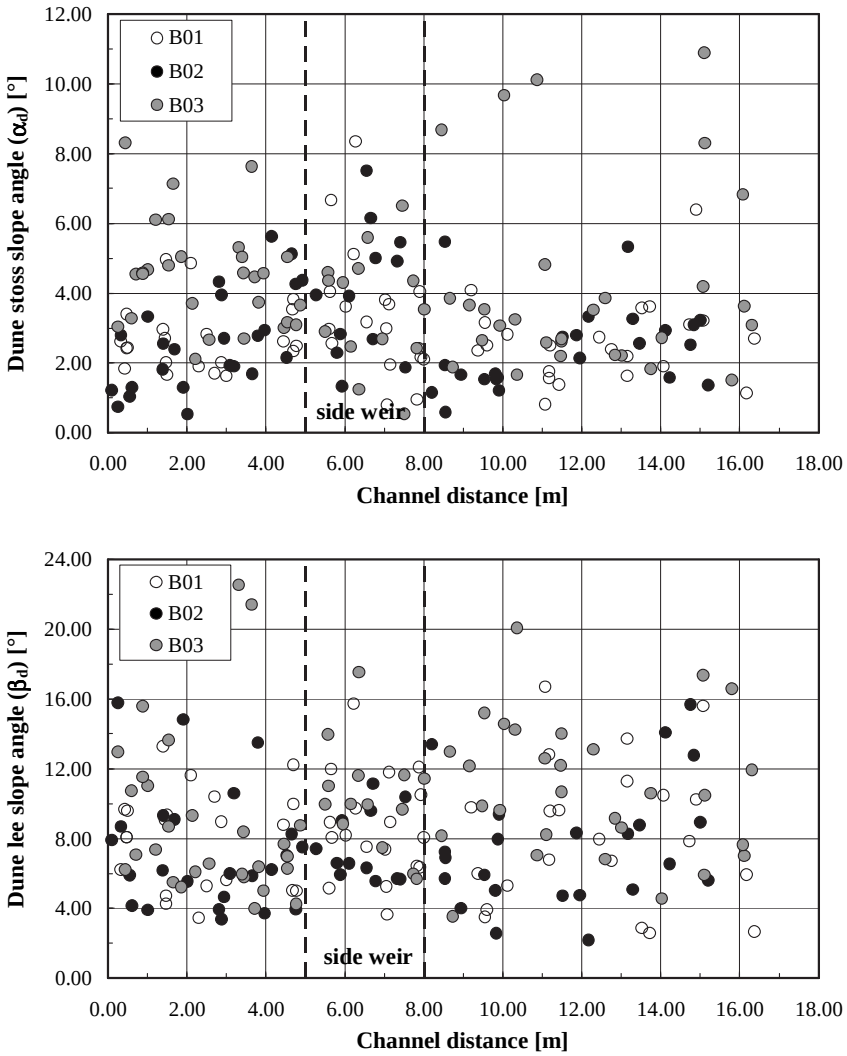

Figure 5.61: Streamwise evolution of dune stoss (α_d) (top) and lee slope angle (β_d) (bottom) for experiments $B01$, $B02$ and $B03$ (all lateralwise positions at $y_B = 0.30\ m$, $0.60\ m$, $0.75\ m$, $0.90\ m$ and $1.20\ m$).

Table 5.25: Geometrical mean bed form (dune) characteristics for experiments $B01$, $B02$ and $B03$. Λ_d = dune length, Δ_d = dune height, δ_d = dune steepness, α_d = dune stoss slope angle and β_d = dune lee slope angle.

N^o of experiment	Λ_d $[m]$	Δ_d $[m]$	δ_d $[-]$	α_d $[°]$	β_d $[°]$
	upstream of weir				
$B01$	1.219	0.038	0.034	2.704	8.032
$B02$	0.969	0.028	0.030	2.616	7.327
$B03$	0.868	0.042	0.054	4.523	8.960
average	1.019	0.036	0.040	3.281	8.106
	weir reach				
$B01$	1.021	0.036	0.038	3.412	8.651
$B02$	1.049	0.041	0.039	3.993	7.492
$B03$	1.118	0.047	0.048	3.586	10.336
average	1.062	0.041	0.042	3.664	8.826
	downstream of weir				
$B01$	1.453	0.053	0.040	2.615	8.266
$B02$	1.642	0.050	0.034	2.402	7.556
$B03$	1.326	0.066	0.054	4.199	10.857
average	1.474	0.056	0.043	3.072	8.893

than ≈ 0.06. Moreover, bed-load will increase dune height and suspended load will decrease dune height. This is due to turbulence being damped by the presence of suspended load (Garde and Ranga Raju (1966)). With respect to Yalin and da Silva (2001) dune height is not constant but first increases, reaches a maximum and then decreases until to disappear at the upper plane bed conditions.

Regarding the bed form shape factor (β_{SF}, see Eq. 5.34 for definition) a characteristic value of $\beta_{SF} = 0.72$ has been determined. Tang and Knight (2006) stated that the simple assumption of $\beta_{SF} = 0.50$ is approximately true for small-scale dunes in experimental flumes. For natural rivers where bed

forms have three-dimensional parabolic characteristics the β_{SF}-factor is closer to 0.66 (Tang and Knight (2006)). Zanke (1982) conducted dune experiments with a β_{SF}-value of 0.60, Wiesemann et al. (2006) reported a value of 0.55 (also for dune experiments).

As far as field conditions are concerned, Chien and Wan (1999) reported that bed form scales in natural rivers are often much larger than in flumes. Sukhodolov et al. (2006) stated that laboratory bed forms have lee side slope angles (β_d) of about 30° (corresponding to the angle of repose of sand), while bed forms in natural rivers have lee side slope angles about half this value. Ogink (1988) reported lee side slopes of river dunes in the range of $1/5 \div 1/7$ ($8° \div 11°$).

Giving some data from field conditions the length of observed bed forms in the Danube river between Straubing and Vilshofen (Germany) varied between $\Lambda_d = 3.00\ m$ and $25.00\ m$. The greatest heights reached up to $\Delta_d = 1.60\ m$ with a mean dune height of $0.22\ m$. The corresponding mean flow and river characteristics have been $Q = 838\ m^3/s$, $y = 3.38\ m$, $S_0 = 0.032\ \%$ and $B = 20\ m$ (Söhngen et al. (1992)).

For the Embarras river in Urbana-Champaign, Illinois (USA), Sukhodolov et al. (2006) reported an average dune length (Λ_d) of $2.00\ m$, a height of $\Delta_d = 0.08\ m$, a stoss slope angle of about $\alpha_d = 5°$ and lee side angle of about $\beta_d = 12°$ for mean flow and river characteristics of $Q = 0.78\ m^3/s$, $v = 0.44\ m/s$, $Fr = 0.24$, $y = 0.35\ m$, $S_0 = 0.057\ \%$ and $B = 5.2\ m$.

Resuming, measured bed forms are not regular but three-dimensional and irregular in size, shape and spacing. No significant difference with respect to geometrical dune properties can be identified for the reach upstream of the weir and in the weir reach itself. However, a higher degree of scattering and increased dispersion can be stated for the channel stretch downstream of the side weir. Looking at flume data given in literature, measured dune properties correspond fairly well to reported ranges.

5.10.3. Comparison of measured and predicted Bed Form Geometry

In the following paragraph measured dune length (Λ_d), height (Δ_d) and steepness (δ_d) for experiment $B01$ are compared with computed dune dimensions according to the approaches presented in appendix A.3.2. The results of this comparison are shown in Figure 5.62. To have an idea of the corresponding bed morphology at the end of the experiment the final longitudinal cross sectional averaged bed profile (moving average, window length $\omega^* = 3.50\ m$, paragraph 6.2) is presented in Figure 5.62.

Until the downstream weir corner dune length (Λ_d) is fairly well presented by the approaches of Yalin (1964), Van Rijn (1984b), Julien and Klaassen

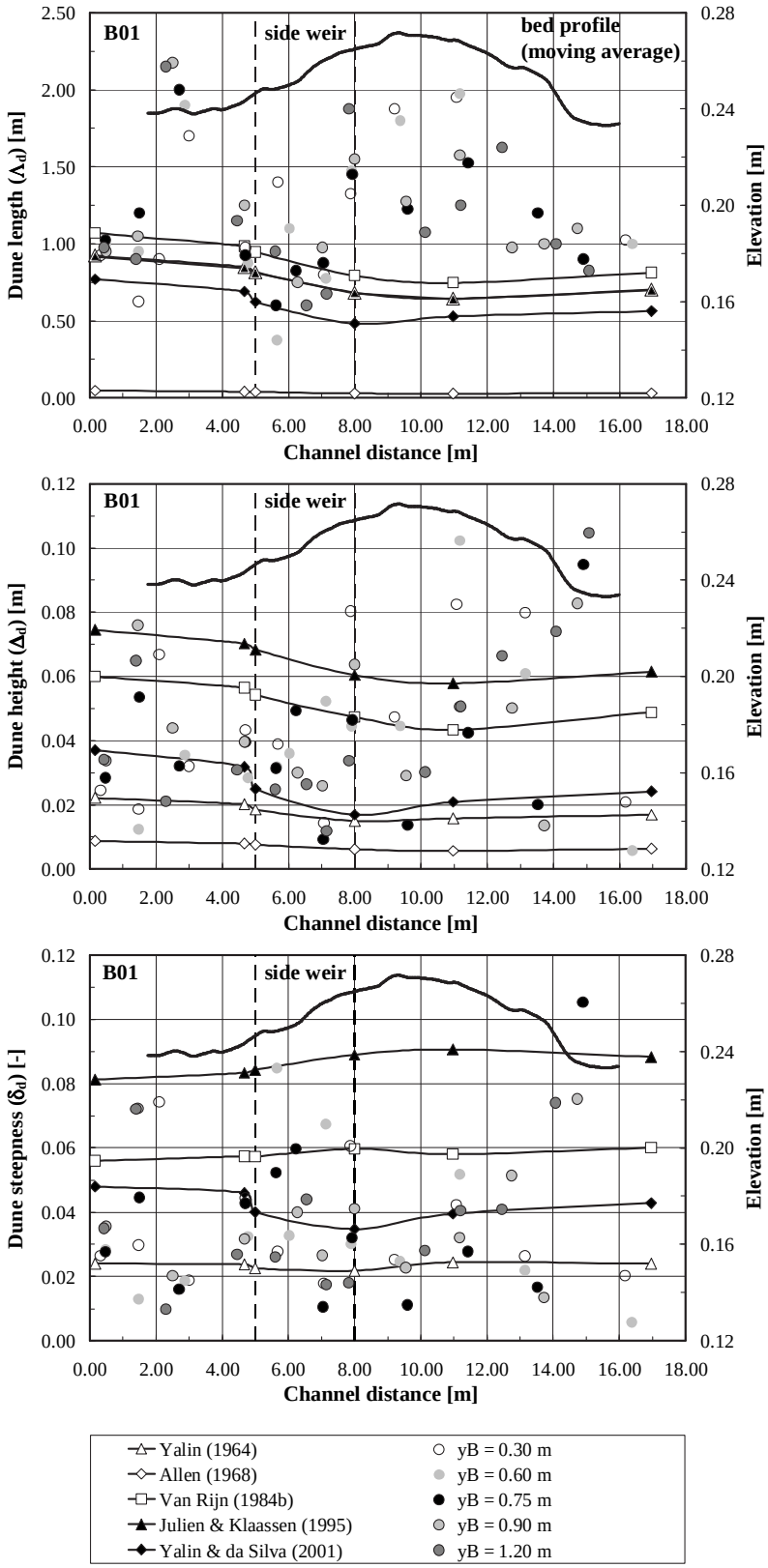

Figure 5.62: Comparison of measured dune length (Λ_d) (top), height (Δ_d) (middle) and steepness (δ_d) (bottom, without Allen (1968)) from experiment $B01$ with approaches from literature. The dashed line indicates the side weir position.

(1995) and Yalin and da Silva (2001). Immediately downstream of the overflow measured dunes are significantly longer and about two orders of magnitude longer than predicted by the approaches from literature. At the end of the testing facility measured dune length smoothly approaches computed values. The outstanding difference might be explained by the fact that the flow on the lee side of the deposit is accelerated downwards towards the channel exit. Due to this reason higher excess shear stresses flattening the dunes are present. The approach by Allen (1968) considerably underestimates dune length for the entire channel stretch.

Despite a certain scattering, measured dune height (Δ_d) satisfies the range of computed dimensions.

Measured dune steepness (δ_d) is in fairly well agreement with predicted values. Data points from the present study are enveloped by the approaches of Yalin (1964) and Julien and Klaassen (1995). It has to be noted that nearly all values are located below the theoretical threshold value of $\delta_d = 0.06$ as reported by Fredsøe (1982), Yalin (1992) and Yalin and da Silva (2001).

Besides streamwise variability a certain lateralwise variability of bed form dimensions appears to be present in Figure 5.62. Since the deposit is two-dimensional, meaning more pronounced on the weir side than opposite to the weir, the main current is deviated and accelerated towards the opposite river bank. Consequently, dunes become somewhat "stretched" in this region, whereas dunes in the wake of the sedimentary deposit almost keep their length. Concluding, however, no clear tendencies for distinct lateralwise variability can be made.

A synoptical comparison of measured and computed dune dimensions is presented in Table 5.26 and Figure 5.63. The approach developed by Allen (1968) is not considered herein, since rather significant differences have been determined (Tab. 5.26). A value of $measured/computed = 1.00$ indicates perfect agreement with the present study (dashed line at 1.00). It can clearly be seen that the upstream reach is best represented by the different approaches (ratio of 1.11). For the downstream reach the less adequate agreement is found (ratio of 1.85). The weir region is located in between (ratio of 1.33). Regarding all three reaches (upstream of weir, weir reach and downstream of weir) it becomes evident that the approaches of Van Rijn (1984b) (ratio of 1.08) and Julien and Klaassen (1995) (ratio of 0.91) represent the measured geometric dune properties in the best way. For Yalin (1964) a mean ratio of 1.99 is determined, for Yalin and da Silva (2001) a value of 1.75 can be stated. Similar findings were reported earlier by Rosier et al. (2007a).

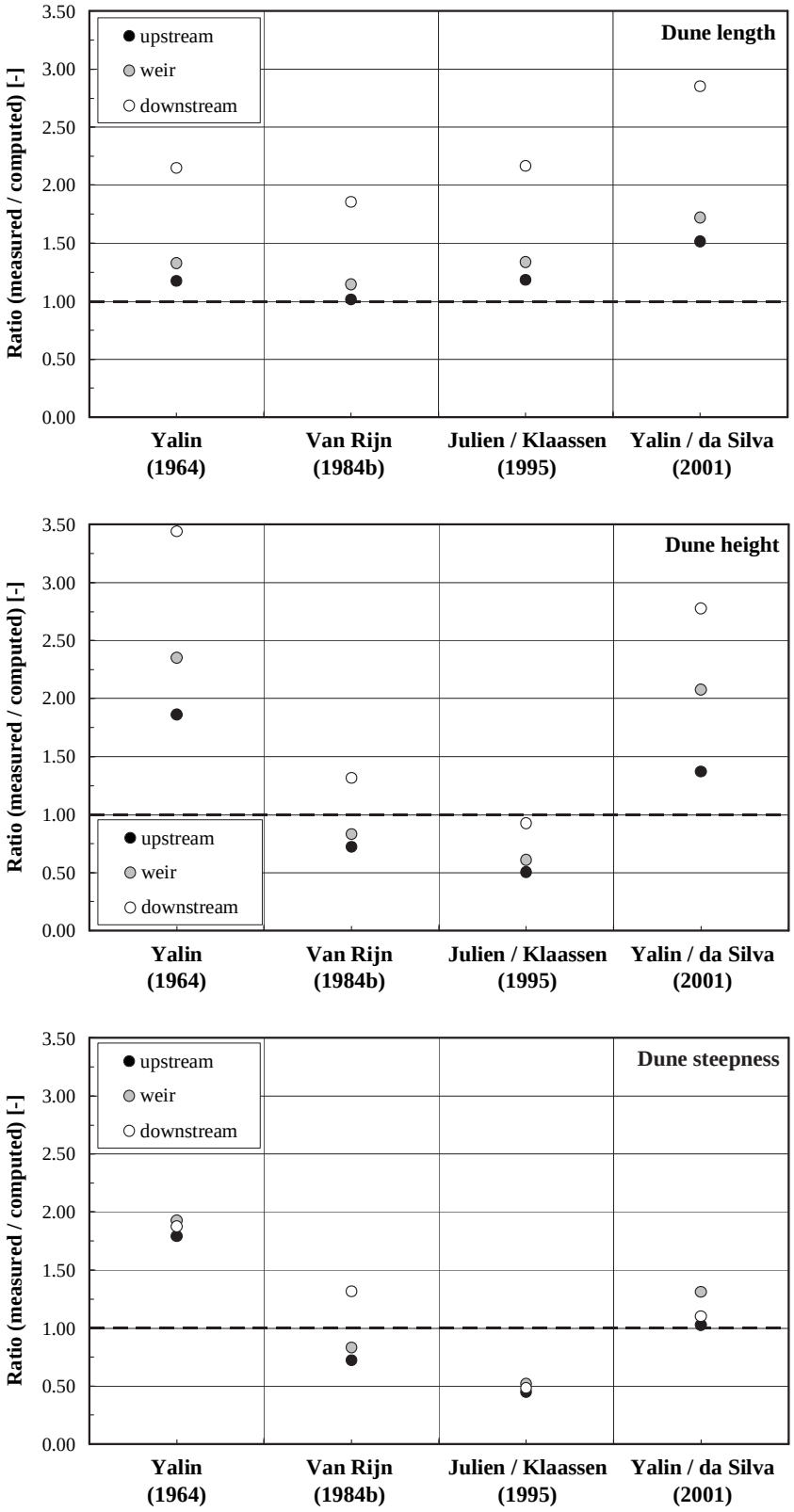

Figure 5.63: Comparison of dune length (Λ_d) (top), height (Δ_d) (middle) and steepness (δ_d) (bottom) (mean values from $B01$, $B02$ and $B03$) with approaches from literature. The dashed line at 1.00 corresponds to perfect agreement.

Table 5.26: Geometrical mean bed form (dune) characteristics from experiments $B01$, $B02$ and $B03$ and comparison with approaches from literature (measured / computed). Λ_d = dune length, Δ_d = dune height and δ_d = dune steepness.

Investigation	upstream of weir			weir reach			downstream of weir		
	Λ_d $[m]$	Δ_d $[m]$	δ_d $[-]$	Λ_d $[m]$	Δ_d $[m]$	δ_d $[-]$	Λ_d $[m]$	Δ_d $[m]$	δ_d $[-]$
Present study	1.019	0.036	0.040	1.062	0.041	0.042	1.474	0.056	0.043
Yalin (1964)	0.867	0.019	0.022	0.800	0.017	0.022	0.686	0.016	0.023
meas. / comp.	1.18	1.86	1.79	1.33	2.35	1.93	2.15	3.56	1.88
Allen (1968)	0.042	0.008	0.194	0.037	0.007	0.200	0.029	0.006	0.213
meas. / comp.	24.34	4.43	0.021	28.79	5.55	0.021	51.20	9.11	0.020
Van Rijn (1984b)	1.004	0.050	0.049	0.927	0.049	0.053	0.795	0.043	0.054
meas. / comp.	1.01	0.72	0.81	1.15	0.83	0.79	1.85	1.32	0.80
Julien / Klaassen (1995)	0.860	0.071	0.083	0.794	0.067	0.085	0.681	0.060	0.089
meas. / comp.	1.18	0.51	0.48	1.34	0.61	0.50	2.17	0.93	0.48
Yalin/da Silva (2001)	0.673	0.026	0.039	0.617	0.020	0.032	0.517	0.020	0.039
meas. / comp.	1.51	1.37	1.03	1.72	2.08	1.31	2.85	2.78	1.10

5.10.4. Duration Development of Bed Forms

As pointed out in appendix A.3.3 the duration of development $T_{b,i}$ of a bed form i can be characterized by the proportionality (Yalin (1992)):

$$T_{b,i} \sim \frac{\Delta_i \cdot \Lambda_i}{q_s} \tag{5.41}$$

In Equation 5.41 $\Delta_i \cdot \Lambda_i$ is ($\approx$ twice) the area of the developed bed form profile. Taking characteristic bed form values (e. g. from experiment $B01$ with a dune stoss slope length of 1.056 m, a lee slope length of 0.231 m and a dune height of $\Delta_d = 0.037\ m$) and assuming a triangular dune shape, an area of 0.024 m^2 is obtained. Hence, twice the area yields $2 \cdot 0.024\ m^2 = 0.048\ m^2 \approx \Delta_i \cdot \Lambda_i$. Using furthermore the bulk bed-load transport rate of $q_{sb} = 0.67 \cdot 10^{-4}\ m^2/s$ ($\rho_s = 1447\ kg/m^3$) from experiment $B01$ results in a T_b-value of 715 sec or $\approx$ 12 min. This means that individual bed forms quickly develop compared to the total duration of the experiment of 188 min, namely after $12/188 = 6.38$ % of the total duration. In Table 5.27 T_b-values from the present study are summarized. In this Table the computation of T_b has been performed using mean dune dimensions upstream of the side weir, assuming a triangular dune shape and using bed-load quantities supplied at the channel entrance. From the average values a duration development of $T_b = 204\ sec$ or $\approx 3.4\ min$ can be derived and individual bed forms develop after $\approx 3.4/137 = 2.5$ % of the total experiment period.

5.10.5. Migration Velocity of Bed Forms

To obtain an approximate idea of the average migration velocity (u_b) of individual bed forms (dunes) photographs taken through the glass-sided channel wall opposite to the weir at different time increments have been analyzed. On these photographs the propagation of the trough region of a dune was fairly well to track. For test series $B01$ and $B02$ the time increment between two photographs has been too long for associating reliably the same bed form on both photographs. For experiments $C02$, $C04$, $C05$, $D02$ and $D03$ no distinct dunes have developed or could have been observed through the channel side wall. The range of measured average values varied between $u_b = 0.83\ mm/s$ and 6.43 mm/s with a mean value of $u_b = 2.85\ mm/s$ (Tab. 5.28).

Taking the average value of 2.85 mm/s and a channel length of $x \approx 18.0\ m$ a bed form will take 6307 sec or 105 min to migrate from the channel entrance to the end. In other words, for a given migration velocity of 2.85 mm/s a bed form is able to advance $\approx 23.50\ m$ within the average test duration of 137 min. Consequently, the experimental conditions chosen allow

Table 5.27: Duration of development (T_b) of an individual bed form for the present study according to Yalin (1992). The value q_{sb} represents the upstream bulk sediment supply ($\rho_s = 1447\ kg/m^3$) and t the duration of the experiment. For experiment $C03$ no clear dunes have developed and the bed has been rather flat all along the channel.

N^o of experiment	q_{sb} $\left[m^2/(s\ m)\right]$	t $[min]$	T_b $[min]$	t/T_b [%]
$A01$	$1.17 \cdot 10^{-4}$	120	6.9	5.8
$B01$	$0.67 \cdot 10^{-4}$	188	11.9	6.3
$B02$	$1.36 \cdot 10^{-4}$	183	2.8	1.5
$B03$	$0.70 \cdot 10^{-4}$	117	14.7	12.6
$B04$	$0.74 \cdot 10^{-4}$	245	9.5	3.9
$B05$	$1.28 \cdot 10^{-4}$	128	4.1	3.2
$B06$	$1.35 \cdot 10^{-4}$	138	8.6	6.2
$C01$	$0.73 \cdot 10^{-4}$	125	3.2	2.5
$C02$	$3.28 \cdot 10^{-4}$	120	0.6	0.5
$C03$	$3.97 \cdot 10^{-4}$	120	$***$	$***$
$C04$	$3.06 \cdot 10^{-4}$	120	0.7	0.6
$C05$	$3.06 \cdot 10^{-4}$	120	7.4	6.2
$D01$	$2.08 \cdot 10^{-4}$	125	1.8	1.5
$D02$	$2.04 \cdot 10^{-4}$	120	1.8	1.5
$D03$	$3.06 \cdot 10^{-4}$	120	0.9	0.8
$D04$	$1.72 \cdot 10^{-4}$	120	3.0	2.5
$D05$	$1.53 \cdot 10^{-4}$	120	2.2	1.8
average	$1.87 \cdot 10^{-4}$	137	3.4	2.5

an individual bed form to migrate from the channel entrance to the channel exit within the given experiment period.

In the following paragraph measured migration velocities are tested against the approaches from literature presented in appendix A.3.3. Relevant

Table 5.28: Average measured bed form migration velocities (u_b) for the present study. For some experiments no u_b-values could be determined ($***$) (explanation in the text).

N^o of experiment	u_b $[mm/s]$	N^o of experiment	u_b $[mm/s]$	N^o of experiment	u_b $[mm/s]$
$A01$	2.30				
.....	.....	.....	.....	.....	.....
$B01$	$***$	$C01$	2.42	$D01$	1.05
$B02$	$***$	$C02$	$***$	$D02$	$***$
$B03$	2.30	$C03$	6.43	$D03$	$***$
$B04$	0.83	$C04$	$***$	$D04$	4.55
$B05$	3.44	$C05$	$***$	$D05$	3.21
$B06$	2.02				
.....	.....	.....	.....	.....	.....
average (all)	2.85				

input parameters such as flow velocity (v) or Froude number (Fr) are computed from section 01 (Fig. 5.13). Bed-load rates (q_{sb}) refer to supplied sediment rates at the channel entrance. Experiments owing Froude numbers greater than 0.85 are not taken into consideration since these flow conditions are located close to the transition from the lower to the upper regime where bed forms (dunes) disappear and plane bed conditions develop. In Table 5.29 measured and computed u_b-values are summarized. A graphical presentation is given in Figure 5.64.

It becomes evident that all approaches from literature considerably overestimate measured dune celerity. The best correlation if found for the approaches of Fredsøe (1982) and Kondratiev et al. (1982). The approach of Nikora et al. (1997) shows the lowest correlation. The relations of Kondap and Garde (1973) and Tang and Knight (2006) are close to each other and a slightly higher overestimation than for Fredsøe (1982) and Kondratiev et al. (1982) can be stated.

Besides the different approaches tested above Yalin (1992) reported values in the range of $u_b = 0.3 \div 6.0\ mm/s$, thus measured migration velocities correspond to this range. Sukhodolov et al. (2006) stated a mean bed form celerity for the Embarras river in Urbana-Champaign, Illinois (USA) of $u_b \approx\ 0.065\ mm/s$ (average field conditions: $Q = 0.78\ m^3/s$, $v = 0.44\ m/s$, $Fr = 0.24$, $y = 0.35\ m$, $S_0 = 0.057\ \%$ and $B = 5.2\ m$). Using a model length

Table 5.29: Comparison of measured and computed bed form migration velocities (u_b) (mean values). The comparison of measured and computed migration velocities refers to mean u_b-values. LSM denotes least squares method $\left(\sum(u_{b,measured} - u_{b,computed})^2\right)$.

Investigation	Eq. in study	u_b min. $[mm/s]$	u_b max. $[mm/s]$	u_b mean $[mm/s]$	meas./ comp. $[-]$	LSM $[mm/s]^2$
present study		0.83	6.43	2.85	1.00	0.00
Kondap & Garde (1973)	A.72	2.42	9.38	6.38	0.45	12.46
Fredsøe (1982)	A.73	1.35	19.89	6.05	0.47	10.19
Kondratiev et al. (1982)	A.74	2.33	8.68	5.96	0.48	9.63
Nikora et al. (1997)	A.75	2.69	27.14	13.58	0.21	115.06
Tang & Knight (2006)	A.76	2.29	9.73	6.48	0.44	13.12
average*)		2.22	14.96	7.69	0.37	32.09

*)approaches from literature only without present study

scale factor of $\lambda_L \approx 1:50$ for the present study and hence a velocity scale factor of $\lambda_L^{1/2}$, a value of $u_b = 0.46\ mm/s$ is obtained. This value is considerably smaller than measured migration velocities. Since the field conditions differ substantially from the experimental boundary conditions (flood conditions with high Froude numbers) this difference is not astonishing. For the river Oder in Germany u_b-values in the order of magnitude of $u_b = 0.064\ mm/s$ are reported (oral communication by B. Hentschel, Bundesanstalt für Wasserbau (BAW), Karlsruhe, Germany). A hydraulic model study ($\lambda_L \approx 1:50$) conducted at the Laboratory of Hydraulic Constructions (LCH-EPFL) for the Rhone river upstream of Lake Geneva (Viège, Canton of Valais) revealed a migration velocity of $u_b = 2.37\ mm/s$.

Tang and Knight (2006) indicated that dune migration rate or celerity (u_b) is small in relation to the mean flow velocity (v) varying in the range of

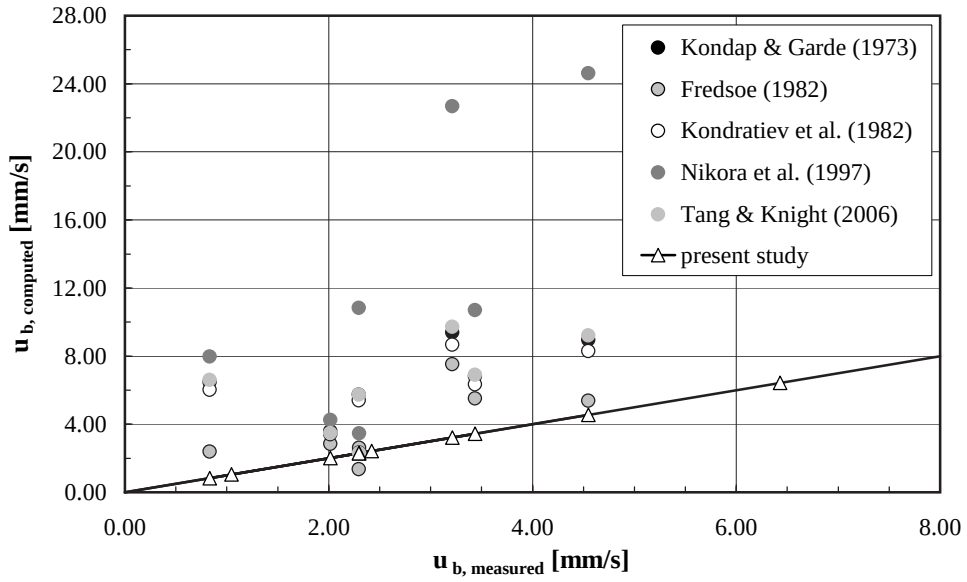

Figure 5.64: Comparison of measured bed form migration velocities (u_b) with different approaches from literature.

$u_b/v = 0.0001 \div 0.003$. For the present study the range varies from 0.0012 to 0.0051 with a mean value of 0.0031.

Concluding, comparing measured and computed u_b-values a great variety can be stated. It has to be kept in mind that measured u_b-values have only been roughly determined via the channel side walls. Moreover, some uncertainties, especially with respect to the bed-load transport rate, usually characterised by an high degree of scatter, are inherent to the data. Finally, the relations from literature have to be seen as approximate estimations as well.

5.10.6. Flow Resistance due to Bed Forms

In the case of a movable bed the total or effective bed roughness mainly consists of grain and form roughness. Depending on flow intensity form roughness effects have to be taken into account for relative roughnesses of $y/d_{90} > 25$ (Jäggi (1984a)). In the present study y/d_{90}-values in the range of 39 to 71 with a mean value of 54 are observed. Hence, form roughness effects are expected to play a certain role.

Typical longitudinal bed surface profiles for each test series at five different lateralwise positions ($y_B = 0.30\ m$, $y_B = 0.60\ m$, $y_B = 0.75\ m$, $y_B = 0.90\ m$ and $y_B = 1.20\ m$) are presented in Figure 5.65. It can be seen that for test series B the final bed surface is covered with dunes. For test series C an almost flat bed is observed. Test series D constitutes an intermediate role. Strickler-values vary in the range of $k_{st} = 42\ m^{1/3}/s \div 77\ m^{1/3}/s$ with a

mean value of 63 $m^{1/3}/s$. It might be noted that bed morphology differs both in longitudinal as well as in lateralwise direction. Moreover, dune crests in the plan view might be inclined over the entire channel width with inclination angles varying between 25° and 60° (Figs 5.58, 5.65). Since passing an inclined dune causes less energy losses than passing a perpendicular one, the impact of bed forms on flow resistance might occasionally be less than expected.

In the following paragraph the influence and repartition of plane bed and form drag induced roughness is investigated and compared with different roughness predictors from literature (appendix A.4).

Necessary input parameters for all calculations have been derived from the respective geometric and hydraulic experimental conditions. To determine experimental plane bed resistance ($k_{st}^{'}$) measured data from the very beginning ($t = 0.0\ min \div 5.0\ min$) of the experiments has been used. Total resistance (k_{st}) has been obtained by applying measured data from the end of the experiments.

Regarding the approaches from literature only data from the end of the experiments is taken to compute total resistance. Within this context no side wall correction procedure has been applied and $y \approx R_h$ is assumed. These assumptions are justified in paragraph 5.7.1. The flat bed resistance from the literature approaches is given explicitly or implicitly by proposing a certain grain roughness (e. g. $k_s^{'} = 2\ d_{50}$) and using flow depth (y) or hydraulic radius (R_h) from the final experimental conditions (here: $y \approx R_h$) (Eq. 5.44). Only for the approach of Brownlie (1981) initial experimental conditions need to be applied to estimate flat bed roughness.

The aim of this analysis is to express the total resistance by means of a ratio "*grain roughness / total roughness*". Since measured resistance has been determined in terms of Strickler-values ($k_{st} = 1/n$) and computed resistance is expressed in terms of Chézy-values (C), Manning's n is used for comparison. C can be transformed into n by the use of Equation A.23. An advantage of the use of n is the fact that small values refer to small resistance and vice versa. For k_{st} and C no such comprehensive and easy to understand ratio can be established [2]. Concluding, the following ratio is applied:

$$\frac{n^{'}}{n} = \frac{n_{grain}}{n_{total}} \tag{5.42}$$

Note that $n^{'}/n$ can be obtained directly by $C/C^{'} = n^{'}/n$ (Eq. A.23).

In Figure 5.66 and Table 5.30 the results of the analysis as well as the comparison with different approaches from literature are presented.

The analysis shows that the ratio $n^{'}/n$ varies in the range of $0.81 \div 0.94$ with a mean ratio of 0.87. This means that about 87 % of the total resistance

[2]Example: $k_{st}^{'}/k_{st} = 80/60 = 1.33$, hence grain roughness is 1.33 times total roughness. This does not appear to be very meaningful, comprehensive and easy to understand

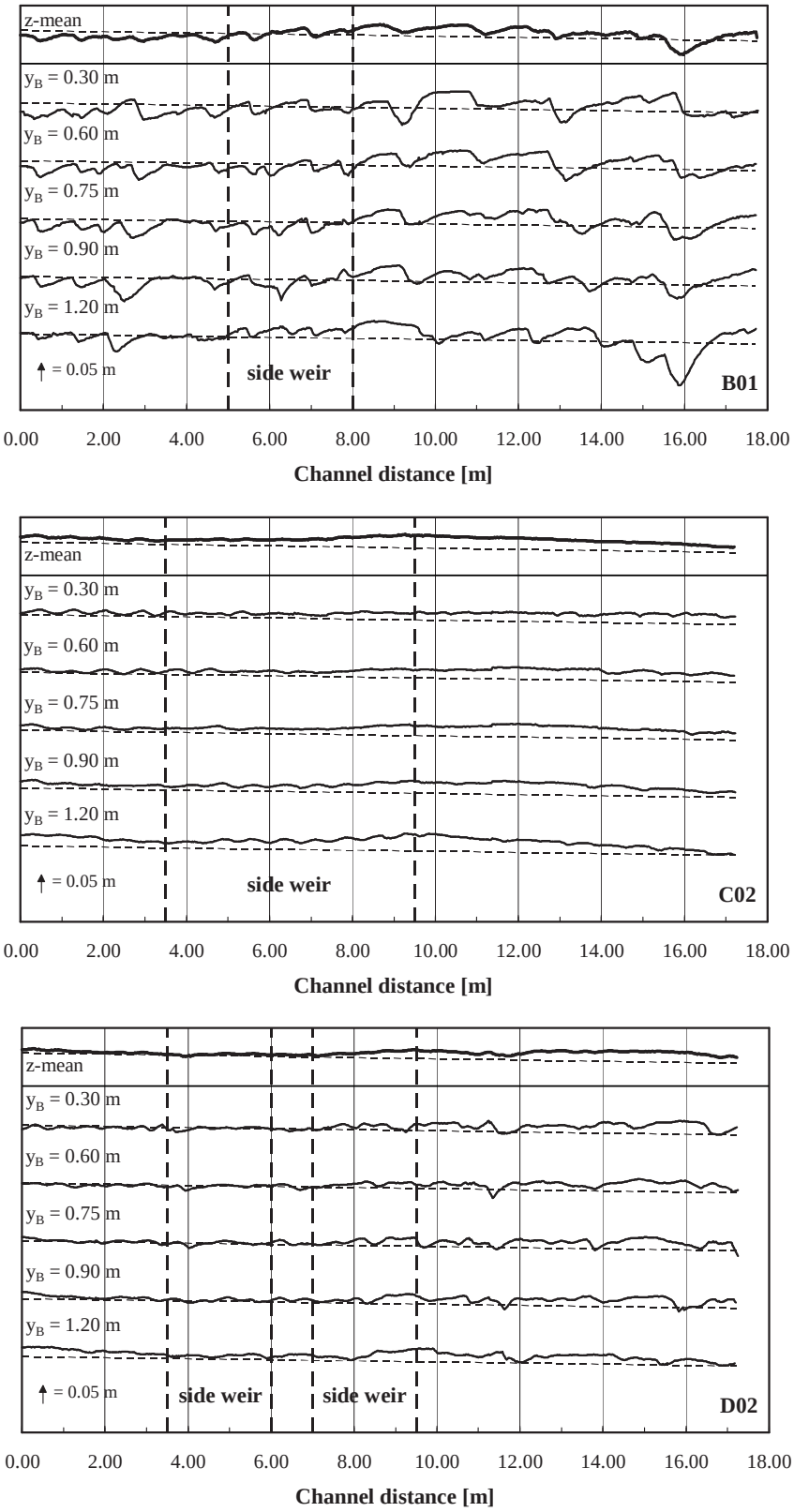

Figure 5.65: Characteristic longitudinal bed surface profiles for each test series at different lateralwise positions. The tiny dashed lines represent the initial bed surface. The side weir is located on the right channel bank at $y_B = 1.50\ m$.

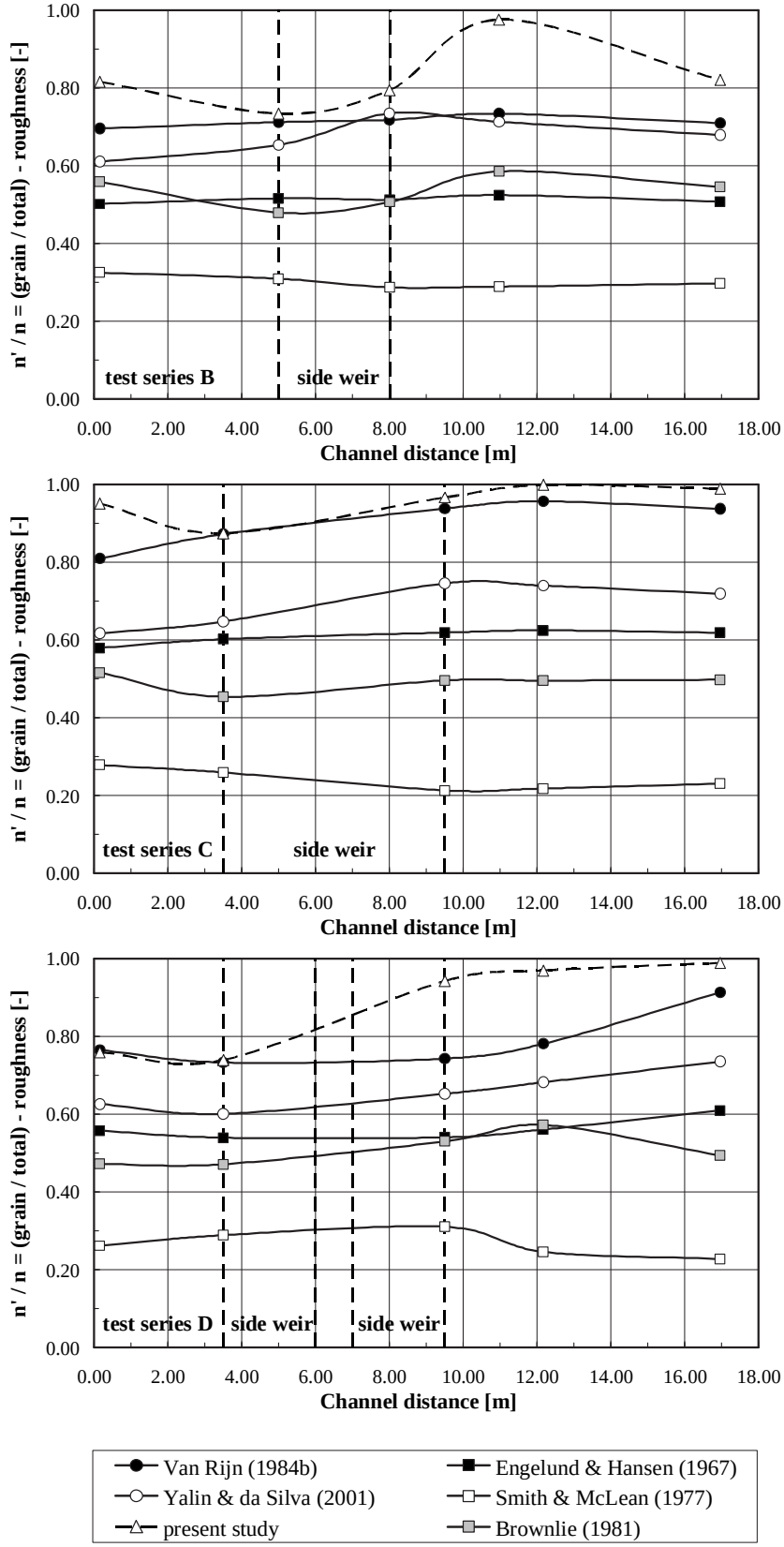

Figure 5.66: Longitudinal evolution of grain to total roughness ($n^{'}/n$) expressed in terms of Manning's n and comparison with approaches from literature for test series B, C and D.

Table 5.30: Ratio of grain to total roughness ($n^{'}/n$) expressed in terms of Manning's n and comparison with approaches from literature. LSM denotes least squares method $\left(\sum(n^{'}/n)_{measured} - (n^{'}/n)_{computed})^2\right)$.

Investigation	Test series			average	meas./ comp.	LSM
	B	*C*	*D*			
	$n^{'}/n$	$n^{'}/n$	$n^{'}/n$	$n^{'}/n$		
	[–]	[–]	[–]	[–]	[–]	[–]
present study	0.81	0.94	0.86	0.87	1.00	0.00
Van Rijn (1984b)	0.71	0.90	0.78	0.80	1.09	0.01
Yalin and da Silva (2001)	0.67	0.69	0.65	0.67	1.30	0.04
Engelund and Hansen (1967)	0.51	0.61	0.56	0.56	1.55	0.10
Smith and McLean (1977)	0.30	0.24	0.27	0.27	3.22	0.36
Brownlie (1981)	0.53	0.49	0.50	0.50	1.74	0.13

is skin friction and about 13 % is from drag. Consequently, bed forms do have a certain influence but this influence is rather mild. In this context it is interesting to mention that G. Parker (IAHR Environmental Fluid Mechanics Short Course - Engineering Graduate School Environment Water (IAHR-EGW), June 2006, University of Karlsruhe, Germany) reported a shear stress repartition for bank full flow in large low-slope sand bed rivers of $\tau^{'}/\tau \approx 0.27$ meaning $\approx$ 27 % of the resistance is related to grain roughness and about 73 % to bed forms.

Looking at $n^{'}/n$-ratios up- and downstream of the weir rather moderate differences are encountered (Tab. 5.31). Since the up- and downstream variation is small ($(n^{'}/n)_{upstream}/(n^{'}/n)_{downstream} = 0.86$) it can be concluded that for both numerical and practical calculations a spatially constant resistance factor (k_{st}, n, C) could be applied. Moreover, in prototype conditions a prediction of the change of resistance values will be difficult anyway, so that in general a constant value will be applied as well.

Referring to plane bed roughness ($n^{'}$) and having Equation A.25 (appendix A.2.1) in mind:

$$\frac{1}{n^{'}} = k_{st}^{'} = \frac{K}{d^{1/6}} \tag{5.43}$$

with K empirical roughness parameter $[m^{1/2}/s]$ and d bed material size,

Table 5.31: Difference of grain/total roughness ratios ($n^{'}/n$) up- and downstream of the side weir.

Test series	upstream $(n^{'}/n)_{up}$ [–]	downstream $(n^{'}/n)_{down}$ [–]	upstream / downstream $(n^{'}/n)_{up}$ / $(n^{'}/n)_{down}$ [–]
B	0.76	0.86	0.88
C	0.90	0.98	0.92
D	0.75	0.97	0.77
average	0.80	0.94	0.86

Strickler (1923) proposed $K = 21.1$ in combination with $d = d_{50}$. By adopting $d = d_{90}$ Meyer-Peter and Müller (1948) obtained $K = 26$. Applying these parameters to the present study, $k_{st}^{'} = 70.4\ m^{1/3}/s$ (for $K = 21.1$ and $d = d_{50}$) and $k_{st}^{'} = 71.7\ m^{1/3}/s$ (for $K = 26$ and $d = d_{90}$). The calculations from the present investigation reveal a plane bed roughness of $k_{st}^{'} \approx 72.4\ m^{1/3}/s$. Applying Equation 5.43 to this value yields $K = 21.7$ for $d = d_{50}$ and $K = 26.3$ for $d = d_{90}$. Obviously, these values are close to 21.1 and 26, respectively. Hence, both approaches might be recommended for the computation of flat bed roughness.

Instead of using a k_{st}-type approach like Equation 5.43 the Chézy resistance coefficient (Eq. A.92) and the Nikuradse equivalent sand grain roughness concept (k_s) can be applied for the determination of flat bed roughness:

$$C^{'} = 18 \cdot log\left(\frac{12 \cdot R_h}{k_s^{'}}\right) \tag{5.44}$$

with $R_h \approx y$ for $B/y > 10$. For the present study a plane bed k_s-value of $k_s^{'} = 2.10\ mm$ was found. Referring to Table A.3 this would correspond to the approach of Engelund and Hansen (1967) proposing:

$$k_s^{'} = 2.0 \cdot d_{65} \tag{5.45}$$

As far as measured total roughness (n) is concerned, a k_s-value according to Equation 5.44 (or Eq. A.92) of $k_s = 5.04\ mm$ is obtained. This would correspond to $\approx 2.5\ d_{90}$ as proposed by Kamphuis (1974) for plane bed (!) roughness (Tab. A.3). The best total roughness prediction is given by the approach of Yalin and da Silva (2001) ($n_{measured}/n_{computed} = 0.85$).

Regarding the repartition of grain and total roughness ($n^{'}/n$) the comparison with different approaches from literature reveals that throughout all three test series the methods based on grain and bed form parameters (Van Rijn (1984b), Yalin and da Silva (2001)) are superior to methods based on integral parameters (Engelund and Hansen (1967), Smith and McLean (1977) and Brownlie (1981)). The best correlation with measured data is obtained for the approaches of Van Rijn (1984b) and Yalin and da Silva (2001) followed by Engelund and Hansen (1967) and Brownlie (1981). The lowest agreement is obtained for the approach by Smith and McLean (1977). Similar observations were made earlier by Rosier et al. (2005d).

Possible explanations for the different prediction qualities are given by Van Rijn (1993) who reported that the slope of a particular river does not change substantially for varying discharges and the slope is mainly imposed by the local bed slope. Consequently, methods which are mainly based on slope as an input parameter are inherently inferior to methods which are based on mean velocity as input parameter. Moreover, it might be stated that the approaches depend, amongst other parameters, on the choice of grain roughness, e. g. Engelund and Hansen (1967) yield satisfying results for grain roughness but considerably overestimate total resistance. Hence, the composed ratio $n^{'}/n$ appears not to be appropriate.

As a conclusion, the approaches of Strickler (1923), Meyer-Peter and Müller (1948) and Engelund and Hansen (1967) might be recommended for the determination of plane bed roughness, whereas for total roughness the method of Yalin and da Silva (2001) is suggested. Concerning the repartition of grain and form roughness a recommendation for the roughness predictor of Van Rijn (1984b) can be given.

Finally, it might be interesting to notice that the ratio of initial overflow discharge (denoted as $Q_D^{'}$ as for plane bed roughness ($k_{st}^{'}$) at the beginning of the experiments) to final overflow discharge (Q_D) is in the range of $Q_D^{'}/Q_D = 0.63$, whereas the ratio of grain to total roughness is in the range of $n^{'}/n = 0.87$ (Tab. 5.30). This means that 87 % of the initial conditions for roughness (corresponding to grain roughness) are maintained but only 63 % of the initial side overflow discharge. In other words the roughness is increased by a factor of $1/0.87 = 1.15$, whereas the overflow discharge is intensified by a factor of $1/0.63 = 1.59$. These ratios are rather indicative but underly that effects other than a change in total roughness is responsable for the transient increase of side overflow discharge. A detailed analysis of form induced roughness and its impact on side overflow has been given in paragraph 5.3.

5.10.7. Conclusion

The dominant bed forms in this study are dunes. Downstream of the weir ripples superimposed on dunes might occur. For experiments owing rather high Froude numbers (≈ 0.90) a slightly wavy or rather flat bed with washed-out dunes could be identified. No significant distinction in bed form type upstream, downstream and in the weir reach can be stated.

A comparison of measured dunes with approaches from literature revealed that the reach upstream of the weir is best represented. For the downstream reach less adequate agreement is found. The weir region is located in between.

Regarding measured dune migration velocity a value of $\approx 2.85\ mm/s$ has been determined. Dune celerity predicted by approaches from literature is considerably overestimated compared to measured values.

The analysis dealing with the repartition of grain, form and total roughness showed that about 87 % of the total roughness is skin friction and about 13 % is from drag. Consequently, bed forms do have a certain influence but this influence is rather mild.

6. Development of an empirical Approach for Prediction of Bed Evolution

In this chapter an empirical $1D$ and $2D$ approach to describe the bed evolution in presence of a side overflow is developed. To account for the shape of the aggraded channel reach by local sediment deposition a Maxwellian distribution function is applied.

6.1. Concept for Description of local Sediment Deposition

With respect to the $1D$-model the moving average of the cross sectional averaged longitudinal bed surface profile is used. This profile represents the overall longitudinal trend of the mobile bed without considering the spanwise variation of the aggraded channel reach. The deposit is uniform over the channel width. Hence, the $1D$-model represents a simplified approach to account for deposition phenomena in presence of a lateral overflow.

To account for the spanwise $2D$-effect of the deposit longitudinal bed surface profiles (moving average) on the left and on the right channel bank are used. The profile on the right channel bank represents the overall aggradation in the weir reach *and* the formation of a local sedimentary deposit forming at the downstream weir corner. In contrast to this, the profile on the left channel bank opposite of the side weir only accounts for the overall bed elevation in the side weir reach. The profiles are coupled by the help of an angle (ϕ^*) or a distance (Δx^*) describing the longitudinal shift between the locations of the maximum bed elevation of each deposit (Fig. 5.51). A schematic overview of the $2D$-concept is presented in Figure 6.1 (top). Thereafter, the two profiles will be intersected as shown exemplarily in Figure 6.1 (bottom).

For the parameterisation of the longitudinal bed surface profiles (moving average) a Maxwell-type distribution function is applied. The input parameters of the distribution function are expressed in terms of dimensionless relationships using relevant variables from the following four groups of parameters:

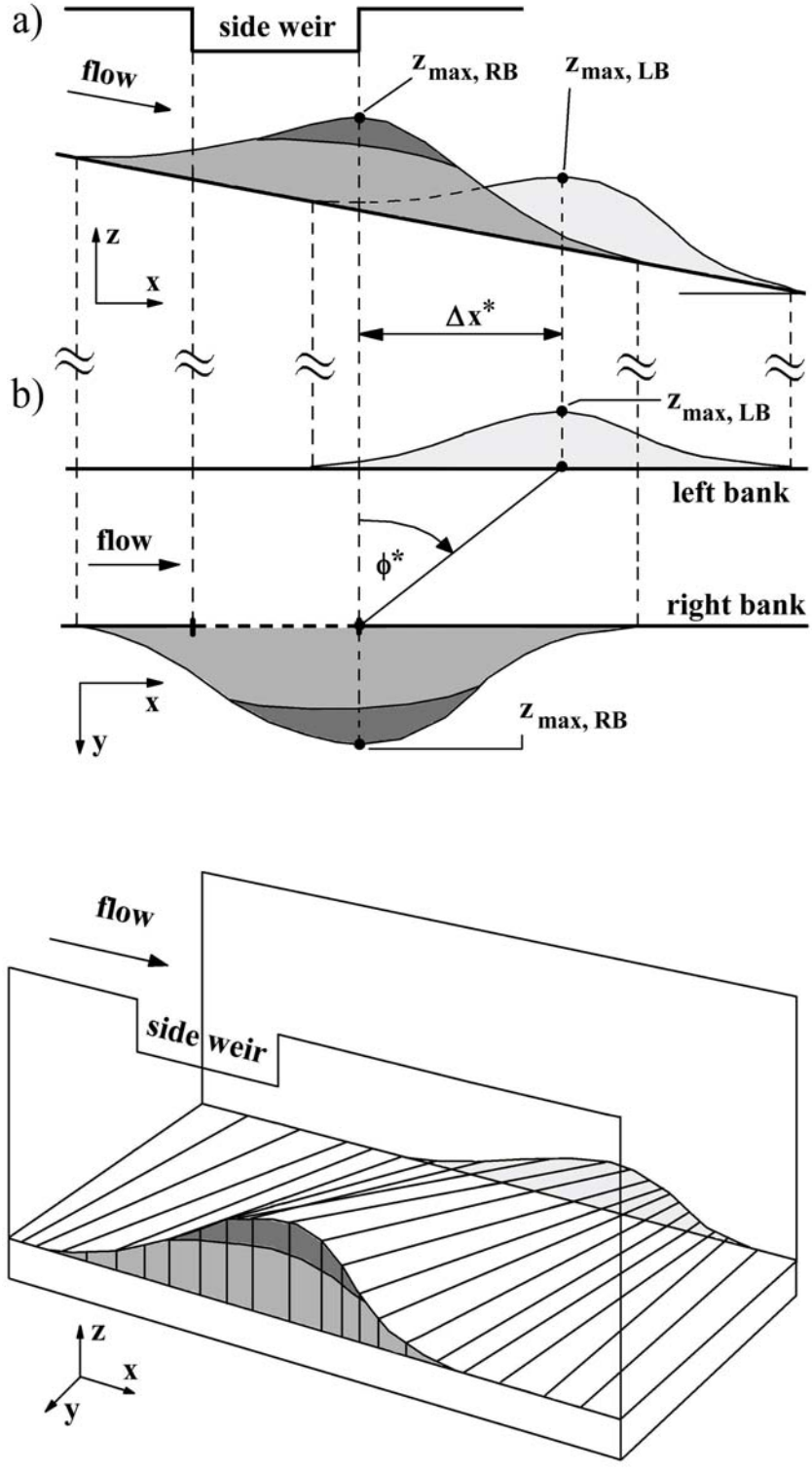

Figure 6.1: Schematic overview of the basic concept to account for the $2D$-effect of the sedimentary deposit. Top: Side view (a) and plan view (b). Bottom: Example for linking the left and right profile linearly. Different intersection types might be imagined using a mesh or grid generator.

- main-channel geometry,
- side weir geometry,
- flow characteristics and
- sediment transport.

Once the bed surface profiles are parameterized the bed evolution model has to be transferred into a channel, river or numerical model. Therefore, a reference or coupling point is needed describing the position of the modelled deposit relative to the side weir.

6.2. Determination of average longitudinal Bed Surface Profiles

As a precursor to the model development the overall trend of the longitudinal bed surface profile is analyzed using a moving average procedure. In this context an appropriate window length has to be chosen. To determine the average longitudinal bed surface profiles bed forms had to be eliminated from each individual data set with the prerequisite that the bed discontinuity (aggradation) in the vicinity of the weir was not to be dampened.

Therefore, the cross sectional averaged longitudinal bed profile is used. This profile is still characterised by oscillations which are not directly linked to individual bed forms (dunes) but a result of the averaging procedure. The periodic variations of the cross sectional averaged longitudinal bed surface are denoted as ω.

The mean ω-values for the entire data set are found to be presented in the best way by a second order polynom (Rosier et al. (2006c):

$$\frac{\omega}{L_D} = y = f(x) = 0.0025 \cdot x^2 + 0.049 \cdot x \tag{6.1}$$

with:

$$x = \frac{Q_1}{L_D^{3/2} \cdot \sqrt{g \cdot h_{D,1} \cdot S_0}} \tag{6.2}$$

where Q_1 upstream discharge, L_D side weir crest length, $h_{D,1}$ side weir pressure head at section 1, g acceleration due to gravity and S_0 initial bed slope. The R^2-value of Equation 6.1 is 0.97. For test series D, L_D has been taken as $2 \cdot 2.50\ m = 5.00\ m$.

The analysis further shows that a moving average procedure with a base of 141 points corresponding to a window length of $\omega^* = 3.50\ m$ yields satisfying

results. The shape of the sediment deposition was not seriously disturbed by this procedure but the effect of bed forms was not completely suppressed.

As a conclusion, the window length of the moving average (ω^*) to determine the overall trend of the longitudinal bed surface evolution smoothing out bed level oscillations might be expressed as follows (Eqs 6.1 and 6.2):

$$\omega^* = 4.542 \cdot \omega \tag{6.3}$$

6.3. Maxwell Distribution Function

The main parameters describing the deposit are the maximum bed elevation (z^*_{max}), the corresponding position of the maximum bed elevation (x^*_{max}), its shape and volume. The shape of the sedimentary deposit is characterised by a rather steep stoss slope and a milder lee slope. Thus, usually the deposit is left skewed. This form is similar to the shape of flood hydrographes.

With regard to these aspects a feasible and satisfying approach for the parameterisation of the deposit is represented by the Maxwell distribution function (Rosier et al. (2006c)). This function is a probability distribution with applications often found in physics and chemistry (e. g. heat and gas transfer) as well as in hydrology to parameterise flood hydrographes. The function is rather simple and straightforward since it is composed of only three dimensionless variables. In addition to that it offers an analytical solution and is continuous and derivable. A further advantageous property, in contrast to e. g. a Gaussian distribution, is given by its boundedness. Another reason for having chosen this kind of function is the fact that it fits the experimental results in the best way.

Introducing the dimensionless parameters referring to the peak values (x^*_{max}, z^*_{max}):

$$X^* = \frac{x^*}{x^*_{max}} \qquad \text{and} \qquad Z^* = \frac{z^*}{z^*_{max}} \tag{6.4}$$

the aggraded channel reach near the side weir can be described by the following Maxwell-type distribution function:

$$Z^*(X^*) = \left(X^* \cdot e^{1-X^*}\right)^{n^*} \tag{6.5}$$

with n^* shape factor of the deposit.

In Figure 6.2 the function $Z^*(X^*)$ is presented for different n^*-values. It can be observed that the shape of the deposit becomes more peaked with increasing n^*. For decreasing n^* the shape is wider and becomes left skewed. Furthermore, by definition, the maxima of both, Z^* and X^*, are located at 1.00.

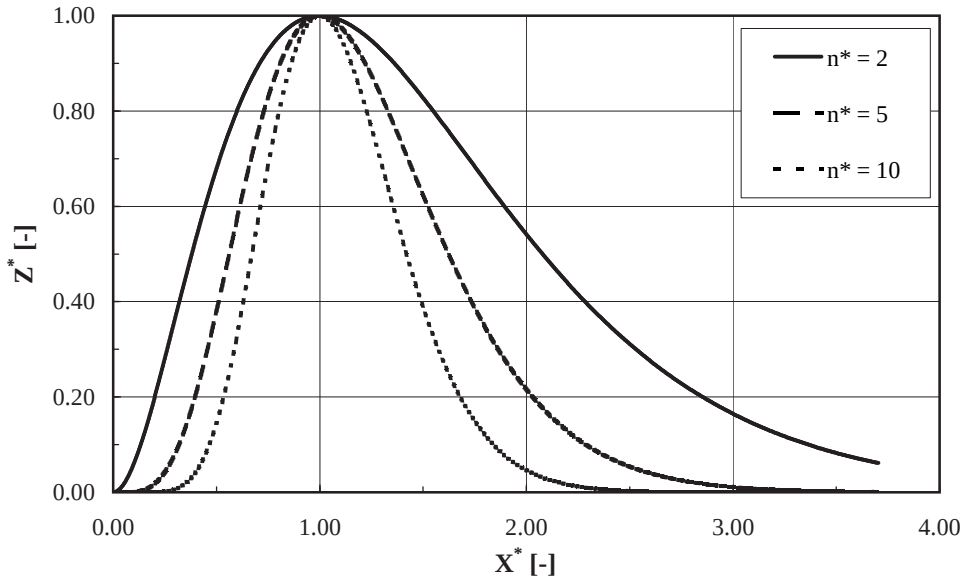

Figure 6.2: Influence of the shape factor n^* in the Maxwell-type distribution function.

6.4. 1D-Model for Prediction of Deposit in longitudinal Direction

In this paragraph a $1D$-model of the aggraded channel reach is developed which allows to predict the evolution of deposition in longitudinal direction. The model represents the overall mobile bed evolution in presence of a side overflow. Effects of vertical convergence are taken into account by the one-dimensional approach, whereas $2D$-effects such as lateralwise variation are not incorporated in the model.

6.4.1. Determination of Shape of Deposit

Within the analysing process the first step consists in defining the starting and end point of the deposit. Due to slight erosion or deposition (non-equilibrium sediment transport) the initial bed level at the beginning of the experiments does not represent an appropriate reference (Fig. 6.3, top). The bed level difference with respect to initial conditions is likely to be attributed to the fact that sediment supply was estimated and consequently pure equilibrium transport conditions might not have been fulfilled at any time step during the experiments. An adequate method within this context appears to be the identification of local minima. For the starting point the local minimum was found when a clear and distinct change of slope from the upstream reach towards the maximum deposit elevation was evident. The end point

was determined applying the same procedure (significant change of slope coming from the maximum in downstream direction). Although this process has mostly been unambiguous a certain degree of interpretation cannot be denied.

Once the local minimum and maximum have been identified they have been linked with a linear function corresponding to the tangent in the respective points. The tangent is then used as reference or baseline to extract the deposit by determining the vertical difference between the deposit and the baseline. By this procedure the deposit is dissociated from the channel and the original data set (Fig. 6.3, middle).

In a next step the maximum elevation (z^*_{max}) of the extracted deposit and its corresponding position (x^*_{max}) have been determined. Thereafter, the Maxwell distribution function has been applied (Fig. 6.3, bottom). The shape factor (n^*) is found by a trial-and error procedure using the least squares method (LSM) for the vertical difference:

$$\Pi = \sum_{i=1}^{n} \left[\left(Z^*_{mov-ave} \right)_i - \left(Z^*_{Maxwell} \right)_i \right]^2 = min \tag{6.6}$$

Once the input parameters of the Maxwell distribution function are determined, dimensionless expressions need to be developed for the shape factor (n^*) and the maximum height of the deposit (z^*_{max}) as well as its corresponding position (x^*_{max}).

6.4.2. Shape Factor n^*

As has been mentioned before, the beginning and the end of the aggraded channel reach could not always be clearly defined. Hence, n^*-values are tainted with a certain scatter and a correction procedure was applied. The correction procedure consisted in eliminating n^*-values exceeding the standard deviation (*stdev*) by 50 %. Within this context, the standard deviation has been determined separately for each test series B, C and D and not for the entire data set. As a consequence, experiments $B04$ and $C05$ have not been considered in the analysis. However, 83 % $6/16 + 80$ % $5/16 + 100$ % $5/16 =$ 87 % of the total data set have been used (the term 6/16 refers to 6 experiments (series B) of total 16 experiments; the term 5/16 refers to 5 experiments (series C and D) of total 16 experiments).

After this correction procedure n^*-values presented in Table 6.1 are obtained. In addition, the corresponding standard deviations are summarized. The Table indicates a mean n^*-value of 4.59.

It has been found out that n^* might be related to the ratio of weir crest length (L_D) to channel width (B) by the following linear correlation (Fig. 6.4):

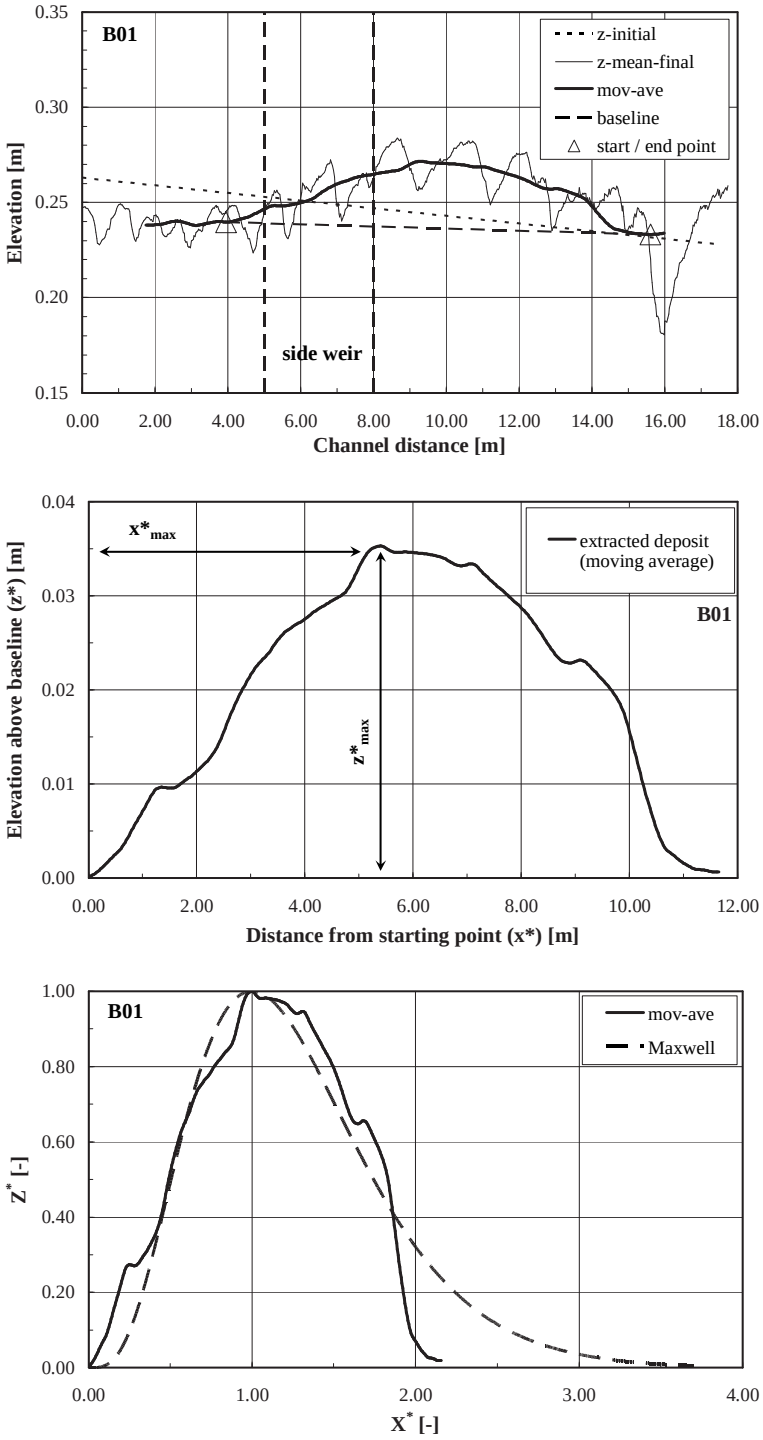

Figure 6.3: Determination of the Maxwell-type distribution function from the original data set (test series $B01$). Top: Initial mobile bed, cross sectional averaged final bed, moving average for the final bed, start and end point of the deposit and baseline connecting the start and end point (local minima). Middle: Extracted deposit. Bottom: Normalized deposit and corresponding Maxwellian distribution function.

Table 6.1: Mean values (after application of a correction procedure) for the shape factor (n^*) and corresponding standard deviations for the $1D$-deposit.

Test series	Shape factor n^* [−]	Standard deviation *stdev* [−]
B	3.78	0.55
C	5.25	1.15
D	4.86	1.18
average	4.59	1.11

$$n^* = \frac{3}{4} \cdot \frac{L_D}{B} + \frac{7}{3} \tag{6.7}$$

Since only three data points are correlated, the R^2-value of Equation 6.7 is rather high ($R^2 = 0.99$). The application range of Equation 6.7 is given by $2.00 \leq L_D/B \leq 4.00$ and Table 6.1.

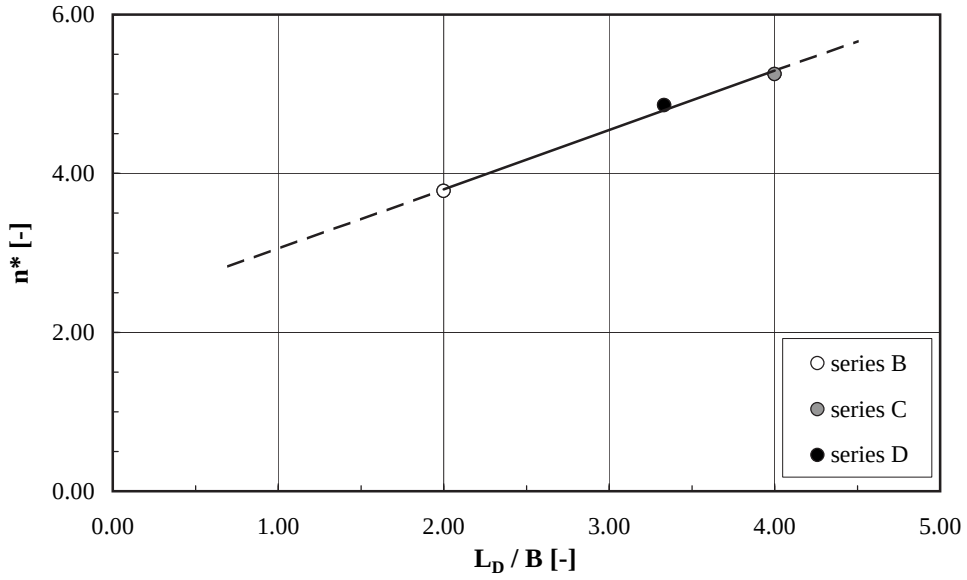

Figure 6.4: Relation of the shape factor (n^*) as a function of crest length to channel width (L_D/B), (Eq. 6.7).

6.4.3. Maximum Deposition Height z^*_{max}

To determine the maximum height of the extracted deposit (z^*_{max}) (Fig. 6.3, middle) parameters from channel and weir geometry as well as flow and sediment transport variables are combined.

Within this context channel geometry, weir geometry and flow conditions are supposed to be represented by the ratio of overflow to approach discharge:

$$\frac{Q_D}{Q_1} = \frac{2/3 \cdot C_D \cdot \sqrt{2 \cdot g} \cdot (y_1 - w_D)^{3/2} \cdot L_D}{R_h^{2/3} \cdot k_{st} \cdot S^{1/2} \cdot B \cdot y_1} \tag{6.8}$$

where Q_D overflow discharge, Q_1 approach flow discharge, C_D side weir discharge coefficient, g acceleration due to gravity, $y_1 - w_D = h_{D,1}$ pressure head above side weir crest, y_1 approach flow depth, w_D weir height, L_D weir crest length, k_{st} Strickler resistance coefficient (here used including form roughness), R_h hydraulic radius ($R_h \approx y_1$ for $B/y_1 > 10$), S slope and B channel width.

Regarding sediment transport, the dimensionless bed-load intensity is supposed to be entirely expressed in terms of the Einstein factor (Φ) (Yalin (1972)). The ratio of bed-load transport up- and downstream of the weir is $\Delta\Phi$ ($\Delta\Phi = \Phi_{downstream}/\Phi_{upstream}$). Characteristic $\Delta\Phi$-ratios from the present study varied in the range of $0.41 \div 0.89$ with a mean value of 0.75. The value of 0.75 indicates that during the operation of the side weir about 25 % of the approach bed-load material has been captured in the deposit. Since the sediment balance has been performed using the DEM (erosion and aggradation ratios based on the DEM refer to bulk volumes and not to pure sediments with $\rho_s = 2650\ kg/m^3$), in the determination of $\Delta\Phi$ a measured sediment bulk density of $\rho_s = 1447\ kg/m^3$ for the conversion of supplied bed material (given in kg/min) has been applied.

To express z^*_{max} in a non-dimensional way the side weir pressure head ($h_{D,1}$) at the upstream weir corner (section 1) has been chosen ($h_{D,1}/z^*_{max}$). In order to find a suitable expression for $h_{D,1}/z^*_{max}$ the genetic program GPKernel (Genetic Programming Kernel) developed by M. Keijzer and V. Babovic at the Danish Hydraulic Institute (DHI) has been used (Keijzer and Babovic (1999), Babovic et al. (2001)). The program looks for mathematical relations based on a set of input parameters, constants, operations, genetic parameters and user-defined targets. The genetic parameters, e. g. the size of the population, the number of generations to produce, run time, different probabilities of mutations and genetic operations can be modified. An advantage of the program is to perform a dimensionally aware genetic programming (Keijzer and Babovic (1999)). Additional information about GPKernel is given in the user's manual (Rodriguez Aguilera (2000)).

Introducing the parameters Q_D/Q_1 and $\Delta\Phi$ to the genetic program several relations in the form $h_{D,1}/z^*_{max} = f(Q_D/Q_1, \Delta\Phi)$ were obtained. Based on the physical meaning and the degree of correlation expressed in terms of R^2-values the following equation has been selected ($R^2 = 0.95$):

$$\begin{aligned}\frac{h_{D,1}}{z^*_{max}} &= \Delta\Phi \cdot (2 \cdot \Delta\Phi - 1.04) \cdot \left[\left(\frac{Q_D/Q_1}{\Delta\Phi - 0.98/\Delta\Phi} + \frac{\Delta\Phi}{Q_D/Q_1} \right) \right. \\ &\quad \left. + \left(\frac{Q_D/Q_1}{Q_D/Q_1 - 0.17} + \frac{2 \cdot \Delta\Phi}{Q_D/Q_1} \right) \cdot \left(\frac{-1.08}{\Delta\Phi} + 2 \cdot \Delta\Phi \right) \right] \\ &\quad + 2 \cdot \Delta\Phi \end{aligned} \tag{6.9}$$

where $h_{D,1}$ is the pressure head at the upstream weir corner, z^*_{max} the maximum deposition height of the extracted deposit, Q_D the overflow discharge, Q_1 the approach discharge and $\Delta\Phi$ the ratio of bed-load transport down- and upstream of the weir.

After regroupement of terms and omission of terms of minor influence the rather complex expression can be reduced to:

$$\frac{h_{D,1}}{z^*_{max}} = \frac{\Delta\Phi}{Q_D/Q_1} \cdot \left(3 \cdot \Delta\Phi - \frac{9}{5} \right) + \frac{9}{4} \tag{6.10}$$

The application range of Equation 6.10 is $0.75 \leq h_{D,1}/z^*_{max} \leq 10.50$. The considerable simplification does not have a significant impact on the R^2-value still being $R^2 = 0.91$. Especially greater values are still fairly well represented. However, a slight decrease of correlation might be identified for small $h_{D,1}/z^*_{max}$-ratios. Since deviations for the greater ratios are more important than for the smaller ones the simplifications appear to be acceptable.

In Figures 6.5 and 6.6 Equations 6.9 and 6.10 are presented and compared with measured $h_{D,1}/z^*_{max}$-ratios.

Regarding the physical meaning of Equation 6.10 it can be stated that for very small Q_D/Q_1-ratios ($Q_D/Q_1 \rightarrow 0.00$ but $\neq 0.00$, overflow discharge almost zero) there is no reason for the bed-load ratio ($\Delta\Phi$) to change, hence $\Delta\Phi$ remains ≈ 1.00 ($\Phi_{downstream} \approx \Phi_{upstream}$). Under this condition the ratio $h_{D,1}/z^*_{max}$ becomes rather great and z^*_{max} is very small (for Q_D/Q_1 close to zero $h_{D,1}$ is also close to zero).

On the contrary, for great Q_D/Q_1-ratios an important portion of the approach discharge is diverted over the weir and $\Delta\Phi$ becomes small (deposition of huge bed-load quantities). In this case $h_{D,1}/z^*_{max}$ becomes small and consequently z^*_{max} increases.

As far as the application of Equation 6.10 is concerned the ratio Q_D/Q_1 is not known a priori. Hence, Equation 6.10 has to be solved by iteration. It is recommended to start with flat bed conditions (no deposit) using the general

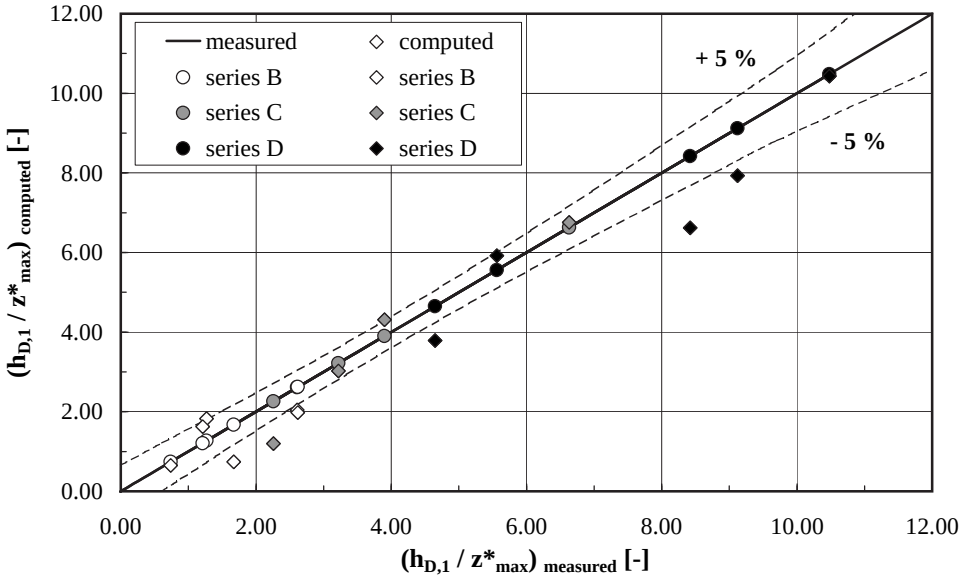

Figure 6.5: Relation for the maximum deposition height (z^*_{max}) of the extracted deposit of the $1D$-model (original formula obtained from GPKernel, Eq. 6.9) and comparison with measured values. The 95 % confidence interval is ± 0.69.

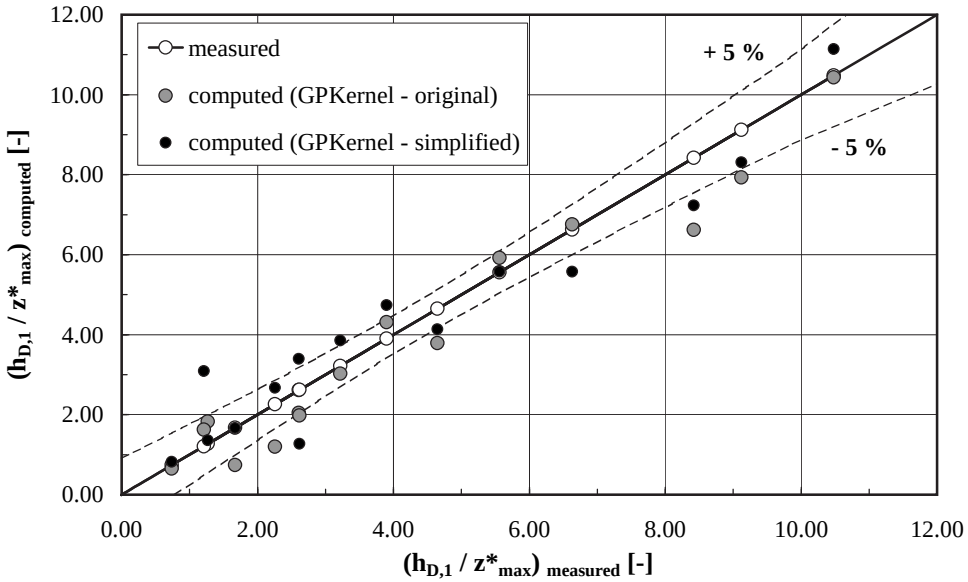

Figure 6.6: Relation for the maximum deposition height (z^*_{max}) of the extracted deposit of the $1D$-model (simplified formula obtained from GPKernel, Eq. 6.10) and comparison with the original GPKernel-formula (Eq. 6.9) and measured values. The 95 % confidence interval is ± 0.85.

equation of weirs (Eq. A.158) and the C_D-coefficient according to Subramanya and Awasthy (1972) or Hager (1987b) (paragraph 5.3.2). Based on the overflow discharge for the flat bed without deposit the up- and downstream Φ-values can be determined and hence $\Delta\Phi$. Once a stable overflow discharge (Q_D) is obtained the iteration can be stopped. An example of the iteration procedure is given in paragraph 7.2.

6.4.4. Location of Maximum Deposition Height x^*_{max}

Since by definition, $X^* = x^*/x^*_{max} = 1.00$, one of the three variables occurring in Equations 6.4 and 6.5 can be constructed. Beginning at $X^* = 0.00$, arbitrarily chosen increments for $0.00 \leq X^* \leq 1.00$ are used. For $X^* > 1.00$, discrete increments until a certain X^*-value depending on the underlaying problem have to be selected. For the present data set an upper range of $X^* = 4.00 \div 6.00$ appears to be reasonable (Fig. 6.3, bottom).

For the transfer of the modelled deposit into a channel, river or numerical model (next paragraph) dimensional values for x^*_{max}, e. g. in $[m]$, are required (analogue to z^*_{max}). The analysis indicated that the distance of $X^* = x^*/x^*_{max} = 0.00$ to 1.00 and from 1.00 to the end of the deposit (Fig. 6.3, bottom) corresponds on average to $x^*_{max} = 3.98\ m \approx 4.00\ m$ of the extracted deposit (Fig. 6.3, middle). Hence, X^*-values ranging from 0.00 to $4.00 \div 6.00$ need to be multiplied by 4.00 m (model scale!).

Indicative values for x^*_{max} might also be derived from Table 6.2.

6.4.5. Location of empirical Deposit relative to Side Weir

Once the shape of the extracted deposit is entirely known it has to be transferred into river, channel or numerical model. To do so, the geometry of the empirical deposit has to be superposed on the initially flat channel bed. In this context the maximum height of the extracted deposit (z^*_{max}) corresponds to the maximum elevation (z_{max}) of the deposit implemented into a river, channel or numerical model (Fig. 6.7).

For the location of the empirical deposit relative to the side weir a horizontal coupling point (cp) is required. Since the position of the downstream side weir corner (section 2) in the main-channel is usually known a priori, this point represents an appropriate reference for the integration of the extracted (modelled) deposit into the channel. The location of the maximum height of the empirical deposit around the downstream weir corner is given by x_{cp} (Fig. 6.7).

Applying the weir crest length (L_D) for normalisation, the ratio x_{cp}/L_D is found to vary in the following range (without experiments $B04$ and $C03$):

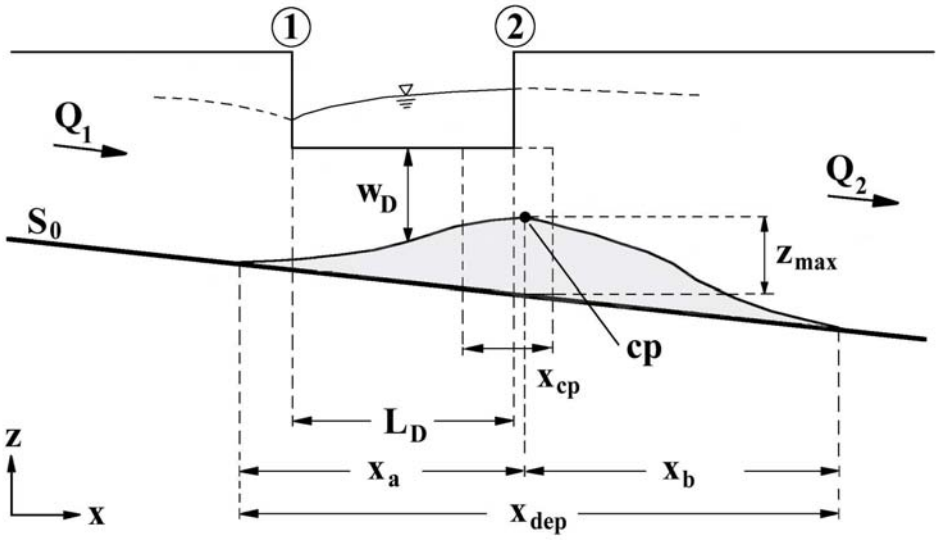

Figure 6.7: Definition sketch illustrating the horizontal location of the maximum height of the deposit relative to the downstream weir corner (cp, x_{cp}) for the implementation of the aggradation model into a river, channel or numerical model.

$$-0.65 \leq \frac{x_{cp}}{L_D} \leq 0.44 \tag{6.11}$$

For negative values the reference point is located upstream of the downstream weir corner; for positive values x_{cp} is located downstream of section 2.

Taking the mean range of Equation 6.11 the location of the horizontal coupling point is supposed to be given by:

$$\frac{x_{cp}}{L_D} = -0.04 \quad \text{or} \quad x_{cp} = -0.04 \cdot L_D \tag{6.12}$$

According to Equation 6.12 the position of the maximum aggradation nearly coincides with the downstream weir corner.

For computations in engineering practice the downstream weir corner is recommended as an anchor point for the horizontal coupling point (x_{cp}). This location might be considered to be on the secure side, since the side overflow discharge (Q_D) is higher for this position than for a deposit being located upstream of the downstream weir corner (Rosier et al. (2007b)). This has been demonstrated in paragraph 5.8.

Since the location of the maximum aggradation constitutes a kind of control section, the range of Equation 6.11 might be reduced considering the approach Froude number at section 1 (Fr_1). From Figure 6.8 the following

threshold values can be derived (Rosier et al. (2006c)):

$$0.60 \leq Fr_1 \leq 0.80: \quad 0.00 \leq \frac{x_{cp}}{L_D} \leq 0.44 \quad \text{(positive range)} \tag{6.13}$$

$$0.80 < Fr_1 \leq \approx 1.00: \quad -0.65 \leq \frac{x_{cp}}{L_D} < 0.00 \quad \text{(negative range)}$$

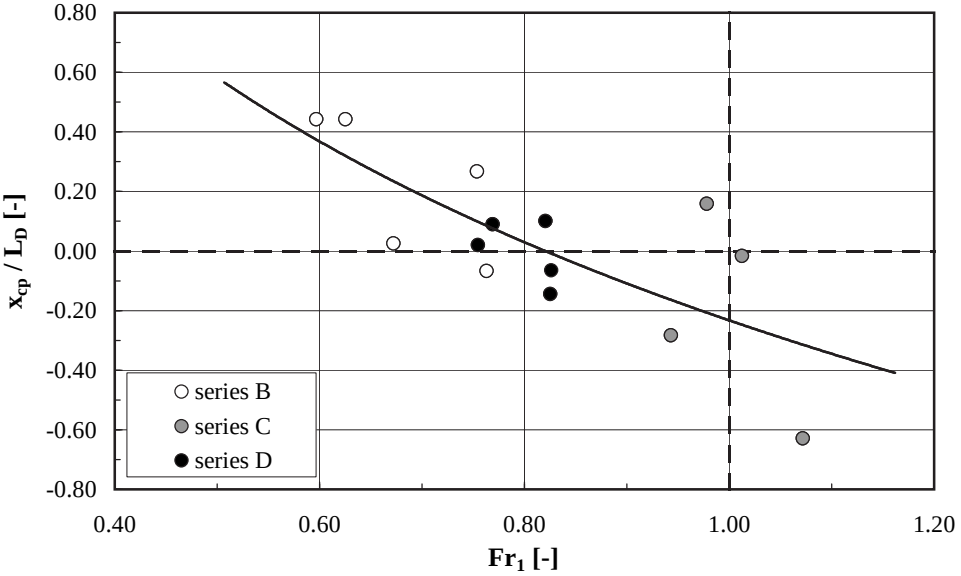

Figure 6.8: Influence of approach Froude number (Fr_1) on the location of the horizontal coupling point (x_{cp}) (Eqs 6.13 and 6.14). The dashed lines indicate $Fr_1 = 1.00$ and $x_{cp}/L_D = 0.00$.

Figure 6.8 might suggest the rather approximative and indicative logarithmic relation ($R^2 = 0.55$):

$$\frac{x_{cp}}{L_D} \approx -6/5 \cdot ln\,(Fr_1) - 1/4 \tag{6.14}$$

To get a rough estimation of the total length of the deposit (x_{dep}) as well as the repartition of the up- and downstream leg (x_a, x_b, Fig. 6.7), the ratios depicted in Table 6.2 might be used.

The average total deposition length (x_{dep}) is given by:

$$\frac{x_{dep}}{L_D} = 2.52 \approx 5/2 \quad \text{or} \quad x_{dep} \approx 5/2 \cdot L_D \tag{6.15}$$

The repartition of the up- and downstream part (x_a, x_b) might be represented by (see Tab. 6.2):

$$\frac{x_a}{x_b} = \frac{0.40}{0.60} = 0.69 \tag{6.16}$$

Table 6.2: Total deposition length (x_{dep}) and repartition of up- and downstream deposition length (x_a, x_b) for the $1D$-model.

Test series	x_a/L_D [–]	x_b/L_D [–]	x_{dep}/L_D [–]	x_a/x_{dep} [–]	x_b/x_{dep} [–]	x_a/x_b [–]
B	1.43	2.02	3.45	0.41	0.59	0.72
C	0.66	1.09	1.75	0.37	0.63	0.61
D	0.75	0.94	1.68	0.44	0.56	0.79
average	1.02	1.50	2.52	0.40	0.60	0.69

From Equation 6.16 it can be concluded that the position of the maximum bed elevation (x^*_{max} or x_{max}) is located upstream of the center. Hence, the deposit is left skewed. The left-skewness also corresponds to the shape of the Maxwellian distribution function (Fig. 6.2).

6.5. Steps for Determination of Bed Morphology by a 1D empirical Approach

In this paragraph the different steps of the computation procedure to determine the shape of the one-dimensional sedimentary deposit as well as the transfer into a channel, river or numerical model are summarized. In principle the determination of the shape of the deposit corresponds to the reverse way of the development procedure (steps depicted in Fig. 6.3 but from bottom to top).

Since the overflow discharge (Q_D) and the bed-load transport ratio ($\Delta\Phi$) are not known at the beginning, an iteration procedure for the determination of the maximum height of the extracted deposit (z^*_{max}) is required.

- Determination of the shape of the deposit:
  - Normalized deposit obtained by the Maxwellian distribution function:
    - Shape factor (n^*) of deposit: Equation 6.7,
    - Arbitrarily chosen increments for X^* (Eq. 6.4): $0.00 \leq X^* \leq 4.00 \div 6.00$,

    - ∗ Height of deposit ($Z^*(X^*)$): Equation 6.5.
  - Geometry of extracted deposit:
    - ∗ Abscissa: $x^* = X^* \cdot x^*_{max}$ with $x^*_{max} \approx 4.00\ m$ (for model scale of $1:30 \div 1:50$) (or using Tab. 6.2),
    - ∗ Ordinate: $z^* = Z^*(X^*) \cdot z^*_{max}$ with z^*_{max} according to Equation 6.10.

- Location of deposit relative to side weir:
  - Horizontal coupling point (x_{cp}) obtained by Equation 6.11 (or Eq. 6.12, simplified):
    - ∗ Reduce location range of x_{cp} applying Equation 6.13 and/or Equation 6.14.
  - Estimation of total deposition length (x_{dep}) using Equation 6.15,
  - Estimation of repartition of up-and downstream deposition length (x_a, x_b) using Equation 6.16.

6.6. Application of 1D empirical Deposition Model in a numerical Flow Calculation

In order to test the prediction accuracy of the $1D$ empirical model, data from the present study has been introduced to the empirical model. Then the empirical model has been implemented into the $1D$-numerical flow simulation code DUPIRO (see paragraph 8.1 for explanation of the numerical code). Form roughness is accounted for by the choice of an appropriate roughness coefficient (k_{st}). The computations indicate that on average the following percentage of the total measured side overflow discharge (Q_D) is predicted (range $75\ \% \div 92\ \%$) (Tab. 6.3):

$$\frac{Q_{D,predicted}}{Q_{D,measured}} \approx 85\ \% \tag{6.17}$$

The missing 15 % are mainly due to the one-dimensional character of the model. Moreover, deviations might be attributed to the one-dimensionality of the numerical code and the choice of an appropriate roughness coefficient (k_{st}).

Consequently, it can be concluded that the side overflow intensity (Q_D) obtained from the $1D$ empirical model implemented into a $1D$-numerical flow model has to be increased by a factor of $\approx 1/0.85 = 1.18$.

Table 6.3: Comparison of measured and computed side overflow (Q_D) for the $1D$ empirical deposition model applied in a $1D$-numerical flow calculation. LSM denotes least squares method $\left(\sum(Q_{D,computed} - Q_{D,measured})^2\right)$.

Test series	Q_D measured $[l/s]$	Q_D computed $[l/s]$	computed/ measured $[-]$	LSM $\left[(l/s)^2\right]$
B	33	29	0.88	591
$C^{*)}$	32	27	0.84	127
D	40	34	0.86	435
average	35	30	0.85	1153$^{**)}$

$^{*)}$without $C03$, $^{**)}$sum

6.7. 2D-Model for Prediction of longitudinal and lateral Shape of Deposit

This paragraph describes the development of an empirical $2D$-model to account on the one hand for the overall mobile bed evolution and on the other for $2D$-effects due to lateralwise variation of the deposit.

6.7.1. Bed Evolution on Left and Right Channel Bank

To determine the profile on the right channel bank the lateralwise distribution of the maximum bed elevation along the side weir has been identified. For this analysis the original DEM data set (without smoothing or applying any moving average) with a spatial discretisation of $\Delta x_i = 1.00\ m$ has been used.

The results indicate a ratio of $y_B/B = 0.80$ for test series B, $y_B/B = 0.94$ for test series C and $y_B/B = 0.88$ for test series D. The average lateralwise location is $y_B/B = 0.88$ (Fig. 6.9). Since this ratio is slightly too short for test series B, a ratio of $y_B/B = 0.85$ and consequently a strip width of $y_B/B = 0.85 \div 1.00$ has been chosen. This range corresponds to an absolute strip width of $0.225\ m$ or $y_B/B = 0.225\ m/1.50\ m = 0.15$ for the right channel bank. In analogy, the same strip width has been selected for the left channel bank, hence $y_B/B = 0.00 \div 0.15$.

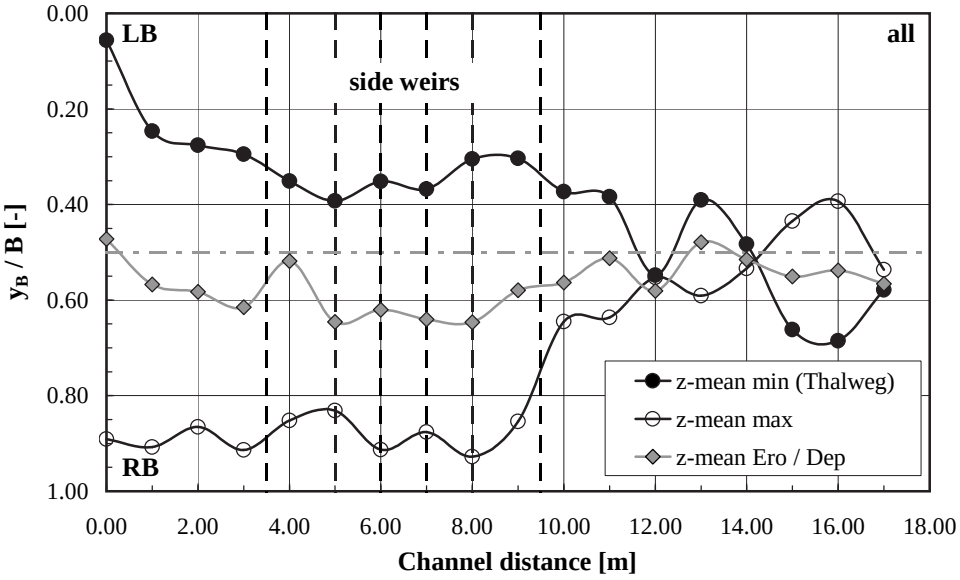

Figure 6.9: Lateralwise location of maximum and minimum bed elevation and transition from erosion/deposition along channel axis for the entire data set. The transition from erosion to deposition for each cross section has been defined by the location where the cross sectional profile crosses the average bed level. If several crossings were present, the maximum vertical difference has been chosen. LB denotes left bank, RB right bank.

Once the two profiles are extracted from the original DEM a moving average is applied (window length $\omega^* = 3.50\ m$, see paragraph 6.2). Typical profiles resulting from this procedure are shown in Figure 6.10. From this Figure it becomes evident that the deposit on the right channel bank is considerably more pronounced than the one on the opposite channel bank. Moreover it can be seen that the locations of the maximum elevation of the deposit on the left and right channel bank are longitudinally shifted. This streamwise offset is dealt with in paragraph 6.7.6.

6.7.2. Determination of Shape of Deposit

The analysing process to define the two deposits on the left and right cannel side corresponds to the same procedure than has been described earlier for the $1D$-model (paragraph 6.4.1). The deposit on the left channel bank has been less prominent than the one on the right bank close to the weir. Hence, the determination process for the shape of the deposit on the left side was characterised by a certain degree of interpretation. In Figure 6.11 an example

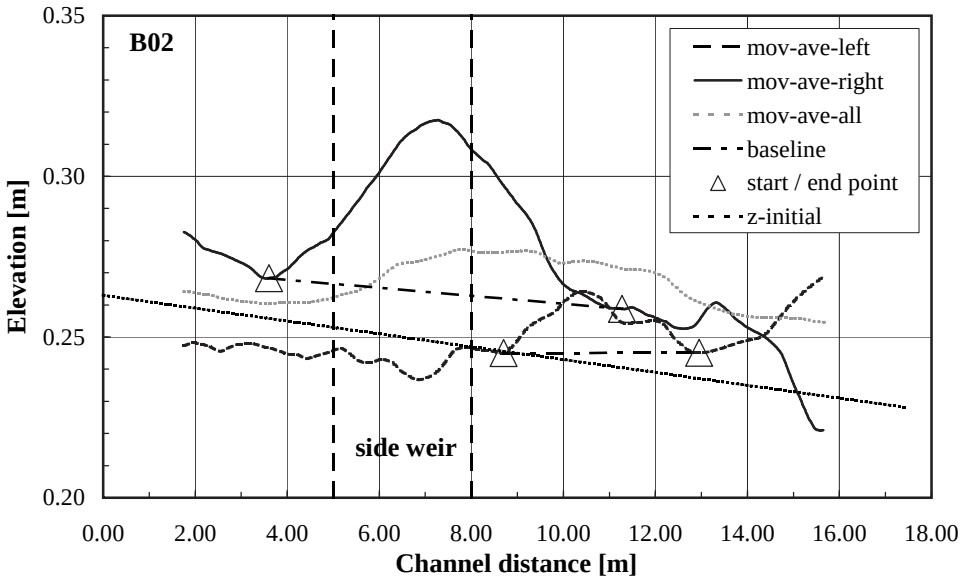

Figure 6.10: Bed evolution (moving average) on left and right channel bank for test series $B02$. In addition, the moving average for the entire cross section is presented. The starting and end points as well as the baseline correspond to the Maxwellian analysis (paragraphs 6.3 and 6.7.2).

for the shape of the deposit on the right channel bank and the determination procedure applying the Maxwellian distribution function is given.

As for the $1D$-model the shape factor (n^*) for the two deposits is found by a trial-and error procedure using the least squares method (LSM). Thereafter, dimensionless expressions for the shape factor (n^*), the maximum height of the deposit (z^*_{max}) and its corresponding position (x^*_{max}) have to be established for the deposits on both sides.

6.7.3. Shape Factor n^*

In contrast to the $1D$-approach the shape factor n^* appears to be less sensitive to the experimental boundary conditions (e. g. upstream discharge, side overflow discharge, weir geometry, bed-load transport). Hence, a rather constant value might be assumed.

Nevertheless, a certain scatter becomes evident and a correction procedure in analogy to the $1D$-method was applied (elimination of n^*-values exceeding the standard deviation (*stdev*) by 50 %). As a result of this correction procedure experiments $B04$, $D01$ and $D05$ on the right bank and experiments $C01$, $C05$ and $D03$ on the left bank have not been considered in the analysis. Despite the elimination of these data points,

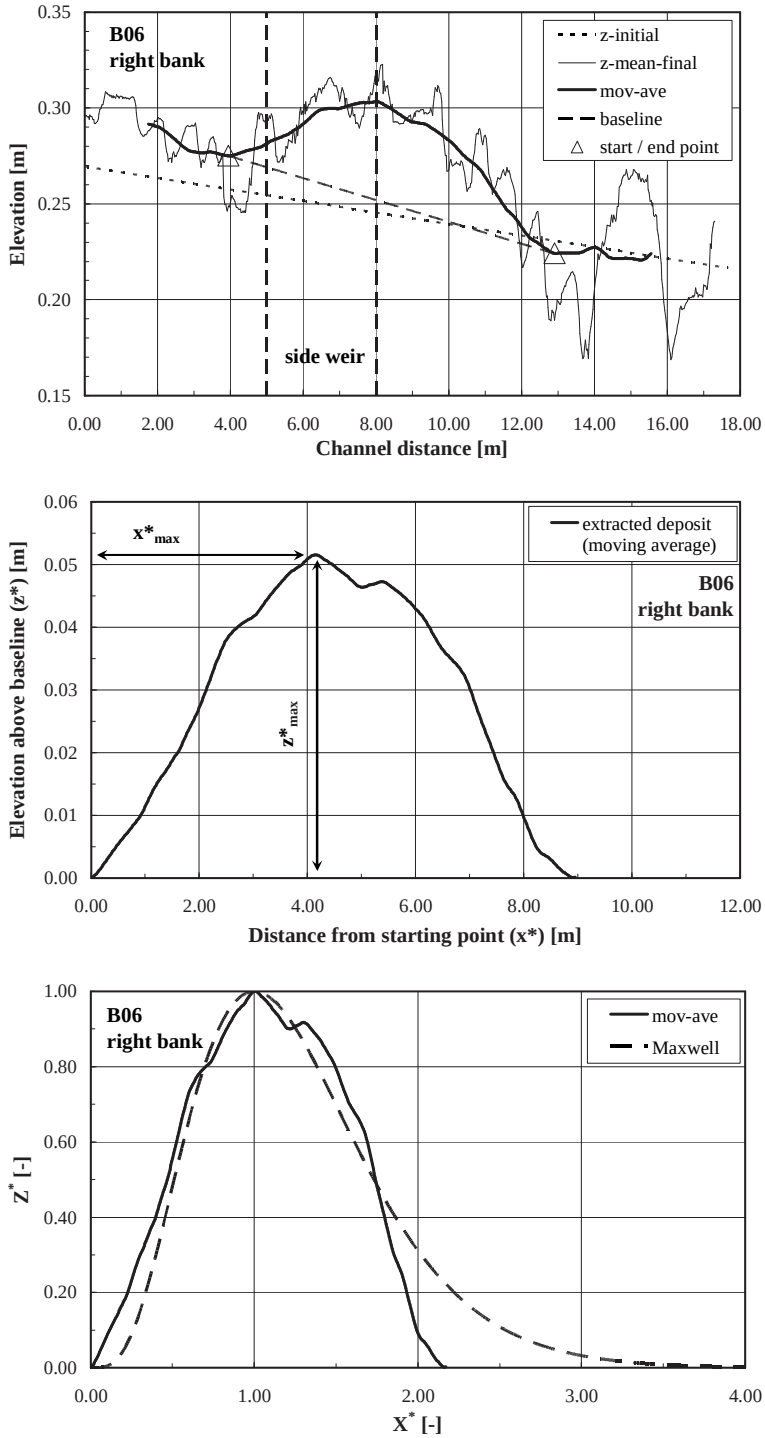

Figure 6.11: Determination of the Maxwell-type distribution function from the original data set (test series $B06$, right channel bank). Top: Initial mobile bed, cross sectional averaged final bed, moving average for the final bed, start and end point of the deposit and baseline connecting the start and end point (local minima). Middle: Extracted deposit. Bottom: Normalized deposit and corresponding Maxwellian distribution function.

83 % 6/16 + 100 % 5/16 + 60 % 5/16 = 81 % of the total data set on the right bank have been used. On the left bank, this ratio corresponds to 100 % 6/16 + 60 % 5/16 + 100 % 5/16 = 88 %.

In Table 6.4 n^*-values and corresponding standard deviations (*stdev*) obtained after the correction procedure are presented. From this Table it can be seen that n^* yields 5.52 for the right (n^*_{RB}) and 3.56 for the left channel bank (n^*_{LB}).

Since the deposit on the right channel bank has always been well and sharply defined and the shape factor does not vary significantly, the following constant value might be used:

$$n^*_{RB} \approx 5.52 \tag{6.18}$$

Table 6.4: Mean values (after application of a correction procedure) for the shape factor (n^*) and corresponding standard deviations (*stdev*) for the deposit on the right and left channel bank.

Test series	Right channel bank		Left channel bank	
	n^*_{RB} [–]	*stdev* [–]	n^*_{LB} [–]	*stdev* [–]
B	5.48	1.22	3.03	0.79
C	5.68	0.90	4.63	1.46
D	5.30	1.49	3.55	0.66
average	5.52	1.08	3.56	1.07

The analysis further shows that for the shape factor on the left channel bank (n^*_{LB}) the ratio of the mean shape factors on the left and right channel bank (n^*_{LB}/n^*_{RB}) is related to the ratio of side weir crest length (L_D) and channel width (B) in the following way (Fig. 6.12):

$$\frac{n^*_{LB}}{n^*_{RB}} = \frac{1}{8} \cdot \frac{L_D}{B} + \frac{2}{7} \tag{6.19}$$

The R^2-value of Equation 6.19 is 0.94. The application range is given by $2.00 \leq L_D/B \leq 4.00$ and Table 6.4.

Equation 6.19 indicates that for increasing crest length values (and $B = const.$) the ratio n^*_{LB}/n^*_{RB} increases as well. This means for longer weirs the shape of the two deposits converges and the overall aggradation is characterised by a more uniform cross sectional distribution. Consequently,

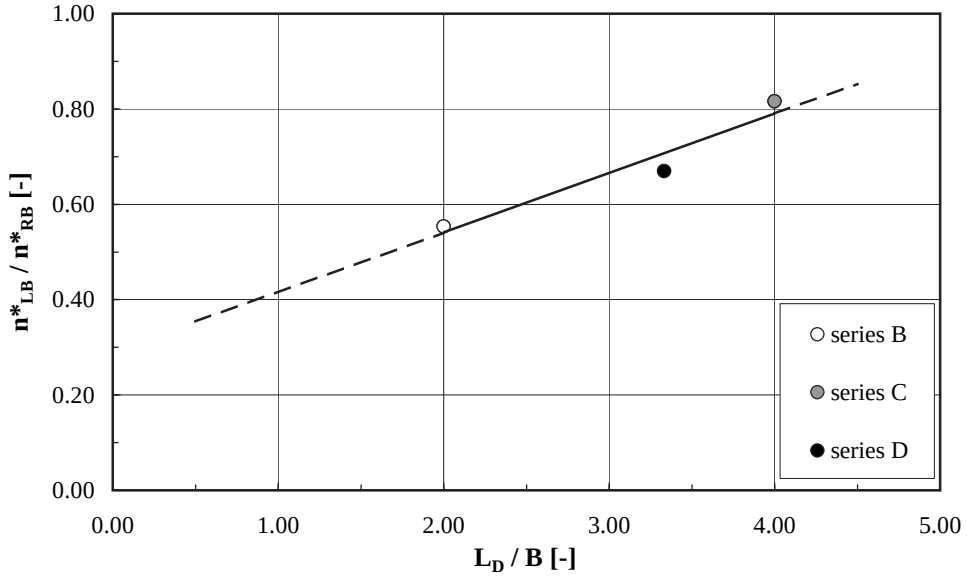

Figure 6.12: Relation between the shape factor (n^*) on the right and left channel bank (n^*_{LB}/n^*_{RB}) as a function of crest length to channel width (L_D/B), (Eq. 6.19).

the local deposition effect on the right bank at the downstream weir corner is reduced. On the contrary, a short weir induces a well defined and more pronounced local deposit on the right bank (side of the weir). The one on the left bank is smoother and more extended. Concluding, the overall deposition is highly two-dimensional and rather uneven.

Instead of applying Equation 6.19 a simplified relationship, e. g. for practical purposes, might be derived from Table 6.4:

$$\frac{n^*_{LB}}{n^*_{RB}} = \frac{3.56}{5.52} = 0.65 \approx 2/3 \quad \text{or} \quad n^*_{LB} \approx 2/3 \cdot n^*_{RB} \tag{6.20}$$

The deviation of the standard deviation with respect to Equation 6.20 is given by $stdev/(n^*_{LB}/n^*_{RB}) = 0.13/0.65 = 20$ %. The deviation of 20 % appears to be satisfying, since, e. g. Van Rijn (1984a), stated that even under controlled flume conditions the prediction inaccuracy of sediment transport related parameters is hardly less than a factor 2.

As has been concluded in paragraph 5.8, the form or shape of the deposit is less important for the intensity of the diverted discharge than the maximum elevation and its location. Therefore, n^* is supposed to be sufficiently described by the use of mean values and a certain scatter within a limited range might be acceptable.

6.7.4. Maximum Deposition Height z^*_{max}

For the determination of the maximum height of the extracted deposit on the right channel bank ($z^*_{max,RB}$) (Fig. 6.11, middle) the expression developed for the maximum deposition of the extracted deposit for the $1D$-model is referred to (Eq. 6.10, repeated here):

$$\frac{h_{D,1}}{z^*_{max}} = \frac{\Delta\Phi}{Q_D/Q_1} \cdot \left(3 \cdot \Delta\Phi - \frac{9}{5}\right) + \frac{9}{4} \tag{6.21}$$

The analysis revealed that the maximum height of the deposit on the right channel bank ($z^*_{max,RB}$) might be related to the maximum deposition height of the $1D$-model (z^*_{max}) by the following expression ($R^2 = 0.91$):

$$\frac{h_{D,1}}{z^*_{max,RB}} = 2/3 \cdot \left(\frac{h_{D,1}}{z^*_{max}}\right)^{4/5} \tag{6.22}$$

Replacing the term $h_{D,1}/z^*_{max}$ with the right hand side of Equation 6.21 (or Eq. 6.10, respectively) yields (Fig. 6.13):

$$\frac{h_{D,1}}{z^*_{max,RB}} = 2/3 \cdot \left[\frac{\Delta\Phi}{Q_D/Q_1} \cdot \left(3 \cdot \Delta\Phi - \frac{9}{5}\right) + \frac{9}{4}\right]^{4/5} \tag{6.23}$$

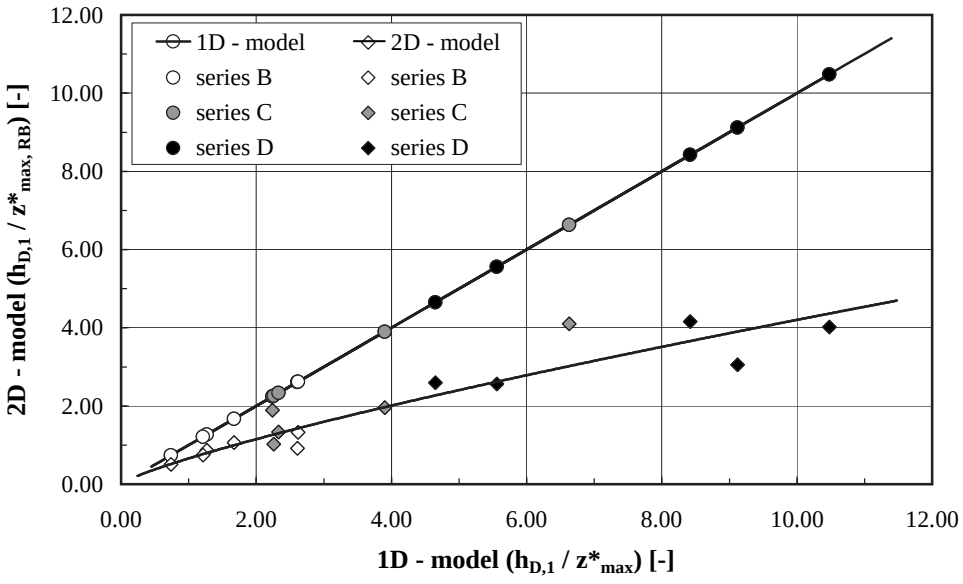

Figure 6.13: Relation for the maximum deposition height ($z^*_{max,RB}$) of the extracted deposit on the right channel bank (Eqs 6.22 and 6.23).

As has been mentioned for the $1D$-approach Equation 6.23 has to be solved by iteration, since Q_D and $\Delta\Phi$ are not known a priori. An example of the iteration procedure is presented in paragraph 7.2.

Knowing $z^*_{max,RB}$ on the right channel side, $z^*_{max,LB}$ on the left channel bank has to be determined. This is achieved by introducing the following relationship describing the ratio between z^*_{max} on the two channel sides:

$$\frac{z^*_{max,LB}}{z^*_{max,RB}} = 0.39 \approx 2/5 \quad \text{or} \quad z^*_{max,LB} \approx 2/5 \cdot z^*_{max,RB} \tag{6.24}$$

For the determination of Equation 6.24 values exceeding the standard deviation by more than 50 % have been eliminated. Herein, the standard deviation has been calculated separately for each test series. Hence, following this criteria, experiments $B03$, $B04$ and $D03$ have not been considered in the analysis. Consequently, $(16 - 3)/16 = 81$ % of the entire data set has been used.

The ratio of the standard deviation with respect to the average of Equation 6.24 is expressed by $stdev/(z^*_{max,LB}/z^*_{max,RB}) = 0.10/0.39 = 26$ %. As has been mentioned for the shape factor (n^*) a prediction inaccuracy of 26 % is in the usual range of parameters derived from experimental flume studies dealing with sediment transport (Van Rijn (1984a)).

Further reflections lead to the assumption that the maximum deposition height on the left channel bank ($z^*_{max,LB}$) might be better represented by an angle instead of a ratio referring to the maximum height of the deposit on the right channel side ($z^*_{max,RB}$) (Eq. 6.24).

This is mainly due to the fact that for, e. g. a wider channel, the deposit close to the weir will probably form approximately in the same way than observed in the present study (since it is a rather local phenomenon), but will not necessarily extend over the entire cross section. It is more likely to show that the deposit will diminish or even disappear approaching the opposite river bank. A discussion concerning the influence of channel width on aggradation is given in paragraph 6.10.2.

As a consequence of these considerations the angle $\phi_{z,LB}$ instead of $z^*_{max,LB}/z^*_{max,RB}$ is introduced (Fig. 6.14). The angle $\phi_{z,LB}$ describes the slope of the crest of the deposit in lateralwise direction. Table 6.5 summarizes average measured $\phi_{z,LB}$-values (without experiments $C03$, $D01$ and $D02$).

In this context $tan\ \phi_{z,LB}$ is supposed to be a function of the product:

$$tan\ \phi_{z,LB} = \frac{\Delta z_{RB-LB}}{B} = y = f(x_i) = f\left(x_1^{\alpha} \cdot x_2^{\beta} \cdot x_3^{\gamma}\right) \tag{6.25}$$

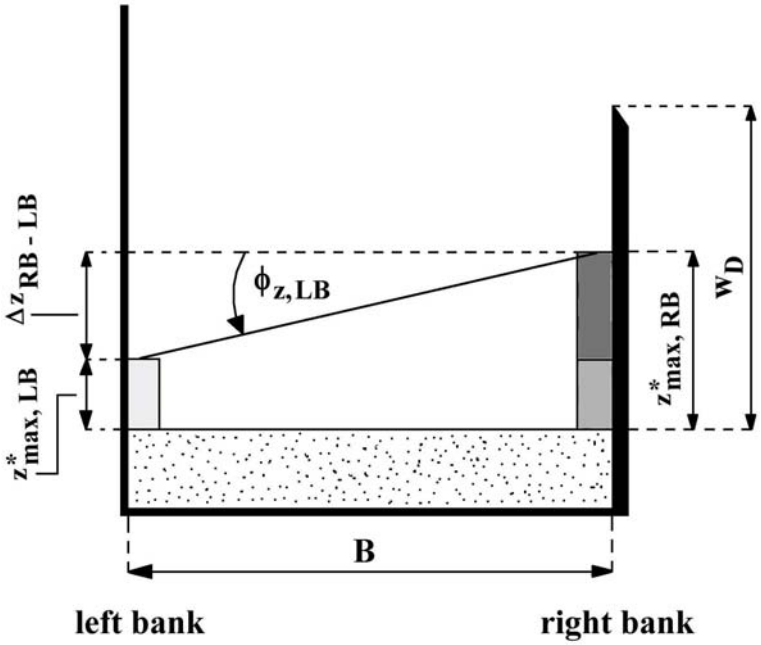

Figure 6.14: Definition sketch for the angle relating the maximum heights of the deposits on the right and left channel bank ($\phi_{z,LB}$) (transverse slope of the crest of the deposit). The grey bars represent the deposit on the right and left channel bank, respectively.

Table 6.5: Mean values for the angle relating the maximum heights of the deposits on the right and left channel bank ($\phi_{z,LB}$). For the definition of $\phi_{z,LB}$ see Figure 6.14.

Test series	$tan\ \phi_{z,LB} = \frac{\Delta z_{RB-LB}}{B}$ [−]	$\phi_{z,LB}$ [°]
B	0.030	1.74
C	0.019	1.10
D	0.019	1.09
average	0.024	1.39

with x_i $(i = 1 \div 3)$:

$$x_1 = \frac{Q_D}{Q_1} \tag{6.26}$$

$$x_2 = \frac{L_D}{B}$$

$$x_3 = \frac{h_{D,1}}{L_D}$$

where Q_D overflow discharge, Q_1 approach discharge in main-channel, L_D weir crest length, B channel width and $h_{D,1}$ side weir pressure head above weir crest at the upstream weir corner (section 1).

The exponents α, β and γ were determined to be $\alpha = -2/3$, $\beta = 1/3$ and $\gamma = 8/5$.

Moreover, the best correlation relating $tan\ \phi_{z,LB}$ with x_i was found to be given by the following outer function:

$$tan\ \phi_{z,LB} = \frac{\Delta z_{RB-LB}}{B} = y = a \cdot x_i^b \tag{6.27}$$

By curve fitting a was determined to be 11.16 and b close to unity.

Consequently, $tan\ \phi_{z,LB}$ might be expressed by the linear relation ($R^2 = 0.89$):

$$tan\ \phi_{z,LB} = 11.16 \cdot \left[\left(\frac{Q_D}{Q_1} \right)^{-2/3} \cdot \left(\frac{L_D}{B} \right)^{1/3} \cdot \left(\frac{h_{D,1}}{L_D} \right)^{8/5} \right] \tag{6.28}$$

A graphical presentation of Equation 6.28 is given in Figure 6.15.

The term Q_D/Q_1 has to be solved by iteration, since Q_D is not known a-priori. It is recommended to start with plane bed conditions (no deposit) using the general equation of weirs (Eq. A.158) and the side weir discharge coefficient (C_D) according to Subramanya and Awasthy (1972) or Hager (1987b) (appendix A.7.3 and 5.3.2).

Finally, using Equations 6.23, 6.27 and 6.28 the maximum height of the deposit on the left channel bank ($z^*_{max,LB}$) can be expressed as (Fig. 6.14):

$$z^*_{max,LB} = z^*_{max,RB} - \Delta z_{RB-LB} \tag{6.29}$$

6.7.5. Location of Maximum Deposition Height x^*_{max}

For the location of the maximum deposition height the same procedure as mentioned for the $1D$-model has to be applied (paragraph 6.4.1).

In contrast to $x^*_{max} = 4.00\ m$ (model scale) for the $1D$-model values of $x^*_{max,RB} = 3.57\ m$ for the right deposit and $x^*_{max,LB} = 2.45\ m$ for the left deposit need to be applied (mode scale!).

Indicative values for $x^*_{max,RB}$ and $x^*_{max,LB}$ might also be derived from Table 6.7.

6.7.6. Location of empirical Deposit relative to Side Weir

As for the $1D$-model a horizontal coupling point (cp) to transfer the modelled deposit into a river, channel or numerical model is needed. In contrast to the

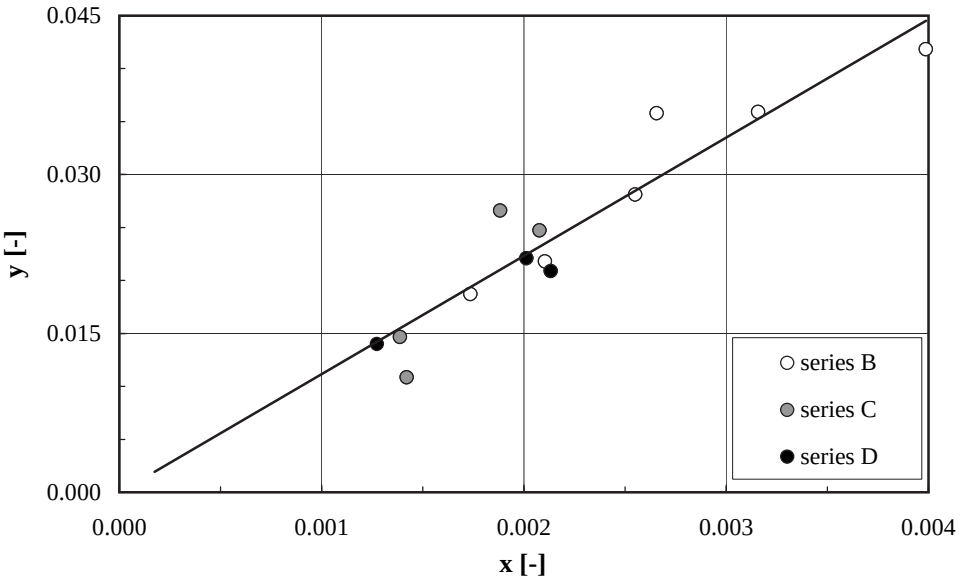

Figure 6.15: Expression to determine the angle between the maximum heights of the deposits on the right and left channel bank ($tan\ \phi_{z,LB}$) (Eqs 6.27 and 6.28).

$1D$-approach a distinction between the shape of the deposit on the right and left channel bank has to be done for the $2D$-model.

In analogy to the $1D$-approach the downstream weir corner has been taken as reference point for the profile on the right bank ($x_{cp,RB}$). For the profile on the left bank the longitudinal shift between the two profiles has been used (Δx^*) (Fig. 6.1 in paragraph 6.1 and paragraph 6.7.1).

- Location of deposit on right channel bank $x_{cp,RB}$:

  Like for the $1D$-model the horizontal coordinate of the coupling point ($x_{cp,RB}$) has been related to the downstream weir corner (section 2). Using the side weir crest length (L_D) the following rather narrow range for the horizontal coupling point on the right channel bank ($x_{cp,RB}$) has been obtained:

$$-0.34 \leq \frac{x_{cp,RB}}{L_D} \leq 0.12 \tag{6.30}$$

  Negative values indicate a location upstream of the downstream weir corner. For positive values $x_{cp,RB}$ is located downstream of the weir end (section 2).

  Applying the average range of Equation 6.30, the horizontal coupling point is supposed to be located at:

$$\frac{x_{cp,RB}}{L_D} = -0.13 \quad \text{or} \quad x_{cp,RB} = -0.13 \cdot L_D \tag{6.31}$$

Following Equation 6.31 the position of the maximum aggradation is located slightly upstream of the downstream weir corner.

As has been mentioned for the $1D$-model the downstream weir corner might be recommended as an anchor point for the horizontal coupling point ($x_{cp,RB}$) in engineering practice. The side overflow intensity (Q_D) will be rather higher for this location than for a deposit situated upstream of the downstream weir corner (paragraph 5.8). Hence, the choice of this position might be considered to be on the secure side.

To reduce the range of Equation 6.30 the approach Froude number at section 1 (Fr_1) is taken into account. Based on this the threshold values represented by Equation 6.32 have been obtained:

$$0.60 \leq Fr_1 \leq 0.85 : -0.34 \leq \frac{x_{cp,RB}}{L_D} \leq 0.12 \quad \text{(entire range)} \tag{6.32}$$

$$0.85 < Fr_1 \leq \approx 1.00 : -0.34 \leq \frac{x_{cp,RB}}{L_D} \leq 0.00 \quad \text{(negative range)}$$

The second line in Equation 6.32 refers to test series C owing rather large L_D/B-ratios ($L_D/B = 4.00$).

For the development of Equations 6.30 to 6.31 experiment $B04$ has not been considered, since it was the only test deviating significantly from the range of the other test series.

- Location of deposit on left channel bank Δx^*:

  As mentioned before, the locations of the maximum elevation of the deposits on each channel side are characterised by a longitudinal displacement (Figs 5.51 and 6.10). To relate the two profiles to each other, the displacement might be expressed via a characteristic angle or distance (Fig. 6.1, top). Herein, a characteristic distance has been chosen (Δx^*). Displacement angles (ϕ^*) between the right and left profile are presented in Table 6.6.

  To develop a relation for the longitudinal shift (Δx^*), parameters accounting for the main-channel flow regime, sediment transport and side weir geometry are combined. With respect to flow conditions, an approach derived by Subramanya and Awasthy (1972) for the lateral outflow angle of water spilled over a side weir is used (Eq. 5.21). The only input parameter in this relation is the approach Froude number in section 1 (upstream weir corner). The resulting equation for Δx^* is a second order polynom having a R^2-value of 0.92. To take further

Table 6.6: Longitudinal displacement angles (ϕ^*) between the maximum bed elevation of the deposit on the right and left channel bank.

N^o of experiment	ϕ^* [°]	N^o of experiment	ϕ^* [°]	N^o of experiment	ϕ^* [°]
$B01$	70	$C01$	29	$D01$	58
$B02$	68	$C02$	22	$D02$	−11
$B03$	66	$C03$	7	$D03$	67
$B04$	77	$C04$	17	$D04$	53
$B05$	54	$C05$	30	$D05$	64
$B06$	71				
average	68		25*)		61**)

*)without $C03$, **)without $D02$

into account a parameter related to sediment transport and to increase the correlation, the shear velocity at section 1 is introduced ($u_{*,1}$) (Eq. 6.33). The second term in Equation 6.33 is made dimensionless by the gravitational acceleration (g) and the weir length (L_D). Hence, this term represents a Froude number. Consequently, the longitudinal displacement of the two deposits is given by:

$$\frac{\Delta x^*}{L_D} = y = f(x) = f\left(\left(1 - \frac{3 \cdot Fr_1^2}{2 + Fr_1^2}\right)^{1/2} \cdot \left(\frac{u_{*,1}}{\sqrt{g \cdot L_D}}\right)^{1/4}\right) \quad (6.33)$$

where Δx^* is the longitudinal displacement of the maximum elevations of the deposit on the left and right channel bank, L_D the weir length, Fr_1 the Froude number at the upstream weir corner, $u_{*,1}$ the shear velocity at the upstream weir corner and g the acceleration due to gravity.

The resulting second order polynom is presented in Figure 6.16 and reads ($R^2 = 0.93$):

$$\frac{\Delta x^*}{L_D} = y = 23.26 \cdot x^2 - 0.11 \cdot x \quad (6.34)$$

For the development of Equation 6.34, test series $B04$ has not been considered since the pair of variates (namely y) from this series scattered

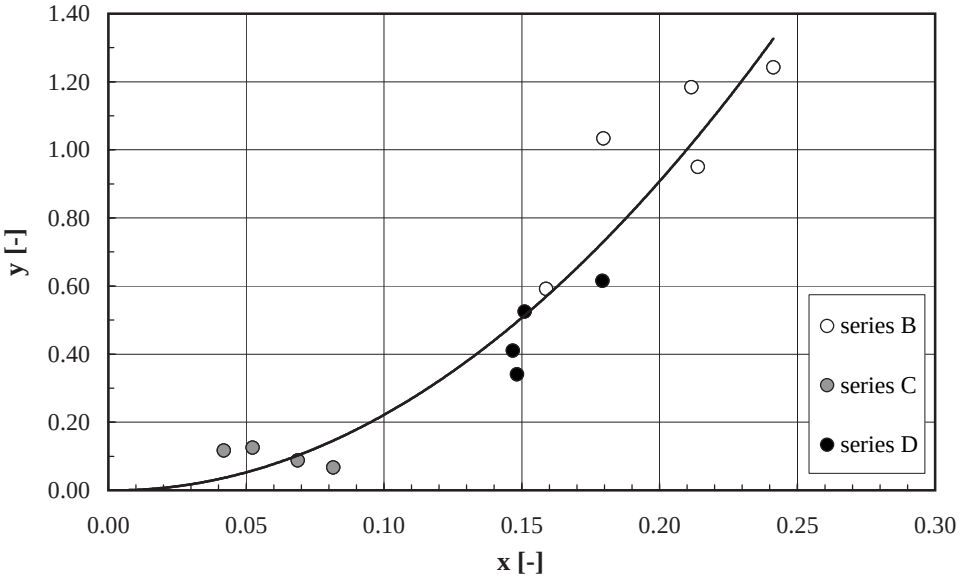

Figure 6.16: Relation to determine the longitudinal displacement (Δx^*) between the deposit on the left and right channel bank (Eqs 6.33 and 6.34).

significantly from the values of the other series ($(x \mid y) = (0.187 \mid 1.90)$). Moreover, experiments $C03$ and $D02$ have not been taken into account because for $C03$ the Froude number exceeded 1.0 and for $D02$ a negative displacement was observed.

The application range is limited by the Froude number. For $Fr_1 = 0.0$, and hence $u_{*,1} = 0.0$, the displacement is zero. The same accounts for $Fr_1 = 1.0$ when the first term in Equation 6.33 becomes equal to zero. Consequently, the theoretical application range is given by $0.0 \leq Fr_1 < 1.0$. This means the displacement increases with increasing Froude numbers until the transition from subcritical to supercritical flow conditions. In the upper regime, the water level along the weir decreases and subsequently the side overflow discharge as well. Hence, the ratio Q_D/Q_1 decreases and a greater portion of the flow remains in the main-channel. Under these conditions, significant bed-load transport occurs. The sediments are most likely to be transported and possible deposits are rather washed out as described before for dunes in the upper regime.

Compared to the first relation (Eq. 5.21), adopting the approach by Subramanya and Awasthy (1972), the R^2-value of Equation 6.34 slightly increases from 0.92 to 0.93. Thus, the additional effect of the second term in Equation 6.33 is smaller compared to the first term. This is also indicated by the different exponents (1/4 to 1/2). However, due to the

incorporation of the second term, a more general and wider application range might be assumed.

As discussed in paragraph 5.9.2 the displacement angle can be seen as the initial angle inducing the formation of an oscillatory erosion gutter downstream of the weir. With increasing distance from the weir the erosion gutter and the oscillation of the flow attenuate and will be damped out further downstream.

Concerning the total deposition length (x_{dep}) as well as the repartition of the up- and downstream leg (x_a, x_b)(Fig. 6.7), the indicative ratios summarized in Table 6.7 might be proposed.

Starting with the total deposition length on the right channel bank ($x_{dep,RB}$):

$$\frac{x_{dep,RB}}{L_D} = 1.74 \approx 7/4 \quad \text{or} \quad x_{dep,RB} \approx 7/4 \cdot L_D \tag{6.35}$$

the repartition of the up- and downstream part is given by:

$$\frac{x_{a,RB}}{x_{b,RB}} = \frac{0.48}{0.52} = 0.92 \tag{6.36}$$

From Equation 6.36 it becomes evident that the position of the maximum bed elevation is located almost in the center of the deposit or slightly upstream of the center. Hence, the deposit is weakly left skewed.

To switch from the right channel bank to the left channel bank, the following equation is suggested:

$$\frac{x_{dep,LB}}{x_{dep,RB}} = \frac{1.12}{1.74} = 0.64 \quad \text{or} \quad x_{dep,LB} = 0.64 \cdot x_{dep,RB} \tag{6.37}$$

Finally, the repartition of the upstream and downstream part of the total aggradation on the left channel side can be estimated by the help of the following expression:

$$\frac{x_{a,LB}}{x_{b,LB}} = \frac{0.53}{0.47} = 1.13 \tag{6.38}$$

Equation 6.38 indicates that the deposit is almost centered or slightly right skewed.

6.7.7. Steps for Determination of Bed Morphology by a 2D empirical Approach

In this paragraph the different computational steps for the determination of the shape of the two-dimensional sedimentary deposit as well as the transfer into a channel, river or numerical model are summarized. As has

Table 6.7: Total deposition length (x_{dep}) and repartition of up- and downstream deposition length (x_a, x_b) for the right and left channel bank.

Test series	Right channel bank					Left channel bank				
	$\frac{x_a}{L_D}$ [−]	$\frac{x_b}{L_D}$ [−]	$\frac{x_{dep}}{L_D}$ [−]	$\frac{x_a}{x_{dep}}$ [−]	$\frac{x_b}{x_{dep}}$ [−]	$\frac{x_a}{L_D}$ [−]	$\frac{x_b}{L_D}$ [−]	$\frac{x_{dep}}{L_D}$ [−]	$\frac{x_a}{x_{dep}}$ [−]	$\frac{x_b}{x_{dep}}$ [−]
B	1.18	1.34	2.52	0.47	0.53	0.75	0.69	1.44	0.50	0.50
C	0.60	0.79	1.39	0.44	0.56	0.50	0.53	1.03	0.49	0.51
D	0.60	0.56	1.16	0.52	0.48	0.51	0.36	0.87	0.61	0.39
average	0.82	0.92	1.74	0.48	0.52	0.59	0.53	1.12	0.53	0.47

been mentioned for the 1*D*-model (paragraph 6.5) the calculation procedure corresponds in principle to the reverse way of the development procedure (steps depicted in Fig. 6.11 but from bottom to top).

As has been mentioned for the 1*D*-model an iteration procedure for the determination of the maximum height of the extracted deposit (here: right bank, $z^*_{max,RB}$) is required, since the overflow discharge (Q_D) and the bed-load transport ratio ($\Delta\Phi$) are not known at the beginning.

- Determination of the shape of the deposit on the right and left channel bank:
  - Normalized deposits (right and left channel bank) obtained by the Maxwellian distribution function:
    - Shape factor for the deposit on the right channel bank (n^*_{RB}): Equation 6.18 (or Tab. 6.4),
    - Shape factor for the deposit on the left channel bank (n^*_{LB}): Equation 6.19 (or Eq. 6.20, simplified),
    - Arbitrarily chosen increments for X^* on the right and left channel bank (Eq. 6.4): $0.00 \leq X^* \leq 4.00 \div 6.00$,
    - Height of deposits ($Z^*(X^*)$) for the right and left channel bank: Equation 6.5.
  - Geometry of extracted deposits (right and left channel bank):
    - Abscissa (right bank): $x^* = X^* \cdot x^*_{max,RB}$ with $x^*_{max,RB} \approx 3.57\,m$ (for model scale of $1:30 \div 1:50$) (or using Tab. 6.7),

  - ∗ Ordinate (right bank): $z^* = Z^*(X^*) \cdot z^*_{max,RB}$ with $z^*_{max,RB}$ according to Equation 6.23,
  - ∗ Abscissa (left bank): $x^* = X^* \cdot x^*_{max,LB}$ with $x^*_{max,LB} \approx 2.45\ m$ (for model scale of $1:30 \div 1:50$) (or using Tab. 6.7),
  - ∗ Ordinate (left bank): $z^* = Z^*(X^*) \cdot z^*_{max,LB}$ with $z^*_{max,LB}$ according to Equations 6.27, 6.28 and 6.29 (or Eq. 6.24, simplified).

- Location of deposits relative to side weir:
  - Horizontal coupling point on the right channel bank ($x_{cp,RB}$) obtained by Equation 6.30 (or Eq. 6.31, simplified):
    - ∗ Reduce location range of $x_{cp,RB}$ applying Equation 6.32.
  - Longitudinal shift of the deposit on the left channel bank with respect to the deposit on the right channel bank (Δx^*) obtained by Equations 6.33 and 6.34,
  - Estimation of total deposition length on the right channel bank ($x_{dep,RB}$) using Equation 6.35,
  - Estimation of repartition of up-and downstream deposition length on the right channel bank ($x_{a,RB}$, $x_{b,RB}$) using Equation 6.36,
  - Estimation of total deposition length on the left channel bank ($x_{dep,LB}$) using Equation 6.37,
  - Estimation of repartition of up-and downstream deposition length on the left channel bank ($x_{a,LB}$, $x_{b,LB}$) using Equation 6.38.

6.8. Application of 2D empirical Deposition Model in a numerical Flow Calculation

In order to analyse the prediction accuracy of the $2D$ empirical model, data from the present study has been introduced to the empirical model. In a next step the empirical model has been implemented into a $1D$-numerical flow code. The numerical program DUPIRO used for testing the $1D$-model appeared not be appropriate, since only a horizontal bottom can be introduced for a cross section (see paragraph 8.1 for description of the numerical code DUPIRO). Due to that reason the $1D$-numerical scheme HEC-RAS (version 3.1.2) has been used.

The HEC-RAS side weir discharge coefficient ($C_{D,HEC-RAS}$) is based on the standard weir equation (Eq. A.158) in the following way:

$$Q_D = C_{D,HEC-RAS} \cdot (y - w_D)^{3/2} \cdot L_D \tag{6.39}$$

with Q_D overflow discharge, $C_{D,HEC-RAS}$ side weir discharge coefficient, y flow depth, w_D weir height and L_D weir crest length.

Hence, the coefficients 2/3 and $(2g)^{1/2}$ occurring in the general equation of weirs (Eq. A.158) are included in the HEC-RAS side weir coefficient:

$$C_{D,HEC-RAS} = 2/3 \cdot C_D \cdot \sqrt{2 \cdot g} \tag{6.40}$$

The results from the present study show that for the determination of $C_{D,HEC-RAS}$ the side weir discharge coefficient (C_D) occurring in Equation 6.40 might be computed according to the approach of Hager (1987b) ($C_D = 0.392$ for the present study, Tab. 5.5).

Form roughness is accounted for by the choice of an appropriate roughness coefficient ($n = 1/k_{st}$).

The HEC-RAS computations indicate that on average the following percentage of the measured side overflow discharge (Q_D) is predicted (range 86 % ÷ 94 %):

$$\frac{Q_{D,predicted}}{Q_{D,measured}} \approx 91\ \% \tag{6.41}$$

Thus, the application of the $2D$-model implemented in a $1D$-numerical scheme increases the prediction accuracy from ≈ 85 % of the $1D$-model to ≈ 91 % for the $2D$-model. As has been stated before deviations from measured Q_D-values might be attributed to the precision of the $2D$-model but also to the one-dimensionality of the numerical code and the choice of an appropriate roughness coefficient (k_{st}).

Concluding, the side overflow intensity (Q_D) obtained from the $2D$ empirical model implemented into a $1D$-numerical flow model has to be increased by a factor of ≈ 1/0.91 = 1.10 (instead of 1.18 for the $1D$-model).

6.8.1. Introduction of an additional Interpolation Point to increase Model Accuracy

Finally, a short reflection concerning the shape of the deposit on the right and left sie and their intersection might be given. As has been mentioned in paragraph 6.7.1 the longitudinal profiles used for the determination of the right and left deposit have been extracted for a spanwise strip width of $y_B/B = 0.15$ close to the channel walls ($y_B/B = 0.00 \div 0.15$ for the left bank, $y_B/B = 0.85 \div 1.00$ for the right bank). The corresponding profiles are located in the middle of the strip width, hence $y_B/B = 0.075$ (left bank) and $y_B/B = 0.925$ (right bank). Linking the two profiles linearly yields the

situation presented in Figure 6.17. The analysis revealed that the transition from erosion to deposition (reference level is the mean final bed elevation) is located approximately at $y_B/B = 0.60$ (Fig. 6.9). Using this information a third interpolation point, in addition to the two points on the right and left bank, might be obtained. The elevation of the additional interpolation point can be estimated as being the average elevation of the two points on the right and left channel bank. However, the gain of precision is limited, since the location of the interpolation point is rather close to the center line of the channel ($y_B/B = 0.60$ close to $y_B/B = 0.50 =$ center line).

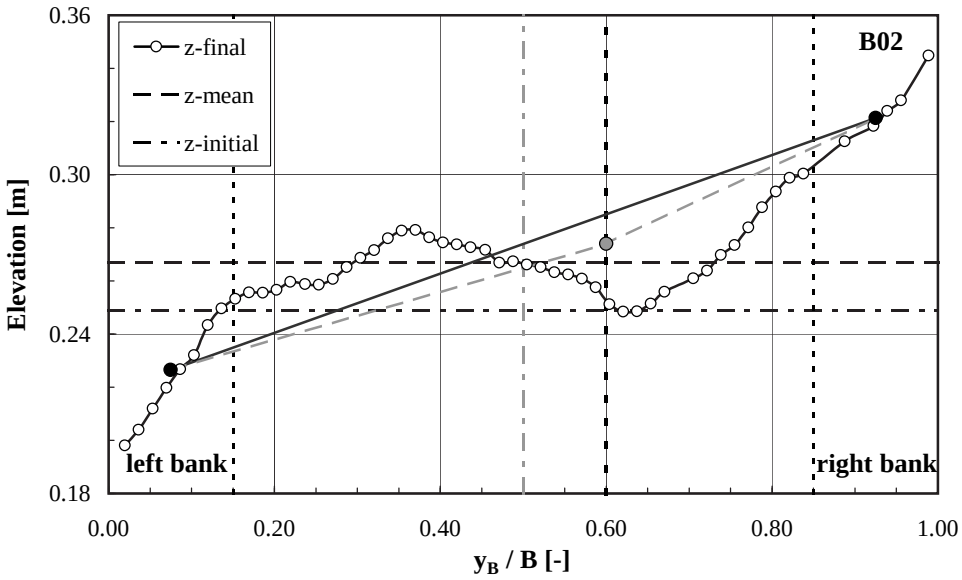

Figure 6.17: Linear intersection of the right and left deposit (profile) with two or three interpolation points. The black thin dotted lines represent the spanwise strip width ($y_B/B = 0.00 \div 0.15$ and $y_B/B = 0.85 \div 1.00$), the two black points the location of the two profiles ($y_B/B = 0.075$ and $y_B/B = 0.925$), the black solid line the intersection between the two profiles, the grey point the additional interpolation point, the black solid dotted line the location of the additional interpolation point ($y_B/B = 0.60$) and the grey dashed line the intersection between the two profiles including the additional interpolation point. The weir crest level elevation is 0.35 m.

6.9. Direct Estimation of Side Overflow

For a detailed determination of side overflow intensity taking into account flow-sediment interaction the empirical models for the description of bed morphology near the weir developed above are suggested to be applied. In some cases, e. g. for the purpose of a pre-design, a first rough estimation of the overflow discharge might be both, desirable as well as sufficient. Therefore, a simple calculation procedure has been developed which is presented in the subsequent paragraph. For the development data from the final experimental conditions has been used. Hence, aggradation phenomena are implicitly incorporated in the equation established.

The approach flow conditions might be expressed by the Gauckler-Manning-Strickler (GMS) equation (Eq A.24):

$$Q_1 = A \cdot k_{st} \cdot R_h^{2/3} \cdot S^{1/2} \tag{6.42}$$

with Q_1 approach flow discharge, $A = B\ y_1$ flow area, B channel width, y_1 approach flow depth, k_{st} Strickler resistance coefficient, R_h hydraulic radius ($R_h \approx y_1$ for $B/y > 10$) and S slope.

The flow over the weir is described by the general equation of weirs (Eq. A.158):

$$Q_D = 2/3 \cdot C_D \cdot \sqrt{2 \cdot g} \cdot (y_1 - w_D)^{3/2} \cdot L_D \tag{6.43}$$

with Q_D overflow discharge, C_D side weir discharge coefficient, g acceleration due to gravity, $y_1 - w_D = h_{D,1}$ pressure head above side weir crest, w_D weir height and L_D weir crest length.

Equations 6.42 and 6.43 are made dimensionless in the following way:

$$\begin{aligned} \frac{Q_1}{B \cdot y_1^{3/2} \cdot \sqrt{g}} &= Fr_1 \\ \frac{Q_D}{L_D \cdot y_1^{3/2} \cdot \sqrt{g}} &= Fr_D \end{aligned} \tag{6.44}$$

with Fr_1 approach flow Froude number and Fr_D weir Froude number since it is based on the overflow discharge and the weir crest length rather than the main-channel discharge and channel width.

Combining Fr_1 and Fr_D and replacing Q_1 and Q_D with Equations 6.42 and 6.43 yields:

$$\frac{Fr_D}{Fr_1} = \frac{Q_D}{Q_1} \cdot \frac{B}{L_D} = \frac{q_D}{q_1} = \frac{2/3 \cdot C_D \cdot \sqrt{2 \cdot g} \cdot (y_1 - w_D)^{3/2}}{k_{st} \cdot S^{1/2} \cdot y_1^{5/3}} \tag{6.45}$$

For the determination of the C_D-value the approaches of Subramanya and Awasthy (1972) and Hager (1987b) are recommended (paragraph 5.3.2).

In Figure 6.18 the ratio Fr_D/Fr_1 is plotted against $h_{D,1}/L_D$.

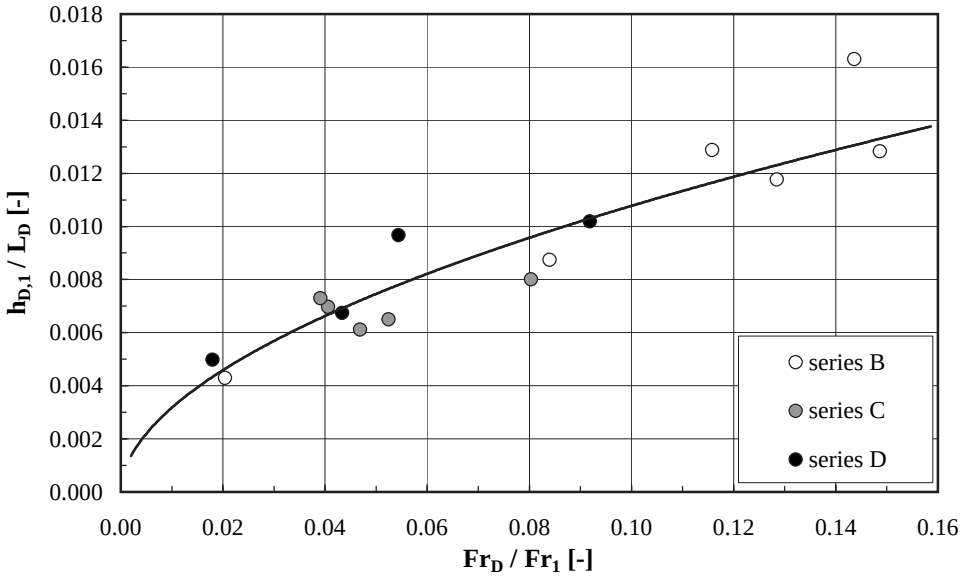

Figure 6.18: Relation of weir Froude number to approach Froude number (Fr_D/Fr_1) versus pressure head to weir length ($h_{D,1}/L_D$) for the determination of side overflow discharge in presence of mobile bed conditions (Eq. 6.46).

The resulting relation is best presented by a power function of the type ($R^2 = 0.87$):

$$\frac{h_{D,1}}{L_D} = 0.037 \cdot \left(\frac{Fr_D}{Fr_1}\right)^{0.53} \tag{6.46}$$

Equation 6.46 indicates that if the pressure head above the weir crest equals zero obviously no outflow occurs. The application range of Equation 6.46 is given by $0.004 \leq h_{D,1}/L_D \leq 0.016$.

Usually, the parameters $h_{D,1}$, L_D and the Froude number (Fr_1) are known or can be easily determined. The side overflow (Q_D) is then computed directly from Equation 6.44.

6.10. Influence of experimental Boundary Conditions

Since the parameter time does not explicitly occur in the models developed, the influence of time is discussed in this paragraph. Moreover, reflections with

respect to the constant channel width in the experiments are given. Finally, the choice of approach flow conditions at the upstream weir corner are reviewed and the downstream boundary conditions with respect to the mobile bed evolution are discussed.

6.10.1. Influence of Time

The formation and the influence of the deposition have to be seen in context with the duration time of the flume experiments. A major concern might be related to the fact whether the aggradation would develop in a different way for longer experiment duration and whether a final bed situation was achieved.

In this context the following three aspects might be discussed:

- Transient evolution of side overflow (Q_D),
- Shape of aggradation downstream of side weir and
- Duration of flood peak while diversion devices such as side weirs are in operation.

Regarding the transient evolution of side overflow the experiments have been stopped when the diverted discharge has been almost constant over a certain time increment (paragraph 5.3.2, Fig. 5.7 and Tab. 5.4). This circumstance might be indicative for the fact that the mobile bed and the sedimentary deposit have developed towards a rather stable situation, shape and (maximum) height at this time increment.

To get an idea of how the bed would develop for a longer experiment duration $1D$-numerical simulations with bed-load transport have been performed using the numerical code DUPIRO. As an example experiment $B02$ with a test duration of 183 min has been chosen. The modelled time was 540 min, thus three times longer than the actual test period. The numerical boundary conditions correspond to those of the experiment with $S_0 = 0.002$, $B = 1.50\ m$, $L_D = 3.00\ m$, $Q_1 = 0.181\ m^3/s$ and $k_{st} \approx 64\ m^{1/3}/s$. Bed-load has been calculated with the simplified formula of Smart and Jäggi (1983) (Eq. A.140). Equilibrium transport conditions were used. The deposition volume per unit width has been determined with reference to the initial flat bed between the upstream weir corner and the channel exit ($x = 5.00 \div 18.00\ m$). The results are presented in Figure 6.19.

It becomes evident from Figure 6.19 that both the deposited volume per unit width as well as the diverted discharge (Q_D) develop towards steady conditions from $t \approx 210\ min$ onwards. The actual experiment duration ($t = 183\ min$) is rather close to this time. Moreover, it might be concluded that no significant changes would occur for considerably longer experiments.

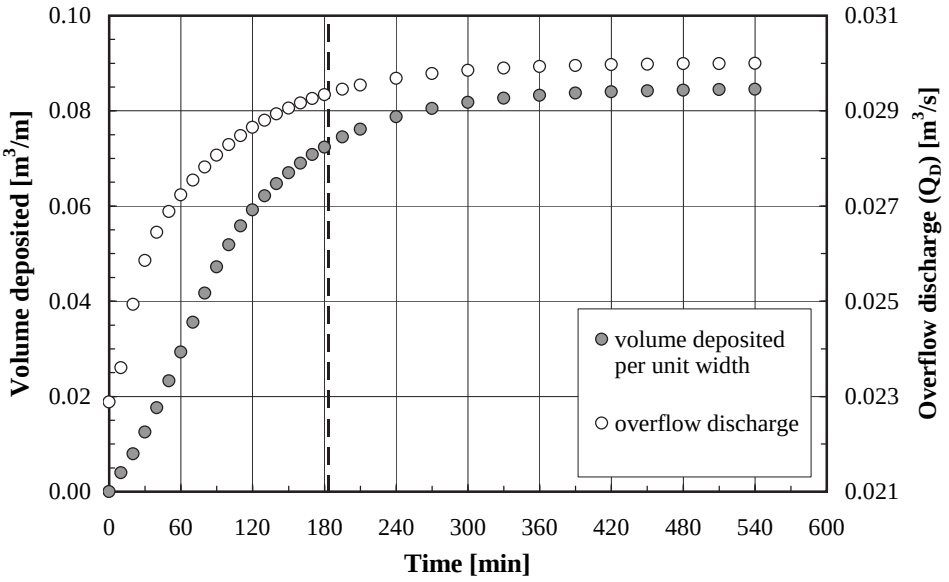

Figure 6.19: Transient evolution of deposition volume per unit width and side overflow discharge (Q_D). Results from a $1D$-numerical simulation using DUPIRO. The boundary conditions for the numerical simulation correspond to experiment $B02$. The dashed line indicates the actual duration of the flume experiment ($t = 183\ min$).

With regard to the shape of the deposit downstream of the weir, if for one reason or other the experiment duration would have been too short, for $t \rightarrow \infty$ the deposit would develop towards a longer and smoother lee side with slightly lower vertical expansion losses but no considerable change in maximum deposition height and location of maximum deposition. This is shown in Figure 6.20. In paragraph 5.8 it has been demonstrated exemplarily that the main properties of the deposit affecting side overflow are its maximum height and location as well as its two-dimensionality (horizontal contraction and expansion losses) but not its lee side shape. Consequently, the dominant aggradation characteristics are adequately represented by the duration chosen for the experiments.

Concerning the duration of flood peaks while overflow devices are in operation, typical flood hydrographes (e. g. October flood 2000) on the Rhone river upstream of Lake Geneva in Switzerland (Branson) have a duration of $t_{prototype} \approx 145\ h$ (rising stage $\approx 45\ h$, peak period $\approx 20\ h$, falling stage $\approx 80\ h$). With respect to the rising stage, during a considerable time increment a lateral diversion structure such as a side weir or an overflow dam will not be in operation since the design discharge usually refers to a flood event with a hundred year return period (HQ_{100}). As far as the falling stage is

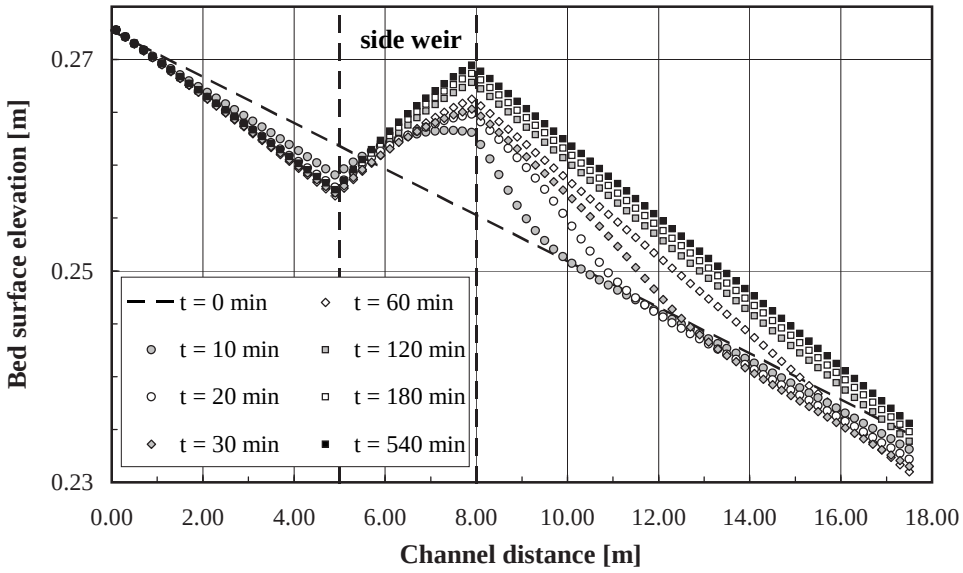

Figure 6.20: Transient evolution of longitudinal bed surface. Results from a $1D$-numerical simulation using DUPIRO. The boundary conditions for the numerical simulation correspond to experiment $B02$. The dashed line indicates the side weir position (crest height at $z = 0.35\ m$). The actual duration of the flume experiment was $t = 183\ min$.

concerned sediments accumulated during the peak period are rather likely to be eroded, thus reducing the effect of the sedimentary deposit (Fig. 8.3). The peak period when the diversion structure is in operation only lasts a rather short time increment. For the Rhone river (Branson) mentioned before the peak period of a hundred year return flood ($HQ_{100} = 1250\ m^3/s$) corresponds to $t_{prototype} \approx 20\ h$. Using the model length scale factor from the present study of $\lambda_L \approx\ 1:50$ (paragraph 4.1) the peak duration of $t_{prototype} \approx 20\ h$ results in $t_{model} \approx 170\ min$, hence corresponding fairly well to the experimental duration time varying between 117 and 245 min.

Furthermore, De Vries (1975) and Kerssens and Van Urk (1986) stated with respect to the morphological time scale that equilibrium conditions may not be achieved in nature. Thus, for a short term flood event final equilibrium conditions will probably never be attained.

Consequently, a rather long experiment duration time including a great part of the rising and falling stage of the hydrograph does not seem to correspond to natural conditions and the duration of the experiments appears to be adequately chosen.

6.10.2. Influence of Channel Width

The channel width represents an important parameter influencing the formation of a sedimentary deposit near the weir. In the following different channel widths and their impact on aggradation and side overflow intensity are investigated. Since the channel width in the experiments has been constant ($B = 1.50\ m$), the width has been varied numerically using the $1D$-code DUPIRO (chapter 8).

The numerical simulations refer to the boundary conditions of experiment $B02$ ($Q_1 = 0.181\ m^3/s$, $S_{0,ini} = 0.002$, $k_{st} \approx 55\ m^{1/3}/s$ (resistance including form roughness), $L_D = 3.00\ m$ and $t = 183\ min$). The different widths studied were $B = 1.00\ m$, $B = 1.20\ m$, $B = 2.00\ m$ and $B = 3.00\ m$. To be dimensionally independent the various widths have been normalized by the constant weir crest length of $L_D = 3.00\ m$. Hence, the following L_D/B-ratios were obtained: $L_D/B = 3.00$, $L_D/B = 2.50$, $L_D/B = 1.50$ and $L_D/B = 1.00$. The reference ratio from the present study is $L_D/B = 2.00$. Thus, the ratios correspond to 1.50, 1.25, 0.75 and 0.50 times the reference ratio (Table 6.8).

Table 6.8: Different crest length to channel width ratios (L_D/B) used for comparison with the reference case $L_D/B = 2.00$ (experiment $B02$) using the $1D$-numerical model DUPIRO.

Case	Crest length L_D $[m]$	Channel width B $[m]$	Ratio L_D/B $[-]$	Multiple of reference ratio $L_D/B = 2.00$ $[-]$
case 1	3.00	1.00	3.00	1.50
case 2	3.00	1.20	2.50	1.25
reference case	3.00	1.50	2.00	1.00
case 3	3.00	2.00	1.50	0.75
case 4	3.00	3.00	1.00	0.50

In Figure 6.21 the results from the numerical computations with bed-load transport are presented. It can be seen that for the smallest L_D/B-ratio ($L_D/B = 1.00$, widest channel) almost no influence of aggradation on the side overflow intensity (Q_D/Q_1) can be identified. Moreover, side overflow does not change with time. For $L_D/B = 1.50$ a slight influence appears to be present but time is of no importance as well. With increasing L_D/B-ratios

the channel becomes narrower and a significant impact on overflow discharge can be observed. For higher L_D/B-ratios transient phenomena occur.

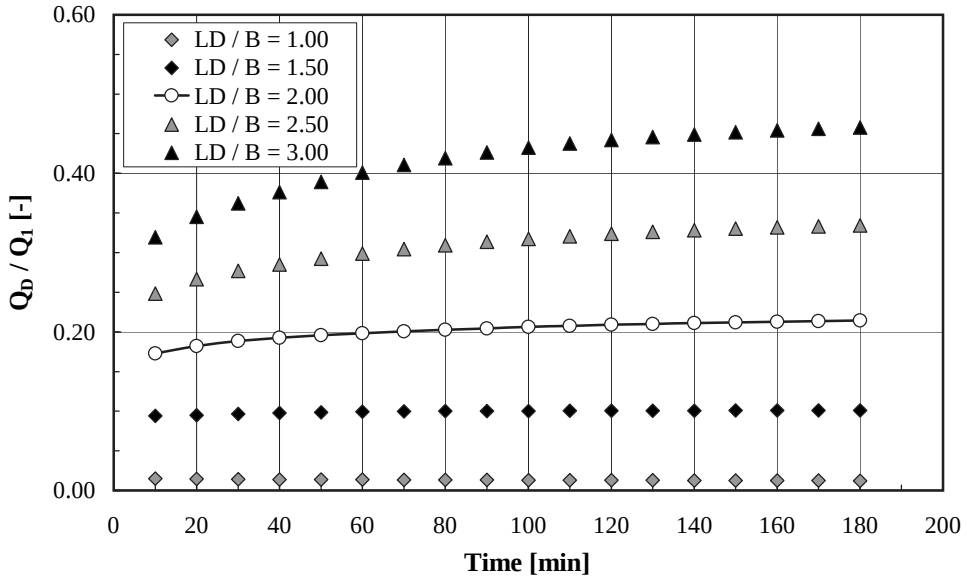

Figure 6.21: Transient evolution of the ratio side overflow to approach discharge (Q_D/Q_1) for different crest length to channel width ratios (L_D/B). The numerical boundary conditions correspond to experiment $B02$ ($Q_1 = 0.181\ m^3/s = const.$, $S_{0,ini} = 0.002$, $k_{st} \approx 55\ m^{1/3}/s = const.$ (resistance including form roughness), $L_D = 3.00\ m = const.$, $t = 183\ min$). The different main-channel widths (B) were chosen to be $B = 1.00\ m$ ($L_D/B = 3.00\ m\ /\ 1.00\ m = 3.00$), $B = 1.20\ m$ ($L_D/B = 2.50$), $B = 1.50\ m$ ($L_D/B = 2.00$, present study), $B = 2.00\ m$ ($L_D/B = 1.50$) and $B = 3.00\ m$ ($L_D/B = 1.00$). Results from a $1D$-numerical simulation using DUPIRO.

The reason for this behavior is based on the fact that the progress of silting-up the cross section is more pronounced for a narrow channel than for a wide channel. In Figure 6.22 the different L_D/B-ratios are plotted against the ratio of final bed elevation to initial bed elevation (z_{fin}/z_{ini}) at the downstream weir corner (location of maximum aggradation). It becomes evident that for a wide channel (small L_D/B-ratio, e. g. $L_D/B = 1.00$) the ratio z_{fin}/z_{ini} is almost equal to unity ($z_{fin} \approx z_{ini}$), whereas for the narrow channel (e. g. $L_D/B = 3.00$) the final bed elevation is 25 % times higher than the initial one ($z_{fin} = 1.25\ z_{ini}$).

Figure 6.23 represents the final Q_D/Q_1-values from Figure 6.21 at $t = 180\ min$ for the different L_D/B-ratios. Assuming roughly that L_D/B and

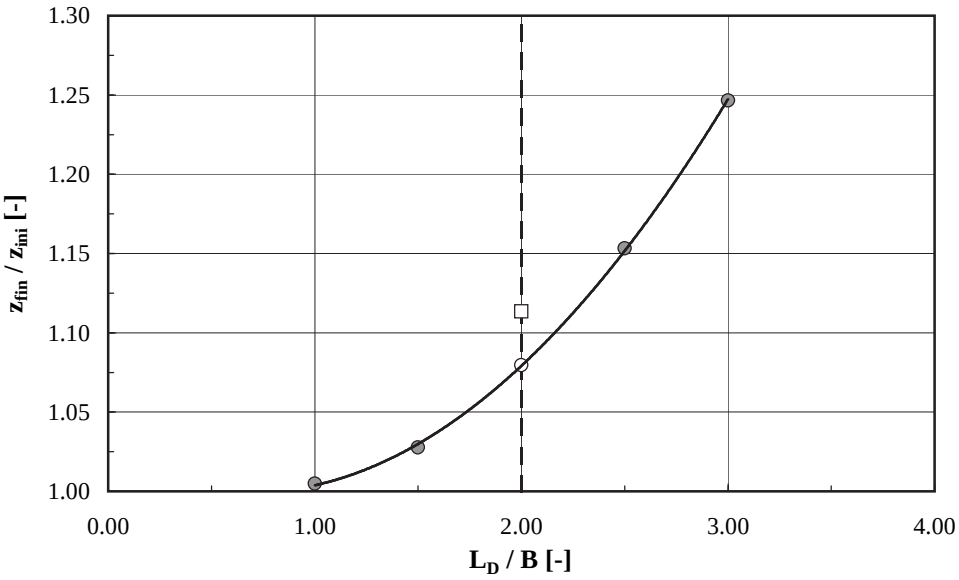

Figure 6.22: Evolution of the ratio final bed elevation to initial bed elevation (z_{fin}/z_{ini}) at the downstream weir corner for different crest length to channel width ratios (L_D/B). z_{fin}/z_{ini} refers to the last time step at $t = 180\ min$ in Figure 6.21. $L_D/B = 2.00$ is the ratio from the present study (dashed line). The white square is the measured z_{fin}/z_{ini}-value for experiment $B02$. The numerical boundary conditions correspond to experiment $B02$. Results from a $1D$-numerical simulation using DUPIRO.

Q_D/Q_1 are related by a linear correlation ($R^2 = 0.99$) it appears that the overflow discharge increases with:

$$\frac{Q_D}{Q_1} = 0.23 \cdot \frac{L_D}{B} - 0.23 \tag{6.47}$$

A physically more meaningful expression is given by the second order polynom of the type ($R^2 = 0.99$):

$$\frac{Q_D}{Q_1} = 0.02 \cdot \left(\frac{L_D}{B}\right)^2 + 0.14 \cdot \frac{L_D}{B} - 0.15 \tag{6.48}$$

The expression indicates that for $L_D/B = 4.75$ the ratio Q_D/Q_1 equals 1.00. Hence, for $B = L_D/4.75 = 0.63\ m$ the total approach discharge would transit over the weir ($Q_D = Q_1$). The value of $B = 0.63\ m$ would correspond to a $0.63\ m/1.5\ m = 42\ \%$ narrower channel or a multiple of $4.75/2.0 = 2.38$ of the reference ratio (Table 6.8). Of course, these reflections are rather

theoretical, since under natural conditions the cross section will not silt up homogenously. Flow will probably pass through at the lowest elevation. Due to local flow acceleration bed material will erode at this location and a certain portion of the flow will always continue in the main-channel.

Comparing measured and computed Q_D/Q_1-ratios for the reference case ($L_D/B = 2.00$) (Fig. 6.23), a difference of $(Q_D/Q_1)_{comp.}/(Q_D/Q_1)_{meas.} = 0.22/0.29 = 0.77$ is determined. This discrepancy is mainly due to the fact that the $1D$-numerical model does not represent the 2-dimensionality of the deposit. Hence, local energy losses induced through lateral constriction and expansion are not captured. Moreover, a certain degree of error might be incorporated in the choice of the Strickler-value ($k_{st} \approx 55\ m^{1/3}/s$).

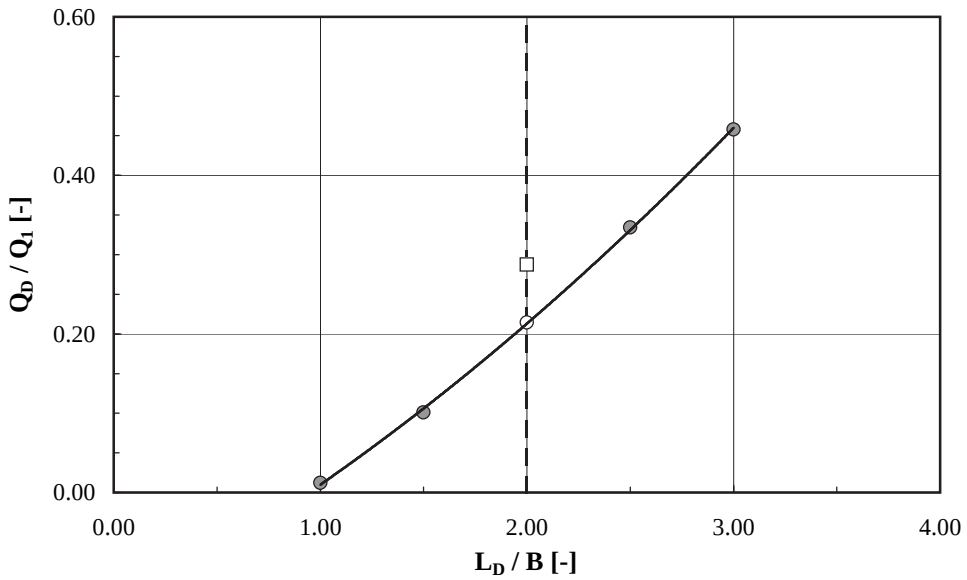

Figure 6.23: Evolution of the ratio side overflow to approach discharge (Q_D/Q_1) for different crest length to channel width ratios (L_D/B). Q_D/Q_1 refers to the last time step at $t = 180\ min$ in Figure 6.21. $L_D/B = 2.00$ is the ratio from the present study (dashed line). The white square is the measured Q_D/Q_1-value for experiment $B02$. The numerical boundary conditions correspond to experiment $B02$. Results from a $1D$-numerical simulation using DUPIRO (Eqs 6.47 and 6.48).

As far as crest length to channel width ratios and their application range are concerned, test series D has a L_D/B-ratio of $5.00\ m/1.50\ m = 3.33$. The corresponding measured Q_D/Q_1-value for experiment $D04$ yields 0.37. Taking the same boundary conditions as in the experiment and using the same L_D/B-ratio of 3.33 but instead of $5.00\ m/1.50\ m = 3.33$ imposing

3.00 m/0.90 m = 3.33 gives a numerically computed Q_D/Q_1-value of 0.44. Obviously, the two Q_D/Q_1-ratios are rather close to each other (0.37 / 0.44 = 84). From these indicative computations it might be concluded that the L_D/B-application range from the present study appears to be generally valid ($2.00 \leq L_D/B \leq 4.00$).

Finally it has to be kept in mind that the results presented in Figures 6.21, 6.22 and 6.23 originate from a $1D$-numerical model. Hence, the aggradation due to lateral water withdrawal is distributed homogeneously over the entire channel width. Under natural conditions deposition effects will be more substantial in the weir region and less pronounced in the channel region far opposite to the side weir.

6.10.3. Influence of Approach Flow Conditions

Usually, approach parameters such as the Froude number or water depth are calculated with normal flow conditions which are considered being similar to flow conditions at the upstream weir corner (section 1) (Fig. A.15, a). Subramanya and Awasthy (1972) stated that the flow depth at section 1 was essentially the same as the one at a section small distance upstream of section 1 ($\approx$ 5 % difference). Furthermore, the draw-down effect of the side weir is assumed to be negligible (e. g. Ranga Raju et al. (1979)).

In the following the assumptions stated above are investigated. In Figure 6.24 measured flow depths (y) at sections 0 (y_0), 01 (y_{01}) and 1 (y_1) are compared (see Fig 5.13 for definition). The Figure suggests that there is almost no difference between flow depths at section 01 and 1. The difference amounts to $y_1/y_{01} = 0.122\ m/0.124\ m = 0.98$. With respect to y_0 a value of 0.128 m has been measured. This section does not appear to constitute an adequate reference cross section, since it is located rather close to the channel entrance (effects of entrance boundary conditions due to sediment supply and others).

In addition to the reflections above numerical calculations using the $1D$-code DUPIRO have been performed. The experimental channel of $L \approx 18.00\ m$ has been extended to $L = 100.00\ m$ in the numerical model. The boundary conditions refer to experiment $B02$ ($Q_1 = 0.181\ m^3/s$, $S_0 = 0.002$, $L_D = 3.00\ m$ and $k_{st} \approx 55\ m^{1/3}/s$). The side weir is introduced at $x = 50.00\ m$. The length of the deposit is $x_{dep} = 9.00\ m$ with a repartition of $x_a/x_b = 3.00\ m/6.00\ m = 0.50$. The height corresponds to $z_{max} = 0.02\ m$.

In a first simulation (scenario 1) neither a side weir nor a deposit have been implemented in the main-channel. The normal flow depth (y_n) for the reference scenario corresponds to $y_n = 0.176\ m$. In a second computation (scenario 2) a side overflow has been installed and in a third simulation (scenario 3) both, a side overflow and a deposit have been introduced.

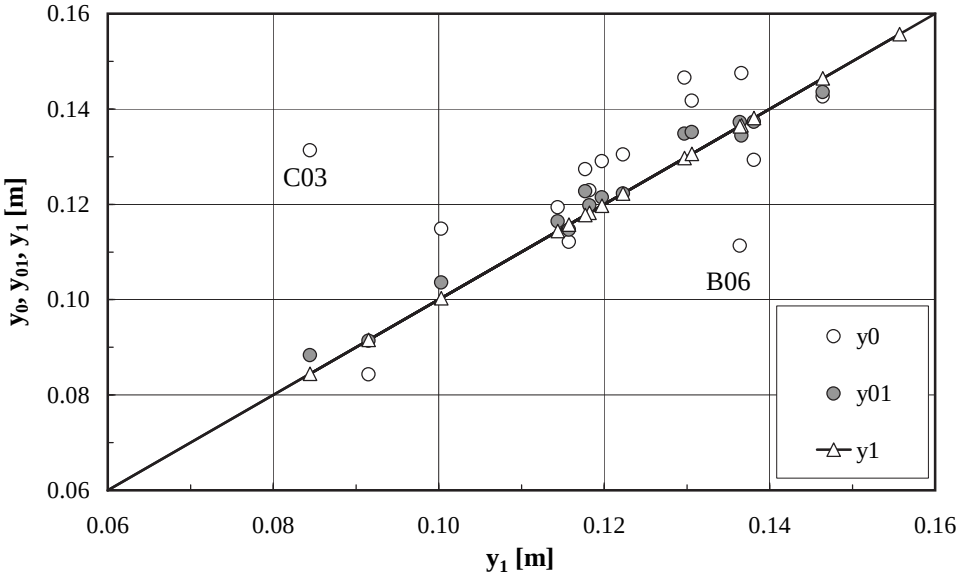

Figure 6.24: Comparison of measured flow depths (y) at different cross sections (see Fig. 5.13 for definition).

Subsequently it has been determined at which distance upstream of the beginning of the weir the flow depth for the two scenarios (scenario 2 and 3) differs by more than 5 % and by more than 10 %, respectively, from the normal flow depth (y_n) of the reference scenario. The computed water levels are presented in Figure 6.25.

The results for the 5 %-threshold indicate that for scenario 2 (overflow but no deposit) the normal flow depth of $y_n = 0.176\ m$ is reached at $x = 31.50\ m$, hence $50.00\ m - 31.50\ m = 18.50\ m$ upstream of the beginning of the weir. This distance would correspond to a factor of $18.50\ m / 3.00\ m \approx 6.2$ or $\approx 6.2 L_D$. Setting a deposit into the main-channel (scenario 3) the distance corresponds to $x = 34.00\ m$, hence $16.00\ m$ or $\approx 5.3 L_D$ upstream of the weir. For the 10 %-threshold the distance amounts to $x = 42.50\ m$ or $\approx 2.5 L_D$ (scenario 2). For scenario 3 a value of $x = 45.00\ m$ or $\approx 1.7 L_D$ is obtained.

These simulations reveal that the deposit reduces the draw-down effect of the water level by the side weir. Hence, approach flow conditions smoothly develop towards normal flow conditions obtained for the case without side weir and without deposit. The assumption referred to above (normal flow conditions similar to approach flow conditions at upstream weir corner (Subramanya and Awasthy (1972))) seems to be even more justified for the situation with deposit than without. This of course depends on the extent and the location of the deposit as has been demonstrated in paragraph 5.8. In the simulations the deposit has been rather flat. For a more pronounced deposit the reduction of the draw-down effect will be even more substantial.

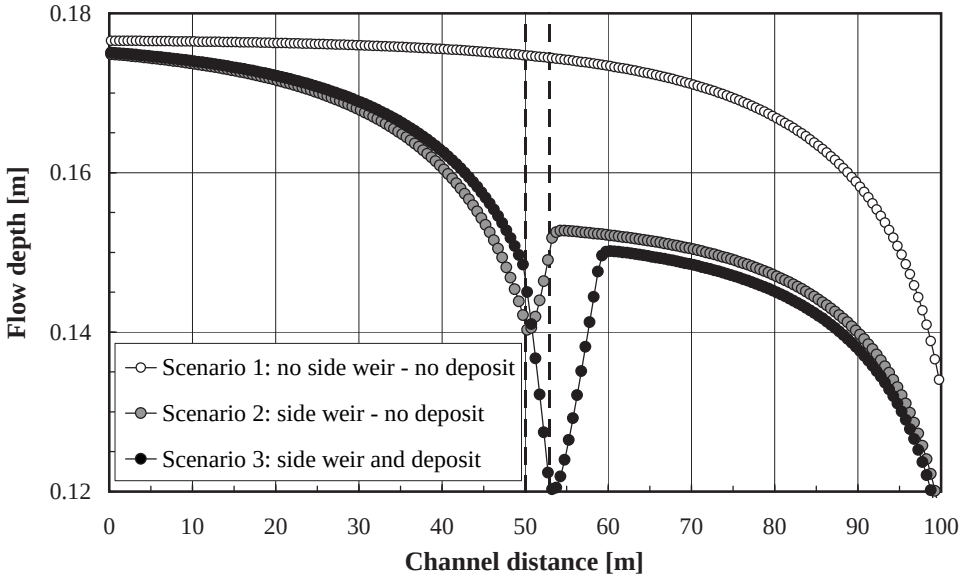

Figure 6.25: Streamwise evolution of flow depth for different scenarios. Scenario 1: No side weir and no deposit. Scenario 2: Side weir but no deposit. Scenario 3: Side weir and deposit. The dashed line indicates the side weir position. Results from a $1D$-numerical simulation using DUPIRO.

Following these reflection it might be concluded that the upstream weir corner represents a reasonable choice for the determination of approach flow conditions.

6.10.4. Influence of downstream Boundary Conditions

The downstream boundary condition of the flume is represented by a plate to fix and keep the sediment layer in place (fixpoint). Under the assumption of the same experiment duration the location of the downstream fixpoint might influence the maximum height of the deposit (z_{max}) by the adjustment of a new equilibrium slope for the reduced bed-load transport capacity (rotational or parallel aggradation). This phenomenon is presented schematically in Figure 6.26.

The figure shows the evolution of the sedimentary deposit for different time steps ($t_1 \div t_4$). At time step t_{4a} a stable deposit has formed for which the side overflow is constant ($Q_D = const.$). For a longer experiment duration ($t \rightarrow \infty$) the height of the deposit will not change any longer and sediments will be deposited downstream of the side weir until the volume to the next fixpoint (fixpoint a) is completely filled up with bed material (see also Figs 6.19

and 6.20). Hence, the maximum height of the deposit is not depending on the location of the downstream fixpoint (fixpoint a).

Assuming now the flume would be somewhat shorter and limited by fixpoint b instead of fixpoint a. In this case the deposit will form in the same way until time step t_3. Thereafter, for time step t_{4b} the fixpoint b will determine the maximum height of the deposit, since a new equilibrium slope for the reduced bed-load transport capacity develops.

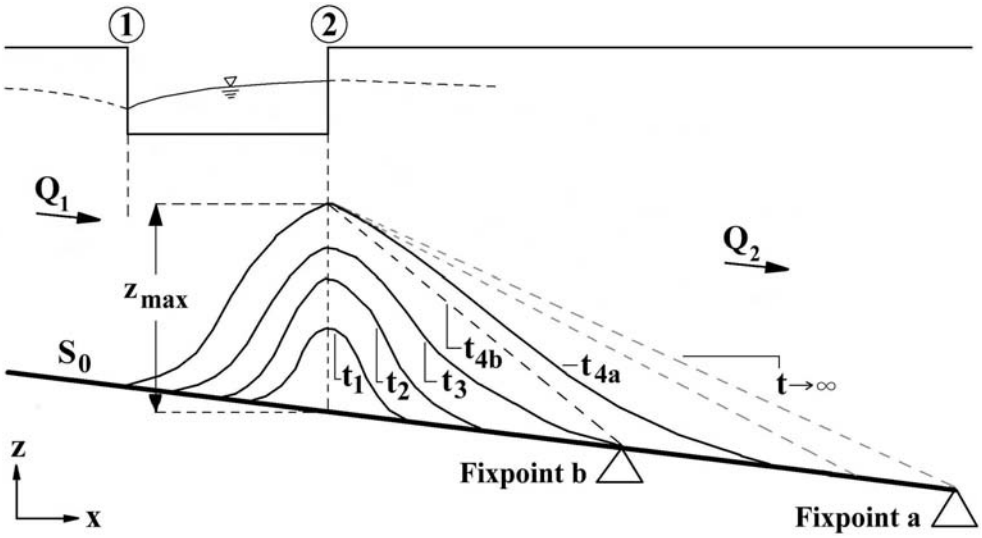

Figure 6.26: Definition sketch illustrating the influence of the location of the downstream fixpoint (fixpoint a and fixpoint b) on the maximum height of the deposit (z_{max}).

To check whether the location of the downstream fixpoint might have influenced the maximum height of the deposit (z_{max}) the downstream equilibrium slope being able to transport the upstream sediment supply ($q_{sb,1}$) with the reduced downstream main-channel discharge (Q_2, q_2) has been determined for the experiments owing large downstream deposition volumes reaching almost until the end of the flume (e. g. experiment $C02$, Fig. 8.2). Based on this slope the bed elevation near the side weir (downstream weir corner) can be computed and compared with the measured maximum height of the deposit. For the determination of the equilibrium slope the bed-load transport formula of Smart and Jäggi (1983) has been used (Eq A.139).

In the following the verification procedure is presented exemplarily for experiment $C02$. Assuming a stable height of the deposit, the sediments supplied at the channel entrance are completely transported through the weir region to the downstream channel reach and $Q_{s,D} = 1.24\ kg/min$ are transported over the weir (Tab. 5.15), the bed-load material to be transported by the reduced main-channel flow (q_2) is $q_{sb,2} = 3.18 \cdot 10^{-4}\ m^2/s$. For this bed-load quantity the equilibrium slope according to the approach of Smart

and Jäggi (1983) yields $S = 0.0125$. Knowing the distance of $x = 9.322\ m$ between the downstream weir corner and the channel exit (plate) and having the height of the plate of $z = 0.26\ m$ in mind a maximum bed elevation of $z_{max,Smart/Jaeggi} = 0.377\ m$ is obtained. This height exceeds the maximum height of the deposit ($z_{max} = 0.284\ m$) and even the height of the weir crest level of $z = 0.35\ m$.

It has been shown in paragraphs 5.7 (Tab. 5.14) and 8 (Tab. 8.1) that the measured bed-load transport might significantly differ from the bed-load transport capacity predicted by approaches from literature. For the present example a factor of about 11.60 has to be applied for the downstream channel reach ($q_{sb,2,measured} = 2.61 \cdot 10^{-4}\ m^2/s$, $q_{sb,2,Smart/Jaeggi} = 2.25 \cdot 10^{-5}\ m^2/s$). Introducing the correction factor of 11.60 the equilibrium slope according to the approach of Smart and Jäggi (1983) amounts to $S = 0.0032$ and the bed elevation at the downstream weir corner to $z_{max,Smart/Jaeggi} = 0.29\ m$. Hence, the measured maximum height of the deposit ($z_{max} = 0.284\ m$) is almost the same than the height obtained by the bed-load transport formula.

The verification indicated that the maximum bed level obtained by the application of a bed-load transport formula has always been less or at least equal to the measured maximum height of the deposit. From these investigations it can be concluded that the location of the downstream fixpoint has no influence on the maximum height of the deposit.

7. Computation Method, Example and Case Study

In this paragraph two examples of the application of the empirical models developed as well as the proposed computation procedure are presented.

The first example of computation refers to boundary conditions related to the flume experiments. The second example refers to prototype conditions and represents a case study on the Rhone river upstream of Lake Geneva in Switzerland.

Basically, the following three steps have to be processed:

- Step 1: Determination of geometry of the empirical deposit.
- Step 2: Implementation of the empirical deposit into a flow calculation program.
- Step 3: Choice of appropriate boundary conditions in the flow calculation program (e. g. flow resistance accounting for bed forms).

7.1. Example of Computation related to experimental Conditions

Since several steps of the computation procedure of the $1D$ and $2D$ empirical approaches are similar but the $2D$ model requires additional calculation steps, the demonstration of the computation process is performed for the $2D$-approach.

Assuming a channel with a bed covered with dunes (no ripples). The following (final) geometrical and hydraulic characteristics are given or have been derived (dimensions refer to the experiments and not to prototype conditions):

- Channel width: $B = 1.50\ m$,
- Bottom slope: $S_0 = 0.10\ \%$,
- Grain diameter of bed material: $d_{50} = 0.72\ mm$, $d_{65} = 1.12\ mm$, $d_{90} = 2.28\ mm$,

- Weir length: $L_D = 3.00\ m$,
- Weir height: $w_D = 0.11\ m$ (absolute crest level $z = 0.35\ m$),
- Approach Discharge: $Q_1 = 0.131\ m^3/s$,
- Outflow Discharge (final situation after iteration): $Q_D = 0.022\ m^3/s$,
- Flow depth at upstream weir corner: $y_1 = R_{h,1} = 0.130\ m$,
- Pressure head at upstream weir corner: $h_{D,1} = 0.026\ m$,
- Froude number at upstream weir corner: $Fr_1 = 0.60$,
- Shear velocity at upstream weir corner: $u_{*,1} = 0.036\ m/s$,
- Ratio of up- to downstream bed-load transport capacity (final situation after iteration): $\Delta\Phi = 0.76$.

Solution:

- Step 1: Determination of the geometry of the empirical deposit on the right and left channel bank:
  - Normalized deposits (right and left channel bank) obtained by the Maxwellian distribution function:
    - Shape factor for the deposit on the right channel bank (n^*_{RB}) obtained by Equation 6.18 (or Tab. 6.4):

$$n^*_{RB} = 5.52.$$

    - Shape factor for the deposit on the left channel bank (n^*_{LB}) obtained by Equation 6.19 (or Eq. 6.20, simplified):

$$n^*_{LB} = \left(\frac{1}{8} \cdot \frac{L_D}{B} + \frac{2}{7}\right) \cdot n^*_{RB}$$

$$= \left(\frac{1}{8} \cdot \frac{3.00}{1.50} + \frac{2}{7}\right) \cdot 5.52 = 2.96.$$

    - Arbitrarily chosen increments for X^* on the right and left channel bank (Eq. 6.4): $0.00 \leq X^* \leq 4.00 \div 6.00$.
    - Height of deposits ($Z^*(X^*)$) for the right and left channel bank obtained by Equation 6.5.
  - Geometry of extracted deposits (right and left channel bank):

* Abscissa (right bank): $x^* = X^* \cdot x^*_{max,RB}$ with $x^*_{max,RB} \approx 3.57\ m$ (for model scale of $1:30 \div 1:50$) (or using Tab. 6.7).

* Ordinate (right bank): $z^* = Z^*(X^*) \cdot z^*_{max,RB}$ with $z^*_{max,RB}$ according to Equation 6.23:

$$z^*_{max,RB} = \frac{h_{D,1}}{2/3 \cdot \left[\Delta\Phi/(Q_D/Q_1) \cdot \left(3 \cdot \Delta\Phi - \frac{9}{5}\right) + \frac{9}{4}\right]^{4/5}}$$

$$= \frac{0.026}{2/3 \cdot \left[0.76/(0.022/0.131) \cdot \left(3 \cdot 0.76 - \frac{9}{5}\right) + \frac{9}{4}\right]^{4/5}}$$

$$= 0.05\ m.$$

* Abscissa (left bank): $x^* = X^* \cdot x^*_{max,LB}$ with $x^*_{max,LB} \approx 2.45\ m$ (for model scale of $1:30 \div 1:50$) (or using Tab. 6.7).

* Ordinate (left bank): $z^* = Z^*(X^*) \cdot z^*_{max,LB}$ with $z^*_{max,LB}$ according to Equations 6.27, 6.28 and 6.29 (or Eq. 6.24, simplified):

$$\Delta z_{RB-LB} = tan\ \phi_{z,LB} \cdot B$$

$$= 11.16 \cdot \left[\left(\frac{Q_D}{Q_1}\right)^{-2/3} \cdot \left(\frac{L_D}{B}\right)^{1/3} \cdot \left(\frac{h_{D,1}}{L_D}\right)^{8/5}\right] \cdot B$$

$$= 11.16 \cdot \left[\left(\frac{0.022}{0.131}\right)^{-2/3} \cdot \left(\frac{3.00}{1.50}\right)^{1/3} \cdot \left(\frac{0.026}{3.00}\right)^{8/5}\right] \cdot 1.50$$

$$= 0.023 \cdot 1.50 = 0.035\ m$$

and (Eq. 6.29):

$$z^*_{max,LB} = z^*_{max,RB} - \Delta z_{RB-LB}$$

$$= 0.05 - 0.035 = 0.015\ m.$$

- Step 2: Implementation of the empirical deposit into a flow calculation program (location of deposits relative to side weir and creation of cross sectional profiles):

– Horizontal coupling point relative to downstream weir corner on the right channel bank ($x_{cp,RB}$) obtained by Equation 6.30 (or Eq. 6.31, simplified). Since $Fr_1 = 0.60$, the entire range of Equation 6.30 is applied (Eq. 6.32):

$$-0.34 \cdot L_D \leq x_{cp,RB} \leq 0.12 \cdot L_D \quad \text{(entire range)}$$

$$-0.34 \cdot 3.00 = -1.02\ m \leq x_{cp,RB} \leq 0.36\ m = 0.12 \cdot 3.00.$$

With reasonable accuracy the downstream weir corner can be chosen as the horizontal coupling point ($x_{cp,RB}$).

– Horizontal coupling point on the left channel bank relative to horizontal coupling point on the right channel bank ($x_{cp,RB}$) determining the longitudinal displacement (Δx^*) obtained by Equations 6.33 and 6.34:

$$\Delta x^* = \left(23.26 \cdot x^2 - 0.11 \cdot x\right) \cdot L_D$$

with:

$$x = \left(1 - \frac{3 \cdot Fr_1^2}{2 + Fr_1^2}\right)^{1/2} \cdot \left(\frac{u_{*,1}}{\sqrt{g \cdot L_D}}\right)^{1/4}$$

$$= \left(1 - \frac{3 \cdot 0.60^2}{2 + 0.60^2}\right)^{1/2} \cdot \left(\frac{0.036}{\sqrt{9.81 \cdot 3.00}}\right)^{1/4}$$

$$= 0.212.$$

Finally, using Equation 6.34:

$$\Delta x^* = \left(23.26 \cdot 0.212^2 - 0.11 \cdot 0.212\right) \cdot 3.00$$

$$= 3.054\ m.$$

– Estimation of total deposition length on the right channel bank ($x_{dep,RB}$) using Equation 6.35:

$$x_{dep,RB} = 7/4 \cdot L_D$$

$$= 7/4 \cdot 3.00 = 5.25\ m.$$

– Estimation of repartition of up-and downstream deposition length on the right channel bank ($x_{a,RB}$, $x_{b,RB}$) using Equation 6.36 and Table 6.7:

$$x_{a,RB} = 0.48 \cdot x_{dep,RB}$$

$$= 0.48 \cdot 5.25 = 2.52\ m,$$

$$x_{b,RB} = 0.52 \cdot x_{dep,RB}$$

$$= 0.52 \cdot 5.25 = 2.73\ m.$$

– Estimation of total deposition length on the left channel bank ($x_{dep,LB}$) using Equation 6.37:

$$x_{dep,LB} = 0.64 \cdot x_{dep,RB}$$

$$= 0.64 \cdot 5.25 = 3.36\ m.$$

.

– Estimation of repartition of up-and downstream deposition length on the left channel bank ($x_{a,LB}$, $x_{b,LB}$) using Equation 6.38:

$$x_{a,LB} = 0.53 \cdot x_{dep,LB}$$

$$= 0.53 \cdot 3.36 = 1.78\ m,$$

$$x_{b,LB} = 0.47 \cdot x_{dep,LB}$$

$$= 0.47 \cdot 3.36 = 1.58\ m.$$

– Creation of cross sectional profiles:

  Herein, the cross sectional profiles have been obtained in the following way:

  The program HEC-RAS has been used as a pure geometrical interpolation tool (without regarding any flow calculations!). In

this context other three-dimensional geometrical measuring tools might be imagined (e. g. AutoCAD, Surfer or other).

The basic idea is to invert the longitudinal and the lateral directions. Thus, in HEC-RAS the two longitudinal profiles, corresponding to the empirical models on both channel sides, are treated as cross sectional (!) profiles. The distance between the two profiles is the channel width (here $B = 1.50\ m$). Both cross sections were chosen to have the same width (corresponding to $x_{dep,RB} = 5.25\ m$, since the right profile is longer than the left one being $x_{dep,RB} = 3.36\ m$).

In a first step the points of maximum deposition have been linked linearly. The same has been done for the left and right side of the cross sectional profiles. Then, a longitudinal interpolation with $\Delta x = 0.10\ m$ has been performed. Consequently, $1.50\ m/0.10\ m = 15$ cross sectional profiles were obtained.

In a second step for each cross sectional increment the corresponding elevation of the 15 cross sectional profiles has been extracted.

These data served then as the actual cross sectional profiles of the skewed deposit which were implemented in a numerical flow simulation program (here HEC-RAS).

As has been been discussed in paragraph 6.10.4 it has to be checked whether the downstream boundary conditions (fixpoint for the evolution of the mobile bed) will not induce a greater maximum height of the deposit by a new equilibrium slope for the reduced bed-load transport capacity than computed by the empirical deposition model.

- Step 3: Choice of appropriate boundary conditions in the flow calculation program:

  Once the empirical model of the deposit is implemented in a numerical flow calculation program, a certain roughness has to be superimposed on the geometry of the deposit. Grain roughness and total roughness, composed of grain and form roughness, might be introduced in the following ways:

  - Grain roughness:
    - Strickler (1923) (Eq. A.27):

$$k_{st}' = \frac{21.1}{d_{50}^{1/6}} = \frac{21.1}{(0.72/1000)^{1/6}} = 71\ m^{1/3}/s.$$

* Meyer-Peter and Müller (1948) (Eq. A.27):

$$k_{st}^{'} = \frac{26}{d_{90}^{1/6}} = \frac{26}{(2.28/1000)^{1/6}} = 72\ m^{1/3}/s.$$

* Engelund and Hansen (1967) (Eq. A.92 and Tab. A.3):

$$C^{'} = 18 \cdot log\left(\frac{12 \cdot R_h}{k_s^{'}}\right)$$

with:

$$k_s^{'} = 2.0 \cdot d_{65}.$$

Hence:

$$C^{'} = 18 \cdot log\left(\frac{12 \cdot 0.130}{2.0 \cdot 0.1.12/1000}\right) = 51\ m^{1/2}/s$$

and (Eq. A.23):

$$k_{st}^{'} = \frac{C^{'}}{R_h^{1/6}} = \frac{51}{0.130^{1/6}} = 72\ m^{1/3}/s.$$

– Total roughness (grain and form roughness):

* Yalin and da Silva (2001) (paragraphs A.3.2 and A.4.1):

$$\frac{1}{c^2} = \underbrace{\frac{1}{c_f^2}}_{grain} + \underbrace{\frac{1}{2 \cdot y} \cdot \underbrace{\left(\delta_d^2 \cdot \Lambda_d\right)}_{dunes}}_{form}$$

with (Eq. A.86):

$$c_f = c^{'} = \frac{1}{\kappa} \cdot ln\left(0.368 \cdot \frac{Z}{2}\right) + B_s$$

$$= \frac{1}{0.40} \cdot ln\left(0.368 \cdot \frac{180.6}{2}\right) + 8.802 = 17.6$$

and (Eqs A.61, A.71)

$$\Lambda_d = 0.55\ m, \quad \delta_d = 0.024.$$

Consequently:

$$\frac{1}{c^2} = \frac{1}{17.6^2} + \frac{1}{2 \cdot 0.130} \cdot \left(0.024^2 \cdot 0.55\right)$$

and:

$$c = 14.9.$$

Finally:

$$k_{st} = \frac{C}{R_h^{1/6}} = \frac{c \cdot \sqrt{g}}{R_h^{1/6}} = \frac{14.9 \cdot \sqrt{9.81}}{0.130^{1/6}} = 65\ m^{1/3}/s.$$

7.2. Case Study on Rhone River upstream of Lake Geneva

To test the three empirical models under prototype conditions a case study on the Rhone river upstream of Lake Geneva between Sion and Branson (km 45.177, downstream of Riddes, Pont Saxon) in Switzerland is performed. In Figure 7.1 a typical reach of the Rhone river is presented. Characteristic cross sectional profiles are depicted in Figure 4.1.

Figure 7.1: Typical reach of the Rhone river upstream of Lake Geneva in Switzerland between Sion and Branson (photo: J. Althaus).

Currently, the hydraulic capacity of the Rhone river is limited to a flood event with a hundred year return period ($HQ_{100} = 1260\ m^3/s$). To assure the degree of protection for a HQ_{100} and increase the protection for a greater flood event (e. g. an extreme flood with $EHQ = 1600\ m^3/s$) a side weir is supposed to be installed in the river dyke. Therefore, the existing elevation

of the dyke is reduced from 467.15 m to 466.50 m on a 200 m long stretch corresponding to a weir crest length of $L_D = 200$ m. To maintain the existing flood protection against a HQ_{100} the side weir is assumed to be equipped with overturning fuse gates (Fig. 7.2).

Figure 7.2: Example of a side weir equipped with overturning fuse gates on the river Engelberger Aa, Switzerland (photos: Swiss Federal Office for the Environment - FOEN). Top left: Construction of the side weir. Top right: Side weir equipped with overturning fuse gates. Bottom left: Side weir in operation. Bottom right: Side weir after flood event.

7.2.1. Application of 1D and 2D empirical Model and Method for direct Estimation of Side Overflow

In the following the impact of a mobile bed on the side overflow intensity is investigated applying the $1D$ empirical deposition model. For the computation the $1D$-numerical code DUPIRO is used (paragraph 8). In addition to the $1D$-approach, indicative results for the $2D$ empirical model and the direct estimation approach are presented.

The following (initial) geometrical and hydraulic characteristics for the Rhone river and the side weir are given:

- Channel width (mean): $B = 40\ m$,
- Bottom slope: $S_0 = 0.10\ \%$,
- Grain diameter of bed material: $d_{50} = 35\ mm$, $d_m = 60\ mm$,
- Grain roughness: $k_{st,grain} = 37\ m^{1/3}/s$,
- Total roughness: $k_{st,total} = 33\ m^{1/3}/s$,
- Weir length: $L_D = 200\ m$,
- Weir height (mean): $w_D = 7.35\ m$ (bed elevation in the middle of the weir $z = 459.15\ m$, absolute crest level $z = 466.50\ m$),
- Approach Discharge (HQ_{100}): $Q_1 = 1260\ m^3/s$,
- Approach Discharge (EHQ): $Q_1 = 1600\ m^3/s$.

Solution:

- Step 1: Determination of the geometry of the empirical deposit:
  - Normalized deposit obtained by the Maxwellian distribution function:
    - Shape factor (n^*) of the deposit obtained by Equation 6.7:

$$n^* = \frac{3}{4} \cdot \frac{L_D}{B} + \frac{7}{3}$$

$$= \frac{3}{4} \cdot \frac{200}{40} + \frac{7}{3} = 6.08.$$

    - Arbitrarily chosen increments for X^* (Eq. 6.4): $0.00 \leq X^* \leq 4.00 \div 6.00$.
    - Height of deposit ($Z^*(X^*)$) obtained by Equation 6.5.
  - Geometry of extracted deposit:
    - Abscissa: $x^* = X^* \cdot x^*_{max}$ with $x^*_{max} \approx 50 \cdot 4.00\ m = 200\ m$ ($x^*_{max} \approx 4.00\ m$ for model scale of $1:30 \div 1:50$) (or using Tab. 6.2).

* Ordinate: $z^* = Z^*(X^*) \cdot z^*_{max}$ with z^*_{max} according to Equation 6.10:

$$z^*_{max} = \frac{h_{D,1}}{\Delta\Phi/(Q_D/Q_1) \cdot \left(3 \cdot \Delta\Phi - \frac{9}{5}\right) + \frac{9}{4}}.$$

Since Q_D/Q_1 and $\Delta\Phi$ are not known at the beginning an iterative computation procedure is required.
It has to be started with a flat bed (total roughness $k_{st,total} = 33\ m^{1/3}/s$) without deposit to obtain an initial overflow discharge (Q_D). Once Q_D is known the discharge in the main-channel downstream of the weir (Q_2) can be determined. Knowing the up- and downstream conditions (discharge, flow depth, flow depth on the weir, slope, roughness) the dimensionless bed-load transport capacities up- and downstream of the side weir can be computed, and hence $\Delta\Phi = \Phi_{downstream}/\Phi_{upstream}$. In the present example $\Delta\Phi$ is calculated according to the approach of Meyer-Peter and Müller (1948) (paragraph A.6.2) with $k_{st}/k'_{st} = k_s/k_r = 33/37 = 0.89$.
Based on these computations a first deposit characterized by n^*, x^*_{max} and z^*_{max} is obtained.

- Step 2: Implementation of the empirical deposit into a flow calculation program (location of deposit relative to side weir):

  - Horizontal coupling point relative to downstream weir corner (x_{cp}) obtained by Equation 6.11 (or Eq. 6.12, simplified):

$$-0.65 \cdot L_D \leq x_{cp} \leq 0.44 \cdot L_D$$

$$-0.65 \cdot 200 = -130\ m \leq x_{cp} \leq 88\ m = 0.44 \cdot 200.$$

The location range of x_{cp} can be reduced applying Equation 6.13 and/or Equation 6.14.

With reasonable accuracy the downstream weir corner can be chosen as the horizontal coupling point (x_{cp}).

As has been been discussed in paragraph 6.10.4 it has to be checked whether the downstream boundary conditions (fixpoint for the evolution of the mobile bed) will not induce a greater maximum height of the deposit by a new equilibrium slope for the reduced bed-load transport capacity than computed by the empirical deposition model.

- Step 3: Choice of appropriate boundary conditions in the flow calculation program:

  Here, the total roughness is given by $k_{st,total} = 33\ m^{1/3}/s$. If the (total) roughness is not known the approaches mentioned in paragraph 7.1 (step 3) are recommended to be used.

The steps 1 to 3 are to be repeated until the side overflow (Q_D) becomes stable. In Figure 7.3 and Table 7.1 the different steps of the iteration procedure as well as the corresponding results are presented. Figure 7.4 shows the evolution of the geometry of the empirical deposit for the different iterations. In Figure 7.5 the evolution of the side overflow (Q_D) is presented for the different iterations.

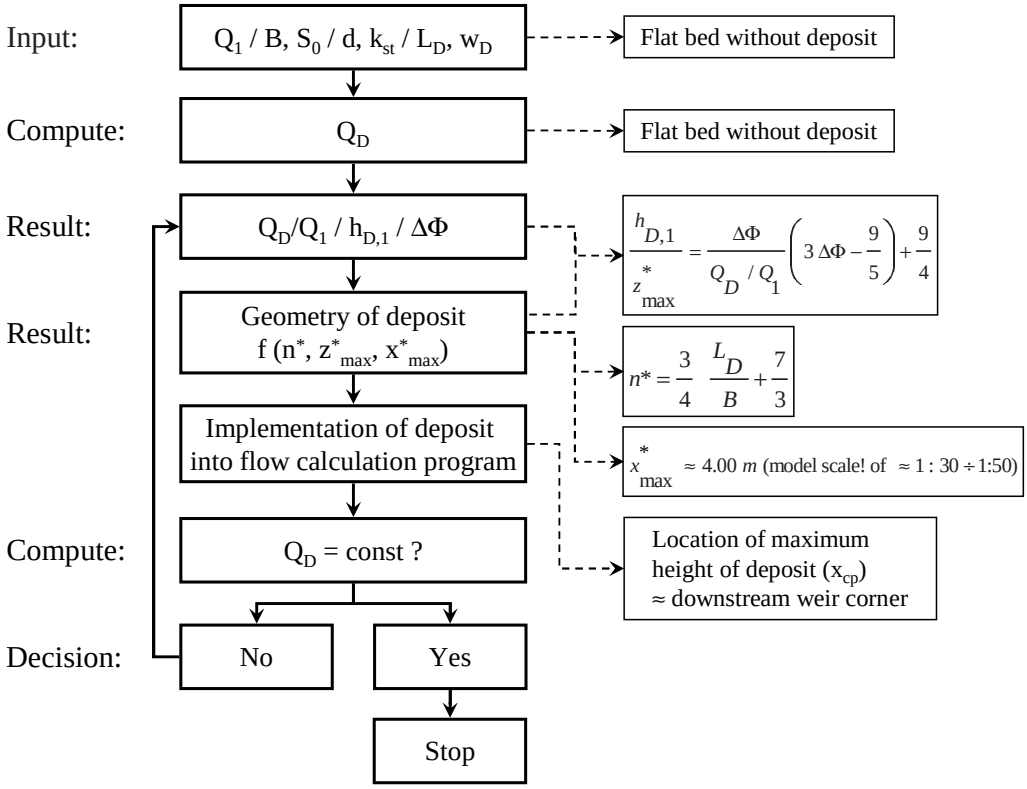

Figure 7.3: Iteration steps for the determination of the geometry of the $1D$ empirical deposit. Regarding the $2D$-deposit the same procedure has to be applied for the two profiles (deposits) on the right and left channel bank. For the implementation into a flow calculation program the longitudinal displacement between the two profiles (Δx^*) has to be determined according to Equations 6.33 and 6.34.

The computations indicate that for a fixed plane bed without deposit the initial side overflow intensity amounts to $Q_{D,ini} = 288\ m^3/s$. After

Table 7.1: Results of the iteration procedure to determine the maximum height of the $1D$-deposit (z^*_{max}). The maximum height (z^*_{max}) refers to the elevation of the initially flat bed level at the downstream weir corner ($z = 459.05\ m$). The approach discharge has been $Q_1 = 1600\ m^{1/3}/s$ (EHQ), the shape factor $n^* = 6.08$ (step 1) and $x^*_{max} = 200\ m$ (step 1). The empirical deposit has been implemented at the downstream weir corner (x_{cp} = downstream weir corner).

N^o of iterations	Q_D $[m^3/s]$	Q_D/Q_1 $[-]$	$h_{D,1}$ $[m]$	$\Phi_{upstr.}$ $[-]$	$\Phi_{downstr.}$ $[-]$	$\Delta\Phi$ $[-]$	z^*_{max} $[m]$
flat bed	288	0.18	1.16	0.035	0.022	0.63	0.00
1	301	0.19	1.24	0.037	0.021	0.56	0.45
2	309	0.19	1.28	0.037	0.020	0.54	0.65
3	312	0.20	1.30	0.037	0.020	0.54	0.73
4	313	0.20	1.31	0.037	0.020	0.53	0.74
5	314	0.20	1.31	0.038	0.020	0.51	0.81
6	315	0.20	1.31	0.038	0.019	0.50	0.84
7	317	0.20	1.33	0.038	0.019	0.50	0.87
8	318	0.20	1.33	0.038	0.019	0.50	0.89

several iterations (here: 8 iterations) a stable deposit and a stable outflow of $Q_{D,fin} = 318\ m^3/s$ are obtained. Hence, the side overflow increases by a factor of $Q_{D,fin}/Q_{D,ini} = 318/288 = 1.10$ (Tab. 7.2).

Having the different prediction accuracies of the $1D$- and $2D$ empirical model implemented in a $1D$-numerical program in mind (85 % for the $1D$-model (Eq. 6.17, paragraph 6.6) and 91 % (Eq. 6.41, paragraph 6.8) for the $2D$-model) it might be concluded that the side overflow will increase by about 6 % from $Q_{D,fin} = 318\ m^3/s$ for the $1D$ empirical approach to $Q_{D,fin} = 1.06 \cdot 318\ m^3/s = 337\ m^3/s$ for the $2D$ empirical approach. This would correspond to an increase of $Q_{D,fin}/Q_{D,ini} = 337/288 = 1.17$ compared to a fixed bed without deposit (Tab. 7.2).

Regarding the approach for direct estimation of the side overflow (paragraph 6.9) using the final values from the last iteration for the $1D$-approach (Tab. 7.1) with $Q_1 = 1600\ m^3/s$, $y_1 = 8.84\ m$, $h_{D,1} = 1.33\ m$, $Fr_1 = 0.486$, $B = 40\ m$ and $L_D = 200\ m$ yields (Eq. 6.46):

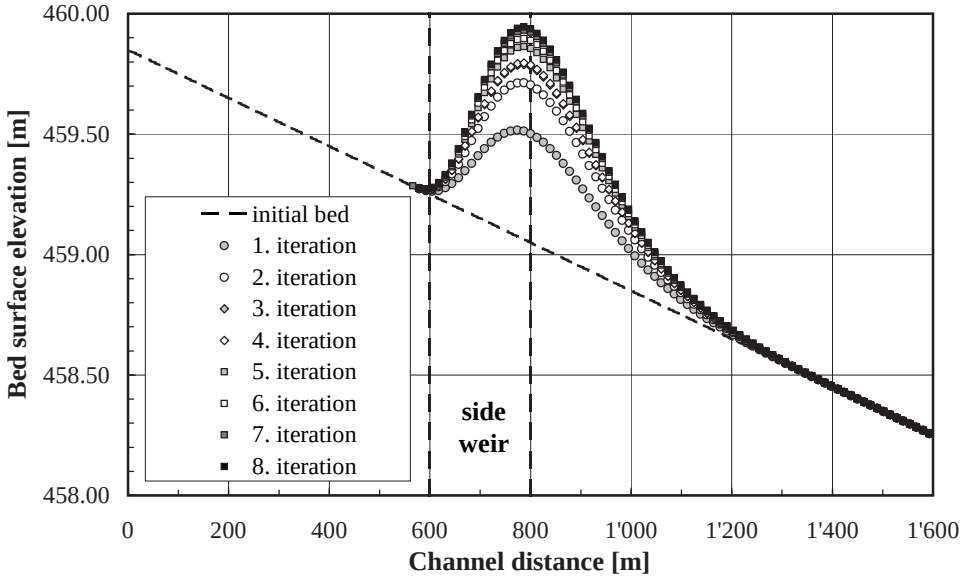

Figure 7.4: Evolution of the geometry of the deposit for the different iterations.

$$Fr_D = \left(\frac{h_{D,1}/L_D}{0.037}\right)^{1/0.53} \cdot Fr_1$$

$$= \left(\frac{1.33/200}{0.037}\right)^{1/0.53} \cdot 0.486 = 0.019.$$

By the help of Equation 6.44 the side overflow follows to be:

$$Q_D = Fr_D \cdot L_D \cdot y_1^{3/2} \cdot \sqrt{g}$$

$$= 0.019 \cdot 200 \cdot 8.84^{3/2} \cdot \sqrt{9.81} = 314\ m^3/s.$$

The overflow discharge of $Q_D = 314\ m^3/s$ is based on the hydraulic parameters obtained from the $1D$-numerical calculations for the $1D$ empirical deposit and is rather close to the one obtained by the $1D$ empirical model ($Q_D = 318\ m^3/s$, Tabs 7.1 and 7.2).

The sedimentary deposit measured in the flume ("reality") is better represented by the $2D$ empirical model than by the $1D$ empirical model (85 % to 91 %, thus a difference of 6 %). To obtain the side overflow for hydraulic parameters based on $1D$-numerical calculations for the $2D$ empirical deposit, the following relation might be introduced (assumption of a similar C_D-value, see also Eq. 5.33):

$$\frac{Q_{D,\ 1D\ empirical\ deposit}}{Q_{D,\ 2D\ empirical\ deposit}} = \frac{1.00}{1.06} = 0.94 = \left(\frac{h_{D,\ 1D\ empirical\ deposit}}{h_{D,\ 2D\ empirical\ deposit}}\right)^{3/2}.$$

Consequently:

$$h_{D,\ 2D\ empirical\ deposit} = \frac{h_{D,\ 1D\ empirical\ deposit}}{\left(Q_{D,\ 1D\ empirical\ deposit}/Q_{D,\ 2D\ empirical\ deposit}\right)^{2/3}}$$

$$= \frac{1.33}{(1.00/1.06)^{2/3}} = 1.38\ m.$$

With $y_1 = 8.84/((1.00/1.06)^{2/3}) = 9.19\ m$ and $Fr_1 = 0.458$ the weir Froude number is:

$$Fr_D = \left(\frac{1.38/200}{0.037}\right)^{1/0.53} \cdot 0.458 = 0.019$$

and the side overflow based on hydraulic parameters derived from the different prediction accuracies of the $1D$ and $2D$ empirical models implemented into $1D$-numerical calculations yields:

$$Q_D = 0.19 \cdot 200 \cdot 9.19^{3/2} \cdot \sqrt{9.81} = 336\ m^3/s.$$

The side overflow of $Q_D = 336\ m^3/s$ is essentially the same than the one obtained by the $2D$ empirical model ($Q_D = 337\ m^3/s$, Tab. 7.2).

The impact and the significance of the computations performed above are presented in Figure 7.5. For the flat bed situation without deposit no overflow will occur for a flood event with a hundred year return period ($Q_1 = HQ_{100} = 1260\ m^3/s = Q_2$). Introducing an approach discharge of $Q_1 = EHQ = 1600\ m^3/s$ will cause serious flooding for the flat bed situation. Taking into account the evolution of the mobile bed applying the three empirical models ($1D$-approach, $2D$-approach and method for direct estimation of side overflow) the side overflow increases and the discharge remaining in the main-channel downstream of the weir (Q_2) decreases. Applying the $2D$ deposition model a protection even for an extreme flood event (EHQ) might be achieved ($Q_{2,EHQ} \approx HQ_{100}$). In this context a sufficiently large retention volume of the flood plain to store the higher overflow discharge has to be ensured.

7.2.2. Conclusion

The computations performed above yield reasonable results for the $1D$- and $2D$ empirical deposition model as well as for the method of direct estimation of side overflow applied under prototype conditions.

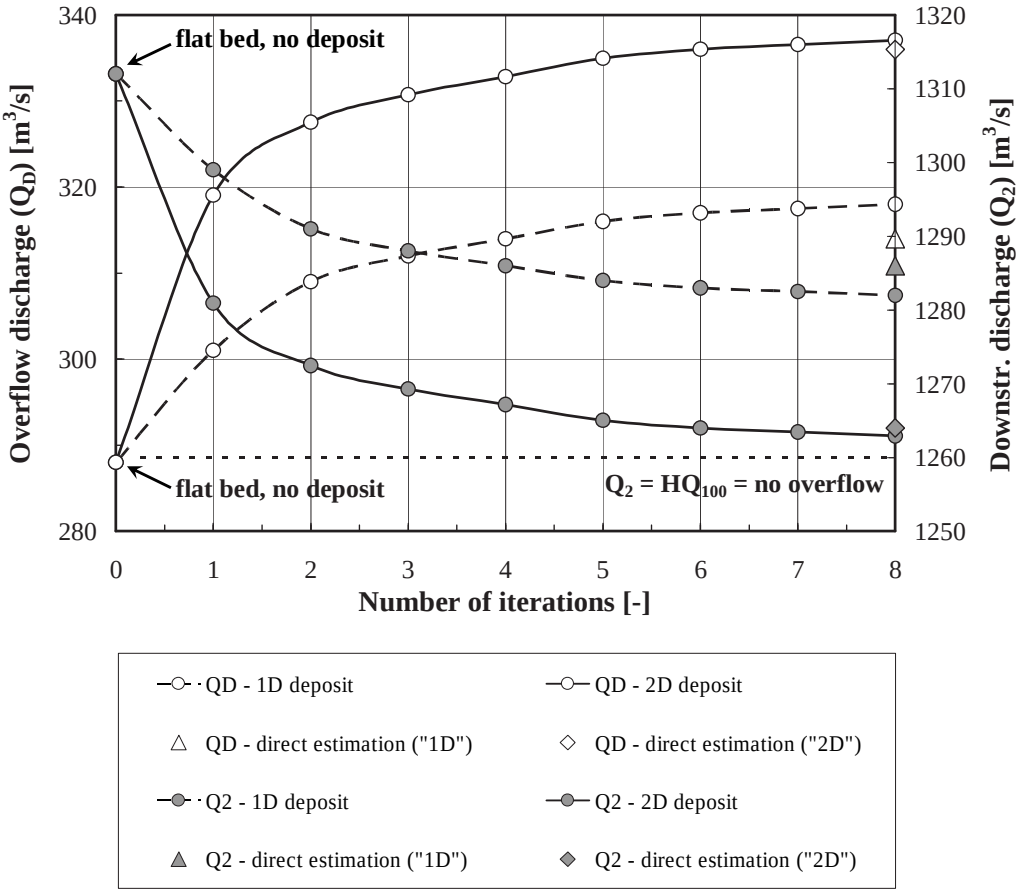

Figure 7.5: Overflow discharge (Q_D) and main-channel discharge downstream of the side weir (Q_2) for an approach discharge of $Q_1 = EHQ = 1600\ m^3/s$ for the $1D$ and $2D$ empirical model as well as the method for direct estimation of side overflow. Iteration number 0 corresponds to the reference case with a flat bed and no deposit.

Table 7.2: Results for the side overflow discharge (Q_D) and comparison with flat bed conditions without deposit applying the $1D$-and $2D$ empirical deposition models as well as the approach for direct estimation to the case study. $Q_{D,ini}$ always refers to the flat bed situation, $Q_{D,fin}$ to the (final) overflow taking into account mobile bed conditions and the formation of a sedimentary deposit. The results for the direct estimation are based on hydraulic parameters ($h_{D,1}$, y_1, Fr_1, Fr_D) obtained from $1D$-numerical calculations with the $1D$ empirical deposit ("$1D$") and the $2D$ empirical deposit ("$2D$").

Approach	Q_1 $[m^3/s]$	Q_D $[m^3/s]$	Q_2 $[m^3/s]$	$Q_{D,fin}/Q_{D,ini}$ $[-]$
flat bed	1600	288	1312	1.00
$1D$ empirical deposit	1600	318	1282	1.10
$2D$ empirical deposit	1600	337	1263	1.17
direct estimation ("$1D$")	1600	314	1286	1.09
direct estimation ("$2D$")	1600	336	1264	1.17

For a fixed plane bed without deposit the degree of protection can only be ensured for a flood event with a return period of hundred years (HQ_{100}). Taking into account the interaction of the side overflow with bed-load transport applying the empirical deposition models the degree of protection progressively increases and might even be assured for an extreme flood event (EHQ) when the $2D$ model is applied. In this context a sufficient storage volume of the retention basin or flood plain has to be provided.

8. Numerical Simulation of Sediment-Flow Interaction in Presence of a Weir

In this paragraph the capability of a $1D$-numerical simulation to predict observed deposition phenomena is investigated. In a first step the numerical model used for the simulations is described. Afterwards, results from the numerical simulations are presented. The presentation of the numerical results is rather brief, since the focus of the present study is laid on the analysis of experimental data.

8.1. Description of 1D-Numerical Model DUPIRO

The $1D$-numerical model used for the simulations is called DUPIRO and has jointly been developed at the Laboratory of Hydraulic Constructions (LCH) and the Institute of Applied Hydrodynamics and Hydraulic Constructions (HACH), University of Liège, Belgium.

The numerical tool is based on the continuity and momentum equations and performs the coupled hydrodynamic simulation of $1D$ flow behavior ($1D$ Saint-Venant shallow water equations) and bed-load transport (Exner equation) employing a finite volume method. The friction head loss is computed according to the Gauckler-Manning-Strickler formula (GMS).

An additional closure relation is required for coupling the bed-load transport and the hydraulic parameters. In the present version of the model the simplified bed-load transport equation of Smart and Jäggi (1983) (Eq. A.140) is implemented. To achieve equilibrium transport conditions the equilibrium transport hypothesis might be applied. This means the solid discharge is able to adapt instantaneously to mild spatial or temporal flow changes (Catella et al. (2007)). The bed-load transport capacity can further be adjusted with a multiplication factor to obtain absolute quantities.

The lateral overflow is taken into account applying the general equation of weirs (Eq. A.158) and using the side weir discharge coefficient (C_D) according to Hager (1987b).

Having the one-dimensionality of the model in mind it has to be stressed that only one value describes the flow or geometry in any point along the channel axis. Consequently, the mobile bed elevation is defined by one single value as well.

As far as the cross sectional geometry is concerned, a definition sketch is given in Figure 8.1. The basic shape of the cross section is trapezoidal. The value z defines the level of the non-erodible fixed bottom. The level z_0 indicates the surface of the mobile bed. The difference $z_0 - z$ characterizes the thickness of the mobile sediment layer. B_z corresponds to the width at the level z, B_0 to the width at the level z_0. B denotes the width of the free water surface and m the slope of the channel or river banks. Usually, z_0 and B_0 refer to the reference conditions (e. g. actual river bed elevation and bottom width). Knowing B_0 at the elevation z_0 and the inclination (m) are sufficient for the definition of the entire cross section (Boillat et al. (2006)). For the present study a rectangular cross section is present, hence $m = 0.00$.

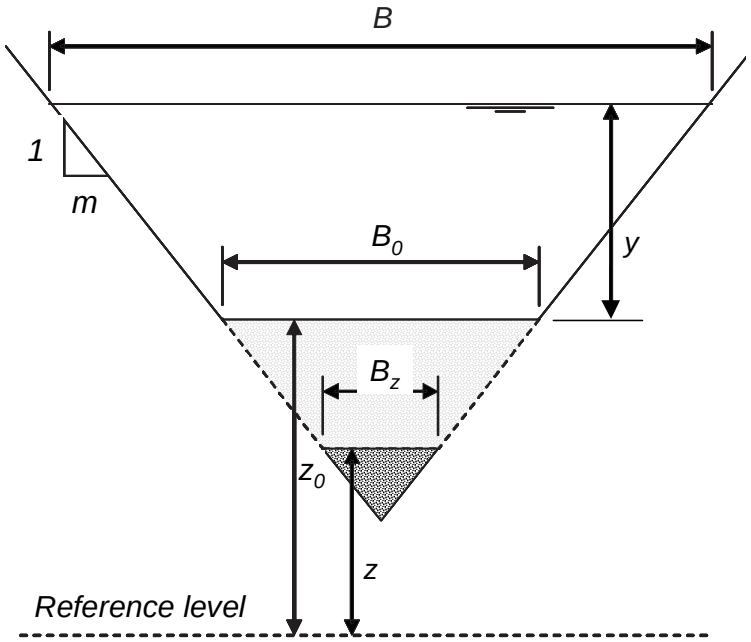

Figure 8.1: Definition sketch illustrating the determination of cross sectional geometry in the numerical model DUPIRO (from Boillat et al. (2006), modified).

The numerical code is developed in the Excel programming environment providing both a graphical user interface and a code in Visual Basic for Applications (VBA). On several worksheets the input parameters, e. g. channel geometry, roughness and reach length, and the boundary conditions are specified. On another worksheet calculation parameters such as time step,

spatial discretisation, computation with or without sediment transport or with or without side overflow are specified.

Once all input parameters are introduced the code is executed. The numerical output is printed onto several worksheets consisting of the position x along the channel axis and e. g. flow depth, flow area, discharge, side overflow discharge, solid discharge or bed elevation as a function of time. Moreover, the evolution with time and the final numerical result are visualized in a plot in the $x - z$-plane on a separate chart.

8.2. Results of Numerical Simulation of Experiments with DUPIRO

8.2.1. Results of Numerical Simulations without Bed-Load Transport

Before performing numerical simulations with bed-load transport several computations have been conducted for fixed bed conditions. Since the most interesting case is the situation with deposition, no results for plane fixed bed conditions are presented herein.

As far as aggradation is concerned, the final longitudinal bed surface profile obtained from the moving average procedure has been implemented in the model. Taking for example experiment $B02$ with a measured Strickler-value of $k_{st} \approx 55\ m^{1/3}/s$ and a measured lateral outflow of $Q_D = 52\ l/s$ ($Q_D/Q_1 = 0.29$), the numerical model yields a Q_D-value of 47 l/s ($Q_D/Q_1 = 0.26$). This rather slight difference might be mainly attributed to the fact that the $1D$-numerical model does not represent the 2-dimensionality of the deposit. Hence, local energy losses induced through lateral constriction and expansion are not captured. However, to a certain extent the $2D$-effect of the deposit is implicitly incorporated in the moving average profile. Moreover, some error might be originated from the determination of the measured Strickler-value of $k_{st} \approx 55\ m^{1/3}/s$.

Although physically incorrect, the compensation of the difference missing due to the disregard of the $2D$-effect of the deposit in the $1D$-model would (!) correspond to an increase in roughness of ≈ 9 % (adaption of $k_{st} = 55\ m^{1/3}/s$ to $k_{st} = 50\ m^{1/3}/s$). Of course, it is more physically based to increase the height of the deposit than increasing roughness. In the example presented above the height of the deposit would have to be slightly increased by $0.01\ m$ to obtain the same lateral outflow as the measured one (adaption of $z_{max} = 0.275\ m$ to $z_{max} = 0.285\ m$). With respect to the initial flat bed level of $z = 0.25\ m$ in the middle of the weir this increase corresponds to $(0.285\ m - 0.25\ m)/(0.275\ m - 0.25\ m) = 0.035/0.025 = 1.40$.

8.2.2. Results of Numerical Simulations including Bed-Load Transport

With respect to simulations including bed-load transport it has to be stated that the bed-load transport capacity, taken into account in the model by the formula of Smart and Jäggi (1983), is underestimated. Measured absolute quantities can be obtained by adopting a multiplication factor. This factor increases or decreases the bed-load transport capacity. In Table 8.1 multiplication factors for the present study are summarized. It appears that on average the bed-load transport capacity predicted by Smart and Jäggi (1983) has to be multiplied by a factor of $\approx$ 5.31. Another option to achieve equilibrium bed-load transport conditions is to apply the equilibrium transport hypothesis, i. g. the solid load is able to adapt instantaneously to mild spatial or temporal flow changes. In the model this is achieved by specifying no value for the solid discharge (empty cell) and a multiplication factor of 1.00.

In Figure 8.2 measured and computed longitudinal bed surface profiles for a characteristic example of each test series are presented. The numerical boundary conditions correspond to the experimental ones (initial state) (Tab. 4.3). For bed-load transport equilibrium transport conditions have been adopted (equilibrium transport hypothesis). Flow resistance has been chosen according to measured Strickler-values ($k_{st} = 55\ m^{1/3}/s$ for experiment $B02$, $k_{st} = 69\ m^{1/3}/s$ for $C02$ and $k_{st} = 61\ m^{1/3}/s$ for $D02$).

It becomes evident that the overall shape of the bed surface is predicted with reasonable accuracy. However, the extent of the aggradation is slightly underestimated for experiment $B02$. A greater difference is observed for experiment $C02$. With respect to experiment $D02$ the small deposit at the first weir and the greater one at the second weir are fairly well reproduced. A comparison of measured side overflow discharge with values obtained from the computations is presented in Table 8.2.

Looking at the shape of the computed deposit a shape factor according to the Maxwellian distribution function of $n^* = 3.3$ has been determined for experiment $B02$. For $C02$ and $D02$ n^*-values of 5.0 and 10.1, respectively, are obtained. The shape factor of the measured deposit (moving average applied to cross sectional averaged final bed surface profile) yields $n^* = 3.0$ for $B02$, $n^* = 5.4$ for $C02$ and $n^* = 9.4$ for $D02$. Hence, the shape factors of measured and computed deposits correlate fairly well.

8.2.3. Results of Numerical Simulations for unsteady Flow with Bed-Load Transport

The numerical model has also been used to investigate unsteady flow conditions. For this, the passage of a flood wave has been simulated. The

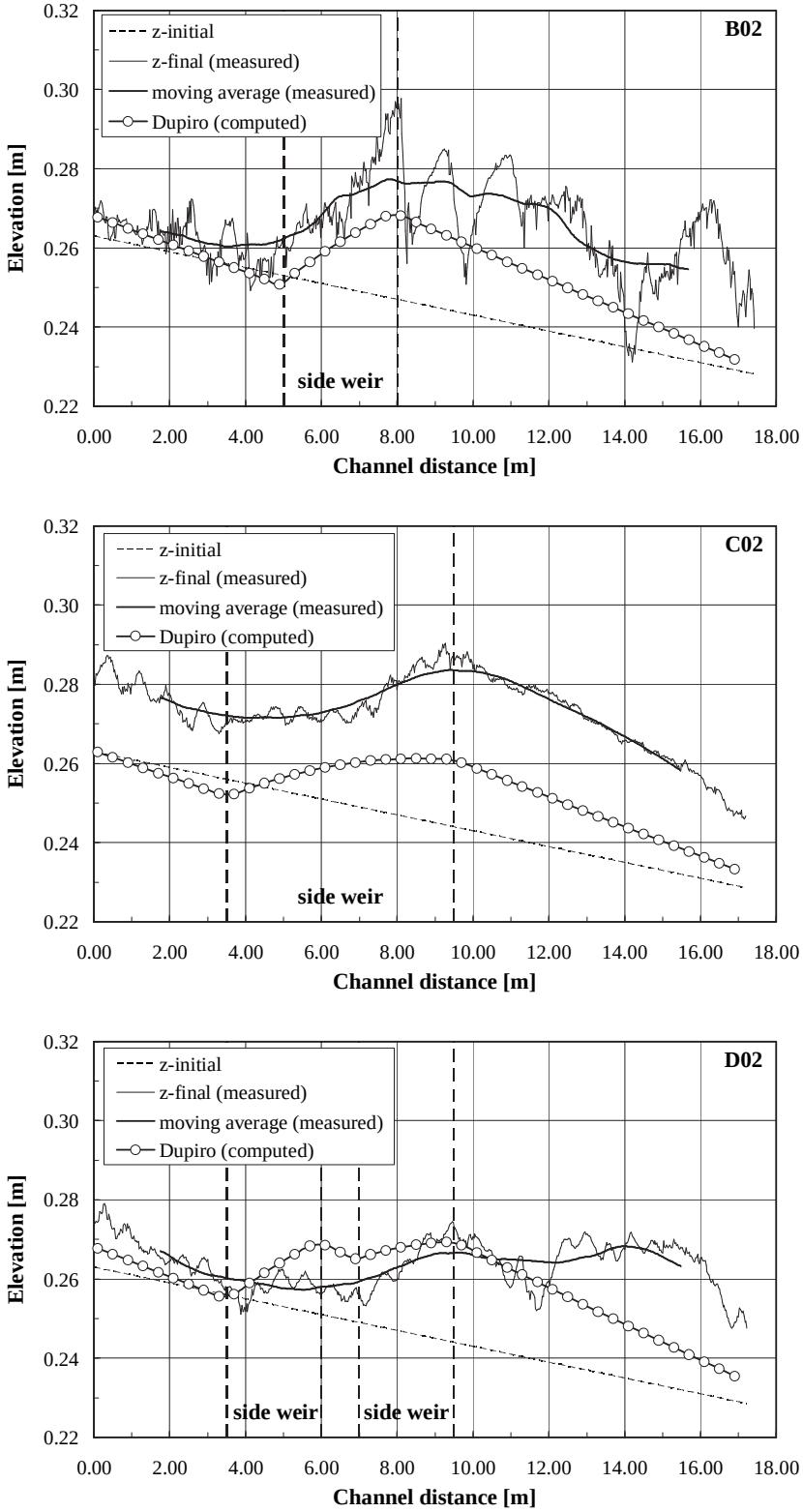

Figure 8.2: Comparison of measured and computed longitudinal bed surface profiles for three emblematic experiments of each test series.

Table 8.1: Ratio of sediment supply ($Q_{sb,in}$) and bed-load transport capacity according to the simplified formula of Smart and Jäggi (1983) (Eq. A.140) ($Q_{sb,SJ}$). The ratio $Q_{sb,in}/Q_{sb,SJ}$ represents the multiplication factor to achieve equilibrium sediment transport conditions in the numerical model.

N^o of experiment	present study $Q_{sb,in}$ $[m^3/s]$	Smart and Jäggi (1983) $Q_{sb,SJ}$ $[m^3/s]$	Multiplication factor $Q_{sb,in}/Q_{sb,SJ}$ $[-]$
$B01$	$5.47 \cdot 10^{-5}$	$2.21 \cdot 10^{-5}$	2.48
$B02$	$11.15 \cdot 10^{-5}$	$4.54 \cdot 10^{-5}$	2.46
$B03$	$5.72 \cdot 10^{-5}$	$6.99 \cdot 10^{-5}$	0.82
$B04$	$6.08 \cdot 10^{-5}$	$0.64 \cdot 10^{-5}$	9.50
$B05$	$10.52 \cdot 10^{-5}$	$2.69 \cdot 10^{-5}$	3.91
$B06$	$11.08 \cdot 10^{-5}$	$3.77 \cdot 10^{-5}$	2.94
average	$8.34 \cdot 10^{-5}$	$3.47 \cdot 10^{-5}$	3.68
$C01$	$6.01 \cdot 10^{-5}$	$2.35 \cdot 10^{-5}$	2.56
$C02$	$26.85 \cdot 10^{-5}$	$3.54 \cdot 10^{-5}$	7.58
$C03$	$32.55 \cdot 10^{-5}$	$4.41 \cdot 10^{-5}$	7.38
$C04$	$25.04 \cdot 10^{-5}$	$2.94 \cdot 10^{-5}$	8.52
$C05$	$25.04 \cdot 10^{-5}$	$3.00 \cdot 10^{-5}$	8.35
average	$23.10 \cdot 10^{-5}$	$3.25 \cdot 10^{-5}$	6.88
$D01$	$17.01 \cdot 10^{-5}$	$2.53 \cdot 10^{-5}$	6.72
$D02$	$16.69 \cdot 10^{-5}$	$3.04 \cdot 10^{-5}$	5.49
$D03$	$25.04 \cdot 10^{-5}$	$4.45 \cdot 10^{-5}$	5.63
$D04$	$14.05 \cdot 10^{-5}$	$3.04 \cdot 10^{-5}$	4.62
$D05$	$12.52 \cdot 10^{-5}$	$2.06 \cdot 10^{-5}$	6.08
average	$17.06 \cdot 10^{-5}$	$3.02 \cdot 10^{-5}$	5.71
average (all)	$15.68 \cdot 10^{-5}$	$3.26 \cdot 10^{-5}$	5.31

hydrograph (model scale) is characterised by a base flow of $Q_1 = 0.035\ m^3/s$

Table 8.2: Measured overflow discharge ($Q_{D,meas.}$) compared with results from numerical computations with bed-load transport ($Q_{D,comp.}$).

N^o of	present study			1D-numerical model			meas. / comp.
exp.	Q_1 $[l/s]$	Q_D $[l/s]$	Q_D/Q_1 $[-]$	Q_1 $[l/s]$	Q_D $[l/s]$	Q_D/Q_1 $[-]$	$Q_{D,meas.}/Q_{D,comp.}$ $[-]$
$B02$	181	52	0.29	181	37	0.20	1.41
$C02$	197	32	0.16	197	37	0.19	0.86
$D02$	182	33	0.18	182	42	0.23	0.79
average	187	39	0.21	187	39	0.21	1.02

(simulated during 10 min, $t_{prototype} \approx 1.2\ h$). After 300 min ($t_{prototype} = 35\ h$) the peak discharge of $Q_1 = 0.181\ m^3/s$ is obtained (rising stage). The peak period corresponds to 170 min ($t_{prototype} = 20\ h$), the falling stage from $Q_1 = 0.181\ m^3/s$ to the base flow has a duration of 500 min ($t_{prototype} = 60\ h$). At the end of the flood event 10 min base flow are simulated once again.

The results of this analysis are presented in Figure 8.3. It can be seen that the maximum overflow occurs at the end of the peak period when the volume deposited reaches its maximum. During the falling stage of the hydrograph the aggradation is continuously washed out until almost initial conditions are obtained at the end of the simulated flood hydrograph.

From these investigations it might be concluded that despite the 1D-character of the numerical model most experimental trends are captured with reasonable accuracy.

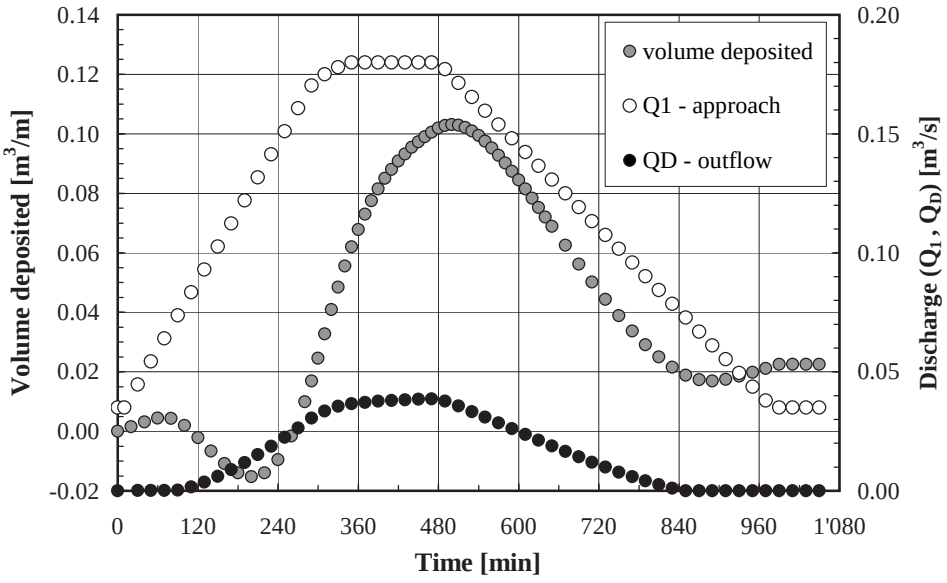

Figure 8.3: Numerical simulation of a flood hydrograph. The boundary conditions correspond to experiment $B02$.

9. Summary, Conclusions, Recommendations and Outlook

9.1. Summary and Conclusions

9.1.1. Problem of Interaction of Side Overflow with Sediment Transport in a Channel

Side overflow devices such as lateral weirs and overflow dams are free overflow regulation and diversion devices commonly encountered in hydraulic engineering. They are set into the side of a channel or river allowing to spill a part of the discharge over their crest when the surface of the flow in the main-channel exceeds a certain level.

The lateral outflow, usually occurring on a rather short stretch of the main-channel, is responsable for the reduction of the bottom shear stress and, hence sediment transport capacity. As a result aggradation and a local sedimentary deposit can form in the vicinity of the weir. The aggraded bed level generates backwater effects and additional contraction and expansion energy losses. Moreover, the mobile bed surface might be covered with alluvial bed forms increasing overall flow resistance. As a consequence the water level and the pressure head above the weir crest increase and the side overflow discharge as well. Hence, the design discharge intended to be diverted over the weir rises in an unforeseen way. The uncontrolled increase of spill discharge might be considerable.

An extensive literature review showed that lateral overflow on fixed bed conditions is well studied and numerous formulae to estimate side overflow discharge exist. The same accounts for bed-load transport capacity and bed morphology, namely alluvial bed forms such as dunes.

Since the interaction of side overflow with bed-load and bed morphology in a channel has not been studied so far, systematic laboratory tests have been performed.

9.1.2. Description of experimental Results

Three test series and one reference experiment without side weir have been carried out in a 20.00 m long, 1.50 m wide and 1.20 m high rectangular flume. The first test series (six experiments) consisted of a 3.00 m long side weir, the second one (five experiments) had a 6.00 m long weir and the third series (five experiments) was characterised by two weirs of 2.50 m length each. The test series covered a wide range of parameters. The approach discharge varied between $0.098\ m^3/s \leq Q_1 \leq 0.222\ m^3/s$, the initial slope of the mobile bed ($d_{50} = 0.72\ mm$) ranged from 0.1 % to 0.4 % and Froude numbers have been in a range of $0.5 \leq Fr_1 \leq \approx 1.00$. Although in a limited number of experiments local Froude numbers exceeded a value of 1.00 the overall flow regime has been subcritical. During the experiments the water surface, the $2D$-velocity field (ultrasonic velocity profiler - UVP), the side overflow discharge and sediment supply were measured. The final bed morphology has been recorded by means of digital photogrammetry.

The ratio of overflow discharge to approach discharge (Q_D/Q_1) rapidly increases at the beginning of the experiments and stabilises after about 26 % of the total duration of the expriment. The average measured overflow ratio amounts to $Q_D/Q_1 \approx 21\%$. In this context the measurement error for the specific side overflow (q_D) related to the precision of the water level measurements and the digital elevation model has been determined to be about $\pm$ 3.85 %. Compared to fixed plane bed conditions the side overflow might increase by a factor of up to $\approx$ 3. Herein, about 25 % of the total increase can be attributed to form roughness effects (dunes) and about 75 % to effects of local sediment deposition near the weir.

Regarding the side weir discharge coefficient (C_D) a value of 0.389 has been determined. A comparison with several approaches from literature indicted that the C_D-value does not change significantly from one approach to the other. The best prediction of C_D is given by the approaches of Subramanya and Awasthy (1972) and Hager (1987b).

Test series D consisted of two weirs of 2.50 m length each. For this configuration it has been found out that 45 % of the total overflow discharge are diverted over the first weir (Q_{D1}) and 55 % over the second one (Q_{D2}). The two weirs behave similarly and the weir composed of the two individual weirs acts in the same way than the two separate weirs. The investigation of the repartition of the overflow discharge for two weirs showed that the repartition on mobile bed conditions is considerably more uniform than for fixed plane bed conditions. The ratio of overflow discharge over the second weir to the one diverted over the first weir corresponds to $Q_{D2}/Q_{D1} = 0.82$ for the mobile bed and $Q_{D2}/Q_{D1} = 0.55$ for the fixed bed. Similar tendencies could be observed for the test series with one single weir. The reason for this more uniform repartition is the local sediment deposit near the weir inducing

so-called pseudo-uniform flow conditions.

The analysis of measured outflow angles indicated that the location of the maximum outflow angle is shifted towards the downstream weir corner with increasing weir length. The average location of the maximum outflow angle corresponds to $\approx 3/4$ of the weir length and is situated close to the maximum elevation of the sedimentary deposit. A comparison with outflow angles predicted by methods from literature showed that the measured angles are significantly smaller than predicted ones. The discrepancy is mainly due to different geometric and hydraulic boundary conditions, e. g. a non-movable bed and substantially smaller Froude numbers in the literature approaches. Therefore, an appropriate relationship for high discharges and elevated Froude numbers ($0.5 \leq Fr_1 \leq \approx 1.00$) has been developed. The input parameters are based on channel and side weir geometry as well as flow variables.

The high discharges are responsable for a strong forward velocity component compared to the spanwise one. For that reason a weak transverse flow circulation superimposed by a strong streamwise current has been discovered. The strength of the secondary circulation increases with increasing overflow to approach discharge ratios (Q_D/Q_1) and from the left bank towards the side overflow on the right bank. The most considerable distortion of the $2D$-velocity profile is encountered in the near-bed region close to the side weir with a rather strong velocity component towards the weir and a comparatively high secondary circulation effect. The near-bed component of the secondary circulation appears to be the dominant mechanism by which sediment is transported to the weir where it accumulates to form the deposit.

As a precursor to the analysis of bed morphology, aggradation and their impact on side overflow intensity, the general situation of a triangular fixed symmetric and non-symmetric obstacle, representing the formation of sediment deposits on the bed, has been investigated theoretically and numerically using the $1D$-numerical code (DUPIRO). From the computations it can be concluded that the height and the position of the local deposit relative to the side weir are of considerable importance regarding side overflow intensity. The downstream shape of the deposit is of minor importance.

With respect to bed-load transport the analysis indicated that as soon as the main-channel flow decreases at the side weir the sediment transport decreases as well and aggradation occurs. This phenomenon appears to be continuous and most significant in the weir reach and a certain distance downstream of the weir. The maximum deposition is observed at the downstream weir corner. The local deposit forming is not uniform but varies both in streamwise and spanwise direction. The skewed shape induces a meander-like erosion channel downstream of the weir which is damped out with increasing distance from the weir. For the description of the oscillatory sine-generated plan shape of the erosion channel (thalweg) indicative expressions are proposed.

The approach sediment transport characteristics can be best expressed by the bed-load formula of Meyer-Peter and Müller (1948) with a correction factor of 1.90 for the absolute transport quantity. The investigations further showed that only rather small portions of sediment have been transported over the weir ($\approx$ 5 % of the upstream sediment supply). In this regard the ramp-like deposit developing in front of the weir might favor the transport of sediments over the weir.

When bed-load transport is present and the flow regime is subcritical alluvial bed forms such as dunes might develop. The dominant bed forms in this study are dunes. Downstream of the weir ripples superimposed on dunes may occur. For experiments owing rather high Froude numbers ($\approx$ 0.90) a slightly wavy or rather flat bed with washed-out dunes could be identified. No significant distinction in bed form type upstream, downstream and in the weir reach can be stated. A comparison of measured dunes with approaches from literature revealed that the reach upstream of the weir is best represented. For the downstream reach less adequate agreement is found. The weir region is located in between. Regarding measured dune migration velocity a value of $\approx$ 2.85 mm/s has been determined. Dune celerity predicted by approaches from literature is considerably overestimated compared to measured values.

Bed forms might induce additional flow resistance. Concerning the repartition of grain, form and total roughness about 87 % of the total roughness is skin friction and about 13 % is from drag. Consequently, bed forms do have a certain influence but this influence is rather mild.

In a last step numerical simulations with bed-load transport have been performed using the $1D$-numerical code DUPIRO. From these simulations it can be concluded that despite the one-dimensional character of the numerical tool the most experimental phenomena such as deposition shape and the location of maximum elevation are captured with reasonable accuracy. The results for the height of the deposit need to be improved.

Besides the development of two empirical models for the description of bed morphology near a side weir (see following paragraphs) a simple relationship for the direct estimation of the side overflow discharge in presence of bed-load transport has been established in paragraph 6.9.

The empirical models have been successfully tested in a case study on the Rhone river upstream of Lake Geneva in Switzerland. Taking into account the evolution of the mobile bed by applying the deposition models the degree of flood protection might increase from a flood event with a hundred year return period (HQ_{100}) to an extreme flood (EHQ).

9.1.3. Development of an empirical Approach for Prediction of Sediment Deposits in longitudinal Direction

For the development of the empirical $1D$-approach the moving average of the cross sectional averaged longitudinal bed surface profile has been used. The window length of the moving average has been chosen in the way that bed forms were eliminated with the prerequisite that the sediment deposit in the vicinity of the weir was not to be dampened.

The approach developed represents the overall longitudinal trend of the mobile bed without considering the spanwise variation of the aggraded channel reach. Hence, the $1D$-model constitutes a simplified approach to account for deposition phenomena in presence of a lateral overflow.

For the parameterisation of the geometry of the deposition model a Maxwell-type distribution function has been applied (paragraph 6.3). The input parameters of the distribution function are expressed in terms of dimensionless relationships using variables referring to main-channel geometry, side weir geometry as well as flow and bed-load transport characteristics:

- Shape factor n^* (Eq. 6.7):

$$n^* = \frac{3}{4} \cdot \frac{L_D}{B} + \frac{7}{3}.$$

- Maximum deposition height z^*_{max} of extracted deposit (Eq. 6.10):

$$\frac{h_{D,1}}{z^*_{max}} = \frac{\Delta\Phi}{Q_D/Q_1} \cdot \left(3 \cdot \Delta\Phi - \frac{9}{5}\right) + \frac{9}{4}$$

  with a 95 % confidence interval of $\pm$ 0.69.

  Since the ratio Q_D/Q_1 and $\Delta\Phi$ are not known a priori an iteration procedure is required. Starting with flat bed conditions (no deposit) an initial Q_D-value and hence a first Φ-value downstream of the weir is obtained. Once the side overflow (Q_D) becomes stable the iteration can be stopped. An example of the iteration procedure is given in paragraph 7.2.

- Location of maximum deposition height x^*_{max} of extracted deposit (paragraph 6.4.4):

$$x^*_{max} \approx 4.00\ m \text{ (for model scale of } 1:30 \div 1:50).$$

The measurement error for the specific side overflow (q_D) related to the precision of the water level recordings and the digital elevation model has been determined to be about ± 3.85 %.

As has been been discussed in paragraph 6.10.4 it has to be checked whether the downstream boundary conditions (fixpoint for the evolution of the mobile bed) will not induce a greater maximum height of the deposit by a new equilibrium slope for the reduced bed-load transport capacity than computed by the empirical deposition model.

The application range of the model corresponds to the domain in which it has been developed. The subsequent (dimensionless) parameters set the limits as follows:

- Initial bottom slope: $0.1\ \% \leq S_0 \leq 0.4\ \%$,
- Ratio of weir crest length to channel width: $2.00 \leq L_D/B \leq 4.00$,
- Approach discharge: $0.098\ m^3/s \leq Q_1 \leq 0.222\ m^3/s$,
- Overflow discharge: $0.004\ m^3/s \leq Q_D \leq 0.071\ m^3/s$,
- Ratio of overflow to approach discharge: $0.04 \leq Q_D/Q_1 \leq 0.037$ and
- Approach Froude number: $0.50 \leq Fr_1 \leq \approx 1.00$.

For the application of the empirical $1D$-model in $1D$-numerical flow calculations a correction factor of ≈ 1.18 for the side overflow (Q_D) has to be applied:

$$\frac{Q_{D,\ numerical\ model}}{Q_{D,\ empirical\ model}} \approx 1.18$$

9.1.4. Development of an empirical Approach for Prediction of longitudinal and lateral Shape of Sediment Deposits

Besides the longitudinal bed evolution the $2D$-approach also accounts for the spanwise variation of the deposit.

Therefore, longitudinal bed surface profiles (moving average) on the left and on the right channel bank have been used. The moving average procedure is the same than has been described for the $1D$-model. The profile on the right channel bank represents the overall aggradation in the weir reach *and* the formation of a local sedimentary deposit forming at the downstream weir corner. In contrast to this, the profile on the left channel bank opposite of the side weir only accounts for the overall bed elevation in the side weir reach. The two profiles are coupled by the help of an angle (ϕ^*) or a distance (Δx^*)

describing the longitudinal shift between the locations of the maximum bed elevation of each profile.

In analogy to the $1D$-model the geometry of the deposition model has been parameterized applying a Maxwell-type distribution function (paragraph 6.3). The input parameters of the distribution function are expressed in terms of dimensionless relationships using variables referring to main-channel geometry, side weir geometry as well as flow and bed-load transport characteristics:

- Profile on right channel bank:
  - Shape factor n^*_{RB} (Eq. 6.18 or Tab. 6.4):

$$n^*_{RB} = 5.52.$$

  - Maximum deposition height $z^*_{max,RB}$ of extracted deposit (Eq. 6.23):

$$\frac{h_{D,1}}{z^*_{max,RB}} = 2/3 \cdot \left[\frac{\Delta\Phi}{Q_D/Q_1} \cdot \left(3 \cdot \Delta\Phi - \frac{9}{5} \right) + \frac{9}{4} \right]^{4/5}$$

    with a 95 % confidence interval of $\pm$ 0.85.

    Since the ratio Q_D/Q_1 and $\Delta\Phi$ are not known a priori an iteration procedure is required. Starting with flat bed conditions (no deposit) an initial Q_D-value and hence a first Φ-value downstream of the weir is obtained. Once the side overflow (Q_D) becomes stable the iteration can be stopped. An example of the iteration procedure is given in paragraph 7.2.
  - Location of maximum deposition height $x^*_{max,RB}$ of extracted deposit (paragraph 6.7.5):

$$x^*_{max,RB} \approx 3.57\ m \text{ (for model scale of } 1:30 \div 1:50).$$

- Profile on left channel bank:
  - Shape factor n^*_{LB} (Eq. 6.19 or Eq. 6.20, simplified):

$$\frac{n^*_{LB}}{n^*_{RB}} = \frac{1}{8} \cdot \frac{L_D}{B} + \frac{2}{7}.$$

  - Maximum deposition height $z^*_{max,LB}$ of extracted deposit (Eqs 6.27, 6.28 and 6.29 or Eq. 6.24, simplified):

$$tan\ \phi_{z,LB} = \frac{\Delta z_{RB-LB}}{B}$$

and (Eq. 6.29):

$$z^*_{max,LB} = z^*_{max,RB} - \Delta z_{RB-LB}.$$

– Location of maximum deposition height $x^*_{max,LB}$ of extracted deposit (paragraph 6.7.5):

$$x^*_{max,LB} \approx 2.45\ m \text{ (for model scale of } 1:30 \div 1:50).$$

The measurement error for the specific side overflow (q_D) related to the precision of the water level recordings and the digital elevation model has been determined to be about ± 3.85 %.

As has been been discussed in paragraph 6.10.4 it has to be checked whether the downstream boundary conditions (fixpoint for the evolution of the mobile bed) will not induce a greater maximum height of the deposit by a new equilibrium slope for the reduced bed-load transport capacity than computed by the empirical deposition model.

The application range of the model corresponds to the domain in which it has been developed. The following (dimensionless) parameters limit the application range:

- Initial bottom slope: $0.1\ \% \leq S_0 \leq 0.4\ \%$,
- Ratio of weir crest length to channel width: $2.00 \leq L_D/B \leq 4.00$,
- Approach discharge: $0.098\ m^3/s \leq Q_1 \leq 0.222\ m^3/s$,
- Overflow discharge: $0.004\ m^3/s \leq Q_D \leq 0.071\ m^3/s$,
- Ratio of overflow to approach discharge: $0.04 \leq Q_D/Q_1 \leq 0.037$ and
- Approach Froude number: $0.50 \leq Fr_1 \leq \approx 1.00$.

For the application of the empirical $2D$-model in $1D$-numerical flow calculations a correction factor of ≈ 1.10 for the side overflow (Q_D) has to be applied:

$$\frac{Q_{D,\ numerical\ model}}{Q_{D,\ empirical\ model}} \approx 1.10$$

9.1.5. Steps proposed for Application of empirical Approaches

The computation procedure for the application of the empirical models can be summarized by the following three steps:

- Step 1: Determination of geometry of the empirical deposit.
- Step 2: Implementation of the empirical deposit into a flow calculation program.
- Step 3: Choice of appropriate boundary conditions in the flow calculation program (e. g. flow resistance accounting for bed forms).

Step 1 has been described in the two preceding paragraphs. An example of the iteration required is presented in paragraph 7.2. To implement the models into a numerical code for flow simulations their location relative to the side weir is needed (horizontal coupling point). Since usually the coordinates of the downstream weir corner are known, this point is taken as a reference for the horizontal coupling point.

- Step 2: Implementation of the empirical deposit into a flow calculation program (location of deposits relative to side weir and creation of cross sectional profiles):
  - $1D$-approach:
    - Horizontal coupling point relative to downstream weir corner (x_{cp}) obtained by Equation 6.11 (or Eq. 6.12, simplified):

      $$-0.65 \leq \frac{x_{cp}}{L_D} \leq 0.44.$$

      With reasonable accuracy the downstream weir corner can be chosen as the horizontal coupling point (x_{cp}).
    - Estimation of total deposition length (x_{dep}) using Equation 6.15:

      $$\frac{x_{dep}}{L_D} = 2.52 \approx 5/2 \quad \text{or} \quad x_{dep} \approx 5/2 \cdot L_D.$$

    - Estimation of repartition of up-and downstream deposition length (x_a, x_b) using Equation 6.16 and Table 6.2:

      $$\frac{x_a}{x_b} = \frac{0.40}{0.60} = 0.69.$$

  - $2D$-approach:
    - Horizontal coupling point relative to downstream weir corner on the right channel bank ($x_{cp,RB}$) obtained by Equation 6.30 (or Eq. 6.31, simplified):

      $$-0.34 \leq \frac{x_{cp,RB}}{L_D} \leq 0.12.$$

With reasonable accuracy the downstream weir corner can be chosen as the horizontal coupling point ($x_{cp,RB}$).

* Horizontal coupling point on the left channel bank ($x_{cp,LB}$) relative to horizontal coupling point on the right channel bank ($x_{cp,RB}$) determining the longitudinal displacement (Δx^*) obtained by Equations 6.33 and 6.34:

$$\frac{\Delta x^*}{L_D} = y = 23.26 \cdot x^2 - 0.11 \cdot x$$

with:

$$x = \left(1 - \frac{3 \cdot Fr_1^2}{2 + Fr_1^2}\right)^{1/2} \cdot \left(\frac{u_{*,1}}{\sqrt{g \cdot L_D}}\right)^{1/4}.$$

* Estimation of total deposition length on the right channel bank ($x_{dep,RB}$) using Equation 6.35:

$$\frac{x_{dep,RB}}{L_D} = 1.74 \approx 7/4 \quad \text{or} \quad x_{dep,RB} \approx 7/4 \cdot L_D.$$

* Estimation of repartition of up-and downstream deposition length on the right channel bank ($x_{a,RB}$, $x_{b,RB}$) using Equation 6.36 and Table 6.7:

$$\frac{x_{a,RB}}{x_{b,RB}} = \frac{0.48}{0.52} = 0.92.$$

* Estimation of total deposition length on the left channel bank ($x_{dep,LB}$) using Equation 6.37:

$$\frac{x_{dep,LB}}{x_{dep,RB}} = \frac{1.12}{1.74} = 0.64 \quad \text{or} \quad x_{dep,LB} = 0.64 \cdot x_{dep,RB}.$$

* Estimation of repartition of up-and downstream deposition length on the left channel bank ($x_{a,LB}$, $x_{b,LB}$) using Equation 6.38:

$$\frac{x_{a,LB}}{x_{b,LB}} = \frac{0.53}{0.47} = 1.13.$$

* Creation of cross sectional profiles:

  In a first step the points of maximum deposition on the two sides of the channel are linked (linearly). The same is done for

the beginning and the end of the profiles on the left and right side of the channel. Then, an interpolation is performed.
To extract profiles (perpendicular to the channel axis) from the interpolated three-dimensional surface of the deposit geometrical measuring tools might be applied (e. g. AutoCAD, Surfer or other).

- Step 3: Choice of appropriate boundary conditions in the flow calculation program:

  Once the empirical model of the deposit is implemented in a numerical flow calculation program, a certain roughness has to be superimposed on the geometry of the deposit. Grain roughness and total roughness, composed of grain and form roughness, might be introduced in the following ways:

  - Grain roughness:
    - Strickler (1923) (Eq. A.27):

$$k_{st}^{'} = \frac{21.1}{d_{50}^{1/6}}.$$

    - Meyer-Peter and Müller (1948) (Eq. A.27):

$$k_{st}^{'} = \frac{26}{d_{90}^{1/6}}.$$

    - Engelund and Hansen (1967) (Eq. A.92 and Tab. A.3):

$$C^{'} = 18 \cdot log\left(\frac{12 \cdot R_h}{k_s^{'}}\right)$$

      with:

$$k_s^{'} = 2.0 \cdot d_{65}.$$

  - Total roughness (grain and form roughness):
    - Yalin and da Silva (2001) (paragraphs A.3.2 and A.4.1):

$$\frac{1}{c^2} = \underbrace{\frac{1}{c_f^2}}_{grain} + \underbrace{\frac{1}{2 \cdot y} \cdot \left(\underbrace{\delta_r^2 \cdot \Lambda_r}_{ripples} + \underbrace{\delta_d^2 \cdot \Lambda_d}_{dunes}\right)}_{form}.$$

9.2. Recommendations for Engineering Purposes

In the first paragraph practical recommendations which have been immediately derived from the present study are presented. In addition, different mitigation measures to reduce deposition are proposed in the second paragraph.

9.2.1. Recommendations derived from present Study

The establishment of the one-dimensional and two-dimensional empirical deposition model has been inspired by the idea to develop rather simple and easy to handle relationships. It has been tried to avoid complexe formulations. Due to this reason for several input parameters besides a more detailed relationship a simplified expression is proposed.

To facilitate the application of the models in engineering practice a synoptical computation procedure is presented in paragraph 6.5 for the $1D$-model and in paragraph 6.7.7 for the $2D$-model. In chapter 7 an example for computation with discrete values is given. In addition to the two empirical deposition models a relationship for direct estimation of side overflow discharge influenced by morphological bed changes is presented in paragraph 6.9.

Some relationships, e. g. Equation 6.10, contain the ratio of overflow to approach discharge (Q_D/Q_1) and the ratio of downstream to upstream bed-load transport capacity ($\Delta\Phi$). Since Q_D is not known a-priori and hence $\Delta\Phi$ is not known as well, an iteration procedure is required. It is recommended to start the iteration with a flat bed (no deposition) using the general equation of weirs (Eq. A.158) and the side weir discharge coefficient (C_D) according to Subramanya and Awasthy (1972) or Hager (1987b) (paragraph 5.3.2). An example of the iteration procedure is given in paragraph 7.2.

Implementing the deposition models into $1D$-numerical schemes a prediction accuracy for the side overflow of 85 % for the $1D$-model and 91 % for the $2D$-model has been obtained. Hence, applying the empirical $1D$-model in a $1D$-numerical program the results for the side overflow need to be multiplied by a factor of ≈ 1.18. For the $2D$-model the multiplication factor corresponds to ≈ 1.10. No recommendations can be given for the use of $2D$- or $3D$-numerical models. However, it is suggested that the prediction accuracy will further increase.

For HEC-RAS computations (version 3.1.2) the side weir discharge coefficient ($C_{D,HEC-RAS}$) might be determined according to Hager (1987b) ($C_D = 0.392$ for the present study, Tab. 5.5) multiplied by the factors 2/3 and $(2g)^{1/2}$ occurring in the general equation of weirs (Eq. A.158).

It has to be noted that the two deposition models as well as the respective formulae should be used within the domain for which they have been established.

The range of approach flow discharge ranged from $0.098\ m^3/s \leq Q_1 \leq 0.222\ m^3/s$. In this context a geometrical model scale factor of $\lambda_L \approx 1 : 30 \div 1 : 50$ has to be kept in mind.

The experiments have been performed at rather high Froude numbers ($Fr_1 > 0.50$) with local(!) Froude numbers even greater than 1.00 (at least numerically). However, the overall flow regime has been subcritical.

Regarding side weir and channel geometry the application range might be expressed in terms of weir crest length to main-channel width being $2.00 \leq L_D/B \leq 4.00$.

As far as the time is concerned the duration of the experimental runs has been orientated towards the time when a diversion structure such as a lateral weir or overflow dam is in operation. Usually, this corresponds to the peak duration of a flood hydrograph, e. g. a flood with a hundred year return period (HQ_{100}). This time might be rather short compared to the total flood event, e. g. the passage of an entire flood hydrograph. The experiment duration in the present study ranged from 117 *min* to 245 *min*. For the conversion from experimental conditions to prototype conditions a geometrical model scale factor of $\lambda_L \approx 1 : 30 \div 1 : 50$ has to be respected.

With respect to measured bed-load transport rates best results have been obtained with the MPM-formula (Meyer-Peter and Müller (1948), appendix A.6.2, Eq. A.130) with a correction factor of 1.90 for absolute transport quantities (Tab. 5.14).

As far as bed form classification methods are concerned satisfying correlation has been identified for the regime predictors of Van Rijn (1984b) and Karim (1999) (appendix A.3.1).

Bed form geometry expressed in terms of length, height and steepness is fairly well represented by the methods of Van Rijn (1984b) and Julien and Klaassen (1995) (appendix A.3.2). Attention should be paid to the geometrical bed form dimensions, since bed form scales in natural rivers might be often much larger than in flumes.

To account for plane bed roughness (grain roughness) the approaches of Strickler (1923) (Eq. A.27), Meyer-Peter and Müller (1948) (Eq. A.27) and Engelund and Hansen (1967) (Eq. A.28 and Tab. A.3) might be recommended. With respect to total flow resistance (effects of grain and form roughness) the method of Yalin and da Silva (2001) is suggested (appendix A.4.1). Concerning the repartition of grain and form roughness a recommendation for the roughness predictor of Van Rijn (1984b) can be given (appendix A.4.1).

The analysis dealing with the determination of an adequate side weir discharge coefficient (C_D) revealed that the approaches of

Subramanya and Awasthy (1972) and Hager (1987b) yield satisfying results (appendix A.7.3).

For practical purposes it might be important to note that the ramp-like deposit could favor sediment intrusion into retention areas, thus, depending on the retention volume, reduce storage capacity (Figs 2.4, 5.38 and 5.39). Moreover, expensive removal by heavy duty machinery has to be taken into account.

Besides having an impact on the intensity of the side overflow discharge the sedimentary deposit influences the bed evolution downstream of the weir. The deposit is responsable for flow diversion towards the opposite river bank. Therefore, appropriate bank protection measures need to be considered to protect the opposite river bank from lateral erosion. Moreover, the thalweg downstream of the overflow develops in an oscillatory way before being damped out. In paragraph 5.9.2 indicative relationships to describe the sine-generated mobile bed evolution downstream of the weir as well the extent of the erosion gutter are presented.

9.2.2. Measures to reduce Aggradation

Parallel to the empirical approaches the sediment problem might be diminished by means of several accompanying mitigation measures, e. g. the installation of erosion-promoting vanes, currently referred to as Iowa-vanes (Odgaard and Spoljaric (1986), Flokstra (2006)), submerged guidewalls, skimming walls or optimized riverbank alignment (Michell et al. (2006)). An important consideration in the successful functioning of submerged vanes is that the ratio of unit discharge of flow over the weir (q_D) should be less than a prescribed proportion of the average unit discharge of the cross flow in the main-channel sweeping past the weir (q_2). This ratio should not exceed a value of about $q_D/q_2 = 0.35$. For the present study a ratio of $q_D/q_2 = 0.10$ is determined, hence conditions appear to be appropriate for the installation of such devices.

Another option is to create a lateral constriction in order to establish so-called pseudo-uniform flow conditions as reported by Hager and Volkart (1986). These modifications might accelerate flow velocity and hence shear stress leading to increased bed-load transport in the weir alignment.

An interesting option to maximize sediment transport is proposed by Yu and Smart (2003). The optimal dimensions of a rectangular channel with rigid banks that maximizes bed-load transport is given by:

$$\frac{B}{y} = \frac{78}{7} \cdot \left(\frac{k_{st,b}}{k_{st,w}} \right)^{3/2} \tag{9.1}$$

with B channel width, y flow depth and $k_{st,b}$ and $k_{st,w}$ Strickler-values related to the bed (including bed form effects) and to the wall, respectively.

For the development of Equation 9.1 common engineering design assumptions and formulas were used, viz, bed-load transport is appropriately expressed by the formula of Meyer-Peter and Müller (1948), flow resistance is described by the Strickler-equation, effects of bed forms of the lower flow regime are incorporated by the procedure of Engelund and Fredsøe (1982) and different bank and bed roughness is accounted for by the side wall correction procedure of Einstein (1942). It is stated that channel banks may require protection to maintain the optimum aspect ratio, the optimum aspect ratio is very sensitive to the ratio of the wall to bed roughness and that natural channels probably do not maximize sediment transport.

Applying Equation 9.1 to the present study ($k_{st,b} \approx 63\ m^{1/3}/s$, $k_{st,w} \approx 100\ m^{1/3}/s$) yields $B/y = 5.57$. With $y \approx 0.10\ m$ downstream of the weir an optimal channel width for maximized bed-load transport would correspond to $B = 0.56\ m$. Using the channel width of the present study ($B = 1.50\ m$) the actual channel would require a width reduction of $0.56/1.50 = 37\ \%$.

9.3. Outlook and further Research

The work done on the behavior of a side weir overflow in presence of a mobile bed and bed-load transport in a flume constitues a first step in developing appropriate models to take into account this flow-sediment interaction.

The present experimental investigations have been conducted for a constant channel width. Moreover, the same grain size distribution has been used throughout all test series. Since both parameters are assumed to have an impact on the formation and the extent of a sedimentary deposit and, hence overflow discharge, additional laboratory tests should be considered. These tests should also focus on a wider range of weir crest lengths to enlarge the variety of weir crest length to main-channel width ratios (L_D/B) already existing from the present work.

Regarding the variation of main-channel width and grain diameter indicative $1D$ numerical simulations have been performed and approximative tendencies could be derived. However, it is suggested to extend the numerical simulations from the $1D$- characteristics to $2D$- or even $3D$-applications. These simulations should refer to both, hydrodynamic as well as computations taking into account bed-load transport. In this context it has to be mentioned that the present study furnishes a very precious data set including free water surface measurements, detailed bed topography (DEM) and the $2D$-velocity field which can be used for calibration and validation of numerical models.

Performing supplementary flume experiments the existing velocity measurements could be extended from the $2D$-flow field to the $3D$-flow field. Hence, further insight into the complex flow pattern and bed-load transport processes in the vicinity of the side overflow can be obtained. Special interest should be laid on the effects of secondary circulation and near-bed flow pattern. The available flow velocity data in the $2D$-plane enriched by additional $3D$-velocity recordings could be further analyzed in terms of turbulence characteristics to complement the process of understanding the three-dimensional flow-sediment interaction at lateral outflow structures.

Additional flume experiments might also deal with mitigation measures to reduce aggradation in the weir reach. Herein, submerged vanes or lateral constrictions to enhance bed-load transport and achieve so-called pseudo-uniform flow conditions could be investigated.

Currently, only experimental investigations exist. Although it appears to be rather difficult to measure flow and bed-load parameters during a major flood event it would be desirable to perform field tests. This would allow to obtain information about the extent of the deposit and its impact on side overflow intensity under prototype conditions.

Acknowledgements

The present research project has been performed at the Laboratory of Hydraulic Constructions (LCH) at the Swiss Federal Institute of Technology in Lausanne (EPFL), Switzerland.

First of all I would like to express my gratitude to Prof. Dr. Anton Schleiss for his outstanding and inspiring attitude during the time I have been working on my dissertation. Under his supervision I got the opportunity to carry out this extremely interesting and challenging project.

I would like to thank him for welcoming me in his team, his confidence, guidance and scientific and financial support and the freedom and opportunities granted to achieve my own ideas and goals. At the same time I strongly appreciate his daily effort and his effectiveness which has always been a great example for me and encouraged me to realize this study.

Moreover, I would like to thank for the excellent working conditions and the opportunity to attend several national and international conferences stimulating on the one hand the scientific exchange with other colleges but also giving the possibility to establish several helpful and beneficial contacts. From these contacts I have deeply profited during my work and they will certainly be of great importance in the future as well.

Dr. Jean-Louis Boillat belongs to the persons I appreciate a lot for the numerous vivid scientific but also non-scientific discussions. It has always been a great pleasure working with him.

The author acknowledges the financial support by the Swiss Innovation Promotion Agency (CTI, grant no. 4898.1) and the Swiss Federal Office for the Environment (FOEN), especially Dr. Gian Reto Bezzola.

Gratitude is dedicated to the members of the jury, Prof. Gerhard Jirka, Dr. Gian Reto Bezzola and Prof. Christophe Ancey for acting as co-examiners, their comments and proof reading.

I appreciated a lot to meet and discuss with Prof. Yves Zech during his two visits in Lausanne as invited professor and at several conferences. His enthusiasm and the intense scientific exchange have been very stimulating and encouraging.

I do not forget the sympathy of Prof. Otto Kölbl and Dr. Julien Vallet from the Laboratory of Photogrammetry (IPHOT, EPFL, Lausanne,

Switzerland) for their substantial support in creating the digital elevation model.

Further, I am thankful to my colleges and friends of the LCH coming from all over the world for their help and the many fruitful discussions and the excellent personal relations.

Appreciation is also due to my colleagues I met and worked with since I graduated from the University of Karlsruhe. Thanks to Nils, Stefan and Ingo for the sound and challenging technical and scientific discussions but especially for just being friends.

Apart from the professional life I would like to thank my longtime friends from Menden, Christian, Jochen, Mark, Thomas and Thorsten, and Karlsruhe, Christian, Ingo, Max, Miro, Nils, Petra, Sebbi, Stefan and Wolfi, for the plenty of fantastic hours we passed together and still do.

Finally I want to express my gratitude to my loving parents for making possible my education, the continuous support and encouragement. Thank also goes to my brothers Markus and Christian.

Last but not least I thank Annette with all my love and heart for her incredible support and patience throughout these years.

Ein ganz besonderer Dank gilt auch der wunderbaren Sophie, die mir in den letzten Jahren so viel Freude bereitet hat und die ich so sehr lieb habe.

Lausanne, July 2007

Burkhard Rosier

References

Ackers, P. (1957). A theoretical consideration of side weirs as storm-water overflows, *Proceedings, Institution of Civil Engineers, London* **6**: 250–269.

Ackers, P. (1993a). Flow formulae for straight two-stage channels, *Journal of Hydraulic Research* **31**(4): 509–531.

Ackers, P. (1993b). Stage-discharge functions for two-stage channels: The impact of new research, *Journal of the Chartered Institution of Water and Environmental* **7**(1): 52–61.

Ackers, P. and White, W. R. (1973). Sediment transport: New approach and analysis, *Journal of the Hydraulics Division, ASCE* **99**(HY11): 2041–2060.

Agaccioglu, H. and Yüksel, Y. (1998). Side-weir flow in curved channels, *Journal of Irrigation and Drainage Engineering* **124**(3): 163–175.

Alam, A. M. Z. and Kennedy, J. F. (1969). Friction factors for flow in sand bed channels, *Journal of the Hydraulics Division, ASCE* **95**(HY6): 1973–1992.

Allen, J. R. L. (1968). *Current ripples*, North-Holland Publishing Company, Amsterdam, The Netherlands.

Allen, J. W. (1957). The discharge of water over side weirs in circular pipes, *Proceedings, Institution of Civil Engineers, London* **6**: 270–287.

Annambhotla, V. S. S., Sayre, W. W. and Livesey, R. H. (1972). Statistical properties of Missouri river bed forms, *Journal of the Waterways, Harbours and Coastal Engineering Division, ASCE* **98**(WW4): 489–510.

Ashida, K. and Tanaka, Y. (1967). A statistical study of sand waves, Proc. 12^{th} IAHR Congress, Fort Collins, Colorado, USA, International Association of Hydraulic Engineering and Research (IAHR), pp. B12, 1–8.

Atabay, S. and Knight, D. W. (1998). Stage-discharge and resistance relationships for laboratory alluvial channels with overbank flow, *in* A. W. Jayawardena, J. H. W. Lee and Z. Y. Wang (eds), *ISRS 1998*, Proc. 7^{th} International Symposium on River Sedimentation - ISRS, Hong Kong, China, Balkema, Rotterdam, The Netherlands, pp. 223–229.

Babovic, V., Keijzer, M., Rodriguez Aguilera, D. and Harrington, J. (2001). An evolutionary approach to knowledge induction: Genetic rogramming in hydraulic engineering, Proc. World Water and Environmental Resources Congress, Orlando, Florida, USA.

Bagnold, R. A. (1966). An approach to the sediment transport problem from general physics, *U.S. Geological Survey* **422**(I).

Balmforth, D. J. and Sarginson, E. J. (1977). Discussion of "Experimental investigation of flow over side weirs" by A. El-Khashab and K.V.H. Smith, *Journal of the Hydraulics Division* **103**(8): 941–943.

Balmforth, D. J. and Sarginson, E. J. (1983a). The effect of curvature in supercritical side weir flow, *Journal of Hydraulic Research* (21): 333–343.

Balmforth, D. J. and Sarginson, E. J. (1983b). An experimental investigation of the discharge capacity of side weirs, *International Conference on the Hydraulic Aspects of Floods and Flood Control*, number F2, BHRA, London, pp. 171–181.

Benson, I., Valentine, E. M., Nalluri, C. and Bathurst, J. C. (1997). Flood channel facility: Expriments in two-stage mobile boundary channels, *in* S. S. Y. Wang and T. Carstens (eds), *Environmental and Coastal Hydraulics: Protecting the Aquatic Habitat*, Proc. 27^{th} IAHR Congress, San Francisco, USA, International Association of Hydraulic Engineering and Research (IAHR), pp. 949–954.

Blanckaert, K. and Graf, W. H. (2001). Experiments on flow in a strongly curved channel bend, 21^{st} *Century: The new era for Hydraulic Research and its Applications*, Proc. 29^{th} IAHR Congress, Beijing, China, International Association of Hydraulic Engineering and Research (IAHR), pp. 371–377.

Boillat, J.-L., Dubois, J. and Nilipour, N. (2006). Migration of a dredging pit in the Rhone river, *in* R. M. L. Ferreira, E. C. T. L. Alves, J. G. A. B. Leal and A. H. Cardoso (eds), *RiverFlow 2006*, Proc. 3^{rd} International Conference on Fluvial Hydraulics - RiverFlow, Lisbon, Portugal, A. A. Balkema Publishers, pp. 1193–1202.

Boisseau, T., Camp'Huis, N.-G. and Gautheron, A. (n.d.). Stratégie d'encrêtement des crues fortes de la Loire moyenne, *Technical report*, Agence de l'eau Loire - Bretagne.

Borghei, S. M., Jalili, M. R. and Ghodsian, M. (1999). Discharge coefficient for sharp-crested side weir in subcritical flow, *Journal of Hydraulic Engineering* **125**(10): 1051–1056.

Bosshard, M. (2000). Hochwasserschutz Reuss - Sicherheit, Effizienz und Ökologie - Wiederaufbau der Dämme an der Reussmündung im Kanton Uri, *Schweizer Ingenieur und Architekt* **36**.

Brownlie, W. R. (1981). Flow depth in sand bed channels, *Tech. Memo 81-3*, W. H. Keck Laboratory of Hydraulics and Water Resources, California Institute of Pasadena, Pasadena, Calif.

Cao, Z., Pender, G. and Meng, J. (2006). Explicit formulation of the Shields diagram for incipient motion of sediment, *Journal of Hydraulic Engineering* **132**(10): 1097–1099.

Catella, M., Bechi, G., Paris, E., Rosier, B. and Schleiss, A. J. (2007). One-dimensional numerical scheme to model bed evolution in presence of a side overflow, *in* C. M. Dohmen-Janssen and S. J. M. H. Hulscher (eds), *RCEM 2007*, Proc. 5^{th} IAHR Symposium on River, Coastal and Estuarine Morphodynamics - RCEM, Enschede, The Netherlands, Taylor and Francis, pp. 1211–1218, Vol. 2.

Chanson, H. (2004). *The hydraulics of open-channel flow: An introduction*, second edn, Elsevier Butterworth-Heinemann.

Cheng, N. S. (1997). Simplified settling velocity formula for sediment particle, *Journal of Hydraulic Engineering* **123**(2): 149–152.

Cheng, N. S. and Chua, L. H. C. (2005). Comparisons of sidewall correction of bed shear stress in open-channel flows, *Journal of Hydraulic Engineering* **131**(7): 605–609.

Cheong, H. F. (1991). Discharge coefficient of lateral diversion from trapezoidal channel, *Journal of Irrigation and Drainage Engineering* **117**(4): 461–475.

Chien, N. and Wan, Z. (1999). *Mechanics of sediment transport*, ASCE, Reston, Virginia, USA.

Chiew, Y. M. (1991). Bed features in non-uniform sediments, *Journal of Hydraulic Engineering* **117**(1): 116–121.

Chow, V. T. (1973). *Open-Channel Hydraulics*, McGraw Hill International Editions.

Clemmens, A. J. (2005). Discussion of "Transition effects in flow over side weirs" by Y. Muslu and E. Yüksel and H. Tozluk, *Journal of Irrigation and Drainage Engineering* **131**(4): 392.

Coleman, G. S. and Smith, D. (1923). The discharging capacity of side weirs, *Institution of Civil Engineers, London, Selected Engineering Papers* (6).

Collinge, V. K. (1957). The discharge capacity of side weirs, *Proceedings, Institution of Civil Engineers, London* **6**: 288–304.

Creager, W. P. and Justin, J. D. (1950). *Hydroelectric Handbook*, second edn, John Wiley and Sons, New York.

Das, A. (1997). Spatially varied flow over an embankment side weir, *Journal of Irrigation and Drainage Engineering* **123**(4): 314–317.

De Marchi, G. (1934). Saggio di teoria del funzionamento degli stramazzi laterali, *L'Energia Elettrica* **11**(11): 849–860.

De Vries, M. (1975). A morphological time scale for rivers, Proc. 16^{th} IAHR Congress, Sao Paulo, Brazil, International Association of Hydraulic Engineering and Research (IAHR).

Del Giudice, G. and Hager, W. H. (1999). Sewer side weir with throttling pipe, *Journal of Irrigation and Drainage Engineering* **125**(5): 298–306.

Dietrich, E. W. (1982). Settling velocity of natural particles, *Water Resources Research* **18**(6): 1626–1982.

Dittrich, A. (1998). Wechselwirkung Morphologie/Strömung natürlicher Fliessgewässer, *Mitteilungen des Instituts für Wasserwirtschaft und Kulturtechnik (IWK) 198*, Universität Karlsruhe (TH), Germany.

Du Boys, P. (1879). Etudes du régime du Rhône et l'action exercée par les eaux sur un lit à fond de graviers indéfiniment affouillable, *Annales des Ponts et Chaussées* **18**(5): 141–195.

Dubois (1999). *DEPERO - User's manual*, LCH - EPFL, Switzerland.

Einstein, H. A. (1942). Formulas for the transportation of bed-load, *Trans. Am. Soc. Civ. Eng.* **107**: 561–577.

Einstein, H. A. (1950). The bed-load function for sediment transportation in open-channel flows, *Technical Bulletin 1026*, U.S. Department of Agriculture Soil Conservation Service, Washington, D.C.

Einstein, H. A. and Barbarossa, N. L. (1952). River channel roughness, *Trans. Am. Soc. Civ. Eng.* **117**: 1121–1146.

El-Khashab, A. and Smith, K. V. H. (1976). Experimental investigation of flow over side weirs, *Journal of the Hydraulics Division* **102**(9): 1255–1268.

Engels, H. (1917). *Forschungsarbeiten auf dem Gebiete des Ingenieurwesens*, Vol. 200 and 201, Berlin, p. 55.

Engelund, F. (1966). Hydraulic resistance of alluvial streams, *Proc. Am. Soc. Civ. Engrs.* **92**(HY2).

Engelund, F. (1977). Hydraulic resistance for flow over dunes, *Progress Report 44, pp. 19-20*, Inst. Hydr. and Hydr. Eng., Technical University of Denmark, Lyngby, Denmark.

Engelund, F. and Fredsøe, J. (1982). Sediment ripples and dunes - annual review of fluid mechanics, *Journal of Fluid Mechanics* **14**: 13–38.

Engelund, F. and Hansen, E. (1967). *A monograph on sediment transport in alluvial streams*, Teknisk Vorlag, Copenhagen, Denmark.

Ervine, A., Fuller, C. and Pender, G. (1997). Sediment transport in a gravel bed channel during overbank flow, *in* S. S. Y. Wang and T. Carstens (eds), *Environmental and Coastal Hydraulics: Protecting the Aquatic Habitat*, Proc. 27^{th} IAHR Congress, San Francisco, USA, International Association of Hydraulic Engineering and Research (IAHR), pp. 1031–1036.

Etheridge, M. J. (1996). The hydraulic analysis of side channel spillways as reservoir outlets, *Journal of the Chartered Institution of Water and Environment* **10**: 245–252.

Favre, H. (1933). Contribution à l'étude des courants liquides, Dunod, Paris.

Favre, H. (1937). Sur les lois régissant le mouvement des fluides dans les conduites en charge avec adduction latérale, *Revue universelle des mines* **13**(12): 502–512.

Favre, H. and Braendle, F. (1937). Expériences sur le mouvement permanent de l'eau dans les canaux découverts, avec apport ou prélèvement le long du courant, *Bulletin Technique de la Suisse Romande* (63): 93–96, 109–114, 129–134.

Ferroglio, L. (1941). Contributo allo studio degli sfioratori laterali, *Energia Elettrica* (18): 783–791.

Führböter, A. (1967). Zur Mechanik der Strömungsriffel - Ein Ansatz zur Berechnung der Höhe der Transportkörper und ihres Einflusses auf den Feststofftransport (in German), Mitteilung, Nr. 29, Franzius-Institut, Technische Universität Hannover (TH), Hannover, Germany, pp. 1–35.

Flokstra, C. (2006). Modelling of submerged vanes, *Journal of Hydraulic Research* **44**(5): 591–602.

Forchheimer, P. (1930). Hydraulik, 3rd edn, Teubner Verlagsgesellschft, Leipzig and Berlin, pp. 406–409.

Frazer, W. (1957). The behaviour of side weirs in prismatic rectangular channels, *Proceedings, Institution of Civil Engineers, London* **6**: 305–328.

Fredsøe, J. (1982). Shape and dimensions of stationary dunes in rivers, *Journal of the Hydraulics Division, ASCE* **108**(8).

Garde, R. J. and Ranga Raju, K. G. (1963). Regime criteria for alluvial streams, *Proc. Am. Soc. Civ. Engrs.* **89**(HY6).

Garde, R. J. and Ranga Raju, K. G. (1966). Resistance relationships for alluvial channel flow, *Proc. Am. Soc. Civ. Engrs.* **92**(HY4).

Geisler, T., Breitenstein, S., Hammer, A., Mayr, D. and Klasinc, R. (2003). Hydraulic modelling - mapping of river bed, *in* J. Granulis and P. Prinos (eds), *Water engineering and research in a learning society: Modern developments and traditional concepts*, Proc. 30^{th} IAHR congress, Thessaloniki, Greece, International Association of Hydraulic Engineering and Research (IAHR).

Gentilini, B. (1938). Ricerche sperimentali sugli sfioratori longitudinali, *Energia Elettrica* **15**(9): 583–595.

Gill, M. A. (1971). Height of sand dunes in open-channel flows, *Journal of the Hydraulics Division, ASCE* **97**(HY12): 2067–2074.

Graf, W. H. (1971). *Hydraulics of sediment transport*, McGraw-Hill Company Inc., London, UK.

Graf, W. H. (1984). *Hydraulics of sediment transport*, Water Resources Publications, LLC, New York, USA.

Graf, W. H. and Altinakar, M. S. (1998). *Fluvial Hydraulics*, John Wiley and Sons.

Graf, W. H. and Altinakar, M. S. (2000). Hydraulique fluviale, *Traité de Génie Civil*, Vol. 16, Presse polytechniques et universitaires romandes, Lausanne, Switzerland.

Hager, W. H. (1982a). Die Hydraulik von Verteilkanälen - Teil 1: Theorie der Verteilkanäle (in German), Mitteilung, Nr. 55, Versuchsanstalt für Wasserbau, Hydrologie und Glaziologie (VAW), Eidgenössische Technische Hochschule Zürich (ETHZ), Zürich, Switzerland.

Hager, W. H. (1982b). Die Hydraulik von Verteilkanälen - Teil 2: Experimente in Verteilkanälen (in German), Mitteilung, Nr. 56, Versuchsanstalt für Wasserbau, Hydrologie und Glaziologie (VAW), Eidgenössische Technische Hochschule Zürich (ETHZ), Zürich, Switzerland.

Hager, W. H. (1984). Discussion of "The effect of curvature in supercritical side weir flow" by D.J.. Balmforth and E.J.. Sarginson, *Journal of Hydraulic Research* (22): 291–298.

Hager, W. H. (1987a). Discussion of "Flow over side weirs in circular channels" by A. Uyumaz and Y. muslu, *Journal of Hydraulic Engineering* **113**(5): 685–690.

Hager, W. H. (1987b). Lateral outflow over side weirs, *Journal of Hydraulic Engineering* **113**(4): 491–504.

Hager, W. H. and Hager, K. (1985). Streamline curvature effects in distribution channels, *Proc. Instn. Mech. Engrs.* **199**(C3): 165–172.

Hager, W. H. and Volkart, P. U. (1986). Distribution channels, *Journal of Hydraulic Engineering* **112**(10): 935–952.

Henderson, F. M. (1966). *Open-channel flow*, Macmillan, New York, USA.

Hersberger, D. S. (2002). Measurement of 3d flow field in a 90 degree bend with ultrasonic Doppler velocity profiler, *ISUD 2002*, Proc. 3^{rd} International Symposium on Ultrasonic Doppler Method for Fluid Mechanics and Fluid Engineering - ISUD, Lausanne, Switzerland, PSI Proceedings 02-01, ISSN 1019-6447, pp. 59–66.

Hersberger, D. S. (2003). Wall roughness effects on flow and scouring in curved channels with gravel bed, Ph.D. dissertation, Communication No. 14, Laboratoire de Constructions Hydrauliques (LCH), Ecole Polytechnique Fédérale de Lausanne (EPFL), Lausanne, Switzerland.

Hey, R. (1979). Flow resistance in gravel bed rivers, *Journal of the Hydraulics Division* **105**(HY4): 365–380.

Hjulström, F. (1935). *The morphological activity of rivers as illustrated by river Fyris*, Vol. 25, chapter 3.

Hunziker, R. P. (1995). Fraktionsweiser Geschiebetransport, *Mitteilungen der Versuchsanstalt für Wasserbau, Hydrologie und Glaziologie (VAW) 138*, Eidgenössische Technische Hochschule Zürich (ETHZ), Zürich, Switzerland.

Jalili, M. R. and Borghei, S. M. (1996). Discussion of "Discharge coefficient of rectangular side weirs" by R. Singh and D. Manivannan and T. Sataynarayana, *Journal of Irrigation and Drainage Engineering* **122**(2): 132.

Jäggi, M. N. R. (1984a). Abflussberechnung in kiesführenden Flüssen, *Die Wasserwirtschaft* **74**(5): 263–267.

Jäggi, M. N. R. (1984b). Der Geschiebetransport in Flüssen nach der VAW-Formel 1983, *Schweizer Ingenieur und Architekt* **47**.

Jäggi, M. N. R. (1999/2000). Flussbau, *Technical report*, Versuchsanstalt für Wasserbau, Hydrologie und Glaziologie (VAW), Eidgenössische Technische Hochschule Zürich (ETHZ), Zürich, Switzerland.

Julien, P. Y. and Klaassen, G. J. (1995). Sand dune geometry of large rivers during floods, *Journal of Hydraulic Engineering* **121**(9): 657–663.

Kamphuis, J. W. (1974). Determination of sand roughness for fixed beds, *Journal of Hydraulic Research* **12**(2).

Karim, F. (1999). Bed-form geometry in sand-bed flows, *Journal of Hydraulic Engineering* **125**(12): 1253–1261.

Keijzer, M. and Babovic, V. (1999). Dimensionally aware genetic programming, *GECCO 1999*, Proc. Genetic and Evolutionary Computation Conference - GECCO, Orlando, Florida, USA.

Kerssens, P. J. M. and Van Urk, A. (1986). Experimental studies on sedimentation due to water withdrawal, *Journal of Hydraulic Engineering* **112**(7): 641–656.

Khorchani, M. and Blanpain, O. (2005). Development of a discharge equation for side weirs using artificial neural networks, *Journal of Hydroinformatics* **7**(1): 31–39.

Kölbl, O. (1988). Cours de photogrammetrie I et II, *Support de cours*, Ecole Polytechnique Fédérale de Lausanne.

Knight, D. W. and Brown, F. A. (2001). Resistance studies of overbank low in rivers with sediment using the flood channel facility, *Journal of Hydraulic Research* **39**(3): 283–301.

Knight, D. W., Brown, F. A., Ayyoubzadeh, S. A. and Atabay, S. (1998). Sediment transport in river models with overbank flow, *in* A. W. Jayawardena, J. H. W. Lee and Z. Y. Wang (eds), *ISRS 1998*, Proc. 7^{th} International Symposium on River Sedimentation - ISRS, Hong Kong, China, Balkema, Rotterdam, The Netherlands, pp. 19–25.

Kobus, H. (1978). Wasserbauliches Versuchswesen, *Deutscher Verband für Wasserwirtschaft-DVWW, Mitteilungsheft Nr.4*.

Kondap, D. M. and Garde, R. J. (1973). Velocity of bed forms in alluvial channels, Vol. 5 of *Proc.* 15^{th} *IAHR Congress, Istanbul, Turkey*, International Association of Hydraulic Engineering and Research (IAHR).

Kondratiev, N. (1962). River flow and river channel formation (translation from Russian (1959)), *Natl. Sci. Found. and U.S. Dept. Interior.* .

Kondratiev, N., Popov, I. and Snishchenko, B. (1982). *Foundations of hydromorphological theory of fluvial processes (in Russian)*, Gidrometeoizdat, Leningrad, Russia.

Kumar, C. P. and Pathak, S. K. (1987). Triangular side weirs, *Journal of Irrigation and Drainage Engineering* **113**(1): 98–105.

Lane, S. N., Chandler, J. H. and Porfiri, K. (2001). Monitoring river channel and flume surfaces with digital photogrammetry, *Journal of Hydraulic Engineering* **127**(10): 871–877.

Langhorne, D. N. (1978). Offshore engineering and navigational problems-relevance of sand wave research, *Technical report*, Inst. of Oceanographic Sciences, Wormley, Godalming, U.K.

Lisle, T. E., Pizzuto, J. E., Ikeda, H. and Iseya, F. (1997). Evolution of a sediment wave in an experimental channel, *Water Resources Research* **33**(8): 1971–1981.

Liu, H. K. (1957). Mechanics of sediment-ripple formation, *Journal of the Hydraulics Division, ASCE* **83**(HY2): 1–21.

Manning, R. (1889). On the flow of water in open-channels and pipes, *Transactions of the Institution of Civil Engineers of Ireland* **20**: 161–207.

Metflow (2000). *UVP Monitor Model UVP-XW User's Guide*, Metflow SA - Lausanne, Switzerland.

Meyer-Peter, E. and Müller, R. (1948). Formulas of bed-load transport, *Report on the second meeting of the IAHSR (today IAHR), 7-9 June*, Stockholm, Sweden, pp. 39–64.

Michell, F., Ettema, R. and Muste, M. (2006). Case study: Sediment control at water intake for large thermal power station on a small river, *Journal of Hydraulic Engineering* **132**(5): 440–449.

Muslu, Y. (2001). Numerical analysis for lateral weir flow, *Journal of Irrigation and Drainage Engineering* **127**(4): 246–253.

Muslu, Y. (2003). Effect of lateral water surface profile on side weir discharge, *Journal of Irrigation and Drainage Engineering* **129**(5): 371–375.

Muslu, Y., Yüksel, E. and Tozluk, H. (2004). Transition effects in flow over side weirs, *Journal of Irrigation and Drainage Engineering* **130**(1): 92–95.

Nadesamoorthy, T. and Thomson, A. (1972). Discussion of "Spatially varied flow over side-weirs" by K. Subramanya and S.C. Awasthy, *Journal of Hydraulics Division* **98**(12): 2234–2235.

Naudascher, E. (1992). *Hydraulik der Gerinne und Gerinnebauwerke*, Springer Verlag, Wien, New York.

Neary, V. S. and Odgaard, A. J. (1993). Three dimensional flow structure at open channel diversions, *Journal of Hydraulic Engineering* **119**(11): 1223–1230.

Neary, V. S., Sotiropoulos, F. and Odgaard, A. J. (1999). Three dimensional numerical model of lateral intake inflows, *Journal of Hydraulic Engineering* **125**(2): 126–140.

Nicollet, G. and Uan, M. (1979). Ecoulements permanents à surface libre en lits composés, *La Houille Blanche* **1**: 21–30.

Nikora, V. I., Sukhodolov, A. N. and Rowinski, P. M. (1997). Statistical sand waves dynamics in the one-directional water flows, *Journal of Fluid Mechanics* **351**: 17–39.

Nikuradse, J. (1933). Strömungsgesetze in rauhen Rohren, *Beilage zur Forschung auf dem Gebiete des Ingenieurwesens; Ausgabe B, Band 4, Juli/ August*, VDI-Verlag GmbH, Berlin NW7.

Odgaard, A. J. and Spoljaric, A. (1986). Sediment control by submerged vanes, *Journal of Hydraulic Engineering* **112**(12): 1164–1181.

Odgaard, A. J. and Wang, Y. (1991a). Sediment management with submerged vanes. I: Theory, *Journal of Hydraulic Engineering* **117**(10): 267–283.

Odgaard, A. J. and Wang, Y. (1991b). Sediment management with submerged vanes. II: Applications, *Journal of Hydraulic Engineering* **117**(10): 284–302.

Ogink, H. (1988). Hydraulic roughness of bed forms, *Report M2017*, Delft Hydraulics, Delft, The Netherlands.

Ramamurthy, A. S. and Carballada, L. (1980). Lateral weir flow model, *Journal of the Irrigation and Drainage Division* **106**(IR1): 9–25.

Ramamurthy, A. S., Qu, J. and Vo, D. (2006). Nonlinear PLS method for side weir flows, *Journal of Irrigation and Drainage Engineering* **132**(5): 486–489.

Ranga Raju, K. G., Prasad, B. and Gupta, S. K. (1979). Side weir in rectangular channel, *Journal of the Hydraulics Division* **105**(5): 547–554.

Ranga Raju, K. G. and Soni, J. P. (1976). Geometry of ripples and dunes in alluvial channels, *Journal of Hydraulic Research* **14**(3).

Raudkivi, A. J. (1990). *Loose boundary hydraulics*, 3rd edn, Pergamon Press, Oxford, New York.

Rehbock, T. (1929). Wassermessung mit scharfkantigen Überfallwehren, *Zeitschrift VdI* **73**(817ff).

Rodriguez Aguilera, D. (2000). *Genetic Programming with GPKernel - User's Manual, version November 2000*, Software developed by V. Babovic and M. Keijzer, Danish Hydraulic Institute (DHI).

Rolland, T. (1995). *Développement d'une instrumentation Doppler ultrasonore: Application aux écoulements turbulents*, PhD thesis, Laboratoire de Recherches Hydrauliques (LRH) (today: Laboratoire d'Hydraulique Environnementale (LHE)), Ecole Polytechnique Fédérale de Lausanne (EPFL), Lausanne, Switzerland.

Rosier, B., Boillat, J.-L. and Schleiss, A. J. (2004e). Mapping of bed morphology for lateral overflow using digital photogrammetry, *ICSE-2 2004*, Proc. 2^{nd} International Conference on Scour and Erosion - ICSE-2, Singapore, Singapore.

Rosier, B., Boillat, J.-L. and Schleiss, A. J. (2004f). Velocity distribution and discharge intensity of lateral overflow on mobile bed, *in* J. H. W. Lee and K. M. Lam (eds), *Environmental hydraulics and sustainable water*

management, Proc. 4^{th} International Symposium on Environmental Hydraulics - ISEH and 14^{th} Congress of the Asia and Pacific Division of IAHR - IAHR-APD, Hong Kong, China, A. A. Balkema Publishers, pp. 1659–1665.

Rosier, B., Boillat, J.-L. and Schleiss, A. J. (2005d). Influence of side overflow induced local sedimentary deposit on bed form related roughness and intensity of diverted discharge, *in* B.-H. Jun, S.-I. Lee, I. W. Seo and G.-W. Choi (eds), *Water Engineering for the Future: Choices and Challenges*, Proc. 31^{th} IAHR Congress, Seoul, South Korea, International Association of Hydraulic Engineering and Research (IAHR), pp. 1639–1650.

Rosier, B., Boillat, J.-L. and Schleiss, A. J. (2005e). Influence of bed morphology on side weir discharge coefficient, *in* G. Parker and M. H. Garcia (eds), *RCEM 2005*, Proc. 4^{th} IAHR Symposium on River, Coastal and Estuarine Morphodynamics - RCEM, Urbana, Illinois, USA, A. A. Balkema Publishers, pp. 1213–1221.

Rosier, B., Boillat, J.-L. and Schleiss, A. J. (2006c). Semi-empirical model to predict mobile bed evolution in presence of a side overflow, *in* R. M. L. Ferreira, E. C. T. L. Alves, J. G. A. B. Leal and A. H. Cardoso (eds), *RiverFlow 2006*, Proc. 3^{rd} International Conference on Fluvial Hydraulics - RiverFlow, Lisbon, Portugal, A. A. Balkema Publishers, pp. 985–996.

Rosier, B., Boillat, J.-L. and Schleiss, A. J. (2007a). Bed form changes in presence of a lateral overflow, *in* G. Di Silvio and S. Lanzoni (eds), *Harmonizing the Demands of Art and Nature in Hydraulics*, Proc. 32^{nd} IAHR Congress, Venice, Italy, International Association of Hydraulic Engineering and Research (IAHR), p. 368 Abstractbook.

Rosier, B., Boillat, J.-L. and Schleiss, A. J. (2007b). Investigation of a sedimentary deposit in presence of a side overflow using a 1D-numercial model, *ISRS 2007*, Proc. 10^{th} International Symposium on River Sedimentation - ISRS, Moscow, Russia.

Rosier, B., Boillat, J.-L., Schleiss, A. J. and Teiller, J. (2004a). Influence d'un débordement latéral sur le transport solide par charriage dans un canal prismatique - Influence of lateral overflow on bed-load transport in a prismatic channel (in French), *in* I. Research Association Interpraevent (ed.), *The defense of populated territories from flooding, debris flows, avalanches and slope movements*, Proc. 10^{th} International Congress Interpraevent, Riva del Garda / Trento, Italy, pp. 257–268, Vol. 4.

Rosier, B., Jordan, F., De Cesare, G., Boillat, J.-L. and Schleiss, A. J. (2004d). Determination of velocity profiles and bed morphology using UVP transducers to investigate the influence of lateral overflow on mobile bed, *ISUD 2004*, Proc. 4^{th} International Symposium on Ultrasonic Doppler Method for Fluid Mechanics and Fluid Engineering - ISUD, Sapporo, Japan, pp. 47–50.

Rouse, H. (1946). *Elemantary mechanics of fluids*, John Wiley and Sons, New York.

Rouse, H. (1965). Critical analysis of open-channel resistance, *Journal of the Hydraulics Division, ASCE* **91**(HY4): 1–25.

Scheuerlein, H. and Schöberl, F. (2001). Integrated conception of hydraulic structures - intake structures, *Technical report*, Laboratoire de Constructions Hydrauliques (LCH)-Ecole Polytechnique Fédérale de Lausanne (EPFL), Switzerland.

Schlichting, H. (1968). *Boundary layer theorie*, McGraw-Hill Book Company, Inc., Verlag G. Braun, 6th edition.

Schmidt, M. (1954). Zur Frage des Abflusses über Streichwehre (in German), Instutut für Wasserbau, Mitteilung Nr. 41, Technische Universität Berlin-Charlottenburg, Berlin, Germany.

Schmidt, M. (1955). Die Berechnung von Streichwehren, *Die Wasserwirtschaft* **45**(4): 96–100.

Schoklitsch, A. (1930). *Handbuch des Wasserbaues*, Springer Verlag, Wien, New York.

Schoklitsch, A. (1950). *Handbuch des Wasserbaues, 2. Ausgabe (2^{nd} edition)*, Springer Verlag, Wien, New York.

Sellin, R. H. J. (1964). A laboratory investigation into the interaction between the flow in the channel of a river and that over its floodplain, *La Houille Blanche* **7**: 793–801.

Shen, H. W. (1962). Development of bed roughness in alluvial channels, *Proc. Am. Soc. Civ. Engrs.* **88**(HY3).

Shields, A. (1936). Anwendung der Ähnlichkeitsmechanik und Turbulenzforschung auf die Geschiebebewegung, *Mitteilungen der Preussischen Versuchsanstalt für Wasser- und Schiffsbau*, Vol. 26, Berlin.

Söhngen, B., Kellermann, J. and Loy, G. (1992). Modelling of the Danube and Isar rivers morphological evolution - Part I: Measurements and formulation, *in* P. Larsen and N. Eisenhauer (eds), *ISRS 1992*, Proc. 5^{th} International Symposium on River Sedimentation - ISRS, Karlsruhe, Germany, Universität Karlsruhe (TH), Germany, pp. 1175–1207.

Simons, D. B. and Richardson, E. V. (1961). Forms of bed roughness in alluvial channels, *Journal of the Hydraulics Division, ASCE* **87**(HY3): 87–105.

Simons, D. B. and Richardson, E. V. (1966). Resistance to flow in alluvial channels, *U.S. Geological Survey Prof. Paper* **422**(J).

Singh, R., Manivannan, D. and Satyanarayana, T. (1994). Discharge coefficient of rectangular side weirs, *Journal of Irrigation and Drainage Engineering* **120**(4): 814–819.

Singh, R. and Satyanarayana, T. (1994). Automated field irrigation system using side weirs, *Journal of Irrigation and Drainage Engineering* **120**(1): 48–59.

Sinniger, R. O. and Hager, W. H. (1989). Constructions hydrauliques, *Traité de Génie Civil*, Vol. 15, Presses polytechniques et universitaires romandes, Lausanne, Switzerland.

Smart, G. M. and Jäggi, M. N. R. (1983). Sedimenttransport in steilen Gerinnen - Sediment transport on steep slopes, *Mitteilungen der Versuchsanstalt für Wasserbau, Hydrologie und Glaziologie (VAW) 64*, Eidgenössische Technische Hochschule Zürich (ETHZ), Zürich, Switzerland.

Smith, J. D. and McLean, S. R. (1977). Spatially averaged flow over a wavy surface, *Journal of Geological Research* **82**: 1735–1746.

Smith, K. V. H. (1973). Computer programming for flow over side weirs, *Journal of the Hydraulics Division* **99**(3): 495–508.

SRCE (2000). Troisième correction du Rhône - Sécurité pour le futur (in French), Rapport de synthèse, Service des routes et cours d'eau du Canton du Valais (SRCE), Switzerland.

Strickler, A. (1923). Beiträge zur Frage der Geschwindigkeitsformel und der Rauhigkeitszahlen für Ströme, Kanäle und geschlossene Leitungen, *Mitteilungen des Eidgenössischen Amtes für Wasserwirtschaft 16*, Eidgenössisches Amt für Wasserwirtschaft, Bern, Switzerland.

Subramanya, K. and Awasthy, S. C. (1972). Spatially varied flow over side-weirs, *Journal of the Hydraulics Division* **98**(1): 1–10.

Sukhodolov, A. N., Fedele, J. J. and Rhoads, B. L. (2006). Structure of flow over alluvial bed forms: an experiment on linking field and laboratory methods, *Earth Surface Processes and Landforms* **31**: 1292–1310.

Swamee, P. K., Pathak, P. K. and Ali, M. S. (1994b). Side-weir analysis using elementary discharge coefficient, *Journal of Irrigation and Drainage Engineering* **120**(4): 742–755.

Swamee, P. K., Pathak, S. K., Mohan, M., Agrawal, S. K. and Ali, M. S. (1994a). Subcritical flow over rectangular side weir, *Journal of Irrigation and Drainage Engineering* **120**(1): 212–217.

Tang, X. and Knight, D. W. (2006). Sediment transport in river models with overbank flows, *Journal of Hydraulic Engineering* **132**(1): 77–86.

Teiller, J. (2000). Comportement hydraulique des digues fusibles, *MS thesis (travail de diplôme)*, Laboratoire de Constructions Hydrauliques (LCH), Ecole Polytechnique Fédérale de Lausanne (EPFL), Lausanne, Switzerland.

Tsubaki, T. and Shinohara, K. (1959). On the characteristics of sand waves formed upon the beds of open-channels and rivers, *Reports of the Research Institute for Applied Mechanics* **VII**(25).

USCE, U. A. C. o. E. (n.d.). *Hydraulic design criteria*, Army Waterways Experiment Station, Vicksburg, Mi., USA, different sheets from various years.

Uyumaz, A. (1992). Side weir in triangular channel, *Journal of Irrigation and Drainage Engineering* **118**(6): 965–970.

Uyumaz, A. and Muslu, Y. (1985). Flow over side weirs in circular channels, *Journal of Hydraulic Engineering* **111**(1): 144–160.

Uyumaz, A. and Smith, R. H. (1991). Design procedure for flow over side weirs, *Journal of Irrigation and Drainage Engineering* **117**(1): 79–90.

Uyumaz, U. (1997). Side weir in U-shaped channels, *Journal of Hydraulic Engineering* **123**(7): 639–646.

Valentine, E. M., Benson, I. A., Nalluri, C. and Bathrust, C. J. (2001). Regime theory and the stability of straight channels with bankfull and overbank flow, *Journal of Hydraulic Research* **39**(3): 259–268.

Van den Berg, J. H. and Van Gelder, A. (1989). Scour and fill sequences in flows over very fine sand and silt, *ICFS 1989*, Proc. 4^{th} International Conference on Fluvial Sedimentology - ICFS, Barcelona, Spain.

Van der Mark, C. F., Blom, A. and Hulscher, S. J. M. H. (2005). On modeling the variability of bed form dimensions, *in* G. Parker and M. H. Garcia (eds), *RCEM 2005*, Proc. 4^{th} IAHR Symposium on River, Coastal and Estuarine Morphodynamics - RCEM, Urbana, Illinois, USA, A. A. Balkema Publishers, pp. 831–841.

Van Rijn, L. C. (1982). Equivalent roughness of alluvial bed, *Journal of the Hydraulics Division, ASCE* **108**(HY10): 1215–1218.

Van Rijn, L. C. (1984a). Sediment transport, part I: Bed-load transport, *Journal of Hydraulic Engineering* **110**(10): 1431–1456.

Van Rijn, L. C. (1984b). Sediment transport, part III: Bed forms and alluvial roughness, *Journal of Hydraulic Engineering* **110**(12): 1733–1754.

Van Rijn, L. C. (1993). *Principles of sediment transport in rivers, estuaries and coastal seas*, Aqua Publications, Amsterdam, The Netherlands.

Vanoni, V. A. and Brooks, N. H. (1957). Laboratory studies of the roughness and suspended load of alluvial streams, *Report E-68*, Sedimentation Laboratory, California Institute of Technology, Pasadena, Calif.

Vanoni, V. A. and Hwang, L. S. (1967). Relation between bed forms and friction in streams, *Journal of the Hydraulics Division, ASCE* **93**(HY3): 121–144.

VAW (1989). Notentlastung der Reuss, *Technischer Bericht 4012*, Eidgenössische Technische Hochschule Zürich (ETHZ), Zürich, Switzerland.

VAW (1995). Hochwasserentlastung Reusskanal, *Technischer Bericht 4065/1*, Eidgenössische Technische Hochschule Zürich (ETHZ), Zürich, Switzerland.

Wang, W. C. and Shen, H. W. (1980). Statistical properties of alluvial bed forms, Proc. 3^{rd} International Symposium on Stochastic Hydraulics, Tokyo, Japan, pp. B9, 1–19.

White, W. R., Paris, E. and Bettess, R. (1980). The frictional characteristics of alluvial streams: A new approach, *Proceedings, Institution of Civil Engineers, London* **69**(2): 737–750.

Wiesemann, J.-U., Mewis, P. and Zanke, U. (2006). Bed levelling investigations on transverse sloped beds, *in* R. M. L. Ferreira, E. C. T. L. Alves, J. G. A. B. Leal and A. H. Cardoso (eds), *RiverFlow 2006*, Proc. 3^{rd} International Conference on Fluvial Hydraulics - RiverFlow, Lisbon, Portugal, A. A. Balkema Publishers, pp. 1203–1210.

Wilbers, A. W. E. (2004). *Prediction of bed form characteristics and bed form roughness in large rivers*, PhD thesis, Utrecht University, Utrecht, The Netherlands.

Williams, G. P. (1970). Flume width and water depth effects in sediment transport experiments, *U.S. Geological Survey Prof. Paper* **562**(H).

Wormleaton, P. R. and Merrett, D. J. (1990). An improved method of calculation for steady uniform flow in prismatic main channel / flood plain sections, *Journal of Hydraulic Research* **28**(2): 157–174.

Wormleaton, P. R., Sellin, R. H. J., Bryant, T., Loveless, J. H., Hey, R. D. and Catmur, S. E. (2004). Flow structures in a two-stage channel with a mobile bed, *Journal of Hydraulic Research* **42**(2): 145–162.

Wu, W. and Wang, S. S. Y. (1999). Movable bed roughness in alluvial rivers, *Journal of Hydraulic Engineering* **125**(12): 1309–1312.

Wu, W. and Wang, S. S. Y. (2006). Formulas for sediment porosity and settling velocity, *Journal of Hydraulic Engineering* **132**(8): 858–862.

Yalin, M. S. (1964). Geometrical properties of sand waves, *Journal of the Hydraulics Division, ASCE* **90**(HY5).

Yalin, M. S. (1972). *Mechanics of sediment transport*, Pergamon Press, Oxford, UK.

Yalin, M. S. (1985). On the determination of ripple geometry, *Journal of Hydraulic Engineering* **111**(8): 1148–1155.

Yalin, M. S. (1992). *River mechanics*, Pergamon Press Ltd.

Yalin, M. S. and da Silva, A. M. F. (2001). *Fluvial processes*, IAHR Monograph, Delft, The Netherlands.

Yen, B. C. (2002). Open-channel flow resistance, *Journal of Hydraulic Engineering* **128**(1): 20–39.

Yen, B. C. and Wenzel, H. G. (1970). Dynamic equations for steady spatially varied flow, *Journal of the Hydraulics Division* **96**(HY3): 801–814.

Yu, G. and Lim, S. Y. (2003). Modified Manning formula for flow in alluvial channels with sand beds, *Journal of Hydraulic Research* **41**(6): 597–608.

Yu, G. and Smart, G. (2003). Aspect ratio to maximize sediment transport in rigid bank channels, *Journal of Hydraulic Engineering* **129**(12): 927–935.

Zanke, U. (1982). *Grundlagen der Sedimentbewegung*, Springer Verlag, Heidelberg, Germany.

Znamenskaya, N. S. (1962). Calculations of dimensions and speed of shifting of channel formations, *Soviet Hydrol. (Am. Geophys. Union)* (No. 2).

Znamenskaya, N. S. (1969). Morphological principle of modeling of river bed processes, Vol. 5.1 of *Proc.* 13^{th} *IAHR Congress, Kyoto, Japan*, International Association of Hydraulic Engineering and Research (IAHR).

List of Figures

List of Tables

A. Theoretical Background

In this appendix basic theoretical aspects being relevant in studying the interaction of lateral side overflow with bed-load transport and bed morphology in a channel are presented. These aspects refer to flow equations, bed material properties, bed forms and flow resistance due to bed forms, bed-load transport, side weirs and spatially varied flow as well as the determination of the discharge coefficient of a side weir.

A.1. Bed Material Properties

Besides hydraulic parameters and channel geometry the bed material characteristics play a dominant role in sediment transport processes. In this paragraph the most important bed material properties such as particle size, particle fall velocity, density and porosity as well as the angle of repose are presented.

A.1.1. Particle Size

Usually, sediments are referred to as gravel, sand, silt or clay. These terms are related to the size of the sediment particle. Various methods are available to determine the particle size (Van Rijn (1993)). Gravel, sand and silt are analyzed by wet or dry sieving methods yielding sieve diameters. In Table A.1 the grain size scale of the American Geophysical Union - AGU is presented. For the present study a median particle size of the mobile bed material of $d_{50} = 0.72\ mm$ has been determined indicating *coarse sand* on the AGU-grain size scale.

A natural sample of sediment particles contains particles of a range of size. The size distribution of such a sample is the distribution of sediment material by percentages of weight, usually presented as a cumulative frequency distribution. The frequency distribution is characterized by:

- Median particle size d_{50}: size at which 50 % by weight is finer.

  Other characteristic values to describe a grain size distribution are the following diameters: d_{10}, d_{16}, d_{30}, d_{50}, d_{65}, d_{84} and d_{90}.

Table A.1: Grain size scale according to the American Geophysical Union - AGU.

Class name	Diameter $[mm]$	Class name	Diameter $[mm]$
Boulders	> 256	Very coarse sand	$2.0 - 1.0$
Cobbles	$256 - 64$	Coarse sand	$1.0 - 0.50$
Gravel	$64 - 2$	Medium sand	$0.50 - 0.25$
		Fine sand	$0.25 - 0.125$
		Very fine sand	$0.125 - 0.062$
Coarse silt	$0.062 - 0.031$	Coarse clay	$0.004 - 0.002$
Medium silt	$0.031 - 0.016$	Medium clay	$0.002 - 0.001$
Fine silt	$0.016 - 0.008$	Fine clay	$0.001 - 0.0005$
Very fine silt	$0.008 - 0.004$	Very fine clay	$0.0005 - 0.00024$
		Colloids	< 0.00024

- Mean particle size d_m:

$$d_m = \frac{\sum(p_i \cdot d_i)}{100} \tag{A.1}$$

with p_i percentage by weight of each grain size fraction d_i.

- Geometric mean size d_g:

$$d_g = \sqrt{d_{84} \cdot d_{16}} \tag{A.2}$$

The geometric mean size represents the first moment of the size frequency distribution.

- Geometric standard deviation σ_d:

$$\sigma_d = \frac{1}{2}\left(\frac{d_{50}}{d_{16}} + \frac{d_{84}}{d_{50}}\right) \tag{A.3}$$

The geometric standard deviation, being a measure based on graphic values, is the second moment of the size frequency distribution describing the variation around the mean.

- Geometric sorting coefficient σ_g:

$$\sigma_g = \sqrt{\frac{d_{84}}{d_{16}}} \tag{A.4}$$

The geometric sorting coefficient is used to characterize the scatter or width, respectively, of the grain size distribution.

Both, Equations A.3 and A.4 are approximations based on the assumption that an ideal sample has a normal (Gaussian) distribution (log-normal distribution). Consequently, results obtained by these two Equations would be close to each other. For the present study σ_d corresponds to σ_g ($\sigma_d \approx \sigma_g$) (Tab. 4.4).

A.1.2. Particle Fall Velocity of Sediments in still and flowing Water

Basically, the fall velocity is a behavioral property. For a sphere falling in a still fluid the terminal fall velocity (w_s) is the fall velocity when the fluid drag force on the particle is in equilibrium with the gravity force. The fall velocity is a function of the sphere diameter (d_s), specific gravity ($s = \rho_s/\rho$), drag coefficient (c_D) and acceleration of gravity (g). The drag coefficient is a function of the Reynolds number ($Re = w_s \cdot d_s/\nu$, with ν kinematic viscosity) and a shape factor. In the Stokes region ($Re < 1$) the drag coefficient is given by $c_D = 24/Re$, yielding (Van Rijn (1993)):

$$w_s = \frac{(s-1) \cdot g \cdot d_s^2}{18 \cdot \nu} \tag{A.5}$$

Outside the Stokes region there is no simple expression for the drag coefficient (c_D). Due to turbulence the particle fall velocity is reduced in flowing water. The effect of temperature on the fall velocity is taken into account by the kinematic viscosity coefficient (ν).

For a natural sediment particle the expressions valid for a sphere cannot be applied because of the differences in shape. Differences in the order of 30 % for shape factors in the range from 0.5 to 1.0 have been observed in experiments (Van Rijn (1993)).

According to Van Rijn (1993), the terminal fall velocity of non-spherical sediment particles can be determined from the following formulae (d is in $[mm]$):

$$0.001 < d \leq 0.1: \quad w_s = \frac{(s-1) \cdot g \cdot d^2}{18 \cdot \nu} \tag{A.6}$$

$$0.1 < d < 1.0: \quad w_s = \frac{10 \cdot \nu}{d} \left[\sqrt{1 + \frac{0.01 \cdot (s-1) \cdot g \cdot d^3}{\nu^2}} - 1 \right]$$

$$d \geq 1.0: \quad w_s = 1.1 \cdot \sqrt{(s-1) \cdot g \cdot d}$$

Wu and Wang (2006) propose the following relationship:

$$w_s = \frac{M_s \cdot \nu}{N_s \cdot d} \cdot \left[\sqrt{\frac{1}{4} + \left(\frac{4 \cdot N_s}{3 \cdot M_s^2} \cdot D_*^3 \right)^{1/w}} - \frac{1}{2} \right]^w \tag{A.7}$$

where $D_* = d[(\rho_s/\rho - 1)g/\nu^2]^{1/3}$ (see Eq. A.123), d nominal diameter of sediment particles and $M_s = 33.9$, $N_s = 0.98$ and $w = 1.33$ coefficients for a Corey shape factor assumed to be 0.7 as suggested by Cheng (1997).

Using Equation A.6 and $d_{50} = 0.72\ mm$ from the present study, a w_s-value of 95 mm/s is obtained. Applying Equation A.7 with $d = d_{50} = 0.72\ mm$, a settling velocity of $w_s = 92\ mm/s$ is computed. According to Zanke (1982), a w_s-value of 91 mm/s is obtained. Following Dietrich (1982), $w_s = 111\ mm/s$.

The particle fall velocity and the median fall diameter represent basic parameters to classify bed forms using bed form classification diagrams (e. g. Liu (1957), Simons and Richardson (1966)) (paragraph A.3.1).

A.1.3. Density and Porosity of alluvial Bed Material

The sediment density of alluvial bed material usually ranges between $\rho_s = 2630\ kg/m^3$ and $\rho_s = 2680\ kg/m^3$. For the present study measurements and indications of the company selling the bed material gave a sediment density of:

$$\rho_s = 2650\ \ kg/m^3 \tag{A.8}$$

As far as the porosity is concerned, the following definition is given:

$$p = \frac{V_p}{V} = \frac{V_p}{V_p + V_s} \tag{A.9}$$

with V_p porosity volume and V_s sediment volume.
Several tests indicate that for the present study a porosity of:

$$p \approx 45.4\ \ \% \tag{A.10}$$

has to be used.

A.1.4. Angle of Repose of Sediment Particles

The angle of repose is a behaviorial property of sediment particles. Grains piled up on each other have an equilibrium slope which is called the angle of natural repose (ϕ_n). This parameter appears to be a function of size, shape and porosity. Values from literature are in the range of $\phi_n = 30°$ to $40°$ for sand sizes from 0.001 to 0.01 m. Observations in nature on the avalanche lee

slope of desert dunes and river bed dunes also show values in the range of 30° to 40° (Van Rijn (1993)).

The angle of repose (ϕ_r), also referred to as the angle of internal friction, is a characteristic angle related to the particle stability on a horizontal or sloping bed. Values for ϕ_r may differ from the angle of natural repose (ϕ_n).

For the design of stable channels the following conservative values are recommended by Van Rijn (1993) (see Tab. A.2):

Table A.2: Angle of repose for stable channel design (silicate material) (from Van Rijn (1993)).

d_{50}	Angle of repose ϕ_r	
$[m]$	Rounded	Angular
≤ 0.001	30°	30°
0.005	32°	37°
0.01	35°	40°
0.05	37°	42°
≥ 0.1	40°	45°

A.2. Flow Equations and Flow Resistance

In this paragraph basic aspects such as velocity distribution, bed shear stress and friction laws of hydraulics in open-channel flow are presented. Furthermore, the different hydraulic regimes and the basic case of plane bed conditions having granular skin roughness are highlighted.

A.2.1. Velocity Distribution, Bed Shear Stress and Friction Laws

Considering a two-dimensional turbulent open-channel flow on a flat bed and assuming a stationary and uniform flow regime with $k_s \ll y$ ($k_s \approx 2d$, with k_s equivalent sand grain roughness and y flow depth), the time average shear stress distribution along z (Fig. A.1, a) is given by the linear relation:

$$\tau = \tau_0 \cdot \left(1 - \frac{z}{y}\right) \tag{A.11}$$

For $z = 0$ this yields the overall time-averaged bed shear stress τ_0:

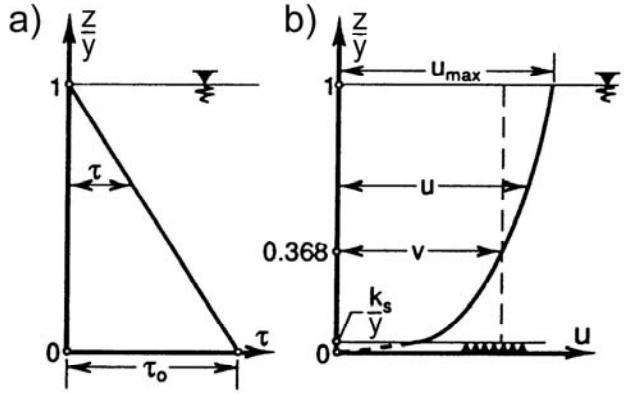

Figure A.1: Time averaged bed shear and velocity distribution for a two-dimensional turbulent open-channel flow on a flat bed assuming a stationary and uniform flow regime with $k_s \ll y$ (Yalin (1992)).

$$\tau_0 = \rho \cdot g \cdot y \cdot S = \rho \cdot u_*^2 \tag{A.12}$$

with ρ density of fluid, g acceleration due to gravity, y flow depth and S slope.

Furthermore, by the definition $\tau_0 = \rho u_*^2$, the bed shear velocity u_* is obtained:

$$u_* = \sqrt{g \cdot y \cdot S} = \sqrt{\frac{\tau_0}{\rho}} \tag{A.13}$$

A general expression for the distribution of flow velocities u is given by the logarithmic form (Nikuradse (1933), Fig. A.1, b):

$$\frac{u}{u_*} = \frac{1}{\kappa} \cdot ln\left(\frac{z}{k_s}\right) + B_s \tag{A.14}$$

where κ is the constant of Van Karman ($\kappa \approx 0.4$), k_s the equivalent sand grain roughness of Nikuradse[1] and B_s an empirical roughness function depending on the roughness Reynolds number (Re^*) (Yalin and da Silva (2001)), being:

[1]The effect of the bottom (or wall) roughness on the velocity distribution in a turbulent flow was first investigated for pipe flow by Nikuradse (1933). In these investigations pipes covered with uniform sand grains at the inside were used. In this context velocity distributions at different Reynolds numbers (Re), pipe diameters and grain sizes (d_{50}) were measured. Referring to these experiments, Nikuradse introduced the concept of the equivalent sand grain roughness or Nikuradse roughness (k_s) as a standard for all other types of roughness elements (k).

$$Re^* = \frac{u_* \cdot k_s}{\nu} \tag{A.15}$$

with ν kinematic viscosity.

Based on experimental results the turbulent hydraulic flow regimes and the empirical roughness function (B_s) can be distinguished in the following way (Nikuradse (1933)):

- Hydraulically smooth:

$$\text{if} \quad Re^* \leq 5 \quad \text{then} \quad B_s = 5.5 \tag{A.16}$$

  The roughness elements are much smaller than the thickness of the viscous sublayer and do not affect the velocity distribution.

- Transition:

$$\text{if} \quad 5 < Re^* < 70 \tag{A.17}$$

  The roughness elements partially stick out of the viscous sublayer and the velocity distribution is affected by viscosity as well as by the bottom roughness. B_s has to be determined graphically (e. g. Schlichting (1968)).

- Hydraulically rough:

$$\text{if} \quad Re^* \geq 70 \quad \text{then} \quad B_s = 8.5 \tag{A.18}$$

  All roughness elements stick out of the viscous sublayer and the velocity distribution is not dependent on the viscosity (ν) of the fluid. This case is the most interesting one for open-channel flow in laboratory flumes and natural rivers.

For any regime of the turbulent flow the depth averaged flow velocity (v) is equal to u at the relative level $z/y = e^{-1} = 0.368$ (Fig. A.1, b). Thus, Equation A.14 yields:

$$\frac{v}{u_*} = \frac{1}{\kappa} \cdot ln\left(0.368 \cdot \frac{y}{k_s}\right) + B_s \tag{A.19}$$

The ratio c_f (or $c^{'}$) relating the average flow velocity (v) and the bed shear velocity (u_*) in Equation A.19 is referred to as the dimensionless Chézy friction factor (Yalin (1992)):

$$c_f = \frac{v}{u_*} \tag{A.20}$$

Equation A.19, which gives the v-value of a uniform two-dimensional flow past a flat bed having a granular roughness of $k_s \approx 2d$ ($d = d_{50}$), gives, at the same time, the value of the friction factor of that flow:

$$c_f = \frac{1}{\kappa} \cdot ln \left(0.368 \cdot \frac{y}{k_s} \right) + B_s \tag{A.21}$$

The friction factor (c_f or $c^{'}$), respectively, can always be replaced by that of the total bed roughness (c) (Yalin (1992)).

Introducing $C = c \cdot \sqrt{g}$ and substituting $u_* = \sqrt{gyS} = \sqrt{\tau_0/\rho}$ (Eq. A.13) in Equation A.20 and y (two-dimensional) with the hydraulic radius (R_h), the traditional and widely used Chézy resistance formula for open-channel flows is obtained:

$$v = C \cdot \sqrt{R_h \cdot S} \tag{A.22}$$

where v is the cross-sectional averaged velocity, C the Chézy resistance coefficient and S the energy slope (S_e).

For a hydraulic rough turbulent flow the Chézy coefficient can be calculated, e. g., with the Manning (n) (Manning (1889)), Strickler (k_{st}) (Strickler (1923)) or Darcy-Weisbach (f) (Rouse (1946)) formula or the Nikuradse equivalent sand grain roughness (k_s) (Nikuradse (1933)), respectively:

$$C = \frac{1}{n} \cdot R_h^{1/6} = k_{st} \cdot R_h^{1/6} = \sqrt{\frac{8 \cdot g}{f}} = 18 \cdot log \left(\frac{12 \cdot R_h}{k_s} \right) \tag{A.23}$$

Using n or k_{st}, the Chézy resistance formula for open-channel flows (Eq. A.22) can be expressed in form of the Gauckler-Manning-Strickler (GMS) equation:

$$v = \frac{1}{n} \cdot R_h^{2/3} \cdot S^{1/2} = k_{st} \cdot R_h^{2/3} \cdot S^{1/2} \tag{A.24}$$

The Manning or Strickler resistance coefficient, respectively, can be related to the bed material size d by:

$$\frac{1}{n} = k_{st} = \frac{K_0 \cdot \sqrt{g}}{d^{1/6}} = \frac{K}{d^{1/6}} \tag{A.25}$$

where K_0 is a dimensionless factor and K an empirical roughness parameter related to the gradation, distribution and shape of the bed material, bed forms and flow conditions. The dimension of $K = K_0\, g^{1/2}$ is $[m^{1/2}/s]$.

In the case of a flat bed only grain roughness induced by skin friction forces has to be taken into account. This topic is dealt with in the following paragraph (paragraph A.2.2).

Furthermore, in practice (and also in the present study), usually a mobile bed with bed forms is observed. Consequently, flow resistance due to form

roughness and subsequently total roughness composed of grain and form roughness has to be taken into account (paragraph A.4)[2].

Moreover, for computing effective bed shear stress in bed-load transport studies it is often necessary to remove sidewall effects and form induced roughness (paragraph A.5).

A.2.2. Granular Skin Roughness

In case of a stationary flat loose bed covered with uniform bed material the grain roughness is generated by skin friction forces. Using Equations A.22, A.23 and A.25, Strickler (1923) suggested a K-value of 21.1 in combination with a "mean diameter" ("mittlerer Korndurchmesser"). This "mean diameter" has not been defined explicitly (Jäggi (1984a)). Meyer-Peter and Müller (1948), e. g., assumed this value to be the median particle size (d_{50}).

Meyer-Peter and Müller (1948) pointed out that the surface roughness for a natural armor layer is best represented by the bigger grains rather than by the smaller ones. Therefore, the Strickler-approach has been modified by adopting $d = d_{90}$ and $K = 26$. Meyer-Peter and Müller (1948) justified the increased constant with a better fit to the results of Nikuradse (1933) and to the fact that the increase from 21.1 to 26 corresponds roughly to a factor of $(d_{90}/d_{50})^{1/6}$. Thus, the higher constant K is partially compensated by the larger grain diameter.

Resuming, n and k_{st}, respectively, can be calculated as follows:

$$\frac{1}{n'} = k'_{st} = \frac{21.1}{d_{50}^{1/6}} \text{ or } \frac{26}{d_{90}^{1/6}} \tag{A.27}$$

Using the Nikuradse equivalent sand grain roughness concept (k_s) for the estimation of the plane bed roughness, bed shear and resistance, the k_s-value is assumed being proportional to a representative sediment size (d_i) ($k_s \approx d_i$ or $k'_s \approx d_i$, respectively). According to Kamphuis (1974), Hey (1979),

[2]In many hydraulic problems a composite channel is present. A composite channel is a channel whose wall roughness changes along the wetted perimeter of the cross section (e. g. compound channels with vegetated flood plains or flume studies with smooth side walls and a rough bed). Customarily, the internal water lines dividing the subsections are not considered as a part of the wetted parameter in computing the subsection hydraulic radii $R_{h,i}$. Only the actual wetted external boundary is used (Yen (2002)). Doing so, e. g. for the calculation of back water curves, an equivalent resistance coefficient $k_{st,eq}$ is used:

$$k_{st,eq} = \left[\frac{U}{\sum_{i=1}^{n} U_i/k_{st,i}^{3/2}}\right]^{2/3} \tag{A.26}$$

Van Rijn (1982) and Jäggi (1984a), flow velocities calculated on the basis of Equations A.22, A.23, A.24 and A.27 are overestimated. This is mainly due to the fact that Equation A.23 has been adopted to to the results of Nikuradse (1933). A detailed explanation for the velocity difference is given by Yalin (1972). As a consequence it has been proposed to increase the sediment size by a correction factor α_s:

$$k_s^{'} = \alpha_s \cdot d_i \tag{A.28}$$

Some values of α_s obtained from the literature are reproduced in Table A.3.

Table A.3: Ratio of Nikuradse equivalent roughness size ($k_s^{'}$) and sediment size (d_i) for plane bed conditions.

Investigator	Measure of sediment size d_i	$\alpha_s = k_s^{'}/d_i$ [−]
Ackers and White (1973)	d_{35}	1.23
Strickler (1923)	d_{50}	3.3
Meyer-Peter and Müller (1948)	d_{50}	1.0
Yalin (1972)	d_{50}	2.0
Einstein and Barbarossa (1952)	d_{65}	1.0
Engelund and Hansen (1967)	d_{65}	2.0
Hey (1979)	d_{84}	3.5
Simons and Richardson (1966)	d_{85}	1.0
Kamphuis (1974)	d_{90}	2.5
Van Rijn (1982)	d_{90}	3.0

A.3. Bed Forms

In this paragraph different methods to classify bed forms are described. Furthermore, geometrical properties such as bed form length, height, steepness and shape as well as bed form migration velocity are presented.

The major feature of alluvial and other sediment-laden channels concerning flow resistance is a boundary consisting of movable particles, and hence the formation of mobile bed forms. The channel bed forms can be

loosely classified as plane bed, ripples, dunes and antidunes. Further and more detailed information on this topic is given later on in this paragraph.

Bed form geometry is always three dimensional. The bed configurations migrate with sediment particles moving on their surface. For channels with finite width the bed forms change across the channel, especially for compound channels and rivers with floodplains (Yen (2002)). This is also the case for the present study where the presence of the side overflow influences dune geometry. The nature of the roughness effects is best represented by the size, shape and spatial distribution of the roughness elements (Rouse (1965)).

A.3.1. Classification of Bed Forms

When the bed form crest is perpendicular (transverse) to the main flow direction the bed forms are called transverse bed forms such as ripples, dunes and antidunes. Ripples have a length scale smaller than the water depth, whereas dunes have a length scale much larger than the water depth. Antidunes have a length scale equal to the length scale of the surface waves (in phase). Figure A.2 shows ripple and dune-type bed forms (dunes, antidunes) as observed in alluvial rivers or channels (Simons and Richardson (1961), Simons and Richardson (1966)).

Ripples and dunes travel downstream by erosion at the upstream face (stoss side) and deposition at the downstream face (lee side). Antidunes travel upstream by lee side erosion and stoss side deposition.

For the purpose of classification of bed forms the morphological regimes for unidirectional currents over a sand bed can be distinguished as follows (see also Fig A.2):

- Lower transport regime with $Fr < 1.0$:

  The typical bed features are the flat bed, ribbons and ridges (crest parallel to flow, longitudinal bed forms), ripples, dunes and bars.

- Transitional transport regime with $Fr \approx 1.0$:

  The typical bed forms are washed-out dunes and sand waves.

- Upper transport regime with $Fr > 1.0$:

  The typical bed forms are the flat bed and sand waves (antidunes).

In the literature several classification methods or regime predictors are available[3]. For a first simple estimation the Froude number (Fr) can be used as a classification parameter (see e. g. Simons and Richardson (1966), Graf

[3]Classification diagrams for gravel bed rivers are not available (Van Rijn (1993)). Usually, the grain size distribution is rather wide and selective transport processes and armoring may occur.

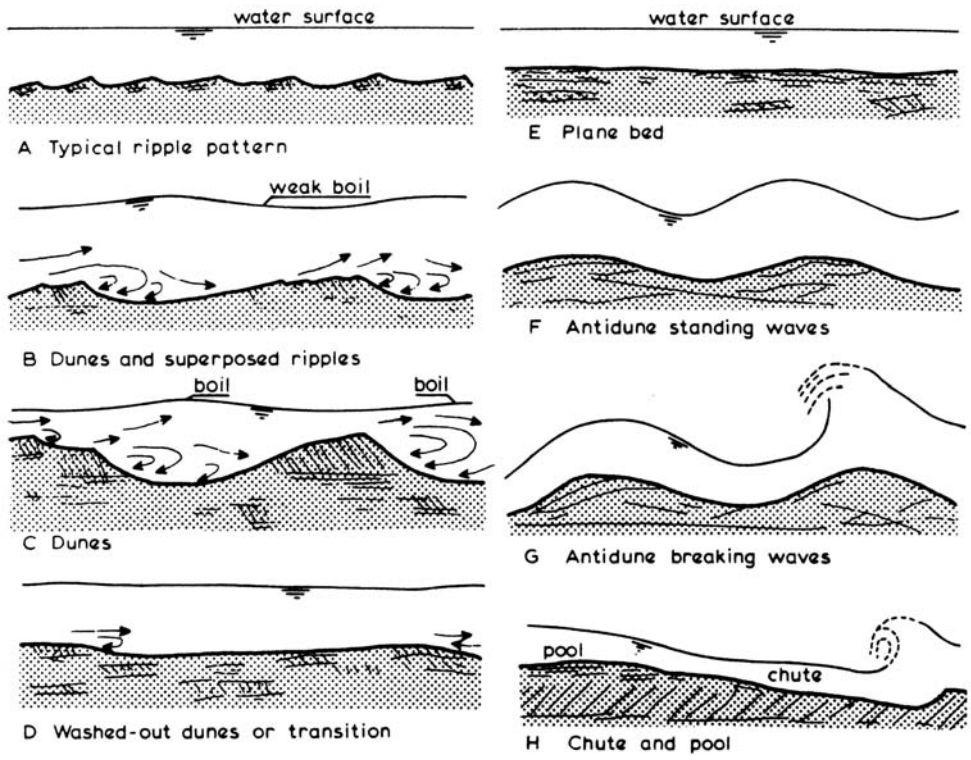

Figure A.2: Bed form types in alluvial rivers according to Simons and Richardson (1966).

and Altinakar (2000)). In Table A.4 the different bed forms according to the Fr-number are presented. However, it must be pointed out that any local Froude number might differ considerably from the averaged Froude number. Consequently, a large variation of Froude numbers may thus appear in any given cross section. Simons and Richardson (1961) remarked that a certain bed form occurs in the laboratory flume at $Fr < 0.6$ and in a large, deep river at $Fr \ll 0.3$.

Table A.4: Froude number (Fr) as bed form classification parameter (e. g. in Graf and Altinakar (2000)).

Flow regime	Sediment transport	Bed form type
$Fr < 1$	no	plane bed
	yes	mini dune, dune
$Fr \approx 1$	yes	plane bed
$Fr > 1$	yes	antidune

In the present study the following classification methods are taken into account:

- Simons and Richardson (1966),
- Van Rijn (1984b),
- Yalin (1992),
- Karim (1999) and
- Yalin and da Silva (2001).

Simons and Richardson (1966) used the stream power(τ_0 v) and the median fall diameter (d_f) as basic parameters. Van Rijn (1984b) used a dimensionless bed shear stress parameter (T) and a dimensionless particle parameter (D_*) to classify bed form types. Yalin (1992) introduced two dimensionless ratios (B/y, y/d), combining the water depth (y) with both, the channel width (B) and a characteristic grain diameter (d). Karim (1999) introduced limiting Froude numbers for the beginning of the transition regime (Fr_t) and for the beginning of the upper regime (Fr_u) as well as a dimensionless number (N^*) to predict ripple-bed configuration. Yalin and da Silva (2001) used the particle Reynolds number ($Re^* = X$) and a relative flow intensity ($\eta^* = Y/Y_{cr} = \theta/\theta_{cr}$). In Table A.5 the different methods and classification parameters are summarized.

- Simons and Richardson (1966):

  Mainly based on flume data, the classification diagram presented in Figure A.3 is proposed.

- Van Rijn (1984b):

  Using a dimensionless particle number (D_*) (Eq. A.123 and paragraph A.6.5) and introducing a transport stage parameter (T) (paragraph A.3.2 and A.6.5):

$$D_* = d_{50} \cdot \left[\frac{(s-1)\cdot g}{\nu^2}\right]^{1/3} \quad \text{and} \quad T = \frac{\left(u_*'\right)^2 - \left(u_{*,cr}\right)^2}{\left(u_{*,cr}\right)^2} \tag{A.29}$$

  the classification in Table A.6 and Figure A.4 is proposed.

  In the lower regime dune-type bed forms are the dominant features for $T \leq 15$ ($\Lambda \gg y$, with Λ bed form length). Mega ripples ($\Lambda \approx y$) and mini ripples ($\Lambda \ll y$) may be superimposed on dunes for $3 \leq T \leq 10$

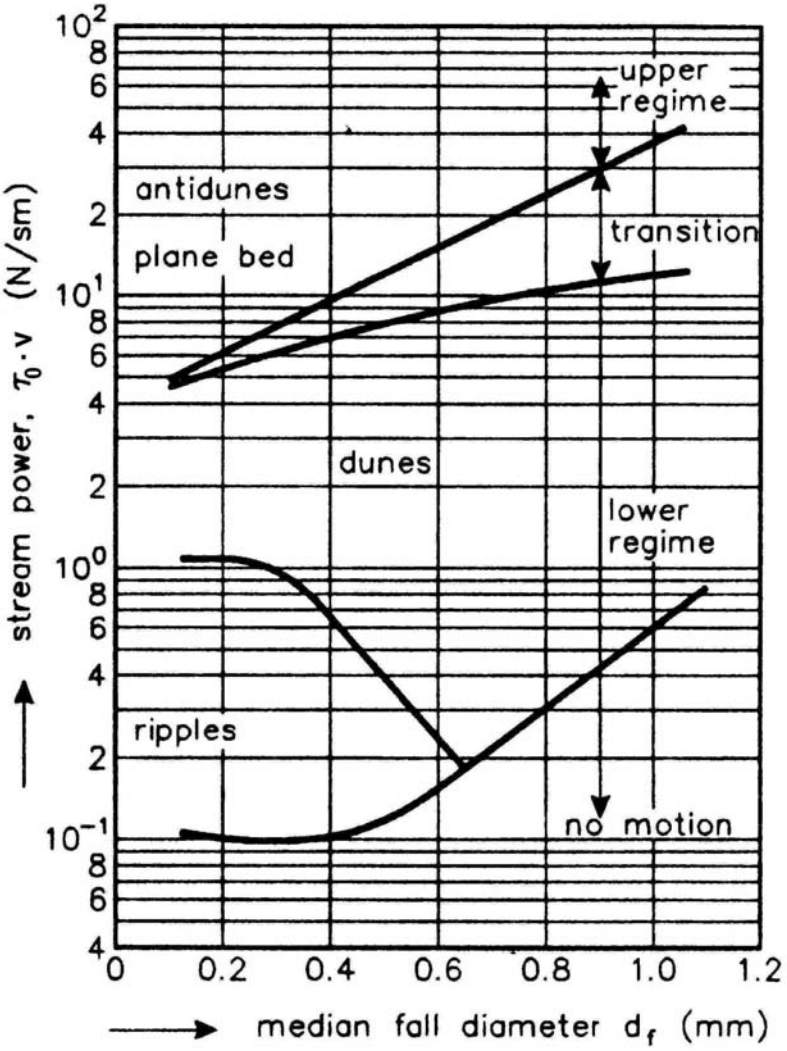

Figure A.3: Bed form classification diagram of Simons and Richardson (1966).

Table A.5: Synopsis of bed form (BF) classification methods taken into account in the present study.

Investigation	Bed form type as a function of classification parameter	Eq., Fig. and/or Tab. in study
Froude number (Fr)	BF type $= f\,(Fr)$	Tab. A.4
Simons & Richardson (1966)	BF type $= f\,(\tau_0 \cdot v, d_f)$	Fig. A.3
Van Rijn (1984b)	BF type $= f\,(T, D_*)$	Fig. A.4 Eq. A.29, Tab. A.6
Yalin (1992)	BF type $= f\,(B/y, y/d)$	Fig. A.5
Karim (1999)	BF type $= f\,(Fr_t, Fr_u, N^*)$	Eqs A.30 to A.34
Yalin & da Silva (2001)	BF type $= f\,(\eta^*, Re^*)$	Fig. A.6 Eqs A.35 to A.41

Table A.6: Classification of bed forms according to Van Rijn (1984b).

Transport regime		Particle size	
		$1 \leq D_* \leq 10$	$D_* > 10$
Lower	$0 \leq T \leq 3$	mini ripples	dunes
	$3 < T \leq 10$	mega ripples & dunes	dunes
	$10 < T \leq 15$	dunes	dunes
Transition	$15 < T < 25$	washed-out dunes, sand waves	
Upper	$T \geq 25$, $Fr < 0.8$	(symmetrical) sand waves	
	$T \geq 25$, $Fr \geq 0.8$	plane bed and/or antidunes	

and $D_* \leq 10$. Mini ripples are the dominant features for $T < 3$ and $D_* < 10$.

The upper regime which is defined to occur for $T \geq 25$ is characterized by a dominating suspended load transport. The characteristic bed forms are nearly symmetrical sand waves ($\Lambda \gg y$, $Fr \ll 0.8$), the plane bed and antidunes ($Fr > 0.8$).

The bed forms in the transition regime ($15 < T < 25$) may range from disappearing dunes (lower regime) to disappearing sand waves (upper regime).

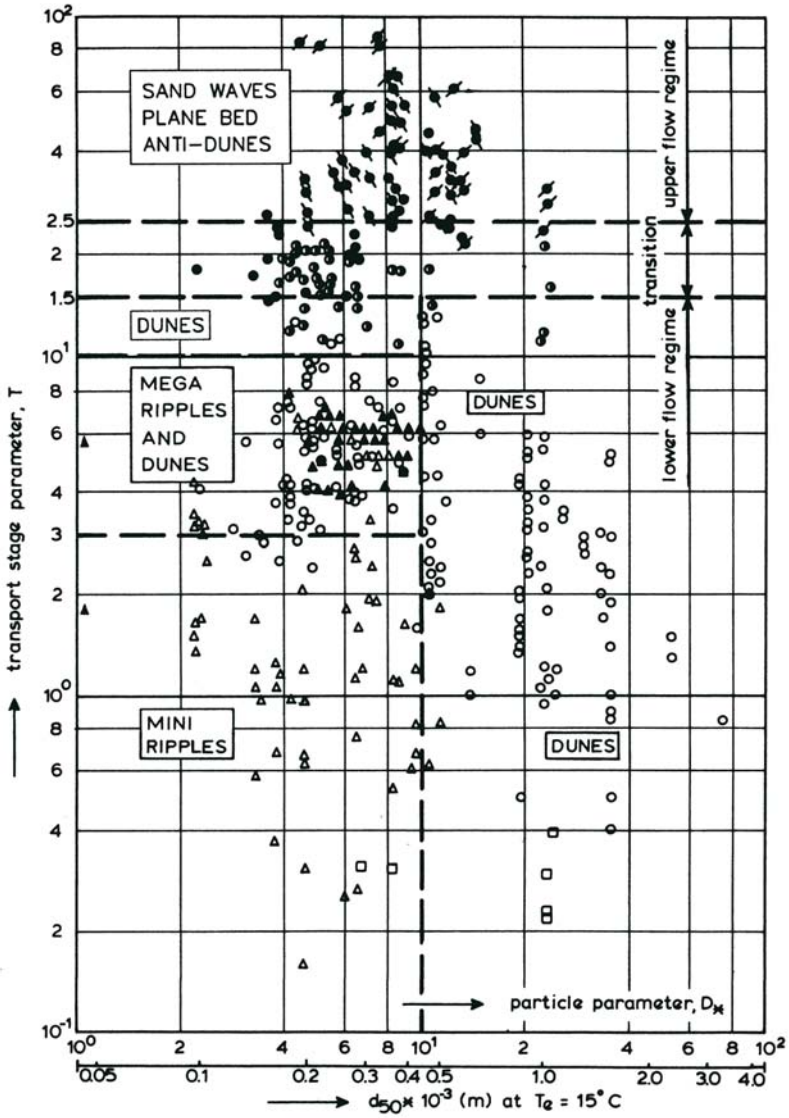

Figure A.4: Bed form classification diagram of Van Rijn (1984b).

- Yalin (1992):

  Available data from a total of 507 data points from 27 sources are plotted on the log-log (B/y, y/d)-plane in Figure A.5. The points A, C and D represent alternate bars, multiple bars and dunes, respectively. Thus, the dominant bed features of the present study (ripples, dunes, plane bed) are not well represented, since the application of this regime predictor

only allows for the estimation of dunes. Ripples and bed features of the transitional and upper regime are not included.

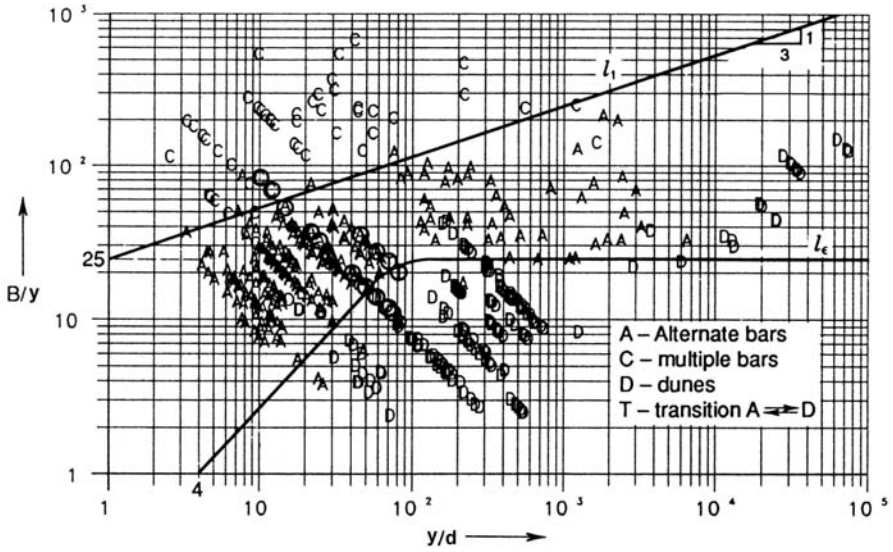

Figure A.5: Bed form classification diagram of Yalin (1992).

- Karim (1999):

  The bed regime predictor by Karim (1999) is based on graphical analysis of laboratory data. Two limiting Froude numbers for the beginning of the transition regime (Fr_t) and the beginning of the upper regime (Fr_u) are defined as:

$$Fr_t = 2.716 \cdot \left(\frac{y}{d_{50}}\right)^{-0.25} \quad \text{and} \quad Fr_u = 4.785 \cdot \left(\frac{y}{d_{50}}\right)^{-0.27} \tag{A.30}$$

  Based on Equation A.30 different bed regimes can be determined from a known Froude number ($Fr = v/\sqrt{gy}$) as follows:

  – Lower regime (ripples, dunes):

$$Fr \leq Fr_t \tag{A.31}$$

  – Transition regime (washed-out dunes):

$$Fr_t \leq Fr \leq Fr_u \tag{A.32}$$

  – Upper regime (plane bed, antidunes):

$$Fr \geq Fr_u \tag{A.33}$$

Equation A.31 is used for predicting dunes, Equation A.32 for transition and Equation A.33 (along with $Fr \geq 0.8$) for antidunes.

For the prediction of the ripple-bed configuration the following dimensionless number (N^*) which is a product of the grain size Reynolds number (Re^*) and the particle Froude number ($Fr_p^* = v/\sqrt{(s-1)gd_{50}}$) is proposed:

$$N^* = Re^* \cdot Fr_p^* = \frac{u_* \cdot d_{50}}{\nu} \cdot \frac{v}{\sqrt{(s-1) \cdot g \cdot d_{50}}} \tag{A.34}$$

It was found that $N^* < 80$ defines the occurrence of ripples for most of the observed flows with ripple beds in the laboratory data.

- Yalin and da Silva (2001):

  Yalin and da Silva (2001) developed a method to determine the existence region of ripples and dunes. According to Yalin and da Silva (2001), ripples and dunes are caused by vertical turbulence. Using Equation A.122 (X_1, X_2 and X_3), the following parameters are (re)introduced:

$$X = X_1 = \frac{u_* \cdot d}{\nu} = Re^* \tag{A.35}$$

$$Y = X_2 = \frac{u_*^2}{(s-1) \cdot g \cdot d} = \frac{\rho \cdot u_*^2}{\gamma_s \cdot d} = \theta \tag{A.36}$$

$$Z = X_3 = \frac{y}{d} \tag{A.37}$$

  with $\gamma_s = (\rho_s - \rho)g$ specific weight of grains in fluid ($\gamma_s = 16186.5\ N/m^3$ for $\rho_s = 2650\ kg/m^3$).

  Furthermore, a material number (Ξ^3):

$$\Xi^3 = \frac{X^2}{Y} = \frac{\gamma_s \cdot d^3}{\rho \cdot \nu} \tag{A.38}$$

  and a modified transport inception function:

$$Y_{cr} = 0.13 \cdot \Xi^{-0.392} \cdot e^{-0.015 \cdot \Xi^2} + 0.045 \left(1 - e^{-0.068 \cdot \Xi}\right) \tag{A.39}$$

  are introduced.

  Finally, the relative flow intensity (η^*) is expressed as:

$$\eta^* = \frac{Y}{Y_{cr}} \left(= \frac{\theta}{\theta_{cr}}\right) \tag{A.40}$$

A bed form is "present" only if it has a detectable non-zero steepness ($\delta > 0$). The dune steepness is supposed to be a function of X, η^* and Z, thus $\delta_d = f_{\delta_d}(X, \eta^*, Z)$. Similarly, the steepness of ripples is supposed to be a function of X and η^* but not depending on Z, thus $\delta_r = f_{\delta_r}(X, \eta^*)$. Finally, the existence region of dunes (D), having $\delta_d = f_{\delta_d}(X, \eta^*, Z)$, is the set of those X, η^* and Z which yields $\delta_d > 0$. The existence region of ripples (R), having $\delta_r = f_{\delta_r}(X, \eta^*)$, is the set of those X and η^* for which $\delta_r > 0$. Since X and η^* are common for both dunes and ripples, it seems to be appropriate to consider R and D in the same (X, η^*)-plane and use Z as a parameter. In Figure A.6 the existence region of R and D are shown.

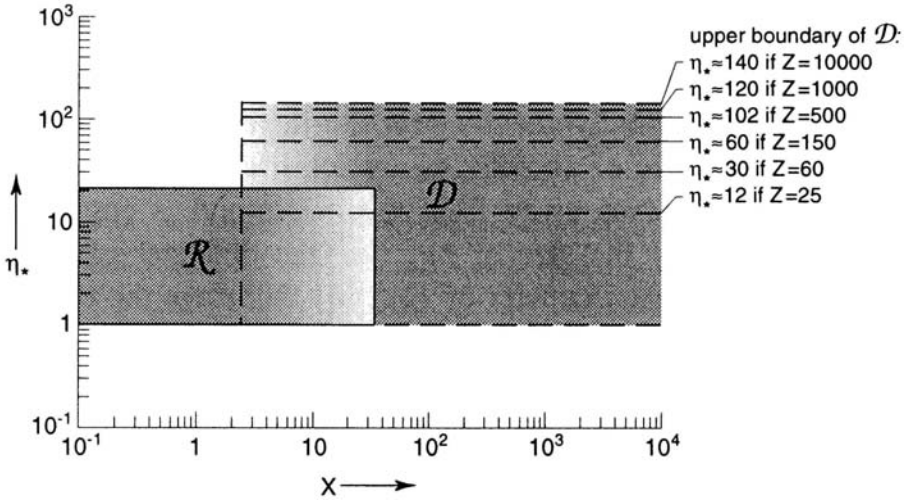

Figure A.6: Bed form classification diagram of Yalin and da Silva (2001).

The lower boundary of R is $\eta^* = 1$, its upper boundary being $\eta^* = 21$. The region D, confined with broken lines, varies depending on Z. The lower boundary of D is the same as that of R, viz $\eta^* = 1$ for all Z. The upper boundary of D varies as an increasing function of Z and η^*. The ripples steepness (δ_r) decreases from $X \approx 2.5$ onwards as to vanish completely at $X \approx 35$, being the right-hand side boundary of R. The dune steepness (δ_d) decreases from $X \approx 35$ downwards as to vanish at $X \approx 2.5$ which is the left-hand side boundary of D. In the interval $\approx 2.5 < X < \approx 35$ ripples and dunes can be present (as ripples superimposed on dunes) simultaneously. Such a superimposition can be realized only if $\Lambda_d \gg \Lambda_r$. Roughly, this condition is written as:

$$\frac{\Lambda_d}{\Lambda_r} \approx \frac{6 \cdot y}{1000 \cdot d} = 0.006 \cdot Z \geq 3 \quad \text{i. e.} \quad Z \geq 500 \tag{A.41}$$

Equation A.41 can be regarded as an additional condition ($\approx 2.5 < X < \approx 35$) for the simultaneous occurrence of dunes and ripples.

A.3.2. Geometry of Bed Forms

Besides an academic interest, dimensions and geometry of bed forms determine practically relevant quantities such as the total or effective roughness of a mobile bed and the resistance factor. In the present study only bed forms of the lower flow regime are taken into account. On the one hand, these are large-scale bed forms whose length is proportional to the flow depth (dunes)[4], on the other hand ripples are considered. Longitudinal ridges and antidunes will not be dealt with herein.

The length of developed bed forms (ripples and dunes) is denoted by Λ, the height is referred to as Δ and the ratio $\Delta/\Lambda = \delta$ is called bed form steepness (Fig A.7).

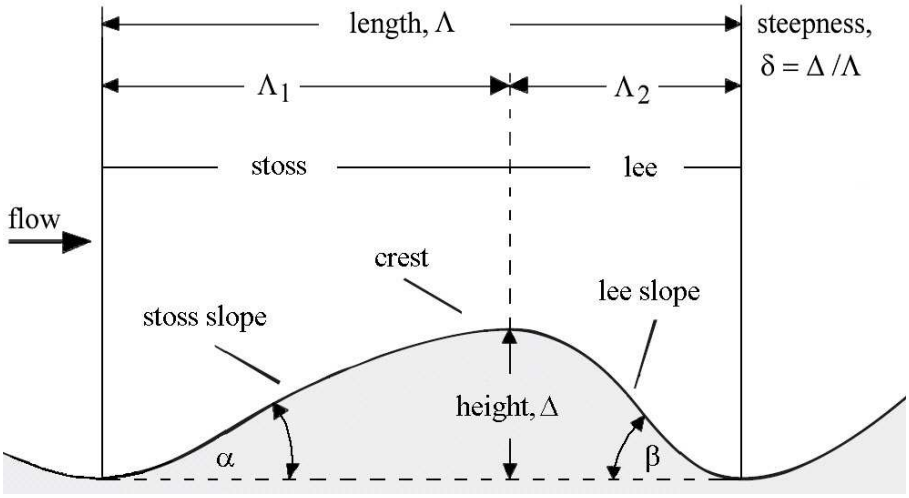

Figure A.7: Definition sketch of bed form geometry.

The following approaches from literature to determine ripple and dune dimensions are taken into account in the present study. Some of them are briefly described (*) below and/or listed (**) in Table A.7 (ripples) and Table A.8 (dunes) at the end of this paragraph.

- Ripples:
  - Yalin (1985)**,
  - Van Rijn (1993)* and
  - Yalin and da Silva (2001)*.

[4]Bed forms whose length is proportional to the flow width are referred to as bars.

- Dunes:
  - Yalin (1964)**,
  - Allen (1968)**,
  - Van Rijn (1982) & Van Rijn (1984b)*,
  - Julien and Klaassen (1995)** and
  - Yalin and da Silva (2001)*.

In the subsequent paragraph the ripple and dune approaches of Van Rijn (1982), Van Rijn (1984b), Van Rijn (1993) and Yalin and da Silva (2001) are presented.

- Van Rijn (1982), Van Rijn (1984b) and Van Rijn (1993):

  Using the dimensionless particle parameter (D_*) and the transport stage parameter (T) (Eq. A.29):

$$D_* = d_{50} \cdot \left[\frac{(s-1)\cdot g}{\nu^2}\right]^{1/3} \quad \text{and} \quad T = \frac{\left(u_*'\right)^2 - \left(u_{*,cr}\right)^2}{\left(u_{*,cr}\right)^2} \tag{A.42}$$

  the following expressions are developed:

  - Ripples:

    When the flow velocities are somewhat larger ($10-20$ %) than the critical velocity for initiation of motion and the median particle size is smaller than about 0.5 mm, small (mini) ripples are generated at the bed surface. The largest ripples may have a length up to the water depth ($0.5\ y - 1.0\ y$) and are commonly called mega ripples. The relative depth of mega ripples varies in the range of 0.02 to 0.06. A clear influence of the T-parameter could not be detected.

    It is assumed that the ripples will completely disappear for $T \approx 10$. The following tentative expressions for the relative length and height of mega ripples are given:

    * Ripple length:

$$\frac{\Lambda_r}{y} = 0.5 \tag{A.43}$$

    * Ripple height:

$$\frac{\Delta_r}{y} = 0.02 \cdot \left(1 - e^{-0.1\cdot T}\right) \cdot (10 - T) \tag{A.44}$$

      The application range of Equation A.44 is given by $1 \leq D_* \leq 10$ and $3 \leq T \leq 10$.

– Dunes:

The relationships for dune length and height are based on the analysis of flume and field data.

∗ Dune length:
The dune height is strongly related to the water depth with values in the range of 3 to $15 \cdot y$. The following relationship is proposed:

$$\frac{\Lambda_d}{y} = 7.3 \tag{A.45}$$

∗ Dune height:

$$\frac{\Delta_d}{y} = 0.11 \cdot \left(\frac{d_{50}}{y}\right)^{0.3} \cdot \left(1 - e^{-0.5 \cdot T}\right) \cdot (25 - T) \tag{A.46}$$

- Yalin and da Silva (2001):

The basic parameters to describe bed form length and steepness are the ones introduced in paragraph A.3.1:

$$X = \frac{u_* \cdot d}{\nu} = Re^* \tag{A.47}$$

$$Y = \frac{u_*^2}{(s-1) \cdot g \cdot d} = \frac{\rho \cdot u_*^2}{\gamma_s \cdot d} = \theta \tag{A.48}$$

$$Z = \frac{y}{d} \tag{A.49}$$

$$\Xi^3 = \frac{X^2}{Y} = \frac{\gamma_s \cdot d^3}{\rho \cdot \nu} \tag{A.50}$$

$$Y_{cr} = 0.13 \cdot \Xi^{-0.392} \cdot e^{-0.015 \cdot \Xi^2} + 0.045 \left(1 - e^{-0.068 \cdot \Xi}\right) \tag{A.51}$$

$$\eta^* = \frac{Y}{Y_{cr}} \left(= \frac{\theta}{\theta_{cr}}\right) \tag{A.52}$$

– Ripples:

∗ Ripple length:
Since ripples forming on the bed of wide channels are (by definition) independent of y and B, the following expression is proposed:

$$\frac{\Lambda_r}{d} \approx \frac{3000}{\Xi^{0.88} \cdot \sqrt{\eta^*} \cdot (1 - 0.22 \cdot \sqrt{\eta^*})} \quad \left(= f_{\Lambda_r}(\eta^*, \Xi)\right) \tag{A.53}$$

∗ Ripple steepness:

The ripple steepness does not depend on Z, thus:

$$\delta_r = f_{\delta_r}(\Xi, \eta^*) \tag{A.54}$$

In a first step it is assumed that the (initial) flow contacting the bed is viscous ($X < \approx 2.5$) and thus the development of δ_r to the full extent is not impeded. At advanced stages ripples disappear (i. e. $\delta_r = 0$ when $\eta^* = \eta^*_{max} \approx 21$) and the maximum ripple steepness of $(\delta_r)_{max} \approx 0.14$ occurs when $\eta^* = \hat{\eta}^*_r \approx 11$. These values do not appear to be affected by Ξ or X, thus the ripple steepness is treated as a function of η^* alone:

$$\delta_r = (\delta_r)_{max} \cdot r \cdot \zeta_r \cdot e^{1-\zeta_r} \quad (= f_{\delta_r}(\eta^*)) \tag{A.55}$$

with

$$\zeta_r = \frac{\eta^* - 1}{\hat{\eta}^*_r - 1} \tag{A.56}$$

and

$$r = 1 \text{ if } \zeta_r \leq 1 \; ; \quad r = \zeta_r \cdot (2 - \zeta_r) \text{ if } 1 < \zeta_r \leq 2 \tag{A.57}$$

Since $(\delta_r)_{max} \approx 0.14$ and $\hat{\eta}^*_r \approx 11$ (which yields $\zeta_r = 0.1(\eta^* - 1)$), relation A.55 is expressed as:

$$\delta_r = 0.014 \cdot r \cdot (\eta^* - 1) \cdot e^{1.1-0.1\cdot\eta^*} \quad (= f_{\delta_r}(\eta^*)) \tag{A.58}$$

which is valid for $1 \leq \eta^* \leq 21$.
With the increment of X from ≈ 2.5 onwards the viscous influence at the bed progressively decreases and the value of δ_r progressively decreases as well (as to vanish completely when $X \approx 35$). This fact can be taken into account by multiplying $(\delta_r)_{max} \approx 0.14$ with a (smaller than unity) function:

$$\Psi_r(X) = \begin{cases} e^{-[(X-2.5)/14]^2} & \text{if} \quad X > 2.5 \\ \\ 1 & \text{if} \quad X \leq 2.5 \end{cases} \tag{A.59}$$

Hence, in total, the ripples steepness is (Eq. A.58 and Eq. A.59):

$$\delta_r = \Psi_r(X) \cdot f_{\delta_r}(\eta^*) \tag{A.60}$$

– Dunes:

  * Dune length:

Taking into account that Λ_d does not depend on Y, the following expression is proposed:

$$\begin{aligned} \frac{\Lambda_d}{d} &= 6Z \cdot \left[1 + 0.01 \frac{(Z-40)(Z-400)}{Z} \cdot e^{-m_\Lambda}\right] \\ (&= f_{\Lambda_d}(X,Y) \cdot 6Z) \end{aligned} \tag{A.61}$$

with

$$m_{\Lambda_d} = 0.055 \cdot \sqrt{Z} + 0.04 \cdot X \tag{A.62}$$

∗ Dune steepness:
Since according to Yalin and da Silva (2001) dunes are generated by vertical turbulence and consequently to be treated as two-dimensional, the dune steepness is determined by the dimensionless variables (see above) as:

$$\delta_d = f_{\delta_d}(X,Y,Z) = f_{\delta_d}(X,\eta^*,Z) \tag{A.63}$$

In the first case of a rough turbulent flow past an initially flat bed ($X > \approx 35$) the Reynolds number X is no longer a variable and Equation A.63 reduces to:

$$\delta_d = f_{\delta_d}(\eta^*,Z) \tag{A.64}$$

For increasing η^*, δ_d (corresponding to a specified $Z = const.$) first increases (starting from $\delta_d = 0$ when $\eta^* = 1$), reaches its maximum value ($\delta = (\delta_d)_{max}$ when $\eta^* = \hat{\eta}_d^*$) before decreasing as to yield the flat bed at advanced stages ($\delta_d \rightarrow 0$). The experimentally determined curves representing the variation of $(\delta_d)_{max}$ and $\hat{\eta}_d^*$ with Z can be reflected by:

$$\begin{aligned} (\delta_d)_{max} &= 0.00047 \cdot Z^{1.2} \cdot e^{-0.17 \cdot Z^{0.47}} \\ &\quad +0.04 \cdot \left(1 - e^{-0.002 \cdot Z}\right) \end{aligned} \tag{A.65}$$

and

$$\hat{\eta}_d^* = 35 \cdot \left(1 - e^{-0.074 \cdot Z^{0.4}}\right) - 5 \tag{A.66}$$

For δ_d, the following equation is obtained:

$$\delta_d = (\delta_d)_{max} \cdot \left(\zeta_d \cdot e^{1-\zeta_d}\right)^{m_\delta} \quad (= f_{\delta_d}(\eta^*,Z)) \tag{A.67}$$

with

$$\zeta_d = \frac{\eta^* - 1}{\hat{\eta}_d^* - 1} \tag{A.68}$$

and

$$m_\delta = 1 + 0.6 \cdot e^{-0.1 \cdot (5 - logZ)^{3.6}} \tag{A.69}$$

Until now a rough turbulent flow ($X > \approx 35$) has been assumed. If, however, the dune-generating turbulent flow is transitional ($\approx 2.5 < X < \approx 35$), then the dune steepness is smaller than that given by the expressions above. For the same remaining conditions, δ_d progressively decreases with X in the interval $\approx 2.5 < X < \approx 35$ as to become $\delta_d = 0$ for all $X < \approx 2.5$ (i. e. for the case of a hydraulically smooth regime of a turbulent flow). This fact is taken into account (as it has been done for the ripple steepness) by multiplying $(\delta_d)_{max}$ with the function $\Psi_d(X)$:

$$\Psi_\delta(X) = 1 - e^{-(X/10)^2} \tag{A.70}$$

Hence, in total, the dune steepness is determined by Equation A.64 and the multiplier-function Equation A.70:

$$\delta_d = \Psi_d(X) \cdot f_{\delta_d}(\eta^*, Z) \tag{A.71}$$

Table A.7: Synopsis of relations to describe ripple dimensions.

Investigator	Relative ripple length	Eq. in study	Relative ripple height	Eq. in study
Yalin (1985)	$\Lambda_r/d = 500 - 1000$	this one	$\Delta_r/d = 50 - 200$	this one
Van Rijn (1993) (mega ripples)	$\Lambda_r/y = 0.5$	Eq. A.43	$\Delta_r/y = 0.02 \cdot \left(1 - e^{-0.1 \cdot T}\right) \cdot (10 - T)$	Eq. A.44
	Relative ripple length		Ripple steepness	
Yalin and da Silva (2001)	$\Lambda_r/d \approx 3000/\left[\Xi^{0.88} \cdot \sqrt{\eta^*} \cdot (1 - 0.22 \cdot \sqrt{\eta^*})\right]$	Eq. A.53	$\delta_r = \Psi_r\left(X\right) \cdot f_{\delta_r}\left(\eta^*, Z\right)$	Eq. A.60

Table A.8: Synopsis of relations to describe dune dimensions.

Investigator	Relative dune length	Eq. in study	Relative dune height	Eq. in study
Yalin (1964)	$\Lambda_d/y = 6.3$	this one	$\Delta_d/y = 1/6 \cdot ((1 - \tau_{0,cr}/\tau_0)$	this one
Allen (1968)	$\Lambda_d/y = y^{0.6}$	this one	$\Delta_d/y = 0.086 \cdot y^{0.19}$	this one
Van Rijn (1984b)	$\Lambda_d/y = 7.3$	Eq. A.45	$\Delta_d/y = 0.11 \cdot (d_{50}/y)^{0.3} \cdot (1 - e^{-0.5 \cdot T}) \cdot (25 - T)$	Eq. A.46
Julien and Klaassen (1995)	$\Lambda_d/y = 6.25$	this one	$\Delta_d/y = 2.5 \cdot (d_{50}/y)^{0.3}$	this one
	Relative dune length		Dune steepness	
Yalin and da Silva (2001)	$\Lambda_d/d = 6Z \cdot [1 + 0.01 \cdot (((Z - 40)(Z - 400))/Z) \cdot e^{-m_\Lambda}]$	Eq. A.61	$\delta_d = \Psi_d(X) \cdot f_{\delta_d}(\eta^*, Z)$	Eq. A.71

A.3.3. Migration Velocity of Bed Forms

In this paragraph the following approaches referring to bed form (dunes) migration velocity (u_b) are briefly introduced and summarized in Table A.9:

- Kondap and Garde (1973),
- Fredsøe (1982),
- Kondratiev et al. (1982),
- Nikora et al. (1997) and
- Tang and Knight (2006).

The main parameters occurring in these approaches are the mean flow velocity (v), the water depth (y), the Froude number (Fr), the bed-load transport rate (q_{sb}), the dune length (Λ_d) and dune height (Δ_d) and the sediment porosity (p).

- Kondap and Garde (1973):

  An approximate equation for the advance velocity of ripples and dunes is given by:

$$u_b = 0.021 \cdot v \cdot \left(\frac{v}{\sqrt{g \cdot y}} \right)^3 = 0.021 \cdot v \cdot Fr^3 \tag{A.72}$$

- Fredsøe (1982):

  Using the continuity equation for the sediment, the migration velocity is determined by the amount of sediment ($q_{s,top}$) which is deposited at the top of the dune immediately before the front:

$$u_b = \frac{q_{s,top}}{(1-p) \cdot \Delta_d} \tag{A.73}$$

  The magnitude of $q_{s,top}$ depends on the rate of sediment transport at the dune crest and the relative amount of suspended load (q_{ss}) and bed-load (q_{sb}). As an approximation, $q_{s,top}$ equals the transport of bed-load at the dune top. The factor p is a porosity factor ranging usually between $0.36 \div 0.40$ for alluvial sand bed material (Chanson (2004)).

- Kondratiev et al. (1982):

  Using a large amount of data substantiating their equation, the dune migration velocity is calculated in the following way (being rather similar to the one proposed by Kondap and Garde (1973)):

$$u_b = 0.019 \cdot v \cdot Fr^{2.9} \tag{A.74}$$

- Nikora et al. (1997):

  Using the mean flow velocity, the Froude number and an average bed form length (Λ_d), the bed form celerity can be computed from the following relation:

$$u_b = \frac{0.66 \cdot v \cdot Fr^{2.9}}{(g \cdot \Lambda_d)/v^2} \tag{A.75}$$

- Tang and Knight (2006):

  Plotting data from laboratory compound channel experiments with a mobile bed as well as data from various other sources (e. g. Kondap and Garde (1973)) led to the relationship:

$$u_b = 0.023 \cdot Fr^{4.25} \cdot \sqrt{g \cdot y} \tag{A.76}$$

Table A.9: Synopsis of bed form (dune) migration velocity approaches taken into account in the present study.

Investigator	Bed form migration velocity	Eq. in study
Kondap and Garde (1973)	$u_b = 0.021 \cdot v \cdot (v/(g \cdot y))^3$	Eq. A.72
Fredsøe (1982)	$u_b = q_{s,top}/((1-p) \cdot \Delta_d)$	Eq. A.73
Kondratiev et al. (1982)	$u_b = 0.019 \cdot v \cdot Fr^{2.9}$	Eq. A.74
Nikora et al. (1997)	$u_b = \left(0.66 \cdot v \cdot Fr^{2.9}\right) / \left(g \cdot \Lambda_d / v^2\right)$	Eq. A.75
Tang and Knight (2006)	$u_b = 0.023 \cdot Fr^{4.25} \cdot \sqrt{g \cdot y}$	Eq. A.76

For the present study the migration velocities of individual bed forms (dunes) range between $u_b = 0.83$ and $u_b = 6.43\ mm/s$, thus corresponding to values reported by Yalin (1992) ($u_b = 0.3 \div 6.0\ mm/s$). The average migration velocity has been determined to be $u_b = 2.85\ mm/s$. A detailed analysis of bed form celerity as well as a comparison with approaches from literature is dealt with in paragraph 5.10.5.

In addition to approaches referring to the determination of bed form migration velocity, Yalin (1992) proposed an expression for the duration of development $T_{b,i}$ of a bed form i by the proportionality:

$$T_{b,i} \sim \frac{\Delta_i \cdot \Lambda_i}{q_s} \tag{A.77}$$

where q_s is an averaged value of the transport rate and $\Delta_i \cdot \Lambda_i$ is ($\approx$ twice) the area of the developed bed form profile.

Applying Equation A.77 to mean values from the present study yields a T_b-value of 204 *sec* or $\approx$ 3.4 *min* (Tab. 5.27). Thus, individual bed forms rapidly develop compared to the average total duration of the experiments of 137 *min*, meaning after $3.4/137 = 2.5$ % of the total duration. The bed form duration development is investigated in paragraph 5.10.4.

A.4. Effective or Total Bed Roughness

In case of a movable bed consisting of sediments the total or effective bed roughness (k_s, c) mainly consists of grain roughness ($k_s^{'}$, $c_f = c^{'}$) generated by skin friction forces and of form roughness ($k_s^{''}$, c_Δ) generated by pressure forces. Depending on flow intensity, form roughness effects have to be taken into account for relative roughnesses of $y/d_{90} > 25$ (Jäggi (1984a)).

Figure A.8 presents a typical relationship between the mean boundary shear stress and the flow velocity. The Figure indicates that the effect of bed forms is particularly substantial with ripples and dunes. In this context it is worthy to mention that the resistance to flow is relatively small for plane bed conditions prior to the beginning of motion. However, flow resistance is larger for this case than it is for the plane bed in the upper flow regime where bed material is in motion. This is explained by the fact that in the first case resistance results from grain roughness that is fixed, whereas in the second case the grain roughness is not fixed but moving and a kind of rolling friction exists (Simons and Richardson (1961)).

Before introducing two methods to estimate total bed roughness, different definitions of the term *effective bed roughness* have to be clarified. According to Van Rijn (1993), the effective bed roughness (and effective bed shear stress) consists of grain and form roughness (n, k_{st}, f, τ_0), whereas Chanson (2004) defines the effective bed roughness (and effective bed shear stress) being the one responsable for bed-load transport, thus being skin roughness only ($n^{'}, k_{st}^{'}, f^{'}, \tau_0^{'}$). In this study, the terms *effective* and *total* bed roughness are used synonymously. The bed shear stress related to bed-load transport is denoted as grain or skin bed shear stress and indicated by a prime ($\tau_0^{'}$).

Basically, two different methods (roughness predictor) to estimate bed roughness can be found in literature (Van Rijn (1993)). The first method is based on grain and bed form related parameters, the second one is based on integral parameters. Herein, the following approaches for each method are considered:

- Methods based on bed form and grain related parameters such as bed form length, height, steepness and bed material size:

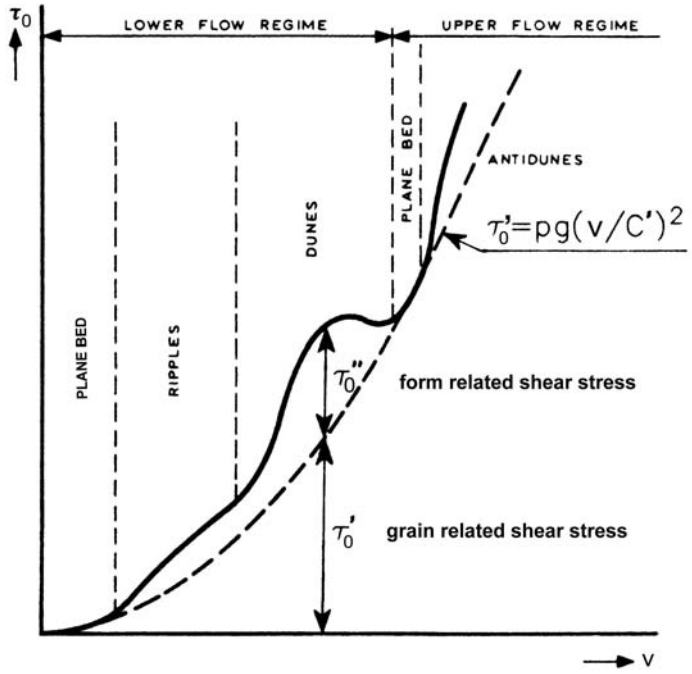

Figure A.8: Bed shear stress as a function of mean flow velocity (Van Rijn (1993)).

  - Van Rijn (1982), Van Rijn (1984b), Van Rijn (1993) and
  - Yalin and da Silva (2001).

- Methods based on integral parameters such as mean flow depth, mean velocity and bed material size:
  - Engelund and Hansen (1967),
  - Smith and McLean (1977) and
  - Brownlie (1981).

A.4.1. Methods for Bed Roughness Estimation based on Grain and Bed Form Parameters

If no sidewall effects have to be taken into account or have already been removed, respectively, (paragraph A.5), the overall Manning or Strickler resistance coefficient (n or k_{st}) for a composite channel cross section can be subdivided into a skin or grain related part (n' or k'_{st}) and a part induced by form drag (e. g. caused by bed forms) (n'' or k''_{st}):

$$k_{st} \begin{cases} k'_{st}: & \text{grain or skin friction} \\ \\ k''_{st}: & \text{form drag (e. g. bed forms)} \end{cases} \tag{A.78}$$

According to the linear separation approach, the resistance coefficient can be expressed as (Naudascher (1992))

$$n = n^{'} + n^{''}, \;\; k_{st} = k_{st}^{'} + k_{st}^{''} \;\text{ or }\; f = f' + f^{''} \tag{A.79}$$

For reasons of simplicity, Van Rijn (1984b) assumed that the effective roughness height of Nikuradse (k_s) can also be divided into a grain related part ($k_s^{'}$) and a form related part ($k_s^{''}$) as follows:

$$k_s = k_s^{'} + k_s^{''} \tag{A.80}$$

Since forces acting in the same direction are algebraically additive, the overall shear stress (τ_0) can be given by the sum of grain and form roughness. This linear superposition was initiated in Zurich, Switzerland, by Meyer-Peter and Müller (1948) and Einstein (1950). They followed the momentum concept assuming the bed shear stress can be separated linearly as:

$$\tau_0 = \tau_0^{'} + \tau_0^{''} \tag{A.81}$$

in which $\tau_0^{'}$ reference plane bed shear and $\tau_0^{''}$ additional bed shear[5].

The distribution of the grain related bed shear stress along a bed form (dune) is shown in Figure A.9. The grain related stress is low in the flow separation zone and high near the crest of the bed form. The form induced bed shear stress is related to the fluid pressure distribution upstream and downstream of the crest. The flow is accelerating near the crest, requiring a decrease of the fluid pressure, whereas the flow is decelerating downstream of the crest requiring an increase of the fluid pressure.

[5]Since for the computation of bed-load transport the shear force that actually causes bed-load transport is needed (τ_0'), this superposition approach might be applied to remove the shear force due to bed forms (τ_0''). At this point it has to be noted that for a sediment plane bed some energy and momentum are spent on picking up, transporting and depositing the bed sediment. This is true even in the case of flow with equilibrium sediment transport for which the plane bed remains constant with respect to time (Yen (2002)). Following Van Rijn (1982), rather large k_s-values have been observed while analyzing a large amount of movable bed experiments which were explicitly indicated as "plane bed" experiments. He pointed out that a completely plane bed does not exist for conditions with active sediment transport and probably, the effective roughness is caused by very small irregularities ("bed forms") of the movable bed.

For a cross section with τ_0 computed as $\rho g R_h S$, linear separation of τ_0 can be accomplished through a linear division of the hydraulic radius (R_h) or the slope (S). For the former, (Einstein (1950)):

$$R_h = R_h^{'} + R_h^{''} \tag{A.82}$$

and the latter (Meyer-Peter and Müller (1948)):

$$S = S^{'} + S^{''} \tag{A.83}$$

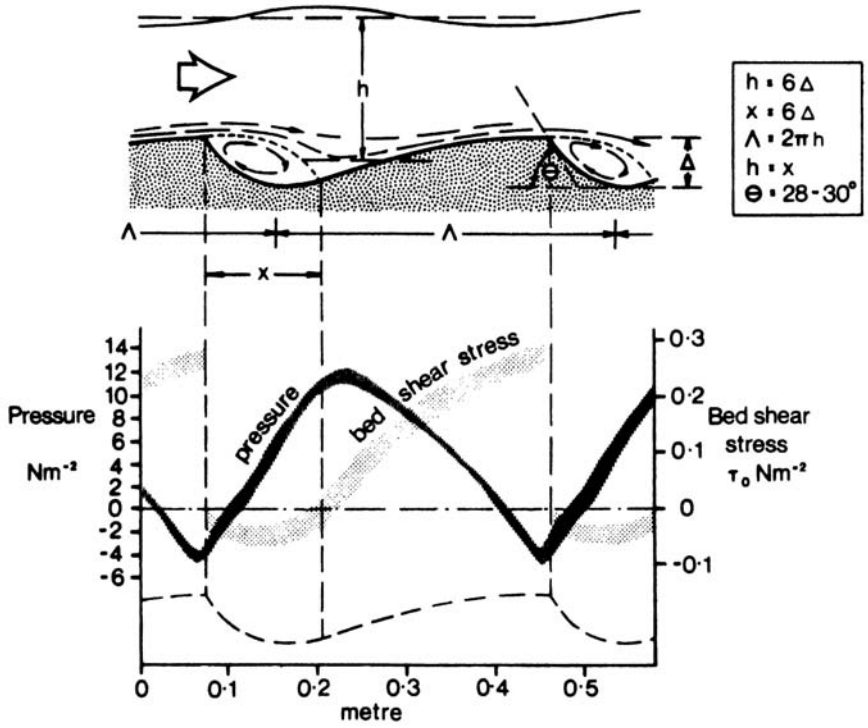

Figure A.9: Fluid pressure and shear stress distribution along a dune (Langhorne (1978)).

In the following paragraph the grain and form roughness concepts as well as the conversion into a total resistance coefficient (e. g. Chézy) of Van Rijn (1984b) and Yalin and da Silva (2001) are presented.

- Grain roughness:

  Grain roughness is the roughness of individual moving or non-moving sediment particles as present in the toplayers of a natural plane movable or non-movable bed.

  – Van Rijn (1982):

    According to Van Rijn (1982), the grain roughness in the lower regime is mainly related to the largest particles of the top layer of the bed (d_{90}). This has already been stated by Meyer-Peter and Müller (1948). The $k_s^{'}$-value of a movable plane bed (moving layer of grains) seems to be somewhat larger than that of a rigid plane bed. Analyzing about 120 sets of flume and field data with and without a mobile bed, the following relation for the lower regime is proposed:

$$k_s^{'} = 3 \cdot d_{90} \tag{A.84}$$

Amongst other values, similar values for sand and gravel beds in the lower regime are summarized in Table A.3.

– Yalin and da Silva (2001):

Using the experimental curve by Schlichting (1968) relating Re^* (where $Re^* = u^* \cdot k_s/\nu$, $k_s \approx 2d$, Eq. A.15) with the roughness function B_s ($B_s = f(Re^*)$), Yalin and da Silva (2001) propose the following analytical equation:

$$B_s = (2.5 \cdot ln\,(Re^*) + 5.5) \cdot e^{-0.0705 \cdot (ln(Re^*))^{2.55}} + 8.5 \cdot \left[1 - e^{-0.0594 \cdot (ln(Re^*))^{2.55}}\right] \quad \text{(A.85)}$$

Furthermore, applying $Re^* = u_* k_s/\nu$ and $X = u_* d/\nu$ with $k_s = 2d$, the Reynolds number yields $Re^* = 2X$. In addition with $Z = y/d$ (and $k_s = 2d$) and using Equation A.21, the grain related resistance factor (friction factor) is expressed by:

$$c^{'} = c_f = \frac{1}{\kappa} \cdot ln\left(0.368 \cdot \frac{Z}{2}\right) + B_s \quad \text{(A.86)}$$

- Form roughness:

Form roughness is related to the fluid pressure distribution on the bed form and to form loss which may be crudely analyzed as a sudden expansion downstream of the bed form crest (Chanson (2004)). The effective form roughness is related to the bed form length (Λ), bed form height (Δ), bed form steepness (δ) and the bed form shape (γ_i).

– Van Rijn (1984b) and Van Rijn (1993):

According to Van Rijn (1982), the most general case is that of a bed consisting of (mega)ripples superimposed on asymmetrical dunes and symmetrical sand waves. Sand waves are defined as bed forms with a length much larger than the water depth. Due to relatively mild leeside slopes no flow separation will occur and form roughness is assumed to be zero. The overall form roughness ($k_s^{''}$) is proposed to be the sum of the individual form roughnesses:

$$k_s^{''} = k_{s,r}^{''} + k_{s,d}^{''} \quad \text{(A.87)}$$

in which $k_{s,r}^{''}$ form roughness related to ripples and $k_{s,d}^{''}$ form roughness related to asymmetrical dunes.

∗ Ripples:

Ripples are defined as bed forms with a length smaller than the water depth. To determine the form roughness related to ripples, the following relationship is proposed:

$$k_{s,r}^{''} = 20 \cdot \gamma_r \cdot \Delta_r \cdot \delta_r \tag{A.88}$$

in which $\delta_r = \Delta_r/\Lambda_r$ ripple steepness and γ_r ripple presence factor. When the bed is fully covered with ripples the γ_r-parameter is $\gamma_r = 1$. When the ripples are superimposed on dunes the region near the crest and the trough of the dunes usually is free of ripples resulting in a γ_r-parameter of about 0.7 .

* Dunes:
  Dunes are defined as asymmetrical bed forms with a length of about 7 times the water depth (Eq. A.45). Based on the analysis of dune data, the following relationship is proposed:

$$k_{s,d}^{''} = 1.1 \cdot \gamma_d \cdot \Delta_d \cdot \left(1 - e^{-25 \cdot \delta_d}\right) \tag{A.89}$$

in which $\delta_d = \Delta_d/\Lambda_d$ dune steepness and γ_d a form factor expressing the influence of dune form on roughness height. Lee side slopes of river dunes are much smaller than those of laboratory dunes (Ogink (1988). Therefore, a considerable reduction of the form roughness for mild lee side slopes is observed because the flow separation effect is less important. Consequently, a form factor of $\gamma_d = 0.7$ for field conditions is recommended.

– Yalin and da Silva (2001):

The hydraulic energy loss due to form roughness is mainly due to a sudden expansion at the bed form crest. The energy loss due to the gradual contraction at the upstream face of the bed form is negligible. Using the Borda-theorem for the sudden expansion, the following expression for the two modes of bed forms, i. e. ripples superimposed on dunes, is assumed to be valid:

* Ripples and Dunes:

$$c^{''} = c_\Delta = \sqrt{2 \cdot y \cdot \left(\frac{1}{\delta_r^2 \cdot \Lambda_r + \delta_d^2 \cdot \Lambda_d}\right)} \tag{A.90}$$

A third mode of bed forms, viz bars (e. g. alternate bars), might be present. Their contribution to form resistance can be ignored since their $\delta^2\Lambda$-values are approximately by one order of magnitude smaller.

Finally, the approaches of Van Rijn and Yalin and da Silva can be summarized as follows:

- Van Rijn (1984b), Van Rijn (1993):

  The total or effective roughness (k_s) is proposed to be computed by means of (Eqs A.80, A.84, A.87, A.88 and A.89):

$$k_s = \underbrace{3 \cdot d_{90}}_{grain} + \underbrace{\underbrace{20 \cdot \gamma_r \cdot \Delta_r \cdot \delta_r}_{ripples} + \underbrace{1.1 \cdot \gamma_d \cdot \Delta_d \cdot \left(1 - e^{-25 \cdot \delta_d}\right)}_{dunes}}_{form} \tag{A.91}$$

  The total Chézy resistance coefficient is calculated as follows (see also Eq. A.23):

$$C = 18 \cdot log\left(\frac{12 \cdot R_b}{k_s}\right) \tag{A.92}$$

  in which R_b hydraulic radius of the bed according to the side wall correction procedure of Vanoni and Brooks (1957) (paragraph A.5).

- Yalin and da Silva (2001):

  Assuming the total or effective dimensionless Chézy resistance factor (c) is the sum of friction losses and energy losses due to the sudden expansion, c is calculated as follows (Eqs A.86 and A.90):

$$\begin{aligned} \frac{1}{c^2} &= \frac{1}{c_f^2} + \frac{1}{c_\Delta^2} \\ &= \frac{1}{(c')^2} + \frac{1}{(c'')^2} \\ &= \underbrace{\frac{1}{c_f^2}}_{grain} + \underbrace{\frac{1}{2 \cdot y} \cdot \underbrace{\left(\delta_r^2 \cdot \Lambda_r\right)}_{ripples} + \underbrace{\delta_d^2 \cdot \Lambda_d\big)}_{dunes}}_{form} \end{aligned} \tag{A.93}$$

  in which $c_f = c^{'}$ dimensionless friction factor related to grain roughness and $c_\Delta = c^{''}$ dimensionless bed form resistance factor.

At this point it has to be noted that the dimensional Chézy resistance factor (C) and the dimensionless Chézy resistance factor (c) are related by:

$$C = c \cdot \sqrt{g} \tag{A.94}$$

A.4.2. Methods for Bed Roughness Estimation based on Integral Parameters

Various methods based on integral parameters such as water depth, mean flow velocity, slope and bed material characteristics have been proposed (Van Rijn (1993)). As mentioned in paragraph A.4 the methods of Engelund and Hansen (1967), Smith and McLean (1977) and Brownlie (1981) are presented herein because the first one gave best results in an extensive appraisal of available methods for river flow conditions (Van Rijn (1993)) and the two other methods because of their simplicity.

- Engelund and Hansen (1967):

  Following the linear separation concept (Meyer-Peter and Müller (1948), Einstein (1950)) and using Equation A.81, the grain and form related bed shear stresses ($\tau_0^{'}$, $\tau_0^{''}$) are defined as:

$$\tau_0^{'} = \rho \cdot g \cdot y^{'} \cdot S \quad \text{or} \quad u_*^{'} = \sqrt{g \cdot y^{'} \cdot S} \tag{A.95}$$

$$\tau_0^{''} = \rho \cdot g \cdot y^{''} \cdot S \quad \text{or} \quad u_*^{''} = \sqrt{g \cdot y^{''} \cdot S} \tag{A.96}$$

  Based on this, it can be derived that:

$$\left(\frac{u_*^{'}}{u_*}\right)^2 = \frac{y^{'}}{y} \quad \text{or} \quad \frac{\theta^{'}}{\theta} = \frac{y^{'}}{y} \tag{A.97}$$

  Moreover it is assumed that $u_*^{'}$ can be found from the following relationship:

$$v = 2.5 \cdot u_*^{'} \cdot ln\left(\frac{12 \cdot y^{'}}{2.5 \cdot d_{50}}\right) \tag{A.98}$$

  Using $v = C\sqrt{yS}$ (Eq. A.22) and $u_*^{'} = \sqrt{gy^{'}S}$ (Eq. A.13), Equation A.98 can be expressed as:

$$C = 2.5 \cdot \sqrt{g} \cdot \sqrt{\frac{y^{'}}{y}} \cdot ln\left(\frac{12 \cdot y^{'}}{2.5 \cdot d_{50}}\right) \tag{A.99}$$

  or

$$C = 2.5 \cdot \sqrt{g} \cdot \sqrt{\frac{\theta^{'}}{\theta}} \cdot ln\left(\frac{12 \cdot y^{'}}{2.5 \cdot d_{50}}\right) \tag{A.100}$$

  For the lower and upper regime, respectively, the following equations are identified:

$$\begin{aligned} \text{lower regime: } \theta^{'} &= 0.06 + 0.4 \cdot \theta^2 && \text{for } \theta \leq 0.7 \quad \text{(A.101)} \\ \text{upper regime: } \theta^{'} &= \theta && \text{for } 0.7 < \theta < 1 \\ \theta^{'} &= \left(0.3 + 0.7 \cdot \theta^{-1.8}\right)^{-0.56} && \text{for } \theta \geq 1 \end{aligned}$$

  Using Equations A.99 or A.100, the Chézy coefficient can be determined.

- Smith and McLean (1977):

  Based on the analysis of river data it is proposed:

$$k_s = d_{50} \cdot [1 + 700 \cdot (\theta - \theta_{cr})] \tag{A.102}$$

  in which θ_{cr} critical Shields parameter. Equation A.102 is only valid in the lower regime ($\theta < 0.7$) with dunes. For $\theta \leq \theta_{cr}$, Equation A.102 yields $k_s = d_{50}$, for $\theta = 0.6$ and $\theta_{cr} = 0.05$, $k_s \approx 400 \cdot d_{50}$. Thus, the k_s-value for the flat bed is $k_s' = d_{50}$.

- Brownlie (1981):

  The Brownlie method predicts the flow depth (y) as a function of the main flow variables. The method is based on dimensional analysis and data fitting using 344 flume data and 550 field data in the lower and upper regime. The following equations are proposed:

$$\begin{aligned} \text{lower regime: } y &= 0.372 \cdot d_{50} \cdot Q_*^{0.654} \cdot S^{-0.254} \cdot \sigma_s^{0.105} \\ \text{upper regime: } y &= 0.284 \cdot d_{50} \cdot Q_*^{0.625} \cdot S^{-0.288} \cdot \sigma_s^{0.08} \\ &\quad \text{for } S \geq 0.006 \text{ or } F_g \geq 1.74 \cdot S^{-1/3} \end{aligned} \tag{A.103}$$

  in which

$$Q_* = \frac{Q}{B \cdot \sqrt{g} \cdot d_{50}^{1.5}}$$

$$F_g = \frac{Q}{B \cdot \sqrt{(s-1) \cdot g \cdot d_{50}}}$$

$$\sigma_s = \frac{1}{2} \cdot \left(\frac{d_{50}}{d_{16}} + \frac{d_{84}}{d_{50}} \right)$$

  The Chézy coefficient follows from:

$$C = \frac{Q}{B \cdot y^{1.5} \cdot S^{0.5}} \tag{A.104}$$

A.5. Sidewall Correction Methods

In studies dealing with sediment transport it is often necessary to remove sidewall effects for computing effective bed shear stress. Thus, a separation of the effects due to the difference in roughness of the channel bed and sidewalls is needed. As pointed out by Naudascher (1992), this is typically the case for channel aspect ratios of $B/y \leq 10$.

The following sidewall correction methods are considered in the present study:

- Einstein (1942),
- Vanoni and Brooks (1957) and
- Williams (1970).

The sidewall correction procedures mentioned above are based on the assumptions of uniform flow velocity throughout the cross section, equal energy slope on the bed and wall regions and partitioning of the overall Manning, Strickler or Darcy-Weisbach resistance coefficient (n, k_{st}, f) in terms of hydraulic radii into a bed and a wall component (n_b, $k_{st,b}$, f_b and n_w, $k_{st,w}$, f_w) (Fig. A.10):

$$k_{st} \begin{cases} k_{st,b}: & \text{bed component} \\ \\ k_{st,w}: & \text{wall component} \end{cases} \tag{A.105}$$

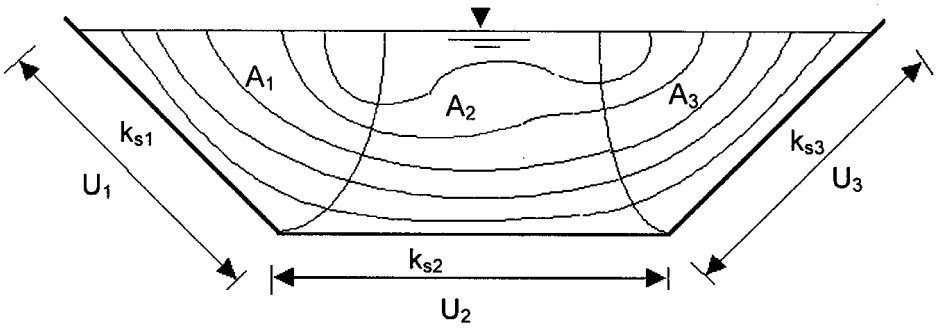

Figure A.10: Partitioning of overall resistance coefficient in terms of hydraulic radii into a bed and a wall component. A represents the flow area, U the wetted perimeter and k_s a resistance coefficient (from Dittrich (1998)).

Customarily, the internal water lines dividing the subsections are not considered as a part of the wetted parameter in computing the subsection hydraulic radii ($R_{h,i}$). Only the actual wetted external boundary is used (Yen (2002)).

The general form of the sidewall correction procedures is the following one:

$$\frac{\tau_b}{\tau_0} = \frac{\tau_b}{\rho \cdot g \cdot R_h \cdot S} = \vartheta \tag{A.106}$$

with $\vartheta \leq 1.0$ sidewall correction coefficient. Thus, the overall shear stress (τ_0) is reduced by the factor ϑ yielding the effective bed shear stress (τ_b).

- Einstein (1942):

  Einstein (1942) has used the Manning resistance coefficient to differentiate flow resistance components associated with the bed and the wall, respectively. The average bed shear stress (τ_b) has been defined as:

$$\tau_b = \rho \cdot g \cdot R_h \cdot S \cdot \left(\frac{n_b}{n}\right)^{3/2} \tag{A.107}$$

  Finally, the following equation has been obtained which has also been used by Meyer-Peter and Müller (1948) in deriving their bed-load formula:

$$\frac{\tau_b}{\rho \cdot g \cdot R_h \cdot S} = 1 - \frac{2 \cdot n_w^{3/2} \cdot v^{3/2}}{B \cdot S^{3/4}} \tag{A.108}$$

- Vanoni and Brooks (1957):

  A major concern with the sidewall correction procedure according to Einstein (1942) is that the wall resistance coefficient (n_w) is set in advance of the actual experiments on bed-load transport. Its value is thus independent of q_w (unit discharge related to the wall region) and B/y; a result that does not seem to have a solid physical background. With respect to this, the Darcy-Weisbach equation for flow resistance has a stronger theoretical foundation and its original formulation for pipe flow can be applied to open-channel flow in the following form:

$$f = \frac{8 \cdot g \cdot R_h \cdot S}{v^2} \tag{A.109}$$

  In the case of a rectangular cross section with wetted parameters B and $2y$ for the bed and wall regions, the resistance coefficient for the bed region (f_b) may be computed as:

$$f_b = f + \frac{2 \cdot y}{B} \cdot (f - f_w) \tag{A.110}$$

  In a formulation such as Equation A.109 the value of f depends on the Reynolds number (Re) which in the case of open-channel flow is computed by using a characteristic length of $4R_h$ ($Re = 4vR_h/\nu$).

  Finally, for a smooth hydraulic boundary the wall friction factor f_w can be calculated iteratively according to Chien and Wan (1999) as follows:

$$\frac{Re}{f} = \frac{10^{\left(1/(2\cdot\sqrt{f_w})+0.40\right)}}{f_w^{3/2}} \tag{A.111}$$

  Cheng and Chua (2005) propose the following function which has been obtained by curve fitting:

$$f_w = \left[20 \cdot \left(\frac{4 \cdot v \cdot R_h}{\nu} \cdot \frac{1}{f}\right)^{0.1} - 39\right]^{-1} \tag{A.112}$$

Applying Equations A.111 and A.112 to the present study no significant difference could be observed between the two expressions. Consequently, due to direct computation instead of an iterative procedure, Equation A.112 has been used for the present investigation.

Concluding, the bed shear stress is expressed as:

$$\frac{\tau_b}{\rho \cdot g \cdot R_h \cdot S} = \frac{B}{B + 2 \cdot y} \cdot \frac{f_b}{f} \tag{A.113}$$

- Williams (1970):

  The approach provided by Williams was achieved experimentally. It is suggested that the bed shear stress could be adjusted simply according to:

$$\frac{\tau_b}{\rho \cdot g \cdot R_h \cdot S} = \frac{B^2}{B^2 + 0.055 \cdot y} \tag{A.114}$$

In Table A.10 the side wall correction procedures taken into account in the present study are summarized.

Table A.10: Synopsis of side wall correction procedures taken into account in the present study. The side wall correction coefficient ϑ is given by Equation A.106.

Investigator	Side wall correction procedure	Eq. in study
Einstein (1942)	$\vartheta = 1 - \left[\left(2 \cdot n_w^{3/2} \cdot v^{3/2}\right) / \left(B \cdot S^{3/4}\right)\right]$	Eq. A.108
Vanoni and Brooks (1957)	$\vartheta = B/\left(B + 2 \cdot y\right) \cdot \left(f_b/f\right)$	Eq. A.113
Williams (1970)	$\vartheta = B^2/\left(B^2 + 0.055 \cdot y\right)$	Eq. A.114

It has to be noticed that it is not clear if a sidewall correction procedure which is derived for a rigid bed is also applicable for mobile beds (Cheng and Chua (2005)). Furthermore, the shear force (τ_0 or τ_b) that actually causes bed-load transport transport is the shear force related to grain roughness (τ_0' or τ_b'). Consequently, the shear force due to bed forms (τ_0'' or τ_b'') has still to be removed (e. g. introducing a factor $(k_{st}/k_{st}')^{3/2}$ as proposed by Meyer-Peter and Müller (1948)). Therefore, taking into account Equation A.78, Equation A.105 might be extended in the following way:

$$k_{st} \begin{cases} k_{st,b} \begin{cases} k'_{st,b}: & \text{grain or skin friction} \\ k''_{st,b}: & \text{form drag (e. g. bed forms)} \end{cases} \\ k_{st,w} \end{cases} \tag{A.115}$$

Since for the present study aspect ratios range from $B/y = 9$ to $B/y = 17$ with a mean value of $B/y = 12$, thus being close or greater than $B/y = 10$, sidewall effects are assumed to play a subordinate role. In fact, a comparison of measured and calculated bed-load transport rates reveals no significant influence of sidewall effects (paragraph 5.7.1).

A.6. Sediment Transport Capacity

In this paragraph the different modes of sediment transport are presented. In addition, the basic (dimensionless) parameters influencing sediment transport are highlighted. Thereafter, several approaches from literature to estimate bed-load transport capacity are described.

A.6.1. Process of Sediment Transport

The transport of sediment particles by a flow of water can be in the form of bed-load and suspended load, depending on the size of the bed material particles and the flow conditions. The suspended load may also contain some wash load which is generally defined as that portion of the suspended load which is governed by the upstream supply rate and *not* by the composition and properties of the bed material (Van Rijn (1984a)). Although in natural conditions there will be *no* sharp division between the bed-load and suspended load transport it is necessary to define a layer with bed-load transport for mathematical representation.

Usually, three modes of particle motion are distinguished:

- Rolling and sliding or both,
- saltation and
- suspended particle motion.

The transport of particles by rolling, sliding and (briefly) saltating is called bed-load transport (Van Rijn (1984a)). This mode of transport is the predominant one in the present study and therefore the only mode considered. The solid particles stay very close to the bed ($0 < z < z_{sb}$, Fig. A.11) which they may leave only temporarily. The displacement of the particles

is intermittent, the random concept of the turbulence plays an important role (Graf and Altinakar (1998)).

$$\text{total load, } q_{s,total} \begin{cases} \text{bed material, } q_s \begin{cases} \text{bed-load, } q_{sb} \\ \text{suspended load, } q_{ss} \end{cases} \\ \text{wash load, } q_{sw} \end{cases}$$

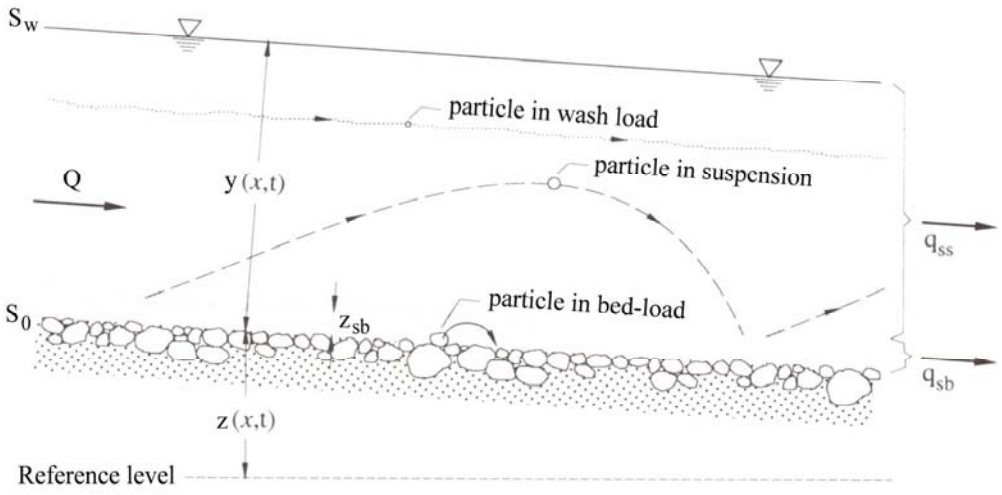

Figure A.11: Different modes of sediment transport according to Graf and Altinakar (2000).

The steady and uniform (two-dimensional) flow of water and sediment particles is defined by seven basic parameters (Van Rijn (1984a), Graf and Altinakar (1998)):

- Density of water: ρ,
- Density of sediment: ρ_s,
- Kinematic viscosity coefficient: ν,
- Particle size: d,
- Flow depth: y or R_h,
- Channel slope: S and
- Acceleration of gravity: g.

A dimensional analysis using the Π-theorem (e. g. Yalin (1972)) shows that these seven components of the two-phase flow can be reduced to a set of four dimensionless parameters, namely:

- Particle or grain size Reynolds number:

$$Re^* = \frac{u_* \cdot d}{\nu} \tag{A.116}$$

- Dimensionless shear stress (Shields factor):

$$\begin{aligned} Fr^* \equiv \tau^* \equiv \theta &= \frac{\tau_0}{(\rho_s - \rho) \cdot g \cdot d} = \frac{\rho \cdot g \cdot R_h \cdot S}{(\rho_s - \rho) \cdot g \cdot d} \\ &= \frac{u_*^2}{(s-1) \cdot g \cdot d} = \frac{R_h \cdot S}{(s-1) \cdot d} \end{aligned} \tag{A.117}$$

  or densimetric Froude number of the particle:

$$Fr_d^* = \frac{u_*}{\sqrt{(s-1) \cdot g \cdot d}} = \frac{\sqrt{\tau_0}}{(\sqrt{\rho_s - \rho}) \cdot g \cdot d} = \sqrt{Fr^*} = \sqrt{\tau^*} = \sqrt{\theta} \tag{A.118}$$

  The critical condition for incipient motion depends on the ratio of the driving and resisting forces acting on the grain (Eq. A.117). According to Shields (1936) the critical condition for Equation A.117 is obtained for

$$Fr_{cr}^* \equiv \tau_{cr}^* \equiv \theta_{cr} = \frac{\tau_{0,cr}}{(\rho_s - \rho) \cdot g \cdot d} = f(Re^*) = 0.06 \tag{A.119}$$

  In Figure A.12 the Shields curve is presented. For the lower and upper regions the determination of θ_{cr} is quite straightforward with sediment and fluid characteristics, whereas for the intermediate region it is inconvenient (Cao et al. (2006)). Explicit θ_{cr}-formulations for the entire Shields diagram (lower, upper and transition region) are given, e. g., by Van Rijn (1984a) ($\theta_{cr} = f(D_*)$), Yalin and da Silva (2001) ($\theta_{cr} = f(\Xi)$) and Cao et al. (2006) ($\theta_{cr} = f(Re^*)$). For the upper region Meyer-Peter and Müller (1948) stated a θ_{cr}-value of 0.047, arguing that at 0.06 a considerable probability of movement already exists. For no motion a value of 0.03 is proposed. Smart and Jäggi (1983) reported a θ_{cr}-value of 0.05.

  For a wide channel the hydraulic radius (R_h) in Equation A.117 generally equals to the flow depth (y), typically if the aspect ratio $B/y > 10$ (Naudascher (1992)). If the aspect ratio of the channel is small ($B/y \leq 10$) the influence of side wall effects has to be considered. In this case the hydraulic radius (R_h) is replaced by the hydraulic radius related to the bed (R_b). In paragraph A.5 different side wall correction methods are presented.

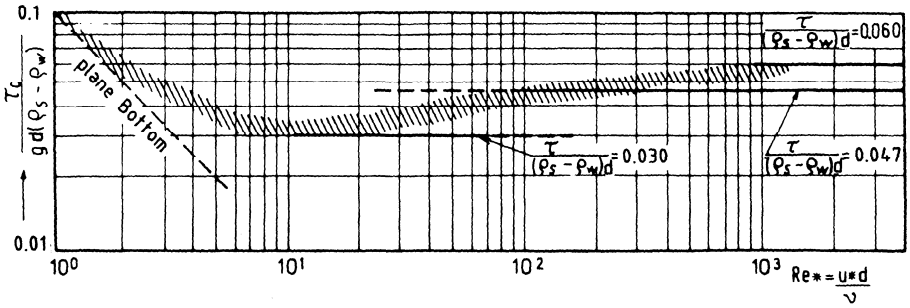

Figure A.12: Shields diagram.

- Depth-particle size ratio or relative depth:

$$\frac{y}{d} \text{ or } \frac{R_h}{d} \tag{A.120}$$

- Specific density parameter or relative density:

$$s = \frac{\rho_s}{\rho} \tag{A.121}$$

Resuming Equations A.116 to A.121, the four dimensionless variables are:

$$\begin{aligned} X_1 &= \frac{u_* \cdot d}{\nu} &&= Re^* \\ X_2 &= \frac{u_*^2}{(s-1) \cdot g \cdot d} &&= \theta \\ X_3 &= \frac{y}{d} \text{ or } \frac{R_h}{d} \\ X_4 &= \frac{\rho_s}{\rho} &&= s \end{aligned} \tag{A.122}$$

In addition, a dimensionless particle diameter (D_*) can be obtained by combining Equation A.116 and Equation A.117:

$$D_* = d \cdot \left[\frac{(s-1) \cdot g}{\nu^2} \right]^{1/3} \tag{A.123}$$

Finally, the transport of sediments can be expressed as a function of these four dimensionless parameters, namely:

$$\Phi = f\left(D_*,\ \theta^*,\ R_h/d,\ \rho_s/\rho\right)$$

Using the Π-theorem (Yalin (1972)) an expression for the dimensionless intensity of the solid discharge as bed-load is obtained. This expression usually is referred to as the Einstein factor and reads:

$$\Phi \equiv q_{sb}^{*} = \frac{q_{sb}}{\sqrt{(s-1) \cdot g \cdot d^3}} \tag{A.124}$$

with q_{sb} the volumetric solid discharge per unit width.

The numerator in Eq. A.124 (q_{sb}) is given by various bed-load transport formulae which are established by experiments performed in the laboratory and in the field (see e. g. Graf (1971), Yalin (1972)). Many of these formulae are of empirical nature but often have incorporated dimensionless numbers. At the present the formulae to predict the bed-load discharge give only reasonable results within a domain of the parameters for which the chosen formula has been established (Graf and Altinakar (1998)). Consequently, the application and use of such formulae has to be done with great care.

Since in the present study only bed-load transport is considered, from the numerous available formulae the following are taken into account in this study and briefly presented in the subsequent paragraphs:

- Meyer-Peter and Müller (1948),
- Schoklitsch (1950),
- Smart and Jäggi (1983) and
- Van Rijn (1984a)

A.6.2. Meyer-Peter and Müller (1948)

A great number of experiments (Tab. A.11) with slopes ranging from 0.04 to 2.3 % were performed at the ETH in Zurich, Switzerland, between 1930 and 1948 resulting in the Meyer-Peter and Müller (1948) formula (MPM).

Table A.11: Characteristic parameters of the bed materials used for the laboratory tests of Meyer-Peter and Müller (1948).

Type of bed material	Mobile bed condition	Density ρ_s $[kg/m^3]$	d_m $[mm]$
uniform	plane bed	2680	5.21 – 28.65
uniform	plane bed	2650	3.17 – 7.01
uniform, non-uniform	plane bed, bed forms	1250 – 4220	0.38 – 5.21

MPM's analysis sought to relate the "available" shear stress ($\tau_0^{'}$) of the flow to the critical shear stress ($\tau_{0,cr}$) necessary for initiation of motion of the sediment and to a transport term with the dimensions of a shear stress (τ_g), i. e. $\tau_0^{'} = \tau_{0,cr} + \tau_g$. These three elements were then converted to dimensionless numbers by dividing by $\rho g(s-1)d_m$. A linear relationship was then sought between the two expressions:

$$\left(\frac{Q_r}{Q}\right) \cdot \left(\frac{k_{st}}{k'_{st}}\right)^{\alpha_0} \cdot \frac{R_h \cdot S}{(s-1) \cdot d_m} \tag{A.125}$$

and

$$\frac{q_{sb}^{2/3}}{(s-1)^{1/3} \cdot g^{1/3} \cdot d_m} \tag{A.126}$$

The exponent α_0 had to be predetermined and was selected to be 1.5. Regression then gave the constants 0.047 and 0.25 as indicated in Figure A.13.

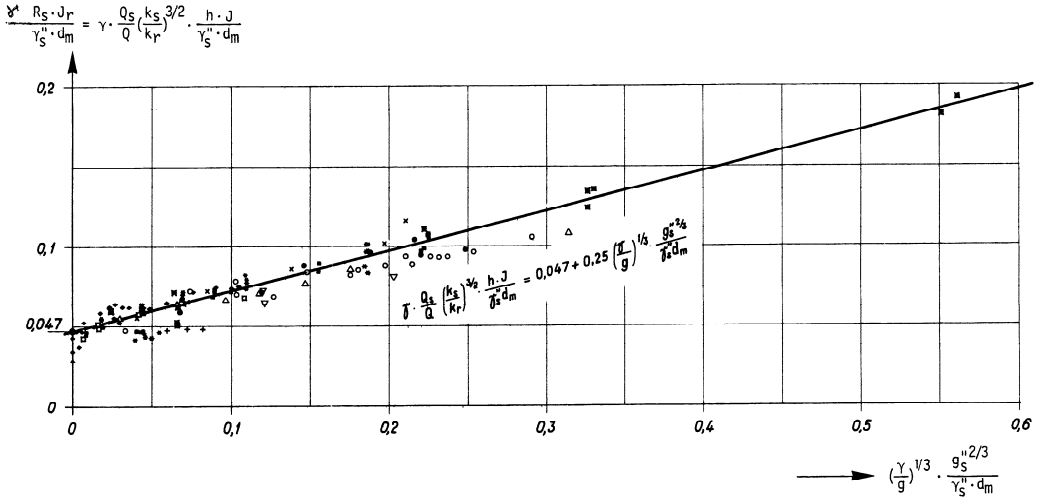

Figure A.13: Dimensionless plot reproduced from the original Meyer-Peter and Müller (1948) publication. This served as a base for the development of their bed-load transport formula.

Thus, the Meyer-Peter and Müller (1948) equation is:

$$\begin{aligned} \rho \cdot g \cdot \left(\frac{Q_r}{Q}\right) \cdot \left(\frac{k_{st}}{k'_{st}}\right)^{3/2} \cdot y \cdot S &= 0.047 \cdot \rho \cdot (s-1) \cdot g \cdot d_m \\ &+ 0.25 \cdot \rho \cdot (s-1)^{2/3} \cdot g^{2/3} \cdot qsb^{2/3} \\ \text{or} \quad \tau_0^{'} &= \tau_{0,cr} + \tau_g \end{aligned} \tag{A.127}$$

where Q_r is a reduced discharge accounting for wall friction according to Einstein (1942) and k_{st} is the overall bed roughness evaluated with the

Gauckler-Manning-Strickler formula (GMS), k'_{st} is the grain roughness, to be evaluated with Equation A.27, resuming:

$$k_{st} = \frac{v}{R_h^{2/3} \cdot S^{1/2}} \quad \text{and} \quad k'_{st} = \frac{26}{d_{90}^{1/6}} \tag{A.128}$$

It has to be noted that $\tau_0^{'}$ is already reduced compared to the mean shear stress (τ_0) by the introduction of the factors Q_r/Q accounting for wall influence and $(k_{st}/k'_{st})^{3/2}$ accounting for bed form roughness. In wide channels Q_r/Q is equal to 1.0 (present study $0.81 < Q_r/Q < 1.00$, mean $Q_r/Q = 0.90$).

In the absence of bed forms it is recommended to take $(k_{st}/k'_{st})^{3/2} = 1.0$; if bed forms are present, $0.35 < (k_{st}/k'_{st})^{3/2} < 1.0$. For gravel bed rivers, Jäggi (1984b) recommends a $(k_{st}/k'_{st})^{3/2}$-value of 0.78. In the present investigation, $(k_{st}/k'_{st})^{3/2}$-values vary in the range of $0.45 < (k_{st}/k'_{st})^{3/2} < 1.00$ with a mean value of $(k_{st}/k'_{st})^{3/2} = (63/72)^{3/2} = 0.83$.

Rearranging for q_{sb}, the bed-load transport is calculated according to:

$$q_{sb} = \left[\frac{\rho \cdot g \cdot \left(\frac{Q_r}{Q}\right) \cdot \left(\frac{k_{st}}{k'_{st}}\right)^{3/2} \cdot y \cdot S - 0.047 \cdot \rho \cdot (s-1) \cdot g \cdot d_m}{0.25 \cdot \rho \cdot (s-1)^{2/3} \cdot g^{2/3}} \right]^{3/2} \tag{A.129}$$

For a non-uniform grain size distribution the mean diameter (d_m) in Equation A.129 is replaced by d_{50}.

Using the Einstein factor (Φ) Equation A.129 can be written in dimensionless form, yielding:

$$\Phi = 8 \cdot \left[\left(\frac{k_{st}}{k'_{st}}\right)^{3/2} \cdot \theta - \theta_{cr} \right]^{3/2} \tag{A.130}$$

In this form the Meyer-Peter and Müller (1948) equation can be compared to other equations expressed with the Einstein factor.

A.6.3. Schoklitsch (1950)

Based on laboratory experiments Schoklitsch (1930) suggested an equation considering a discharge relationship of the type:

$$q_{sb} = \chi \cdot S^k \cdot (q - q_{cr}) \tag{A.131}$$

where χ is a characteristic sediment coefficient and q_{cr} is a water discharge at which the bed material begins to move (incipient motion criteria). Thus, the rate of movement is proportional to the excess power.

In a first step it was tried to determine the critical flow rate at which bed-load starts to move. Using both uniform sands and sand mixtures (laboratory and field bed-load measurements) the critical discharge (q_{cr}), usually expressed by τ_{cr}, is given with the use of the Gauckler-Manning-Strickler formula such as:

$$q_{cr} = 0.26 \cdot (s-1)^{5/3} \cdot \frac{d^{3/2}}{S^{7/6}} \tag{A.132}$$

valid for $d \geq 6\ mm$. For non-uniform granulometric sediment mixtures d_{40} is taken as the equivalent diameter.

From the different empirical formulae proposed by Schoklitsch, the one developed in 1950 is presented:

$$q_{sb} = \frac{2.5}{s} \cdot S^{3/2} \cdot (q - q_{cr}) \tag{A.133}$$

Equation A.133 implicitly incorporates the critical shear stress concept and is valid for larger grain sizes ($d \geq 6\ mm$) being rather uniform and for bed slopes being moderate to strong (0.3 to 10 %).

A.6.4. Smart and Jäggi (1983)

Sediment transport tests have been performed in a tilting flume (6.0 m long and 0.2 m wide) at the VAW (Versuchsanstalt für Wasserbau, Hydrologie und Glaziologie) in Zurich, Switzerland, with a live bed with mean diameters ranging from 2.0 to 10.5 mm (Tab. A.12), slopes ranging from 3 to 20 % and discharges going from 0.005 m^3/s to 0.03 m^3/s. Material II and IV are comparatively uniform whereas material I and III represent mixtures.

Table A.12: Characteristic parameters of the bed materials used for the live bed laboratory tests of Smart and Jäggi (1983).

Material	Angle of repose ϕ_n [°]	Density ρ_s $[kg/m^3]$	d_m $[mm]$	d_{30} $[mm]$	d_{90} $[mm]$
I	35	2670	4.3	1.3	11.0
II	33	2670	4.2	3.6	5.2
III	33	2680	2.0	1.0	4.6
IV	32.5	2680	10.5	9.0	12.1

The formula according to Smart and Jäggi (1983) has been derived by a stepwise multiple regression technique relating the transport rate principally

to the water discharge (Q) and the slope (S). A correlation was not only found for the range of the new tests (Tab. A.12) but also for the test range of Meyer-Peter and Müller (1948).

Since no change in behavior was found between experiments on slopes less than 2 % (Meyer-Peter and Müller (1948)) and those with slopes in the range $3\ \% \leq S \leq 20\ \%$ (steep flume tests), it was postulated that one formula could apply to both situations. For this reason an attempt was first made to extend the Meyer-Peter and Müller (1948) formula to higher slopes. Subsequently, a more general approach was adopted to find a common law for both data sets. However, it was also considered that this attempt could conceivably yield a new equation.

A first improvement compared to the Meyer-Peter and Müller (1948) formula has been achieved by varying the value of θ_{cr} with the grain Reynolds number instead of keeping it constant at 0.047. Additionally, the use of the flow mixture depth (y_m) instead of the clear water depth (y) has increased the correlation. Using a product of the excess shear stress ($\theta - \theta_{cr}$) and a power function of θ resulted in a better fit to the experimental data than could be obtained with a power function of the excess shear stress only (as in the Meyer-Peter and Müller (1948) formula). Furthermore, additional correlation was obtained by introducing the total resistance to flow of the bed (in this case with $c = v/u_*$) and the slope. Attempts to improve the correlation by introducing a factor representing form roughness (such as k_{st}/k'_{st}) remained unsatisfactory. An equation which fitted the experimental data best was of the form:

$$\Phi = f\left(S^{0.6} \cdot c \cdot \theta^{0.5} \cdot (\theta - \theta_{cr})\right) \tag{A.134}$$

To account for the conditions at the beginning of motion of the bed material a correction had to be applied to one of the independent parameters. A critical slope (S_{cr}) was introduced which can be considered to represent that part of the flow energy required to detach particles from the bed. This slope was calculated from θ_{cr} as a function of flow depth. It proved to be more successful to apply this correction to the slope rather than to the flow depth.

For sediments of nearly uniform size the best fit was obtained with the equation of the form:

$$q_{sb} = \left(\frac{a}{(s-1)}\right) \cdot S^{\alpha_1} \cdot q^{\alpha_2} \cdot (S - S_{cr})^{\alpha_3} \tag{A.135}$$

A logarithmic regression showed that the values of the exponents α_2 and α_3 were very close to unity.

As a result of the analysis of the steep flume data and the original Meyer-Peter and Müller (1948) data the following bed-load transport formula was derived:

$$q_{sb} = \frac{4}{s-1} \cdot \left(\frac{d_{90}}{d_{30}}\right)^{0.2} \cdot S^{0.6} \cdot q_r \cdot (S - S_{cr}) \tag{A.136}$$

with q_r reduced discharge per unit width accounting for sidewall effects (Einstein (1942), Jäggi (1984b)):

$$q_r = \frac{Q}{B} \cdot \left[1 - \left(\frac{v}{k_{st,w} \cdot S^{1/2}}\right)^{3/2} \cdot \frac{U_w}{A}\right] \tag{A.137}$$

with U_w sidewall part of the total wetted perimeter (U).

Using the Einstein factor (Φ) the following dimensionless equation is obtained:

$$\Phi = 4 \cdot \left(\frac{d_{90}}{d_{30}}\right)^{0.2} \cdot S^{0.6} \cdot c \cdot \theta^{0.5} \cdot (\theta - \theta_{cr}) \tag{A.138}$$

For practical calculations the formula (Eq. A.136) may be written as:

$$q_{sb} = \frac{4}{s-1} \cdot \left(\frac{d_{90}}{d_{30}}\right)^{0.2} \cdot S^{1.6} \cdot q \cdot \left(1 - \frac{\theta_{cr} \cdot (s-1) \cdot d_m}{y_m \cdot S}\right). \tag{A.139}$$

The effect due to sediment gradation was able to be compensated for by a week power function of d_{90}/d_{30}. If this factor is neglected it should be replaced by 1.05. Considering $s = 2.68$ (natural sand or gravel) and $\theta_{cr} = 0.05$ (fully developed turbulence and moderate slopes), Equation A.139 can be written as:

$$q_{sb} = 2.5 \cdot q \cdot S^{0.6} \cdot \left(S - \frac{d_m}{12.1 \cdot y_m}\right) \tag{A.140}$$

In dimensionless form the simplified formula (Eq. A.140) can be expressed in the following way:

$$\Phi = 4.2 \cdot S^{0.1} \cdot Fr \cdot \theta^{0.5} \cdot (\theta - \theta_{cr}) \tag{A.141}$$

The correction parameter in the Meyer-Peter and Müller (1948) formula (Eq. A.130) corresponds to the Froude number in the Smart and Jäggi (1983) formula (Eq. A.141). For the same flow depth Fr represents a measure for the kinetic energy of the flow (Jäggi (1984b)). Accordingly, for the same bed shear stress the sediment transport also depends on the flow velocity.

The application range of the bed-load transport formula is given by the range of the experimental data used, meaning slopes varying between

0.2 % and 20 % and relative roughnesses $y_m/d_m < 100$ (Jäggi (1984b)). The slope of the present investigation (average initial bottom slope $S_0 = 0.21$ %) corresponds to the lower slope range, whereas the average y_m/d_m-values slightly exceed the limit ($y_m/d_m = 119$).

A.6.5. Van Rijn (1984)

Following the approach of Bagnold (1966) it is assumed that the motion of the bed-load particles is dominated by gravity forces while the effect of turbulence on the overall trajectory is supposed to be of minor importance. Furthermore, all particles with a jump height smaller than the maximum saltation height are assumed to be transported as bed-load by rolling and saltating along the bed surface. The bed-load transport (q_{sb}) is the product of the saltation height (δ_b), the particle velocity (u_p) and the bed-load concentration (c_b) resulting in:

$$q_{sb} = \delta_b \cdot u_p \cdot c_b \tag{A.142}$$

According to Van Rijn (1984a) the bed-load transport rate can be described with sufficient accuracy by only two of the four dimensionless parameters described in paragraph A.6.1, being the dimensionless particle number (D_*, Eq. A.123) and a transport stage parameter (T):

$$D_* = d_{50} \cdot \left[\frac{(s-1)\cdot g}{\nu^2}\right]^{1/3} \tag{A.143}$$

and

$$T = \frac{\left(u_*^{'}\right)^2 - \left(u_{*,cr}\right)^2}{\left(u_{*,cr}\right)^2} \tag{A.144}$$

in which $u_*^{'} = \left(\sqrt{g}/C^{'}\right) v$ bed shear velocity related to grains, $C^{'}$ Chézy-coefficient related to grains, v mean flow velocity and $u_{*,cr}$ critical bed shear velocity according to Shields (1936) as given analytically by Van Rijn (1984a) [6]:

$$\text{Shields curve} \begin{cases} & D_* \leq 4 & \theta_{cr} = 0.24 \cdot (D_*)^{-1} \\ 4 < & D_* \leq 10 & \theta_{cr} = 0.14 \cdot (D_*)^{-0.64} \\ 10 < & D_* \leq 20 & \theta_{cr} = 0.04 \cdot (D_*)^{-0.10} \\ 20 < & D_* \leq 150 & \theta_{cr} = 0.013 \cdot (D_*)^{0.29} \\ & D_* > 150 & \theta_{cr} = 0.055 \end{cases} \tag{A.145}$$

[6] Yu and Lim (2003) proposed a single equation within a ± 2 % error for Equation A.145.

Using different sets of hydraulic conditions ($d = 0.1 - 2\ mm$, $u_* = 0.02 - 0.14\ m/s$), the T- and D_*-parameters were computed and related to the saltation height resulting in the following simple expression:

$$\frac{\delta_b}{d} = 0.3 \cdot D_*^{0.7} \cdot T^{0.5} \tag{A.146}$$

Furthermore, the particle velocity (u_p) is given by

$$\frac{u_p}{\sqrt{(s-1) \cdot g \cdot d}} = 1.5 \cdot T^{0.6} \tag{A.147}$$

When bed forms are present the influence of form drag, which does not not contribute to bed-load transport, must be eliminated. For this reason an effective grain shear velocity must be defined. In a first step the average (effective) grain shear stress ($\tau_b^{'}$) at the upsloping part of the bed form is computed:

$$\tau_b^{'} = \rho \cdot g \cdot \frac{v^2}{(C')^2} \tag{A.148}$$

As the transport stage parameter (T) in Equation A.144 is given in terms of the grain shear velocity ($u_*^{'}$), Equation A.148 is transformed to

$$u_*^{'} = \frac{\sqrt{g} \cdot v}{(C')^2} \tag{A.149}$$

The Chézy-coefficient related to the surface (or grain) roughness of the sediment bed is defined as (Eq. A.23):

$$C' = 18 \cdot log\left(\frac{12 \cdot R_b}{3 \cdot d_{90}}\right) \tag{A.150}$$

in which R_b hydraulic radius related to the bed according to the sidewall correction method of Vanoni and Brooks (1957) (paragraph A.5).

With respect to the value of $3d_{90}$ in Equation A.150, in an earlier study, Van Rijn (1982) has analyzed about 100 flume and field movable bed experiments which were explicitly indicated as "plane bed" experiments resulting in k_s-values in the range of 1 to $10D_*$ with a mean value of about $3D_*$. It is pointed out that these values, which are rather large, show that a completely plane bed does not exist for conditions with active sediment transport. Probably, the effective roughness is caused by very small irregularities ("bed forms") of the movable bed. Yen (2002) stated that for a sediment plane bed some energy and momentum are spent on picking up, transporting and depositing the bed sediment, thus underlining the observation of rather large k_s-values. Finally, the roughness height of a movable "plane" bed surface is supposed to be about $3d_{90}$.

Using measured bed-load transport rates (q_{sb}), the bed-load concentration (c_b) was determined using Equation A.142 as:

$$c_b = \frac{q_{sb}}{u_p \cdot \delta_b} \tag{A.151}$$

Taking into account 130 flume experiments with particle diameters ranging from 0.2 to 2.0 mm, flow depths greater than 0.1 m and Froude numbers not larger than 0.9, the bed-load concentration can be represented by

$$\frac{c_b}{c^*} = 0.18 \cdot \frac{T}{D_*} \tag{A.152}$$

with c^* maximum (bed) concentration = 0.65.

Using Equations A.146, A.147 and A.151 the bed-load transport (in m^2/s) for particles in the range of 0.2 to 2.0 mm can be computed as (Van Rijn (1984a)):

$$q_{sb} = 0.053 \cdot \frac{T^{2.1}}{D_*^{0.3}} \cdot \left(\sqrt{(s-1) \cdot g} \cdot d_{50}^{3/2}\right) \tag{A.153}$$

For the verification of Equation A.153, 580 flume and field data regarding bed-load transport only have been used.

The computation procedure of the bed-load transport is as follows:

- Compute particle parameter (D_*) using Equation A.143,
- compute critical bed shear velocity ($u_{*,cr}$) according to Shields (Eq. A.145),
- compute Chézy-coefficient related to grains (C') using Equation A.150,
- compute effective bed shear velocity (u'_*) (with a maximum value equal to u_*) using Equation A.149,
- compute transport stage parameter (T) using Equation A.144,
- compute bed-load transport (q_{sb}) using Equation A.153.

Finally, it has been stressed by Van Rijn (1984a) that an investigation of flume experiments performed under similar flow conditions by various researchers showed deviations up to a factor 2. Thus, even under controlled flume conditions, it is hardly possible to predict the transport rate with an inaccuracy less than a factor 2.

Table A.13: Synopsis of bed-load transport equations taken into account in the present study.

Investigator	Bed-load transport equation	Eq. in study
MPM (1948)	$q_{sb} = \Big[\Big(\rho \cdot g \cdot (Q_r/Q) \cdot (k_{st}/k'_{st})^{3/2} \cdot y \cdot S - 0.047 \cdot \rho \cdot (s-1) \cdot g \cdot d_m\Big) / \left(0.25 \cdot \rho \cdot (s-1)^{2/3} \cdot g^{2/3}\right)\Big]^{3/2}$	Eq. A.129
Schoklitsch (1950)	$q_{sb} = \frac{2.5}{s} \cdot S^{3/2} \cdot (q - q_{cr})$	Eq. A.133
Smart & Jäggi (1983)	$q_{sb} = \frac{4}{s-1} \cdot (d_{90}/d_{30})^{0.2} \cdot S^{0.6} \cdot q_r \cdot (S - S_{cr})$	Eq. A.136
Van Rijn (1984a)	$q_{sb} = 0.053 \cdot T^{2.1}/D_*^{0.3} \cdot \left(\sqrt{(s-1) \cdot g} \cdot d_{50}^{3/2}\right)$	Eq. A.153

A.6.6. Synopsis of Bed-load Transport Equations

In Table A.13 the bed-load transport approaches taken into account in the present study are summarized.

A.7. Side Weirs and Spatially Varied Flow

In this paragraph an introduction of spatially varied flow with decreasing discharge in the subcritical flow regime is given. For this purpose the dynamic equation for spatially varied flow with decreasing discharge is introduced and the general equation of weirs is derived. Since the side weir discharge coefficient represents an important parameter, several approaches from literature are briefly presented.

A.7.1. Types of Flow over a Side Weir

The flow over a side weir is a typical case of spatially varied flow with decreasing discharge. Side weirs can be used in a channel with sub- or supercritical flow. Each type of flow has its own hydraulic behavior. However, subcritical flow is more practical in engineering projects and is the focus of this study. The behavior of subcritical flow in a channel at a side weir region can be of three types, depending on the approach and downstream depth. Although in subcritical flow the normal depth is always greater than the critical depth,

due to the outflow discharge at the side weir section, the depth just upstream of the weir is less than the normal depth. When the flow depth at or near the weir is greater then the critical depth, the water level in the channel rises in the downstream direction with subcritical flow, while the discharge decreases (Fig. A.14, a). On the other hand, if there is a discontinuity in the flow, due to the downstream depth being greater than the critical one, a transition from subcritical to supercritical flow followed by a hydraulic jump is expected (Fig. A.14, b). Finally, if at or near the weir the depth in the channel is close to the critical depth, than a supercritical condition occurs and the flow depth decreases to the end of the weir (Fig. A.14, c). The case presented in (Fig. A.14, a) is a typical design and Figures b and c are not a designers preference (Borghei et al. (1999)).

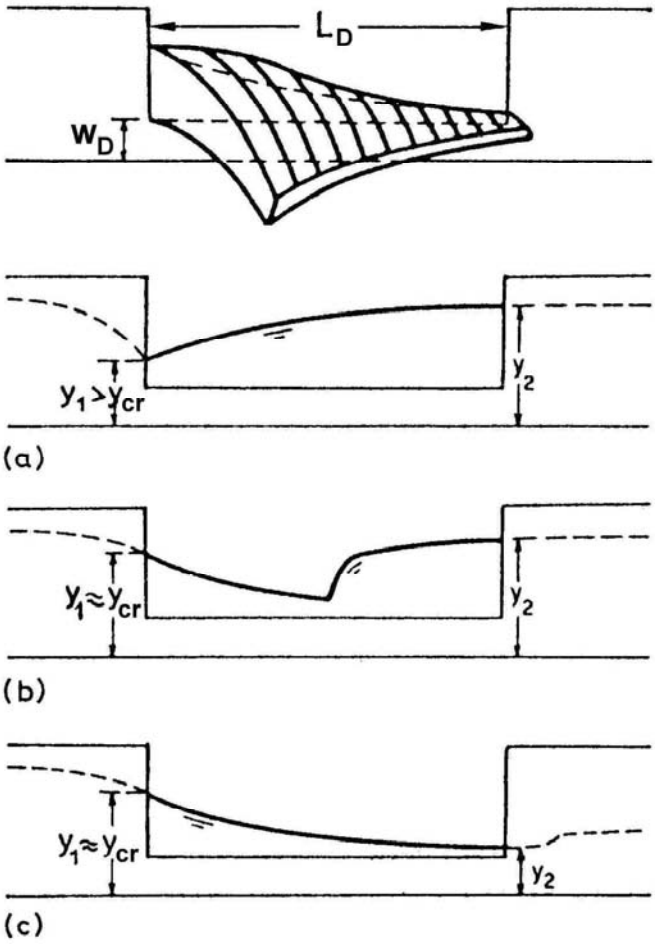

Figure A.14: Water profile in channel at side weir: a) subcritical flow, b) hydraulic jump and c) supercritical flow (from Naudascher (1992)).

A.7.2. Side Weir Equation

As mentioned in paragraph 2.3 in the present study only flow with decreasing discharge in the subcritical flow regime is of interest. This type of spatially varied flow may be treated as a flow diversion where the diverted water does not affect the energy head. Therefore, the use of the energy equation will be found more convenient than the use of the momentum principle in solving this problem (Chow (1973)).

For the analysis of this type of spatially varied flow the energy principle is directly applicable. The total energy H at a channel section is (Fig. A.15, a):

$$H = z + y + \frac{\alpha \cdot Q^2}{2 \cdot g \cdot A^2} = h + \frac{\alpha \cdot Q^2}{2 \cdot g \cdot A^2} \tag{A.154}$$

with z distance of the bottom of the channel section above a horizontal datum, y water depth in main-channel, α kinetic energy correction coefficient, Q discharge, g acceleration due to gravity and A flow area. The term $z + y$ is the pressure head h without velocity head ($h = z + y$) (Fig. A.16).

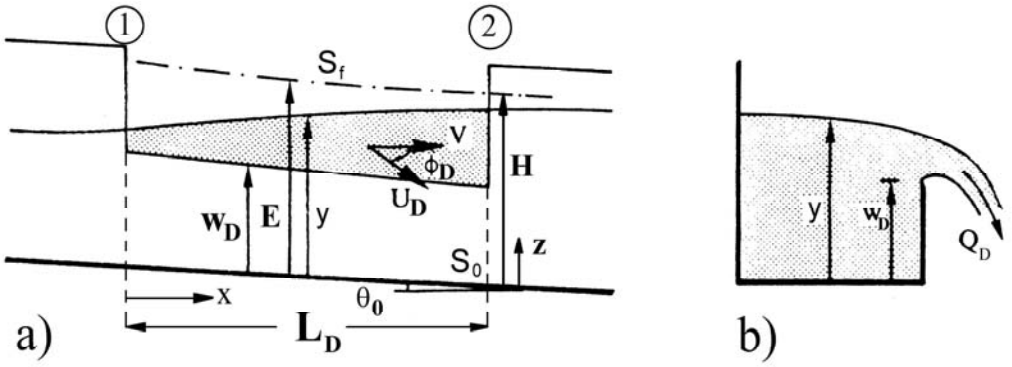

Figure A.15: Definition sketch of geometrical and hydraulic side weir parameters: a) longitudinal section, b) cross section (from Sinniger and Hager (1989), modified).

Differentiating this equation with respect to x (longitudinal direction) yields:

$$\frac{dH}{dx} = \frac{dz}{dx} + \frac{dy}{dx} + \frac{\alpha}{2 \cdot g} \cdot \left(\frac{2Q\ dQ}{A^2\ dx} - \frac{2Q^2\ dA}{A^3\ dx} \right) \tag{A.155}$$

Noting that $dH/dx = -S_f$ (energy slope (S_e) or friction slope (S_f), respectively), $dz/dx = -S_0$ (channel bottom slope) and:

$$\frac{dA}{dx} = \left(\frac{dA}{dy} \right) \cdot \left(\frac{dy}{dx} \right) = \frac{B\ dy}{dx} \tag{A.156}$$

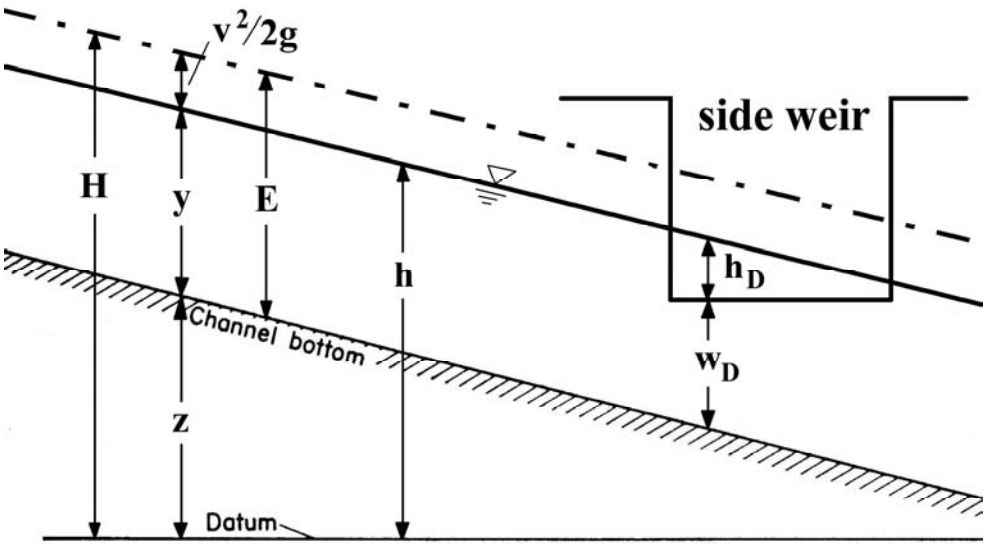

Figure A.16: Definition sketch of total energy head (H), specific energy head (E), pressure head (h) and side weir head (h_D).

with B constant channel width, the above equation may be reduced to:

$$\frac{dy}{dx} = \frac{S_0 - S_f - \left(\frac{\alpha \cdot Q}{g \cdot A^2}\right) \cdot \left(\frac{dQ}{dx}\right)}{1 - \left(\frac{\alpha \cdot Q^2 \cdot B}{g \cdot A^3}\right)} \tag{A.157}$$

which is the dynamic equation for spatially varied flow with decreasing discharge. It should be noted that the momentum principle can also be used for the derivation of Equation A.157.

Assuming that $S_0 - S_f = 0$ (i. e. constant specific energy $E = y + Q^2/(2gA^2)$ across the weir) and $\alpha = 1$ (constant and uniform velocity distribution across the channel), the general equation of weirs can be written as follows:

$$q_D = -\left(\frac{dQ}{dx}\right) = \left(\frac{dQ_D}{dx}\right) = \frac{2}{3} \cdot C_D \cdot \sqrt{2 \cdot g} \cdot (y - w_D)^{3/2} \tag{A.158}$$

where q_D discharge per unit length over the weir, Q_D weir outflow discharge, C_D discharge coefficient and w_D weir height. The term $y - w_D = h_D$ represents the pressure head (without velocity head) above the side weir crest and the term $[2g\ (y - w_D)]^{1/2} = (2g\ h_D)^{1/2}$ is the approach overflow velocity (Del Giudice and Hager (1999)). Multiplying Equation. A.158 with the side weir crest length (L_D) the lateral outflow discharge Q_D is obtained.

Because the specific energy (E) was assumed to be constant along the side weir the discharge in the channel at any section is given by:

$$Q = B \cdot y \cdot \sqrt{2g \cdot (E - y)} \tag{A.159}$$

Substituting Equation A.158 and Equation A.159 in Equation A.157, integrating the resultant equation and arranging for C_D, De Marchi (1934) has introduced the coefficient of discharge as follows (Chow (1973)):

$$C_D = C_M = \frac{3 \cdot B}{2 \cdot L_D} \cdot \phi + const. \tag{A.160}$$

in which ϕ varied flow function which was first solved by De Marchi (1934). Honoring De Marchi, C_D is also referred to as C_M. The varied flow function is given by:

$$\phi_i = \frac{2E_i - 3w_D}{E_i - w_D} \cdot \sqrt{\frac{E_i - y_i}{y_i - w_D}} - 3 \cdot arcsin\sqrt{\frac{E_i - y_i}{E_i - w_D}} \tag{A.161}$$

with $i = 1$ (section 1) and 2 (section 2), respectively (Fig. A.15). The argument of $arcsin$ has to be entered in RAD. Designating the beginning and end of a side weir of length L_D (Fig. A.15, a) by suffixes 1 and 2, respectively, the discharge coefficient can be expressed as:

$$C_D = \frac{3 \cdot B}{2 \cdot L_D} \cdot (\phi_2 - \phi_1) \tag{A.162}$$

Knowing conditions at section 1 (i. e. Q_1 and y_1), ϕ_2 and thus Q_2 can be found, provided C_D is known. The total discharge over the side weir will be:

$$Q_D = Q_1 - Q_2 \tag{A.163}$$

Using dimensional analysis, C_D can be formulated as:

$$C_D = f\left(Fr_1, \frac{w_D}{y_1}, \frac{y_1}{L_D}, \frac{L_D}{B}, \frac{E_1}{L_D}, S_0, ...\right) \tag{A.164}$$

where Fr_1 approach Froude number in the main-channel at section 1 (Fig. A.15, a). The variation of parameters appearing in Equation A.164 can be measured or determined experimentally.

Several expressions relating C_D to the parameters in Equation A.164 have been developed (Borghei et al. (1999)). Some of the proposed formulas are presented in the following paragraph.

A.7.3. Discharge Coefficient of a Side Weir

A side weir is designed to divert a certain discharge, hence, the knowledge of an accurate discharge coefficient is important. A basic assumption for several side weir discharge formulae or side weir discharge coefficients, respectively, (e. g. Subramanya and Awasthy (1972), Borghei et al. (1999), Muslu (2001)) is based on the fact that the main design objective is to estimate the total overflow discharge and the depth is of secondary importance (Borghei et al. (1999)).

Usually, the weir is relatively short compared to the channel length. Therefore, water level changes are too small and depth depth is not a decisive design criteria. Due to this reason, approach parameters such as the Froude number or water depth are usually calculated with normal flow conditions which are considered being similar to flow conditions at section 1 (Fig. A.15, a). Subramanya and Awasthy (1972) stated that the flow depth at section 1 was essentially the same as the one at a section small distance upstream of section 1 ($\approx$ 5 % difference). Furthermore, most of the C_D-relations are based on flow depth measurements in the channel centerline and not in the weir plane, since the draw-down effect of the side weir is assumed to be negligible (e. g. Ranga Raju et al. (1979)).

From the numerous available discharge coefficient formulas reported in literature several refer to non-rectangular main-channel geometry, e. g. Cheong (1991) and Das (1997) (trapezoidal), Uyumaz and Muslu (1985) (circular), Uyumaz (1997) (u-shaped) and Uyumaz (1992) (triangular), non-rectangular side weir geometry, e. g. Kumar and Pathak (1987) (triangular), or broad crested weirs. Since both, the channel and side weir geometry of the present study have been rectangular and the side weir has been sharp crested, only the ones enumerated below are considered:

- Frazer (1957),
- Subramanya and Awasthy (1972),
- Ranga Raju et al. (1979),
- Hager (1987b),
- Singh et al. (1994),
- Borghei et al. (1999) and
- Swamee et al. (1994a).

In the following the approaches mentioned above are briefly described and the proposed relations for the side weir discharge coefficient are presented. In

Table A.14 the discharge coefficient equations are summarized. More detailed information with respect to the basic experimental boundary conditions is given in Tables 2.1, 2.2, 2.3 and 2.4 and in paragraph 2.3.

- Frazer (1957):

  The experiments by Frazer (1957) on lateral outflow over a side weir in a rectangular channel indicated a C_D-value of:

$$C_D = 0.55 - 0.115 \cdot Fr_1^2 - \frac{0.017 \cdot E_1}{L_D} \tag{A.165}$$

- Subramanya and Awasthy (1972):

  Assuming little or no effects of the geometrical configuration of the flow (L_D/B, y_1/L_D, w_D/y_1), the discharge coefficient for a lateral opening for zero ($w_D = 0.00\ m$) or finite height in a rectangular main-channel has been determined by:

$$C_D = 0.611 \cdot \sqrt{1 - \frac{3 \cdot Fr_1^2}{2 + Fr_1^2}} \tag{A.166}$$

- Ranga Raju et al. (1979):

  The discharge coefficient for a sharp-crested side weir diverting part of the main flow into a branch channel from a rectangular main-channel has been given by Ranga Raju et al. (1979) as:

$$C_D = 0.81 - 0.60 \cdot Fr_1 \tag{A.167}$$

  The difference with respect to Frazer (1957) might be ascribed to the empirical correction factor applied to compute the effective weir length and to the presence of side walls of the branch channel in the experiments (Fig. 5.6, b).

- Hager (1987b):

  Investigating the lateral outflow mechanism of side weirs using a one-dimensional approach, the discharge coefficient relation for a sharp-crested side weir of zero height ($w_D = 0.00\ m$) located in a rectangular main-channel is assumed to be:

$$C_D = 0.485 \cdot \sqrt{\frac{2 + Fr_1^2}{2 + 3 \cdot Fr_1^2}} \tag{A.168}$$

  It has to noted that the term 2/3 in Equation A.158 is already incorporated in Equation A.168.

- Singh et al. (1994):

  Since the sill height determines the ratio of the surface flow to the bed flow that is deflected through the weir, the ratio of sill height to upstream flow depth (w_D/y_1) is added to the upstream Froude number (Fr_1) in the determination of the side weir discharge coefficient:

$$C_D = 0.33 - 0.18 \cdot Fr_1 + 0.49 \cdot \frac{w_D}{y_1} \tag{A.169}$$

- Borghei et al. (1999):

  In addition to the upstream Froude number (Fr_1) and w_D/y_1, the ratio of side weir crest length to channel width is incorporated in the relation for the side weir discharge coefficient. The channel slope appears to be negligible. The equation reads:

$$C_D = 0.7 - 0.48 \cdot Fr_1 - 0.3 \cdot \frac{w_D}{y_1} + 0.06 \cdot \frac{L_D}{B} \tag{A.170}$$

- Swamee et al. (1994a):

  The dominant variable is supposed to be the ratio of side weir head to weir height ($(y-w_D)/w_D$). Except Singh et al. (1994), this parameter has not been considered in the previous investigations. Due to this reason, a concept of an elementary discharge coefficient for the discharge of an elementary rectangular strip along the weir crest is proposed:

$$C_D = 0.447 \cdot \left[\left(\frac{44.7 \cdot w_D}{49 \cdot w_D + y} \right)^{6.67} + \left(\frac{y - w_D}{y} \right)^{6.67} \right]^{-0.15} \tag{A.171}$$

  Thus, the input variables do not only refer to section 1 but vary along the spill crest. Therefore, the calculation of the side overflow discharge using Equation A.158 requires an integration along the weir crest.

Table A.14: Synopsis of formulas for the determination of the discharge coefficient of a side weir used for comparison in the present study.

Investigator	Relation for side weir discharge coefficient	Eq. in study
Frazer (1957)	$C_D = 0.55 - 0.115 \cdot Fr_1^2 - \frac{0.017 \cdot E_1}{L_D}$	Eq. A.165
Subramanya and Awasthy (1972)	$C_D = 0.611 \cdot \sqrt{1 - \frac{3 \cdot Fr_1^2}{2 + Fr_1^2}}$	Eq. A.166
Ranga Raju et al. (1979)*	$C_D = 0.81 - 0.60 \cdot Fr_1$	Eq. A.167
Hager (1987b)	$C_D = 0.485 \cdot \sqrt{\frac{2 + Fr_1^2}{2 + 3 \cdot Fr_1^2}}$	Eq. A.168
Singh et al. (1994)*	$C_D = 0.33 - 0.18 \cdot Fr_1 + 0.49 \cdot \frac{w_D}{y_1}$	Eq. A.169
Borghei et al. (1999)	$C_D = 0.7 - 0.48 \cdot Fr_1 - 0.3 \cdot \frac{w_D}{y_1} + 0.06 \cdot \frac{L_D}{B}$	Eq. A.170
Swamee et al. (1994a)	$C_D = 0.447 \cdot \left[\left(\frac{44.7 \cdot w_D}{49 \cdot w_D + y} \right)^{6.67} + \left(\frac{y - w_D}{y} \right)^{6.67} \right]^{-0.15}$	Eq. A.171

*)restricted outflow (branch channel, sidewalls)

B. Experimental Data and Documentation

B.1. Test Series A (without side weir)

Table B.1: Channel geometry, sediment supply and experiment duration for test series A.

N^o of exp.	Channel width B $[m]$	Bottom slope $S_{0,ini}$ [%]	Weir crest length L_D $[m]$	Weir height $w_{D,ini}$ $[m]$	N^o of weirs n_D $[-]$	Sediment supply $Q_{sb,in}$ $[kg/min]$	Exp. duration t $[min]$
$A01$	1.50	0.20	$***$	$***$	$***$	15.25	120

Table B.2: Flow parameters for test series A.

N^o of exp.	Upstream discharge Q_1 $[l/s]$	Overflow discharge $Q_{D,fin}$ $[l/s]$	Flow depth $y_{1,fin}$ $[m]$	Flow velocity $v_{1,fin}$ $[m/s]$	Froude number $Fr_{1,fin}$ $[-]$	Pressure head $h_{D,1,fin}$ $[m]$
$A01$	153	$***$	0.150	0.679	0.560	$***$

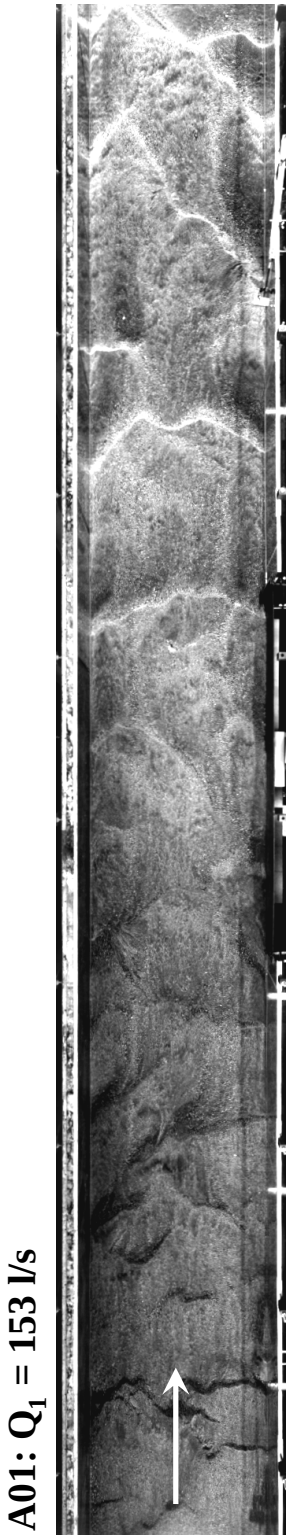

Figure B.1: Final bed morphology for experiment $A01$.

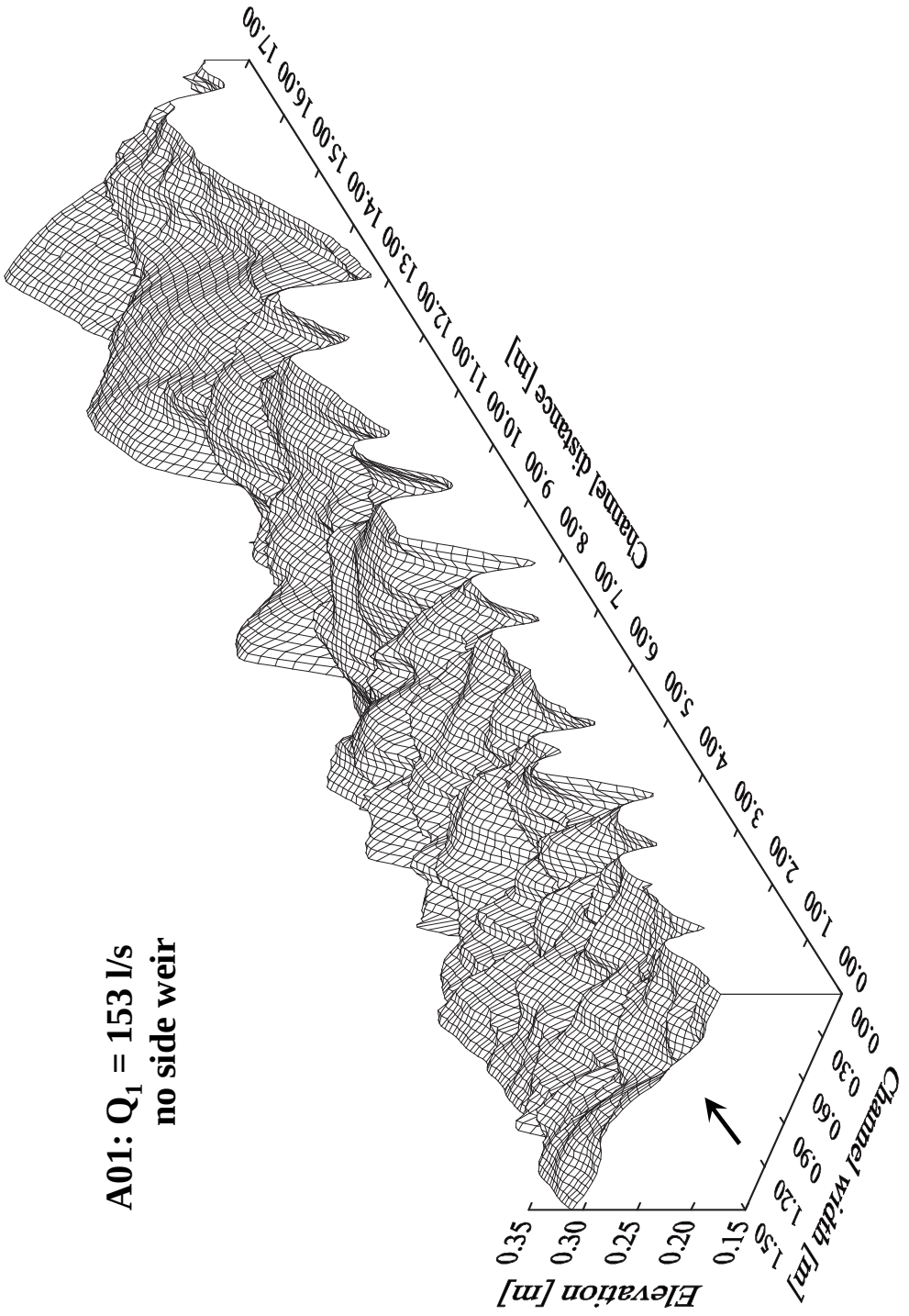

Figure B.2: 3*D*-view of the final bed morphology for experiment *A*01.
Note: The left and right channel bank are inverted!

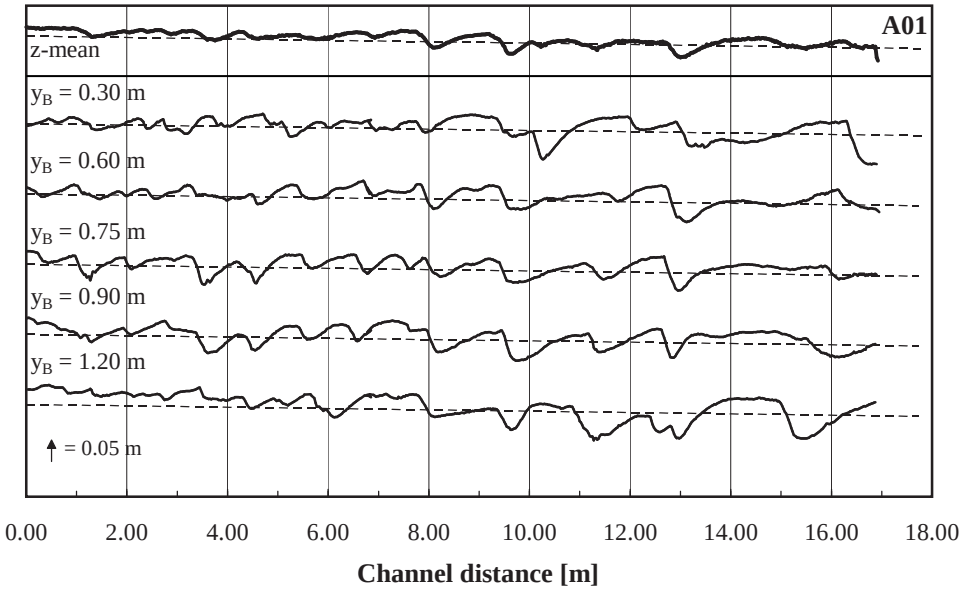

Figure B.3: Longitudinal final bed surface profiles at different spanwise positions (y_B) for experiment $A01$. The tiny dashed lines represent the initial bed surface.

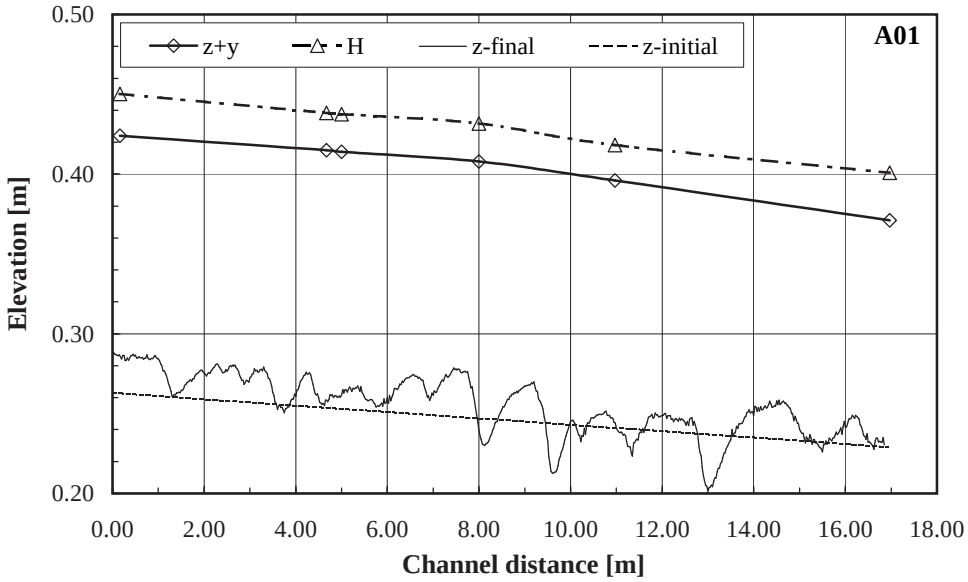

Figure B.4: Streamwise cross sectional averaged final bed surface profile (z_{final}), water level elevation ($z + y$) and total energy head (H) for experiment $A01$.

B.2. Test Series B (weir length $L_D = 3.00\ m$)

Table B.3: Channel geometry, weir geometry, sediment supply and experiment duration for test series B.

N^o of exp.	Channel width B $[m]$	Bottom slope $S_{0,ini}$ [%]	Weir crest length L_D $[m]$	Weir height $w_{D,ini}$ $[m]$	N^o of weirs n_D $[-]$	Sediment supply $Q_{sb,in}$ $[kg/min]$	Exp. duration t $[min]$
$B01$	1.50	0.20	3.00	0.10	1	8.70	188
$B02$	1.50	0.20	3.00	0.10	1	17.73	183
$B03$	1.50	0.40	3.00	0.10	1	9.10	117
$B04$	1.50	0.10	3.00	0.10	1	9.67	245
$B05$	1.50	0.20	3.00	0.10	1	16.72	128
$B06$	1.50	0.30	3.00	0.10	1	17.61	138

Table B.4: Flow parameters for test series B.

N^o of exp.	Upstream discharge Q_1 $[l/s]$	Overflow discharge $Q_{D,fin}$ $[l/s]$	Flow depth $y_{1,fin}$ $[m]$	Flow velocity $v_{1,fin}$ $[m/s]$	Froude number $Fr_{1,fin}$ $[-]$	Pressure head $h_{D,1,fin}$ $[m]$
$B01$	131	22	0.130	0.673	0.597	0.026
$B02$	181	52	0.137	0.883	0.763	0.049
$B03$	177	41	0.146	0.806	0.672	0.039
$B04$	98	4	0.092	0.714	0.753	0.013
$B05$	144	37	0.118	0.812	0.754	0.035
$B06$	148	44	0.136	0.723	0.625	0.038

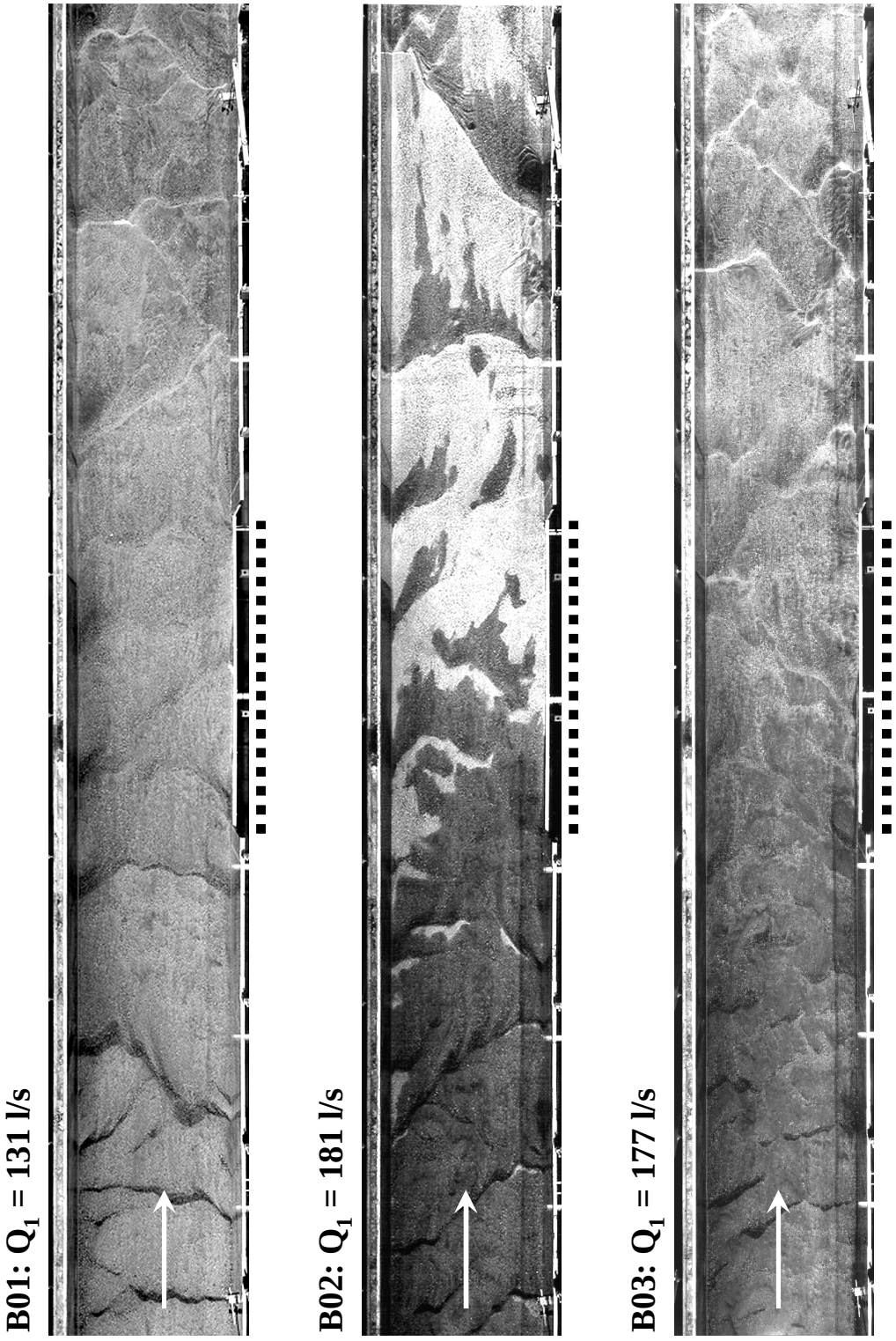

Figure B.5: Final bed morphology for experiments $B01$, $B02$ and $B03$.

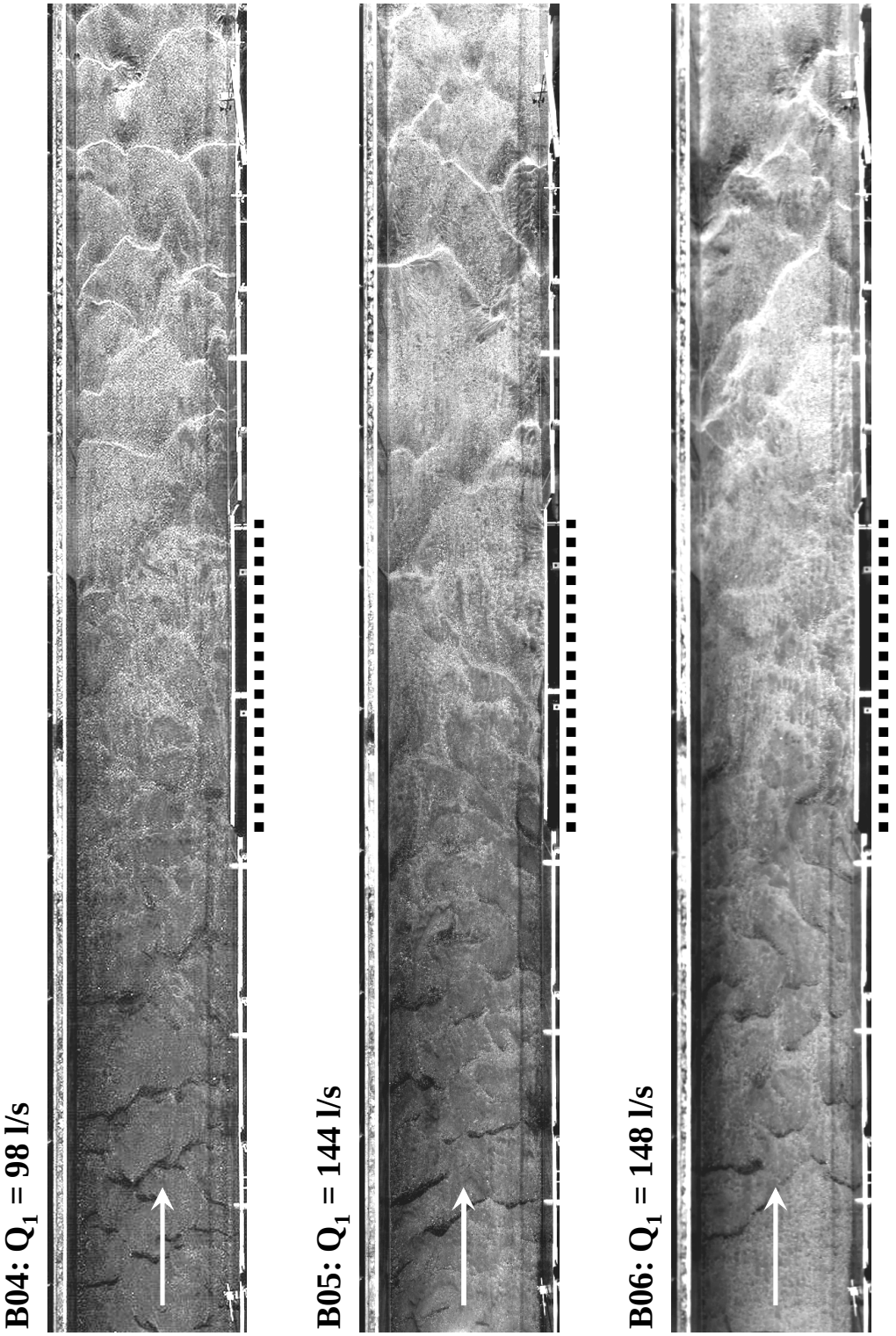

Figure B.6: Final bed morphology for experiments $B04$, $B05$ and $B06$.

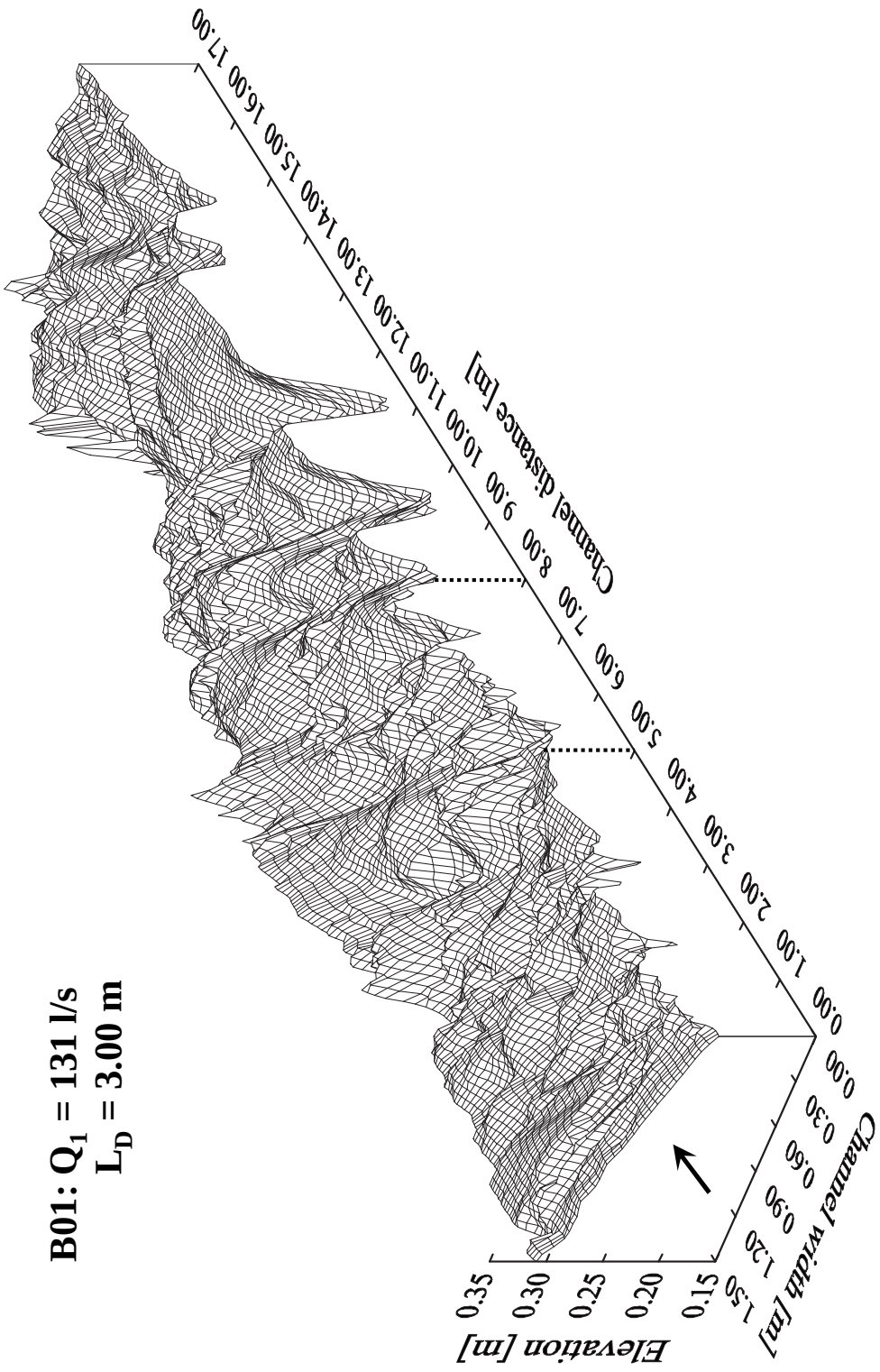

Figure B.7: 3*D*-view of the final bed morphology for experiment *B*01. The dotted line indicates the side weir location. Note: For better visibility of the deposit the left and right channel bank are inverted!

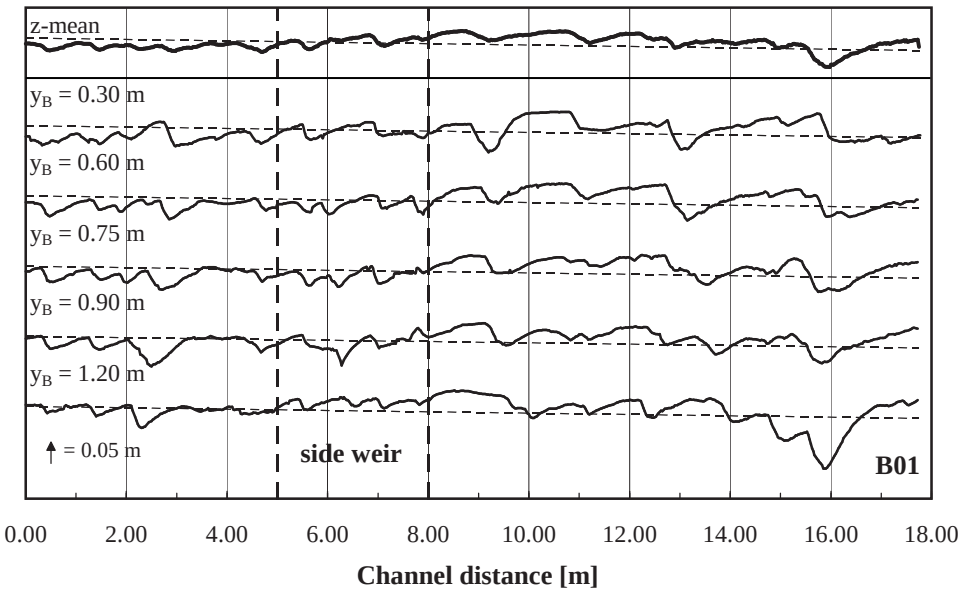

Figure B.8: Longitudinal final bed surface profiles at different spanwise positions (y_B) for experiment $B01$. The tiny dashed lines represent the initial bed surface. The side weir is located on the right channel bank at $y_B = 1.50\ m$.

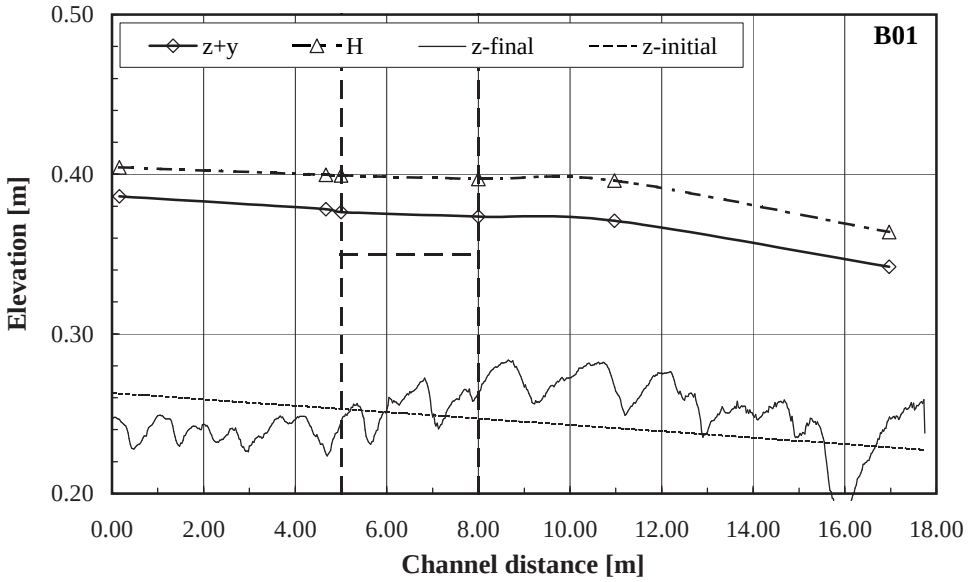

Figure B.9: Streamwise cross sectional averaged final bed surface profile (z_{final}), water level elevation ($z + y$) and total energy head (H) for experiment $B01$.

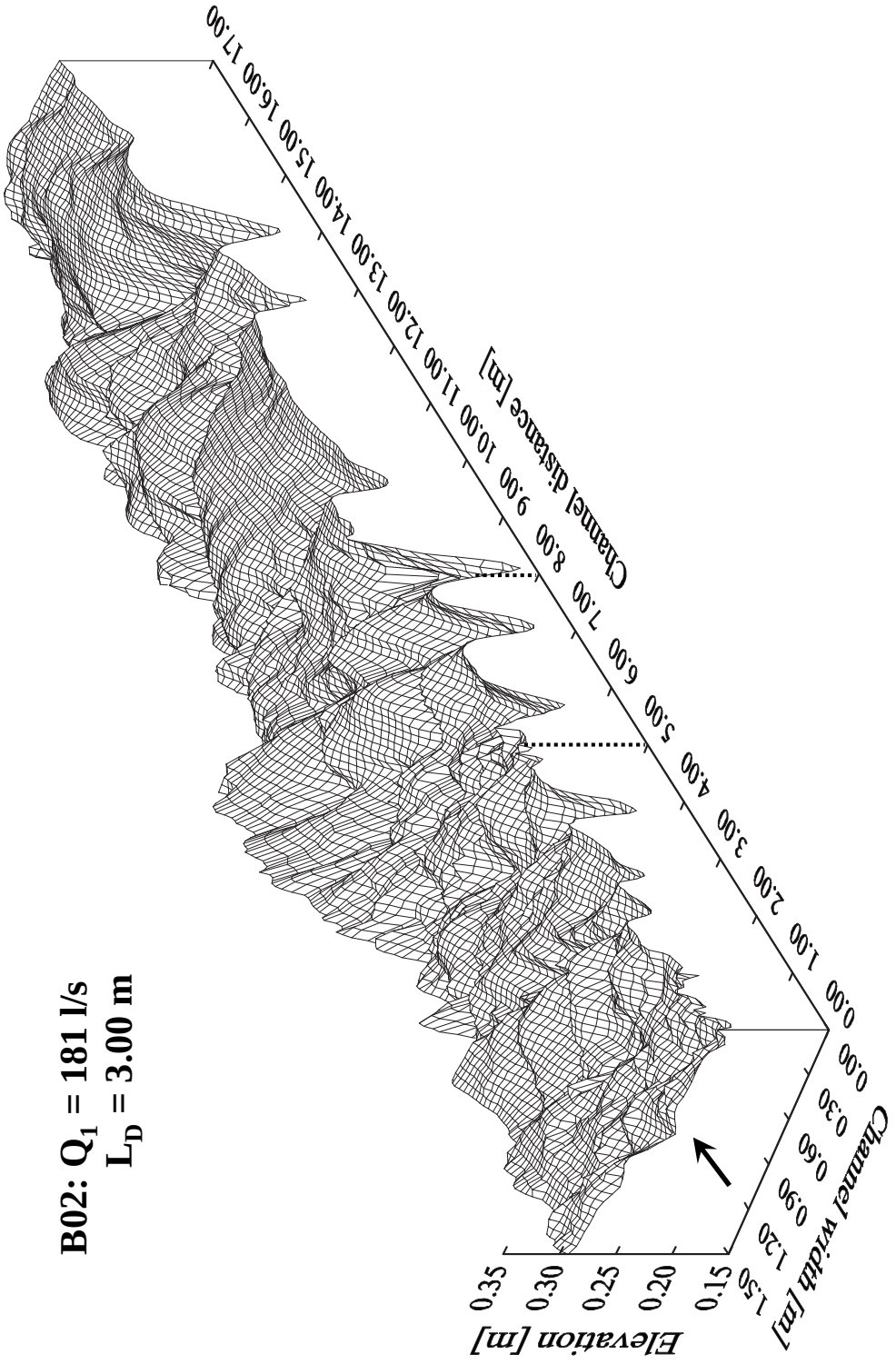

Figure B.10: 3*D*-view of the final bed morphology for experiment *B*02. The dotted line indicates the side weir location. Note: For better visibility of the deposit the left and right channel bank are inverted!

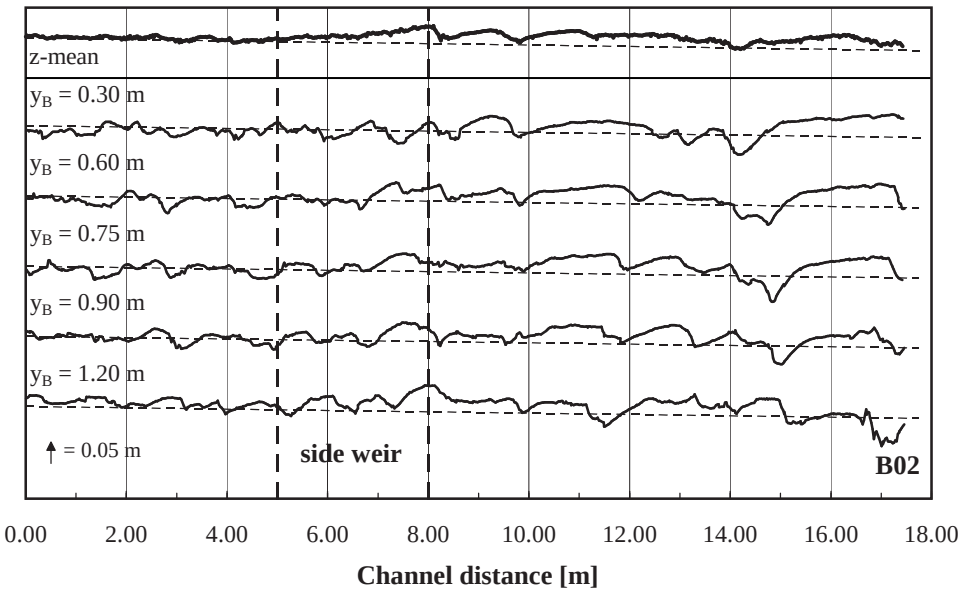

Figure B.11: Longitudinal final bed surface profiles at different spanwise positions (y_B) for experiment $B02$. The tiny dashed lines represent the initial bed surface. The side weir is located on the right channel bank at $y_B = 1.50\ m$.

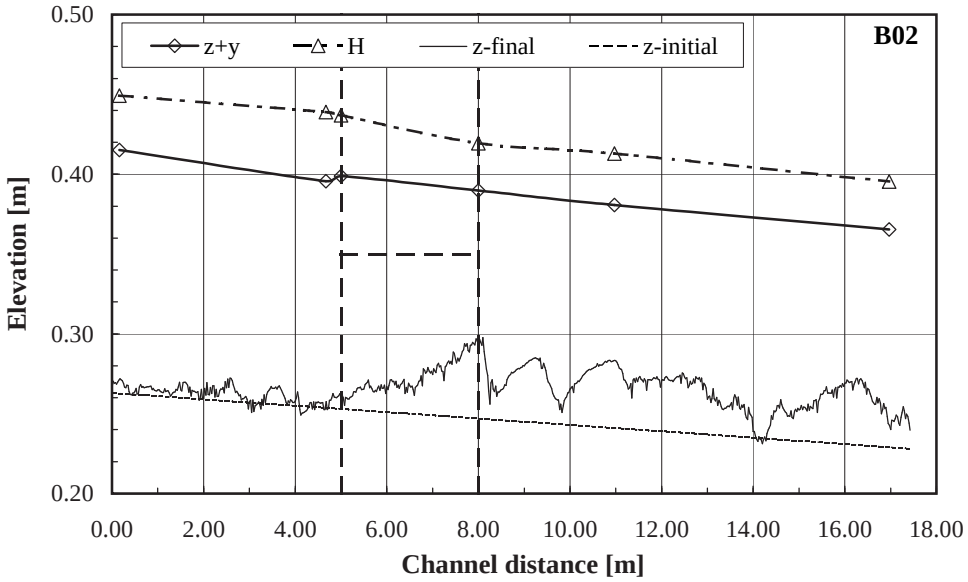

Figure B.12: Streamwise cross sectional averaged final bed surface profile (z_{final}), water level elevation ($z + y$) and total energy head (H) for experiment $B02$.

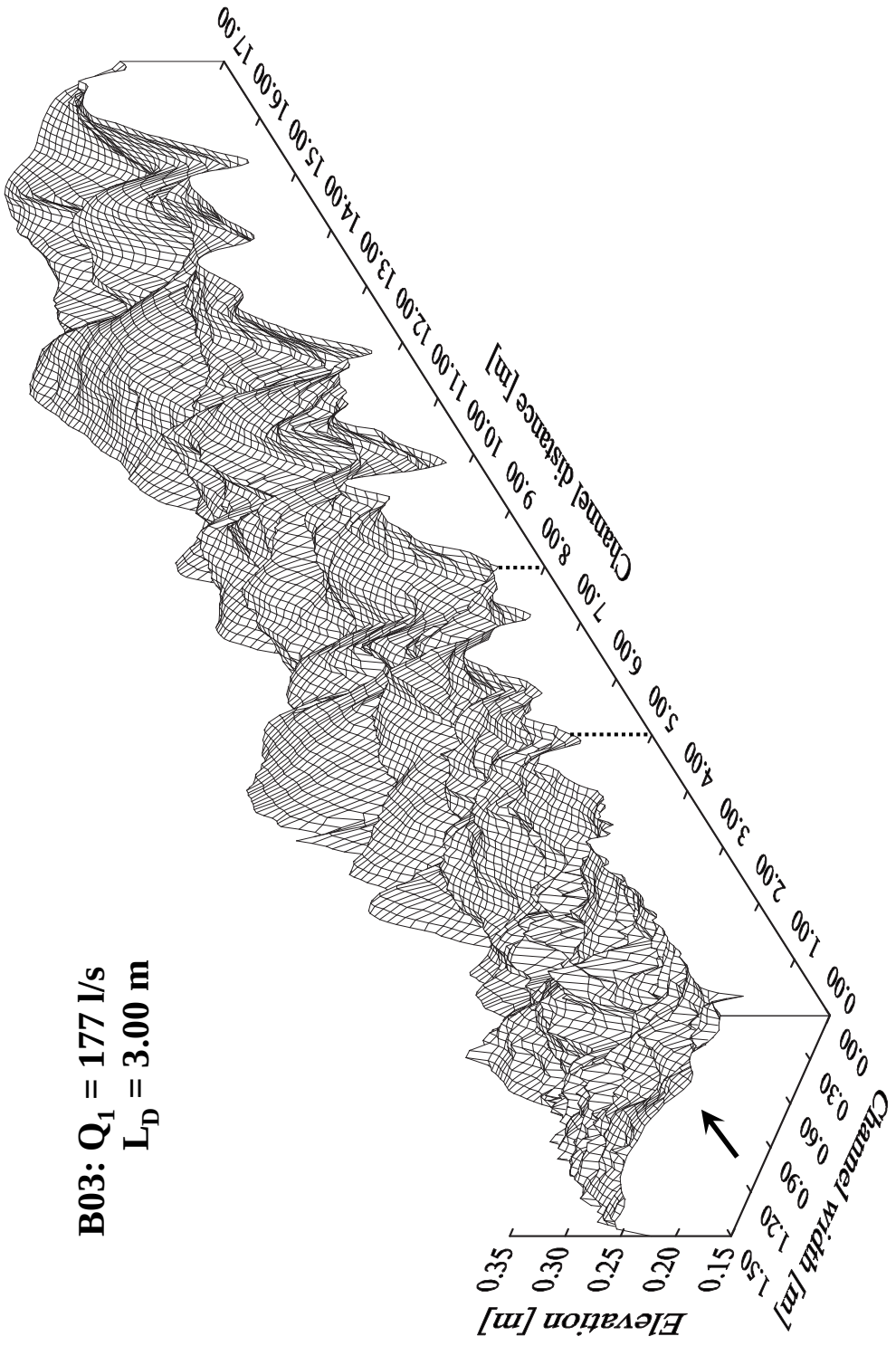

Figure B.13: 3*D*-view of the final bed morphology for experiment *B*03. The dotted line indicates the side weir location. Note: For better visibility of the deposit the left and right channel bank are inverted!

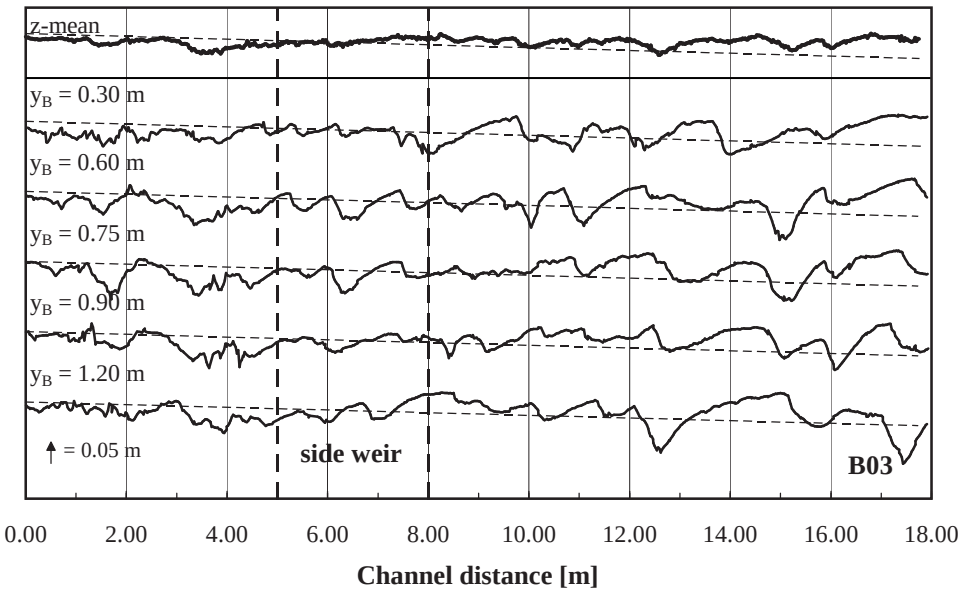

Figure B.14: Longitudinal final bed surface profiles at different spanwise positions (y_B) for experiment $B03$. The tiny dashed lines represent the initial bed surface. The side weir is located on the right channel bank at $y_B = 1.50\ m$.

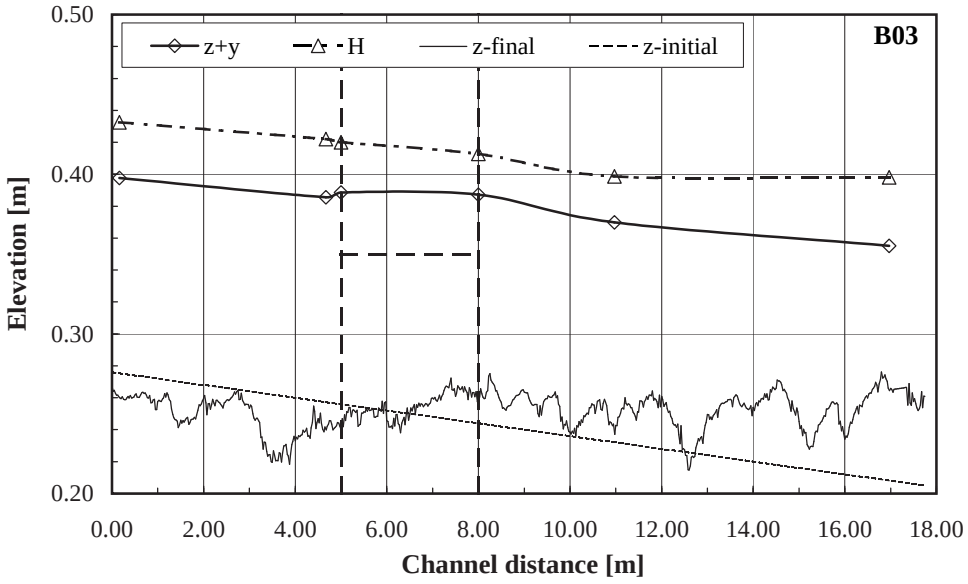

Figure B.15: Streamwise cross sectional averaged final bed surface profile (z_{final}), water level elevation ($z + y$) and total energy head (H) for experiment $B03$.

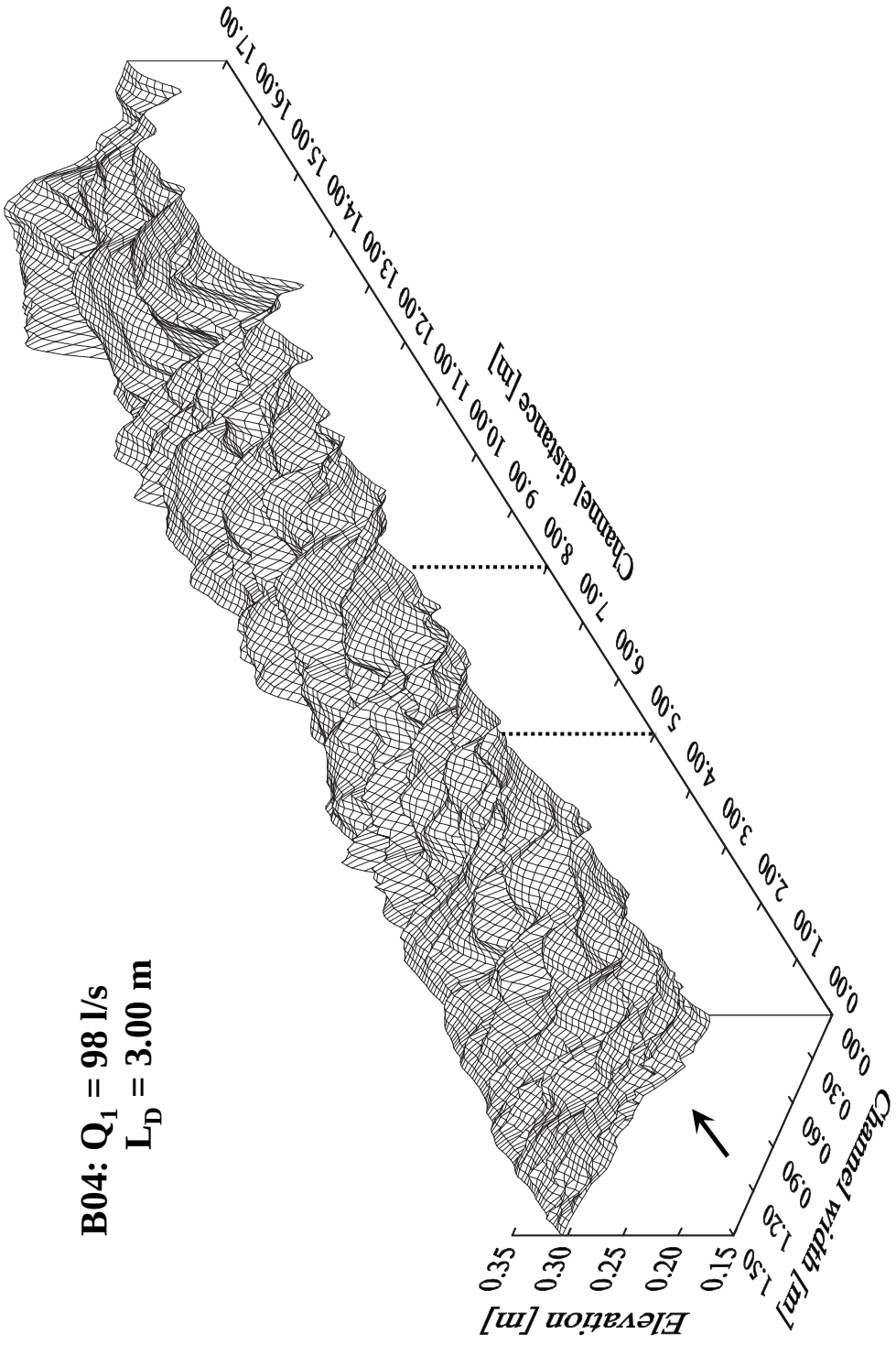

Figure B.16: 3*D*-view of the final bed morphology for experiment *B*04. The dotted line indicates the side weir location. Note: For better visibility of the deposit the left and right channel bank are inverted!

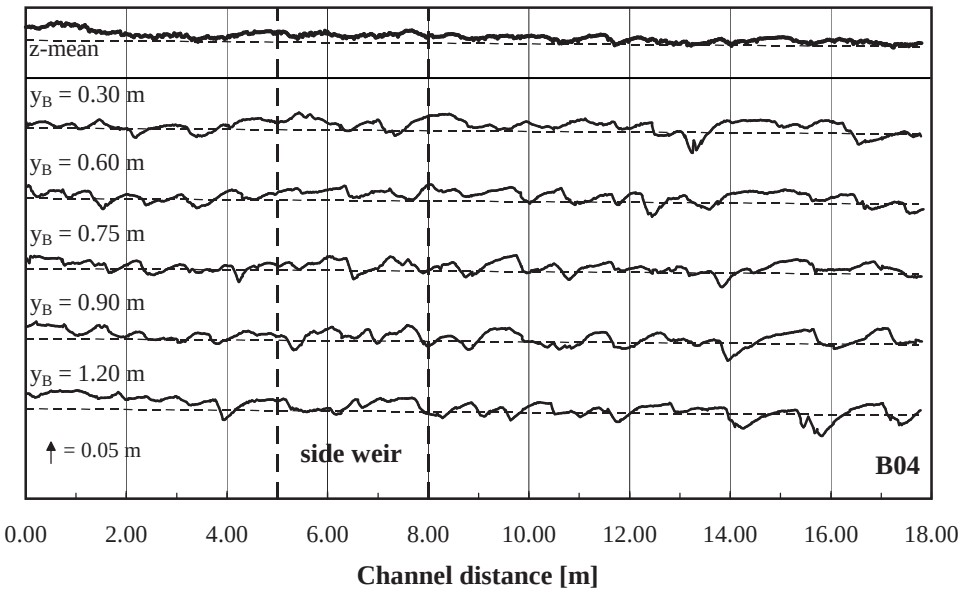

Figure B.17: Longitudinal final bed surface profiles at different spanwise positions (y_B) for experiment $B04$. The tiny dashed lines represent the initial bed surface. The side weir is located on the right channel bank at $y_B = 1.50\ m$.

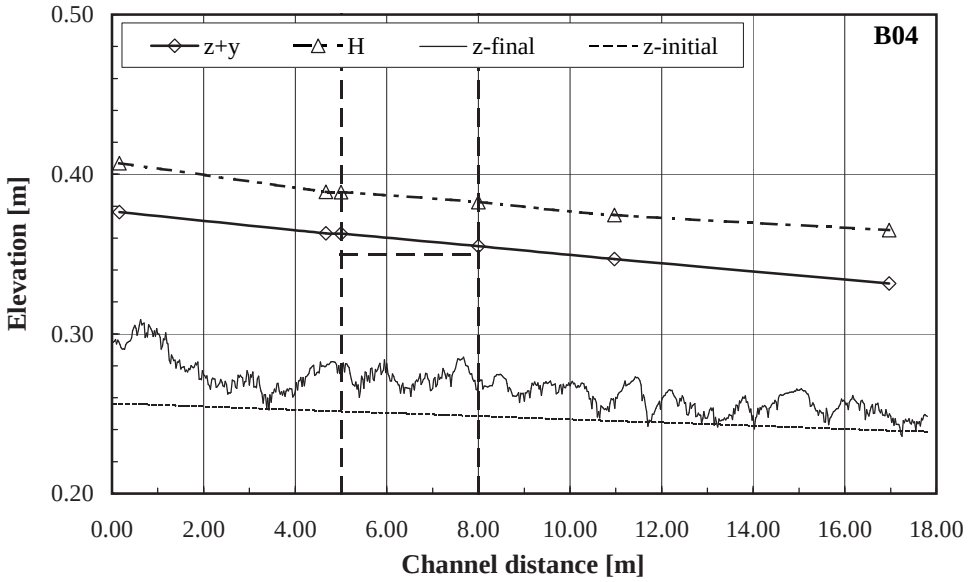

Figure B.18: Streamwise cross sectional averaged final bed surface profile (z_{final}), water level elevation ($z + y$) and total energy head (H) for experiment $B04$.

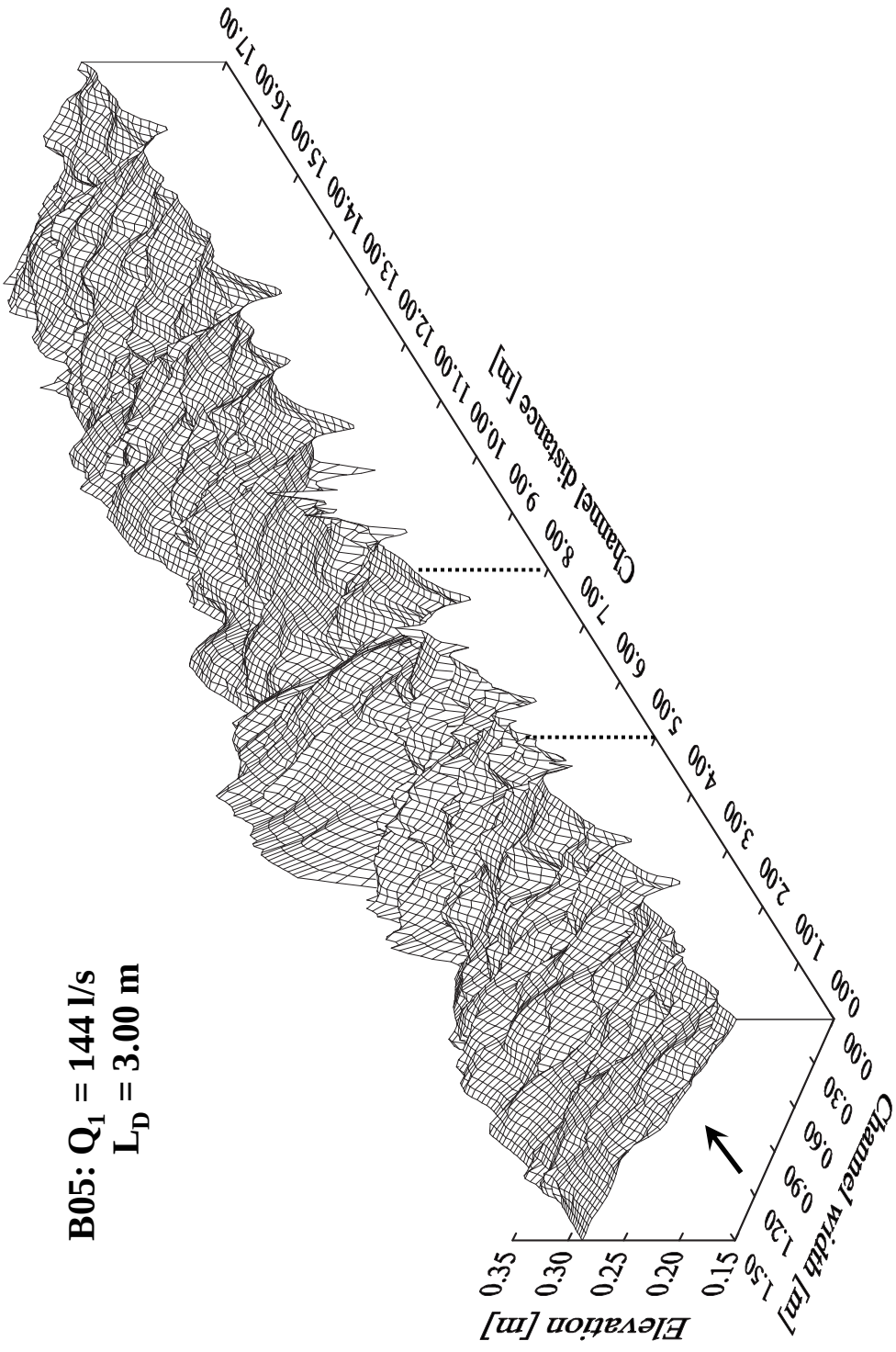

Figure B.19: 3*D*-view of the final bed morphology for experiment *B*05. The dotted line indicates the side weir location. Note: For better visibility of the deposit the left and right channel bank are inverted!

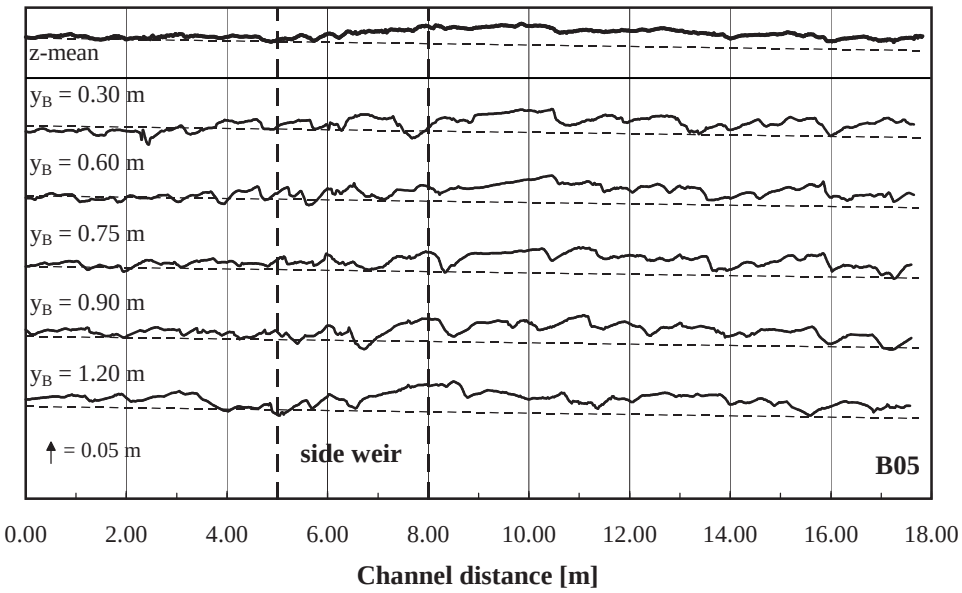

Figure B.20: Longitudinal final bed surface profiles at different spanwise positions (y_B) for experiment $B05$. The tiny dashed lines represent the initial bed surface. The side weir is located on the right channel bank at $y_B = 1.50\ m$.

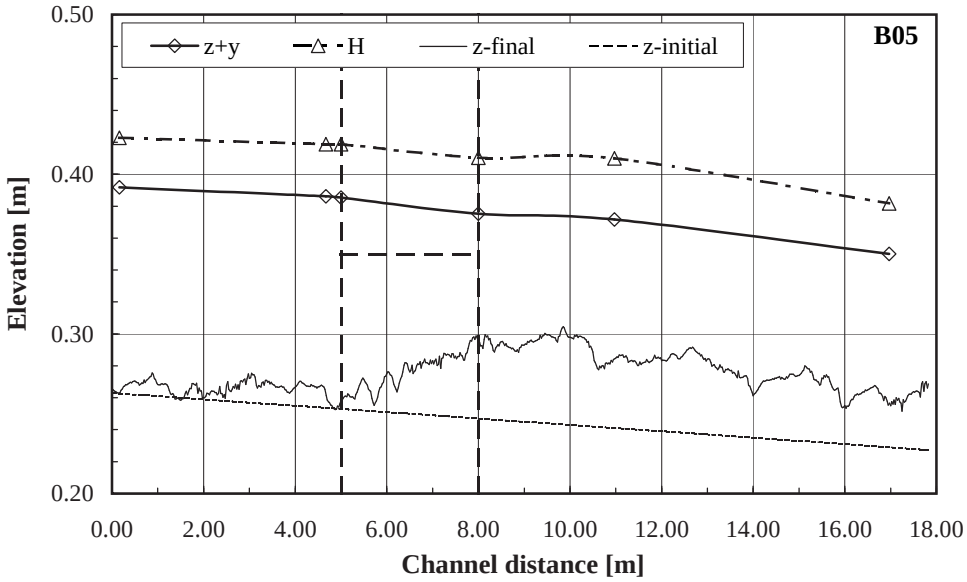

Figure B.21: Streamwise cross sectional averaged final bed surface profile (z_{final}), water level elevation ($z + y$) and total energy head (H) for experiment $B05$.

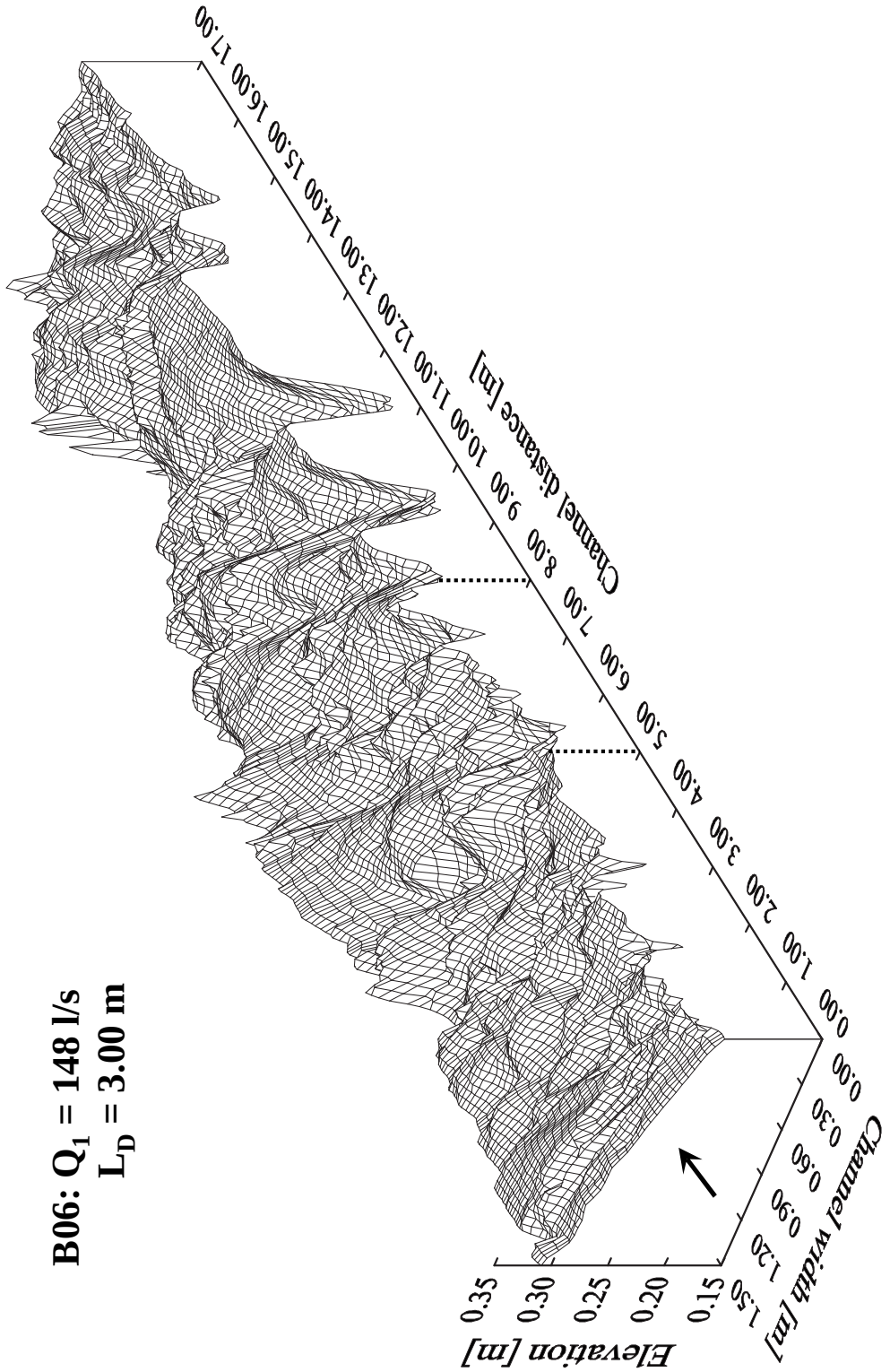

Figure B.22: 3*D*-view of the final bed morphology for experiment *B*06. The dotted line indicates the side weir location. Note: For better visibility of the deposit the left and right channel bank are inverted!

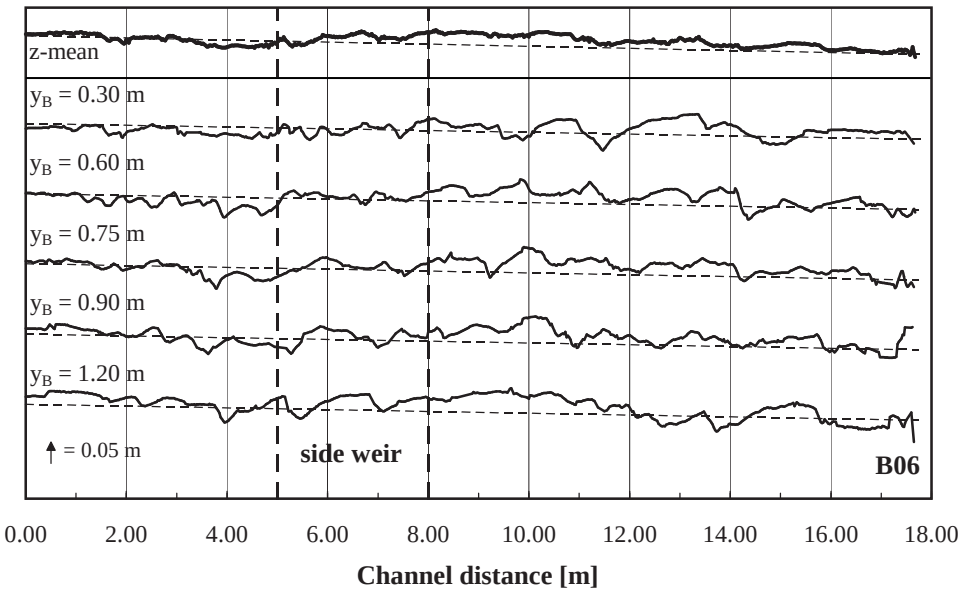

Figure B.23: Longitudinal final bed surface profiles at different spanwise positions (y_B) for experiment $B06$. The tiny dashed lines represent the initial bed surface. The side weir is located on the right channel bank at $y_B = 1.50\ m$.

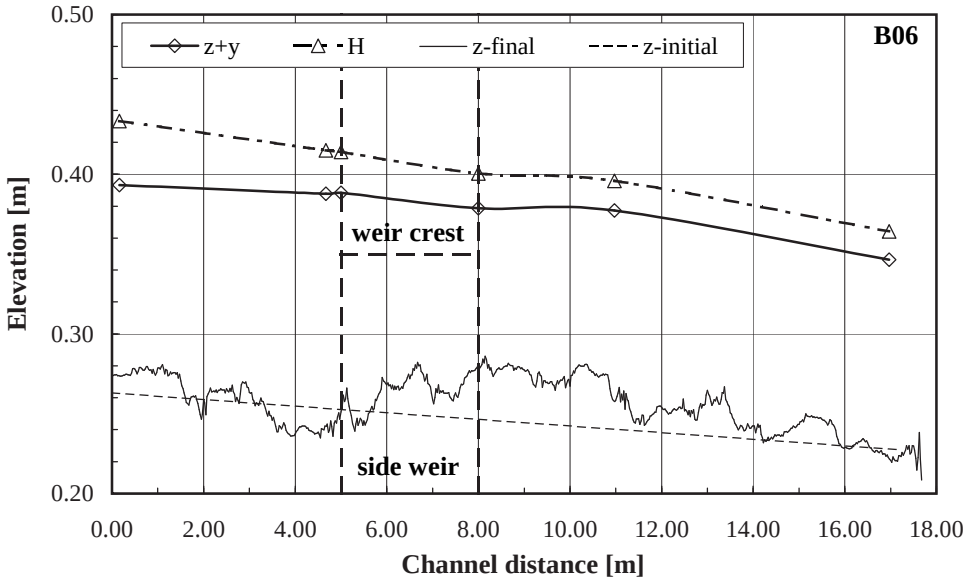

Figure B.24: Streamwise cross sectional averaged final bed surface profile (z_{final}), water level elevation ($z + y$) and total energy head (H) for experiment $B06$.

B.3. Test Series C (weir length $L_D = 6.00\ m$)

Table B.5: Channel geometry, weir geometry, sediment supply and experiment duration for test series C.

N^o of exp.	Channel width B $[m]$	Bottom slope $S_{0,ini}$ [%]	Weir crest length L_D $[m]$	Weir height $w_{D,ini}$ $[m]$	N^o of weirs n_D $[-]$	Sediment supply $Q_{sb,in}$ $[kg/min]$	Exp. duration t $[min]$
$C01$	1.50	0.20	6.00	0.09	1	9.56	125
$C02$	1.50	0.20	6.00	0.09	1	42.69	120
$C03$	1.50	0.20	6.00	0.09	1	51.76	120
$C04$	1.50	0.20	6.00	0.09	1	39.82	120
$C05$	1.50	0.20	6.00	0.09	1	39.82	120

Table B.6: Flow parameters for test series C.

N^o of exp.	Upstream discharge Q_1 $[l/s]$	Overflow discharge $Q_{D,fin}$ $[l/s]$	Flow depth $y_{1,fin}$ $[m]$	Flow velocity $v_{1,fin}$ $[m/s]$	Froude number $Fr_{1,fin}$ $[-]$	Pressure head $h_{D,1,fin}$ $[m]$
$C01$	160	30	0.100	1.063	1.072	0.037
$C02$	197	32	0.120	1.097	1.012	0.042
$C03$	221	71	0.084	1.744	1.916	0.048
$C04$	179	28	0.118	1.014	0.943	0.044
$C05$	181	38	0.116	1.042	0.978	0.039

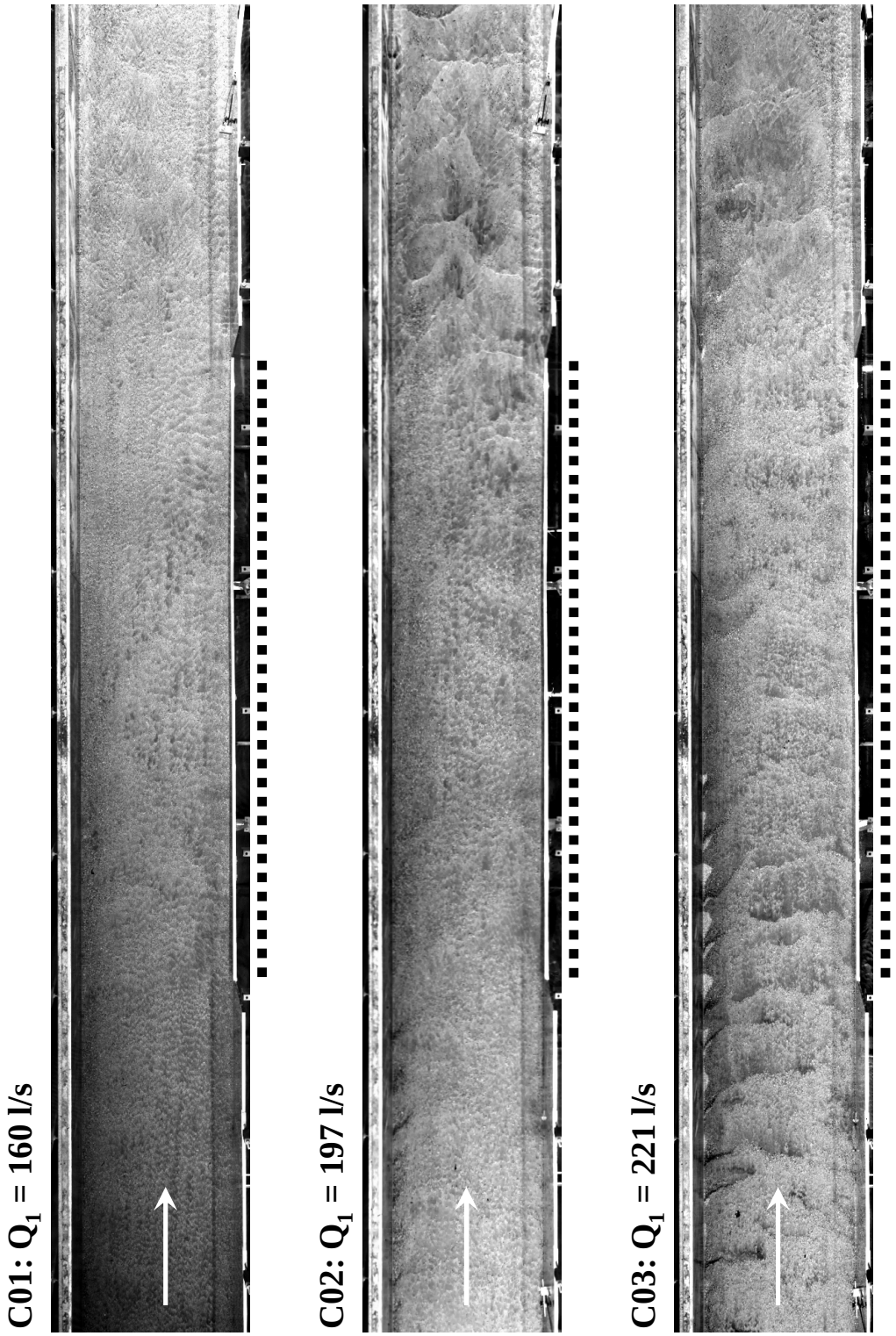

Figure B.25: Final bed morphology for experiments $C01$, $C02$ and $C03$.

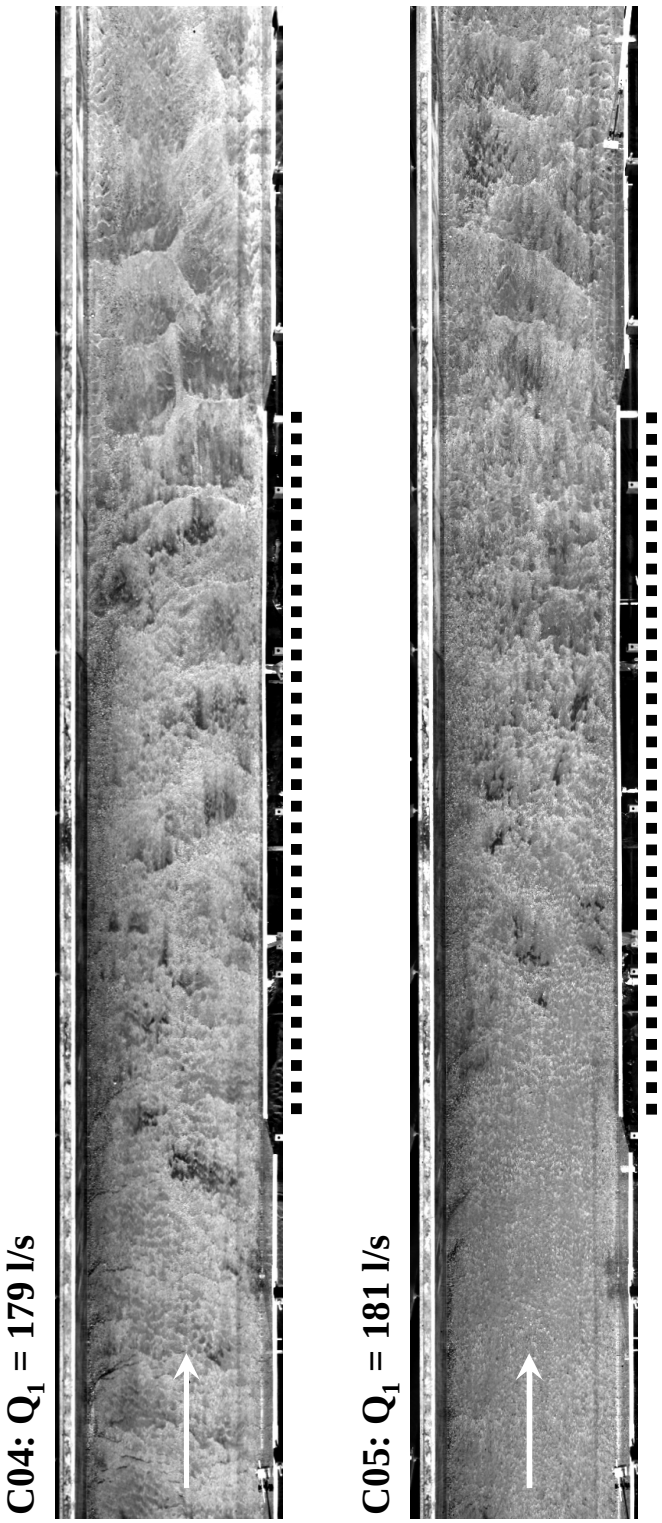

Figure B.26: Final bed morphology for experiments $C04$ and $C05$.

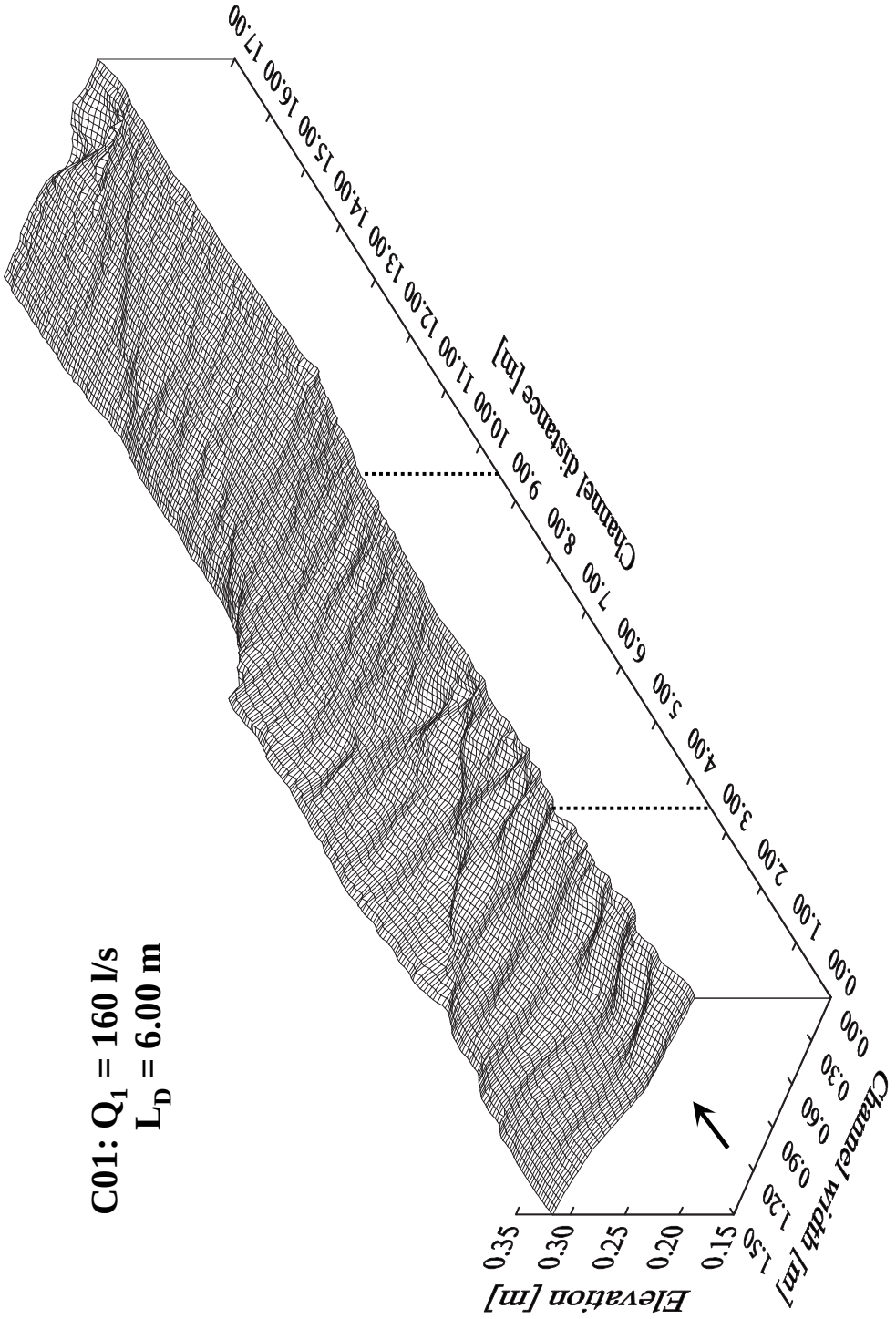

Figure B.27: 3*D*-view of the final bed morphology for experiment *C*01. The dotted line indicates the side weir location. Note: For better visibility of the deposit the left and right channel bank are inverted!

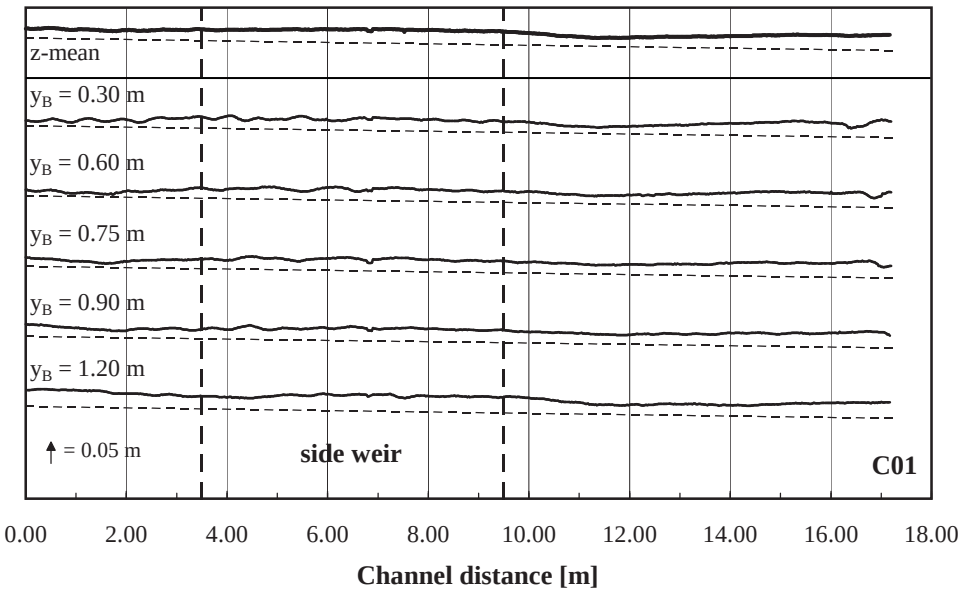

Figure B.28: Longitudinal final bed surface profiles at different spanwise positions (y_B) for experiment $C01$. The tiny dashed lines represent the initial bed surface. The side weir is located on the right channel bank at $y_B = 1.50\ m$.

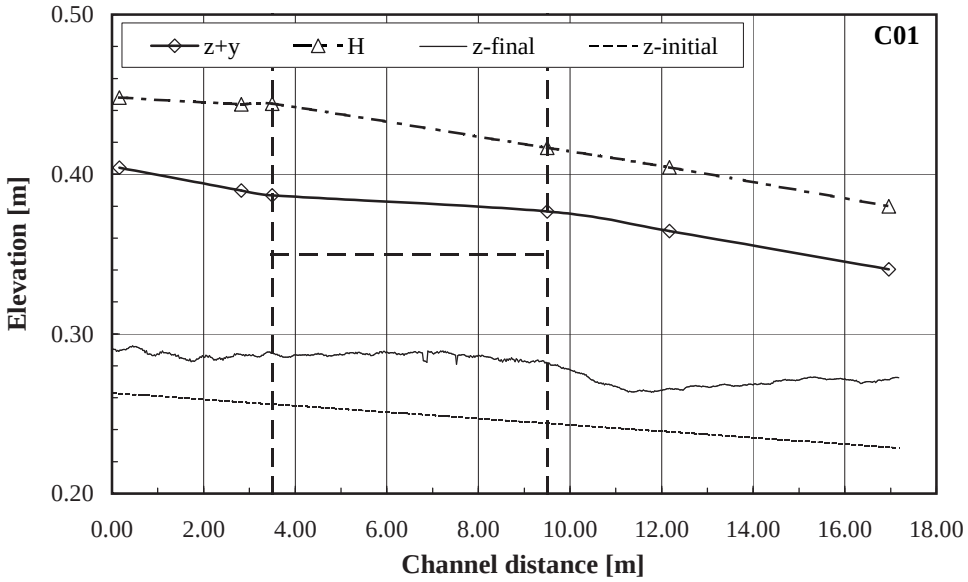

Figure B.29: Streamwise cross sectional averaged final bed surface profile (z_{final}), water level elevation ($z + y$) and total energy head (H) for experiment $C01$.

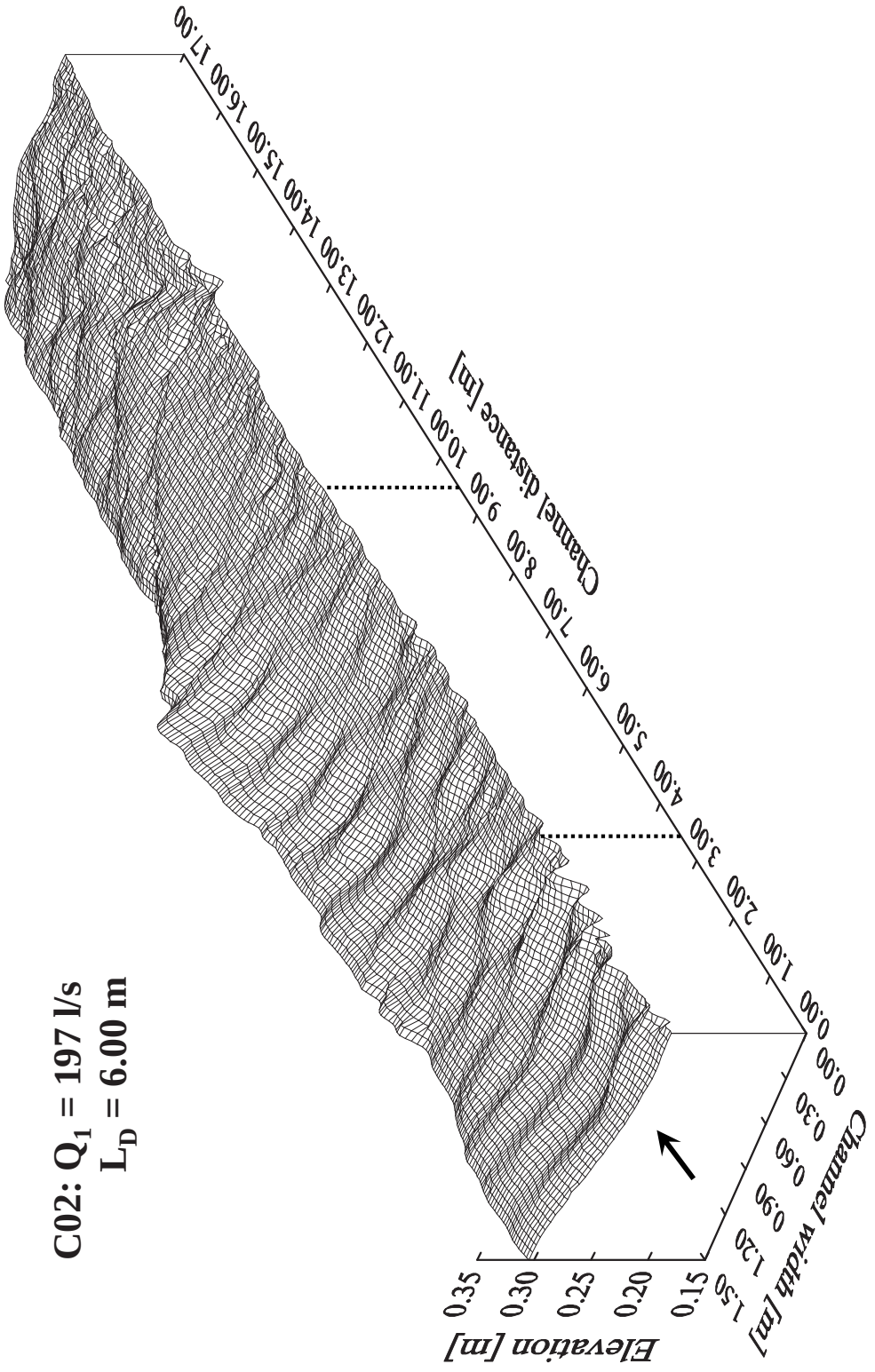

Figure B.30: 3*D*-view of the final bed morphology for experiment *C*02. The dotted line indicates the side weir location. Note: For better visibility of the deposit the left and right channel bank are inverted!

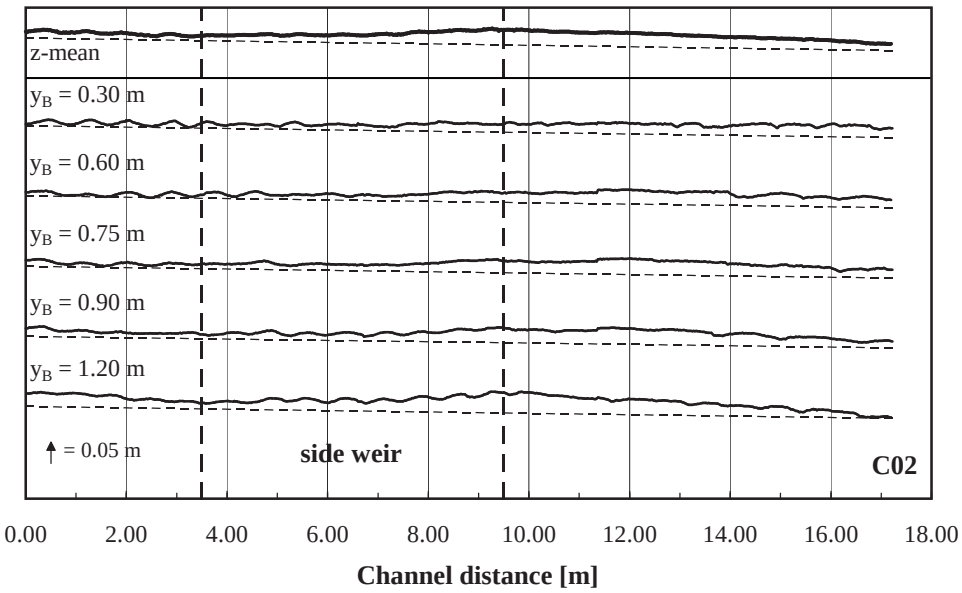

Figure B.31: Longitudinal final bed surface profiles at different spanwise positions (y_B) for experiment $C02$. The tiny dashed lines represent the initial bed surface. The side weir is located on the right channel bank at $y_B = 1.50\ m$.

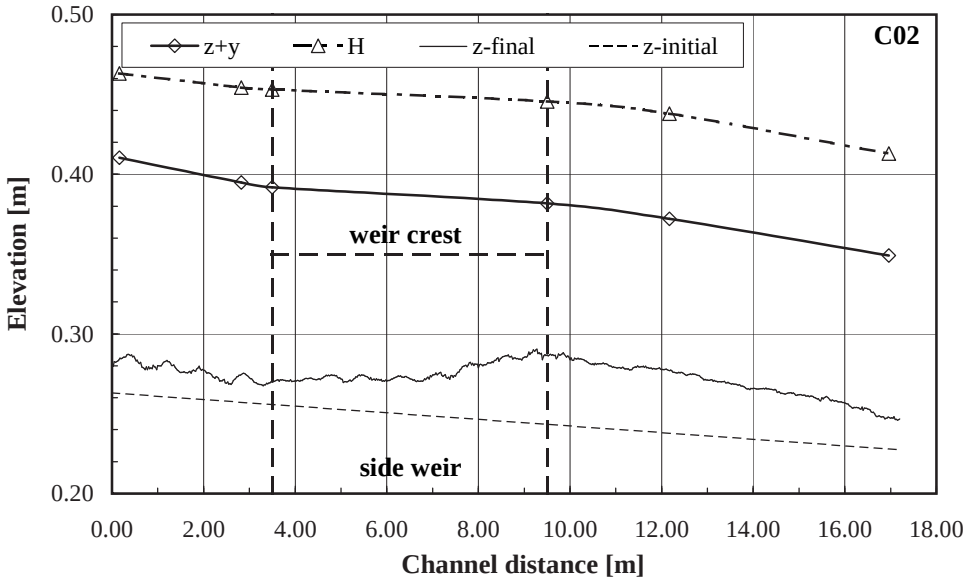

Figure B.32: Streamwise cross sectional averaged final bed surface profile (z_{final}), water level elevation ($z + y$) and total energy head (H) for experiment $C02$.

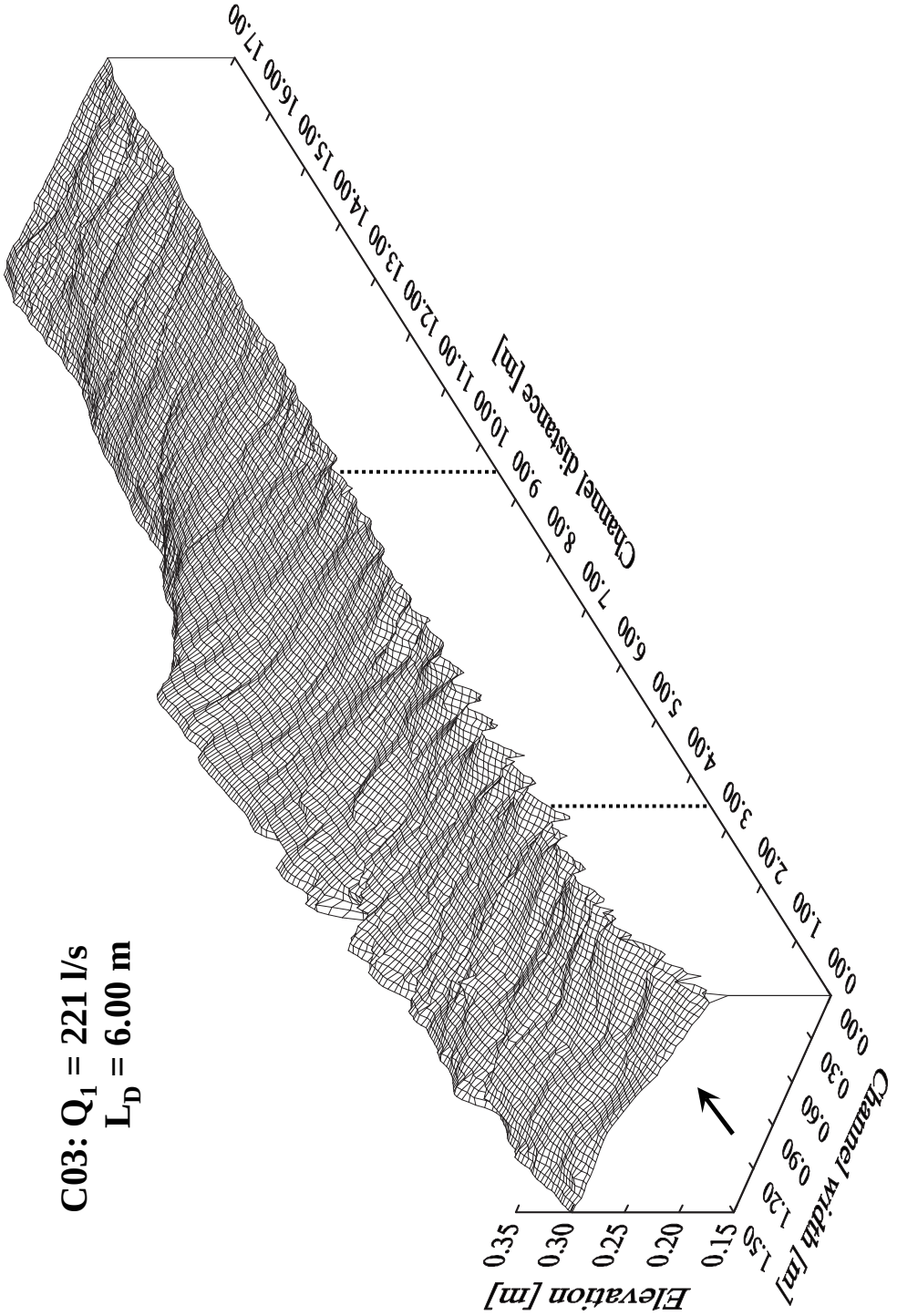

Figure B.33: 3*D*-view of the final bed morphology for experiment *C*03. The dotted line indicates the side weir location. Note: For better visibility of the deposit the left and right channel bank are inverted!

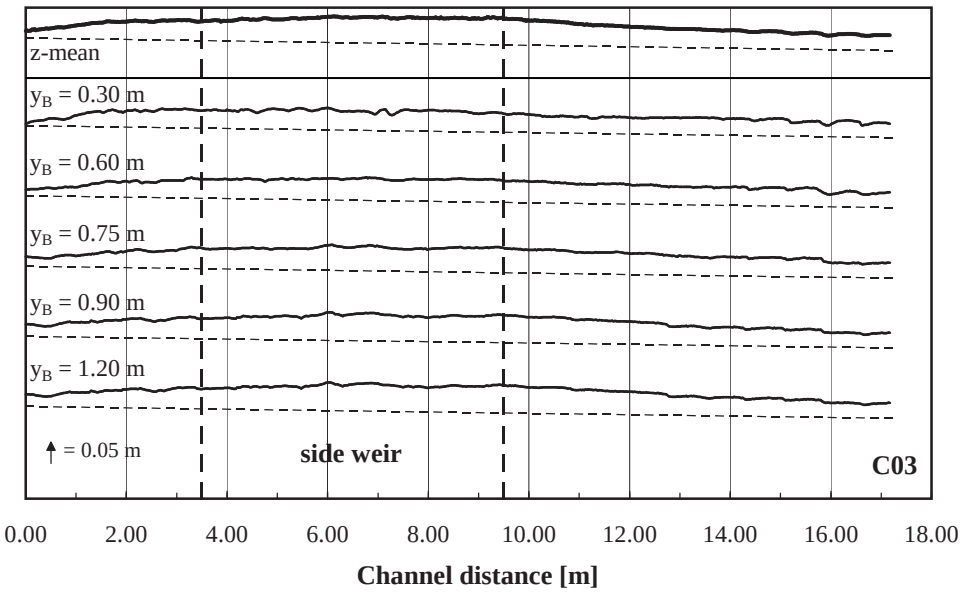

Figure B.34: Longitudinal final bed surface profiles at different spanwise positions (y_B) for experiment $C03$. The tiny dashed lines represent the initial bed surface. The side weir is located on the right channel bank at $y_B = 1.50\ m$.

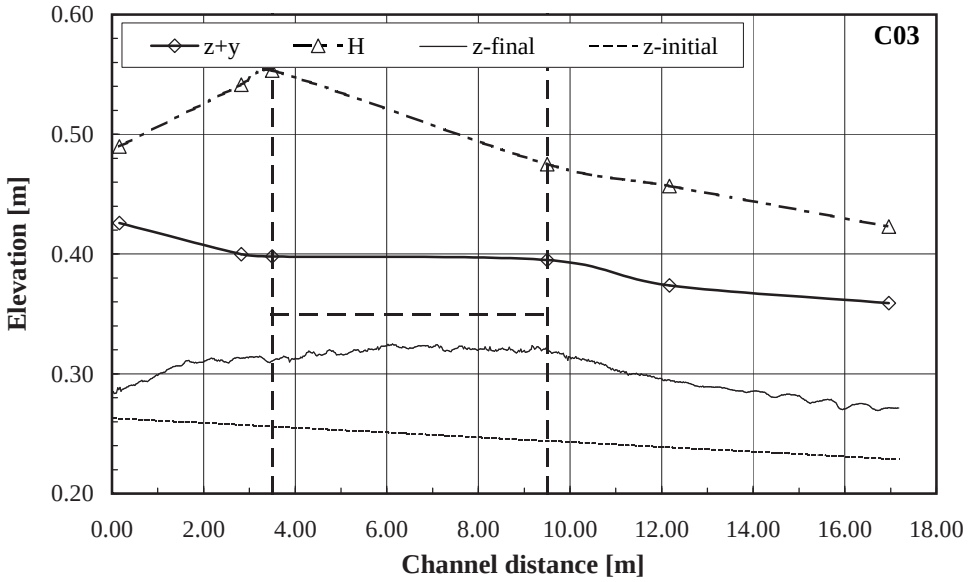

Figure B.35: Streamwise cross sectional averaged final bed surface profile (z_{final}), water level elevation ($z + y$) and total energy head (H) for experiment $C03$.

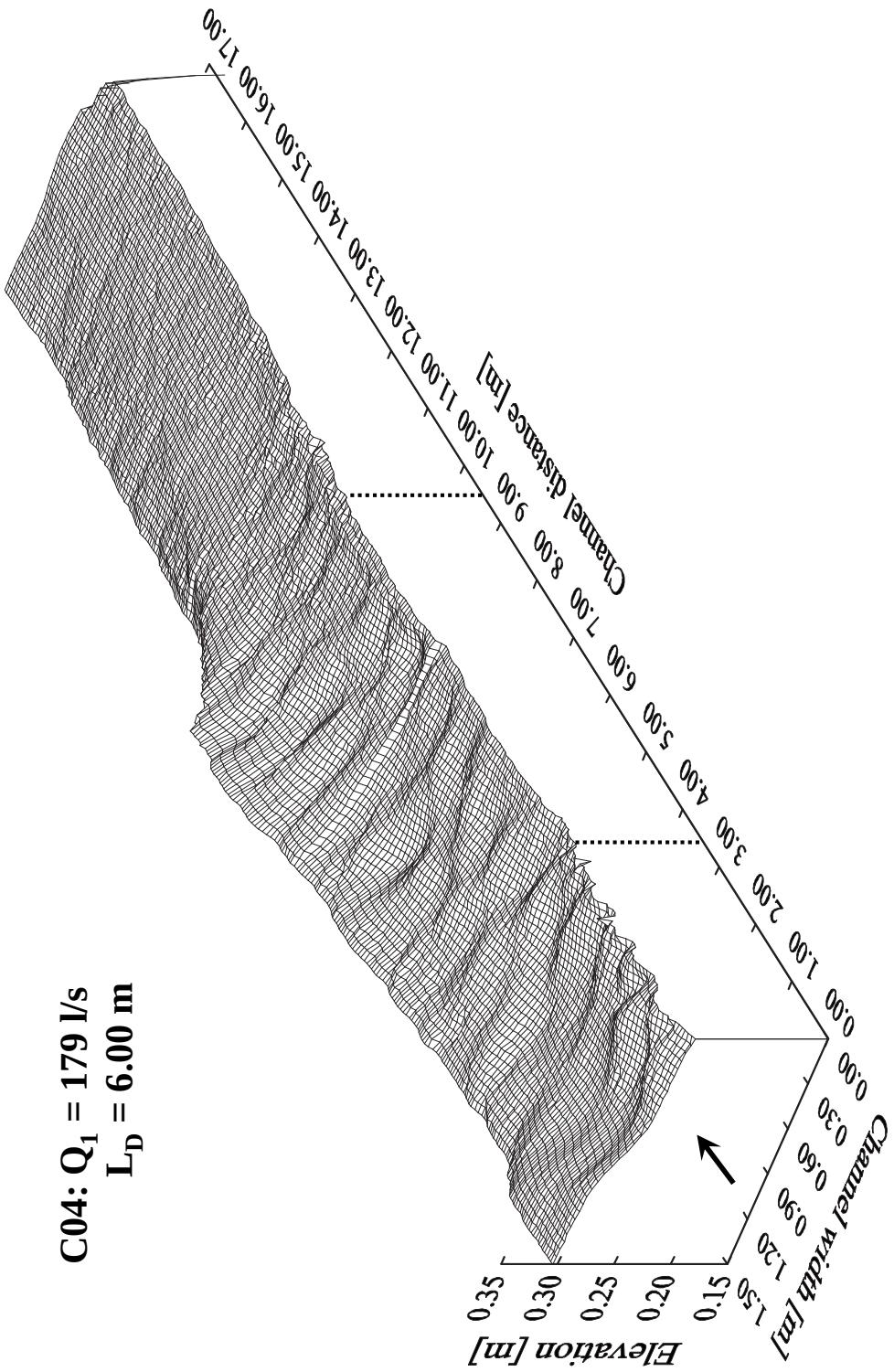

Figure B.36: 3D-view of the final bed morphology for experiment $C04$. The dotted line indicates the side weir location. Note: For better visibility of the deposit the left and right channel bank are inverted!

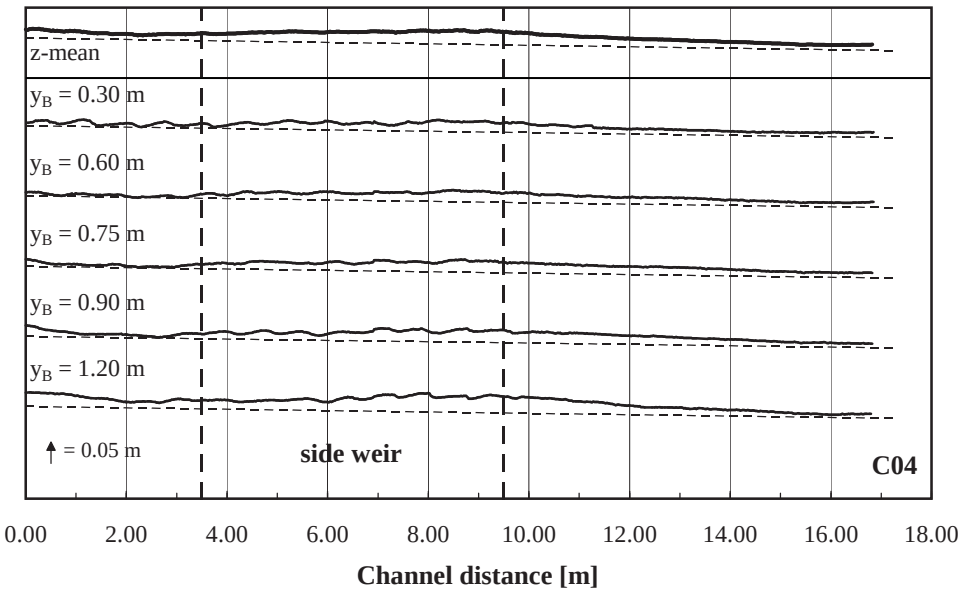

Figure B.37: Longitudinal final bed surface profiles at different spanwise positions (y_B) for experiment $C04$. The tiny dashed lines represent the initial bed surface. The side weir is located on the right channel bank at $y_B = 1.50\ m$.

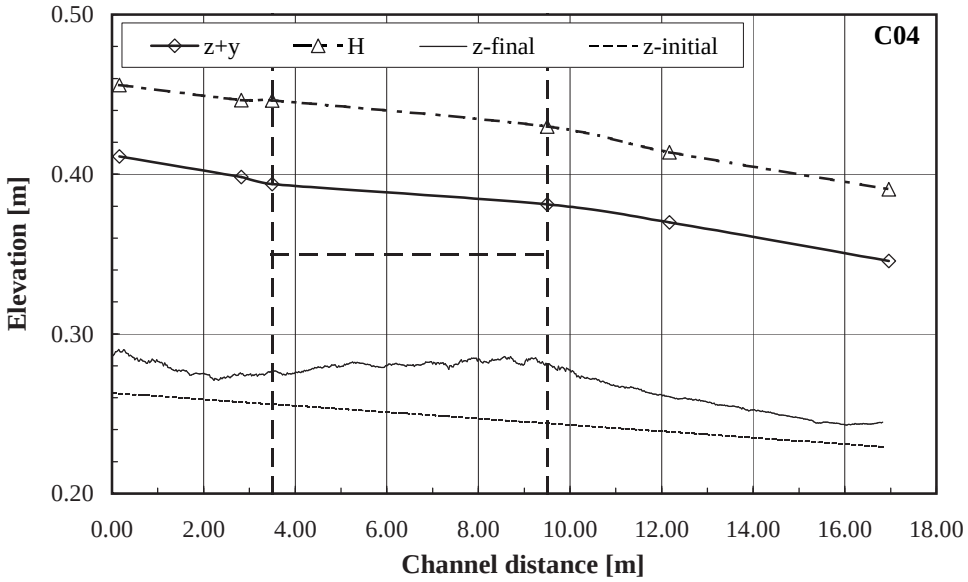

Figure B.38: Streamwise cross sectional averaged final bed surface profile (z_{final}), water level elevation ($z + y$) and total energy head (H) for experiment $C04$.

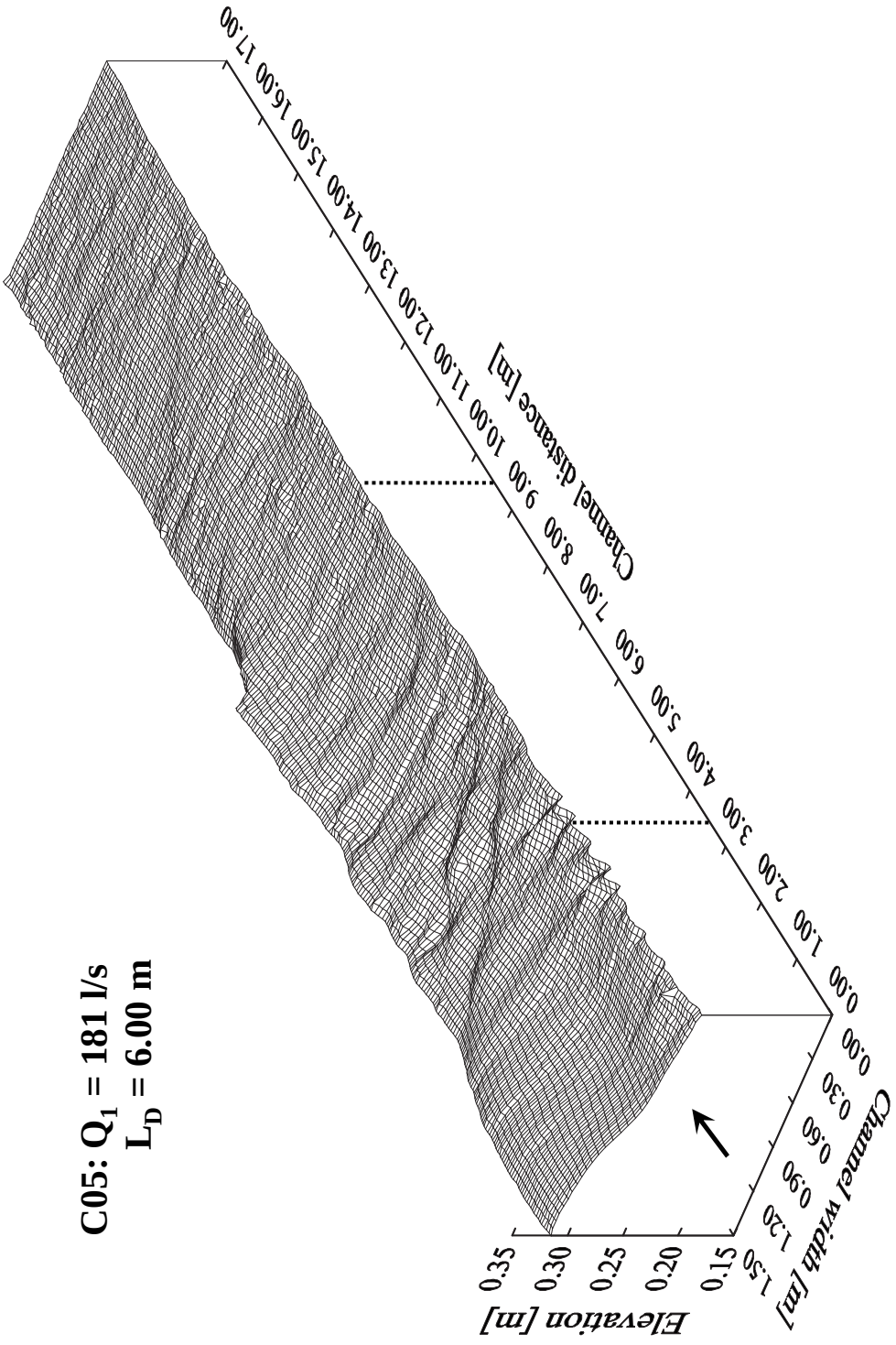

Figure B.39: 3D-view of the final bed morphology for experiment $C05$. The dotted line indicates the side weir location. Note: For better visibility of the deposit the left and right channel bank are inverted!

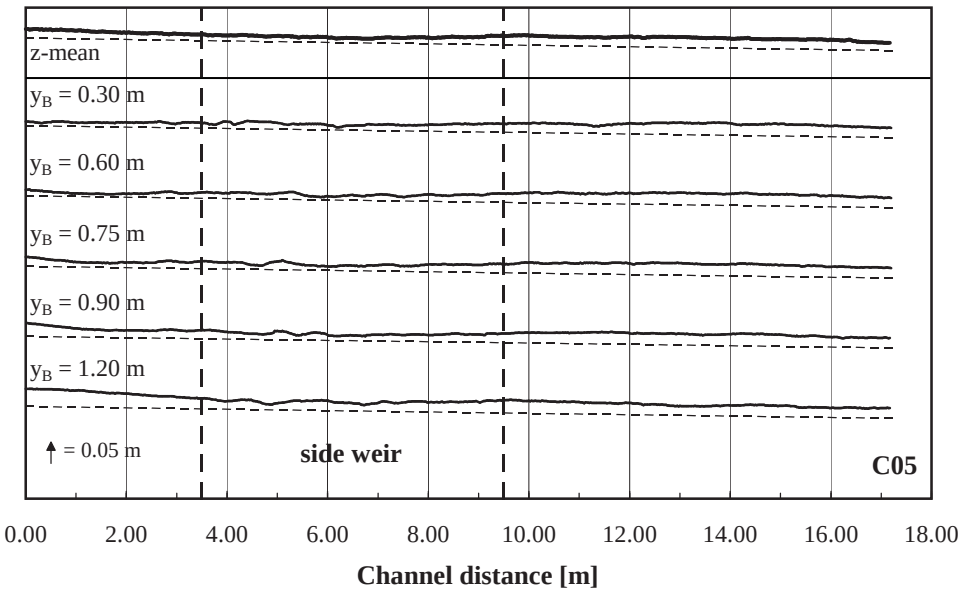

Figure B.40: Longitudinal final bed surface profiles at different spanwise positions (y_B) for experiment $C05$. The tiny dashed lines represent the initial bed surface. The side weir is located on the right channel bank at $y_B = 1.50\ m$.

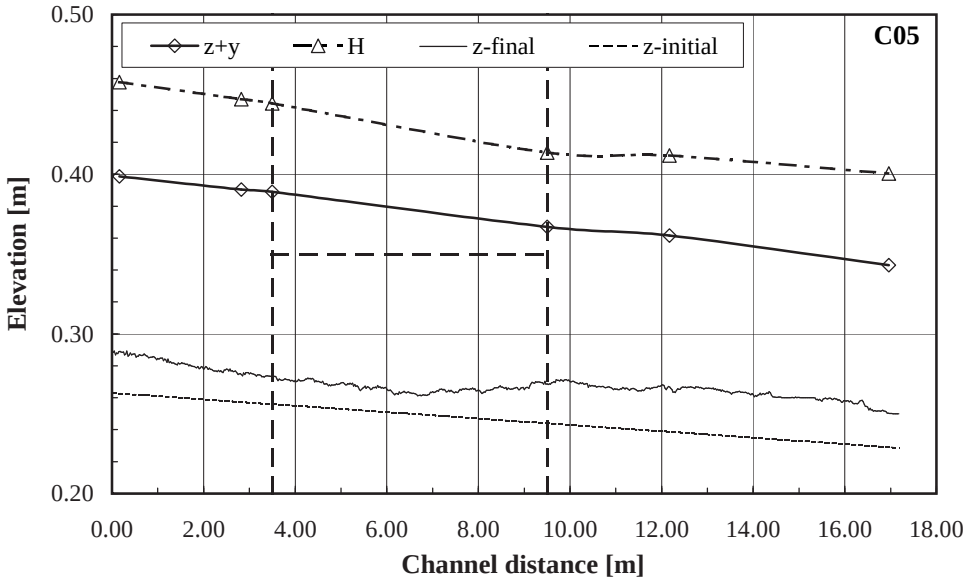

Figure B.41: Streamwise cross sectional averaged final bed surface profile (z_{final}), water level elevation ($z + y$) and total energy head (H) for experiment $C05$.

B.4. Test Series D (weir length $L_D = 2 \cdot 2.50\ m$)

Table B.7: Channel geometry, weir geometry, sediment supply and experiment duration for test series D.

N^o of exp.	Channel width B $[m]$	Bottom slope $S_{0,ini}$ [%]	Weir crest length L_D $[m]$	Weir height $w_{D,ini}$ $[m]$	N^o of weirs n_D $[-]$	Sediment supply $Q_{sb,in}$ $[kg/min]$	Exp. duration t $[min]$
D01	1.50	0.20	$2 \cdot 2.50$	0.09	2	27.04	125
D02	1.50	0.20	$2 \cdot 2.50$	0.09	2	26.54	120
D03	1.50	0.20	$2 \cdot 2.50$	0.09	2	39.82	120
D04	1.50	0.20	$2 \cdot 2.50$	0.09	2	22.34	120
D05	1.50	0.20	$2 \cdot 2.50$	0.09	2	19.91	120

Table B.8: Flow parameters for test series D.

N^o of exp.	Upstream discharge Q_1 $[l/s]$	Overflow discharge $Q_{D,fin}$ $[l/s]$	Flow depth $y_{1,fin}$ $[m]$	Flow velocity $v_{1,fin}$ $[m/s]$	Froude number $Fr_{1,fin}$ $[-]$	Pressure head $h_{D,1,fin}$ $[m]$
D01	166	24	0.122	0.905	0.826	0.034
D02	182	33	0.138	0.879	0.755	0.048
D03	222	68	0.156	0.951	0.769	0.051
D04	182	67	0.131	0.929	0.821	0.040
D05	150	9	0.114	0.874	0.825	0.025

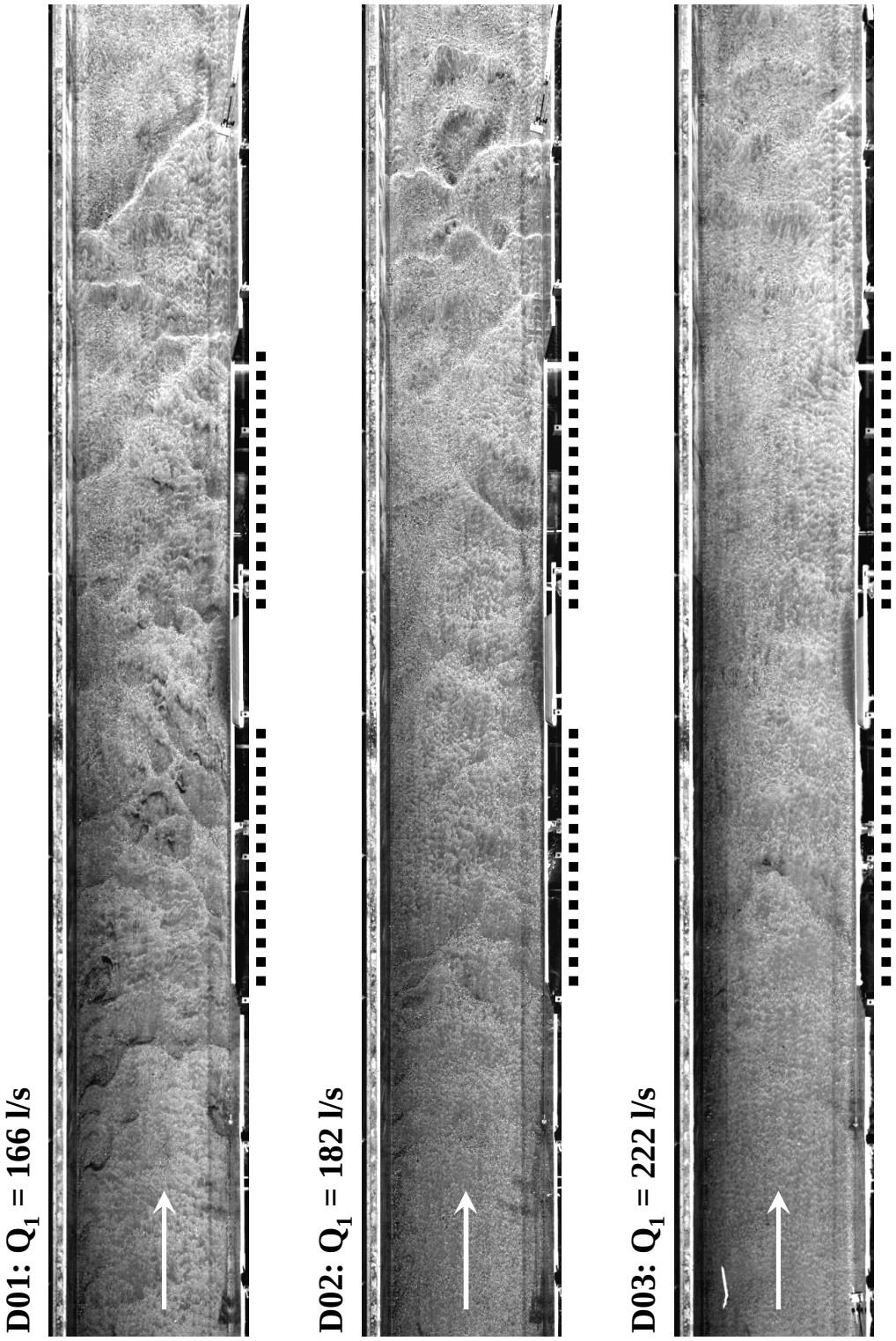

Figure B.42: Final bed morphology for experiments $D01$, $D02$ and $D03$.

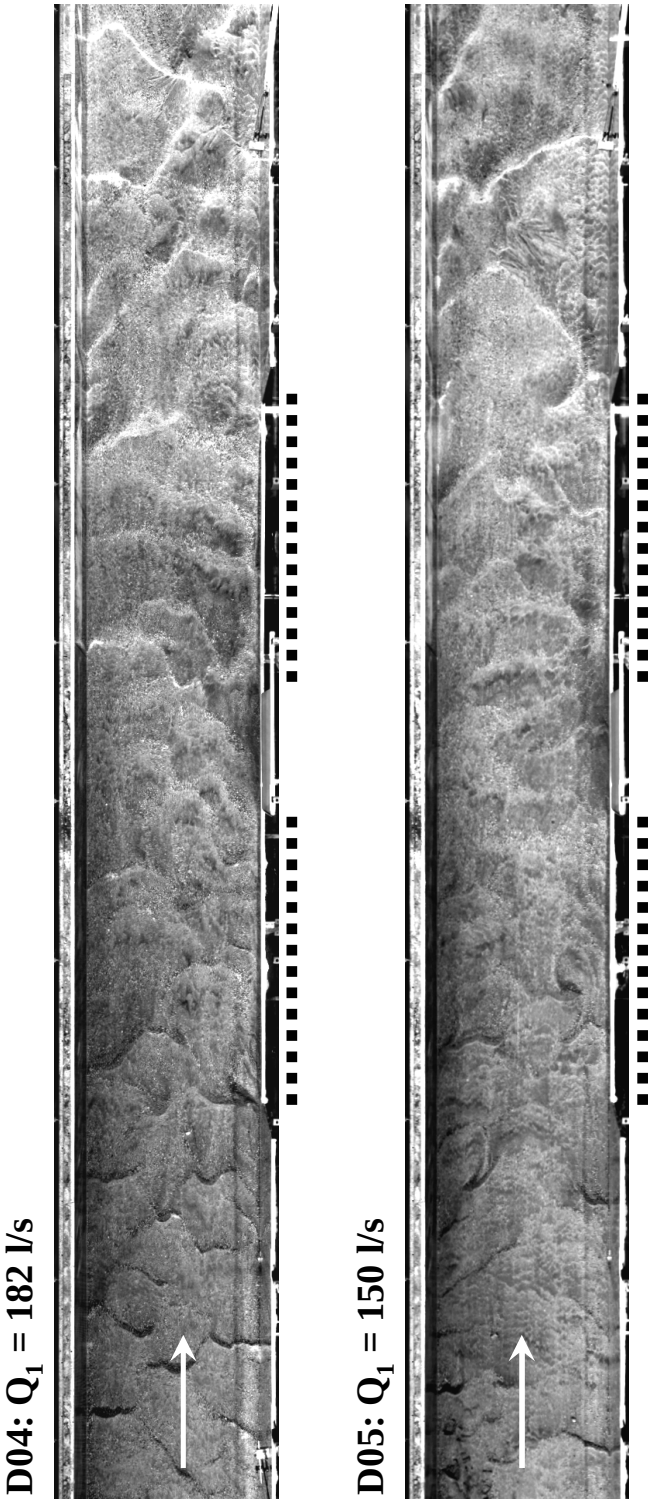

Figure B.43: Final bed morphology for experiments $D04$ and $D05$.

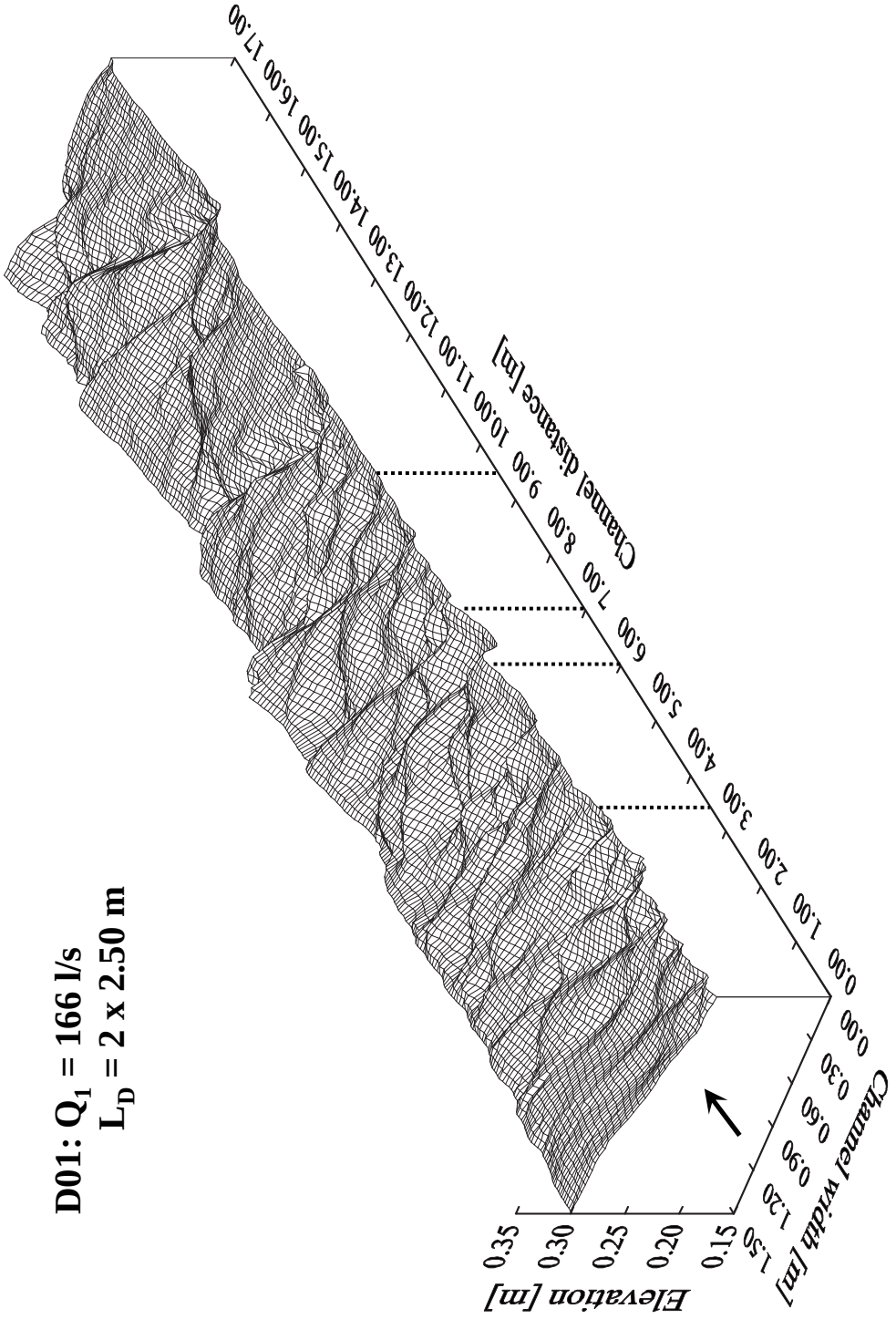

Figure B.44: 3*D*-view of the final bed morphology for experiment *D*01. The dotted line indicates the side weir location. Note: For better visibility of the deposit the left and right channel bank are inverted!

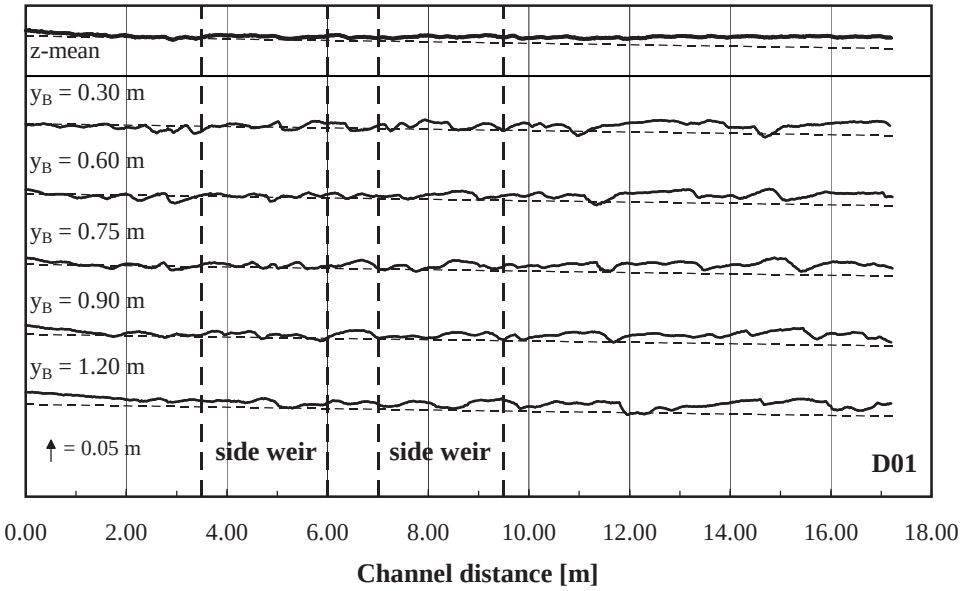

Figure B.45: Longitudinal final bed surface profiles at different spanwise positions (y_B) for experiment $D01$. The tiny dashed lines represent the initial bed surface. The side weir is located on the right channel bank at $y_B = 1.50\ m$.

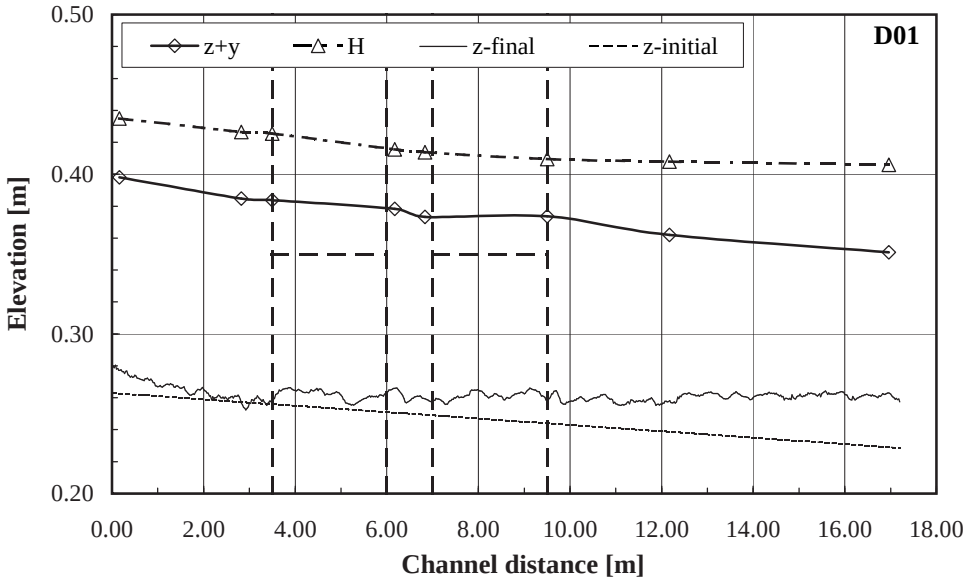

Figure B.46: Streamwise cross sectional averaged final bed surface profile (z_{final}), water level elevation ($z + y$) and total energy head (H) for experiment $D01$.

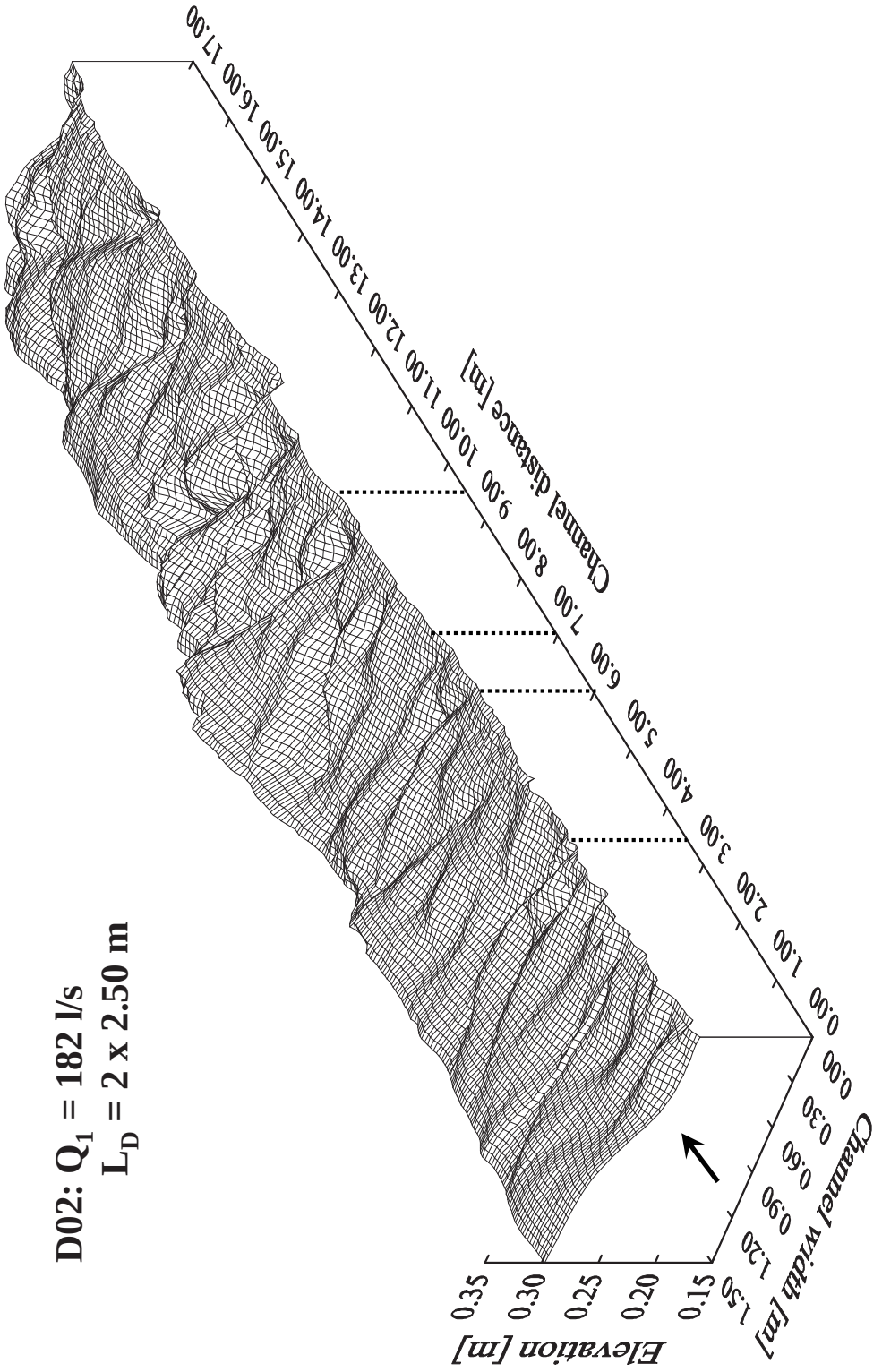

Figure B.47: 3*D*-view of the final bed morphology for experiment *D*02. The dotted line indicates the side weir location. Note: For better visibility of the deposit the left and right channel bank are inverted!

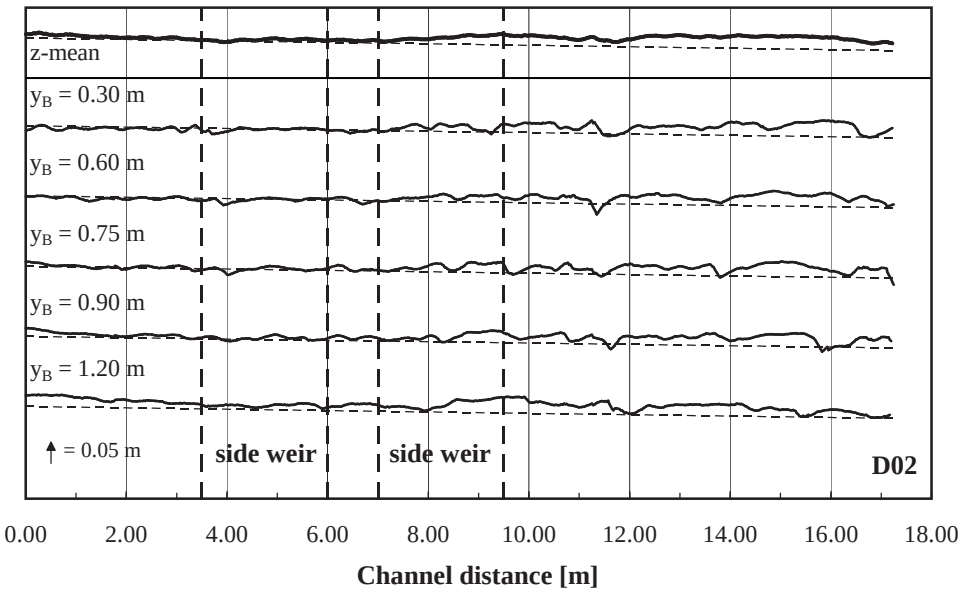

Figure B.48: Longitudinal final bed surface profiles at different spanwise positions (y_B) for experiment $D02$. The tiny dashed lines represent the initial bed surface. The side weir is located on the right channel bank at $y_B = 1.50\ m$.

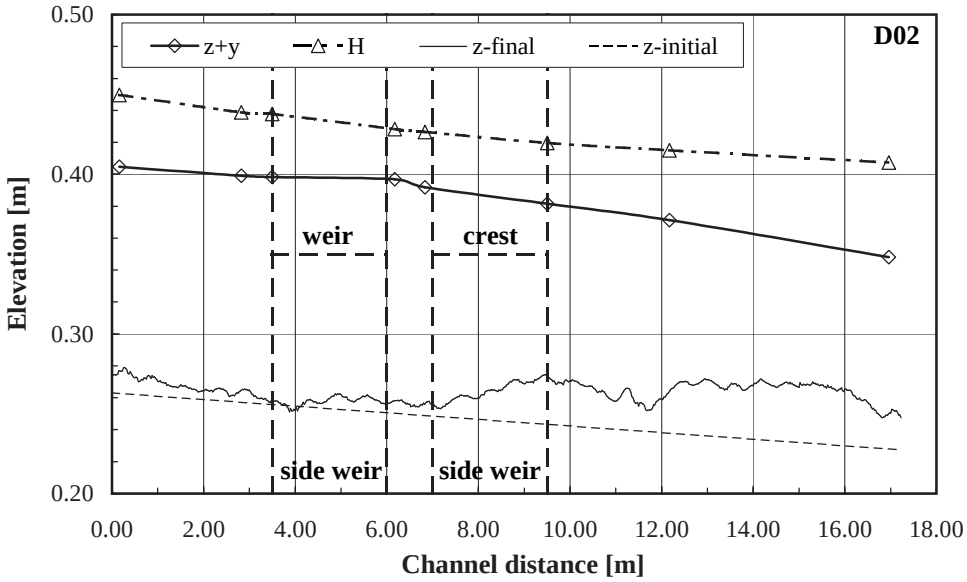

Figure B.49: Streamwise cross sectional averaged final bed surface profile (z_{final}), water level elevation ($z + y$) and total energy head (H) for experiment $D02$.

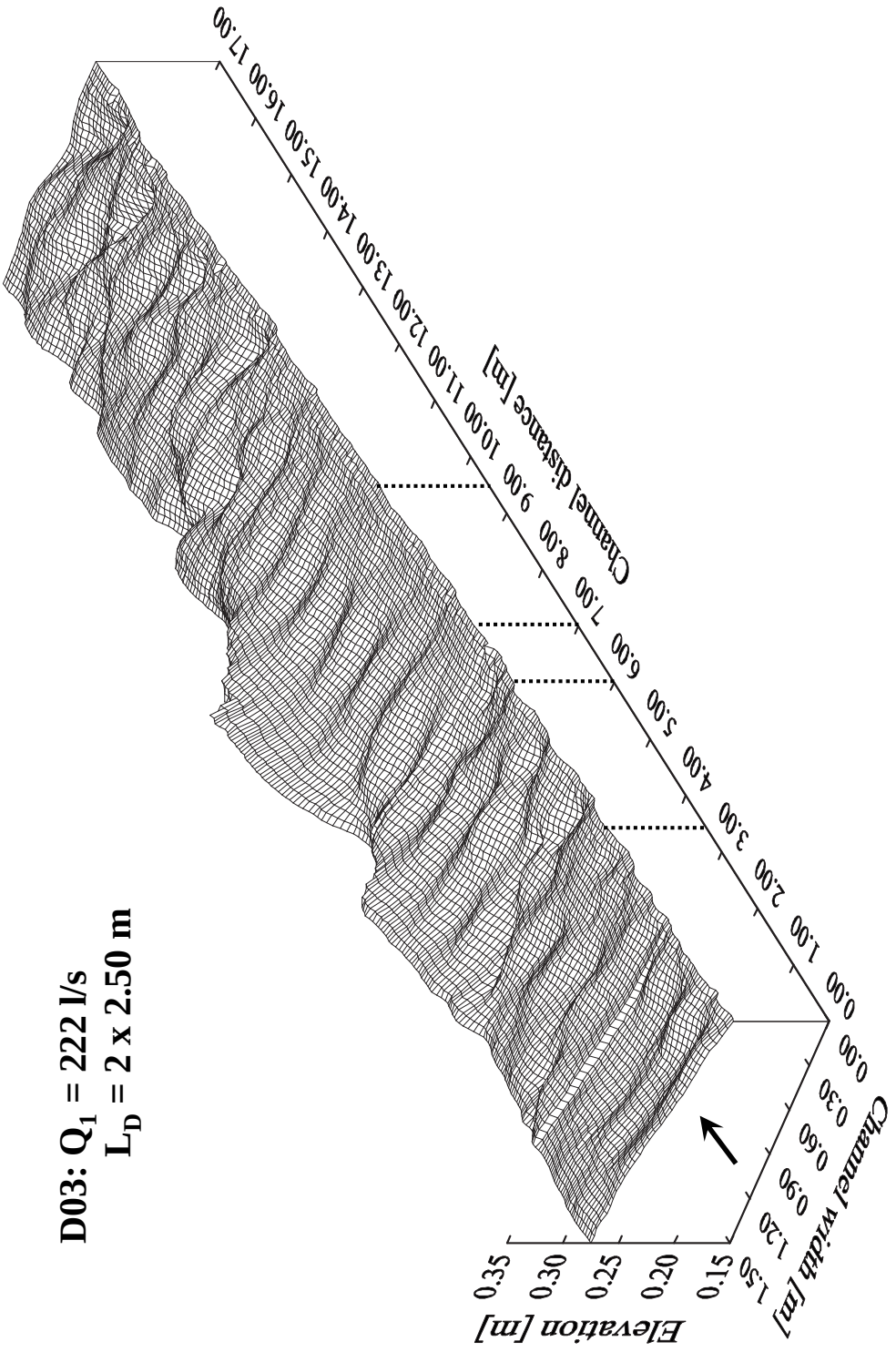

Figure B.50: 3*D*-view of the final bed morphology for experiment *D*03. The dotted line indicates the side weir location. Note: For better visibility of the deposit the left and right channel bank are inverted!

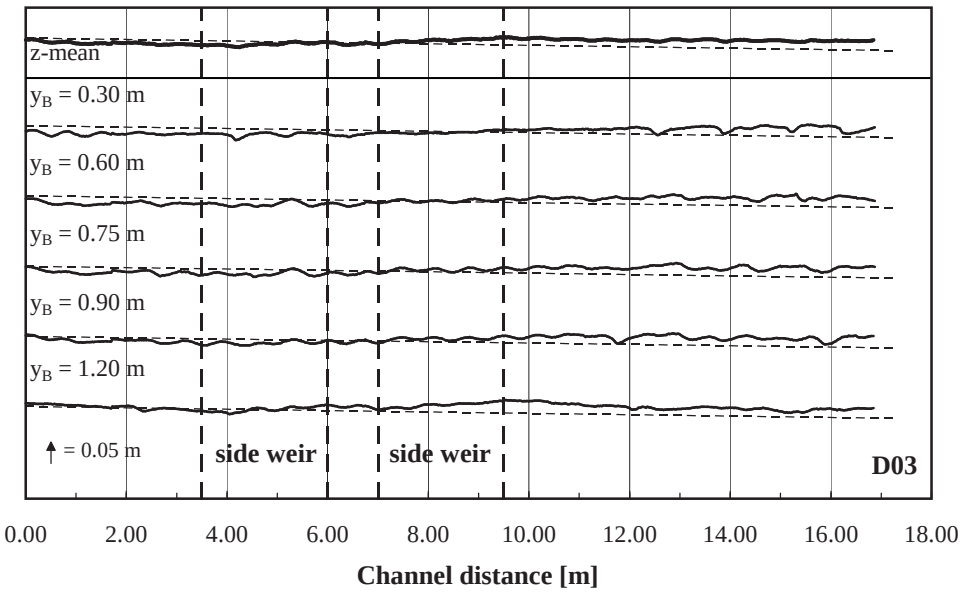

Figure B.51: Longitudinal final bed surface profiles at different spanwise positions (y_B) for experiment $D03$. The tiny dashed lines represent the initial bed surface. The side weir is located on the right channel bank at $y_B = 1.50\ m$.

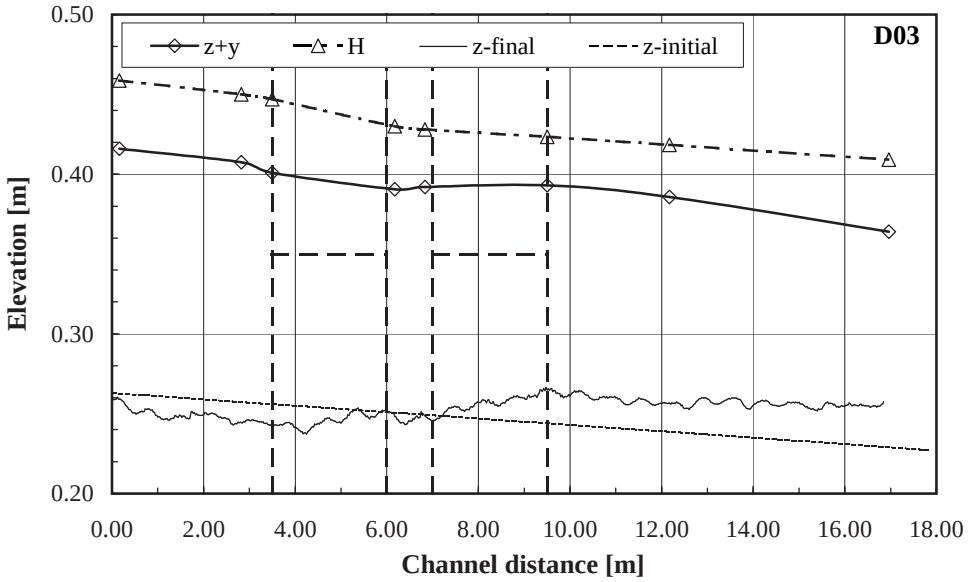

Figure B.52: Streamwise cross sectional averaged final bed surface profile (z_{final}), water level elevation ($z + y$) and total energy head (H) for experiment $D03$.

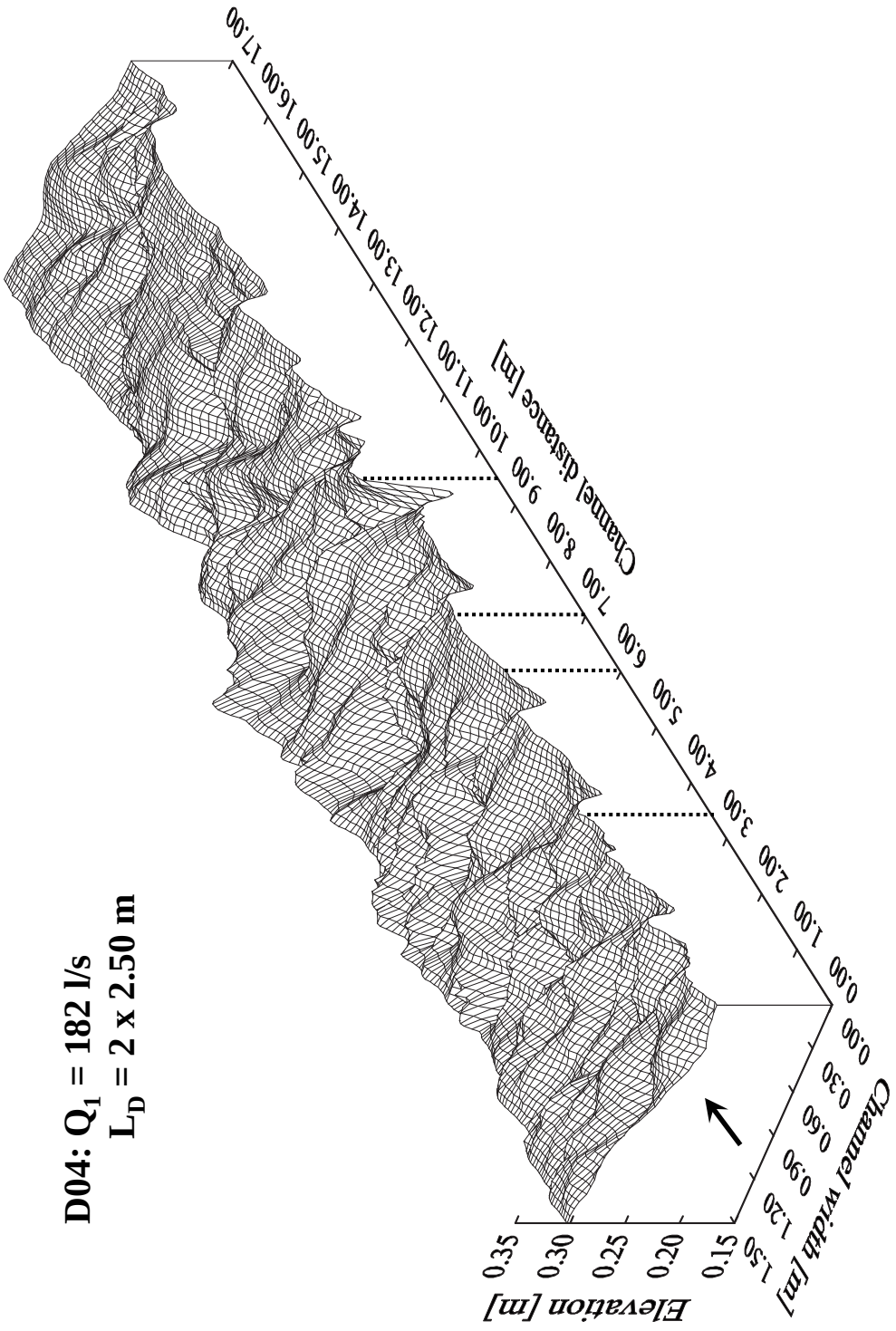

Figure B.53: 3*D*-view of the final bed morphology for experiment *D*04. The dotted line indicates the side weir location. Note: For better visibility of the deposit the left and right channel bank are inverted!

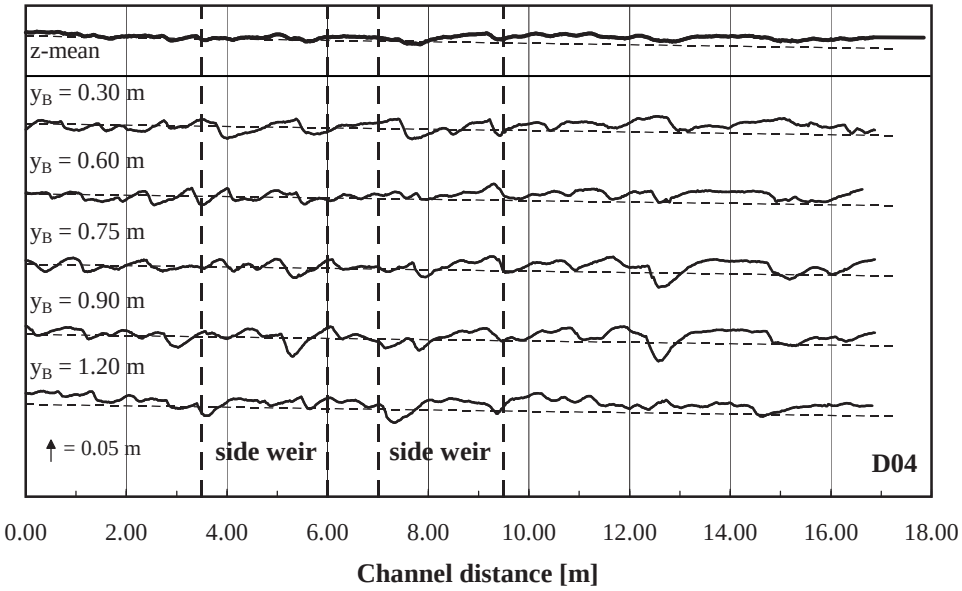

Figure B.54: Longitudinal final bed surface profiles at different spanwise positions (y_B) for experiment $D04$. The tiny dashed lines represent the initial bed surface. The side weir is located on the right channel bank at $y_B = 1.50\ m$.

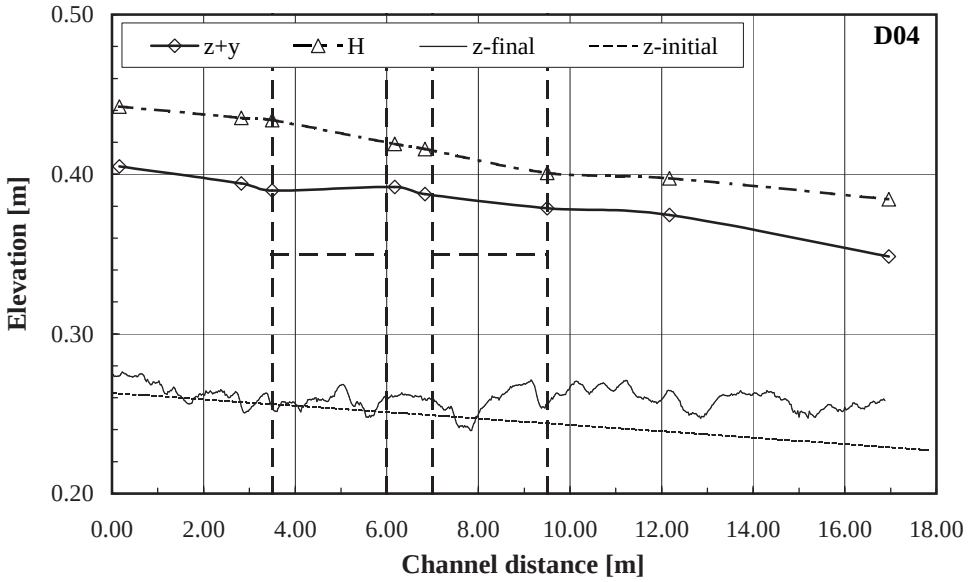

Figure B.55: Streamwise cross sectional averaged final bed surface profile (z_{final}), water level elevation ($z + y$) and total energy head (H) for experiment $D04$.

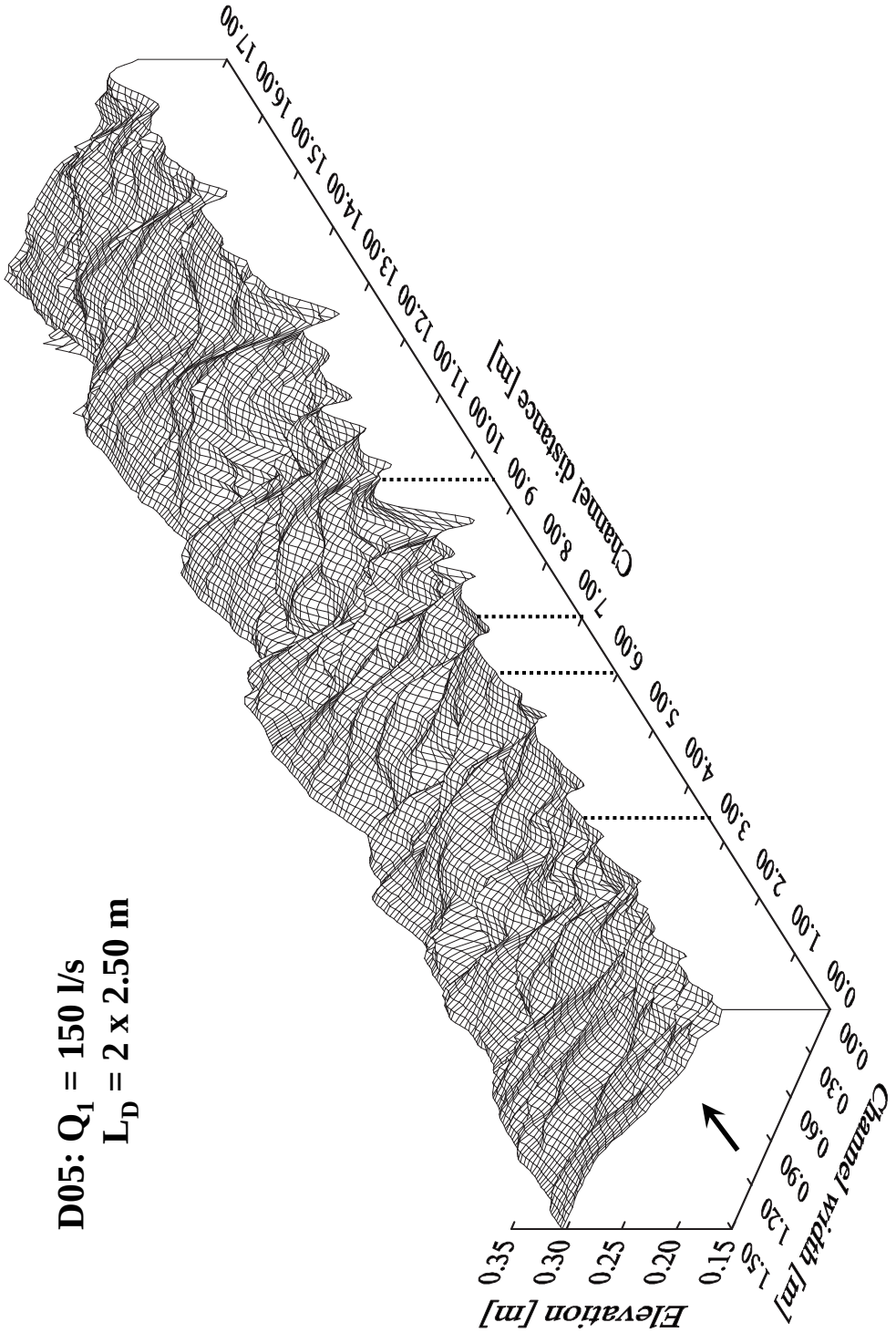

Figure B.56: 3*D*-view of the final bed morphology for experiment *D*05. The dotted line indicates the side weir location. Note: For better visibility of the deposit the left and right channel bank are inverted!

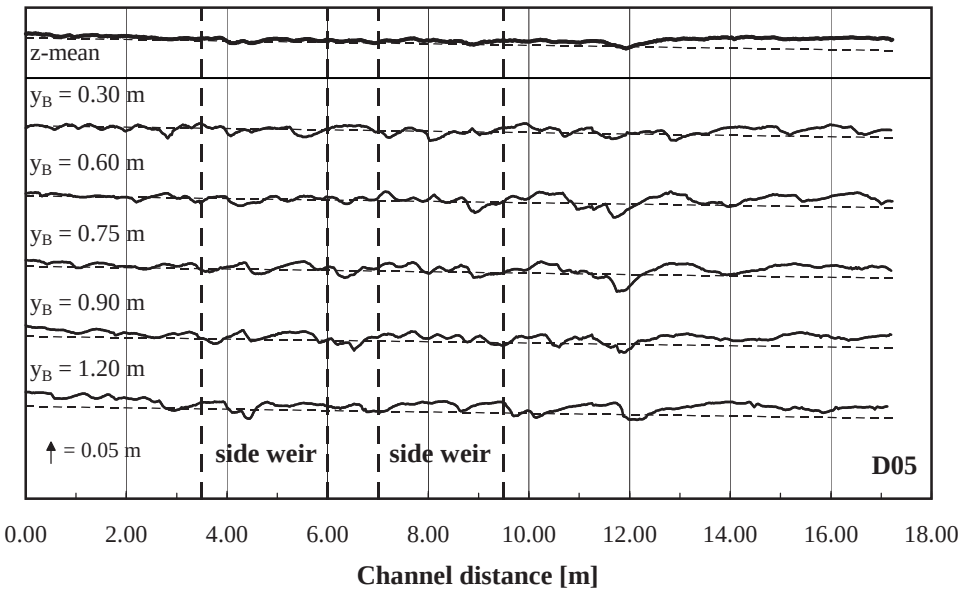

Figure B.57: Longitudinal final bed surface profiles at different spanwise positions (y_B) for experiment $D05$. The tiny dashed lines represent the initial bed surface. The side weir is located on the right channel bank at $y_B = 1.50\ m$.

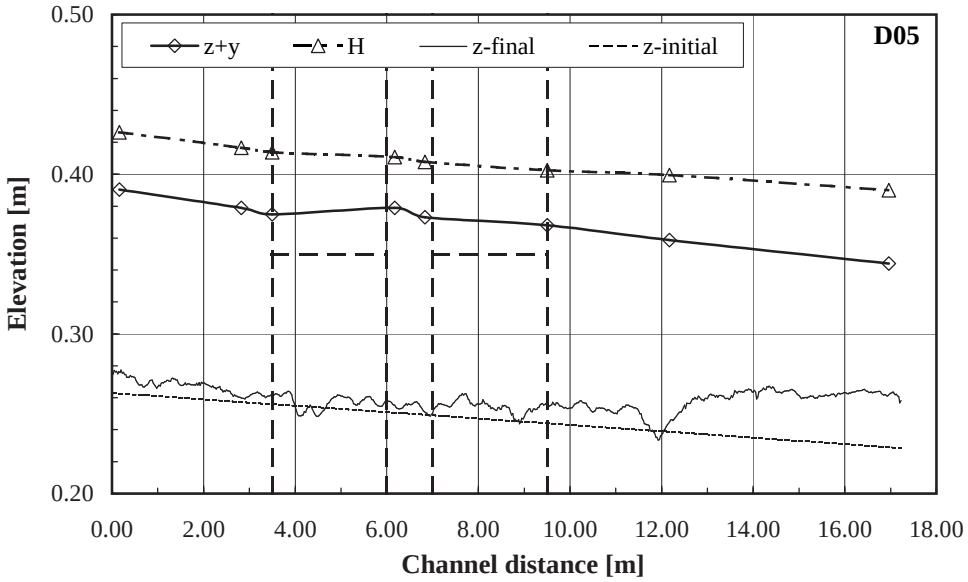

Figure B.58: Streamwise cross sectional averaged final bed surface profile (z_{final}), water level elevation ($z + y$) and total energy head (H) for experiment $D05$.

Communications du Laboratoire de Constructions Hydrauliques ISSN 1661-1179
Ecole Polytechnique Fédérale de Lausanne
Editeur: Prof. Dr A. Schleiss

N° 22	2005	INTERREG IIIB - Projet ALPRESERV. Conférence sur la problématique de la sédimentation dans les réservoirs - Gestion durable des sédiments dans les réservoirs alpins
N° 23	2005	Master of Advanced Studies (MAS) in hydraulic schemes Collection des articles des travaux de diplôme
N° 24	2006	S. Sayah Efficiency of brushwood fences in shore protection against wind-wave induced erosion
N° 25	2006	P. Manso The influence of pool geometry and induced flow patterns in rock scour by high-velocity plunging jets
N° 26	2006	M. Andaroodi Standardization of civil engineering works of small high-head hydropower plants and development of an optimization tool
N° 27	2006	Symposium érosion et protection des rives lacustres Bases de dimensionnement des mesures de protection des rives lacustres
N° 28	2007	A. Vela Giró Bank protection at the outer side of curved channels by an undulated concrete wall
N° 29	2007	F. Jordan Modèle de prévision et de gestion des crues - Optimisation des opérations des aménagements hydroélectriques à accumulation pour la réduction des débits de crue
N° 30	2007	P. Heller Méthodologie pour la conception et la gestion des aménagements hydrauliques à buts multiples
N° 31	2007	P. Heller Analyse qualitative des systèmes complexes à l'aide de la méthode de Gomez & Probst
N° 32	2007	J. García Hernández, F. Jordan, J. Dubois, J.-L. Boillat Routing System II - Modélisation d'écoulements dans des systèmes hydrauliques
N° 33	2007	Symposium - Flussbauliche Massnahmen im Dienste des Hochwasserschutzes, der Umwelt, Gesellschaft und Wirtschaft / Mesures d'aménagement des cours d'eau pour la protection contre les crues, l'environnement, la société et l'économie
N° 34	2007	B. Rosier Interaction of side weir overflow with bed-load transport and bed morphology in a channel

ISSN 1661-1179

Prof. Dr A. Schleiss
Laboratoire de constructions hydrauliques - LCH
EPFL, Bât. GC, Station 18, CH-1015 Lausanne
http://lchwww.epfl.ch
e-mail: secretariat.lch@epfl.ch